

**NUMERICAL AND EXPERIMENTAL FATIGUE
ANALYSIS OF SHORT GLASS FIBRE REINFORCED
POLYMERS**

YAHIR ABRAHAM LIZAMA CAMARA

A Thesis Presented for the Degree of

Doctor of Philosophy



The
University
Of
Sheffield.

Department of Mechanical Engineering
Faculty of engineering

The University of Sheffield, UK.

2020

ABSTRACT

This dissertation proposes a stress-based, multi-scale and multi-stage modelling approach, developed to predict the effect of the fibre orientation distribution on the fatigue life of an injection moulded short-glass fibre reinforced nylon 6,6 composite ($v_f=30\%$). The main objectives of this research were: to analyse the effect of the fibre orientation distribution in the material tensile and fatigue behaviour; to develop a stress-life (S-N), multi-stage computer-aided engineering (CAE), modelling methodology to produce sensible (± 3 std. dev.) fatigue life predictions; and to understand the damage mechanisms that incentivise crack initiation and propagation under constant amplitude cyclic loading. The novelty of the present work also included the full experimental validation at every step of the modelling phase to assess the accuracy of the numerical simulation and the effect of the propagation of these inaccuracies on the final fatigue life prediction.

The composite material presented highly anisotropic behaviour. This is a product of the variation of the fibre orientation through the thickness, produced during the injection moulding process. This non-homogenous fibre distribution showed a skin-shell-core microstructure.

Good agreement, qualitative and quantitative, was obtained between the finite element simulations and the experimental results in terms of: the fibre orientation tensor, full strain-fields and fatigue lives. However, a limitation of the stress-life based approach was revealed for fully reversed stress ratios, $R = \frac{\sigma_{min}}{\sigma_{max}} = -1$. Therefore, a new energy approach was investigated, allowing the introduction of a fatigue parameter derived from the analysis of the cyclic stabilised hysteresis loops, herein expressed in terms of Dissipated Energy vs Life curves. Initial results of this approach revealed a reduction in the spread of the fatigue data that was seen with the S-N method.

Finally, the analysis of specimens' fracture surfaces, via optical and scanning electron microscopy (SEM); together with high-speed camera images, digital image correlation results, and in conjunction with the stress and strain modelling results; suggested that the development of damage in the material follows a multi-crack nature, with initiation likely occurring below the surface, in locations where the maximum stress/energy is present. Additionally, evidence of several crack planes were observed, which implied the presence of multiple cracks developing and propagating at different points in the fatigue life of the specimens.

Numerical and Experimental Fatigue Analysis of Short Glass Fibre Reinforced Polymers

YAHIR ABRAHAM LIZAMA CAMARA

Reg. no. 150247953

A Thesis Presented for the Degree of

Doctor of Philosophy

Department of Mechanical Engineering

The University of Sheffield

2020

*This dissertation is dedicated to
my mother Martha and my father Pedro.*

Thank you!

ACKNOWLEDGEMENTS.

I personally would like to thank my research supervisor Dr. Christophe Pinna, for his continuous support, patience and guidance during the last four years.

I would also like to acknowledge the Mexican government, through CONACyT, and Jaguar Land Rover, in specific Dr. Zongjin Lu, Dr. Mark Blagdon and Robert Crow; for providing with financial and technical support for this project.

Finally, additional acknowledgements go to BASF for their material and technical support and, to Autodesk (Moldflow), HBM Prenscia (nCode) and e-Xtream (Digimat) for the support provided in the use of their software.

CONTENTS

1. INTRODUCTION	1
1.1 MOTIVATION	1
1.2 AIM AND KEY OBJECTIVES	3
1.2.1 <i>Key project objectives</i>	3
1.3 NOVELTY	4
1.4 OUTLINE OF WORK	4
2. LITERATURE REVIEW	5
2.1 APPLICATIONS OF SHORT FIBRE REINFORCED POLYMERS (SFRP's)	5
2.2 INTRODUCTION TO SFRP'S	6
2.2.1 <i>Reinforcement fibres and glass fibres</i>	6
2.2.1.1 Fibre length distribution and critical fibre length (l_c)	8
2.2.2 <i>Thermoset and thermoplastic matrices</i>	11
2.2.3 <i>Moulding techniques for thermoplastic SFRP's</i>	14
2.3 FIBRE ORIENTATION DISTRIBUTION, MEASUREMENT AND PREDICTION	17
2.3.1 <i>Fibre orientation distribution</i>	17
2.3.2 <i>Measurement of fibre orientation and orientation tensor</i>	19
2.3.3 <i>Prediction of fibre orientation</i>	23
2.4 MONOTONIC BEHAVIOUR OF SFRP'S	25
2.4.1 <i>Fibre length effect</i>	31
2.4.2 <i>Humidity, strain rate and temperature effects</i>	32
2.4.3 <i>Modelling monotonic behaviour of SFRP's</i>	35
2.4.3.1 Multi-scale modelling	37
2.5 FATIGUE BEHAVIOUR OF SFRP'S	40
2.5.1 <i>Summary of fatigue concepts and stress-life approach</i>	40
2.5.2 <i>Cyclic behaviour of short fibre reinforced polymers</i>	42
2.5.2.1 Effects of fibre orientation anisotropy	42
2.5.2.2 Fibre length effect	44
2.5.2.3 Cyclic response of SFRP's	47
2.5.3 <i>Modelling fatigue of SFRP's</i>	51
2.5.3.1 Stress-Life based methods	51
2.5.3.2 Energy-based methods	54
2.6 DAMAGE IN SFRP'S	59
2.6.1 <i>Stiffness degradation</i>	59
2.6.2 <i>Damage mechanisms</i>	60
2.6.3 <i>Damage mechanisms under fatigue loading</i>	62
2.7 DISCUSSION OF LITERATURE	68

3.	EXPERIMENTAL METHODOLOGY	70
3.1	INTRODUCTION	70
3.2	MATERIAL DESCRIPTION.....	70
3.2.1	<i>Material conditioning</i>	73
3.3	SPECIMENS GEOMETRIES.....	76
3.3.1	<i>Uniaxial specimens</i>	76
3.3.1.1	Specimen orientation	77
3.3.1.2	Machining.....	79
3.4	APPARATUS AND DATA ACQUISITION	80
3.4.1	<i>Uniaxial testing</i>	80
3.4.1.1	Alignment control	81
3.4.1.2	Analogue data acquisition	83
3.5	MONOTONIC TENSILE TESTING PROCEDURE.....	86
3.6	FATIGUE TESTING PROCEDURE.....	87
3.6.1	<i>Constant amplitude</i>	87
3.6.2	<i>Block loading</i>	89
3.7	MATERIAL ANALYSIS TECHNIQUES	91
3.7.1	<i>Digital Image Correlation (DIC)</i>	91
3.7.1.1	High speed DIC.....	92
3.7.1.2	DIC Resolution	93
3.7.2	<i>Optical microscopy</i>	93
3.7.3	<i>Scanning Electron Microscopy</i>	94
3.7.4	<i>Computed tomography</i>	95
3.8	CONCLUSION	97
4.	MODELLING METHODOLOGY	98
4.1	INTRODUCTION	98
4.2	INJECTION MOULDING PROCESS.....	98
4.3	MATERIAL MODELLING	101
4.3.1	<i>Mean field homogenization</i>	101
4.3.2	<i>Reverse engineering</i>	104
4.3.3	<i>Cyclic Stress-Strain behaviour</i>	106
4.4	STRESS ANALYSIS.....	107
4.4.1	<i>Structural model</i>	107
4.4.2	<i>Analysis setup</i>	109
4.4.2.1	Boundary conditions.....	109
4.4.2.2	Analysis type.....	109
4.4.2.3	Input of material properties	110
4.4.3	<i>Fibre orientation tensor mapping</i>	110
4.5	FATIGUE MODELLING.....	113

4.5.1	<i>Stress-Life (S-N) approach</i>	113
4.5.1.1	Introduction	113
4.5.1.2	Stress tensor results and stress combination method	115
4.5.1.3	Calibration of the model and fatigue calculations	115
4.5.2	<i>Mean stress correction</i>	119
4.5.3	<i>Energy-based approach</i>	121
4.6	CONCLUSION	123
5.	EXPERIMENTAL RESULTS	125
5.1	FIBRE ORIENTATION DISTRIBUTION	125
5.1.1	<i>Fibre distribution</i>	125
5.1.2	<i>Fibre orientation tensor</i>	129
5.2	MONOTONIC TESTING	130
5.2.1	<i>Stress-Strain behaviour</i>	130
5.2.1.1	Poisson's ratio	133
5.2.2	<i>Tension-Compression behaviour</i>	134
5.3	FATIGUE TESTING	135
5.3.1	<i>Constant amplitude</i>	135
5.3.1.1	Stiffness evolution	137
5.3.1.2	Temperature evolution	139
5.3.1.3	Hysteresis loops	142
5.3.1.4	Hysteresis area	145
5.3.1.5	Cyclic Stress-Strain behaviour	146
5.3.1.6	Stress-Life at 1Hz	147
5.3.2	<i>Block loading</i>	149
5.3.2.1	Block loading hysteresis loops	151
5.4	FULL-FIELD STRAIN MEASUREMENTS	153
5.4.1	<i>Tensile strain fields (DIC)</i>	153
5.4.2	<i>Fatigue strain fields (high speed DIC)</i>	161
5.5	MATERIAL DAMAGE AND FAILURE	166
5.5.1	<i>Optical inspection of failed specimens</i>	166
5.5.1.1	Uniaxial tensile specimens	166
5.5.1.2	Uniaxial fatigued specimens	167
5.5.2	<i>Surface quality, as-moulded and as-machined</i>	170
5.5.2.1	As-moulded surface	170
5.5.2.2	As-machined surface	171
5.5.3	<i>Tensile specimens, fracture surface</i>	174
5.5.3.1	Fracture surface of 0° reference specimens	174
5.5.3.2	Fracture surface of a 90° reference sample	176
5.5.4	<i>Fatigue specimens, fracture surface</i>	177
5.5.4.1	Fracture surface of 0° reference specimens	178

5.5.4.2	Fracture surface of a 90° reference sample.....	182
5.5.4.3	Fracture surface of a 45° reference sample.....	184
5.6	CONCLUSION	186
6.	MODELLING RESULTS	188
6.1	PREDICTED FIBRE ORIENTATION DISTRIBUTION	188
6.1.1	<i>Injection moulding simulation results</i>	<i>188</i>
6.1.1.1	Plate's through-thickness fibre orientation tensor	190
6.1.2	<i>Fibre orientation tensor after mapping onto structural mesh</i>	<i>192</i>
6.2	PREDICTED MATERIAL PROPERTIES	194
6.2.1	<i>Mean Field Homogenization and Reverse engineering results</i>	<i>194</i>
6.2.2	<i>Finite Element Stress-Strain curves</i>	<i>196</i>
6.3	FE STRESS AND STRAIN RESULTS	198
6.3.1	<i>Dog-bone specimens</i>	<i>198</i>
6.3.1.1	0° specimens.....	198
6.3.1.2	90° specimens.....	200
6.3.1.3	45° specimens.....	202
6.3.1.4	30° specimens.....	204
6.3.1.5	0° Edge specimens	206
6.3.1.6	90° Edge specimens	208
6.4	FATIGUE MODELLING RESULTS.....	210
6.4.1	<i>Stress-Life fatigue modelling.....</i>	<i>210</i>
6.4.1.1	Stress ratio R=0.0 results	210
6.4.1.2	Stress ratio R=-1.0 results	215
6.4.1.3	Mean stress correction	217
6.4.2	<i>Extension of the Energy-based approach.....</i>	<i>220</i>
6.4.2.1	Mean stress correction	222
6.5	CONCLUSION	224
7.	DISCUSSION.....	226
7.1	INTRODUCTION	226
7.2	FIBRE ORIENTATION DISTRIBUTION	226
7.3	MONOTONIC TENSILE MATERIAL BEHAVIOUR.....	230
7.3.1	<i>Predicted coupon tensile material response</i>	<i>232</i>
7.3.2	<i>Strain field distributions</i>	<i>233</i>
7.4	FATIGUE ANALYSIS	237
7.4.1	<i>Stress-Life approach.....</i>	<i>237</i>
7.4.2	<i>Energy based approach.....</i>	<i>239</i>
7.4.3	<i>Fatigue damage mechanisms</i>	<i>243</i>
8.	CONCLUSION	252

8.1 FUTURE WORK	253
APPENDIX.....	256
A APPENDIX CHAPTER 4.	256
<i>A.1 Example of material input card for stress analysis.....</i>	<i>256</i>
<i>A.2 Mapped orientation tensor global error.....</i>	<i>258</i>
B APPENDIX CHAPTER 5	261
<i>B.1 Hysteresis loops</i>	<i>261</i>
<i>B.2 Fatigue failed specimens</i>	<i>264</i>
REFERENCES	269

LIST OF FIGURES

Figure 1-1 Al vs PA66GF50 CO₂ footprint of a production car component. With the courtesy of Jaguar Land Rover..... 1

Figure 1-2 Automobile engine air intake manifold made of PA66 GF30 [7]..... 2

Figure 2-1 Examples of parts using short fibre reinforced composites [13] 5

Figure 2-2 Decrease in tensile strength for a carbon fibre with diameter [6]..... 6

Figure 2-3 Different forms of glass fibre: a) chopped strand, b) continuous yarn, c) roving, d) fabric [6]..... 8

Figure 2-4 Specimen types and fibre length distribution for glass fibre reinforced PA66 coupons [16]. SGF and LGF stand for, respective, short and long glass fibre..... 10

Figure 2-5 Schematic of a SFRP's fibre arrangement a) before, and b) after specimen failure. c) Frequency histogram of fibre length and critical length (l_c) [17]. 10

Figure 2-6 Fibre length variation of reinforced PA6 and calculated l_c [20]. 11

Figure 2-7 Effect of fibre length as reinforcement material. a) Longer and b) shorter fibres [22]. 11

Figure 2-8 Schematic representation of a) thermoplastic and b) thermoset polymer [13].....12

Figure 2-9 "Variation of tensile modulus with temperature for three different types of polymers: a) amorphous thermoplastic, b) semi-crystalline thermoplastic, and c) thermoset. d) Effects of loading rate and temperature on stress-strain behaviour of polymeric solids" [13].14

Figure 2-10 Extrusion and compression moulding process [6].....16

Figure 2-11 Schematic of injection moulding [28]17

Figure 2-12 Diagram of evolution of the fibre orientation during the injection moulding process [37].....18

Figure 2-13 a) Variation of fibre orientation distribution throughout the thickness of a SFRP injection moulded part, b) higher magnification in the centre [38].....19

Figure 2-14 Microstructure of PA66/GF30 observed by micro-CT [41].19

Figure 2-15 "Definition of orientation angles (ρ and γ) of a fibre" [32].20

Figure 2-16 Tracking of fibre centres (ellipses) during 5 frames to calculate the fibre orientation via confocal laser scanning microscopy. Straight lines represent a fitting between the centre coordinates through the frames [30]20

Figure 2-17 a) Identifying fibres in a 2D X-ray image and extracting the (L, Φ) values. b) Calculating the out-of-plate angle, θ , from the stage height, H , and the fibre projection, L [43].22

Figure 2-18 Fibre orientation tensor definition [45]23

Figure 2-19 Original formulation for the second order orientation tensor proposed by Advani and Tucker based on the Folgar-Tucker model [48].23

Figure 2-20 Comparison of fibre orientation data with 3D predictions. Folgar-Tucker (F-T) and RSC models are used. a_{11} and a_{22} are the orientation tensor components [50].24

Figure 2-21 Fibre orientation component in the flow direction (a_{11}) depicted at the cross section of a specimen (FEA prediction) [51].25

Figure 2-22 Influence of flow type and normalized part thickness on the predicted and measured fibre orientation (a_{11} as function of thickness at the centre position) [33]. Note: MF stands for Moldflow.25

Figure 2-23 Stress-Strain curves for unreinforced and reinforced SFRP samples at different orientations [52].27

Figure 2-24 Stress–Strain curves of SFRP specimens at different orientations [53].27

Figure 2-25 “Variations of average tensile properties with temperature and fibre orientation for duplicate tension tests of PBT and PA6 conducted at displacement rate of 1 mm/min for (a) tensile strength, (b)

elastic modulus, and (c) strain at tensile strength. d) Variations of fibre length and orientation on the test gage section surface of a PA6 sample machined in the mould flow direction" [20].28

Figure 2-26 "Stress-Strain curves showing the effect of thickness at displacement rate of 1mm/min at 23°C for PA6 in the: a) longitudinal (L) and, b) transverse (T) direction" [20].29

Figure 2-27 a)Stress-Strain curve showing the effect of mould flow direction and displacement rate PBT. b) Variation of strength with strain rate for PBT [54].....29

Figure 2-28 Comparison of strain field from DIC (left) and FEA (right). Showing range of largest principal strain [55].30

Figure 2-29 "Stress-strain curve and DIC images for a static tensile test" [56].30

Figure 2-30 Variation of the Stress-Strain response with fibre length for two sample types of reinforced PA66 (adapted from [16]).31

Figure 2-31 Typical stress-strain curves for short carbon fibre reinforced epoxy containing 1, 5 and 15 mm length fibres [57].32

Figure 2-32 Relation between fibre and tensile strength for a) carbon fibre –epoxy resin composite; and b) glass fibre-epoxy resin composite [58].32

Figure 2-33 "a) Influence of humidity content of a reinforced polyamide on mechanical behaviour (static tensile test) b) Humidity evolution for different reinforcing materials in water at 40°C" [59].....33

Figure 2-34 Nominal stress-strain curve for a) unreinforced and b) reinforced polyamide 6 (PA6GF30) at different strain rates. Dotted: sample transversally to injection flow direction. Solid: sample longitudinally [60].....34

Figure 2-35 Effect of temperature on tensile curves of a SFRP at different strain rates [61].....34

Figure 2-36 "a) Direction and location of specimens cut from injection moulded plates (arrows indicate the injection moulding direction and the dashed areas are the discarded materials. b)Tensile curves showing effect of anisotropy at different temperatures and displacements rates for polyamide-6" [20].....35

Figure 2-37 "Comparison of experimental elastic modulus values in the longitudinal, transverse and 45° directions at displacement rate of 1mm/min and predictions models for a) polybutylene terephthalate with 30wt% glass fibre (PBT) and b) polyamide-6 with 35wt% glass fibres and 10 wt% rubber (PA6)" [20]......36

Figure 2-38 a) Proposed empirical relationships for tensile strength and Young's modulus. b) Comparison of stress-strain curves of a PA6-SFRP

at different directions, at strain rate 0.05min^{-1} and at different temperatures [61]37

Figure 2-39 a) P is a material point or material element surrounded by a material neighbourhood, i.e., a macro-element. b) Possible microstructure of an RVE for the material neighbourhood of P [65]....38

Figure 2-40 Depiction of Mori-Tanaka technique [66].....39

Figure 2-41 "Calibration of linear elastic material model to tensile test expressed in true stress-strains. Dashed lines correspond to experimental data and solid lines represent the calibrated elastic material response of the SFRP" [71].....40

Figure 2-42 Stress contours showing the largest principal stress on a a) 0° specimen (parallel to the mould flow) and b) 90° specimen (transversal to the flow) [55]......40

Figure 2-43 Constant amplitude testing and definition of cyclic stress concepts [73].....41

Figure 2-44 Tensile-compression ($R=-1$) stress-life (SN) curves measured at 23°C and at 0° , 30° and 90° on PA66GF35 [3].43

Figure 2-45 Effect of the flow direction on the fatigue life of PBTGF30 at 23°C and under $R=-1$ [75].....43

Figure 2-46 Uniaxial fatigue curves at room temperature for PA66GF35 at a) $R=-1$ and b) $R=0$ for thickness= 3mm at different orientation angles ($\theta=0^\circ$, 30° and 90°) [76].44

Figure 2-47 Stress-Life curves at 110°C for three sample orientations (0°,45° and 90°) and at R=0.1 and R=-1 [77].	44
Figure 2-48 Peak stress-fatigue life data for composites with 1, 5 and 15 mm length fibres [57].	46
Figure 2-49 a) Variation with fibre length of the cycles to failure vs normalised stress. b) Cycles to failure vs fibre aspect ratio for an applied stress of 60, 70, 80 and 90% UTS [78].	46
Figure 2-50 Variation of the surface temperature of polypropylene for: unreinforced neat resin (UPP), reinforced with long fibres (LFPP) and reinforced with short fibres (SFPP) [79].	47
Figure 2-51 "Calculated and experimental ratcheting strain values over stress cycles for short fibre GFRP with $V_f=40\%$ at a) 45+/-35MPa and b) 45+/-15MPa" [81].	48
Figure 2-52 "Evolution of mechanical response during fatigue life (expressed in percentage of lifetime) of PA66GF35 under stress-controlled sinusoidal loading. a)Stress-strain response during fatigue testing. b) Residual strain" [82].	48
Figure 2-53 a) Stress-strain curves for a loading step. b) hysteresis area evolution [83].	49
Figure 2-54 Midlife stress-displacement loops for dried (solid curve) and wet (dashed curve) samples of PA6-SFRP at the same stress amplitude for R=0.1 in: a) longitudinal and b) transverse directions. c) S-N curves	

at ambient temperature showing the effect of water absorption in both longitudinal and transverse direction [84].....50

Figure 2-55 Graphs from a-i present the effect of humidity and fibre orientation on the cyclic mechanical properties. Graphs j-l are the hysteresis area evolution, the slope and the mean strain through the life of the specimens at 10Hz [86].....51

Figure 2-56 Fatigue data fitted by using Tsai-Hill failure surface (grid surface) for 23°C, at a)R=0, b)R=-1 for PA66GF35 specimens [76].53

Figure 2-57 "Fatigue strength data as function of specimen angle and Tsai-Hill criterion for PBT at 23°C for a) R=-1 and b)R=0.1 conditions" [91].53

Figure 2-58 a) Correlation of the high cycle fatigue behaviour (model prediction vs experimental data) on PA66GF35 at uniaxial R=-1. b) Prediction at critical locations (right) compared to measurements (left) [3].....54

Figure 2-59 a) Fatigue results using the strain energy (W_{mean}) approach. b) Fatigue results of engine mount parts using the " W_{mean} " approach [2].....55

Figure 2-60 Uniaxial fatigue data at ambient temperature in terms of averaged strain energy density range over a control volume [92].....56

Figure 2-61 "Comparison between experimental a) and FE simulated b) distribution of strain fields obtained at 5000 cycles of the Meuwissen

specimen configuration fatigue test. c) Comparisons between experimental and simulated longitudinal damage (d_{LL}) evolutions versus number of cycles (N) for PA6-GF30. Displacement controlled fatigue tests" [93].....57

Figure 2-62 Surface strain on a) pressure vessel gated from top without weldline, b) gated from side with weldline, c) closer view of the strain contour on the weldline. d) Pressure vessels SSED results for different temperatures, R ratio, pressure levels for non-well-lined samples [94].58

Figure 2-63 Illustration of the typical stiffness degradation curve for composite materials [14].....59

Figure 2-64 Stiffness evolution at $T=23^{\circ}\text{C}$, $R=0$, thickness= 3mm specimens with fibre orientation specimens cut at 0° [76].....60

Figure 2-65 Axial stiffness VS Relative number of cycles, for two specimens with different notch tip radius [95].60

Figure 2-66 Location of failure on samples tested at a) $R=0.1$ and $R=-1$ [77].....61

Figure 2-67 a) Damage initiation at fibre end and interface decohesion at the location where the fibres are close one another for a load of $P=56\%$ of σ_{UTS} . b) Crack propagation in the form of interface debonding and transverse crack for a load $P=81\%$ of σ_{UTS} [98]62

Figure 2-68 "Surface A; fragile behaviour at magnification of a) x200 and b) x3000. Surface B; ductile behaviour at a magnification of c) x200 and b) x3000" [99].63

Figure 2-69 0° specimen $N_R=2,468$ cycles. a) Damage at fibre ends. b) Fibre failure. c) and d) Debonding [100].64

Figure 2-70 PA66GF35 specimen at $R=0$. a) Localisation of temperature at the stress concentrator (shoulder tip). b) Specimen failure after 1 second from temperature localisation. c) Crack path after specimen failure [101].64

Figure 2-71 "Fiber distribution at crack initiation for a notched specimen, interrupted fatigue test; (b), (c), (d) are magnified views of the crack" [101].65

Figure 2-72 Model for the crack plane deviation in chopped glass fibre reinforced polypropylene at low fibre loading [102].65

Figure 2-73 a) Fibre failures, b) Debonding and c) Micro-cavitation (95% of specimen life) [96].66

Figure 2-74 Rendered μ CT image of fatigue loaded specimen which shows damage in the form of fibre/matrix interfacial debonding [103].67

Figure 2-75 "Analysis of the fibre orientation distribution and fibre content; 8 x 8 x 8 discretization for six different sections along the

thickness. In the X-ray CT micrographs (first column from the left side) the crack path is indicated in red" [104].....67

Figure 3-1 Measurements of a) fibre diameter and b) fibre length. c) Histogram of fibre diameter and d) fibre length showing critical length (l_c).....71

Figure 3-2 Histogram of average specimen thickness.....73

Figure 3-3 Followed conditioning process.74

Figure 3-4 Specimens in a warm water bath for conditioning.....74

Figure 3-5 Measured temperature of the warm water bath.75

Figure 3-6 Specimen weight a) before condition (Dry), and b) after conditioning (Wet). c) Final percentage of humidity content (Condition).
.....76

Figure 3-7 Dog-bone specimen geometry. Nominal dimensions shown in millimetres.....77

Figure 3-8 Project's specimens orientations (θ) and locations on the injection moulded plate.78

Figure 3-9 Locations for "Edge" specimens. Dimensions in millimetres.
.....78

Figure 3-10 Specimen manufacturing workflow procedure.....79

Figure 3-11 After-milling histograms for a) specimen's gauge length width (in millimetres), and b) calculated gauge length cross-sectional area (in mm²).....80

Figure 3-12 Hydraulic testing machine setup.....81

Figure 3-13 a) Schematic of alignment specimen. b) Gripped specimen during calibration. d) LabVIEW code used for calibration.82

Figure 3-14 Strain gauges readings without and with the alignment system.82

Figure 3-15 Position of grips before and after calibration.83

Figure 3-16 LabVIEW program used for measurement of the Force, Displacements, Strain and Temperatures.....84

Figure 3-17 Data acquisition sampling rate error.....84

Figure 3-18 Measured machine's displacement and forced feedback.84

Figure 3-19 a) External LVDT used for displacement measurements. b) Comparison of raw data (Volts) between Machine's LVDT and external LVDT.85

Figure 3-20 Extensometer used to measure the material's strain.....86

Figure 3-21 Thermocouple locations to measure a) specimen's surface temperature, b) grips temperature and c) reference temperature.86

Figure 3-22 Schematic of wave forms for each R ratio.89

Figure 3-23 Example of BL test at R=-1 for a 0° specimen tested at High-to-Low sequence. Only first two blocks are shown.....90

Figure 3-24 a) Depiction of a subset before deformation and after deformation. b) Example of specimens speckled for DIC.91

Figure 3-25 3D DIC hardware configuration.....92

Figure 3-26 Typical configuration for High Speed DIC testing.....92

Figure 3-27 DIC technique showing a) minimum subset size and b) achieved minimum resolution.....93

Figure 3-28 a) Specimens mounted on epoxy resin. b) Optical microscope used for observations.94

Figure 3-29 a) Example of SEM-ready specimens showing the aluminium stubs, the gold coating and the silver DAG compound. b) Sputtering machine used for gold coating. c) Hitachi microscope.95

Figure 3-30 Bruker Skyscan 1172 microCT scanner.96

Figure 3-31 a) X-ray preview of specimen before analysis. b) Specimen mounted ready for scanning. c) Specimen inside CT chamber.....96

Figure 4-1 Computer aided engineering (CAE) workflow map.....98

Figure 4-2 Optimised injection moulded plate's finite element mesh. 100

Figure 4-3 Comparison in the through-thickness orientation tensor result at the specimen's gauge length's centre location for three difference mesh densities. 100

Figure 4-4 Schematic of material model workflow..... 101

Figure 4-5 General Stress-Strain curves for GF and PA66 used for the MFH technique. 102

Figure 4-6 Digimat procedure for the 2-step MFH in a composite with misaligned inclusions [66]. 104

Figure 4-7 Comparison of the macro behaviour between material experimental data, and the before and after RE MFH material model for a 0° reference specimen of PA66GF50 (thickness=4mm and $V_f=30\%$).
..... 105

Figure 4-8 a) Definition of terms for the cyclic Stress-Strain curves. b) True stress amplitude vs True plastic strain amplitude log-log plot.. 107

Figure 4-9 Uniaxial specimen's structural mesh, showing element's nodes (N1-N8) and integration point (I1) location..... 108

Figure 4-10 Mesh independence analysis conducted over the gauge length. Stress results from a unitary load case in tension..... 109

Figure 4-11 Uniaxial specimen boundary conditions. 110

Figure 4-12 Example of fibre orientation distribution along the flow direction. Superposition of Donor (plate) and Receivers (uniaxial specimens) meshes. 111

Figure 4-13 Visualization of the mapping of fibre orientation tensor results from the injection moulded plate (Donor) to the specimens structural mesh (Receiver). 112

Figure 4-14 Specimen's mapped fibre orientation data..... 112

Figure 4-15 Error analysis in terms of transferred of orientation tensor data between the composite Plate and the 0° Specimen. 113

Figure 4-16 High level schematic of algorithm for S-N approach..... 114

Figure 4-17 a) Schematic representation of the calibration of fully fibre-oriented Stress-Life material curves. b) Interpolation of S-N parameters 118

Figure 4-18 a) Simplified schematic description of the limitations of the S-N approach and, b) the advantages of using an Energy formulation. 121

Figure 4-19 High level schematic of algorithm for a W-N approach for SFRP's..... 123

Figure 5-1 CT 2D slices at the centre of the gauge length of specimen showing the qualitative distribution of fibres through the thickness. Flow in the out- of-plane direction with respect to *Cross-section* view. 126

Figure 5-2 Optical microscopy picture of fibre distribution at the core layer of a 0° specimen with nominal thickness of 4mm. Flow in the out of plane direction..... 127

Figure 5-3 Optical microscopy picture of fibre distribution at the shell layer of a 0° specimen with nominal thickness of 4mm. Flow in the out of plane direction..... 127

Figure 5-4 Optical microscopy picture of fibre distribution at the skin layer of a 0° specimen with nominal thickness of 4mm. Flow in the out of plane direction..... 128

Figure 5-5 Interval plot (95%CI) of the percentage that the Skin, Shell and Core layers represent from the total material thickness. Created with information documented in [29], [33], [50]. 128

Figure 5-6 Orientation tensor components (a_{11} , a_{22} and a_{33}) measurements using two different CT scanners in a 4mm thick plate. 130

Figure 5-7 Stress-Strain curves for conditioned PA66GF50 at room temperature..... 132

Figure 5-8 Interval plots for PA66GF50 specimens. a) Strain at break, b) Strength, c) Chord (Young's) modulus, and d) 0.2%Yield strength... 132

Figure 5-9 Interval plots for Poisson's ratio of PA66GF50 specimens. 134

Figure 5-10 Quasi-static (2mm/min) tension-compression (R=-1) test for a) 0° and b) 90° reference specimens.....	135
Figure 5-11 Constant Amplitude, coupon based S-N curves for conditioned PA66GF50 at ambient temperature and at different R ratios.	136
Figure 5-12 Stiffness evolution for PA66GF50 specimens at R=-1. Total life (Nf) is given in Cycles. Initial stiffness (K ₀) is given in kN/mm.	138
Figure 5-13 Stiffness evolution for PA66GF50 specimens at R=0. Total life (Nf) is given in Cycles. Initial stiffness (K ₀) is given in kN/mm.	139
Figure 5-14 Stiffness evolution for PA66GF50 specimens at R=0.3. Total life (Nf) is given in Cycles. Initial stiffness (K ₀) is given in kN/mm.	139
Figure 5-15 Histogram of ambient temperature.....	140
Figure 5-16 Temperature evolution for PA66GF50 specimens at R=-1. Total life (Nf) is given in Cycles.....	141
Figure 5-17 Temperature evolution for PA66GF50 specimens at R=0. Total life (Nf) is given in Cycles.....	141
Figure 5-18 Temperature evolution for PA66GF50 specimens at R=0.3. Total life (Nf) is given in Cycles.....	141
Figure 5-19 Hysteresis loops (Stress vs Strain), and evolution of strain (Strain vs Cycle) curves for 0°, R=-1 at a) $\sigma_a=50\text{MPa}$, b) $\sigma_a=40\text{MPa}$ and R=0 c) $\sigma_a=41\text{MPa}$, d) c) $\sigma_a=33\text{MPa}$	143

Figure 5-20 Hysteresis loops (Stress vs Strain), and evolution of strain (Strain vs Cycle) curves for 30°, R=-1 at a) $\sigma_a=46\text{MPa}$, b) $\sigma_a=36\text{MPa}$ and R=0 c) $\sigma_a=33\text{MPa}$, d) c) $\sigma_a=25\text{MPa}$ 144

Figure 5-21 Evolution of the hysteresis area at R=-1 for a) 0°, b)90°, c)45° and d) 30° specimens. 145

Figure 5-22 Cyclic Stress-Strain curves for PA66GF50 at different orientations, overlapping the stabilised hysteresis curves at different stress amplitudes. 147

Figure 5-23 Effect of the frequency on the fatigue life of PA66GF50. 148

Figure 5-24 Evolution of a) Stiffness and b) Temperature with frequency. 148

Figure 5-25 Average number of BL blocks to failure for each specimen orientation and load sequence. 151

Figure 5-26 Estimated number of blocks to failure (D=1) VS Experimental number of blocks to failure for different specimens orientations and load sequences. 151

Figure 5-27 Stabilised hysteresis loops (Stress vs Strain), and evolution of strain (Strain vs Cycle) curves for a) 0°, b)90° and c)45° specimens under Block loading High-Low sequence. 152

Figure 5-28 Stabilised hysteresis loops (Stress vs Strain), and evolution of strain (Strain vs Cycle) curves for a) 0°, b)90° and c)45° specimens under Block loading Low-High sequence.....	153
Figure 5-29 Definition of the specimen's surfaces.	154
Figure 5-30 Strain distribution on the main surface for a 0° specimen loaded in tension at a) 55MPa, and b) 100MPa with $V_f=30\%$	155
Figure 5-31 Strain distribution on the main surface for a 90° specimen loaded in tension at a) 40MPa, and b) 75MPa with $V_f=30\%$	156
Figure 5-32 Strain distribution on the thickness surface for a a) 0°, b) 90° and c)45° specimen loaded in tension at 40MPa.....	156
Figure 5-33 Main surface for 0° specimen tested in tension showing the strain distribution and a macro crack of 4.18mm in the centre prior to failure , and the failure plane.....	158
Figure 5-34 Main surface for 0° specimen tested in tension showing the strain localization, and the exponential evolution of a macro crack from onset to failure.....	159
Figure 5-35 Main surface for 90° specimens tested in tension showing the strain distribution prior to failure. Specimen B showing a 2.82mm macro crack close to the edge.....	159
Figure 5-36 Main surface for 45° specimens tested in tension showing the strain distribution prior to failure.....	160

Figure 5-37 Main surface for 30° specimens tested in tension showing the strain distribution and macro cracks prior to failure..... 160

Figure 5-38 Main surface for 0° Edge specimen tested in tension showing the strain distribution and macro crack growth evolution.. 161

Figure 5-39 Main surface for 90° Edge specimen tested in tension showing the strain distribution prior to failure..... 161

Figure 5-40 Main surface of 0° specimen tested at R=-1 and $\sigma_a=33\text{MPa}$.
..... 163

Figure 5-41 *Thickness surface* strain evolution at the beginning of a fatigue test for a 0° specimen at R=0 and $\sigma_a=35\text{MPa}$. Showing the gauge length area only..... 163

Figure 5-42 *Thickness surface tensile e_{yy}* strain evolution throughout the life of a 0° specimen at R=0 and $\sigma_a=35\text{MPa}$. a) Specimen failure. b) DIC Strain fields at different number of cycles. c) Evolution of the localised tensile strain. d) Eng. Stress vs Eng. Strain (virtual extensometer) curves at different number of cycles. 164

Figure 5-43 Evolution of fatigue crack through the thickness. a) to f) show a sequential time lapse capture via High speed cameras..... 165

Figure 5-44 Optical view of the fracture surface for tensile tested specimens at a) 0°, b) 90° and c) 45° orientations..... 166

Figure 5-45 Visual inspection of failure plane for tensile specimens. 167

Figure 5-46 Failure plane of fatigued specimens at $R=-1$ 168

Figure 5-47 Failure plane of fatigued specimens at $R=0$ 169

Figure 5-48 Failure plane of fatigued specimens at $R=0.3$ 169

Figure 5-49 As-moulded surface, full specimen' width (10mm).
Specimen not tested. $V_f=30\%$ 170

Figure 5-50 Close-up of the as-moulded, near the edge. $V_f=30\%$ 171

Figure 5-51 Close-up of the as-moulded, near the middle. $V_f=30\%$. 171

Figure 5-52 As-machined surface showing the different fibre orientation
layers through the thickness. Specimen not tested. $V_f=30\%$ 172

Figure 5-53 Close-up of the as-moulded, near the edge. $V_f=30\%$ 173

Figure 5-54 Close-up of the as-moulded, near the middle. $V_f=30\%$. 173

Figure 5-55 Fracture surface of 0° reference specimen 1 tested in
tension and close-up images. $V_f=30\%$ 175

Figure 5-56 Fracture surface of 0° reference specimen 2 tested in
tension and close-up images. $V_f=30\%$ 176

Figure 5-57 Fracture surface of 90° reference specimen tested in tension
and close-up images. $V_f=30\%$ 177

Figure 5-58 Fracture surface of 0° reference specimen 1 tested in fatigue
 $R=-1$ and close-up images. $V_f=30\%$ 179

Figure 5-59 Fracture surface of 0° reference specimen 2 tested in fatigue
 $R=-1$ and close-up images. $V_f=30\%$ 180

Figure 5-60 View of the main surface of a failed 0° specimen at R=-1. V _f =30%.	181
Figure 5-61 Close up near the fracture surface showing a macro crack. V _f =30%.	181
Figure 5-62 Close up near the fracture surface showing a macro crack between fibres. V _f =30%.....	182
Figure 5-63 Fracture surface of 90° reference specimen tested in fatigue R=-1 and close-up images. V _f =30%.	183
Figure 5-64 Close-up of the fracture surface of a 90° reference specimen tested in fatigue at R=-1 with V _f =30%; showing holes in the matrix due to possible fibre pull-out.	184
Figure 5-65 Fracture surface of 45° reference specimen tested in fatigue R=-1 and close-up images. V _f =30%.	185
Figure 6-1 Cavity filling.....	189
Figure 6-2 Moldflow a ₁₁ component results. Surface and thickness view for reference location.	189
Figure 6-3 Fibre orientation distribution across the surface and through the thickness of the plate showing the location of the centres of the different specimens.....	190
Figure 6-4 Through-thickness orientation tensor components at different points in the plate. Moldflow results only.....	191

Figure 6-5 Through-thickness orientation tensor between Moldflow (before mapping) and Abaqus (after mapping) at different locations. 193

Figure 6-6 a_{11} orientation tensor distribution for a) reference, b) 0° Edge and c) 90° Edge specimens. 193

Figure 6-7 Assumed fibre distribution for the MFH model. 196

Figure 6-8 Comparison between MFH using standard values and further calibration via Reverse Engineering. 196

Figure 6-9 Predicted coupon Stress-Strain data. 197

Figure 6-10 Evolution of the FE stress/strain distribution for a 0° reference specimen with $V_f=30\%$. Braces denote the approximate division between the shell and core layers in the structural model... 199

Figure 6-11 Cross sections of a 0° coupon under a 4kN tensile load showing the stress (a, b) and strain (c, d) distributions through the specimen's shoulder and middle section. 200

Figure 6-12 Evolution of the FE stress/strain distribution for a 90° reference specimen with $V_f=30\%$. Braces denote the approximate division between the shell and core layers in the structural model... 201

Figure 6-13 Cross sections of a 90° coupon under a 3kN tensile load showing the stress (a, b) and strain (c, d) distributions through the specimen's shoulder and middle section. 202

Figure 6-14 Evolution of the FE stress/strain distribution for a 45° reference specimen with $V_f=30\%$. Braces denote the approximate division between the shell and core layers in the structural model...203

Figure 6-15 Cross sections of a 45° coupon under a 3.3kN tensile load showing the stress (a, b) and strain (c, d) distributions through the specimen's shoulder and middle section.....204

Figure 6-16 Evolution of the FE stress/strain distribution for a 30° reference specimen with $V_f=30\%$. Braces denote the approximate division between the shell and core layers in the structural model...205

Figure 6-17 Cross sections of a 30° coupon under a 3.9kN tensile load showing the stress (a, b) and strain (c, d) distributions through the specimen's shoulder and middle section.....206

Figure 6-18 Evolution of the FE stress/strain distribution for a 0° Edge specimen with $V_f=30\%$. Braces denote the approximate division between the shell and core layers in the structural model.....207

Figure 6-19 Cross sections of a 0° edge coupon under a 4.2kN tensile load showing the stress (a, b) and strain (c, d) distributions through the specimen's shoulder and middle section.....208

Figure 6-20 Evolution of the FE stress/strain distribution for a 90° Edge specimen with $V_f=30\%$. Braces denote the approximate division between the shell and core layers in the structural model.....209

Figure 6-21 Cross sections of a 90° edge coupon under a 3kN tensile load showing the stress (a, b) and strain (c, d) distributions through the specimen's shoulder and middle section..... 210

Figure 6-22 Result of the S-N fatigue modelling for R=0.0. Model uses 0°, 45° and 90° reference specimens for calibration..... 212

Figure 6-23 FEA-Life distribution for 0°, 45° and 90° reference specimens under R=0 and $\sigma_a=30$ MPa (Cut-off at 1×10^7 cycles). 212

Figure 6-24 FEA-Life distribution for 30° reference, 0°Edge and 90°Edge Specimens under R=0 and $\sigma_a=30$ MPa (Cut-off at 1×10^7 cycles)..... 213

Figure 6-25 Result of the S-N fatigue modelling for R=0.0. Model uses only 0° and 90° reference specimens for calibration..... 214

Figure 6-26 Result of the S-N fatigue modelling at the reference location for R=-1.0. Model uses 0°, 45° and 90° reference specimens for calibration..... 216

Figure 6-27 Result of the S-N fatigue modelling at the reference location for R=-1.0. Model uses only 0° and 90° reference specimens for calibration..... 217

Figure 6-28 Mean stress correction for 0° reference specimens at R=0 and 0.3..... 219

Figure 6-29 Mean stress correction for 90° reference specimens at R=0 and 0.3..... 219

Figure 6-30 Mean stress correction for 45° reference specimens at R=0 and 0.3.....220

Figure 6-31 Experimental Dissipated Energy vs Life data for specimens at different orientations.....222

Figure 6-32 Experimental Dissipated Energy vs Life curves for specimens at different orientations at R=-1 and R=0.....222

Figure 6-33 Mean stress correction. Corrected dissipated energy vs Life curve.....224

Figure 7-1 a) Variation of the predicted a_{11} orientation tensor component at reference location with the interaction coefficient (C_i). b) Location of measurement.....229

Figure 7-2 FE vs CT comparison of the orientation tensor information.229

Figure 7-3 Boxplot of the variation of the predicted a_{11} orientation tensor component in a 12 x 12 mm² area around the reference location.230

Figure 7-4 FE vs Experimental Stress-Strain curves for specimens at different orientations for PA66GF50 and $V_f=30\%$233

Figure 7-5 Thickness surface comparison between FEA and DIC for a) 0°, b)90°, and c) 45° reference specimens at 1.5kN tensile load.....235

Figure 7-6 Comparison between FEA and DIC for calibration a) 0° and b) 90° reference location specimens loaded in tension ($V_f=30\%$). 236

Figure 7-7 Comparison between FEA and DIC for validation a) 0° Edge and b) 90° Edge locations specimens loaded in tension ($V_f=30\%$). ... 236

Figure 7-8 Boxplot of DIC vs FEA comparison for a) 0° reference, b) 90° reference, c) 0° Edge and d) 90° Edge specimens..... 237

Figure 7-9 Model validation for $R=0$ a) using 30° reference specimens (calibrated with 0°, 45° and 90° reference); b) using 30° and 45° reference specimens (calibrated with 0° and 90° reference)..... 239

Figure 7-10 Dissipated energy vs Stress amplitude. 241

Figure 7-11 FE Elemental Stress-Strain curves of a 0° reference specimen. Location of inspection corresponded to the most common fracture plane for the specimen at that particular load level..... 242

Figure 7-12 FE Elemental Stress-Strain curves at 1.6kN for a a) 90° reference specimen and b) 45° reference specimen. Location of inspection corresponded to the most common fracture plane for the specimen at that particular load level. 242

Figure 7-13 FE elemental localised energy on difference specimens seen through the thickness on the most common fracture plane. a) 0° reference, b) 90° reference and c) 45° reference..... 243

Figure 7-14 a) Comparison of stiffness evolution for different reference specimens at $R=-1$ and applied force amplitude of 1.6KN. b) Depiction of possible cracks lengths due to fibre orientation.....247

Figure 7-15 Optical analysis of specimens' fracture location.247

Figure 7-16 Comparison of locations of a) FEA Maximum Principal Stress and b) first crack appearance and c)second crack appearance on the thickness for a 0° reference fatigue specimen..... 248

Figure 7-17 Comparison of 0° reference specimen's fracture surface with $V_f=30\%$. Tensile vs Fatigue ($N=235,800$ cycles, $R=-1$, $\sigma_a=40\text{MPa}$) samples.....249

Figure 7-18 Comparison of 90° reference specimen's fracture surface with $V_f=30\%$. Tensile vs Fatigue ($N=30,260$ cycles, $R=-1$, $\sigma_a=40\text{MPa}$) samples.....249

Figure 7-19 Stress and strain distributions and fracture surface of a fatigue 0° reference specimen with $V_f=30\%$ at $R=-1$ and $\sigma_a=40\text{MPa}$ ($N=235,800$ cycles). Arrows denote example of packets seen on the fracture surface.....250

Figure 7-20 Stress and strain distributions and fracture surface of a fatigue 90° reference specimen with $V_f=30\%$ at $R=-1$ and $\sigma_a=40\text{MPa}$ ($N=30,260$ cycles). Arrows denote example of packets seen on the fracture surface..... 250

Figure 7-21 Stress and strain distributions and fracture surface of a fatigue 45° reference specimen with $V_f=30\%$ at $R=-1$ and $\sigma_a=40\text{MPa}$ ($N=66,646$ cycles). Arrows denote example of packets seen on the fracture surface..... 251

Figure A-0-1 Mapping global error for 0° Edge uniaxial specimens.. 258

Figure A-0-2 Mapping global error for 30° uniaxial specimens 258

Figure A-0-3 Mapping global error for 45° uniaxial specimens 259

Figure A-0-4 Mapping global error for 90° uniaxial specimens 259

Figure A-0-5 Mapping global error for 90° Edge uniaxial specimens 260

Figure A-0-6 Hysteresis loops (Stress vs Strain), and evolution of strain (Strain vs Cycle) for 0°, $R=-1$ samples at a) $\sigma_a=50\text{MPa}$, b) $\sigma_a=40\text{MPa}$ and c) $\sigma_a=38\text{MPa}$ 261

Figure A-0-7 Hysteresis loops (Stress vs Strain), and evolution of strain (Strain vs Cycle) for 0°, $R=0$ samples at a) $\sigma_a=41\text{MPa}$, b) $\sigma_a=33\text{MPa}$.
..... 262

Figure A-0-8 Hysteresis loops (Stress vs Strain), and evolution of strain (Strain vs Cycle) for 90°, $R=-1$ samples at a) $\sigma_a=31\text{MPa}$, b) $\sigma_a=41\text{MPa}$.
..... 262

Figure A-0-9 Hysteresis loops (Stress vs Strain), and evolution of strain (Strain vs Cycle) for 45°, $R=-1$ samples at a) $\sigma_a=31\text{MPa}$, b) $\sigma_a=46\text{MPa}$
..... 263

Figure A-0-10 Hysteresis loops (Stress vs Strain), and evolution of strain (Strain vs Cycle) for 30°, R=-1 samples at a) $\sigma_a=36\text{MPa}$, b) $\sigma_a=46\text{MPa}$ 263

Figure A-0-11 Hysteresis loops (Stress vs Strain), and evolution of strain (Strain vs Cycle) for 30°, R=0 samples at a) $\sigma_a=25\text{MPa}$, b) $\sigma_a=33\text{MPa}$ 264

Figure A-0-12 Fracture specimens for 0° coupons at R=-1 264

Figure A-0-13 Fracture specimens for 90° coupons at R=-1 265

Figure A-0-14 Fracture specimens for 45° coupons at R=-1 265

Figure A-0-15 Fracture specimens for 30° coupons at R=-1 266

Figure A-0-16 Fracture specimens for 0° coupons at R=0. 266

Figure A-0-17 Fracture specimens for 90° coupons at R=0. 266

Figure A-0-18 Fracture specimens for 45° coupons at R=0. 267

Figure A-0-19 Fracture specimens for 30° coupons at R=0. 267

Figure A-0-20 Fracture specimens for 0° coupons at R=0.3. 267

Figure A-0-21 Fracture specimens for 90° coupons at R=0.3. 268

Figure A-0-22 Fracture specimens for 45° coupons at R=0.3. 268

LIST OF TABLES

Table 2-1 Typical values for commonly used long fibre reinforcements [13].	7
Table 2-2 Typical matrix properties [5].	13
Table 2-3 Comparison of fibre reinforced polymer composite manufacturing processes [5].	15
Table 3-1 Material properties for PA66GF50 conditioned at 23°C/50%R.H. [111].	72
Table 3-2 Stress levels used for uniaxial fatigue testing.	88
Table 3-3 Block loading stress levels and sequence definition.	90
Table 4-1 Optimisable parameters during RE.	105
Table 5-1 Basquin's equation parameters in terms of Stress amplitude (σ_a), and life cycles (N).	137
Table 5-2 Calculated Ramberg-Osgood's cyclic strength coefficient (K') and cyclic strain hardening exponent (n') values for the different specimens orientations.	147
Table 5-3 Block loading testing results.	150
Table 6-1 Composite phases' material parameters.	196
Table 6-2 Experimental and modelling Basquin's equations for R=0. Model uses 0°, 45° and 90° reference specimens for calibration.	213

Table 6-3 Experimental and modelling Basquin's equations for R=0.
Model uses only 0° and 90° reference specimens for calibration.....215

Table 6-4 Experimental and modelling Basquin's equations for R=1.
Model uses 0°, 45° and 90° specimens for calibration.....216

Table 6-5 Experimental and modelling Basquin's equations for R=1.
Model uses only 0° and 90° reference specimens for calibration.....217

Table 6-6 Walker coefficient (γ) for different orientation and stress ratios.....220

NOMENCLATURE

Symbol	Unit	Description
σ_a	MPa	Stress amplitude
$\%W_{cond}$	%	Percentage of Weight increase
$\Delta\sigma$	MPa	Stress range
a	-	Orientation tensor component
C0	-	Uniform stiffness
Ci	-	Interaction coefficient
D	-	Miner's rule damage
δ	mm	Displacement
E_c	MPa	Compressive Young's modulus
E_t	MPa	Tensile Young's modulus
F	kN	Force
I	-	Shape and the orientation of the ellipsoidal volume
l_c	μm	Critical fibre length
k	-	Fitting parameters
k	kN/mm	Stiffness
m	-	Strain rate strengthening coefficient
N	cycles	Fatigue life
n_i	Cycles	Accumulated cycles
R	-	Stress ratio
R(p)	MPa	Hardening stress
T	$^{\circ}\text{C}$	Temperature
T0	$^{\circ}\text{C}$	Reference temperature
$T_{ambient}$	$^{\circ}\text{C}$	Ambient temperature
T_{coupon}	$^{\circ}\text{C}$	Temperature of coupon
T_g	$^{\circ}\text{C}$	Glass transition temperature
U	-	Translations
ν	-	Poisson's ratio
W	MJ/m ³	Energy
$W_{corrected}$	MJ/m ³	Corrected dissipated energy.
W_{dry}	gr	Dry Weight
W_{wet}	gr	Wet Weight
ϵ^*	-	Reference strain rate
θ	$^{\circ}$	Angles
λ	-	Fibre share
ρ, γ	$^{\circ}$	Angles
σ_{b0}	MPa	Reference tensile strength
σ_{eq}	MPa	Equivalent stress
σ_{ij}	MPa	Direction stress

σ_L	MPa	Longitudinal stress
σ_m	MPa	Mean stress
σ_{max}	MPa	Maximum stress
σ_{min}	MPa	Minimum stress
σ_t	MPa	Ultimate tensile strength
σ_T	MPa	Transversal stress
σ_y	MPa	Yield stress

ACRONYMS

Al	aluminium
BL	Block loading
CAE	Computer-aided engineering
CLSM	Confocal laser scanning microscopy
CMR	Contact micro-radiography
CNC	Computer numerical controlled machining
CT	Computed tomography
DIC	Digital image correlation
FEA	Finite element analysis
FOD	Fibre orientation distribution
HCF	High cycle fatigue
H-L	High to Low
HS	High speed
I	interpolating factor
LAA	laminar analogy approach
L-H	Low to High
LVDT	Linear Variable Differential Transformer
MFH	Mean field homogenization
MIL	Mean Intercept Length
NI	National instruments
OT	Orientation tensor
PA	Nylon
PBT	polybutylene terephthalate
PET	Polyethylene terephthalate
PMC	Polymer matrix composites
RE	Reverse engineering
RH	Relative humidity
RP	Reference point
RSC	Reduced strain closure
RVE	representative volume element
SEM	Scanning electron microscopy
SFRP	Short fibre reinforced polymer
SG	Strain gauge
S-N	Stress-Life curves
SSED	surface strain energy density
StDev	Standard deviation
UTS	Ultimate tensile stress
W-N	Dissipated energy vs Life curves

1. INTRODUCTION

1.1 Motivation

Interest in the use of Short Fibre Reinforced Polymer composites (SFRP's) in load bearing applications has significantly increased as industries move into materials and manufacturing technologies that are less expensive but, at the same time, maintain good levels of performance in terms of strengths, stiffness, etc. of final parts. This trend is more evident if we examine the automotive industry, which in the last five years has invested a significant amount of resources on research projects with the purpose of increasing the understanding of this type of composites [1]–[3]. One of the key aspects driving this initiative is the challenging requirement that cars manufacturers are facing in Europe in terms of the reduction of fuel consumption and more importantly CO₂ emissions. The European Parliament established a goal for new cars to achieve 40% less carbon dioxide emissions by 2020 making the new target 95g/km, in comparison to the 2007's carbon emissions requirement of 158.7 g/km [4]. If not met, cars manufacturers would face penalties of €95.00 per g/km of CO₂ in excess. In this regard, Figure 1-1 shows the advantage of using this type of composites in terms of the CO₂ footprint relative to a specific automobile component, where total emissions could be reduced by more than 50% if the material is changed from Aluminium (Al) to PA66GF50.

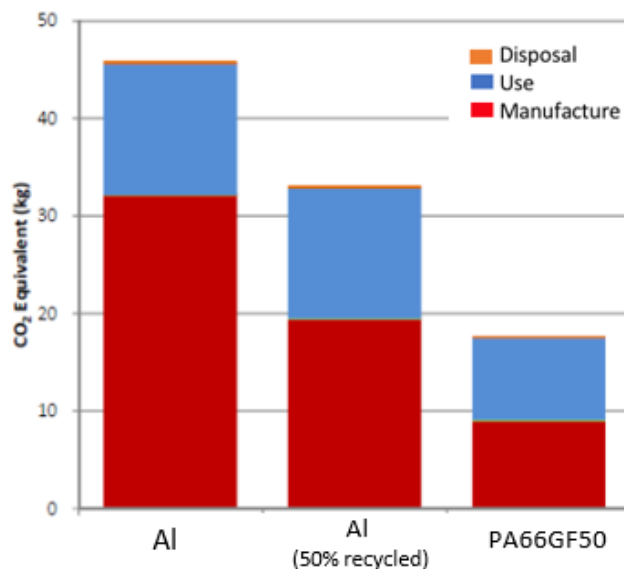


Figure 1-1 Al vs PA66GF50 CO₂ footprint of a production car component.
With the courtesy of Jaguar Land Rover.

The most interesting quality of SFRP's is that they allow for tailoring of the material properties, in terms of Young's modulus, tensile strength, fatigue life, etc.; while weight, material and production costs can be greatly reduced. However, this comes at the price of a significantly more complex material behaviour that, as of today, is still not fully understood.

In SFRP's, most reinforcements are available as chopped fibres. The best mechanical performance is achieved in this shape than in any other; i.e. particles, flakes, etc [5]. Glass fibres are consistently employed as they are inexpensive and have a medium to high material performance. In regard to resins, thermoplastic polymers present low mould shrinkage, have better toughness and impact resistance, refrigeration is not needed and they can be remoulded making them ideal for flow forming [6]. Components in cars, ships, drones and airplanes, tooling cases, engines and appliances spare parts, are some examples of the use of this type of composites. Figure 1-2 shows an air intake manifold made out of SFRP PA66GF30 used on production cars.



Figure 1-2 Automobile engine air intake manifold made of PA66 GF30 [7].

Field failures of this type of composites are mostly due to the fatigue loading conditions experienced during duty cycle. This is characterised by the degradation of the structural mechanical properties due to one, or a combination of, known composite damage mechanisms, such as: fibre breakage, matrix failure (cracking or large plastic deformation), interface failure (fibre pull out), etcetera [8]. However, the particular mechanical state, in terms of stresses and strains, that incentives the initiation of cracks on SFRP's parts are still being researched.

The fatigue life behaviour of metals is long understood and existing models are, for the most part, well established. This is not the case for composites, where large gaps

of knowledge still exist. Even more so in regard to injection moulded SFRP's, where their fatigue behaviour and failure mechanisms are in general driven by: the highly complex fibres distribution, stochastic damage propagation, and the complex matrix material response. Current modelling methodologies used for these short fibre reinforced composites borrow heavily from the better understood composite laminate theory [9]–[11].

Therefore, in order to use these materials safely, with more confidence and to avoid over-designing; a physically-based and integrated model for fatigue prediction of SFRP's is needed. In specific, one that not only includes the effect that the fibre orientation has on the material's life, but also the effect of the mean stresses and changes in the loading conditions, as well as, the known viscoelastic response that the resin has on the overall performance of the composite. This model should also include, and be drawn in combination with, the physical understanding of the complex damage mechanisms that appear at the different regions of the material thickness. The present work proposes a modelling methodology with said characteristics and contributes to addressing the gaps in knowledge that currently exist in the understanding of the fatigue response of short glass fibre reinforced polymer composites.

1.2 Aim and key objectives

The aim of this project is to develop, and validate, a modelling methodology for the fatigue behavior of injection moulded short glass-fibre reinforced polymers, as well as, to generate new insight about the fatigue damage mechanisms of this type of composite materials.

1.2.1 Key project objectives

- To review existing published experimental and modelling techniques, as well as, to identify gaps in the knowledge of SFRP's.
- To characterise the material properties of SFRP's under tensile and, in particular, under fatigue loads.
- To characterise the complex fibre distributions through the material thickness.
- To investigate the degradation of the material properties due to damage accumulation.
- To understand the specific micro and macro-mechanisms that lead to crack initiation-propagation within the distinguishable regions of the material.

- To develop a modelling methodology to produce a reliable fatigue life prediction for SFRP's based on the gained understanding of the material behaviour.

1.3 Novelty

The present dissertation helps addressing the gaps in the knowledge regarding the fatigue behaviour and prediction of short glass-fibre reinforced polymer composites. It builds from the limitations of current published methodologies and from experimental analysis of the material response, and damage mechanisms, carried out using state-of-the-art techniques. It proposes a new multi-scale modelling approach to predict the effect of the local fibre orientation, and includes the experimental validation at every step of the modelling phase to assess the accuracy of the numerical prediction, and the effect of the propagation of these inaccuracies on the final fatigue life calculation. This work also investigates an energy-based approach and introduces a fatigue parameter based on the stabilised dissipated energy in order to mitigate the effect of the fibre orientation in the material cyclic behaviour, while taking into account the plasticity effects inherent of this type of materials. Finally, it generates new knowledge regarding the location and conditions, in terms of stress and strain, for crack appearance and propagation in this type of materials.

1.4 Outline of work

This dissertation is divided in the following manner: Chapter 2, presents an in-depth review of the most relevant published literature regarding short fibre reinforced polymers composites. Chapter 3, describes the experimental methodology in detail. It defines the material, specimen geometry and equipment used. The conditions used for monotonic and fatigue testing are also described. Chapter 4, presents the modelling methodology and the computer aided engineering (CAE) approach used in this project. Each step from the injection moulding simulation to the fatigue prediction is described in detail. For clarity of presentation, the project's results are divided in two chapters: Experimental results (Chapter 5) and Modelling results (Chapter 6). Chapter 7, presents the in-depth analysis and discussion of the body of work. Finally, Chapter 8 presents the overall conclusions and future work.

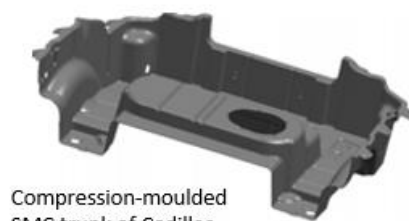
2. LITERATURE REVIEW

2.1 Applications of Short Fibre Reinforced Polymers (SFRP's)

Short fibre reinforced polymer composites, or SFRP's, are being used more extensively in engineering parts and consumer products. This is due to the unique combination of material properties that they can achieve, due to the relatively lower bulk cost and due to the wide range of geometries that they can be shaped into. The relatively ease of forming is one of the key characteristics, and a reason of its extensive use, that distinguish SFRP's from other type of composites.

SFRP's can be processed similarly to non-reinforced plastics, and in the case of thermoplastics matrices like Nylon (polyamide) they can be mass produced through universal methods, such as injection moulding. This allows the manufacturing of complex shapes in bulk at low prices. Material properties are partly determined by the fibre volume fraction and partly by the process [12]. This creates a wide range of options in terms of properties and costs that needs to be considered prior to the selection of any particular combination.

A large number of industries make use of SFRP's. This ranges from the aircraft and space industry, to the automotive industry and sporting goods, etc. The automotive industry in particular benefits highly from the crash resistance capabilities, overall good mechanical properties and of the weight reduction of parts that SFRP's allow in comparison to metallic materials. In cars, SFRP's can be found alone or as part of a wide range of components, such as: dashboards, mirrors, valves, cases, radiators, manifolds, etc. Figure 2-1 shows examples of car parts made with short fibre reinforced composites materials.



Compression-moulded SMC trunk of Cadillac Solstice



Compression-moulded valve cover for a truck engine

Figure 2-1 Examples of parts using short fibre reinforced composites [13]

2.2 Introduction to SFRP's

2.2.1 Reinforcement fibres and glass fibres

In a composite material the reinforcement's main function is to bare the load while improving the overall strength and stiffness of the part. It can be made out of different materials (organic, metallic, synthetic or mineral [5]); and, can take many forms; such as: long, chopped, woven fabrics, natural fibres, particles, flakes, whiskers, sheets, etc. Although, fibres provide with the highest strength and stiffness among the different shapes. The reasons fibres are used on structural materials can be summarized as follows [6]:

- Fibres allow for a relative small diameter, which reduces the probability of flaws and defects, and increases the fraction of the theoretical strength that can be achieved. An early example of the reduction of strength with increase diameters was measured by Lamotte and Perry in 1970 [6], and the results can be seen in Figure 2-2 .
- Fibres also allow for a high aspect ratio (length divided by the diameter), to maximize the amount of load that is passed to the reinforcement from the resin.

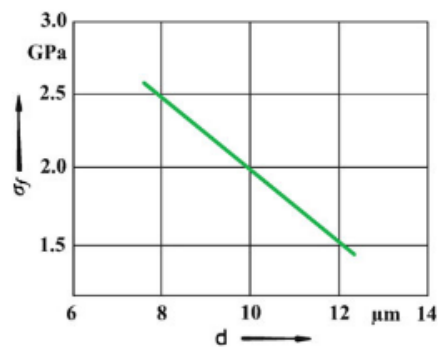


Figure 2-2 Decrease in tensile strength for a carbon fibre with diameter [6].

Reinforcement fibres can be found with different generic names, such as: glass fibres, carbon fibres, graphite, Kevlar (Du Pont's trade name for aramid fibres), etc. Fibre type, volume or weight fraction, fibre length and fibre orientation; are key factors that impact the final mechanical characteristics of the composite [14], such as: stiffness and tensile strength, fatigue performance and damage mechanisms, electrical and thermal conductivities and finally, cost [13]. Table 2-1 show typical values for tensile and compressive strengths for commonly used fibres.

Table 2-1 Typical values for commonly used long fibre reinforcements [13].

Fibre	Tensile Strength (GPa)	Compressive Strength (GPa)
E-glass fibre	3.4	4.2
T-300 carbon fibre	3.2	2.7 - 3.2
AS 4 Carbon fibre	3.6	2.7
GY-70 carbon fibre	1.86	1.06
P100 carbon fibre	2.2	0.5
Kevlar 49 fibre	3.5	0.35-0.45
Boron	3.5	5

In the case of glass fibres, there is a wide range of designations depending on their specific chemical constitution. Silica (SiO_2) is the main component and its content ranges from anywhere between 50% to 60% [6]. Glass fibre types can be divided in the following [15]:

- Type E (Electrical); low electrical conductivity.
- Type S (Strength); high strength.
- Type C (Chemical); high chemical durability.
- Type M (Modulus); high stiffness.
- Type A (Alkali); high alkali or soda lime glass.
- Type D (Dielectric); low dielectric constant.

From this classification, glass fibre type E is widely used due to its good strength and reasonable Young's modulus (as shown in Table 2-1), and good electrical insulation capabilities. Although its electrical applications are only a small part of the overall uses for this material [6]. Glass fibre can be manufactured into different forms, chopped, yarn, fabric, etc. as shown in Figure 2-3. From where chopped glass fibres are widely used in the injection moulding industry and can be typically found in lengths up to ~12mm [15].

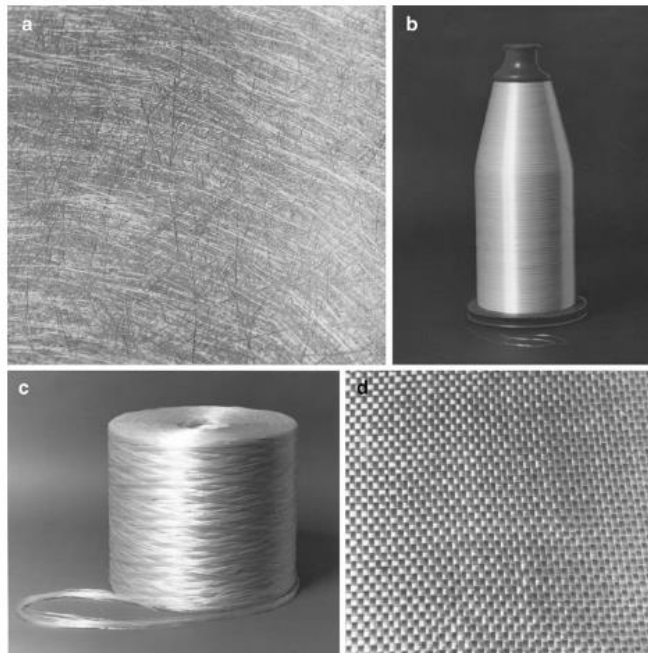


Figure 2-3 Different forms of glass fibre: a) chopped strand, b) continuous yarn, c) roving, d) fabric [6].

2.2.1.1 Fibre length distribution and critical fibre length (l_c)

The distribution of the fibre length in short fibre reinforced composites has been studied in the past to assess the effects that the different lengths might have in the material response. In Chapters 2.4.1 and Chapter 2.5.2.2., those effects are detailed in regards to tensile and fatigue performance, respectively. As a general introduction, an example of the fibre length distribution of SFRP's is presented in a work by Sasayama et.al. [16], for two different specimens' shapes, Figure 2-4a; and reinforced with two types of fibre lengths: long (LGF) and short (SGF). The distribution of the fibres' lengths is presented in Figure 2-4b-e; where the average fibre length for each specimen were: For Type 1, 385 μ m (SGF) and 537 μ m (LGF) and for Type 2, 391 μ m (SFG) and 611 μ m (LGF). From these images, it can be seen that for the case of short fibres (SGF) the distribution presents a more uniform range of lengths, Figure 2-4b & d. Whereas in the specimens reinforced with long fibres (LGF), Figure 2-4c & e, a specific length is clearly seen above any other, and is denoted by a peak in the frequency observed. From the analysis of the fibres, the critical length (l_c) can be identified as: "the minimum fibre length which, embedded into the matrix, breaks under tensile load" [17]. In other words, the minimum fibre length that achieves the maximum reinforcement, or maximum fibre strength, possible. This l_c has been estimated for SFRP's via several methods: for example, Vas et.al. [17], estimated the l_c using a mathematical approach based on the "barbe" or "beard" length distribution

calculated from the measured fibre length distribution of fibres protruding out of specimens' fracture surfaces, a schematic is depicted in Figure 2-5a and b, on reinforced poly(ethylene-terephthalate) samples. The estimation using this approach calculated a $l_c=683\mu\text{m}$, significantly higher than the average length of $156\mu\text{m}$, as shown in Figure 2-5c. A simpler model by Kelly and Tyson [18], proposed that in short fibre reinforced materials the external load is transferred to the fibre by the shear force at the fibre-matrix interface, and that l_c , which is the "minimum length to build up enough stress to fracture the fibre"[19], is then given by:

$$l_c = \frac{\sigma_f \cdot d}{2\tau}$$

Equation 2-1

Where σ_f is the fibre tensile strength, d the fibre diameter, and τ the interfacial shear strength between the fibre and matrix. A simplification can be done if a strong interfacial bond is assumed [19]. Then τ will be restricted by the shear strength of the matrix, τ_{m_i} ; and if the matrix is assumed isotropic, therefore:

$$\tau = \frac{\sigma_m}{\sqrt{3}}$$

Equation 2-2

Where σ_m is the strength of the matrix. In a work by Mortazavian and Fatemi [20], a burn off test was conducted on a short fibre reinforced PA6 to measure the average fibre length present in the composite, which was 0.253mm . In comparison, the obtained critical length for this material using Equation 2-1 and Equation 2-2 was significantly larger than the actual average, at $l_c=0.67\text{mm}$, as presented in Figure 2-6.

That the actual fibre lengths are lower than l_c is the case for most injection moulded short fibre reinforced polymers, which suggests that the final strength of the composite is not really related to the strength of the fibre per se, but on the fibre-matrix interfacial shear strength [19]. As concluded in [21], final fibres in the material tend to be shorter than the critical length due to the breakage that occurs due to the high-shear mixing and plasticization that takes place inside the barrel of the injection moulding machine. In a study conducted in this same work [21], fibre lengths in pre-moulding pellets of short E-glass and polypropylene were in average 0.71mm , after the injection moulding the average fibre length had reduced to 0.274mm , i.e. a lost of almost 62% of the initial length. Finally, some of the effects that different fibre lengths, and diameters, have in the material are presented in [22], and summarized in Figure 2-7. In an ideal unit volume sample, longer fibres would have an effect in the crack

path length. As the cracks propagate through the fibre/matrix interface, Figure 2-7a, this crack path is made longer which in turns helps in improving the composite strength and toughness. On the other hand, in the same volume sample but with shorter fibres there would be significantly higher number of individual fibres that in turns increases the stress concentrators at the fibres ends, Figure 2-7b; which are responsible for the initiation of microcracks, and thus decreases the composite strength and toughness [22].

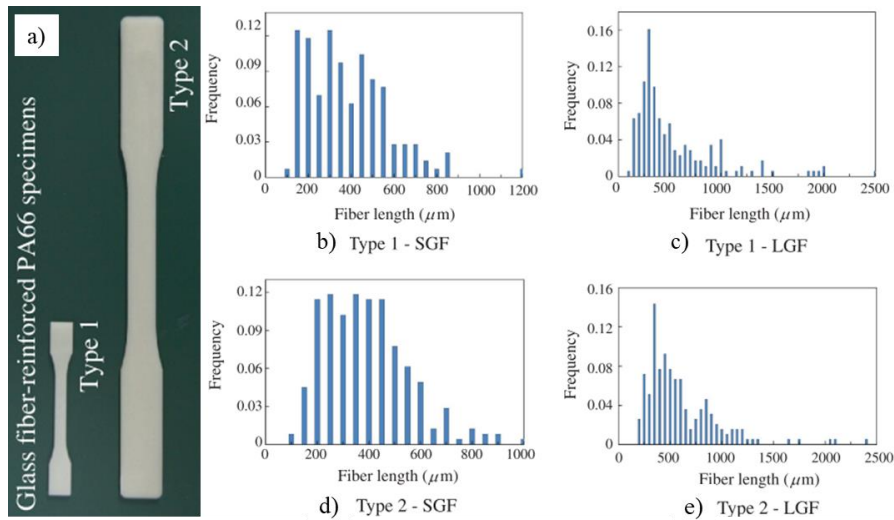


Figure 2-4 Specimen types and fibre length distribution for glass fibre reinforced PA66 coupons [16]. SGF and LGF stand for, respective, short and long glass fibre.

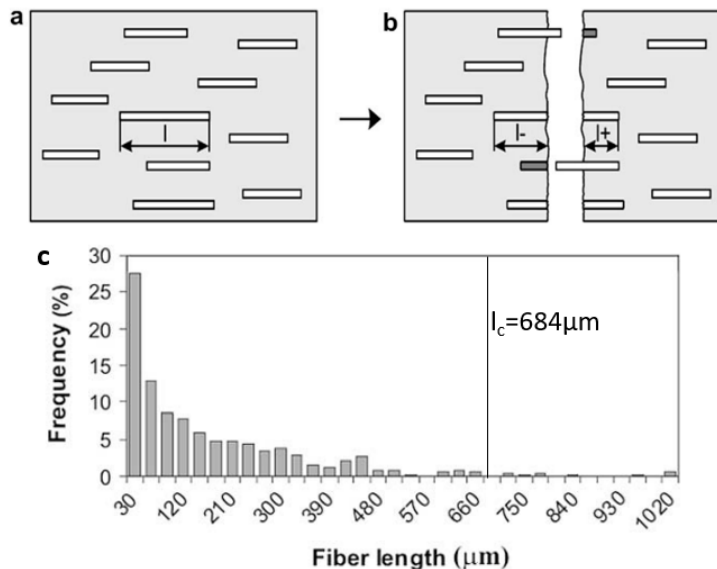


Figure 2-5 Schematic of a SFRP's fibre arrangement a) before, and b) after specimen failure. c) Frequency histogram of fibre length and critical length (l_c) [17].

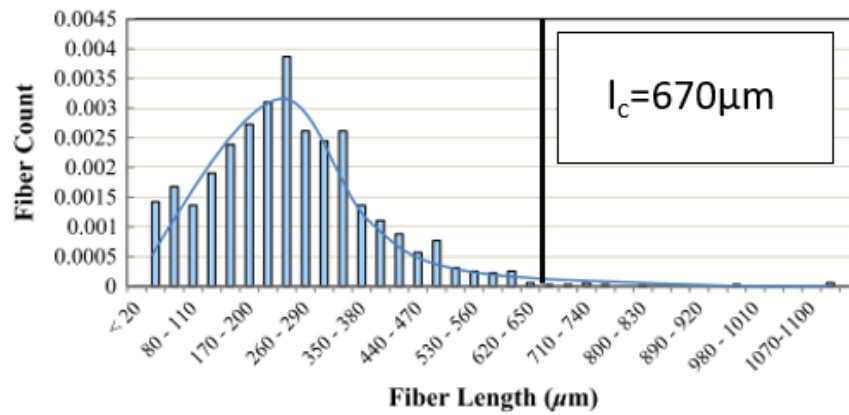


Figure 2-6 Fibre length variation of reinforced PA6 and calculated I_c [20].

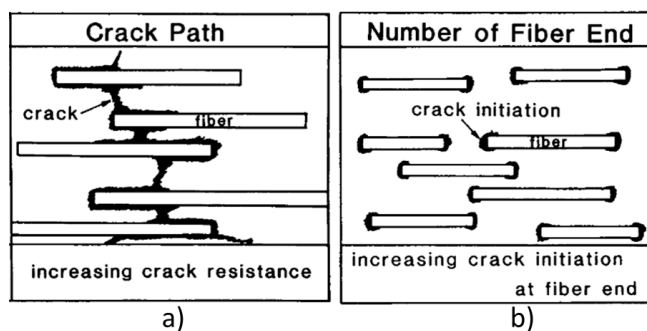


Figure 2-7 Effect of fibre length as reinforcement material. a) Longer and b) shorter fibres [22].

2.2.2 Thermoset and thermoplastic matrices

The principal goal of the resin is to transfer the load, to serve as medium to protect and bond the reinforcement (fibres) together. SFRP's are, for the most part, easier to fabricate than other composites due to the relative low processing temperature needed for the part manufacture and lower cost of the polymer [12]. In SFRP's, the matrix is constituted by a polymeric resin that can either be a thermoplastic or a thermoset [23].

In thermoplastics, the individual molecules are not chemically joined together, as shown in Figure 2-8a, they are held in place by weak secondary bonds such as van der Waals bonds and hydrogen bonds [13]. This results in the softening they experienced when heated, allowing them to be moulded and remoulded, they also present good crash resistance. Low- and high-density polyethylene, polystyrene, PMMA, Polyvinyl chloride (known as PVC) and Nylon (from the Polyamide family) are examples of commonly used thermoplastics [6]. In contrast, in thermoset resins their molecules are

chemically joined together by cross-links, as presented in Figure 2-8b, forming a rigid three-dimensional network structure after polymerization (curing) [13]; as result thermosets decompose when heated, but they present good resistance against solvents and corrosives, are an excellent option for high temperature applications, and there is a wider option of available manufacturing processes. Epoxy, polyester, vinyl ester and other polyimides are examples of thermoset resins. The advantages of thermoplastic resins over thermosets can be summarized into two main aspects [12]:

- 1) *Lower manufacturing cost*, which translates to no cure needed, unlimited shelf life, possibility of recycling, low moisture content, fusion possible; and
- 2) *Better performance*, due to their higher toughness, higher environmental tolerances and good dry and humid properties.

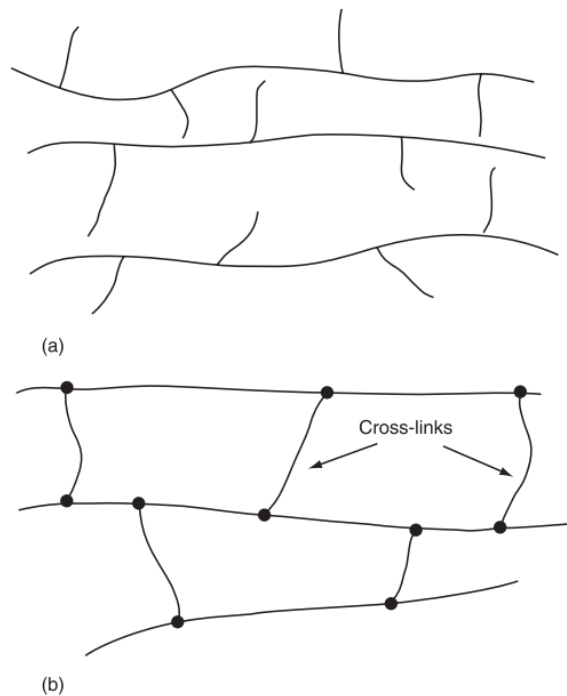


Figure 2-8 Schematic representation of a) thermoplastic and b) thermoset polymer [13].

Table 2-2 shows typical tensile material properties for commonly use thermoplastic and thermoset resins. Where E_t and E_c are the tensile and compressive moduli, σ_t and σ_c are the ultimate tensile strengths, ν is the Poisson's ratio, and α is the coefficient of thermal expansion [5].

Table 2-2 Typical matrix properties [5].

Material	Density (kg/m³)	E_t (GPa)	E_c (GPa)	σ_t (MPa)	σ_c (MPa)	N	α (10⁻⁶/°C)
Polyester	1200-1400	2.5-4.0	-	45-90	100-250	0.37-0.40	100-200
Epoxy	1100-1350	3.0-5.5	-	40-100	100-200	0.38-0.40	45-65
NARMCO 2387 (epoxy)	1210	3.38	3.86	29	158	-	-
PVC	1400	2.8	-	58	-	-	50
Nylon	1140	2.8	-	70	-	-	100
Polyethylene	960	1.2	-	32	-	-	120

Finally, polymeric resins (both thermoplastics and thermosets) present a unique characteristic in comparison to metals, their response is usually viscoelastic or viscoplastic. As result, the material properties show a dependency on the ambient temperature, moisture and the loading rate [5]. Figure 2-9a to c show examples of the variation of the polymer modulus with temperature and loading rate, for thermoplastics and thermoset resins. Approximately around the point of the glass transition temperature (T_g), the polymer changes from a solid state to a more soft, ductile one. This change can present a reduction of their modulus of up to five orders of magnitude [13]. At this temperature the material is also highly viscoelastic. This means that when a load is applied, it shows an immediate elastic deformation followed by a slow viscous one [24]. In this regard, Figure 2-9d presents the effect that the change in loading rate and temperature have in the polymer's material response. It can be seen that at low temperature the polymer behaviour is very close to a brittle material, it might not show signs of yielding and the strain-to-failure is very low. As the temperature increases, yielding might occur; but the yield strength decreases rapidly. On the other hand, the strain-to-failure increases at higher temperatures, transforming the polymer into a more ductile material. In regards to the loading rate, the opposite relation to the temperature effects is seen. In other words, at low loading rates the material might show a more ductile behaviour, presenting a relatively higher toughness. On the other hand, at high loading rates, or short duration of loading, the material presents a more rigid, or brittle, response [13].

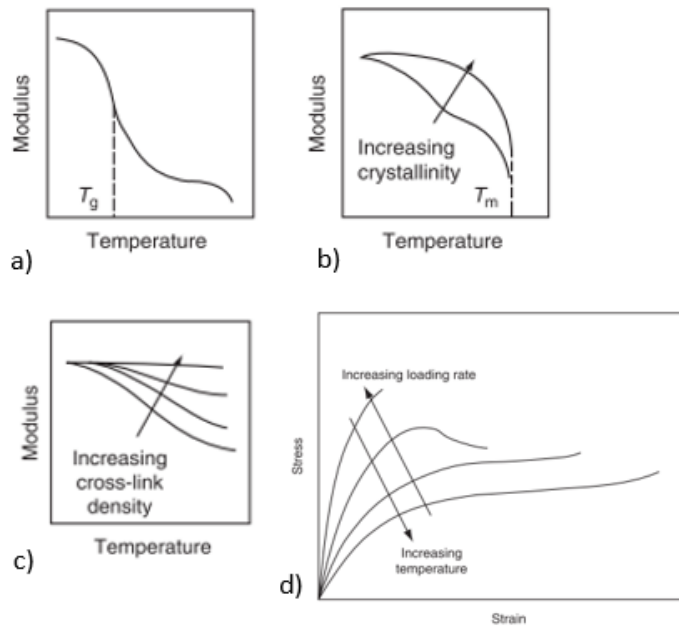


Figure 2-9 "Variation of tensile modulus with temperature for three different types of polymers: a) amorphous thermoplastic, b) semi-crystalline thermoplastic, and c) thermoset. d) Effects of loading rate and temperature on stress-strain behaviour of polymeric solids" [13].

2.2.3 Moulding techniques for thermoplastic SFRP's

In general, there is a large range of available manufacturing techniques for fibre reinforced polymer composites such as: hand lay-up, vacuum bag moulding, pultrusion, injection moulding, etc. [5]. Table 2-3 provides with a summary of the key characteristics of these processes; in terms of initial cost, part strength, part complexity, etc. For short fibre polymer composites in particular, available moulding techniques are the same as the ones used for non-reinforced plastics and are discussed next.

**Table 2-3 Comparison of fibre reinforced polymer composite
manufacturing processes [5].**

Manufacturing process	Equipment costs	Rate of production	Part strength	Operator skill required	Part complexity	Reproducibility	Possible fibre forms (R-Random/Continuous)
Hand lay-up	L	L	L	H	H	L	R,C
Spray-up	M	M	L	H	H	L	R
Tape lay-up (manual)	L	L	-	H	N	L	C
Tape lay-up (automated)	H	H	-	L	M	H	C
Vacuum bag moulding (wet lay-up)	L	M	M	H	H	L	R,C
Autoclave moulding (tape lay-up)	H	M	H	M	M	H	C
Filament winding	M	M	H	L	L	H	C
Pultrusion	H	H	H	L	L	H	C
Compression moulding	H	H	-	M	H	H	R,C
Resin transfer moulding	M	M	-	M	H	H	R,C
Reaction injection moulding	M	H	-	M	H	H	R,C
Injection moulding	H	H	L	H	H	H	R
Stitched / thermoform preforms	M	H	M	M	M	H	R,C
Random fibre preforms	M	L	L	H	H	L	R
3-d woven/braided preforms	H	M	H	L	H	H	C
Legend: H-high, M-medium, L-low.							

Short fibre reinforced polymer composites are first fabricated by pre-mixing fibres (of ~2-3mm in length or less) in a liquid resin. Un-polymerized or partially polymerized matrix in the case of thermoset; or the molten, or dissolved in a solvent, polymer in the case of thermoplastics [12].

For the case of thermoplastic resins, main moulding methods include: thermoforming, extrusion and injection moulding, among other. *Thermoforming* characterises by the production of a composite sheet (which includes the short chopped fibres) that is then heated and stamped into the desired shape, followed by a vacuum or pressure forming [6]. *Extrusion* characterises by forcing the reinforcement/resin mixture (in the form of pellets, rods or tapes, etc.) through an open die by using a screw mechanism [12], a diagram of the full extrusion process is presented in Figure 2-10. Finally, *injection moulding* is widely used due to its short processing time and relatively simple mechanism. Typically, short fibre reinforced thermoplastics are supplied as cylindrical

granulates of ~3-5mm long and 3mm in diameter [25]. For the case of injection moulded parts, correct establishment of the injection point, also called gate, and the overall process parameters are important to optimize the performance of the part [26]. These parameters are: mould surface, material melt temperature and material transition temperature, injection time, viscosity, injection rate, injection pressure, clamping force, filling time, cooling time, packing pressure, among other [27]. Figure 2-11 shows a simplified schematic of the injection moulding process. The resin/reinforcement pellets are first fed into the machine, from where the material is pushed forward via a screw-drive arrangement. This screw increases in diameter producing a compressive effect that rises the temperature of the material, melting it and directing the flow into the injection chamber. Finally, it is poured into the mould and pressed. After the part has cooled it is ejected, and the process is repeated as necessary.

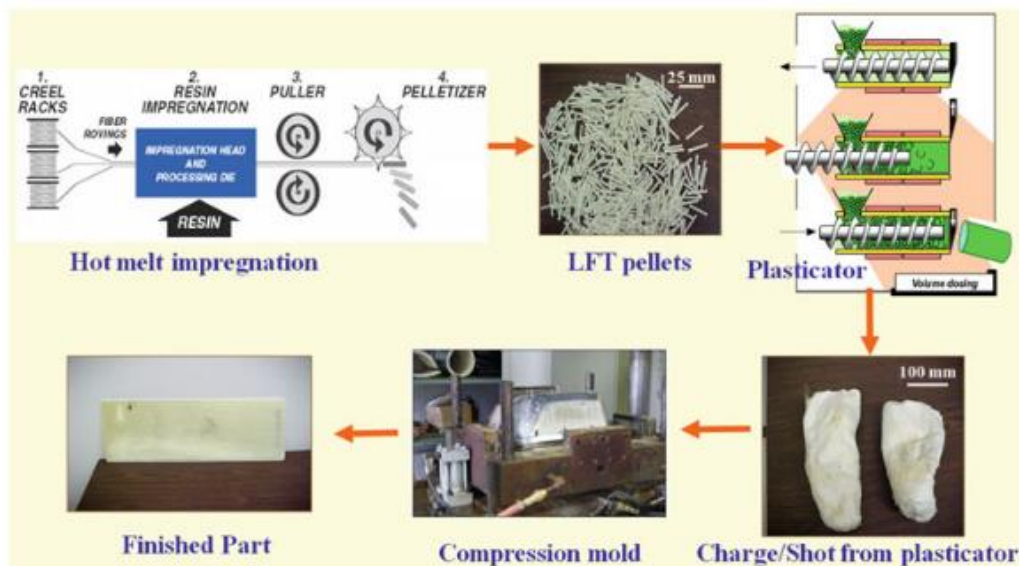


Figure 2-10 Extrusion and compression moulding process [6].

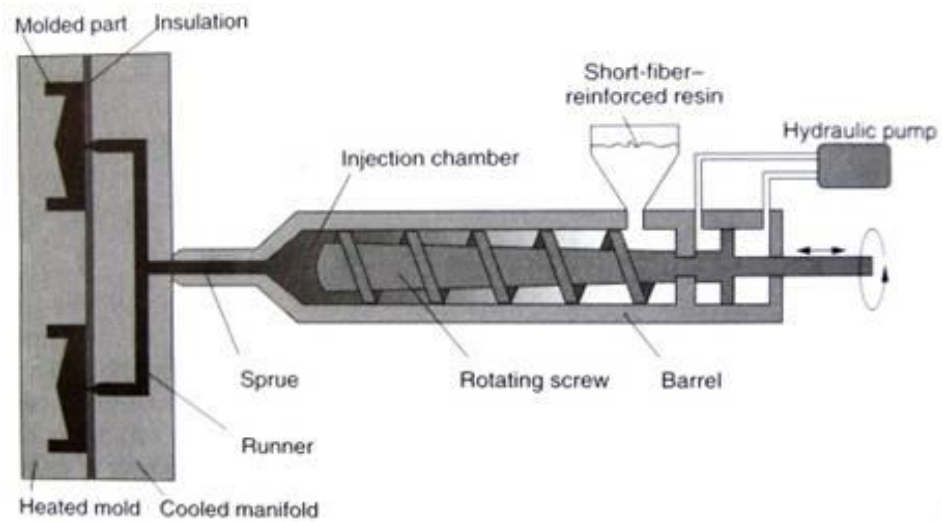


Figure 2-11 Schematic of injection moulding [28]

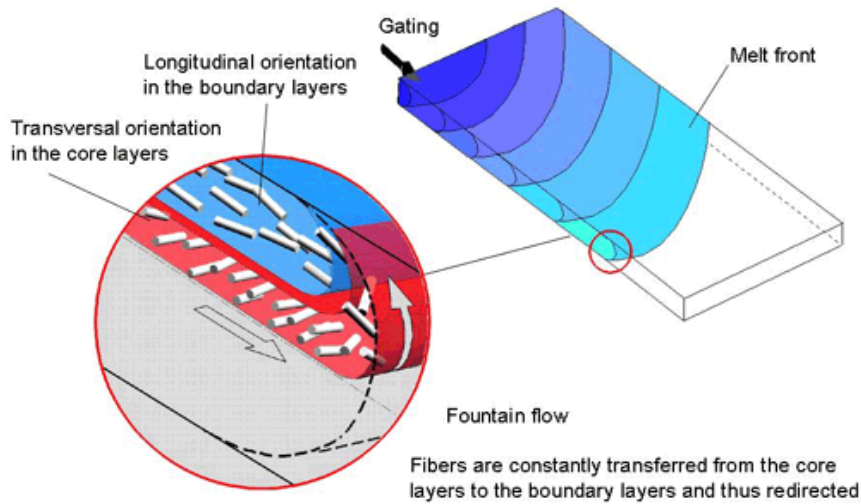
2.3 Fibre orientation distribution, measurement and prediction

2.3.1 Fibre orientation distribution

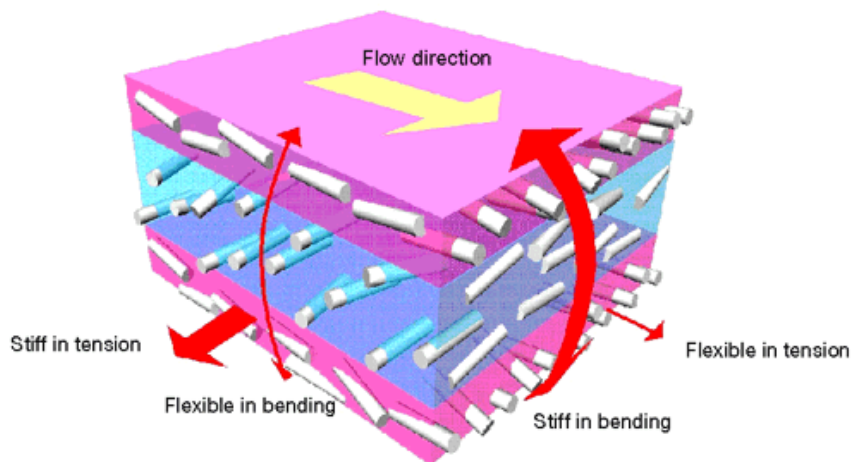
Injection moulded SFRP's present a highly anisotropic response product of a through-thickness continuous fibre orientation distribution (FOD), which is defined during the injection moulding of the part. A particular skin-shell-core structure can be identified [29], and its constitution drives the final material properties. Therefore, it has been of particular research interest the correct identification, measurement and prediction of this distribution [29]–[36]. A simplified representation of the evolution of the fibre orientation distribution in short fibre reinforced injection moulded plastics is shown in Figure 2-12. As the molten flow of polymer fills the mould, it creates distinctive regions of fibre distribution that are dominated by different flow mechanisms [30]. The fibres are constantly moving from the centre to the outer layers due to the fountain effect that takes place at the front flow [32]. In terms of fibre distribution, three main layers or regions can be clearly identified: A section where the preferred orientation of the fibres is parallel to the flow direction; a region of fibres aligned mostly transverse to the flow direction and; outer layers with seemingly random orientation [25]. This distribution occurs due to the interaction of the material being injected and the mould. During the injection process the part of the liquid material that gets in contact with the mould solidifies before the rest, this produces the seemingly random distribution on the outer layers of the composite. In pure shear flow fibres are mainly oriented in the flow direction. Stresses produced between the

solidified outer layers and the still flowing centre tend to align the fibres in this direction [32]. On the other hand, at the centre of the stream the divergent, axial, flow aligns the fibres perpendicular to the flow direction. Faster injection speeds tend to produce fibres more transversally aligned, whereas slower speeds more parallel to the flow [36].

Evolution of Fiber Orientation in Mold Filling Process



Evolution of Fiber Orientation in Mould Filling Process



Mechanical behaviour of anisotropic layered shells

Figure 2-12 Diagram of evolution of the fibre orientation during the injection moulding process [37].

2.3.2 Measurement of fibre orientation and orientation tensor

As early as the 1970's experimental measurement has been done to visualise and measure the fibre distribution. In 1975 Darlington and McGinley [38] investigated by contact micro-radiography (CMR) the orientation distribution of a Nylon 66 SFRP. Figure 2-13 shows their early findings, where the skin-core structure is visible. Since then, newer novel techniques have been developed to unambiguously measure the fibre orientation. Current widely spread methodologies use a combination of optical techniques or scanning-electron-microscopy (SEM) and image processing [30], [32], [35], [39]; or through the use of computed tomography (CT) and reconstruction software [31], [33], [40], as shown in Figure 2-14 for the case of a nylon-66 reinforced with short glass fibre 30wt% composite.

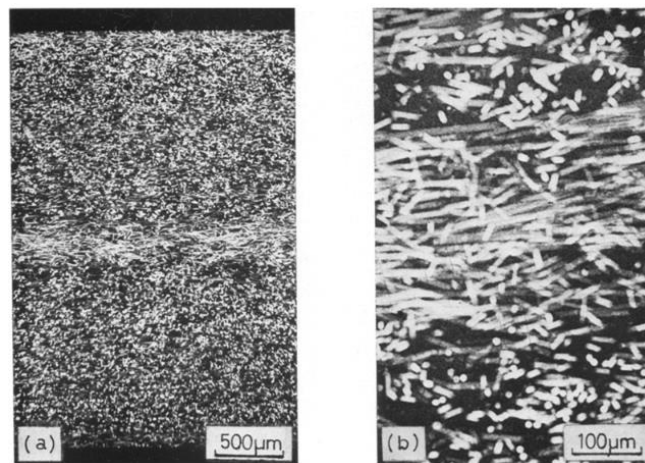


Figure 2-13 a) Variation of fibre orientation distribution throughout the thickness of a SFRP injection moulded part, b) higher magnification in the centre [38].

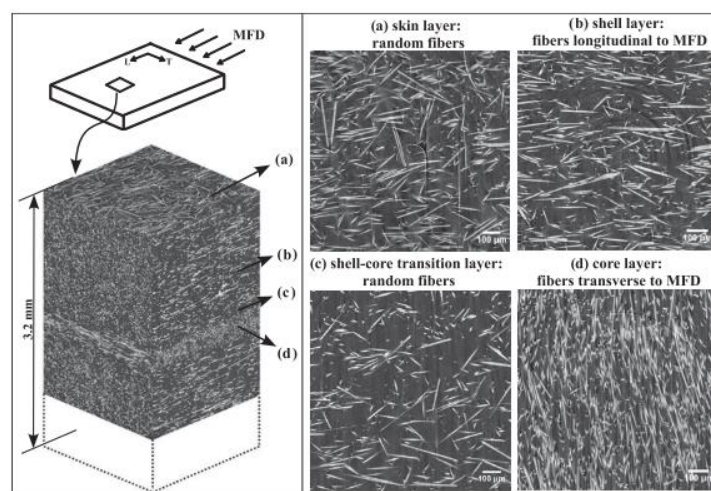


Figure 2-14 Microstructure of PA66/GF30 observed by micro-CT [41].

In simpler terms, the orientation of a single fibre can be described in a three-dimensional space with two angles in a polar coordinate system, ρ and γ , as represented in Figure 2-15. If a cross-sectional plane is then taken along the fibre, an ellipse of axes a and b is formed [32], which are related to the original orientation; i.e. an ellipse of axes $a=b$ (a circle) would mean the fibre is fully oriented in the out-of-plane direction with $\gamma=\rho=0$, and so on. Different analysis techniques, and methodologies, can then be used to measure the ellipses, calculate the angles and obtain the orientation of the fibres. An example of optical techniques is shown in Figure 2-16, where confocal laser scanning microscopy, or CLSM, was used to take sub-surface images and track the displacement of the fibre centres, in this figure four fibres were followed over five different frames, with the orientation of the fibre being calculated by fitting a line through the centre of the formed ellipses. The direction of the ellipses' major axes are identified by the blurring visible on the edges of the cross-section, as highlighted in Figure 2-16. This eliminates the angle ambiguity that occurs due to the ellipses dimensions being product of either ρ or $\rho+180^\circ$ as shown in Figure 2-15, and then calculate the fibre orientation [30].

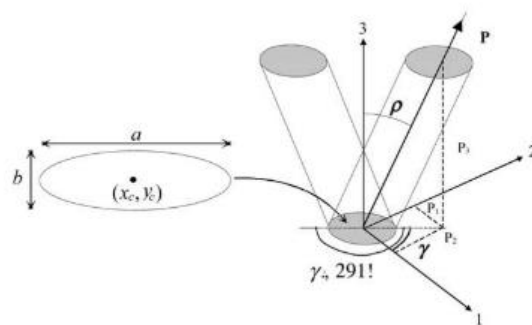


Figure 2-15 "Definition of orientation angles (ρ and γ) of a fibre" [32].

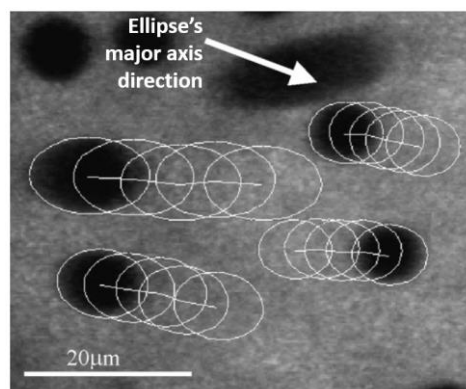


Figure 2-16 Tracking of fibre centres (ellipses) during 5 frames to calculate the fibre orientation via confocal laser scanning microscopy. Straight lines represent a fitting between the centre coordinates through the frames [30]

While optical techniques are still widely used, they are heavily dependent on the surface preparation, which is not only time consuming but requires a significant amount of expertise to produce good results. To mitigate this problem, research effort has been focused into using non-destructive techniques. A 2012 study by Bernasconi et. al. [42], compared the fibre orientation distribution of a SFRP measured via optical-image analysis and by tomographic methods, using a micro-CT for acquiring the X-ray images, and the Mean Intercept Length (MIL) concept for reconstruction and analysis. Initially, the found differences were attributed to the inaccuracies of the optical methods at measuring almost perpendicular orientations. Later analysis at the same location, but closer to the core layer, showed better match between both methods. It finally concluded that although micro-CT requires more expensive experimental facilities, it is non-destructive and it is less dependent of the section-plane chosen for analysis, as is the case for the optical methods. Another example of the used of CT for measurement of fibre orientation distribution was carried out by Nguyen Thi et. al. [43]. A high resolution 3D X-ray CT system XVA-160 α was used obtained 2D X-ray slices of a 30wt% glass fibre reinforced Nylon-6 SFRP composite. Similar to the optical method, the process used to measure the FOD can be summarized in the following steps:

1. Identify each fibre and extract the corresponding values for: the length of the fibre projection on the 1-2 plane, or L , and the angle between the fibre projection on the 1-2 plane and the axis 1, or Φ ; from the X-ray image, as shown in Figure 2-17a. An Auto-CAD software function was used for this case.
2. Calculate the out-of-plane angle, θ , as shown in Figure 2-17b. Where the H , or stage height, is the gap between the first and last 2D slice in which the measured fibre appears, from a series of consecutives 2D X-ray images.
3. With θ and Φ calculate the fibre orientation tensor components using:

$$\begin{aligned}
 a_{11} &= \langle \sin^2\theta \cos^2\Phi \rangle & a_{12} &= \langle \sin^2\theta \cos\Phi \sin\Phi \rangle \\
 a_{22} &= \langle \sin^2\theta \sin^2\Phi \rangle & a_{13} &= \langle \sin\theta \cos\theta \cos\Phi \rangle \\
 a_{33} &= \langle \cos^2\theta \rangle & a_{23} &= \langle \sin\theta \cos\theta \sin\Phi \rangle
 \end{aligned}$$

Equation 2-3

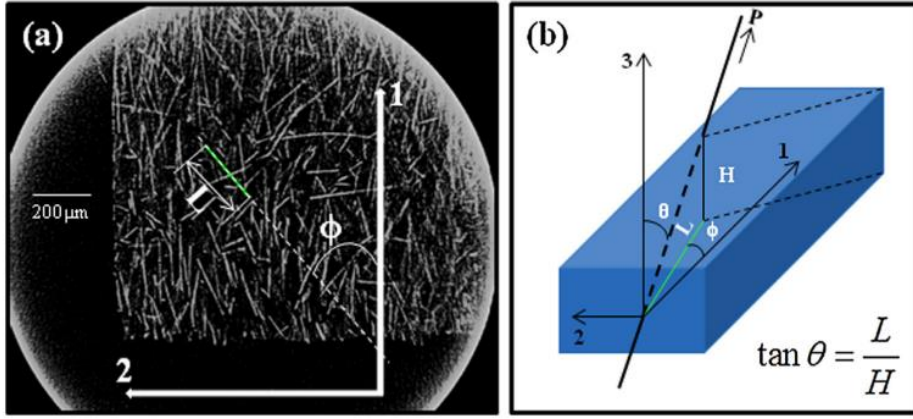


Figure 2-17 a) Identifying fibres in a 2D X-ray image and extracting the (L, Φ) values. b) Calculating the out-of-plate angle, θ , from the stage height, H , and the fibre projection, L [43].

In all cases, and independent of the method used, due to the extremely large number of fibres that can be part in a composite, the fibre orientation distribution (FOD) at any given point is described by using a probability distribution function $\psi(\rho, \gamma)$ [30], which is then briefed, to reduce the computational requirements, into a second order orientation tensor of the form:

$$a_{ij} = \int_{\bar{p}} p_i p_j \psi(\bar{p}) d\bar{p}$$

Equation 2-4

where \bar{p} is a unit vector parallel to a fibre, with components p_{ij} , which are related to angles, ρ and γ (as described in Figure 2-15), and $\psi(\bar{p})$ is the orientation distribution function, such that

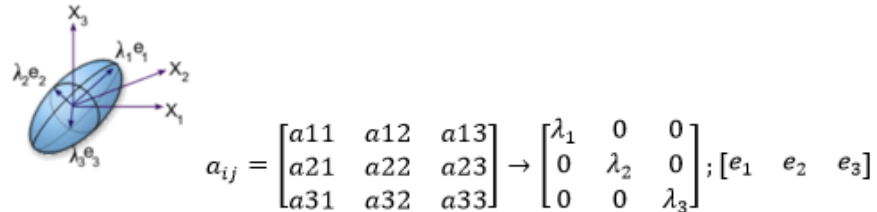
$$\psi(\rho, \gamma) \sin \rho d\rho d\gamma$$

Equation 2-5

gives the probability of finding a fibre between angles ρ and $\rho+d\rho$, and between γ and $\gamma+d\gamma$ [32]. In other words, the fibre orientation tensor components shows the probability of fibre alignment in the three main cartesian directions. A high probability is indicated by a value closed to 1, a low probability is indicated by a value closed to 0 [44]. The depiction of the tensor is presented in Figure 2-18. The eigenvectors (e_i) indicate the principal directions of alignment, and the eigenvalues (λ_i) give the proportions (0 to 1) of fibres aligned with the eigenvectors [45]. Finally, from the same

figure, it can be seen that the fibre orientation tensor possesses several characteristics which can be summarized as [46]:

- It is real and symmetric ($a_{ij}=a_{ji}$),
- The terms through the diagonal cannot be negative terms, and
- Tensor is normalized such as the summation of its diagonal components is equal to 1.



$$a_{ij} = \begin{bmatrix} a_{11} & a_{12} & a_{13} \\ a_{21} & a_{22} & a_{23} \\ a_{31} & a_{32} & a_{33} \end{bmatrix} \rightarrow \begin{bmatrix} \lambda_1 & 0 & 0 \\ 0 & \lambda_2 & 0 \\ 0 & 0 & \lambda_3 \end{bmatrix}; [e_1 \ e_2 \ e_3]$$

Figure 2-18 Fibre orientation tensor definition [45]

2.3.3 Prediction of fibre orientation

Research effort is also focused on the prediction of the fibre orientation distribution. Most work is based on the 1984 work by Folgar and Tucker [47], which established a mathematical model to describe the orientation behaviour of a fibre in suspension. Later, Advani and Tucker [48], built on this model by using tensors to predict the fibre orientation in short fibre composites, the original second order tensor formulation is shown in Figure 2-19. From where, a_{ij} is the orientation tensor, ω_{ij} represents the vorticity tensor, $\dot{\gamma}_{ij}$ the strain-rate tensor, λ is a constant that depends on the geometry of the fibre, and δ_{ij} is a unit tensor [45]. D_r can also be replaced by $C_i \dot{\gamma}$ [48]. $\dot{\gamma}$ being the magnitude of the strain-rate tensor, and C_i the original fibre interaction coefficient proposed by Folgar and Tucker [47]; which is material dependent and obtained from fitting experimental results. For example, $C_i = 0.0018$ and $C_i = 0.0002$, are interaction coefficients for two SFRP's of same fibre content and aspect ratio, but different matrix, PAA30 and PAA50 respectively [32].

$$\begin{aligned} \frac{D\mathbf{a}_2}{Dt} = \frac{D\mathbf{a}_{ij}}{Dt} = & -\frac{1}{2}(\omega_{ik}\mathbf{a}_{kj} - \mathbf{a}_{ik}\omega_{kj}) \\ & + \frac{1}{2}\lambda(\dot{\gamma}_{ik}\mathbf{a}_{kj} + \mathbf{a}_{ik}\dot{\gamma}_{kj} - 2\dot{\gamma}_{kl}\mathbf{a}_{ijkl}) \\ & + 2D_r(\delta_{ij} - \alpha\mathbf{a}_{ij}) \end{aligned}$$

Figure 2-19 Original formulation for the second order orientation tensor proposed by Advani and Tucker based on the Folgar-Tucker model [48].

Research has been done to improve the accuracy of the prediction methods. Wang et. al. [49] modified the Folgar-Tucker model and proposed a *reduced strain closure* model, or RSC, which reduces the change of fibre orientation with respect to the strain by only reducing the growth rates of the eigenvalues of the tensor and keeping the rotation rates of the eigenvectors unchanged. This achieved a better correlation with experimental measurements and predictions than the original model. Wang and Jin [50] compared prediction results using the original Folgar-Tucker model and the RSC model against experimental data, using commercial software Autodesk Moldflow Insight 3D. Figure 2-20, shows that better correlation for a_{11} and a_{22} components is achieved with the RSC. Jerabek et. al. [51] also performed a comparative analysis of the fibre orientation distribution by using CT and Autodesk Moldflow in short fibre reinforced polypropylene composites. For this case a commercial grade GD301FE with 32wt% of fibres was used. Figure 2-21 shows the magnitude of the calculated fibre orientation tensor component, a_{11} , through the thickness, each element represents at least 3,000 fibres. This investigation found best fit values with experimental data for RSC and C_i constants of 0.05 and 0.001 respectively. The difference in the thickness of the material also has an effect in the distribution of the fibres. Gsellman et. al. [33] conducted an analysis to demonstrate this, 2 and 3.5 mm material were used, at different flows. This analysis was mostly numerical in 3D structure using commercial software (Autodesk Moldflow). Results of this investigation, Figure 2-22, showed a relative good correlation with CT data in the area between the core and the skin. Whereas, in the centre of the specimen, a more pronounced mismatch was seen for the different thicknesses used.

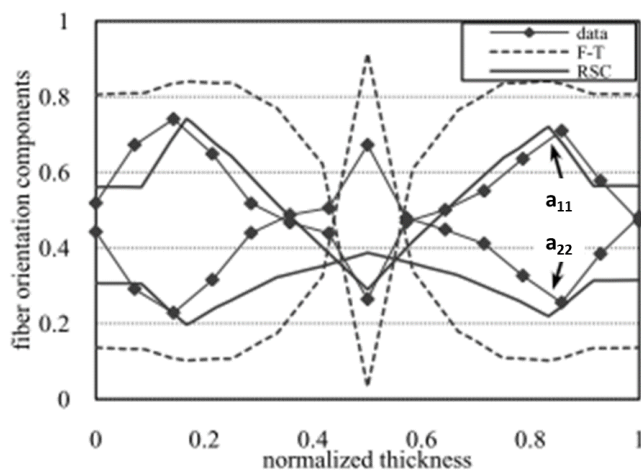


Figure 2-20 Comparison of fibre orientation data with 3D predictions. Folgar-Tucker (F-T) and RSC models are used. a_{11} and a_{22} are the orientation tensor components [50].

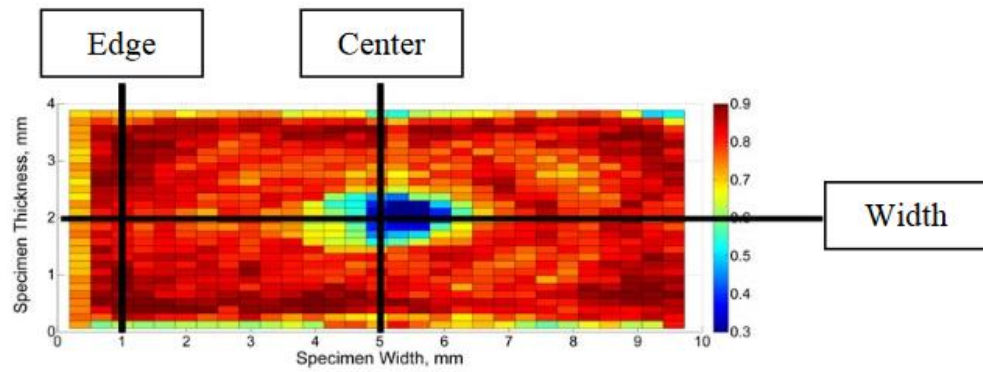


Figure 2-21 Fibre orientation component in the flow direction (a_{11}) depicted at the cross section of a specimen (FEA prediction) [51]

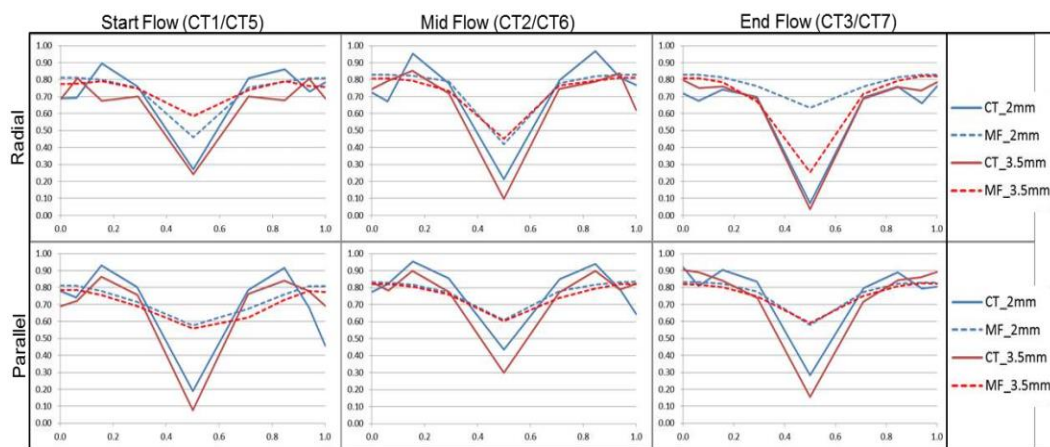


Figure 2-22 Influence of flow type and normalized part thickness on the predicted and measured fibre orientation (a_{11} as function of thickness at the centre position) [33]. Note: MF stands for Moldflow.

2.4 Monotonic behaviour of SFRP's

The material response of short fibre reinforced polymers is heavily dependent of the distribution of the fibres and the behaviour of its constituents. Research work has been carried out to assess, and to model, the material properties of these composites under different conditions. On a work by Gupta et.al. [52] on a short glass-fibre reinforced polypropylene showed a clear variation of the tensile properties of the composite with the specific angle of the specimen. Samples were taken at 0° (longitudinal to flow), 15° , 30° , 45° , 60° , 75° and 90° (transversal to flow). Results, presented in Figure 2-23, shown that specimens oriented closer to the flow direction, 0° and 15° , had the highest strengths and Young's moduli. On the other hand, specimens oriented at 45° , 60° , 75° and 90° , presented very similar values of strength and Young's modulus, which were lower than the ones seen on 0° and 15° . A middle point was reached on the specimen

oriented at 30°, where the stress-strain curve laid approximate in-between the 0° and 90° curves. Similar results were obtained by Bernasconi et.al. [53] on a PA6GF30 composite. Dog-bone specimens taken at 0°, 30°, 60° and 90° were tested in tension. Results, presented in Figure 2-24, also shown a clear effect of the fibre distribution on the material behaviour. Similar to the previous case, 0° and 90° samples presented the highest and lowest values of strength and Young's modulus, with the 60° oriented specimens laying very close to the 90°; and with the 30° oriented samples laying in between 0° and 90° material curves. Works from Mortazavian and Fatemi [20], [54], investigated the anisotropic effects, due to thickness and fibre orientation, on two different SFRP's: polybutylene terephthalate (PBT) with 30wt% glass fibres and polyamide-6 (PA6) with 35wt% glass fibres and 10wt% rubber. Specimens oriented at 0°, 18°, 45°, 90° were tested in tension. Figure 2-25a-c shows the results in terms of the tensile material parameters, where it can be seen that the 0° and 18° specimens showed the highest strengths and Young's modulus, at ambient temperature. On the other hand, 90° and 45° specimen showed lower and very close values of strength, although 45° presented higher strain at tensile strength. An analysis of the variation of the fibre lengths and orientation of the PA6 specimens' gauge section is presented in Figure 2-25d. In this figure it is shown that longer fibres are more oriented toward the flow direction (closer to 0°); whereas shorter fibres are more randomly oriented. Approximate 20% of the fibres were oriented between 45° and 90° with shorter lengths than those at 0° direction. This could explain why 45° and 90° specimens presented similar strengths, and why 0° specimens showed a higher tensile strength, as shown in Figure 2-25a. In terms of coupling the flow with the fibre length and orientation, Figure 2-25d also suggests that during the injection moulding process longer fibres tend to be affected more by the shear stresses, which occurs in the shell layers, produced between the seemingly solidified skin layer and the still flowing centre; therefore orienting these longer fibres mainly in the flow direction. While shorter fibres, seem to be affected more by the divergent, or axial, flow that occurs in the core layer. The analysis of the results also showed that PA6 specimens with smaller thickness presented smaller core regions (~2 times smaller), but the shell layers remained a large percentage of the specimen's cross section. This meant that the tensile moduli and strengths for the longitudinal specimens were similar for both thicknesses, as shown in Figure 2-26a. This is because in longitudinal specimens, independent of thickness, most of the load is bared by the shell layer. For the case of the transversal specimens, where the load is mainly bared in the core layer, a bigger difference with the thickness was seen; with thicker specimens presenting a higher

Young's modulus and strength [20], as shown in Figure 2-26b. Meaning that the higher the ratio of the core thickness to the specimen thickness, the tensile properties of the longitudinal and transverse specimens become closer [20]. In a similar manner, by analysing results of PBT specimens cut at 0° (longitudinal), 18° and 45° (mix-axis), and 90° (transversal), showed that there is little difference in terms of tensile properties for the transversal, 90°, and 45° specimens, as presented in Figure 2-27a. although the later presented larger ductility than any other orientation. Finally, a correlation between tensile strength and strain rate was drawn, as shown in Figure 2-27b; where it was seen that at least for longitudinal and transversal specimens the tensile strength linearly increased with the log strain rate [54].

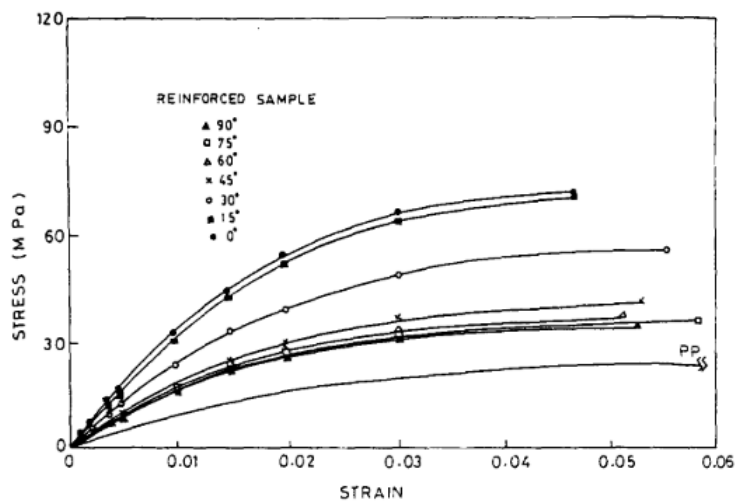


Figure 2-23 Stress-Strain curves for unreinforced and reinforced SFRP samples at different orientations [52].

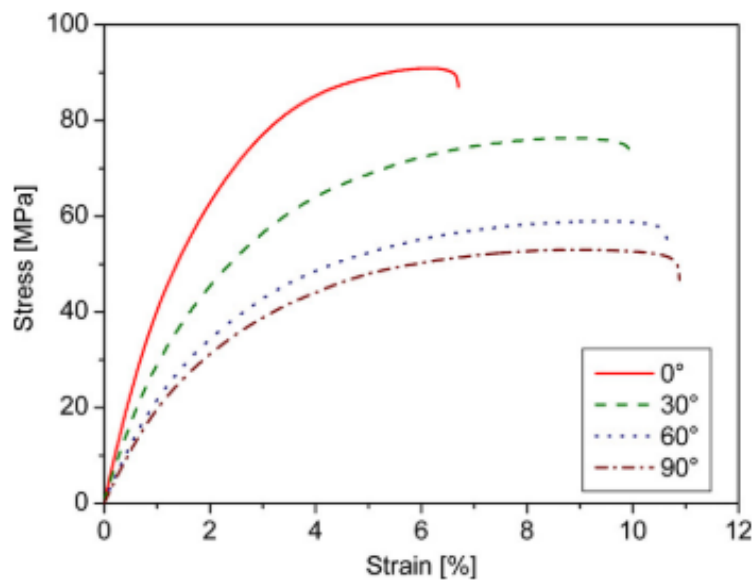


Figure 2-24 Stress-Strain curves of SFRP specimens at different orientations [53].

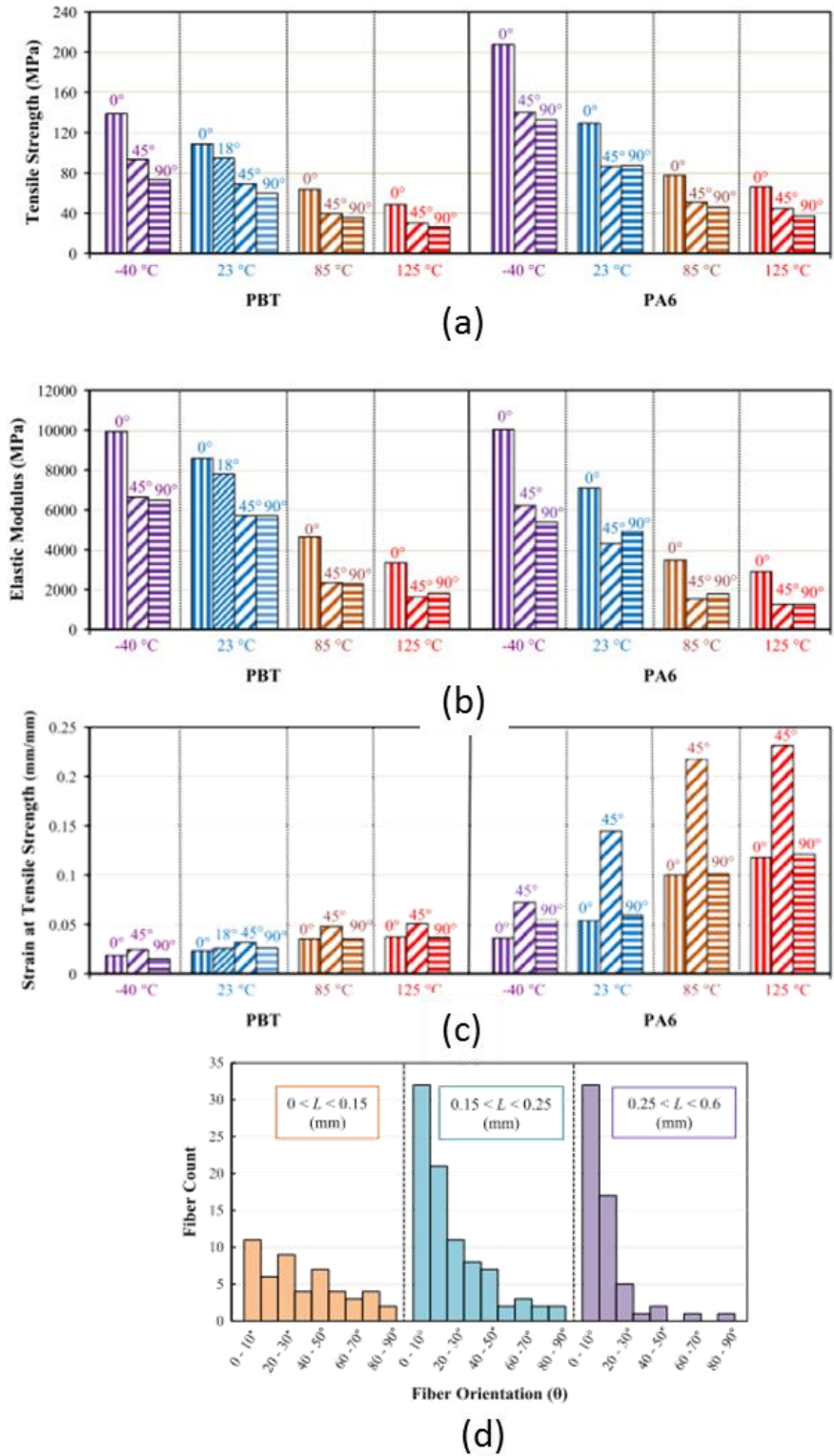


Figure 2-25 “Variations of average tensile properties with temperature and fibre orientation for duplicate tension tests of PBT and PA6 conducted at displacement rate of 1 mm/min for (a) tensile strength, (b) elastic modulus, and (c) strain at tensile strength. d) Variations of fibre length and orientation on the test gage section surface of a PA6 sample machined in the mould flow direction” [20].

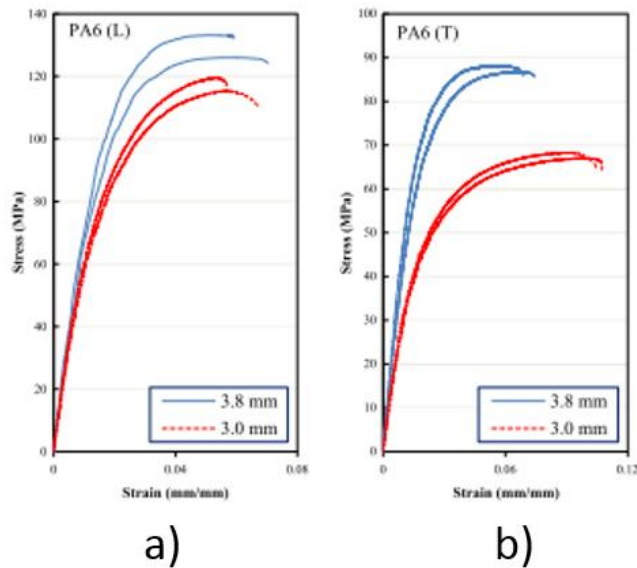


Figure 2-26 "Stress-Strain curves showing the effect of thickness at displacement rate of 1 mm/min at 23°C for PA6 in the: a) longitudinal (L) and, b) transverse (T) direction" [20].

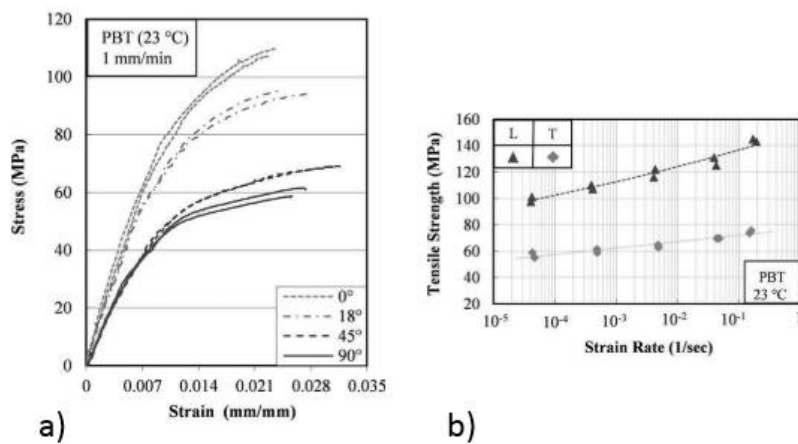


Figure 2-27 a) Stress-Strain curve showing the effect of mould flow direction and displacement rate PBT. b) Variation of strength with strain rate for PBT [54].

Experimental techniques have also been used to characterise the local behaviour of short fibre reinforced polymers. Heyes [55], used full-field strain results obtained via optical Digital Image Correlation (DIC) to compared against finite element analysis (FEA) results for a SFRP grade. Although for this particular study only qualitative validation was achieved, as shown in Figure 2-28 for a 45° specimen. In a similar manner, Crupi et. al. [56] made use of DIC technique to analyse the stress-strain response of longitudinal specimens cut from plates made out of Nylon-66 reinforced with 35wt% short glass fibres composite, with fibres of nominal diameter of 10

microns and 280 microns in length. As shown in Figure 2-29, a clear stress-strain curve for the material was obtained via this technique while at the same time it provides a highlight of the evolution of strain in the fracture zone, where even at lower strains, ~0.4%, the fracture zone was already visible.

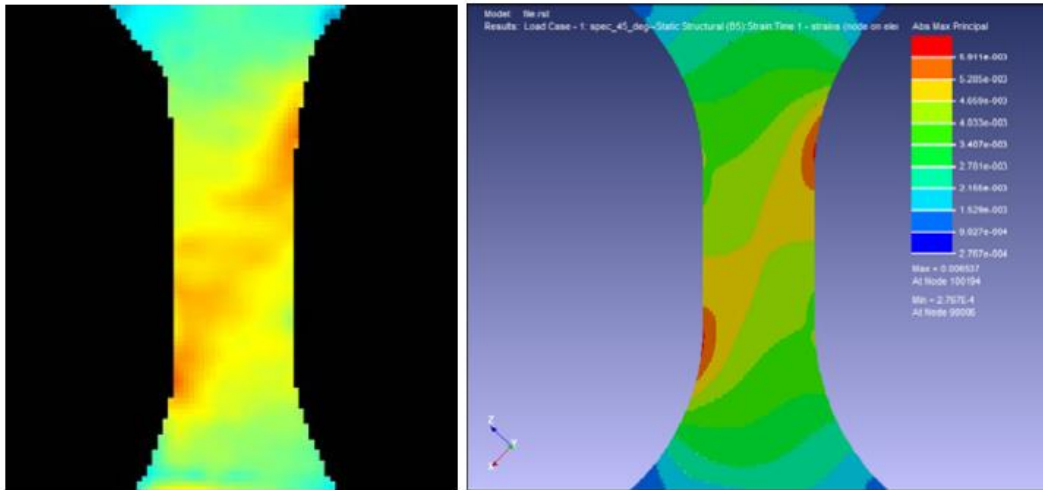


Figure 2-28 Comparison of strain field from DIC (left) and FEA (right). Showing range of largest principal strain [55].

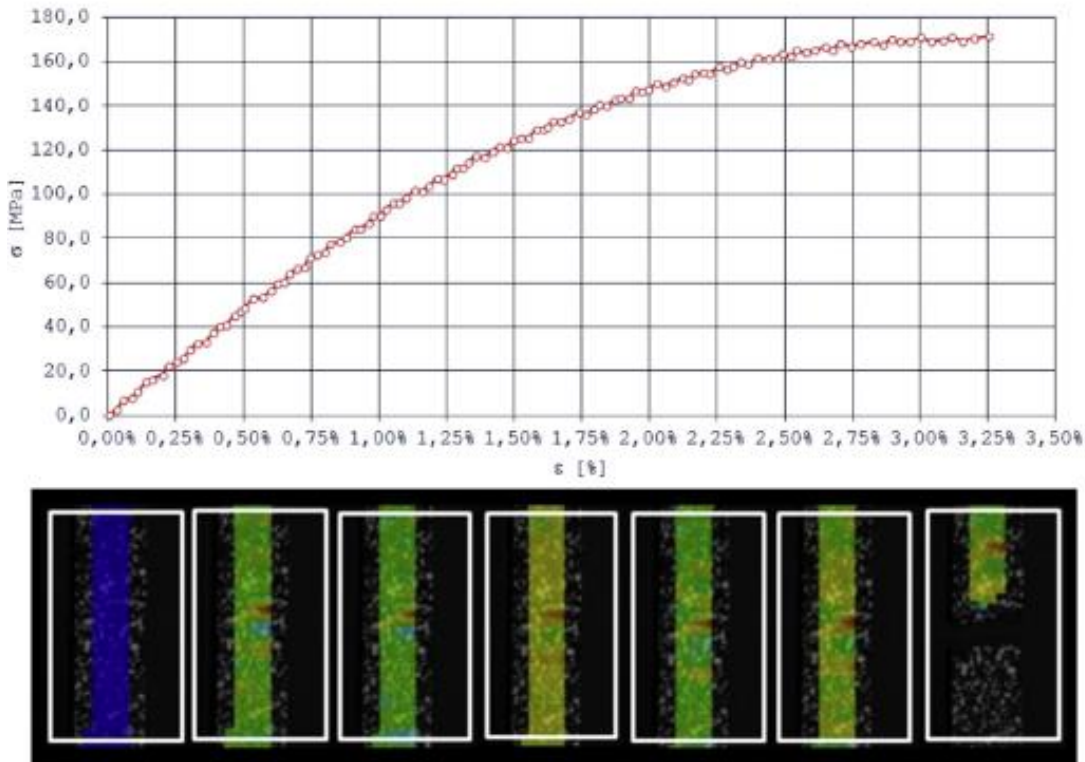


Figure 2-29 "Stress-strain curve and DIC images for a static tensile test" [56].

2.4.1 Fibre length effect

The fibre length in composites has been shown to present an effect on the overall response of the material. In an investigation conducted by Sasayama et.al. [16], on two different PA66 reinforced specimen types, Figure 2-4a, showed that the fibre length had an effect on the quasi-static Stress-Strain curve of the material. In Figure 2-30 it can be seen that, for both specimens type, longer fibres presented higher tensile strengths; while at the same time showing lower strain-at-break. In average, in Type 1 specimens, fibres were 40% larger in the long glass fibre coupon (LGF), in comparison to the short glass fibre one (SGF). On the other hand, for Type 2 specimens, LGF presented an average fibre length of 59% higher than the ones in the SGF coupon. Similar Stress-Strain behaviour was seen by Hitchen et.al. [57], on short fibre reinforced epoxy. Specimens with three different fibre lengths were investigated, 1, 5 and 15mm. As it can be seen in Figure 2-31, the longer the fibre, the stiffer the response and higher final strength was achieved. On the other hand, the shorter the fibres the higher strain-at-break was obtained, with a behaviour seemly more ductile. In particular, this change of the tensile strength was investigated by Miwa and Horiba [58], on two different type of short fibre reinforced epoxy composites: short glass fibre samples and short carbon fibre samples. Results of the variation of the tensile strength with the fibre length, and with the temperature, can be seen in Figure 2-32a and b. From this figure it can be seen that, as expected, in neat resin the change in strength is only due to the temperature. For the case of the short carbon and short glass fibre samples, the longer the fibre the higher the strength, but a plateau is rapidly reached at approximate 1mm length. The effect of the temperature can also be seen in this figure, and again as expected, at higher temperatures the strength rapidly drops.

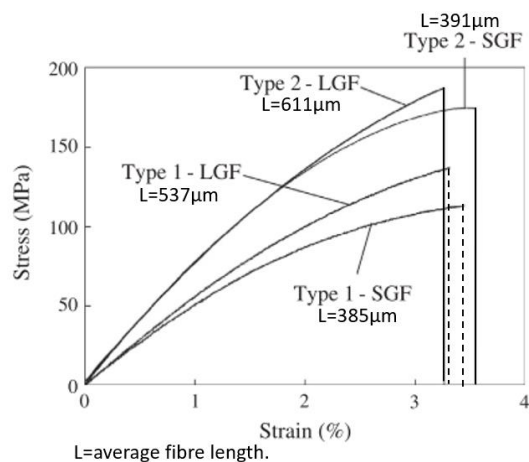


Figure 2-30 Variation of the Stress-Strain response with fibre length for two sample types of reinforced PA66 (adapted from [16]).

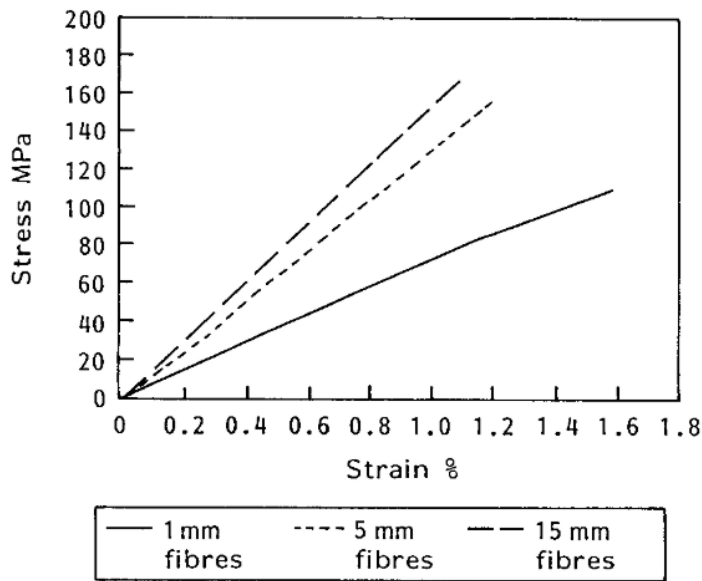


Figure 2-31 Typical stress-strain curves for short carbon fibre reinforced epoxy containing 1, 5 and 15 mm length fibres [57].

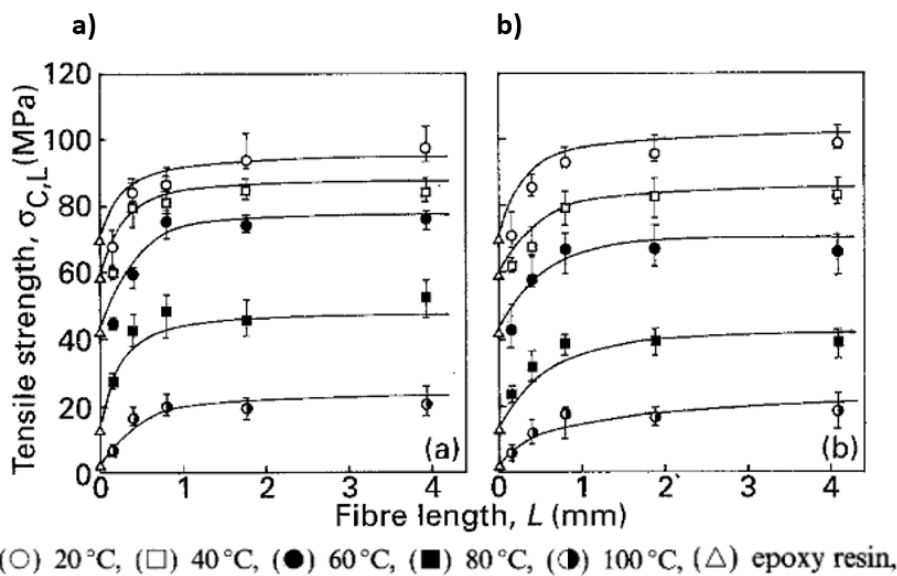


Figure 2-32 Relation between fibre and tensile strength for a) carbon fibre – epoxy resin composite; and b) glass fibre-epoxy resin composite [58].

2.4.2 Humidity, strain rate and temperature effects

Under monotonic conditions, SFRP's material response is also heavily influenced by the level of humidity (water) in the matrix. Carrascal et. al. [59], conducted an experimental study on glass fibre reinforced nylon (PA6) to evaluate this effect. Both the water-bath temperature and the immersion time were controlled during the

experiment. Results of this work showed that PA6 is highly susceptible to water absorption. Figure 2-33a presents the effect in terms of tensile mechanical properties that different percentage of humidity content had in the SFRP, showing a negative relationship with increased humidity up to saturation. Figure 2-33b shows the percentage levels of saturation for different glass fibre reinforcement (0, 25 and 35wt%) when submerged in a water bath at 40°C. The higher the amount of reinforcement (GF35) the lower the maximum amount of water absorption due to the decrease in the total volume of hygroscopic matrix in the composite [59].

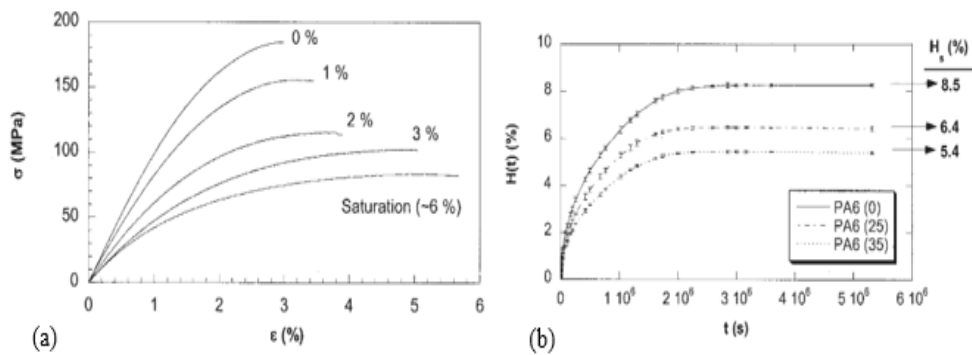


Figure 2-33 "a) Influence of humidity content of a reinforced polyamide on mechanical behaviour (static tensile test) b) Humidity evolution for different reinforcing materials in water at 40°C" [59].

In terms of the effect of loading rates, Glaser and Wust [60], conducted uniaxial tensile testing on unreinforced and reinforced nylon, PA6 and PA6GF30 respectively, at displacement rates between 5 and 50mm/min (strain rates between 10^{-3} /s and 10^{-2} /s). Figure 2-34 shows the different behaviours observed between the pure matrix and the reinforced composite. It can be seen that for both materials the strain rate has an effect on the material response due to the matrix viscous behaviour, although this is more significant for the case of the reinforced plastic. The matrix is also softer and more ductile, whereas the composite is significantly stiffer and tough, which is the expected effect of the fibre reinforcement. The level of anisotropy can also be seen in the case of the reinforced plastic, where longitudinally cut samples were stronger.

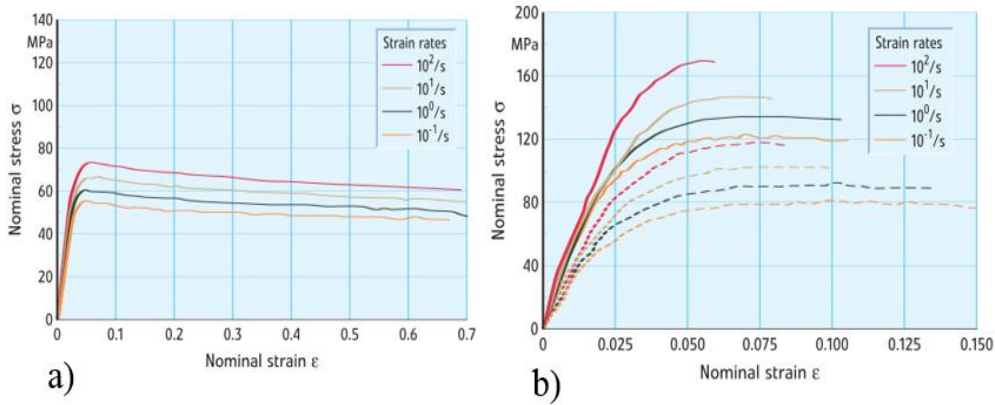


Figure 2-34 Nominal stress-strain curve for a) unreinforced and b) reinforced polyamide 6 (PA6GF30) at different strain rates. Dotted: sample transversally to injection flow direction. Solid: sample longitudinally [60].

Wang et. al. [61] investigated the combined effect of temperature and strain rate on short type E glass fibre and nylon-6 composite sheets at 21.5, 50, 75 and 100°C; and 0.05, 0.5 and 5min⁻¹, respectively. Results of this work presented in Figure 2-35, showed that the material is dependent of both conditions and that the tensile strength and modulus increased with strain rate and decreased with temperature. The glass transition temperature showed to have a clear effect in the material response in a region between 50 to 75°C. Similar results were seen in [20] on short glass fibre and rubber reinforced nylon-6. Specimens were cut from plates at different orientations, 0 (along extrusion), 90 (normal to extrusion) and 45°, per Figure 2-36a. It showed the effect of the temperature and displacement rate in the material, in particular at colder temperatures where higher tensile strengths were seen [20], as shown in Figure 2-36b. Specimens cut at 45° also presented higher levels of ductility.

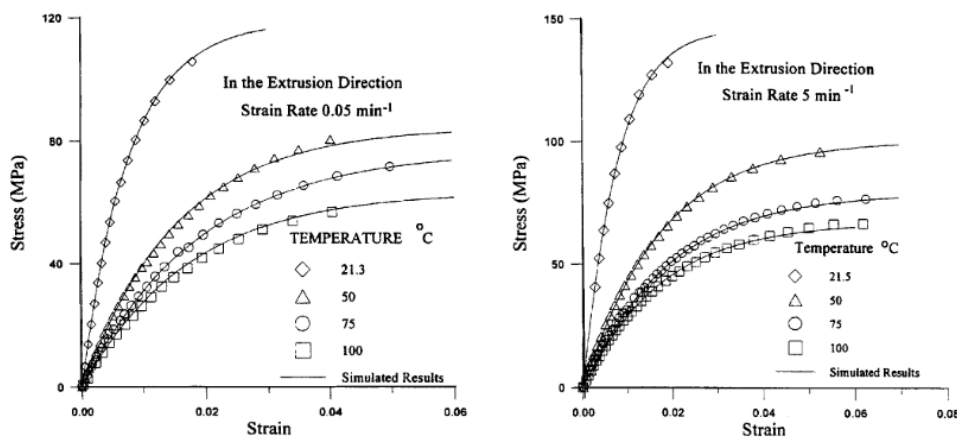


Figure 2-35 Effect of temperature on tensile curves of a SFRP at different strain rates [61].

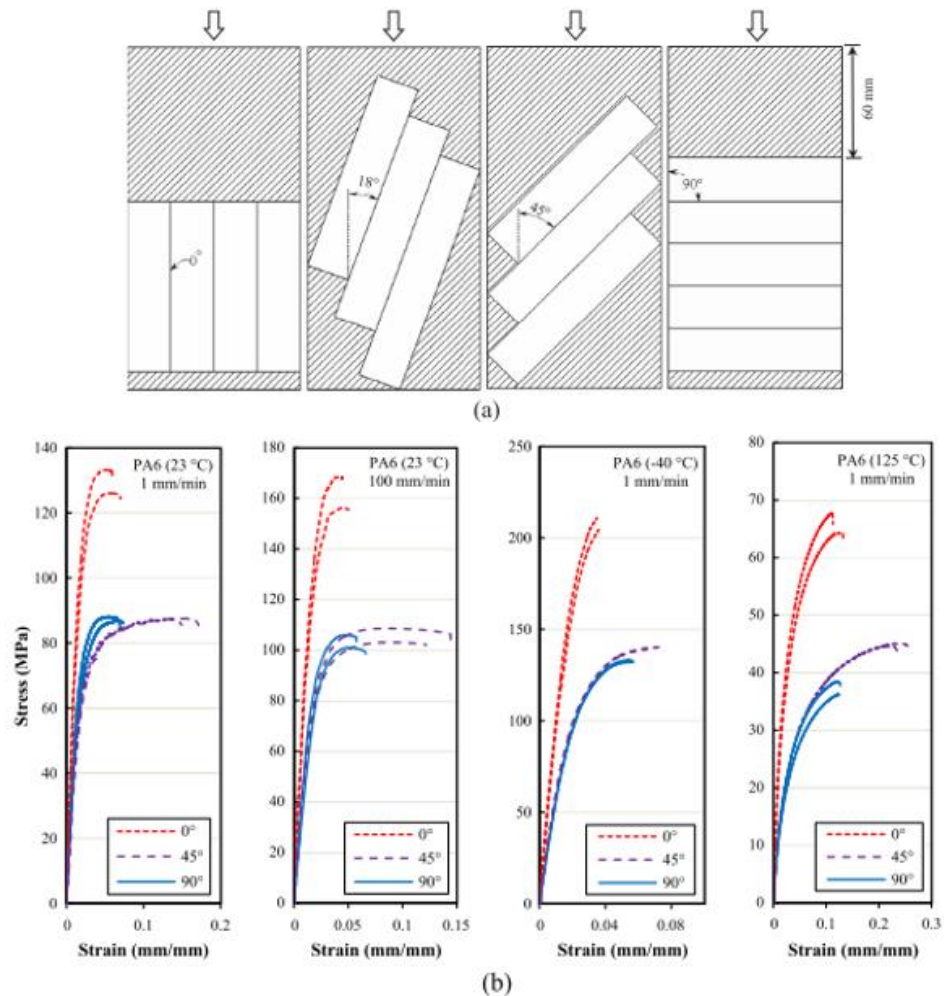


Figure 2-36 "a) Direction and location of specimens cut from injection moulded plates (arrows indicate the injection moulding direction and the dashed areas are the discarded materials. b)Tensile curves showing effect of anisotropy at different temperatures and displacements rates for polyamide-6" [20].

2.4.3 Modelling monotonic behaviour of SFRP's

Different methodologies have been proposed to model the monotonic response of SFRP's. In a work by Mortazavian and Fatemi [20] several models were compared against experimental results in terms of elastic modulus and tensile strength. Two different SFRP's were used, as well as, specimens oriented in the longitudinal, transverse and 45° directions. Results of this comparison, in terms of elastic modulus, are shown in Figure 2-37. Predicted values using Halpin-Tsai (H-T) [62], originally proposed for unidirectional oriented plies, were in the order of 12% and 47% higher than the experimentation for longitudinal specimens; and between 45% and 15% lower for the transversal specimens. This difference was concluded to be due to the inability of the H-T model to deal with the fibre orientation distribution in SFRP's, as

well as, with the stochastic variation of fibres' aspect ratios. A modified linear rule of mixtures, including a fibre orientation factor and a fibre length factor [63], was also used to estimate the longitudinal elastic modulus. Again a large divergence between prediction and experimentation was seen for both composites. A laminate analogy approach (LAA) [64], was used to estimate the longitudinal and transverse elastic modulus. This modelling methodology provided with the closer predictions in comparison to other models. Similarly, based on experiments done on short glass fibre reinforced nylon-6 at different temperatures and strain rates, Wang et. al. [61] developed empirical relationships to fit the tensile modulus and strength, as shown in Figure 2-38a. Where E , σ_{b0} , ϵ^* and T_0 are reference elastic modulus, reference tensile strength, reference strain rate and reference temperature, respectively. Two additional coefficients were defined for better fit, m and λ , named strain rate strengthening coefficient and thermal softening coefficient, respectively. Results, Figure 2-38b, showed good initial correlation with data, although highly depend of m and λ . It also showed a noticeable difference in properties depending of the direction tested, along or normal to the extrusion direction. Finally, it is also good to mention that in [54] it was seen that the classical Ramberg-Osgood non-linear relationship was adequate to fit the experimental data on both non-reinforced polymers and short glass-fibre reinforced, to a certain extent.

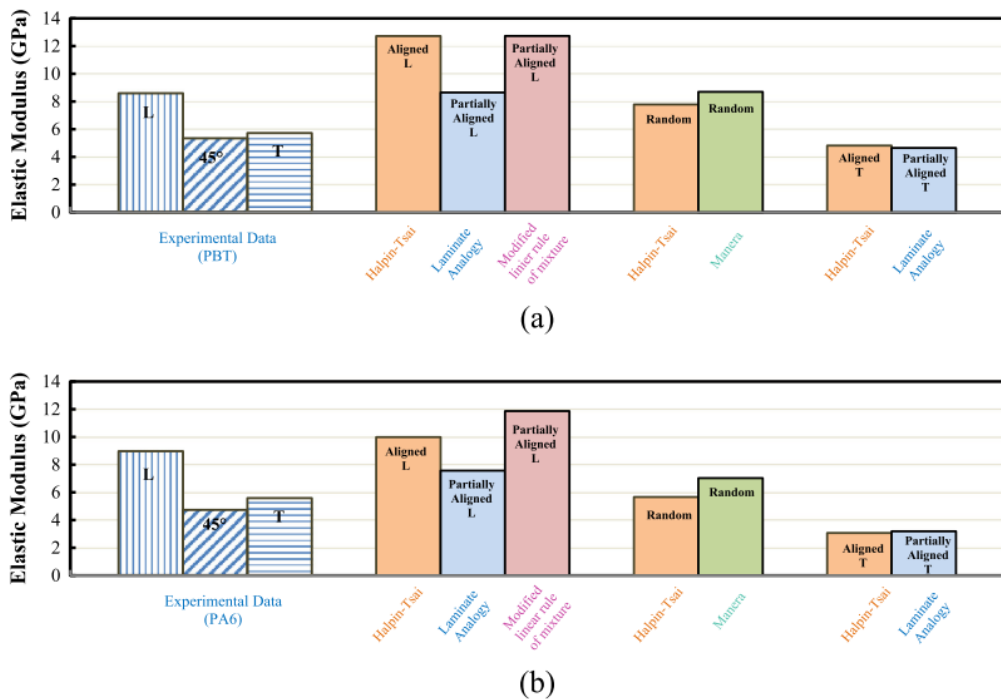


Figure 2-37 "Comparison of experimental elastic modulus values in the longitudinal, transverse and 45° directions at displacement rate of 1mm/min and predictions models for a) polybutylene terephthalate with 30wt% glass fibre

(PBT) and b) polyamide-6 with 35wt% glass fibres and 10 wt% rubber (PA6)" [20].

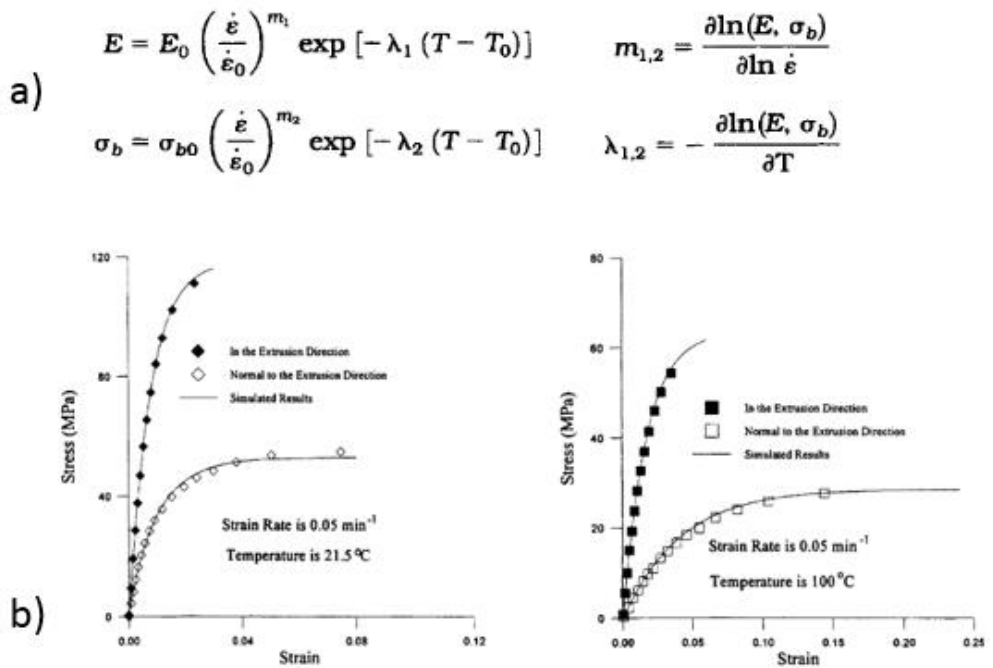


Figure 2-38 a) Proposed empirical relationships for tensile strength and Young's modulus. b) Comparison of stress-strain curves of a PA6-SFRP at different directions, at strain rate 0.05min⁻¹ and at different temperatures [61]

2.4.3.1 Multi-scale modelling

Continuum mechanics assumes the uniformity of the material (stresses and strains within an infinitesimal section are uniform) at any point, macro-elements. This is not the case on the microscopic level, where infinitesimal material regions are not uniform and are formed by constituents of different properties and shapes with their respective stresses and strains, micro-elements. Therefore, to represent the continuum mechanics response using parameters that describe the microstructure and properties at the microscopic level a representative volume element, or RVE, was introduced, which is an statistically meaningful representation of the infinitesimal material region [65]. This modelling methodology based on micromechanics or multi-scale approach, tries to predict the macro composite response based on the influence of the microstructure [66]. A schematic of the macro and micro-elements is depicted on Figure 2-39.

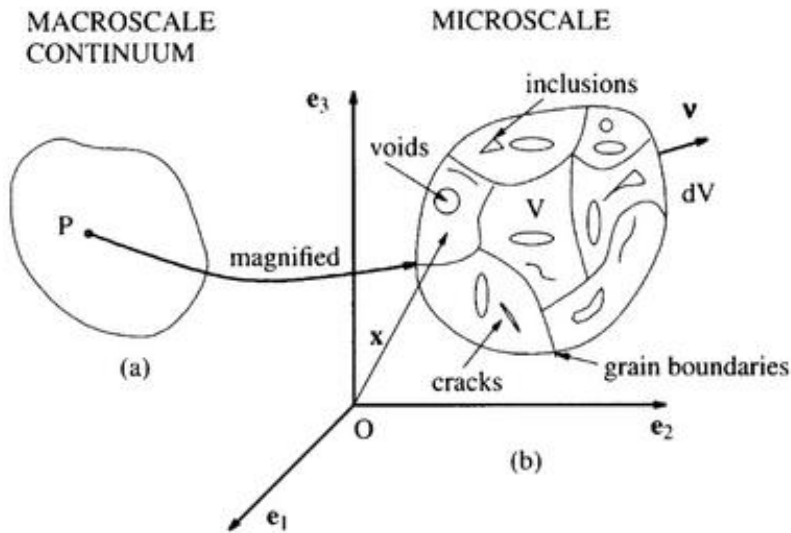


Figure 2-39 a) P is a material point or material element surrounded by a material neighbourhood, i.e., a macro-element. b) Possible microstructure of an RVE for the material neighbourhood of P [65].

Homogenization techniques aim to represent the overall properties of the heterogeneous solid with the characteristic that any suitable subvolume can be used as and RVE to obtain the overall macroscopic parameters [65]. In simpler terms, for the case of linear elasticity, it would mean finding an equivalent homogenous material, such that its overall macro stiffness is equivalent to the real heterogeneous composite under the same boundary conditions [66].

Eshelby [67] based mean-field homogenization models are widely use. In general, it describes the strain changes observed in a solid infinite material when a single ellipsoidal shape is cut and welded back, such that:

$$\boldsymbol{\varepsilon}(\mathbf{x}) = \boldsymbol{\zeta}(\mathbf{I}, \mathbf{C}_0) : \boldsymbol{\varepsilon}^*, \quad \forall \mathbf{x} \in (\mathbf{I})$$

Equation 2-6

Where, $\boldsymbol{\varepsilon}^*$ is a stress-free eigenstrain, $\boldsymbol{\zeta}(\mathbf{I}, \mathbf{C}_0)$ is the Eshelby's tensor, depending on the uniform stiffness (\mathbf{C}_0) and the shape and the orientation of the ellipsoidal volume (\mathbf{I}) [66]. For the case of two-phase composite, one matrix and one fibre/inclusion type, two models are commonly used: the Mori-Tanaka [68] (M-T) model; and the double inclusion (D-I) model proposed by Nemat-Nasser and Hori [69].

For the particular case of the Mori-Tanaka model. Benveniste [70] proposed, and is further explained in [66], that M-T describes the behaviour of each inclusion as an isolated particle in the matrix, thus reducing the overall problem to the Eshelby's single

inclusion model. Therefore, the solid is infinite and is subjected to the average matrix strains in the real RVE as in the far field strain. A depiction of this is shown in Figure 2-40. A very simple application of this model methodology is shown in Figure 2-41, where Lindhult and Miranda [71], used M-T as means calibrate a linear-elastic model for PA6GF30 composite, good correlation can be observed in terms of elastic properties. A similar application was also carried out by Heyes [55] on injection moulded coupons. An heterogeneous distribution of the largest principal stress through the thickness was observed, which depended on the orientation of the sample, as is shown in Figure 2-42. It is also good to mention that although the M-T approach is widely used to model SFRPs properties, it is not without limitations. In a work by Bohm [72], it was shown that M-T methodology assumes that the inhomogeneities can be described as perfect ellipsoids that keep their aspect ratio throughout the complete deformation history, so in composites with a high void content, or highly porous, it would tend to overestimate the resultant material stiffness. Similarly, in two-phase composites where the reinforcement is significantly stiffer than the matrix, the prediction of the elastic moduli are always on the low side. On the other hand, if the reinforcement is more compliant in a stiffer matrix, the estimated moduli are on the higher side.

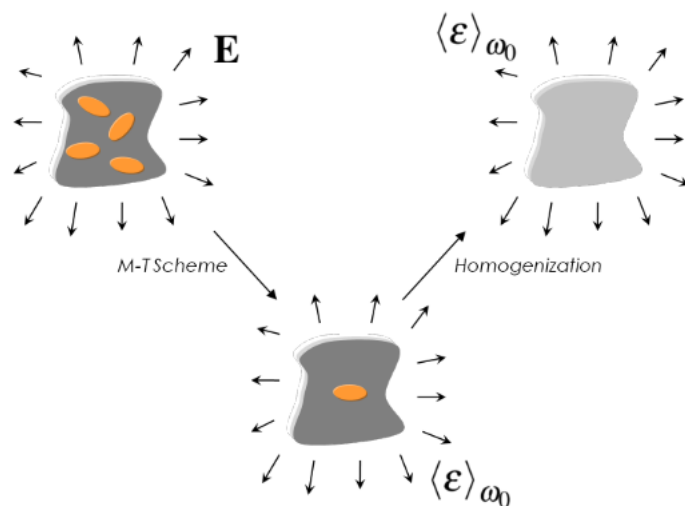


Figure 2-40 Depiction of Mori-Tanaka technique [66].

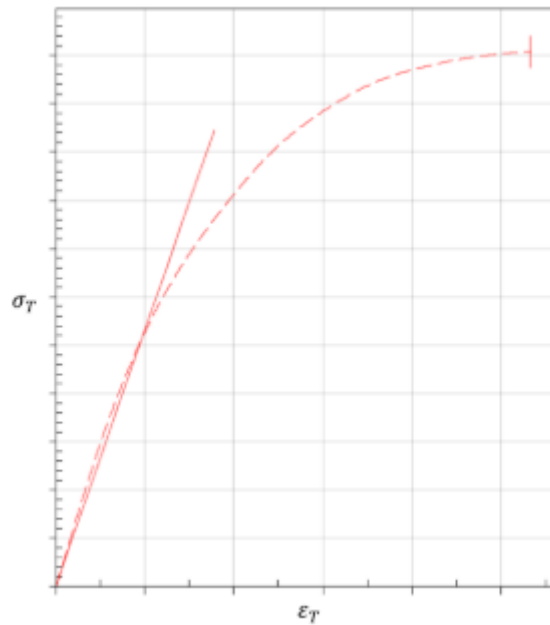


Figure 2-41 "Calibration of linear elastic material model to tensile test expressed in true stress-strains. Dashed lines correspond to experimental data and solid lines represent the calibrated elastic material response of the SFRP" [71].

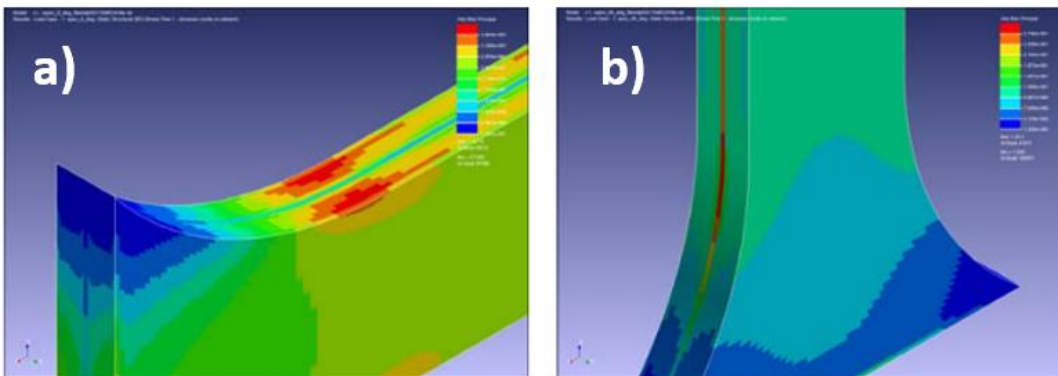


Figure 2-42 Stress contours showing the largest principal stress on a a) 0° specimen (parallel to the mould flow) and b) 90° specimen (transversal to the flow) [55].

2.5 Fatigue behaviour of SFRP's

2.5.1 Summary of fatigue concepts and stress-life approach.

During the 1800's, August Wöhler formulated the idea of representing the fatigue loading against the total number of cycles to failure to quantify the results of his experiments, with the only requirement of the cycles up to failure and the alternating

stress [14]. Figure 2-43 presents the typical representation of a constant amplitude cyclic testing.

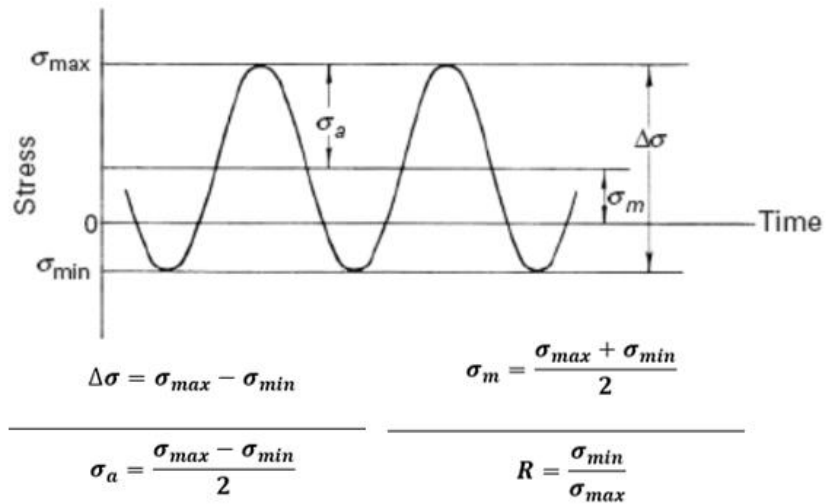


Figure 2-43 Constant amplitude testing and definition of cyclic stress concepts [73].

In 1910, Basquin established that the material fatigue life increases, as a power law, when the stress amplitude decreases [74]. Therefore this relationship can be described, in terms of the cyclic stress, as a power function of the form:

$$\sigma = \sigma_o \cdot N^{-\frac{1}{k}}$$

Equation 2-7

Where σ represents any cyclic stress like: stress amplitude, stress range, maximum stress, etc. and N is the number of cycles before failure for that cyclic stress. σ_o denotes the fatigue coefficient which is defined as the intercept at 1 cycle, and $-\frac{1}{k}$ is the slope of the resultant power function curve, and is related to the material. Ranges for the slope has been documented the literature [74], to vary between 0.04 to 0.15, with lower values for unidirectional carbon and higher for multidirectional glass fibre composites. One of the main limitations of this approach, is that this type of relationships are purely empirical and therefore do not have any direct physical meaning, which means that the best S-N curve for a given material is just the one that can best fit the available experimental data. Finally, if required, a further transformation can be carried out to define Equation 2-7 in terms of the life cycles, if:

$$\sigma \cdot N^{\frac{1}{k}} = \sigma_o$$

$$\left(\sigma \cdot N^{\frac{1}{k}}\right)^k = (\sigma_o)^k$$

Therefore

$$\sigma^k \cdot N = \sigma_o^k$$

And if

$$C = \sigma_o^k$$

Therefore the relationship can be written as:

$$N \cdot \sigma^k = C$$

Equation 2-8

2.5.2 Cyclic behaviour of short fibre reinforced polymers

2.5.2.1 Effects of fibre orientation anisotropy

Similarly to monotonic conditions, material response of SFRP's under cyclic loading is depended of the distribution and individual behaviour of the constituents. In particular, fibre orientation distribution have a large effect on the fatigue performance of SFRP's.

A study conducted by Malo et. al. [3], carried out fatigue testing on Nylon-66 reinforced with 35wt% short glass fibre composites, from where specimens at different orientations (0°, 30° and 90°) were tested under fully reverse loading conditions (R=-1) at 3Hz and at ambient temperature. Specimens' buckling was controlled via precise alignment of the grips through a specialized alignment fixture. From the results shown on Figure 2-44, 0° presented with the highest life at this conditions, several orders of magnitude in comparison to the other orientations. Whereas, no significant difference could be seen between 30° and 90° specimens. A similar response was observed by Fatemi et. al. [75], on a polybutylene terephthalate (PBT) reinforced with 30wt% short glass fibre composite. Dog-bone specimens were cut at 0°, 18°, 45° and 90° orientations from injection moulded plates. Fully reverse fatigue testing was done at ambient temperature. Again as in the previously mentioned work, 0° specimens showed the largest life, and more importantly, no significant difference was observed for specimens at 45° and 90°, as it is shown in Figure 2-45. Additionally, in [76] fatigue testing was also carried out at R=-1 and at R=0 on PA66GF35 oriented specimens (0°, 30° and 90°) at room temperature and with frequencies between 5-10Hz. Results of the material characterization can be seen in Figure 2-46, from where similar results to

the previous cited work were found, including positive stress ratios. Finally, Fouchier et. al. [77], conducted similar uniaxial fatigue testing on a PA66GF30 composite at two different stress ratios, $R=0.1$ and $R=-1$, but at a higher temperature. Results, presented in Figure 2-47, shown that the fully reverse loading has a particular effect on the fatigue behaviour of 45° and 90° coupons, with lives very close to each other. From these works it is then clear that, in terms of fatigue performance, there is a high dependence on the fibre orientation and mould flow direction. The specimens with closer orientation to the flow direction, i.e. 0° , showed higher endurance limits in all cases.

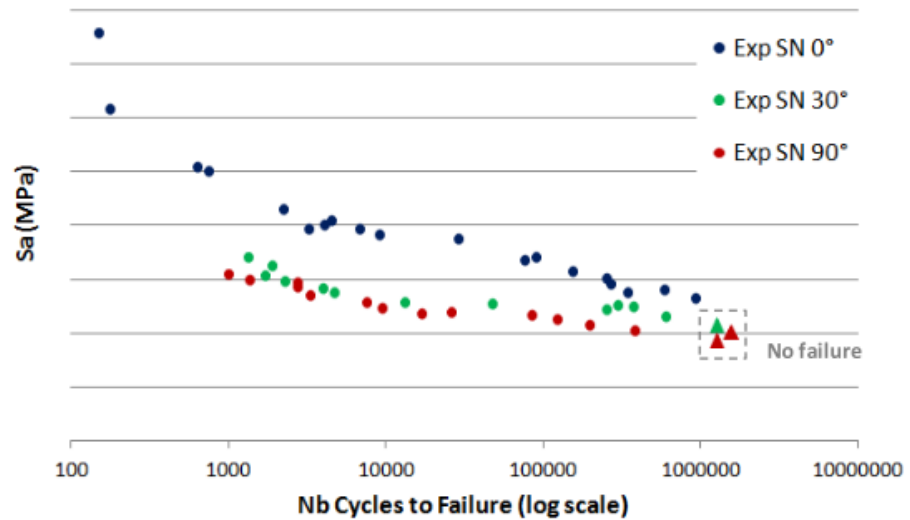


Figure 2-44 Tensile-compression ($R=-1$) stress-life (SN) curves measured at 23°C and at 0° , 30° and 90° on PA66GF35 [3].

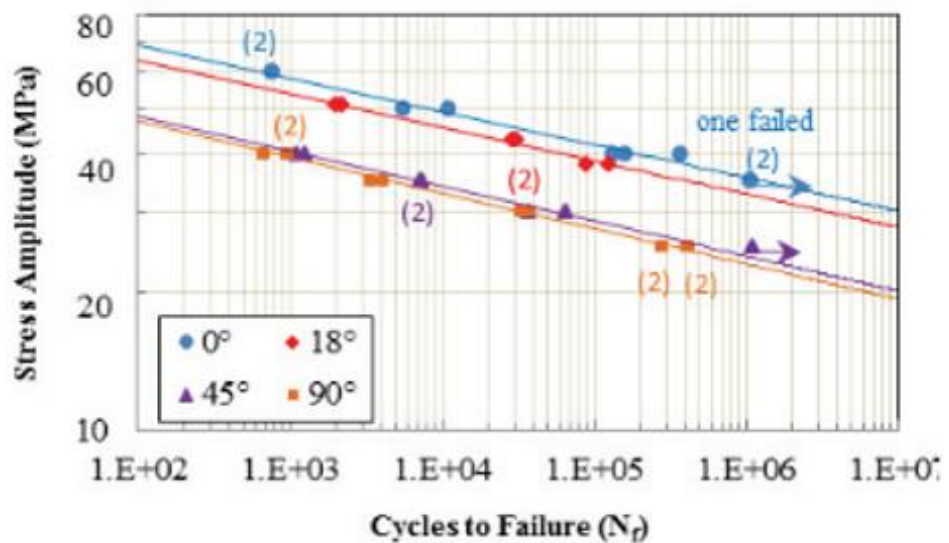


Figure 2-45 Effect of the flow direction on the fatigue life of PBTGF30 at 23°C and under $R=-1$ [75].

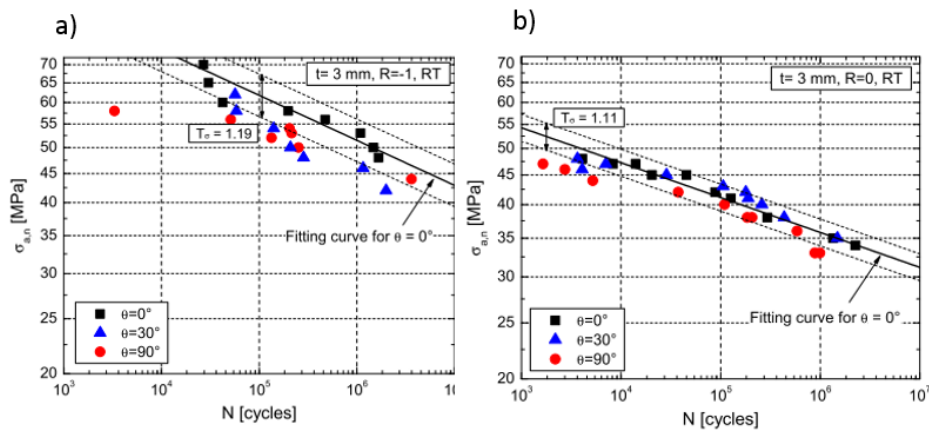


Figure 2-46 Uniaxial fatigue curves at room temperature for PA66GF35 at a) R=-1 and b) R=0 for thickness= 3mm at different orientation angles ($\theta=0^\circ$, 30° and 90°) [76].

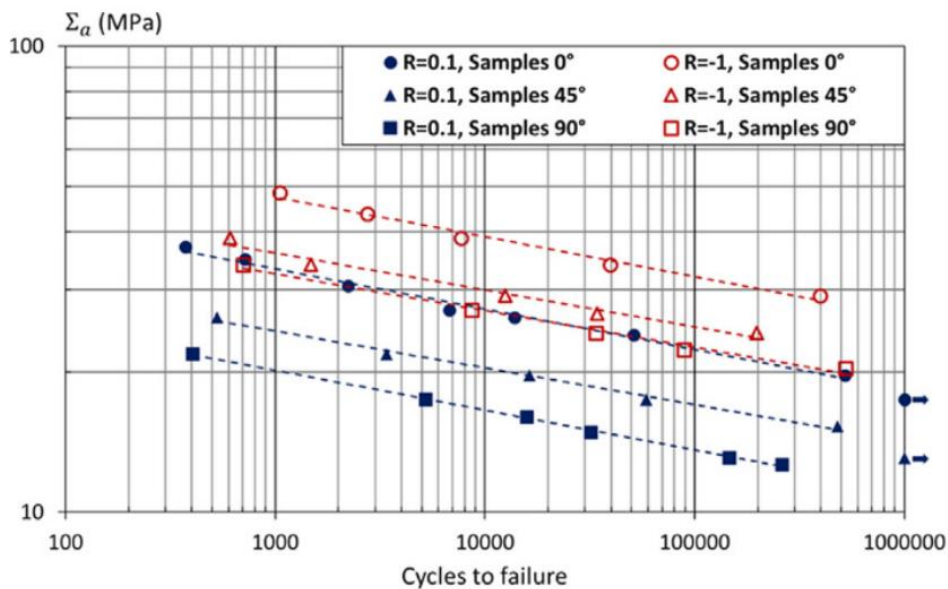
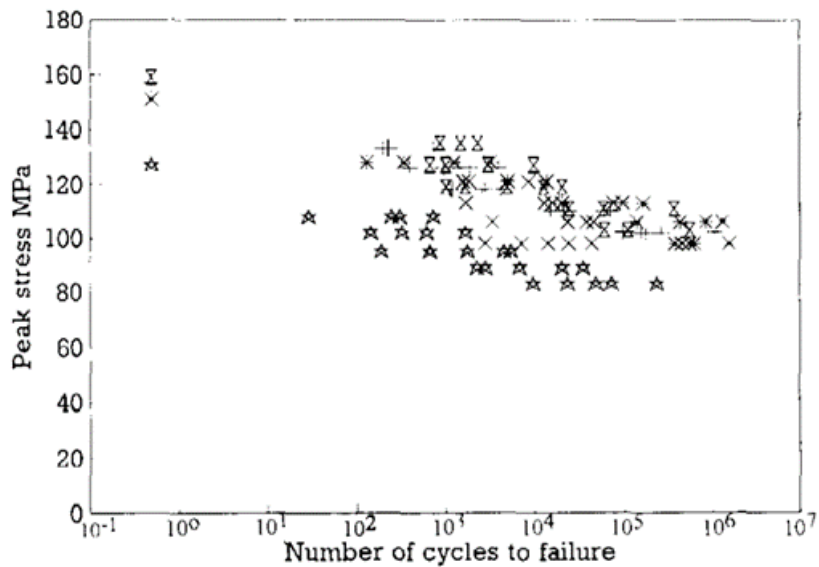


Figure 2-47 Stress-Life curves at 110°C for three sample orientations (0° , 45° and 90°) and at $R=0.1$ and $R=-1$ [77].

2.5.2.2 Fibre length effect

The fatigue performance of short fibre reinforced composites is also affected by the fibre length. In a work by Hitchen et.al. [57], conducted on short fibre reinforced epoxy, tension-tension fatigue test was carried out on material reinforced with 1, 5 and 15mm fibres. Results, of this experimentation suggested that higher fatigue lives were achieved with longer fibres at a given peak stress, as shown in Figure 2-48. On this image, a variation of the fatigue life can be seen between the different fibre lengths, 1, 5 and 15mm, with the later one presenting better fatigue strength. Interestingly, the effect seems to be related to the length and not so much to the fibre content, as

results for the same fibre length but different volume fraction seem to be closer to each other, i.e. similar lives for 15mm with $V_f=19.8\%$ and 15mm with $V_f=18\%$. This effect of the fibre length was also investigated by Lavengood and Gulbransen in [78], where flexural fatigue testing, with positive stress ratio, was conducted on short boron fibre reinforced composites. Fibres of 4, 1, 0.5 and, 0.25 inches (101, 25.4, 12.7 and 6.37 mm, respectively) were used for this investigation. Figure 2-49a and b show the results in terms of Life-Stress curves (where the stress was normalised to remove the bias caused by dissimilar strengths), and the variation of the fatigue life with the aspect ratio of the fibres. These figures suggest that the fatigue life of the material increases with the length and aspect ratio of the fibres, which is also dependent of the length. At the same level of stress, specimens with shorter fibres have significant lower fatigue resistances. From Figure 2-49b is also interesting to see that a plateau is reached in terms of the aspect ratio, and as the difficulty of composite fabrication increases with the aspect ratio, it is therefore suggested to use the lowest aspect ratio possible. The level of self-heating in the material was also affected by the fibre length, as investigated by Subramanian and Senthilvelan [79]. In this work, uniaxial fatigue testing at $R=0$ was conducted on short fibre reinforced polypropylene. Three type of specimens were used: neat unreinforced resin, reinforced resin with fibres of 0.28mm in average length (SFPP), and of 1.38mm in average length (LFPP). Results of the surface temperature, presented in Figure 2-50, show that for the pure resin the heat build-up was purely due to the hysteresis of the matrix. When the reinforcement is included, the self-heating is also increased due to the stress concentration effect at the fibre ends and due to friction between the fibre and the matrix. It was also suggested, that the reason the shorter fibres seems to increase the temperature higher than longer fibres was due to the relatively larger number of fibres present in any given volume of material.



* 15mm fibre, Vf=19.8% x 15mm fibre, Vf=18.0% Δ 5mm fibre, Vf=22.5%
 × 5mm fibre, Vf=17.5% ☆ 1mm fibre, Vf=14.1%

Figure 2-48 Peak stress-fatigue life data for composites with 1, 5 and 15 mm length fibres [57].

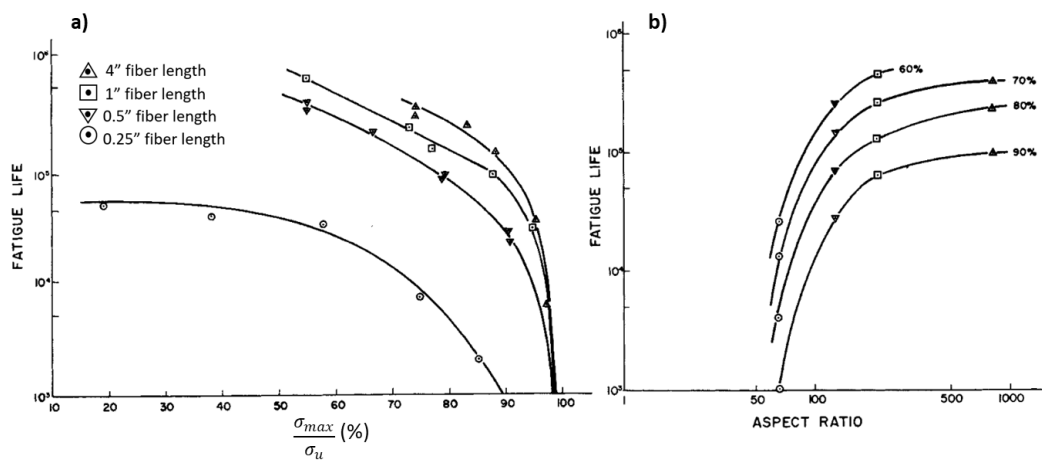


Figure 2-49 a) Variation with fibre length of the cycles to failure vs normalised stress. b) Cycles to failure vs fibre aspect ratio for an applied stress of 60, 70, 80 and 90% UTS [78].

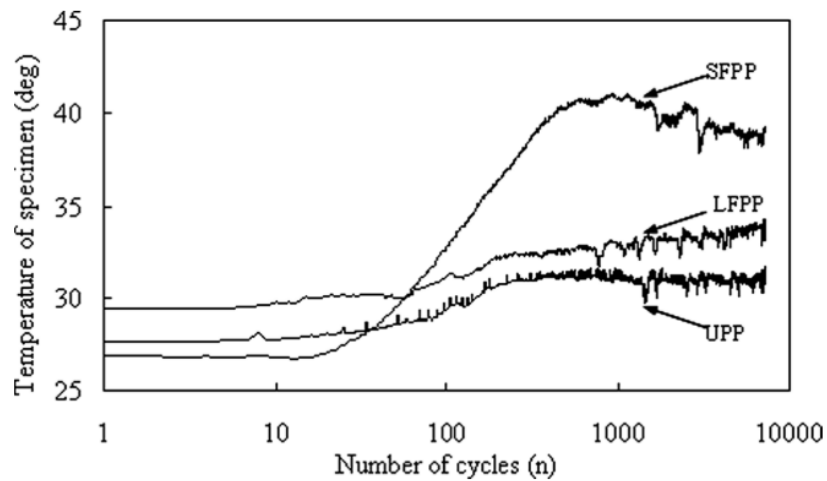


Figure 2-50 Variation of the surface temperature of polypropylene for: unreinforced neat resin (UPP), reinforced with long fibres (LFPP) and reinforced with short fibres (SFPP) [79].

2.5.2.3 Cyclic response of SFRP's

Material response under cyclic loading is of important analysis for the study of SFRP's fatigue performance. A clear effect in terms of the evolution of strain has been seen on cyclic non-zero mean stress loading conditions. Under these type of loading a progressive accumulation of deformation occurs, this is also known as ratcheting [80]. Work done by Ahmadzadeh and Varvani-Farahani [81], in short glass-fibre reinforced polymers, exhibited the evolution of ratcheting thought the life of the material. This work showed that as stress amplitude increases so does the ratcheting strain resulting on smaller lifespans, as seen Figure 2-51. Shifting of the hysteresis curves, due to strain accumulation, was observed by Launay et. al. [82] on PA66GF35 composites during R=0 fatigue testing. A rapid shift, and thinning, in the hysteresis loops is seen corresponding to a reduction in the dissipated energy density (hysteretic area). Material softening was also observed. The residual strain, indicator of accumulation of viscoplastic strain, was seen to reach a linear positive gradient within initial stages of the life of the material; this is presented in Figure 2-52. A similar behaviour was seen by Serrano-Abello et. al. [83], for this work the focus was at the beginning of the life on a SFRP with PA66. Cyclic testing was carried out at R=0 and 1Hz under different loading stress amplitudes. Material was conditioned under a humidity ratio of 50%. As is shown in Figure 2-53, a shift in the hysteresis loop was seen, residual strain. A rapid reduction in the hysteresis area is also observed right at the beginning of the life in

the specimens up to around the fourth cycle from where a steady state is reached, again this corresponds to a reduction in the material energy dissipation.

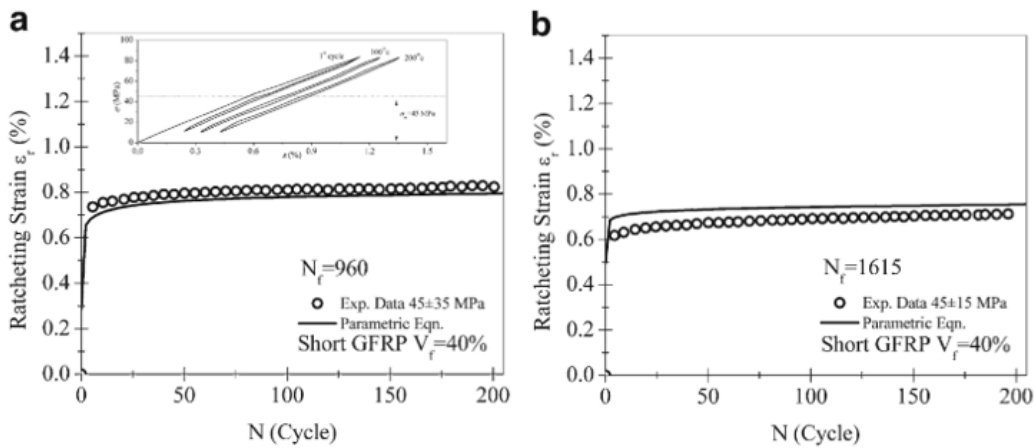


Figure 2-51 "Calculated and experimental ratcheting strain values over stress cycles for short fibre GFRP with $V_f=40\%$ at a) $45\pm 35\text{MPa}$ and b) $45\pm 15\text{MPa}$ "

[81].

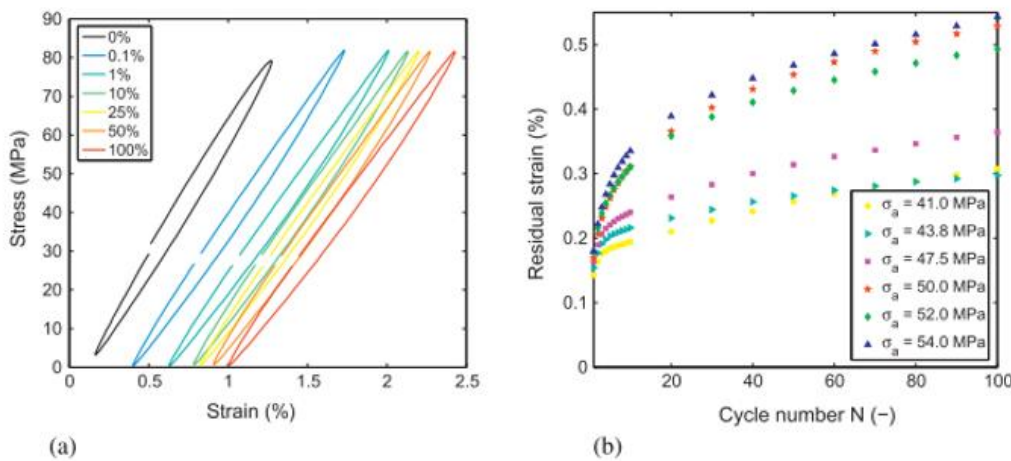


Figure 2-52 "Evolution of mechanical response during fatigue life (expressed in percentage of lifetime) of PA66GF35 under stress-controlled sinusoidal loading.

a) Stress-strain response during fatigue testing. b) Residual strain" [82].

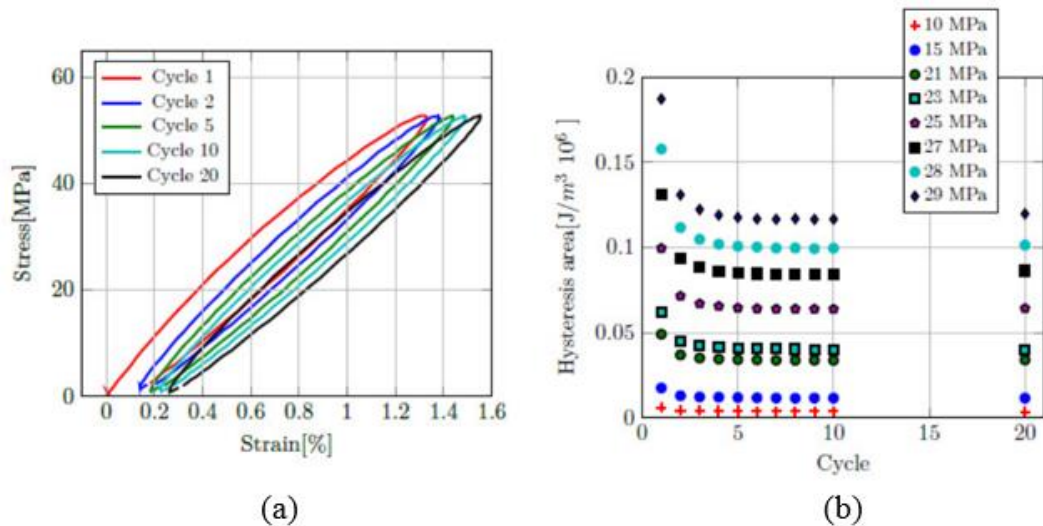


Figure 2-53 a) Stress-strain curves for a loading step. b) hysteresis area evolution [83].

Similarly to monotonic conditions, humidity (matrix water absorption) has a large effect in the material behaviour under cyclic loading. Analogue to the reduction in tensile strength in quasi-static loading; under wet conditions toughness and overall fatigue strength is significantly reduced. An example of this is presented in [84] for dry and wet short glass fibre reinforced PA6 composites. For dry conditions, the specimens were desiccated at 80°C for 6 hours prior to testing. For wet conditions, the specimens were immersed in a room-temperature water bath between 1 and 140 days prior to testing. The material was seen to follow Fick's law for moisture absorption [85]. The effects of water content in the matrix were significant in both low cycle fatigue (LCF) and high cycle fatigue (HCF) regions, as it can be seen in Figure 2-54c.

Additionally, under the same cyclic stresses, wet samples presented larger stress-deformation loops, Figure 2-54a and b, which was hypothesized to be due to a plasticizing effect of the water in the matrix, this was not seen on dry specimens. Effect of the hygrometric state, level of water absorption, on mechanical properties of SFRP's was also observed by Benaarbia et. al. [86] in terms of strain accumulation on a short fibre reinforced PA66 composite. 0°, 45° and 90° oriented specimens were used. Testing was carried out at 10Hz. Figure 2-55 shows the results obtained for the different oriented specimen at different levels of relative humidity (RH). Progressive mean strain accumulation was seen with drifting of the hysteresis loop with fatigue cycles, which seemed to be sensitive to the humidity level. Ratcheting did not reach a stabilized state and the trend was altered depending the water content, as well as, the

fibre configuration. In terms of fibre orientation, hysteresis loops in 0° seemed to be thinner in comparison to 45° and 90° for all humidity.

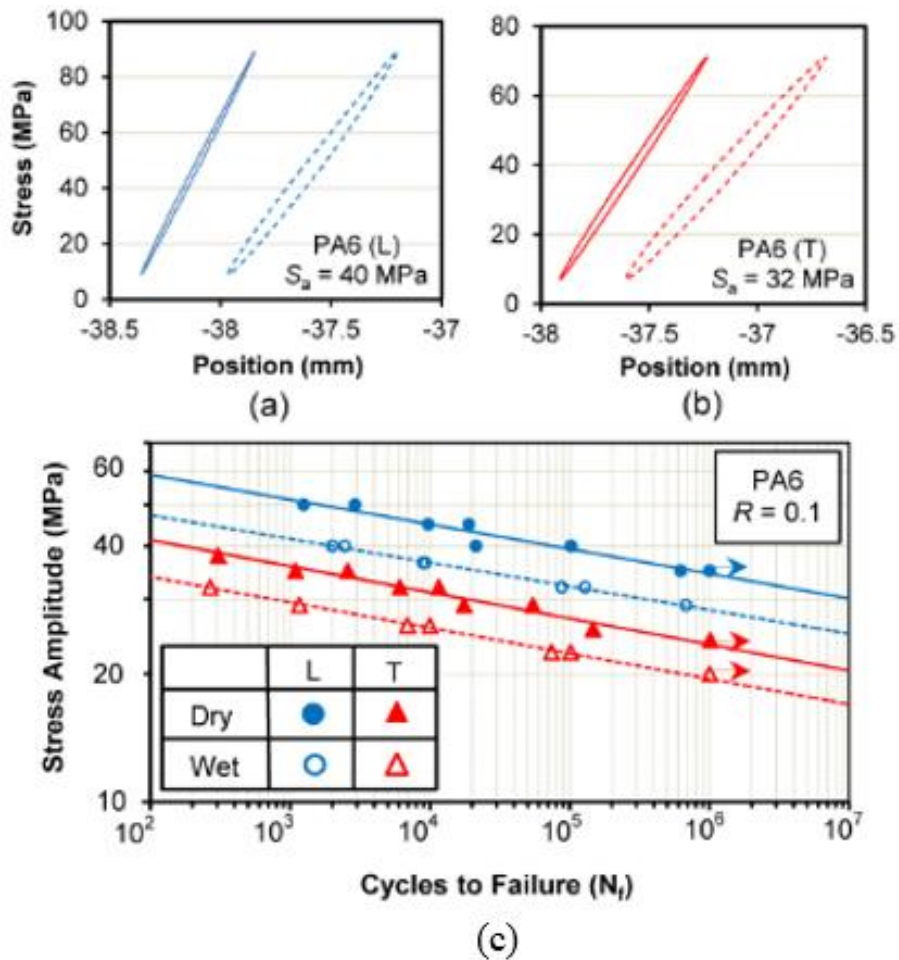


Figure 2-54 Midlife stress-displacement loops for dried (solid curve) and wet (dashed curve) samples of PA6-SFRP at the same stress amplitude for $R=0.1$ in: a) longitudinal and b) transverse directions. c) S-N curves at ambient temperature showing the effect of water absorption in both longitudinal and transverse direction [84].

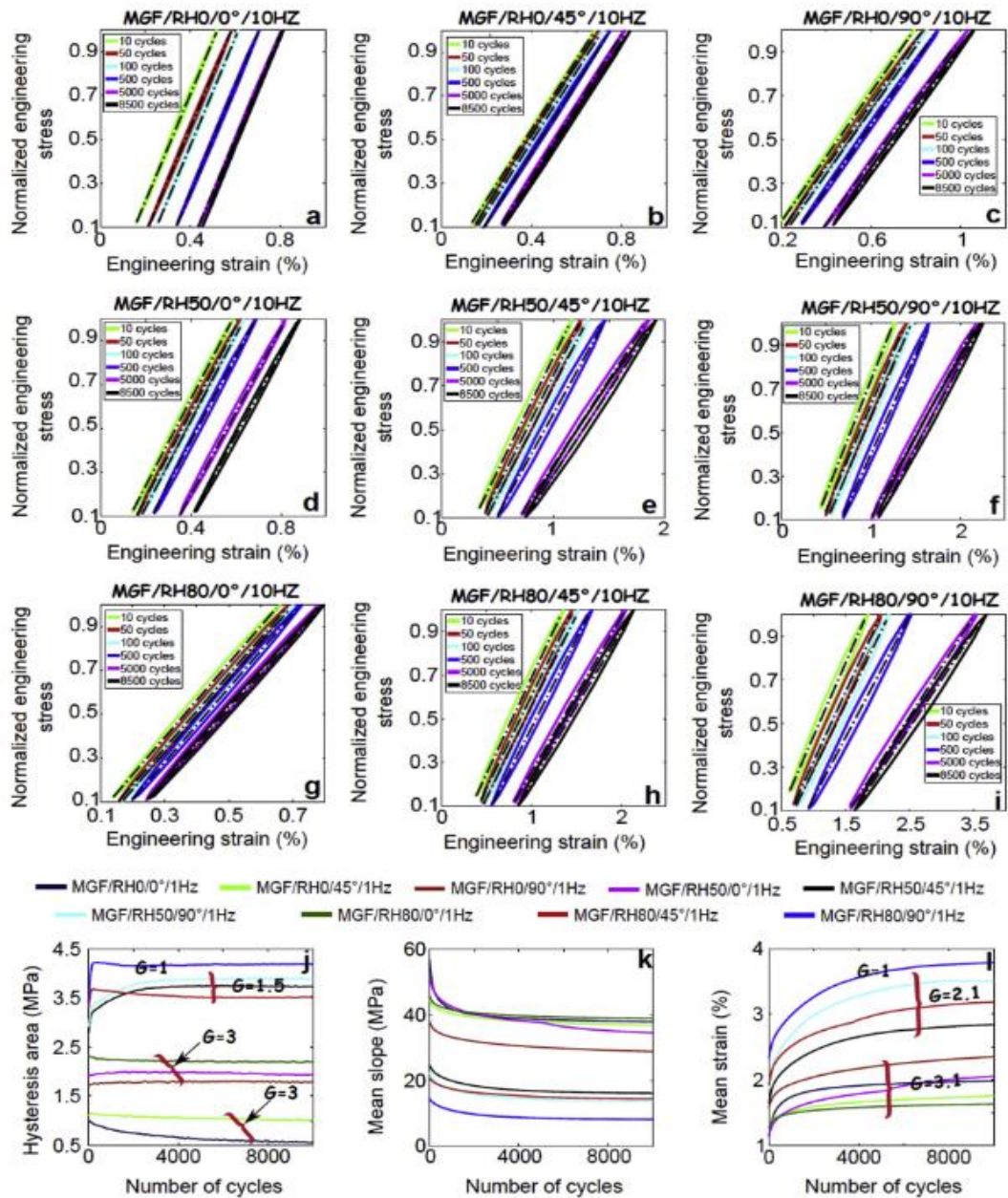


Figure 2-55 Graphs from a-i present the effect of humidity and fibre orientation on the cyclic mechanical properties. Graphs j-l are the hysteresis area evolution, the slope and the mean strain through the life of the specimens at 10Hz [86].

2.5.3 Modelling fatigue of SFRP's

2.5.3.1 Stress-Life based methods

In terms of Stress-Life approach, one of the most used methodologies corresponds to the fatigue-modified Tsai-Hill (T-H) criterion. Early in 1948 Hill postulated a yield criterion for anisotropic materials based on von Mises' for isotropic materials, this was further developed by Tsai for laminated composites [87]. T-H considers the distortion

energy (energy that produces a change in shape) from the total energy due to loading, the other energy is the dilation energy that produces a volume change [88]. Thus, T-H can identify material failure but it cannot distinguish between failure modes, such that [89]:

$$\frac{\sigma_{11}^2}{S_{11}^2} - \frac{\sigma_{11}\sigma_{22}}{S_{11}^2} + \frac{\sigma_{22}^2}{S_{22}^2} + \frac{\sigma_{12}^2}{S_{12}^2} \geq 1.0$$

Equation 2-9

From where σ_{11} , σ_{22} and σ_{12} correspond to the longitudinal, transverse and shear stresses, and the coefficients S_{ij} correspond to the σ_{ij} values at either tensile or compressive failure. This criterion was later modified in 1977 by Sims-Brogdon [90] for its applications in fatigue. Although, the above explained T-H method was initially proposed for composite laminates, more recently it has been applied successfully in fatigue prediction of short fibre reinforced polymers. De Monte et. al. [76] applied the modified T-H on a PA66GF35 composite. Specimens cut at different orientations were used. Stress controlled fatigue testing, at $R=0$ and $R=-1$, was carried out to characterised the material and a fatigue strength limit was established at 10^6 cycles. Figure 2-56 show three-dimensional failure surfaces result of using this criterion on SFRP's in terms of fatigue strength, where the level of anisotropy seemed to be less pronounced for the case of $R=0$ at higher life cycles. A proposed explanation for this was that it might be possible that at higher fatigue lives damage is controlled by the core layer and the overall morphology of the specimens is not as important for failure. Although this study provided with good results a better validation was needed in terms of a different orientation not used in the calibration of the model. Mortazavian and Fatemi [91] carried out this validation by using the modified T-H on a polybutylene terephthalate (PBT) short fibre reinforced composite. 0° , 18° , 45° and 90° oriented samples were used, under $R=0.1$ and $R=-1$ stress ratios. Figure 2-57 shows that for both cases, the effect of the mould flow direction on the fatigue behaviour was successfully predicted, where most of the 18° specimens' fatigue lives were estimated within a factor of two of the experimental life. Finally, a component-level demonstration of this methodology was presented by Malo et. al. [3] for an automobile oil cooler bracket made out of PA66GF35. On this work a numerical model based on a representative volume element (RVE) was used to calculate the global stiffness and fatigue response, assuming a linear-elastic material behaviour. Coupon-

level experimentation was used as input for the model calibration, as shown in Figure 2-58a. Industry software (Digimat) was then used to decompose the material fibre anisotropy into two-phase pseudo-grains, composed by fully aligned fibres only. Mori-Tanaka homogenization technique was then used to calculate the anisotropic stiffness in each pseudo-grain, as well as, and the Tsai-Hill criterion's fatigue life. Validation of this work was done at component level by comparing physical crack locations on the part against the model results. Although the model predicted the locations corresponding the said cracks, results in terms of actual fatigue life were not presented, as shown in Figure 2-58b.

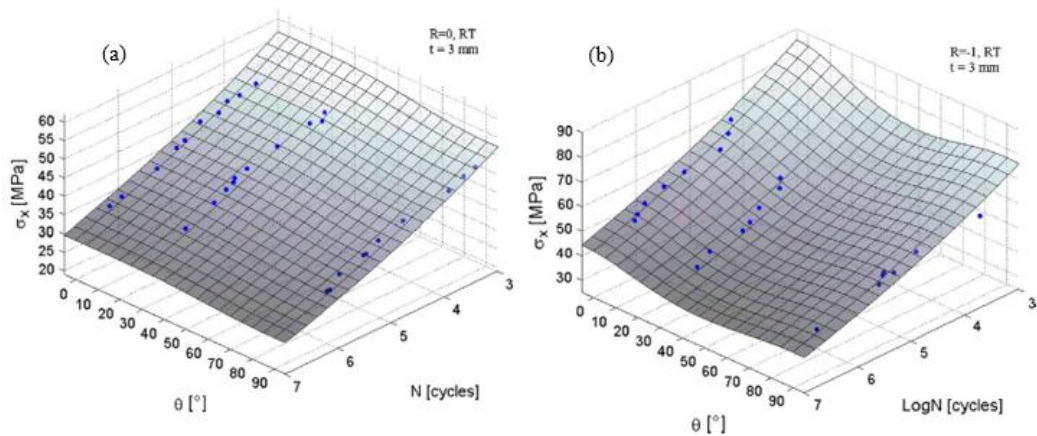


Figure 2-56 Fatigue data fitted by using Tsai-Hill failure surface (grid surface) for 23°C, at a)R=0, b)R=-1 for PA66GF35 specimens [76].

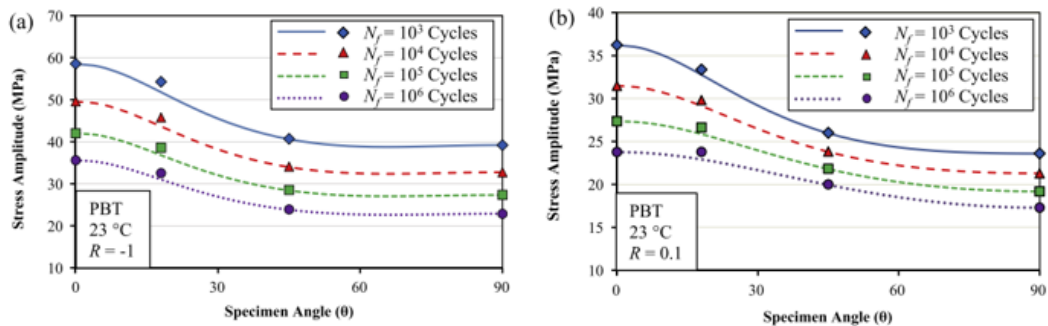
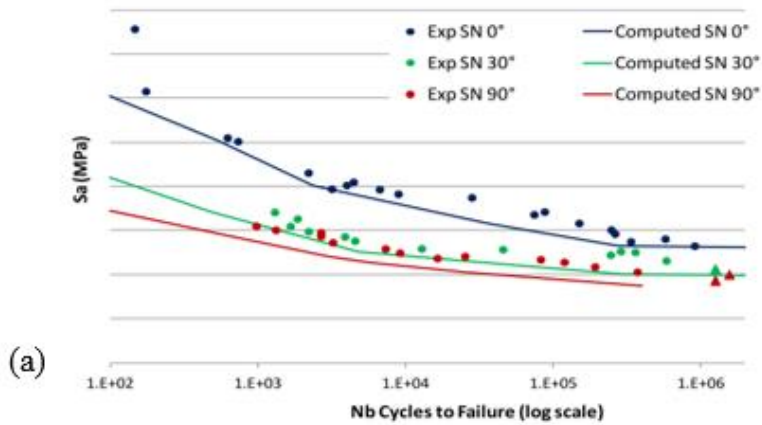


Figure 2-57 "Fatigue strength data as function of specimen angle and Tsai-Hill criterion for PBT at 23°C for a) R=-1 and b)R=0.1 conditions" [91].



(b)

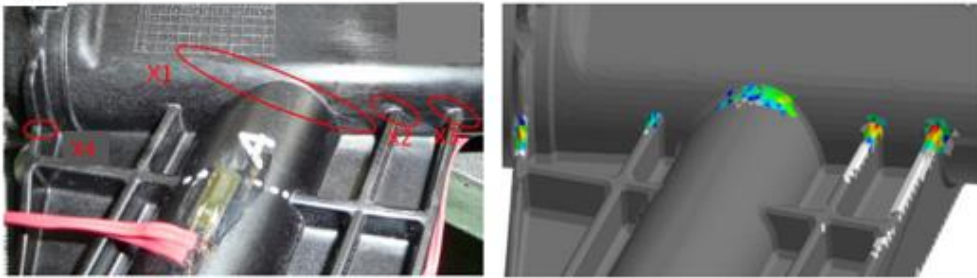


Figure 2-58 a) Correlation of the high cycle fatigue behaviour (model prediction vs experimental data) on PA66GF35 at uniaxial R=-1. b) Prediction at critical locations (right) compared to measurements (left) [3].

2.5.3.2 Energy-based methods

Energy models are less sensitive to the anisotropy of the material, as it relates the fatigue life to a single parameter. In its most basic form the elastic strain energy density can be formulated as:

$$\Delta W_e = \frac{1}{2} \sigma \epsilon_e$$

Equation 2-10

Where; ΔW_e is the elastic strain energy density, σ the stress and ϵ_e the elastic strain. Wilson and Heyes [2], applied this methodology to predict the failure of an engine mount, by relating the strain energy density to the fatigue life of the material as:

$$N = A \Delta W_e^b$$

Equation 2-11

Where; A and b are material fitting parameters. A conditioned (23°C/50%R.H.) PA66-GF50 composite was used in the form of dog-bone coupons cut from injection

moulded plates of 3mm in thickness. Material was assumed linear elastic and characterization was done via Constant Amplitude testing at R=0.1. The model was implemented via FEA and by averaging the strain energy density results for all elements. Coupons oriented at 0°, 90° and 45° (in respect to the flow direction) were used to train the model (Figure 2-59a), and validation was done at component level (Figure 2-59b). Using this approach, good results were obtained, although slightly conservative ones (lower predicted life). Similarly, De Monte et al. [92] used the strain energy density as a mean to reduce the effects of stress concentrations due to notches (and radii), as well as, stress ratios, on a PA66-GF35 composite. Two stress ratios were considered for this investigation: R=0 and R=-1. A fatigue model was proposed to describe the experimental data:

$$\Delta W(N) = \Delta W(10^6) * \left(\frac{10^6}{N} \right)^{\frac{1}{k}}$$

Equation 2-12

Where; $\Delta W(10^6)$ and k are two fitting parameters, and the function was treated in the logarithm form. Material was considered linear elastic and transverse isotropic (only one direction of anisotropy). Figure 2-60 shows the results for different stress ratio (R) and different notch radii (ρ), from where they seemed to converge into a singular material master curve for the prediction of fatigue life.

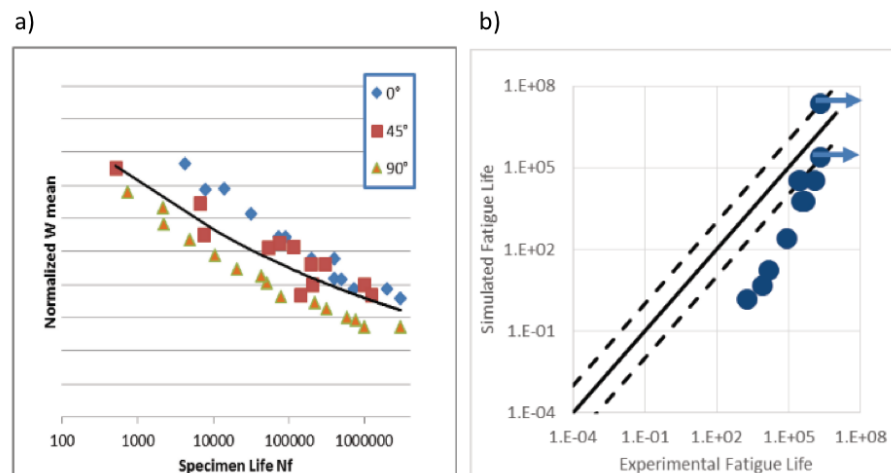


Figure 2-59 a) Fatigue results using the strain energy (W mean) approach. b) Fatigue results of engine mount parts using the “W mean” approach [2].

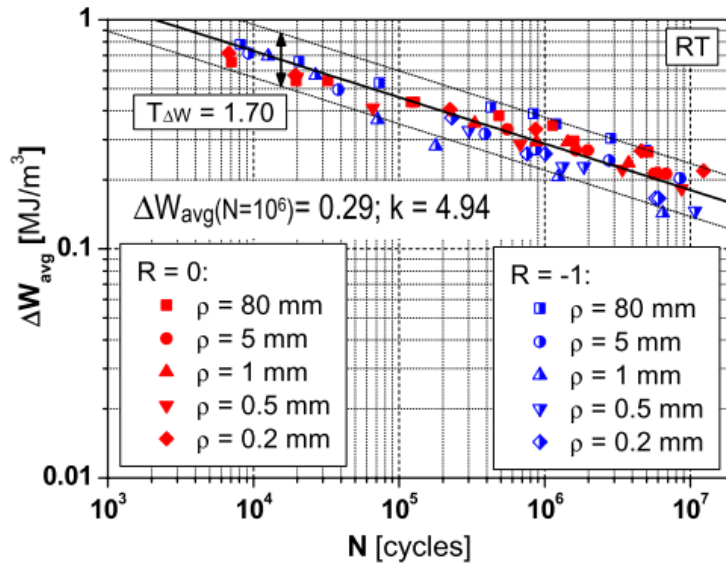


Figure 2-60 Uniaxial fatigue data at ambient temperature in terms of averaged strain energy density range over a control volume [92].

Meraghni et. al. [93], proposed a phenomenological model based on Lavedeze and Dantec [9], but in conjunction with full-field strain measurements taken via digital image correlation for identification of model fitting parameters. This work was carried out on a Nylon-6 reinforced short glass fibre (30wt%) composite. This model establishes that the elastic strain energy of the material, in pristine conditions and after damage onset, can be described by using damage parameters (d_{ij}), this is:

$$2W_d = \frac{1}{1-\nu_{12}\nu_{21}} [E_{11}^0(1-d_{11})\epsilon_{11}(\epsilon_{11} + \nu_{21}\epsilon_{22}) + E_{11}^0\epsilon_{11}(\epsilon_{11} + \nu_{21}\epsilon_{22})] + \frac{1}{1-\nu_{12}\nu_{21}} [E_{22}^0(1-d_{22})\epsilon_{22}(\epsilon_{22} + \nu_{12}\epsilon_{11}) + E_{22}^0\epsilon_{22}(\epsilon_{22} + \nu_{12}\epsilon_{11})] + G_{12}^0(1-d_{12})\gamma_{12}^2 + G_{13}^0(1-d_{13})\gamma_{13}^2 + G_{23}^0(1-d_{23})\gamma_{23}^2$$

Equation 2-13

Where; W_d is the strain energy, E_{ij}^0 and G_{ij}^0 are the Tensile and Shear modulus of the pristine, undamaged, material, ϵ_{ij} and γ_{ij} are the tensile and shear strains, ν_{ij} is the Poisons' ratio, and d_{ij} are the directional damage parameters. Parameter identification was done using full strain fields measured with digital image correlation and an objective function representing the difference between experimental and numerical data, as shown in Figure 2-61a and Figure 2-61b. Comparison between model results and experimentation showed a good correlation, as shown in Figure 2-61c, although only mapping of the onset and steady damage propagation was achieved.

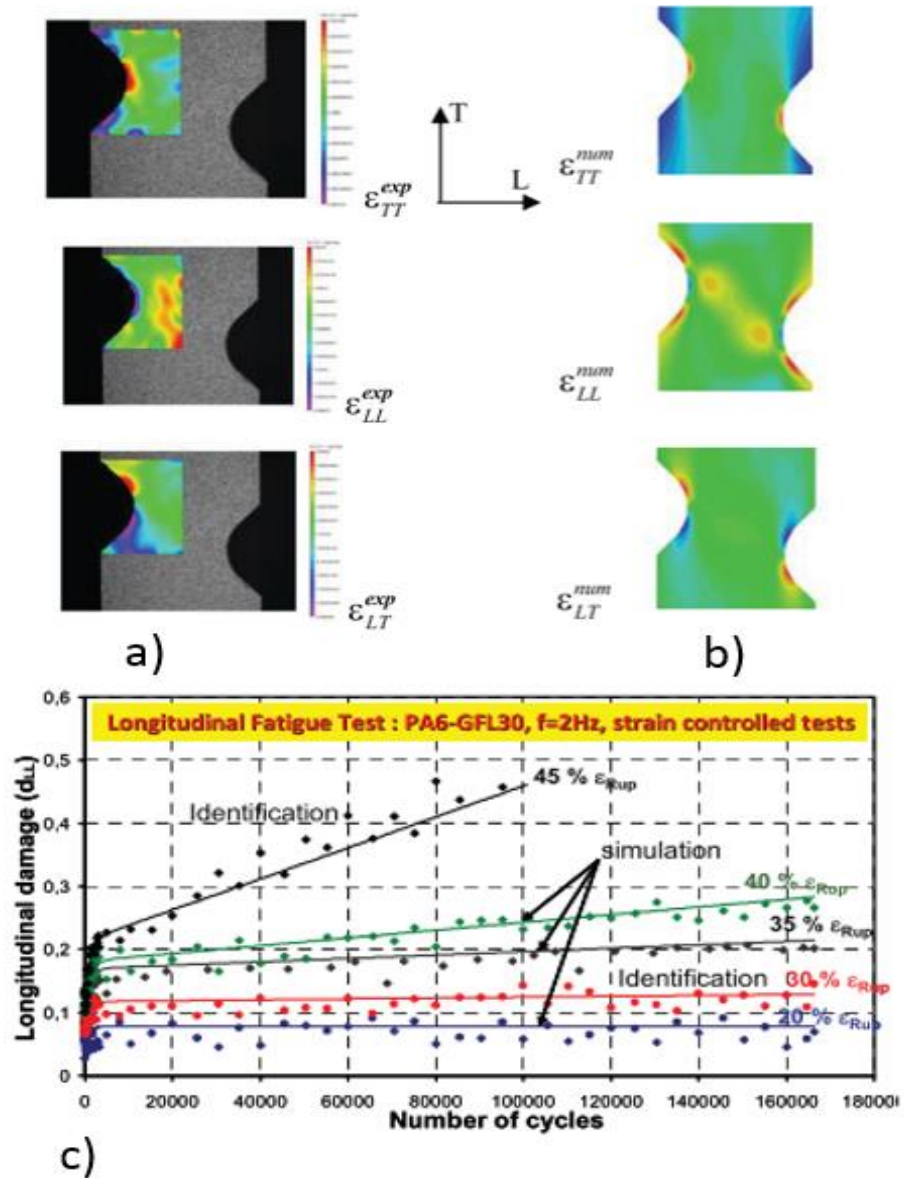


Figure 2-61 "Comparison between experimental a) and FE simulated b) distribution of strain fields obtained at 5000 cycles of the Meuwissen specimen configuration fatigue test. c) Comparisons between experimental and simulated longitudinal damage (d_{LL}) evolutions versus number of cycles (N) for PA6-GF30. Displacement controlled fatigue tests" [93].

Experimental measurements via digital image correlation have also been applied more directly in fatigue energy models. Thambi et. al. [94], used full strain-fields to characterise the surface strain energy density (SSED) of a pressure vessel made out of PPO/PS (p-phenylene oxide/Polystyrene) blend resin reinforced with 30% short glass. Fatigue test at 1Hz with internal water pressure were conducted. The energy formulation is based on Equation 2-10, such that a relationship between fatigue loading and strain-stress amplitudes can be described as:

$$\Delta W = f(\Delta \varepsilon \cdot \Delta \sigma)$$

Equation 2-14

From where a model correlating life (cycles) to the strain energy was proposed. This is:

$$N_f^m \cdot \Delta W = C$$

Equation 2-15

Where, ΔW is the surface strain energy density (SSED), m is a fatigue exponent and, C the material ductility coefficient. Digital image correlation measurements of the first principal strain over the surface were used for the fatigue evaluation, as the elastic strain energy was calculated based on the hysteresis loops obtained with this technique. A homogenous area was selected for non-weldline specimens, Figure 2-62a; whereas for weldline samples the evaluation was based on the location of the actual weldline, Figure 2-62b and Figure 2-62c. Results presented in Figure 2-62d, shown a good correlation of this model for different temperatures and different positive stress ratios, showing a linear relationship with respect to the log-life of the part.

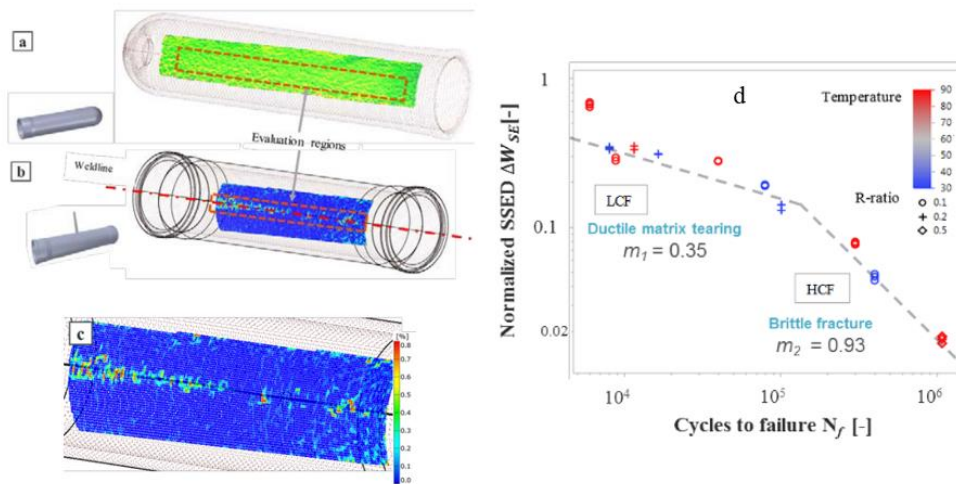


Figure 2-62 Surface strain on a) pressure vessel gated from top without weldline, b) gated from side with weldline, c) closer view of the strain contour on the weldline. d) Pressure vessels SSED results for different temperatures, R ratio, pressure levels for non-well-lined samples [94].

2.6 Damage in SFRP's

2.6.1 Stiffness degradation

Measurement of residual stiffness, or stiffness degradation, can be used to assess material's damage accumulation and propagation. Figure 2-63 shows a schematic of a typical stiffness degradation curve. Three main regions have been identified [9], [14]: At the beginning (up to 10% of fatigue life) there is a sudden drop due to matrix softening, onset of damage and micro-cracks formation. A second region characterised for a more stable decay with slow coalescence of defects and propagation on the interfaces. Finally, a steeper deterioration of the material due to macro-crack propagation and failure.

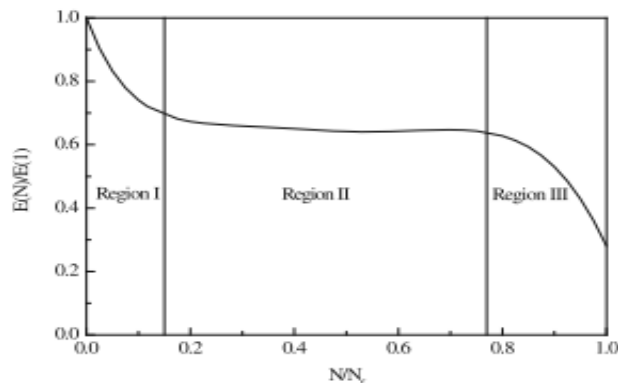


Figure 2-63 Illustration of the typical stiffness degradation curve for composite materials [14].

De Monte et. al. [76] measured the evolution of stiffness of 1mm thick specimens along the flow direction for short glass fibre reinforced nylon-66, Figure 2-64. No stable steady state was achieved, continuous degradation. At point of failure, a reduction of original stiffness up to 15% was seen. A similar approach was used by Meneghetti et. al. [95] on notched PA66GF35 samples. Uniaxial fatigue testing at two different frequencies was conducted, 2 and 7.5Hz depending the load level, and at $R=0.1$ stress ratio. Measurement of the normalized axial stiffness for the specimens, as seen in Figure 2-65, showed a comparable stiffness decay for both geometries up to half the life. Implying that larger part of the fatigue life in the samples was spent propagating the damage up to the point where geometry had a significant effect in the material failure.

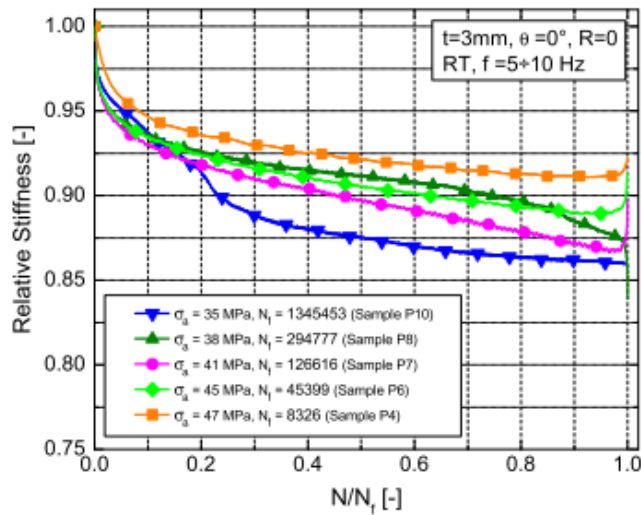


Figure 2-64 Stiffness evolution at $T=23^{\circ}\text{C}$, $R=0$, thickness= 3mm specimens with fibre orientation specimens cut at 0° [76].

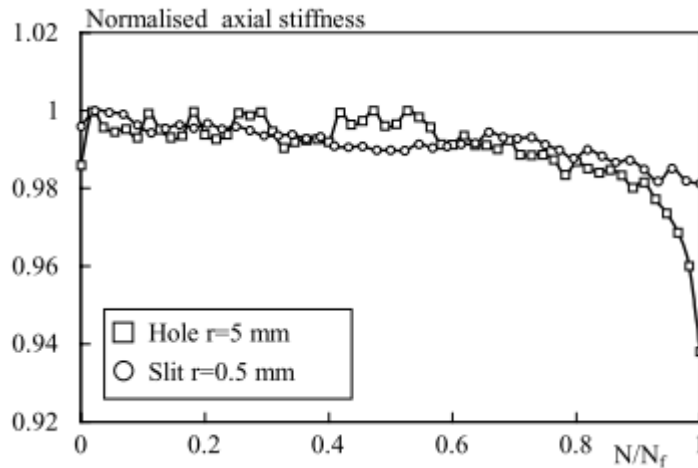


Figure 2-65 Axial stiffness VS Relative number of cycles, for two specimens with different notch tip radius [95].

2.6.2 Damage mechanisms

Uniaxial tested specimens has shown locations of failure to be located all along the gauge section, in particular close to the end of the specimens' shoulders and/or closer to the middle section, as shown in Figure 2-66a-b and Figure 2-70c. Figure 2-66a-b are of particular interest as they show that for two different fatigue stress ratios, $R=0.1$ and $R=-1$, the failures for the 45° specimens are consistently at an angle of approximate 45° and going from one corner near the shoulder of the specimens. Similarly, an argument can be made that the failures of the 0° and 90° specimens are for the most part flat and normal to the load direction. It will be presented later on

this thesis that these documented results correlate with the failure locations observed during this project.

Damage in composites is caused by changes in the microstructure due to a combination of failure mechanisms such as: matrix cracking, fibre breakage, fibre pull-out, debonding, fibre bridging, etc.[14]. A series of damage stages can be identified as [96], [97]:

- Initiation of damage at fibre ends,
- Growth of damage and debonding along the interface,
- Bridging between crack walls.
- Cracks grow until final critical size and sample fails.

Experimental techniques, such as Optical and Scanning Electron Microscopy (SEM), and Computed Tomography (CT), have been used to observe and analyse the different mechanisms for SFPR's failure, in both monotonic and fatigue conditions. Figure 2-67a and b, show the aforementioned first stage (crack initiation at the fibre edges) and second stage (debonding at the interface) respectively; on a Nylon-66 and GF30 SFRP composite via in situ SEM, during monotonic testing [98].

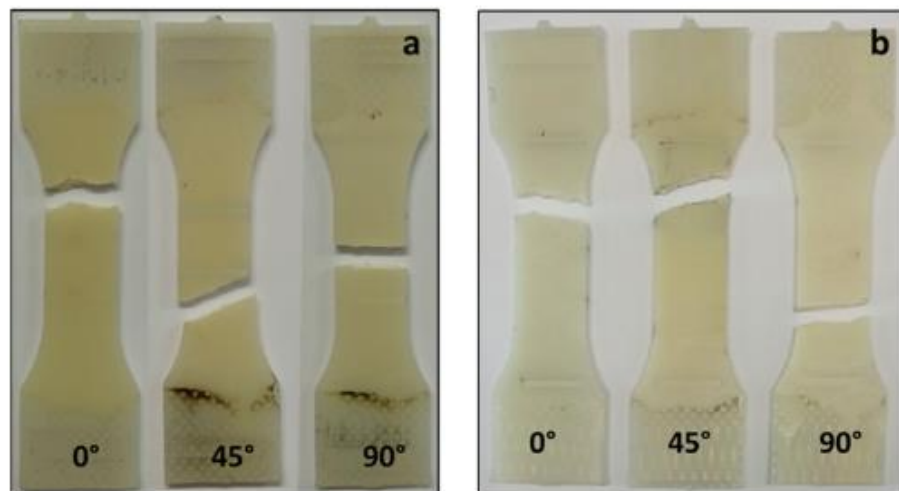


Figure 2-66 Location of failure on samples tested at a) R=0.1 and R=-1 [77].

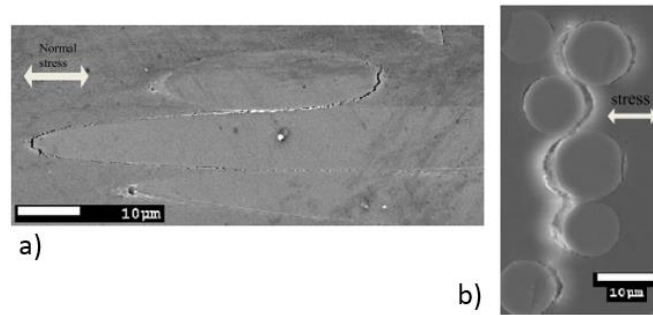


Figure 2-67 a) Damage initiation at fibre end and interface decohesion at the location where the fibres are close one another for a load of $P=56\%$ of σ_{UTS} . b) Crack propagation in the form of interface debonding and transverse crack for a load $P=81\%$ of σ_{UTS} [98]

2.6.3 Damage mechanisms under fatigue loading

SEM has been used for macroscopic analysis of the failure mechanisms of SFRP's under fatigue loading. Klimkeit et. al. [99] observed the fracture surfaces of PBT-PET (Polybutylene terephthalate - Polyethylene terephthalate) reinforced with 30wt% short glass fibres specimens after fatigue testing. Two main regions were found: A first area where the matrix failed in a quasi-brittle manner with no signs of shear. Significant evidence of clean fibre pulled-out (Figure 2-68a), and roughness on the matrix seen at higher magnification (Figure 2-68b). A second region where a more ductile behaviour was seen. Evidence of fibre pulled-out was found in this region as well but with evidence of having deformed the matrix around (Figure 2-68c). At higher magnification, larger deformation of the matrix could be seen (Figure 2-68d).

In a work by Rolland et. al. [100], a short fibre reinforced composite (nylon 6,6 and 30wt% short-glass fibre), was inspected using a synchrotron at relatively low number of cycles, <2,500 cycles. The above described damage mechanism were identified at different points in the life of the specimen, as observed in Figure 2-69. Within the first 20% of the life of the specimen micro-cracks at the fibre ends, and fibre failure was seen, Figure 2-69a and b. After this point crack started to bridge between cracks ends or by breaking the actual fibres. Debonding on the other hand, was observed later on the life of the specimens at approximate 40% of the life, Figure 2-69c-d. A work by Belmonte et. al. [101], studied the fatigue damage mechanism of a nylon-glass fibre short fibre reinforced composite, PA66-GF35. Using infrared thermography during fatigue testing on the main surface of a sample, the location for unstable failure was located due to the localised dissipated heat at an area near to the shoulder of the sample. Figure 2-70a shows that surface temperature readings can serve as a method

to measure the energy localization caused by stress concentrators, shoulder tips, which act as points of failure initiation under fatigue conditions. This location showed a temperature of approximate 2°C higher than the rest of the surface temperature, and was concentrated in a very small area. Interestingly, failure occurred ~1s after this temperature localization was seen, Figure 2-70b, which suggests that final material failure is very fast under fatigue loading. Figure 2-70c, shows a zoom-in image of the final failure, where it can be seen, clearly, the macro crack path; starting from the shoulder tip on one side of the specimen to end at the other side of the coupon.

On a different experiment using notched specimens, fatigue test was interrupted at the point when crack initiation was found, Figure 2-71a. The location where the crack started was not the tip of the notch, but in an area where a bundle of similar oriented fibres were found, Figure 2-71b. This crack went around the boundaries of the fibres, through the matrix in a very clean manner with low deformation of the resin, as it can be observed in Figure 2-71c and d. Finally, in a work by Karger, et.al. [102], several planes, or plateaus, were observed as the crack tip progressed through the composite. A depiction of these planes is shown in Figure 2-72, where the stress concentrations at the fibre ends result in plastic deformation of the surrounding matrix (p), then craze is form into different plateaus (c), and finally coalescing of the plateaus through individual shear steps (s). Higher fibre volume fractions increase the number of (p) regions and thus locally higher pasticity of the fibres surrounding matrix.

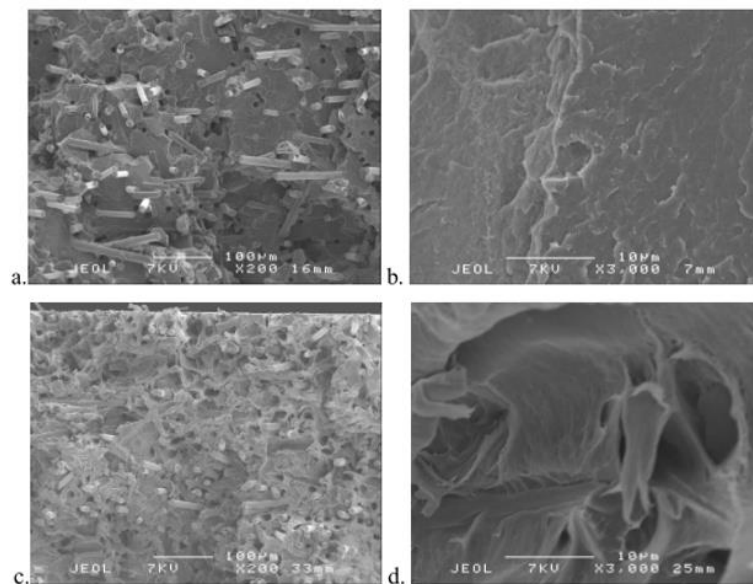


Figure 2-68 "Surface A; fragile behaviour at magnification of a) x200 and b) x3000. Surface B; ductile behaviour at a magnification of c) x200 and b) x3000"

[99].

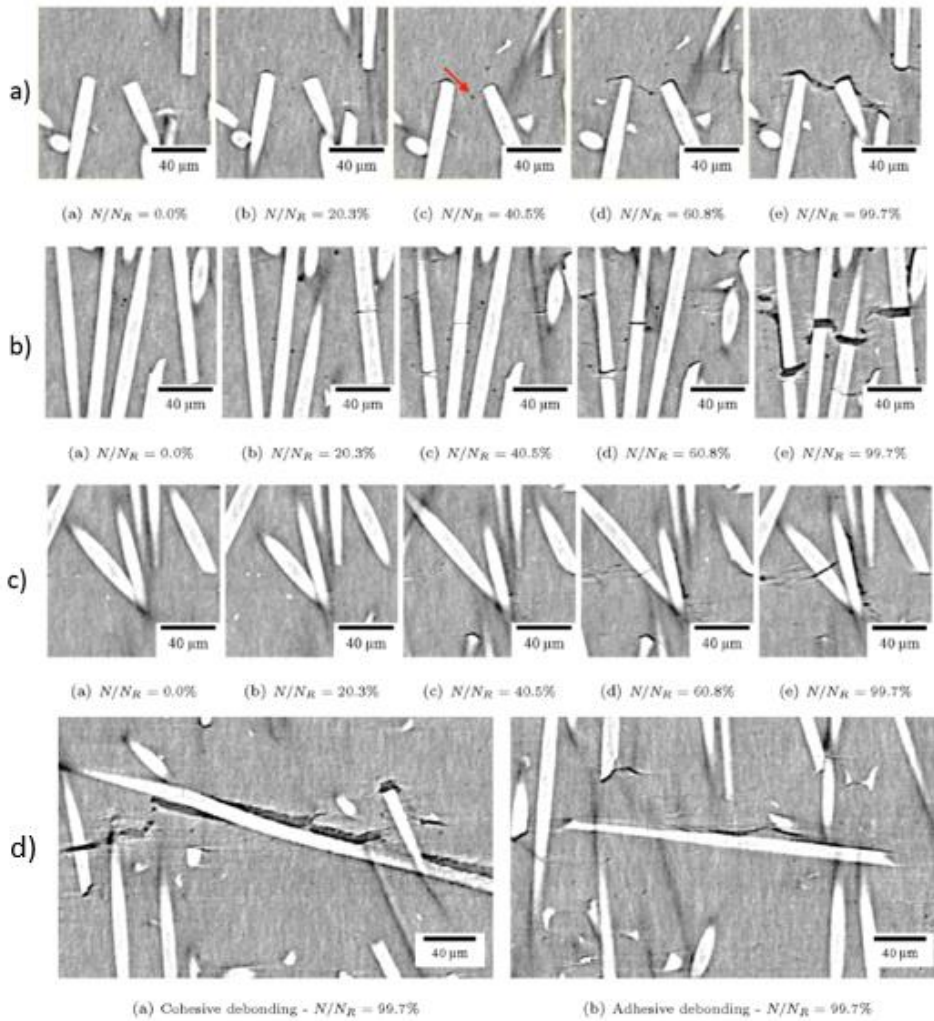


Figure 2-69 0° specimen $N_R=2,468$ cycles. a) Damage at fibre ends. b) Fibre failure. c) and d) Debonding [100].

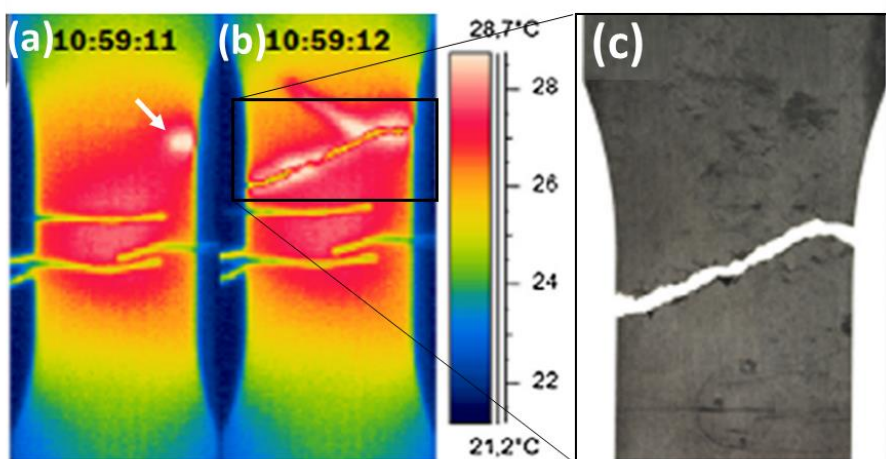


Figure 2-70 PA66GF35 specimen at $R=0$. a) Localisation of temperature at the stress concentrator (shoulder tip). b) Specimen failure after 1 second from temperature localisation. c) Crack path after specimen failure [101].

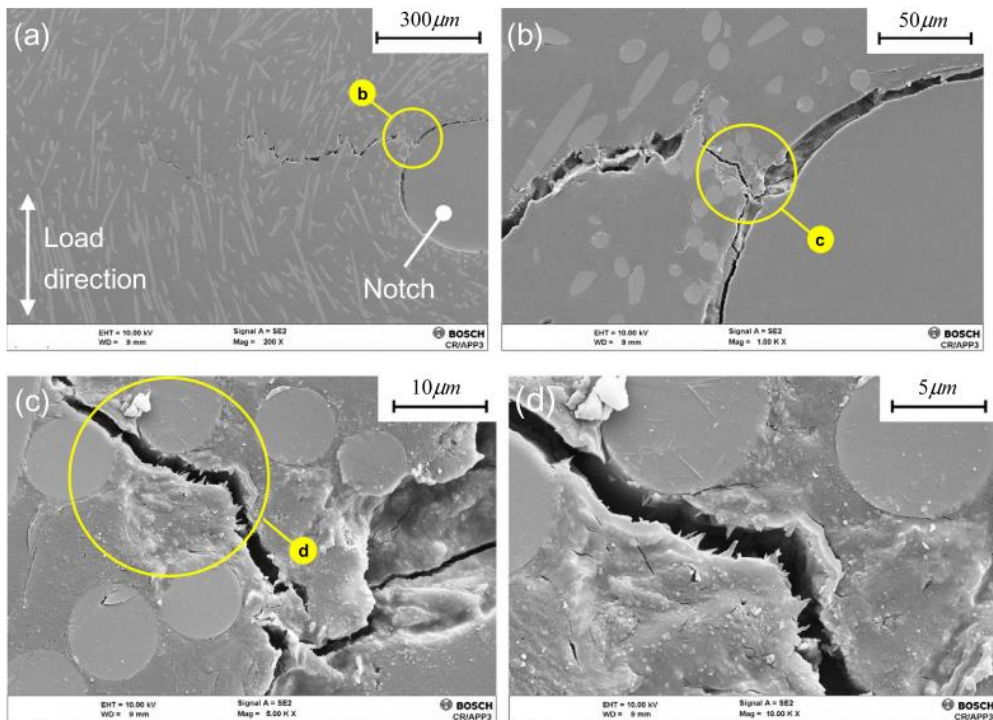


Figure 2-71 "Fiber distribution at crack initiation for a notched specimen, interrupted fatigue test; (b), (c), (d) are magnified views of the crack" [101].

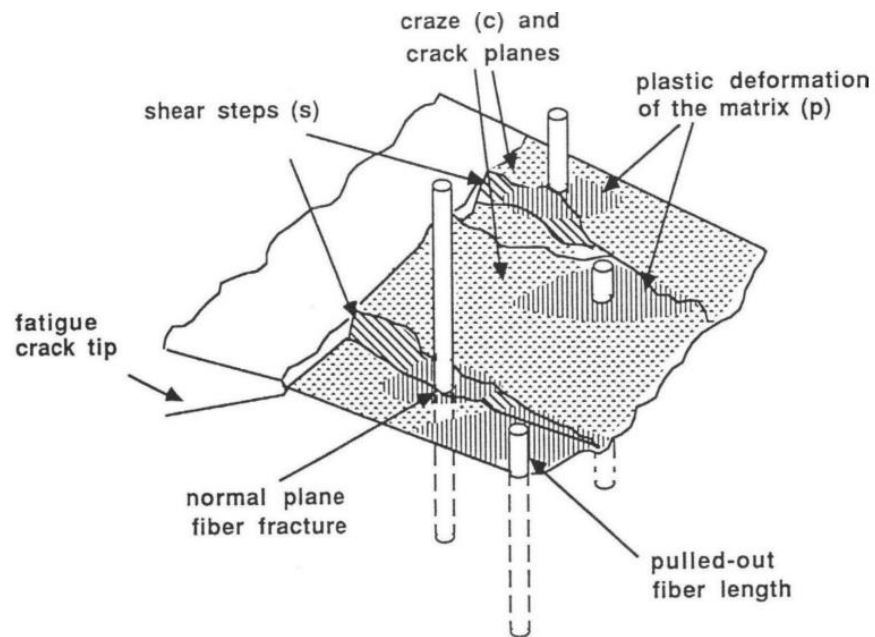


Figure 2-72 Model for the crack plane deviation in chopped glass fiber reinforced polypropylene at low fibre loading [102].

In terms of computed tomography applications, Rolland et. al. [96] used X-ray micro-tomography with a resolution of $0.65\mu\text{m}$, to analyse the evolution of quasi-static and

fatigue damage at different points in life of the specimens. Polyamide-66 with 30wt% short glass fibre was used. Damage at fibre ends was found for both load conditions. Fibre failure, with the space between fibre ends of up to $520 \mu\text{m}^3$; and debonding was widespread through the specimen, this is presented in Figure 2-73a to b. Evidence of matrix micro-cavitation, with maximum void diameter of $5 \mu\text{m}$, was also observed in this study, presented in Figure 2-73c. A similar application of this technology in fatigue of composites was carried out by Arif et. al. [103] on a PA66GF30 SFRP. Tension-tension fatigue loading at a frequency of 3Hz was used. Under CT inspection, significant amount of fibre/matrix interfacial debonding along the fibre was seen. Figure 2-74 presents a CT image separating the physical fibres (blue coloured) and the localized debonding (green coloured). This type of damage appeared in the shell layers in earlier stages of the fatigue testing; whereas, in the core layer only appearing at the end of the life of the specimen. Belmonte et. al. [104] use this technology to analyse the particular effect that the fibre distribution had in the fatigue damage onset on PA66GF35. Figure 2-75 shows the analysis of a crack growing on a notched specimen and the fibre orientation distribution, and volume fraction, around the notched region. Through thickness oriented fibres were seen in the vicinity of the surface of the specimen. Groups of fibres were also seen to vary unevenly indicating that the orientation is not constant but changes along the material.

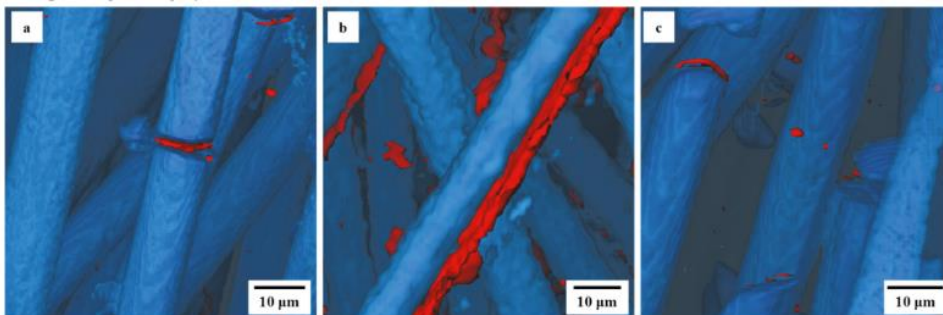


Figure 2-73 a) Fibre failures, b) Debonding and c) Micro-cavitation (95% of specimen life) [96].

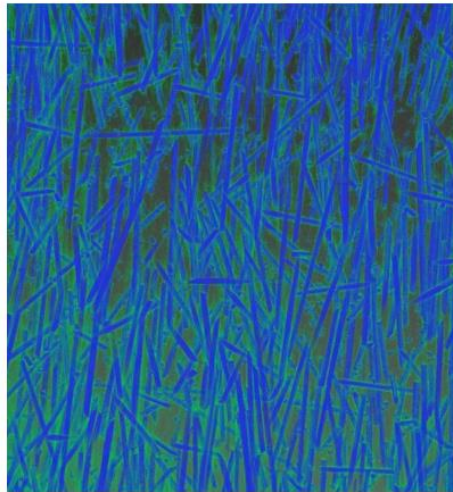


Figure 2-74 Rendered μ CT image of fatigue loaded specimen which shows damage in the form of fibre/matrix interfacial debonding [103].

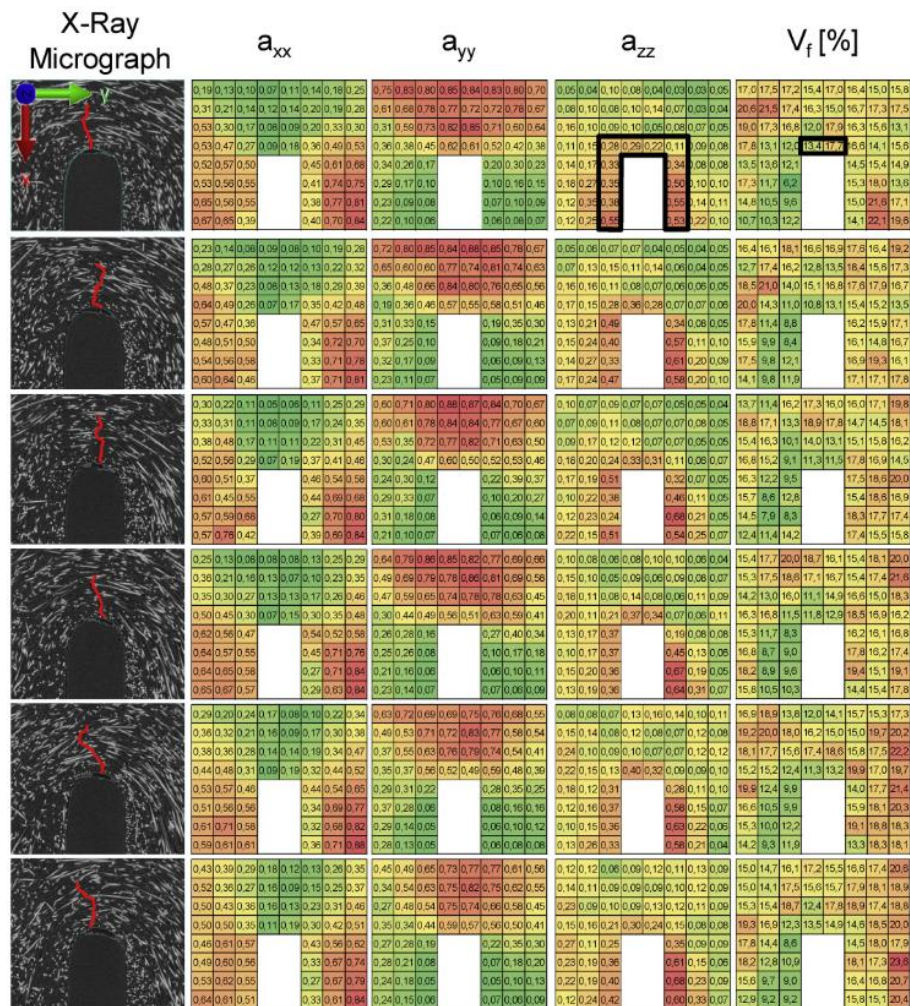


Figure 2-75 "Analysis of the fibre orientation and fibre content; 8 x 8 x 8 discretization for six different sections along the thickness. In the X-ray CT micrographs (first column from the left side) the crack path is indicated in red"

[104].

2.7 Discussion of literature

After reviewing the relevant published literature on short fibre reinforced polymer composites, it is clear that these materials are highly complex, in terms of their microstructure and mechanical properties. The material response of SFRP's is dependent of factors such as: the level of anisotropy due to fibre orientation distribution, the size of the different skin-shell-core regions, fibre length and critical length, the geometry and amount of reinforcement, the overall thickness of the part, the environmental conditions at which the composite is being subjected to, the loading conditions, the matrix's material response, etc. Of particular interest is the effect of the fibre orientation distribution product of the material manufacturing procedure, i.e. injection moulding, on the material properties. Although methodologies have been proposed to predict this distribution, a perfect correlation has not yet being found when comparing results with experimental measurements. This is key, as the fibre orientation distribution has a large effect on the material response. Research has shown that specimens of the same material but cut at different orientations would show completely dissimilar results when tested under monotonic and fatigue loading conditions. This is due to either the matrix, the reinforcement, or a mixture of both, driving the material properties. Similar results have been found in regards to the fibre length effect on the material performance. In terms of fatigue life, this means that to fully describe the material response it requires a significant amount of experimental characterisation, as the distribution of fibres would change depending of the composite grade. To mitigate this problem different type of methodologies haven been proposed with the objective to mitigate and/or predict the effect that the anisotropy has in the material's fatigue life, as well as, to try to reduce the amount of experimental data needed. Upon close analysis of the current published work a set of existing gaps in the knowledge can be identified and are summarized as follows: 1) validation of the model is done at the last step, at the fatigue prediction level, ignoring that such complex procedure would produce a stack-up of uncertainties. 2) The material formulation is assumed to be linear-elastic, proper analysis of the application is needed to address whether the resultant stresses-strains lay within said region. 3) The plastic and viscous response of the thermoplastic matrix is not fully considered. 4) During experimental material characterization more than one specimen is cut out from the same composite plate, this translates into dissimilar fibre orientation distribution for specimens sharing the same orientation and thus adding unwanted uncertainties to the results. 5) Some studies have reported information about fatigue

damage development mechanisms in injection moulded composites, but there is still a lack of understanding of the actual stress and strain conditions below the surface that relate to crack initiation and propagation. Therefore, in order to address these gaps in the knowledge the present work proposes a new more robust methodology which builds from the current published work. Each step will be validated by state-of-the-art experimental techniques, to address and to quantify the uncertainties at each stage in the modelling methodology. Material experimental characterisation will be done with careful care of the material orientation distribution to avoid adding unwanted uncertainties to the result. The experimental work will consider the damage mechanisms in the material, as well as, the effect of the mean stress on the geometries to make it more applicable to real working conditions.

3. EXPERIMENTAL METHODOLOGY

3.1 Introduction

The following chapter presents the experimental methodology followed throughout the project. The characteristics of the composite material, the preparation of the specimens, the experimental equipment and the experimental procedures are outlined and described in detail. Additionally, the techniques used for the material analysis are also presented.

3.2 Material description

In general terms, the short glass-fibre reinforced polymer composite chosen for the present project is formed by:

- **Resin (Matrix):** Polyamide 66, also known as, Nylon 6,6 or PA66.
- **Reinforcement (Fibre):** Short glass fibre type E (electrical).

More specifically, the resin used on this composite is manufactured by BASF [105], with A3W designation, black coloured and with a neat resin density of 1.13 g/cm³ [106]. The short glass fibre is bought by the composite manufacturer and has a nominal aspect ratio of 20 (~200µm in length by ~10µm in diameter), an areal weight of 900gsm (unidirectional fibre), and a density of 2.6 g/cm³ [107]. Typically, the sizing for glass fibre is composed by a coupling agent to improve adhesion, and a film former to lubricate, protect and hold fibres together prior to the composite manufacture. Commonly found, in the literature, glass fibre coupling agents include: γ -aminopropyltriethoxysilane, γ -glycidoxypropyltrimethoxysilane, γ -methacryloxypropyltrimethoxysilane and vinyltriethoxysilane; whereas, film formers include: polyvinyl acetates, polyurethanes, polyolefins, polyesters, epoxies and modified epoxies [108].

Additionally, measurements for the diameter and length were carried out on a number of fibres. ImageJ [109] (image processing software) was used to calculate the dimensions of seemingly in-plane aligned fibres on images of the cross-section of the composite taken via optical microscopy. This was done by using the software to measure the cross sections of the fibres, from where diameters and lengths could be calculated, an example of this is shown in Figure 3-1a and b. As it can be seen in these figures, only fibres that were seemingly circular or rectangular were counted, this is as fibres at any other orientation than perfectly aligned would show up as stretched

ellipses. In average, the measured fibre diameter was approximate $9.9\mu\text{m}$; whereas, the average measured fibre length was approximate $215\mu\text{m}$. The histogram of the distribution of the measurements taken is presented in Figure 3-1c and d. The main limitation of this approach is that it relies on fibres being perfectly, or seemingly perfectly, aligned in-plane with the cut of the specimen used for microscopy. Only fibres that appear as circles and rectangles would be counted, as any fibre at a different angle would appear as an ellipse, as shown in Figure 2-16. This meant the number of fibres available for direct measurement was relatively small and restricted to the specimens observed. Nevertheless, this approach, although limited, provided with a sensible idea of the distribution of the fibre dimensions inside the composite. Finally, the fibre critical length (l_c) was calculated according to Equation 2-1. Where the fibre strength was obtained from textbook values for Type-E glass fibre at $\sigma_f=3,100\text{MPa}$ [15]. From Equation 2-2 the interfacial shear strength was calculated based on the matrix strength, after assuming a strong fibre-matrix bonding. Therefore, from available public data for neat PA66 resin [110], the matrix strength was taken as $\sigma_m=80\text{MPa}$, which meant an interfacial shear strength of $\tau=46.2\text{MPa}$ (per Equation 2-2). After using the measured average for the fibre diameter, $d=9.92\mu\text{m}$, this meant that the critical fibre length (l_c) for the present material is in the order of $l_c=665\mu\text{m}$, and therefore, the fibres used are below the critical length, as presented in Figure 3-1d. This calculated l_c is also close to the ones reported in the literature for other SFRP's, as shown in Figure 2-5c and Figure 2-6 . It is then clear that, for all these cases the fibre length used on SFRP's is smaller than the critical l_c for that material.

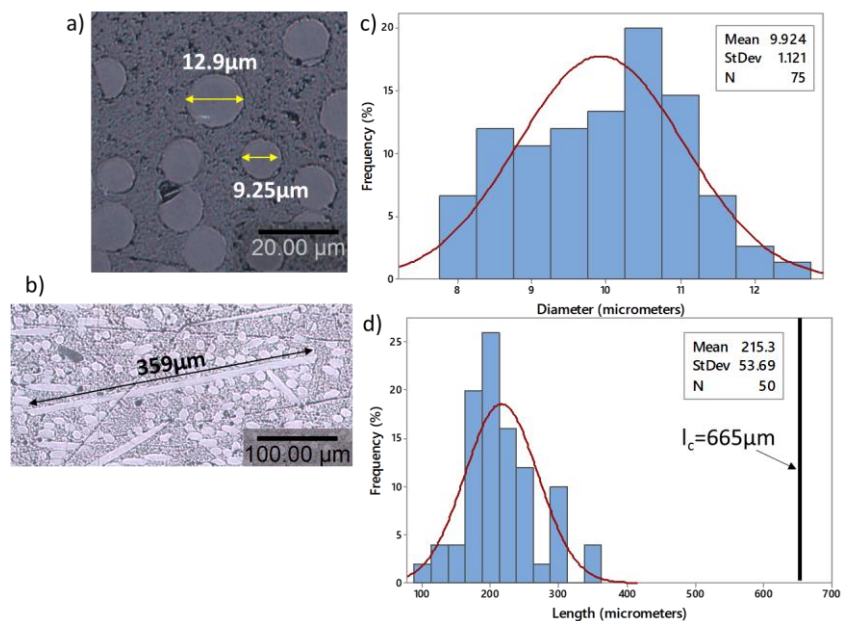


Figure 3-1 Measurements of a) fibre diameter and b) fibre length. c) Histogram of fibre diameter and d) fibre length showing critical length (l_c).

In regards to the composite, its denomination is PA66GF50 [111], it consists of a fibre weight ratio of 50wt% ($V_f=30\%$), with a bulk material density of 1.57 kg/m^3 , and a glass transition temperature (T_g) between $65\text{-}70^\circ\text{C}$. The material is injection moulded at a temperature of 300°C , with a mould surface temperature of 85°C , and injection time of 1.8s. It shows a constrained moulding shrinkage of between 0.30 to 0.35%. Manufacturer bulk material properties at ambient temperature are provided by the supplier and are shown in Table 3-1. In terms of processing, the injection rate is $5,000 \text{ cm}^3/\text{s}$, with a maximum injection pressure of 180MPa and a maximum clamping force of 7,000 tonne. The injection moulding considers the filling and packing of the material with a cooling time of 20s, where the pressure used for packing is 60% of the filling pressure. The composite is provided by the supplier in a dry, as moulded, condition in the form of plates with nominal dimensions of 150mm by 150mm and 4mm in thickness. To assess the real material thickness, a random set of 70 manufactured specimens were measured at different locations, gauge length and shoulders as shown in Figure 3-7. Then an average value was taken from these values. Figure 3-2 shows the histogram of said measurements, where the average thickness was 3.91mm. For all geometric dimensions measured throughout this document, a digital caliper [112] with a total length of 0-150mm and a resolution of $\pm 0.01 \text{ mm}$ was used.

Table 3-1 Material properties for PA66GF50 conditioned at $23^\circ\text{C}/50\%\text{R.H.}$ [111].

Properties	Unit	Values
Tensile Modulus	MPa	11,500
Stress at break	MPa	160
Strain at break	%	4.1

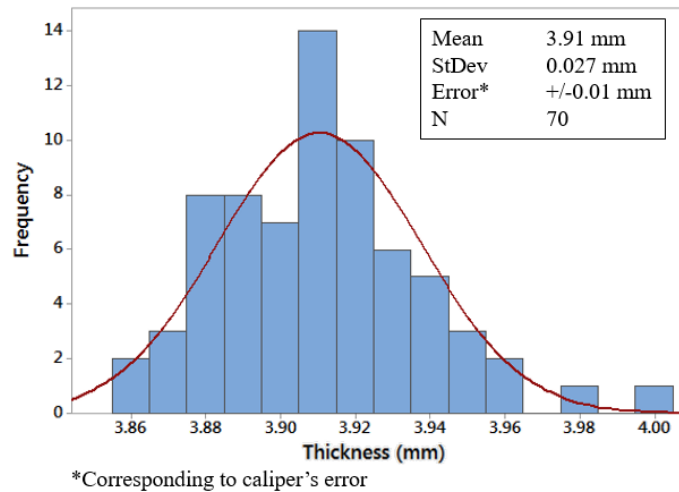


Figure 3-2 Histogram of average specimen thickness.

3.2.1 Material conditioning

The process of adding moisture to the composite material is known as *Conditioning* and, besides influencing the material properties [59], it allows for a reference for the replicability and validation of results. As it was presented in Chapter 2, Nylon based composites are known to absorb water significantly. Figure 2-33a shows the Stress-Strain behaviour of a similar Nylon 6 based Short Glass Fibre composite at different levels of conditioning. This made critical the establishment of a controlled humidity (Condition) baseline for the experimental procedure, from where standard laboratory condition (23°C/50%R.H. per BS EN ISO 527-1:2012 [113]) is widely used. The moisture content of the PA66GF50 used in this project reaches equilibrium at said laboratory conditions when the total weight of the material has increased, from dry state, between 1.00 to 1.40% [111]. From this point forward, any mention to the condition level refers to this range.

The conditioning of the material was carried out after the machining of the specimens to allow for a more efficient use of time and space. After conditioning, the specimens were kept on individual sealed aluminium bags, to avoid transfer of humidity with the atmosphere, and testing was conducted as soon as possible. The overall process followed for the conditioning of the material is mapped in Figure 3-3.

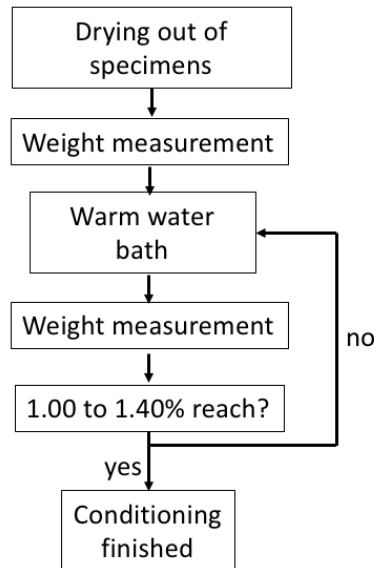


Figure 3-3 Followed conditioning process.

Specimens were dried out for 48hrs at 40°C to obtain an individual weight baseline and at a temperature below T_g to avoid material structural changes. Measurements were taken using a XPR105 balance [114], with a maximum capacity of 120g and error of +/-0.1mg. A warm water bath at 55°C was used to accelerate the absorption of water, via a convection oven, this method is widely used throughout industry [115]. Figure 3-4 shows specimens being conditioned. The temperature of the bath was monitored via a LabVIEW [116] code created by the author, a National Instruments (NI) data acquisition card NI-9211, and a thermocouple type T [117], with a temperature range of -270°C to +370°C with an accuracy of +/-1°C, and measures were taken at a sampling rate of 1Hz (1 data point per second). Figure 3-5 shows the trend of the warm water bath temperature, from room temperature up to stabilization of the water temperature.



Figure 3-4 Specimens in a warm water bath for conditioning.

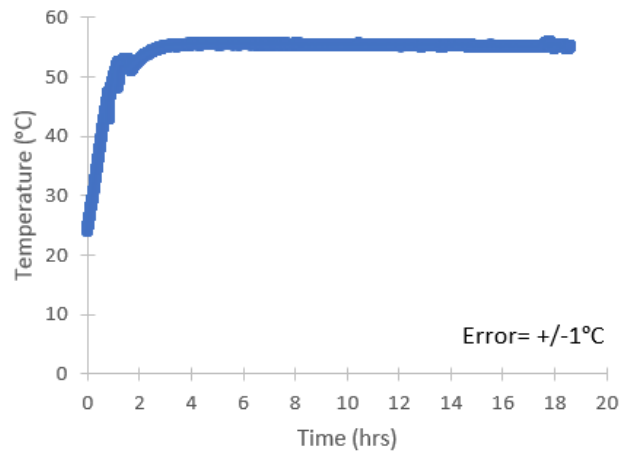


Figure 3-5 Measured temperature of the warm water bath.

Weight measurements were taken every 24 hours. Material condition was calculated accordingly to:

$$\%W_{cond} = \frac{W_{wet} - W_{dry}}{W_{dry}} \times 100\%$$

Equation 3-1

Where, W_{dry} and W_{wet} are, respectively, the weight of the material in its dry and wet condition in grams. $\%W_{cond}$ is the level of humidity in the material in percentage. In average 72hrs were sufficient to reach the target range. Figure 3-6 shows the histograms for the random set of 70 specimens, measurements are for before conditioning (Dry) and after (Conditioned). Specimens showed a dry weight of 15.19g (average) and a wet weight if 15.39g (average), whereas the final percentage of humidity content reached was 1.32% (average), which is in compliance with the aforementioned range with no specimens over or below these limits.

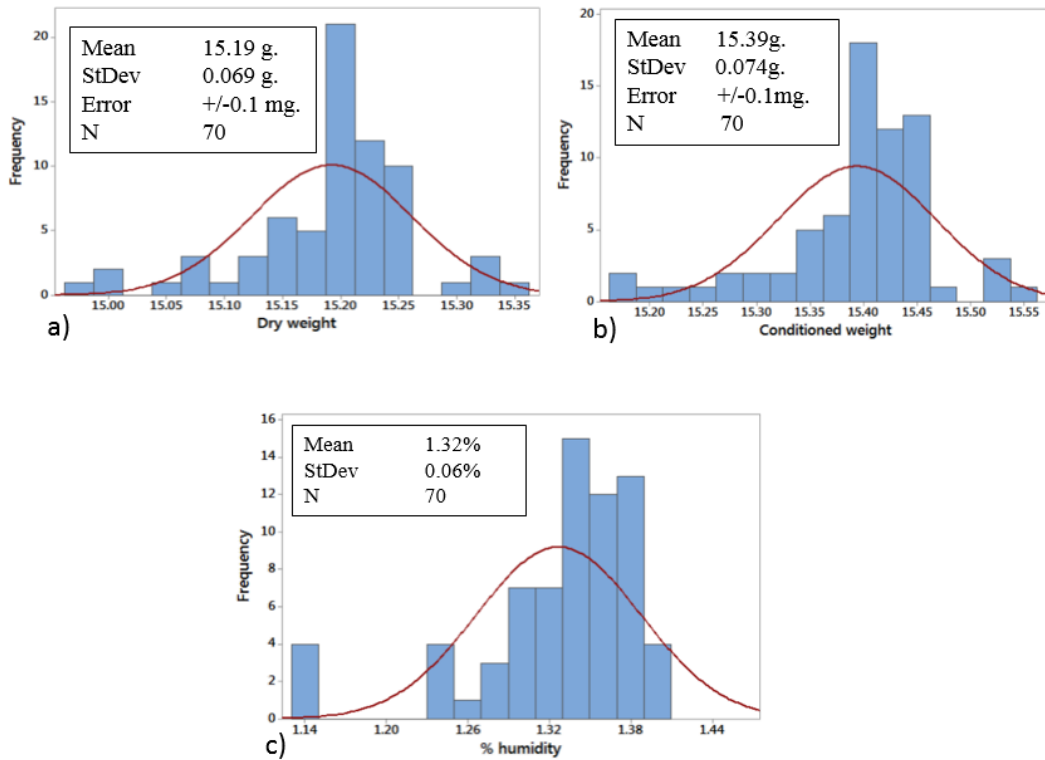


Figure 3-6 Specimen weight a) before condition (Dry), and b) after conditioning (Wet). c) Final percentage of humidity content (Condition).

3.3 Specimens geometries

3.3.1 Uniaxial specimens

Dog-bone coupons were used to characterise the material anisotropic behaviour under uniaxial loading conditions, both in tensile and fatigue. The specimen geometry was also designed to reduce the effects of machine/frame induced misalignment [3], [118]. This was achieved by analysing similar specimen geometries used in other relevant published work, i.e. Fatemi et. al. [75] and De Monte et. al. [76], as well as, per BS EN ISO 527-4:1997 [119]; and by adjusting the coupon's dimensions to perfectly fit the testing hardware. Final specimen's dimensions are shown in Figure 3-7. The 4mm thickness corresponds to the nominal thickness of the plates and is set by the injection moulding process and not by the specimen machining, as shown in Figure 3-2. The 6 mm diameter holes located at the coupon shoulders were created for ease of manufacture, they allow the machining of several samples at the same time. These shoulder regions are gripped during the experimental testing and, as such, have no influence in the material structural response.

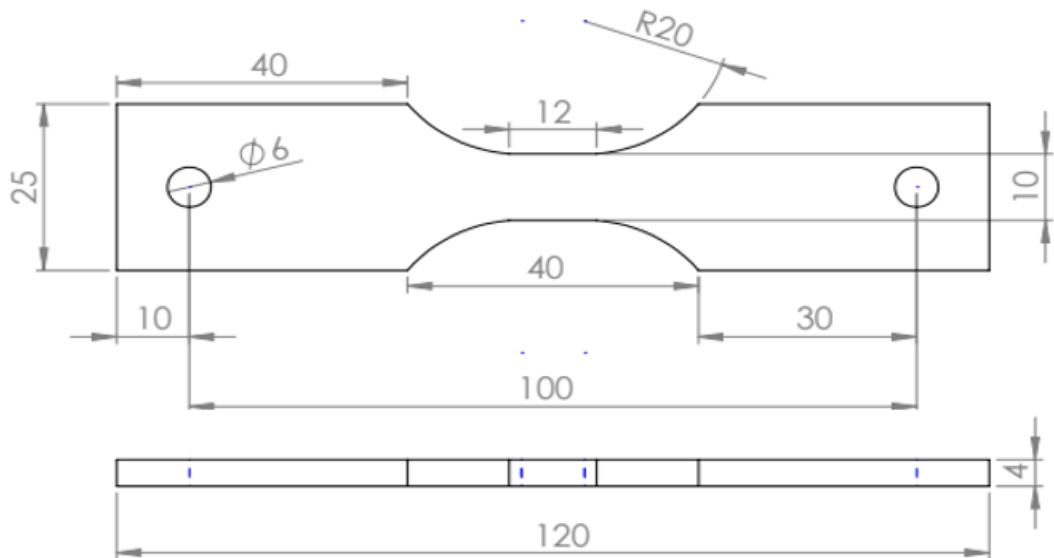


Figure 3-7 Dog-bone specimen geometry. Nominal dimensions shown in millimetres.

3.3.1.1 Specimen orientation

Four different reference specimen orientations, with respect to the mould flow direction, were used to characterise the material anisotropy due to the fibre orientation distribution, in both monotonic and fatigue conditions. These reference orientations are: longitudinal ($\theta=0^\circ$), transversal ($\theta=90^\circ$) and two mid-axis ($\theta=30^\circ$ and $\theta=45^\circ$). To minimize uncertainties in the experimental results, only one specimen was cut from each of the plates and every time was done at the same location, this assured the same fibre distribution at the specimen's gauge length location. Figure 3-8 shows the location and orientations (θ) of the specimens on the injection moulded plates, as well as the gauge-length area shared by all coupons. Additionally, in order to assess the effect of injection moulding on the material response, two Edge locations were also selected for validation of the modelling approach: Near the mould's side edges and along the flow direction ($\theta=0^\circ$ Edge), and close to the gate ($\theta=90^\circ$ Edge). Figure 3-9 shows the exact location of these specimens.

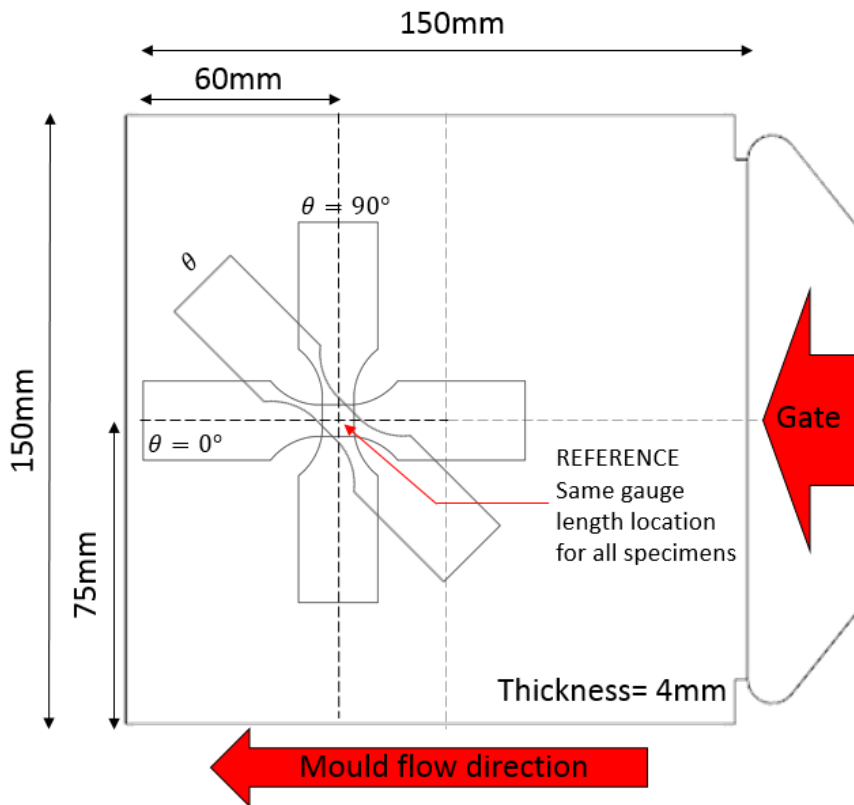


Figure 3-8 Project's specimens orientations (θ) and locations on the injection moulded plate.

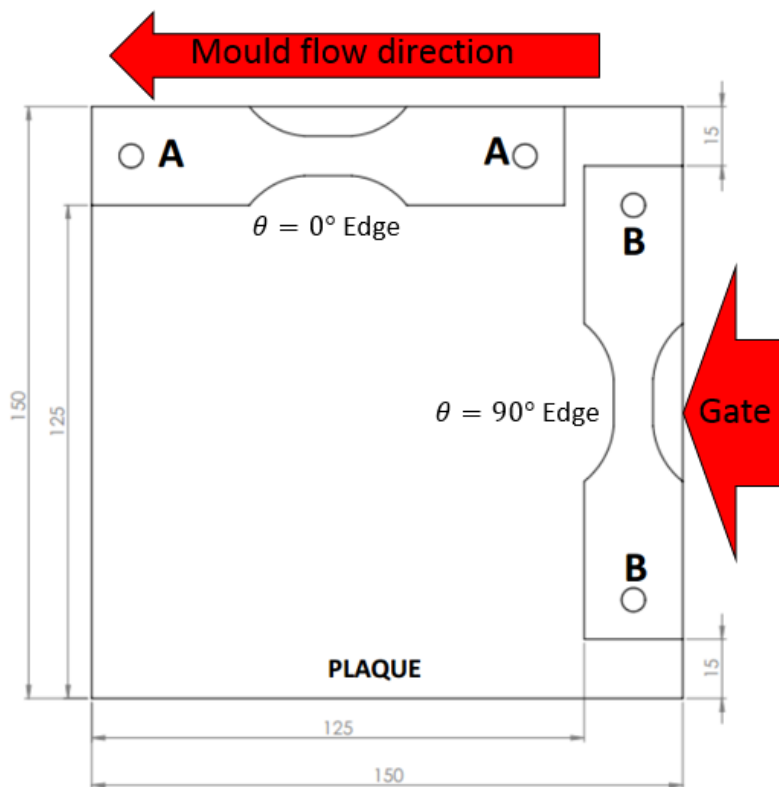


Figure 3-9 Locations for "Edge" specimens. Dimensions in millimetres.

3.3.1.2 Machining

Different machining methods were initially considered, but due to restrictions in terms of cost, time, in-house availability, etc., CNC milling was finally chosen as the manufacturing process for the specimens. The general milling procedure is shown in Figure 3-10, and is done at a spindle speed of 3500 RPM, feed rate of 350 mm/min and a depth of cut of 8 mm. The general process is the following:

- 1) Rectangles of close overall dimensions to the final specimens are cut from the 150 x 150mm plates at the required location depending the orientation (θ) of the samples, per Figure 3-8.
- 2) A special jig was created in order machine several samples at the same time. Rectangles from step (1) are then stacked up together.
- 3) A machining instruction program was created to cut the dog-bone shape per Figure 3-7 dimensions.
- 4) CNC milling is done per step (3) instructions.
- 5) Final coupon produced.

Specimen dimensions in terms of the gauge length's width and cross-sectional area were measured and calculated, respectively. These are shown in Figure 3-11, where an average of 10.11mm for the width, and an average of 39.55mm² for the cross-sectional area were found. Finally, the thickness was not machined from the original plate and measurements are shown in Figure 3-2.

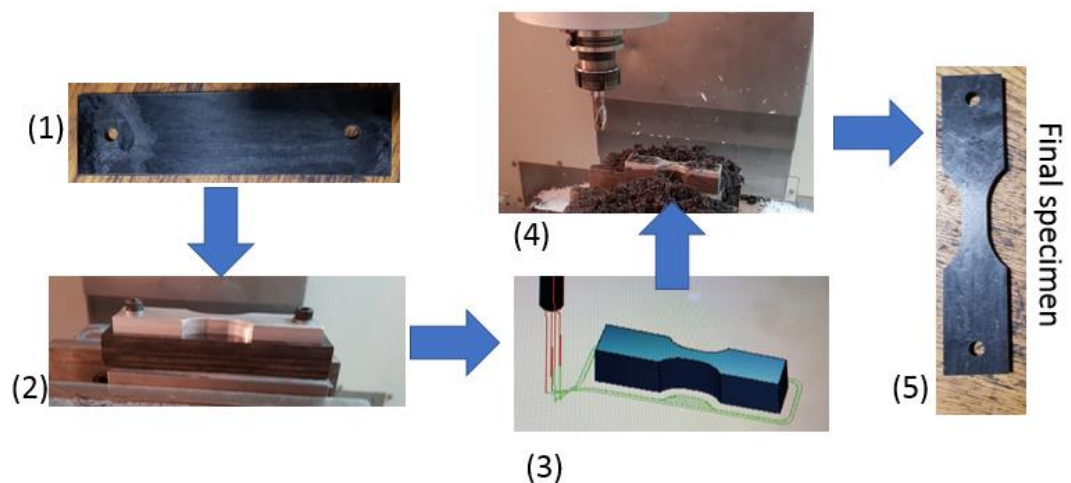


Figure 3-10 Specimen manufacturing workflow procedure.

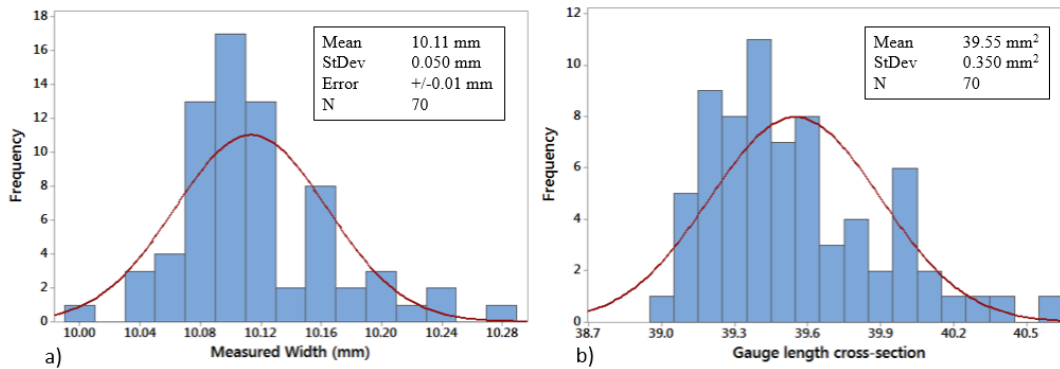


Figure 3-11 After-milling histograms for a) specimen's gauge length width (in millimetres), and b) calculated gauge length cross-sectional area (in mm²).

3.4 Apparatus and data acquisition

3.4.1 Uniaxial testing

Material characterisation under uniaxial conditions, both tensile and fatigue, was carried out using a Nene Testing System servo-hydraulic machine equipped with an Interface 1020 load cell [120], with a capacity of +/-12.5kN (total force range of 25kN) with a static error of +/-0.04% and fatigue rated for up to 10⁸ cycles. Additionally, the testing frame has a built-in actuator LVDT (Linear Variable Differential Transformer) with a stroke range of +/-50mm (total displacement of 100mm) and a measured error of +/-1%. The machine is controlled by a MOOG SmartTest ONE test controller [121]. Force and displacement, as well as temperature and strain, were recorded for each test. The particulars of the data acquisition are presented in detail later in this chapter. Figure 3-12 shows the testing frame and setup used during fatigue testing.

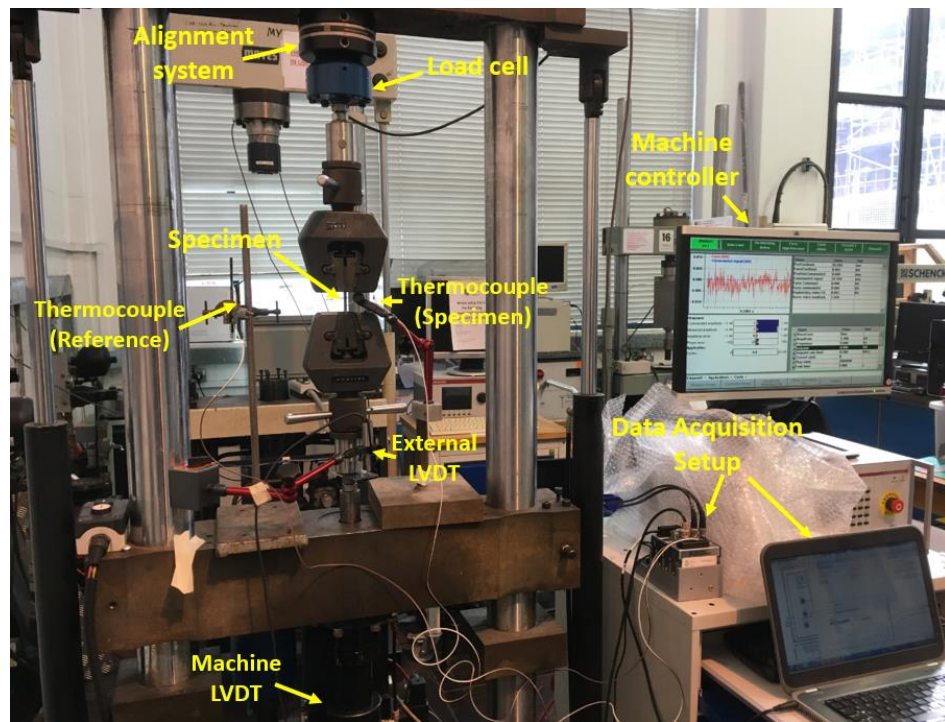


Figure 3-12 Hydraulic testing machine setup.

3.4.1.1 Alignment control

Alignment was of importance during testing as misaligned specimens could introduce multiaxial loads that would not be representative of the required testing conditions. For this effect a MTS 609 Alignment fixture [122] was used to carefully control of the gripping position, and therefore the specimen's alignment, with respect to the actuator and machine's load cell, as is shown in Figure 3-12. Measurement of the alignment was done via an eight-channel strain-gauged rectangular specimen constructed per ASTM E1012-14 [123]. Single-element strain gauges with a 2 mm active grid and 5% strain limit (FLA-2-17 [124]) were used. Dimensions, locations of the sensing strain gauges and final specimens are shown in Figure 3-13a-b; a protective silicone layer was also applied to the gauges. Measurement of the specimen used was carried out using a combination of LabVIEW [116] code (Figure 3-13c) and two NI-9237 data acquisition cards to measure the 8 channels in synchrony. In an ideal scenario with no load, no deformation should occur (zero strain). Under this condition, misalignment or bending in the out-of-plane direction (with respect to Figure 3-13a plane) occurs if strain gauges SG01 and SG02 read a positive strain (Tension), and opposite strain gauges SG05 and SG06 read a negative strain (Compression), or vice versa. In-plane bending occurs when this same behaviour is seen but for the set of strain gauges SG03-SG04 and SG07-SG08, respectively. Based on this principle alignment correction was carried out by: First, assessing the current level of alignment

via strain readings (before). Second, correcting the gripping position, by controlling the alignment fixture, until the strain gauge readings are minimized (after). Figure 3-14 shows a comparison of strain readings when using and not using the alignment fixture. Figure 3-15 shows the before and after position the grips when the alignment system is used.

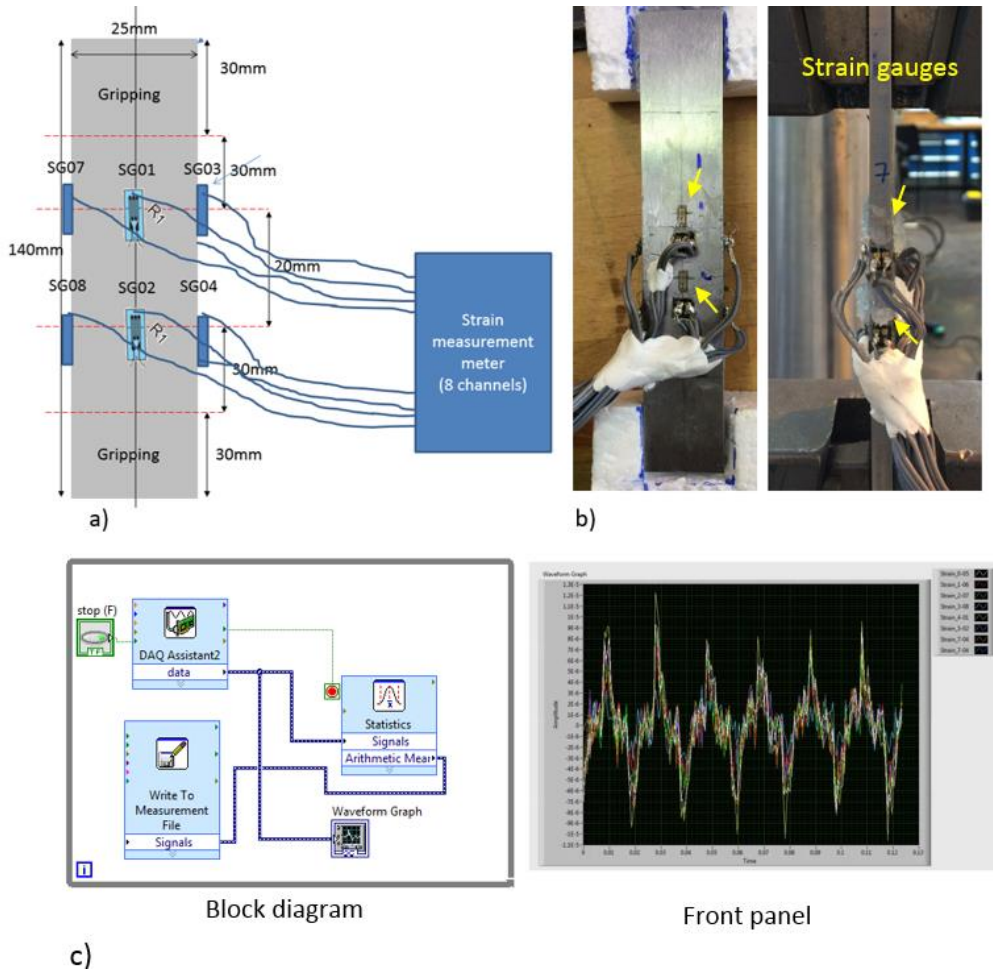


Figure 3-13 a) Schematic of alignment specimen. b) Gripped specimen during calibration. d) LabVIEW code used for calibration.

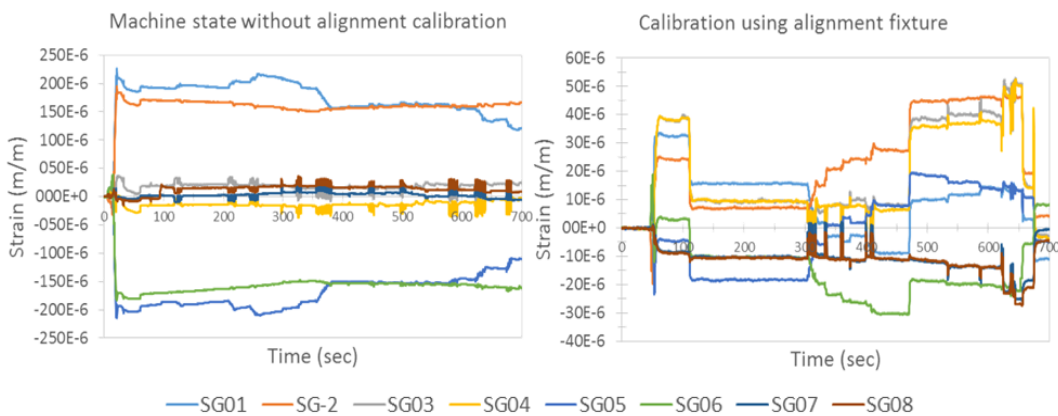


Figure 3-14 Strain gauges readings without and with the alignment system.

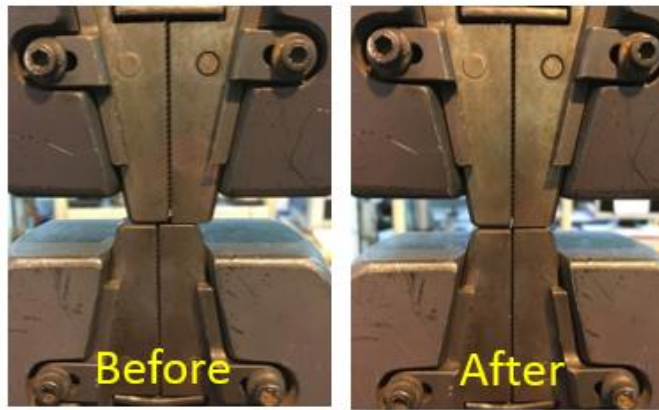


Figure 3-15 Position of grips before and after calibration.

3.4.1.2 Analogue data acquisition

Important data corresponding to the material response under fatigue loading conditions was acquired for each fatigue cycle. This analogue data corresponded to:

1. The testing Force
2. The machine's Displacement,
3. The specimen Strain, and
4. The Temperatures of the specimens surface, the grips and a reference (room temperature).

Acquisition of the data was done simultaneously during the fatigue testing via a LabVIEW [116] code in combination with several NI data acquisition cards: NI-9211 (for the thermocouples), NI-9215 (for the force and displacements) and NI-9237 (for the strain gauges and extensometer). An image of the LabVIEW [116] code, created by the author to acquire the information, is shown in Figure 3-16. An adequate sampling rate was also necessary as to correctly capture the peaks and troughs. This rate could not be too low to avoid aliasing (distortion of the measured wave form) [125], nor too high to avoid unnecessary large data files. Figure 3-17 shows the calculated error for different sampling rates. A sampling frequency of two times the testing frequency is commonly used, a.k.a. Nyquist sampling rate [125]. For the case of the present project, the corresponding Nyquist sampling frequency would be 10Hz, or 10 samples per cycle, but this seemed to provide with a large error in terms of identifying the actual maximums, approximate 20%. A frequency of 50Hz, or 50 samples per cycles, was finally chosen as it provides with less than one percent or error, <1%, and also corresponded to exactly ten times the testing frequency.

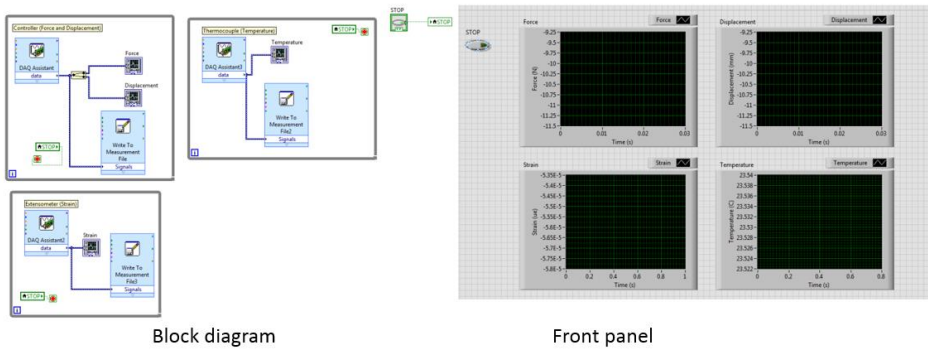


Figure 3-16 LabVIEW program used for measurement of the Force, Displacements, Strain and Temperatures.

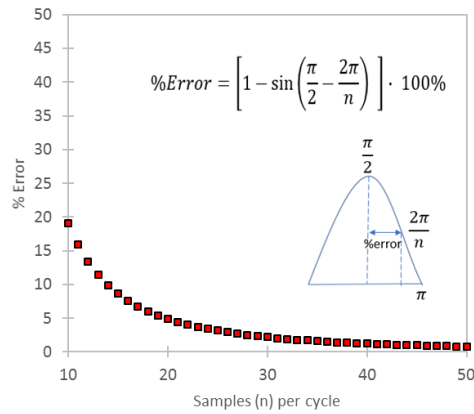


Figure 3-17 Data acquisition sampling rate error.

The machine testing force, corresponding to the feedback measured by the machine load cell; and machine displacement, corresponding to the built-in LVDT feedback, were both recorded. Figure 3-18 shows a measurement example of the Machine's force and displacement signals.

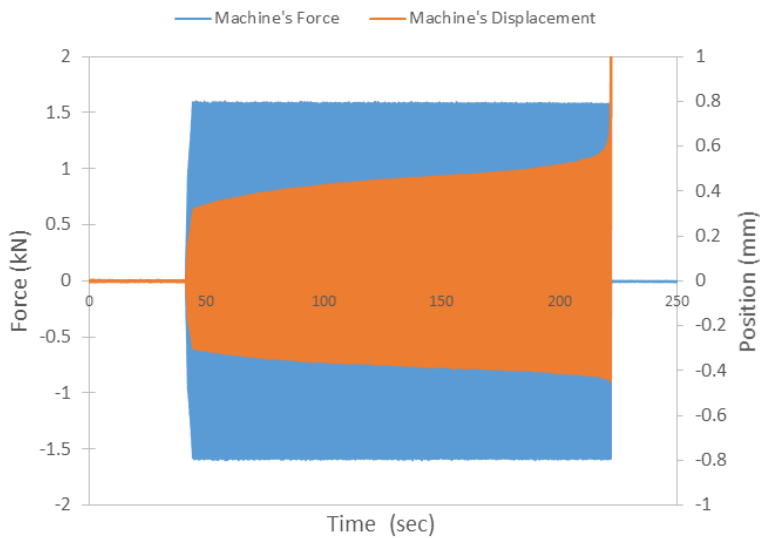


Figure 3-18 Measured machine's displacement and forced feedback.

More accurate displacements were measured with an external Ametek DG2.5/S MK II LVDT [126], with a total travel of 5mm and a linear resolution of $< \pm 2\%$. The external LVDT was instrumented using an independent power supply of 15VDC. Figure 3-19a shows the sensor located in the testing rig before a fatigue testing. Figure 3-19b presents a comparison of raw signals (Volts) between the Machine's LVDT and the external LVDT. It can be seen that a less-noisy, more defined, wave form is obtained using the independent sensor.

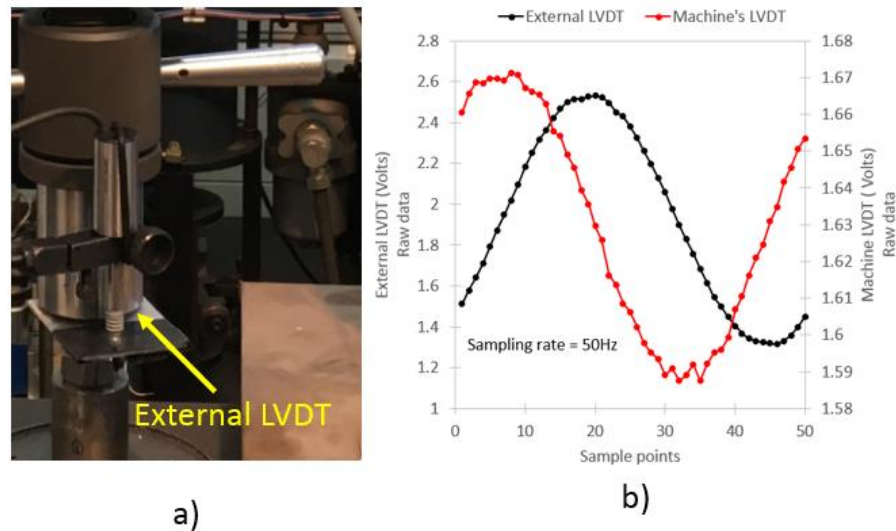


Figure 3-19 a) External LVDT used for displacement measurements. b) Comparison of raw data (Volts) between Machine's LVDT and external LVDT.

Material strains were measured using an Instron 2620 Series [127] fatigue rated extensometer, with a full-scale range of $\pm 5\text{mm}$ and a linearity error of $\pm 0.15\%$. Power was supplied directly by the NI-9237 card through a Wheatstone full-bridge configuration. Figure 3-20 shows the extensometer installed on a fatigue specimen prior to testing.

Finally, temperatures were measured at: the centre of the specimen, the grips, and at a reference specimen. Three separate thermocouples type T [117], with temperature range of -270°C to $+370^{\circ}\text{C}$ and an accuracy of $\pm 1^{\circ}\text{C}$ were used for this. Figure 3-21 shows the location of the thermocouples prior to fatigue testing.

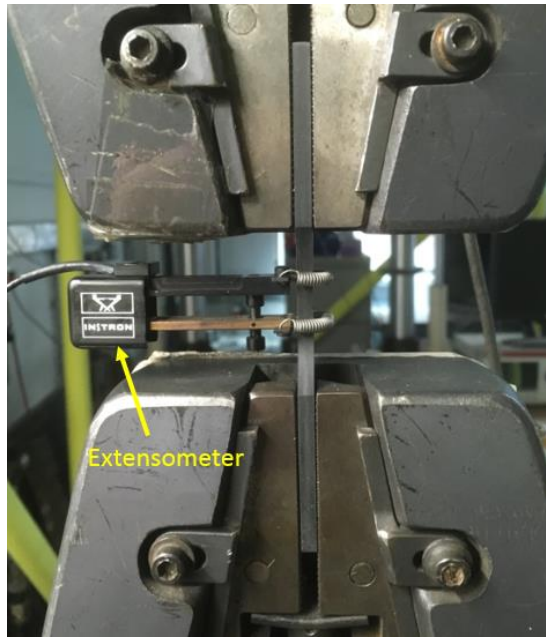


Figure 3-20 Extensometer used to measure the material's strain.

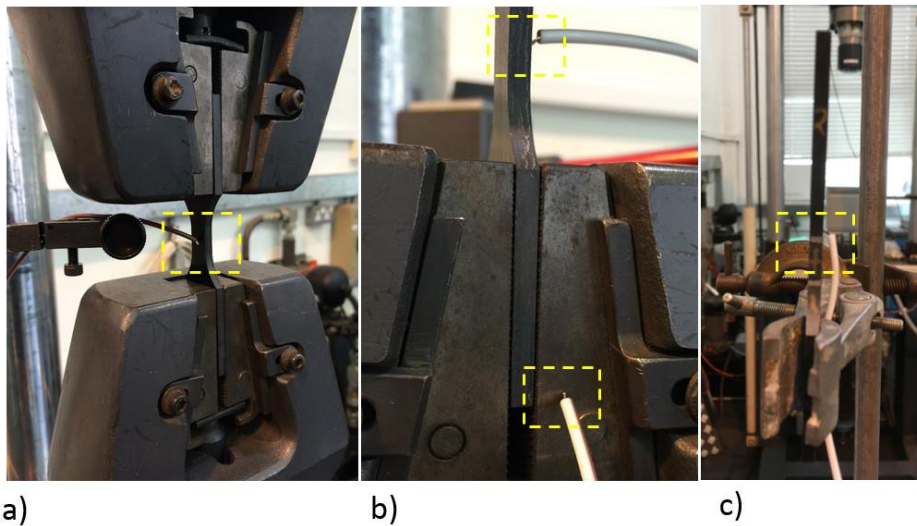


Figure 3-21 Thermocouple locations to measure a) specimen's surface temperature, b) grips temperature and c) reference temperature.

3.5 Monotonic tensile testing procedure.

Quasi-static testing was performed on specimens at all orientations to characterise the material properties. Tensile testing was carried using the uniaxial testing machine previously described, under displacement controlled conditions. An extension rate of 2 mm/min was used for this per ASTM D3039 [128] *Constant Head-Speed Tests* recommendation.

3.6 Fatigue testing procedure

3.6.1 Constant amplitude

Fatigue testing under uniaxial constant amplitude (CA) loading was carried out using force-controlled conditions. The frequency used was 5Hz, this allowed for relatively fast testing times at longer lives and, at the same time, allowed for lower self-heating temperatures, where specimens' surface temperature was monitored for this case (Figure 3-21). Different load levels were established to allow for good spread of the data, in terms of fatigue life, and with a target of 10,000, 100,000 and 1,000,000 cycles, at the industrial partner request. Nominal stresses were later calculated from the machine's loads to plot the specimens' Stress-Life (S-N) curves for each particular orientation per:

$$\text{Stress (MPa)} = \frac{\text{Max. or Min. Load (N)}}{\text{Measured width (mm)} \times \text{Measured thickness (mm)}}$$

Equation 3-2

Three different stress, R, ratios were used to characterise the effect of mean stresses in the composite material. A fully-reversed tension-compression stress ratio, R=-1; and two positive stress ratios, R=0 and R=0.3. The actual stress levels used were selected based on basic manufacturer-provided S-N data, and by conducting a series of early dummy testing to assured specimens' life data was close to the before mentioned industrial partner targets. This did not account for the stochastic nature of fatigue testing, but provided with a good idea to obtain a range of life cycles as close as possible to the request. The stress levels used for the proper testing, are shown in Table 3-2 for each of the different stress ratios, in brackets is the percentage in relation to the tensile strength results shown in Figure 5-8b for each orientation. A schematic of the wave forms, with respect to mean stress, for each R ratio is shown in Figure 3-22. Corresponding $\Delta\sigma$, σ_m and σ_a , were calculated using the equations shown in Figure 2-43. S-N curves were then drawn using the calculated stress amplitude (σ_a), and the final fatigue life (N). Similar to relevant published work [76], [129], a fatigue cut-off limit was set at 10^6 cycles, corresponding to the high cycle fatigue (HCF) regime.

Table 3-2 Stress levels used for uniaxial fatigue testing

Stress "R" ratio	Specimen Orientation	Max. stress /Min. stress in MPa (% of Tensile Strength)		
-1.0	0°	±50 (±48%) ±37.5 (±36%)	±42.5 (±41%)	±40 (±38%)
	30°	±45 (±46%)	±40 (±40%)	±35 (±35%)
	45°	±45 (±49%) ±30 (±32%)	±40 (±43%) ±27.5 (±30%)	±35 (±38%)
	90°	±45 (±56%) ±30 (±37.5%)	±40 (±50%)	±35 (±43%)
0.0	0°	+80 / 0.0 (77% / 0%)	+65 / 0.0 (62% / 0%)	+50 / 0.0 (48% / 0%)
	30°	+65 / 0.0 (66% / 0%)	+50 / 0.0 (51% / 0%)	
	45°	+65 / 0.0 (70% / 0%)	+57.5 / 0.0 (62% / 0%)	+45 / 0.0 (49% / 0%)
	90°	+57.5 / 0.0 (71% / 0%)	+50 / 0.0 (62.5% / 0%)	+40 / 0.0 (50% / 0%)
0.3	0°	+100 / +30 (96% / 29%) +57 / +17 (54% / 16%)	+82.5 / +25 (80% / 24%)	+75 / +22.5 (72% / 21%)
	45°	+71.2 / +21.2 (77% / 23%)	+67 / +20 (72% / 21%)	+57 / +17 (62% / 18%)
	90°	+71.2 / +21.2 (89% / 26%)	+67 / +20 (83% / 25%)	+57 / +17 (71% / 21%)

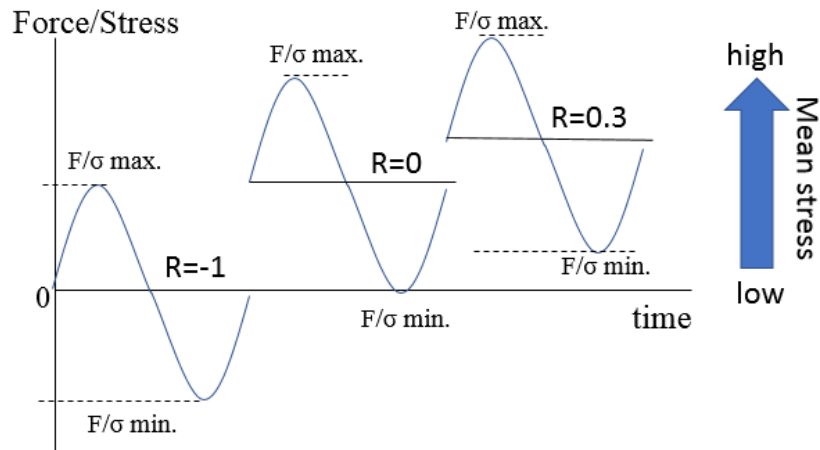


Figure 3-22 Schematic of wave forms for each R ratio.

3.6.2 Block loading

Block loading (BL) was carried out to assess the effect of damage accumulation and load sequence in the material fatigue response. Stress levels were established by analysing the results of the coupon level SN curves, drawn after completing the Constant Amplitude testing; and by calculating a linear damage (D) per block by using Miners' rule for cumulative damage:

$$\sum_{i=1}^k \frac{n_i}{N_i} = D$$

Equation 3-3

Where, n_i is the number of cycles accumulated at stress σ_i . N_i the total life at σ_i . Failure occurs when $D=1$. To allow for a relatively significant amount of blocks before failure, and for progressive damage propagation, D was set to be $<0.5\%$ per block for all specimens orientations. This value was set arbitrarily, in order to obtain an estimated life of at least a couple of hundred blocks per specimen orientation. This meant that for each 0° , 90° and 45° specimens, the estimated total number of blocks to reach $D=1$ would be, respectively, 300 blocks, 222 blocks and 192 blocks. It is also good to mention that although Miner's rule is widely used, it does have several limitations, in particular it just accounts for a proportion of the total life consumed at each stress level and then adds together all the proportions for all the stress levels in a particular block, therefore it does not consider any effect that the load sequence can have in the material response. This method also does not distinguish whether the damage is due to a particular mechanism, so is not possible to pinpoint the physical nature of the

material failure. This also means that the accumulation is just linear, and does not account for any non-linear damage accumulation that might occur due to the progressive degradation of the material properties caused by the propagation of damage. Nevertheless, due to its simplicity of implementation, it represented a sensible starting point. Finally, R=-1 was selected for this test to avoid the inclusion of mean stress effects in this analysis. Testing stress levels, load sequence and estimated D per block per orientation can be seen in Table 3-3. Figure 3-23 shows the first two blocks of a BL test for a 0° specimen with High-to-Low load sequence.

Table 3-3 Block loading stress levels and sequence definition.

R ratio	Orientation	Nominal σ_a (MPa)	Cycles per block	Damage per block (%)	Load sequence		
					High - Low	Low - High	
-1	0°	45	40	0.11	↓	↑	
		40	250	0.09			
		37.5	1,000	0.12			
		Total Miners' rule damage per block (D)					0.3%
	45°	40	40	0.2	↓	↑	
		35	200	0.19			
		30	1,000	0.11			
		Total Miners' rule damage per block (D)					0.5%
	90°	40	40	0.2	↓	↑	
		35	200	0.15			
		30	1,000	0.1			
		Total Miners' rule damage per block (D)					0.45%

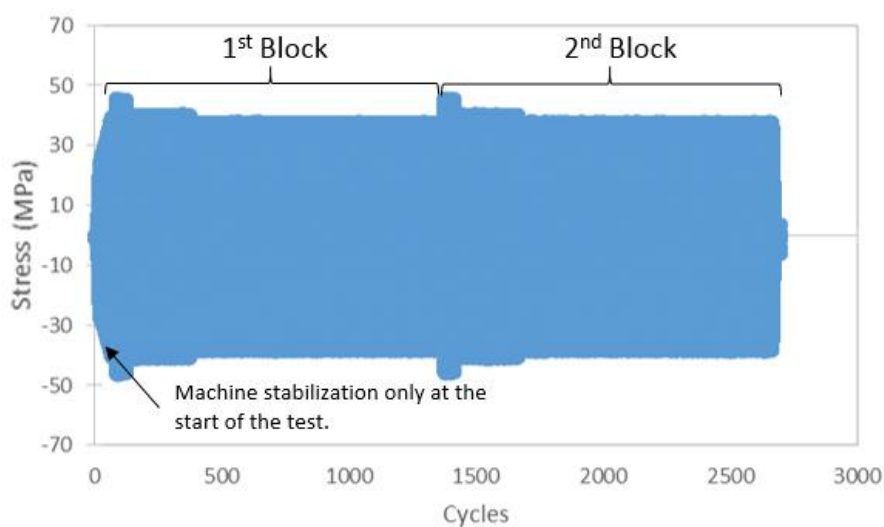


Figure 3-23 Example of BL test at R=-1 for a 0° specimen tested at High-to-Low sequence. Only first two blocks are shown.

3.7 Material analysis techniques

3.7.1 Digital Image Correlation (DIC)

Digital Image Correlation or DIC, is an optical (image) based experimental technique used to measure displacements, motion and strains [130]. This methodology allows for full-field measurements, in-plane (2D) and out-of-plane (3D, stereoscopy). Full strain fields are calculated by comparing the movement of after-deformation images, in relation to a reference frame (zero deformation). An area of interest is selected in the specimen, which is then subdivided into smaller interrogation windows (subsets). Displacements are calculated by selecting individual points inside each subset in the reference image [131], e.g. $A(x_0, y_0)$ and $B(x_1, y_1)$, and tracking their respective location in the deformed frame, e.g. $A'(x'_0, y'_0)$ and $B'(x'_1, y'_1)$, as shown in Figure 3-24a. To allow this tracking, the testing specimens were speckled using a spray paint technique. Matte black droplets over a base primer white, to minimize shining and overexposure of the images. Examples of the speckled samples used in this project are shown in Figure 3-24b. Finally, Figure 3-25 shows the configuration for the 3D DIC system, which consists in the acquisition cameras, a source of white light, the specimen under study and the analysis software (not in frame). One of the main characteristics of this technique is that it can reliably resolve displacements of up to $1/100^{\text{th}}$ of a pixel. In other words, a 5 Megapixel camera (current setup) looking at a 100 mm sample, would be able to resolve displacements with a resolution of ~ 1.5 microns (theoretically) [132].

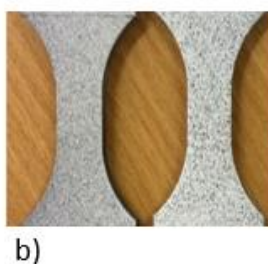
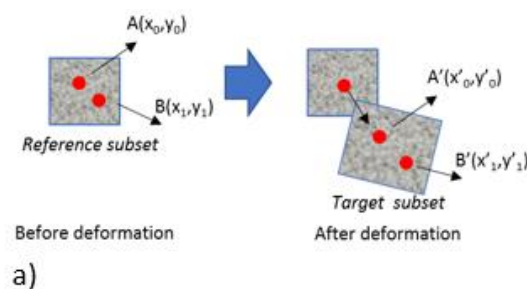


Figure 3-24 a) Depiction of a subset before deformation and after deformation.
b) Example of specimens speckled for DIC.

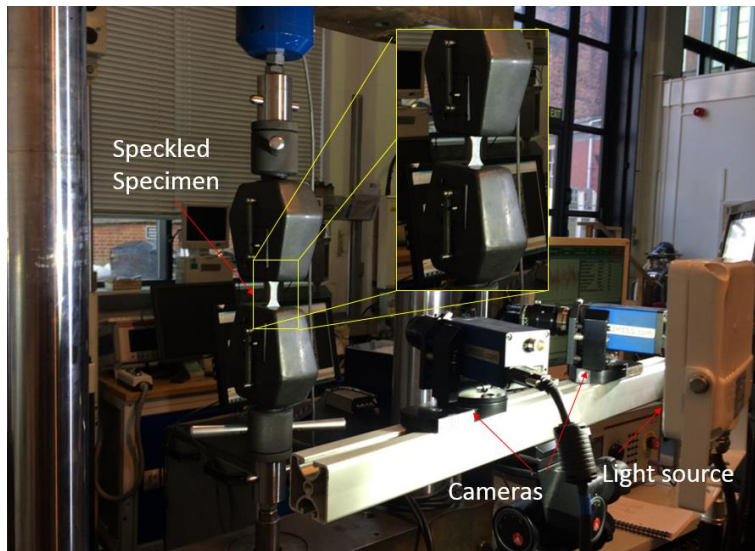


Figure 3-25 3D DIC hardware configuration.

3.7.1.1 High speed DIC

Material softening under fatigue loading conditions could not be measured with the typical DIC setup due to the high testing frequency. High speed (HS) DIC was then used to measure the material strain field distributions under this cyclic conditions. For this case HS Phantom VEO 410 L [133] cameras were used. These cameras have a maximum resolution of 1280x800 pixel with a maximum frame rate, at this resolution, of 5.2kHz and a reacting time of 9.6 seconds. A total of 100 frames per fatigue cycle were capture to correctly characterise the strain fields during fatigue testing. The corresponding capturing rate was 500Hz. Figure 3-26 shows the typical configuration for HS DIC testing.

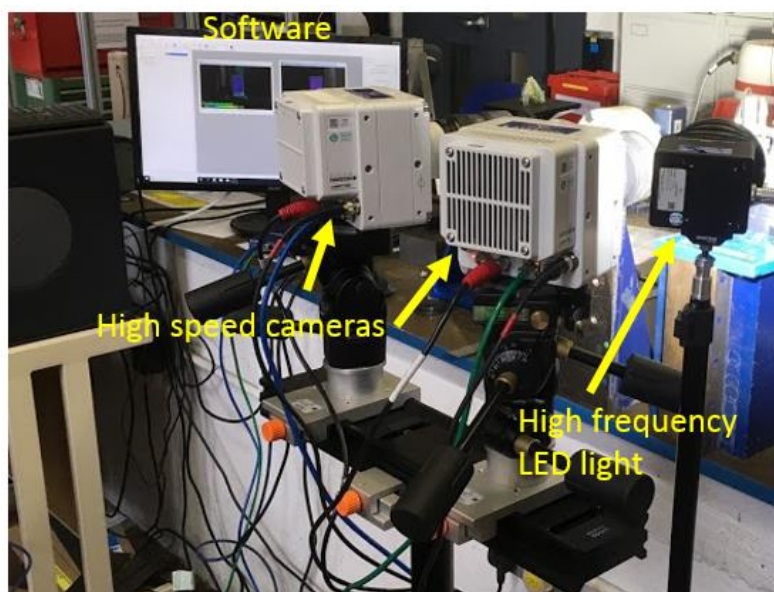


Figure 3-26 Typical configuration for High Speed DIC testing.

3.7.1.2 DIC Resolution

The system resolution was needed to assess the confidence in the strain results obtained with this technique. Three samples were tensile tested for this case. A minimum subset size of 8.5x8.5 pixel was achieved for each sample (Figure 3-27a), below this size the correlation would either fail, frames would be skipped or some data would be lost in the area of analysis. After inspecting the result of the correlation, a minimum confidence range of between 0.0001 to 0.0003 m/m was found for this technique, below this range only noise is detected. The results can be seen in Figure 3-27b.

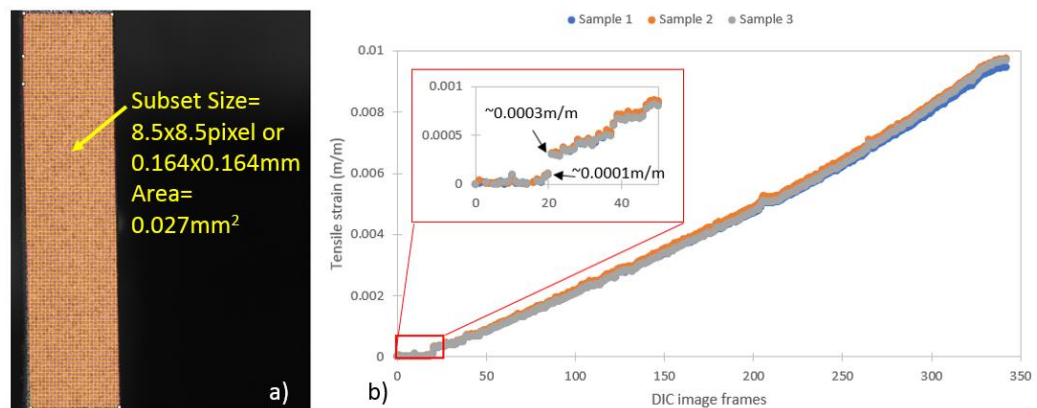


Figure 3-27 DIC technique showing a) minimum subset size and b) achieved minimum resolution.

3.7.2 Optical microscopy

The analysis of the specimens under optical microscopy was done to assess and measure the fibre distribution throughout the thickness of the material. For this, a careful sample preparation was needed. It was first started by selecting a region of interest, e.g. specimen's gauge length, and then cutting through using a diamond blade to avoid damaging the fibres. After this, and to facilitate the observation of the fibres, the samples were cold mounted in epoxy resin at a ratio of 4 to 1 (resin to hardener) and left to dry for 24 hrs. Afterwards, to remove the surface imperfections, the specimens were grinded and polished at different steps, velocities and times. The main stages are listed below:

1. A coarse grinding using P800 grind paper.
2. A finer grinding using diamond suspension of 9 microns.
3. A coarse polishing using diamond suspension of 6 microns.
4. A final polishing using diamond suspension of 1 micron.

Finally, the specimens were observed using an optical microscope Nikon Eclipse LV150N [134], with available magnifications of 5x, 10x, 20x, 50x and 100x. Epoxy-mounted specimens and the microscope used are shown in Figure 3-28.

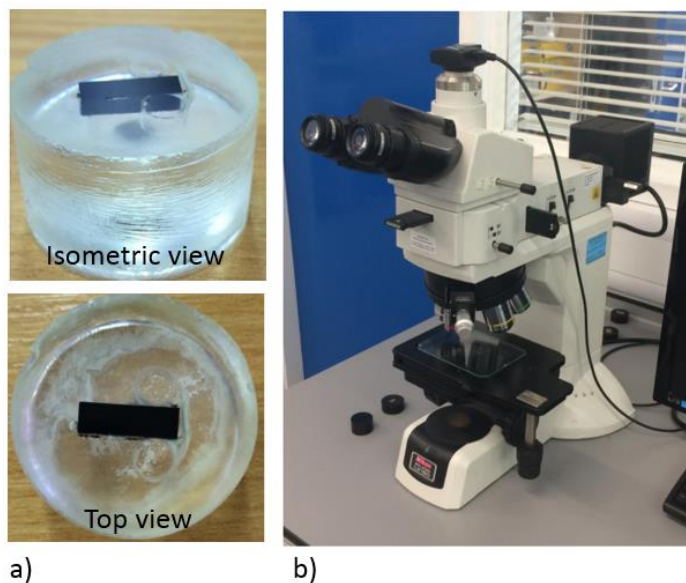


Figure 3-28 a) Specimens mounted on epoxy resin. b) Optical microscope used for observations.

3.7.3 Scanning Electron Microscopy

This technique was used on the material with the objective of analysing: The fracture surface of failed specimens, the as-moulded surface of the composite, and the as-machined surface of the testing coupons. For all cases, a careful preparation of the samples was needed. As the composite is non-conductive a layer of conductive coating was required prior to analysis, also the samples needed to be small enough to fit the microscope chamber. Specimens were first cut with a diamond blade to avoid damage to the fibres. Samples were then mounted on aluminium (Al) stubs with the help of Acheson Silver (Ag) DAG compound, both being conductive materials. Mounted specimens are finally coated with a thin gold (Au) layer via sputtering, this creates a conductive close circuit for electrons to travel through the polymer. Observations of the samples was done using a SEM Hitachi TM3030 Tabletop Microscope [135] with an available magnification of 15 to 60,000x (digital zoom: 2x, 4x). Figure 3-29a to c show an example of the sample preparation, the final SEM-ready specimen and the actual microscope.

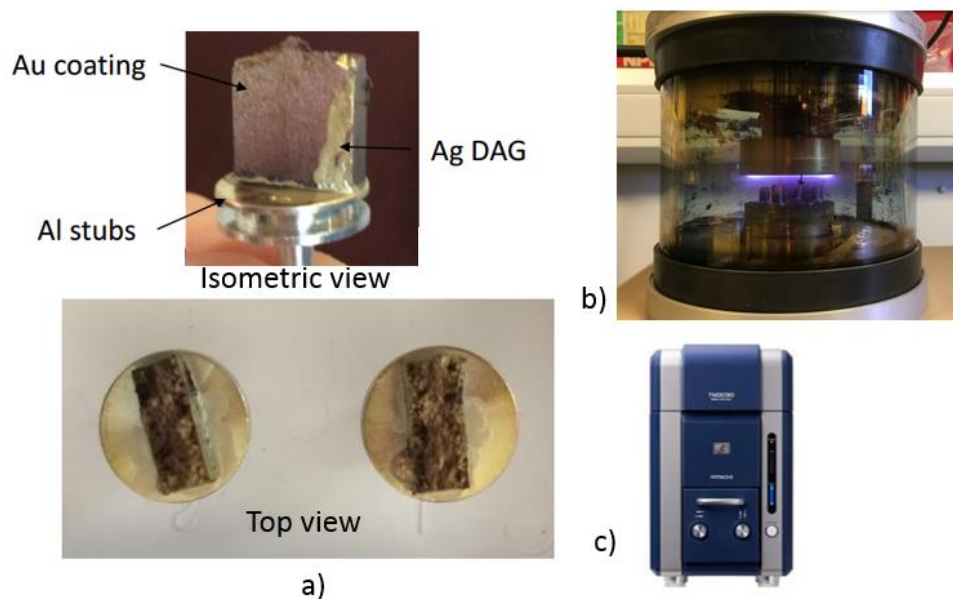


Figure 3-29 a) Example of SEM-ready specimens showing the aluminium stubs, the gold coating and the silver DAG compound. b) Sputtering machine used for gold coating. c) Hitachi microscope.

3.7.4 Computed tomography

While using microscopy techniques allowed the observation of the surface of the material, there was important information that could only be extracted from inside, e.g. fibre distribution. Additionally, these are destructive techniques which implied the possibility of losing important data during the sample preparation. For this reason, micro-computed tomography (μ CT) was performed to inspect the internal structure of the material in a non-destructively manner. The μ CT system used was a Bruker Skyscan 1172 [136] desktop x-ray with a 100kV X-ray tube source, power of 10W (0-250 μ A), a minimal focal spot size of <5micrometres and a detail detectability of <1micrometre. The scanner setup can be seen in Figure 3-30. The specimen preparation was simpler than for the other techniques, a maximum sample size of <5mm per side was used. In specific, the average size of the specimen was \sim 5x5mm by \sim 4mm in thickness, which allowed the full thickness of the plate to be inspected. The scanner settings that produced the best image quality were found by trial and error. These were: a camera binning mode of 2000x1024 and a 0.5mm aluminium filter; this allowed a maximum voxel resolution between 2.53 - 3 μ m. The scanning was also done with a rotation step of 0.7° and an image averaging of 2 with a 180° rotation. The bigger the specimen, the lower the maximum resolution achievable, in specific inside the material. The main limitation faced using this technique was the equipment itself. At maximum resolution

the final scan struggled to show: individual fibres, a clear boundary between the fibres and the matrix, and any feature in the matrix itself, such as cracks, voids, etc. Nevertheless, it was possible to distinguish the different microstructural layers produced by the fibre orientation distribution as whole, as shown in Figure 5-1. Finally, Figure 3-31a-c shows a sample being readied for scanning and then installed into the scanner chamber.



Figure 3-30 Bruker Skyscan 1172 microCT scanner.

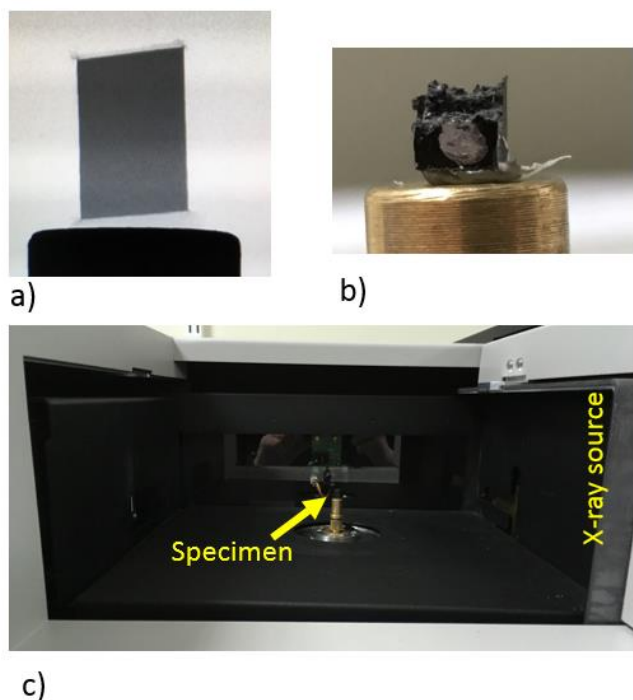


Figure 3-31 a) X-ray preview of specimen before analysis. b) Specimen mounted ready for scanning. c) Specimen inside CT chamber.

3.8 Conclusion

The present experimental methodology described the process followed to characterise the material properties of a SFRP made out of a nylon 6,6 resin and a relatively high amount of reinforcement, 50wt% short glass-fibre. In contrast, more commonly used nylon/short glass-fibre reinforced polymers include up to 35wt% of fibre reinforcement, e.g. [137], [138]. Similarly, the material thickness investigated on this project is relatively high at 4 mm. This is significantly larger than what it is normally investigated and documented in the literature, which typically is around 3 mm or less, e.g. [138], [139]. Additionally, unlike other published work [20], to maintain the consistency of the fibre distributions and therefore reduce the sources of inaccuracies in the analysis, only one specimen was machined out of each composite plate and every single time at the same location. Application of state-of-the-art high-speed camera equipment was also implemented to allow the analysis of the material behaviour under cyclic conditions. As part of the model calibration and validation effort, three different locations on the composite plate were chosen to assess the effect of the fibre distribution on the material's mechanical response: a reference location, close to the central part of the plate; and two Edge locations, close to the fan gate and to the mould's side edges, respectively. Additionally, to better understand the material fatigue response, three different stress ratios were also studied, two positive and one fully reverse. A comprehensible methodology for specimen conditioning, water/humidity absorption, with careful control of the water bath temperature was also established and documented for further reference. Measurement of the key analogue data, such as: displacements, strains, forces and surface temperatures, was conducted by using state-of-the-art instrumentation techniques via the implementation of hardware and software solutions, programmed by the author. An analysis of the recommended sample frequency to minimize aliasing and sampling errors was carried out and also documented for further reference. To assure the repeatability of the results, and as to reduce the sources of systematic errors, an industry grade alignment system was used as part of the experimental program, calibration of the alignment was done via a 8-channel synchronous measurement.

4. MODELLING METHODOLOGY

4.1 Introduction

This chapter presents the technique used to predict the fatigue life of short fibre reinforced polymer composites. Due to the complexity of the material behaviour a multistage modelling methodology was proposed, which covered from the injection moulding simulation of the material, to the final fatigue prediction of the specimens. In this regard, a map of the inputs and outputs of each modelling step is shown in Figure 4-1. In summary; the process started with the injection moulding simulation which provides with the fibre alignment information. The anisotropic material properties were then predicted based on the material constituents, fibre and matrix, via a mean field homogenization technique. In the following stage, both the fibre information and the material model were introduced into the specimen's structural model and the stress analysis was setup. Finally, the fatigue calculations were carried out depending on the load history, the stress states and the fibre information, in the case of the S-N approach, to produce a fatigue prediction.

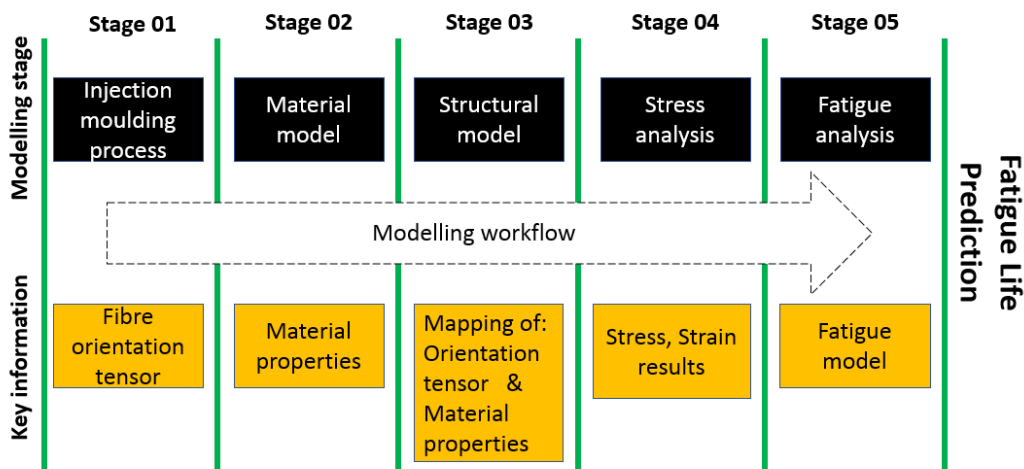


Figure 4-1 Computer aided engineering (CAE) workflow map.

4.2 Injection moulding process

The modelling methodology was started with the simulation of the injection moulding process, which provided with the prediction of the fibre orientation tensor information, a key driver of the final anisotropic material properties.

With information provided by the material manufacturer (BASF) on how the actual composite material was manufactured, the structural model of the injection moulded

plate was created. For this analysis Autodesk Moldflow Insight 2017 [140] software was used. To better characterise the behaviour of the fibres, and as best practice, not only the cavity (plate) was modelled, but the fan gate (which allows the distribution of the material), and the runner (the canal through which the material flows into the gate-cavity), were also modelled [141]. At the end of the runner, the injection point (the simulated sprue) was positioned. The overall model of the part can be seen in Figure 4-2.

The boundary conditions for the injection moulding simulation followed the material manufacturing process. The material melt temperature was set at 300°C, whereas the mould surface temperature at 85°C, this lower mould temperature allows to solidify the material as soon as the cavity is filled reducing the processing time. Fibre aspect ratio of 20 (200 microns by 10 microns in average). The injection time was 1.8s, with a dynamic viscosity of 0.354. In terms of the process settings; the injection rate is 5,000 cm³/s, with a maximum injection pressure of 180MPa and a maximum clamping force of 7,000 tons, typical values go from 5 to ~6,000 tonnes [141]. In other to fully characterise the fibre information, the injection moulding considered the filling and the packing stage of the material; with a total cooling time of 20s. The pressure used for the packing stage was 108MPa. Additionally to this, the simulated mould for the injection moulding was set as software default, this is a steel P20 mould with a density of 7.8 g/cm³ Young's modulus of 200,000 MPa and 0.33 Poisson's ratio.

In terms of the injection simulation, the fibre orientation analysis was done under the *3D analysis technology* option in Moldflow [44]. The result is a 3x3 symmetric tensor with six different components, as shown in Figure 2-18, at each node on the tetrahedral mesh (default element type). The fibre analysis model used was based on the Folgar-Tucker [47] model, available in the software, the definition of this model was explained in the Literature review section of this thesis. This meant that the orientations of the fibres were mainly dependent on the interaction coefficient (C_i). In theory this coefficient can vary anywhere from 0 to 1. With values close to 0 meaning that the fibres do not interact with each other, and larger values meaning that the fibres become less aligned [142]. In reality C_i values range from between 0 to 0.1, as it has been found that higher values do not improve fibre alignment in this method. In a validation study carried out on Moldflow 2017 release, it was found an average error of less than 0.2% using the Folgar-Tucker model [143]. This study was done on a 3mm, in thickness, plate of PA66GF50 of the same manufacturer than the present project's material (BASF). Calibration of the present analysis was done against Computed

tomography measurements by comparing the fibre orientation tensor components. The results are shown in a later chapter of this thesis. A mesh independence study was also conducted in terms of the orientation tensor components. Figure 4-3 shows the variation of the matrix components through the thickness with the mesh density, from coarse to fine (selected mesh), with values taken in the middle of the plate. Finally, Figure 4-2 shows the mesh chosen for the injection moulding simulation (including gate and runner). The final mesh consisted of a total of 1,379,406 four-node solid tetrahedral elements, this is shown in Figure 4-3 as "Fine mesh". A comparison between the simulation results using the selected mesh, and experimental measurements is shown in Figure 5-6 in Chapter 5.

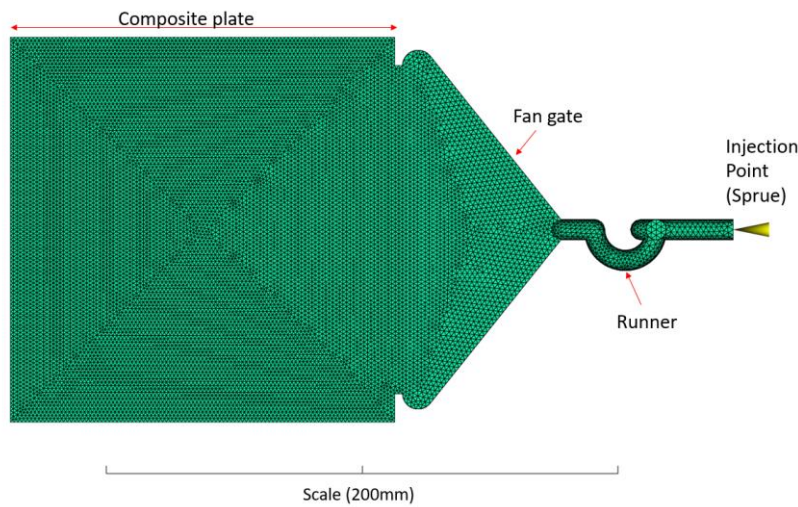


Figure 4-2 Optimised injection moulded plate's finite element mesh.

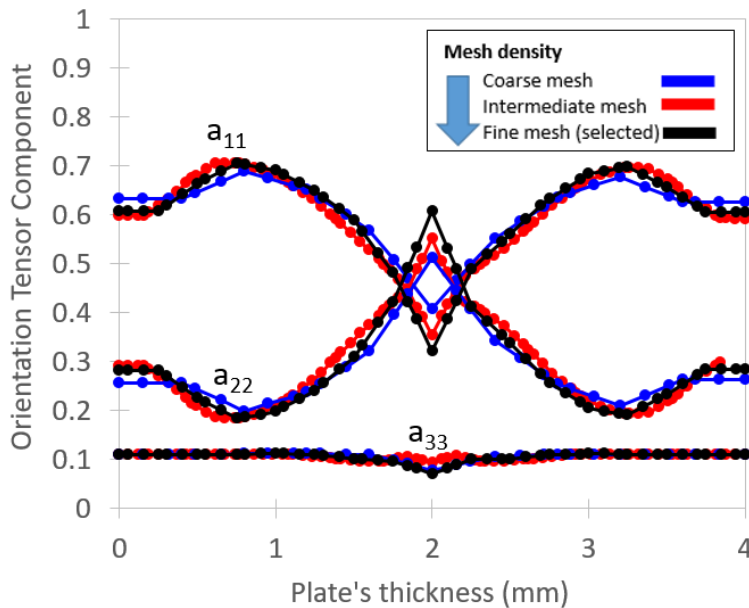


Figure 4-3 Comparison in the through-thickness orientation tensor result at the specimen's gauge length's centre location for three different mesh densities.

4.3 Material modelling

Defining the material properties was a critical step to obtain correct levels of stresses and strains, which would later be used in the fatigue life prediction of the composite material. Due to the effect that the fibre orientation distribution has in the material behaviour, a more complex material model needed to be used. For the case of the present project, a two-stage procedure was implemented to obtain the anisotropic material properties. First, a mean-field-homogenization technique (MFH) was used to obtain a base, or general, material model of the composite under study. Second, an iterative reverse engineering (RE) approach was also carried out using experimental data to further calibrate the material model. This two-stage approach is depicted in Figure 4-4. The modelling of the material was carried out using Digimat [144], which allowed the implementation of the MFH technique, as well as, the linkage with the RE approach to better define the model. The final material model was also validated against experimental measurements. The following section describes, in detail, the methodology used in both stages, which defined the composite's material properties.

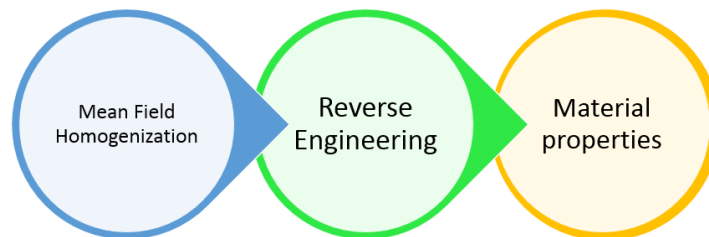


Figure 4-4 Schematic of material model workflow.

4.3.1 Mean field homogenization

In general terms, the goal of the MFH technique is to find an equivalent homogenous material with similar properties to the composite, by estimating volume averages of stresses and strains fields [66]. An example of this method is depicted in Figure 2-40. For the present project, the Mori-Tanaka (M-T) model [68] was used, as it had been found to correlate well for two-phase composites (a matrix and a single type of inclusion) with success at relatively larger concentrations of inclusions. Similar work has been documented in past [71] to model the material behaviour of SFRP's, although under linear-elastic conditions only. The problem with that approach was that behaviour of this type of composite is complex and needed a different material model to represent the correct behaviour. For the present project an elasto-plastic material model was considered instead.

The MFH procedure started with the characterisation of the material properties of the constituents. In other words, the fibre and the matrix. Textbook properties were used for the case of the Type-E glass fibre [15], an example of these properties is shown in Table 2-1. The matrix material properties were obtained using the CAMPUS material data base, freely accessible in [145]. Based on this information, the general Stress-Strain curves, for the glass fibre and the nylon matrix, used in the MFH technique are shown in Figure 4-5. Where the glass fibre (GF) was considered to be elastic, while the matrix (PA66) elasto-plastic via using the J_2 -plasticity model, already integrated in the software. In this regard, it is good to mention that the application of this theory for the prediction of the properties of short fibre reinforced polymers considers several assumptions. The J_2 plasticity model is only applied to the matrix stress/strain curve (as shown in Figure 4-5) with the matrix assumed to be isotropic. The MFH mixes the stress/strain curves of both fibre (linear behaviour) and matrix (non-linear isotropic) and produces curves with hardening rates which depend on fibre orientation. The full mathematical details of this formulation are presented in [66]. Additionally, in a work by Doghri and Friebel [146], it was shown that this methodology is restricted to only two-phase composites, it also tends to produce a stiffer material response with longitudinal oriented fibres, and the strain hardening of the material might not be adequately modelled. Nevertheless, and although this formulation does not completely describes the full behaviour of the material, e.g. viscosity, strain rate dependence, creep, etc.; for the particular application presented herein, this methodology did show a good correlation between the results of the numerical model and the experimental validation, as is presented in Figure 7-4.

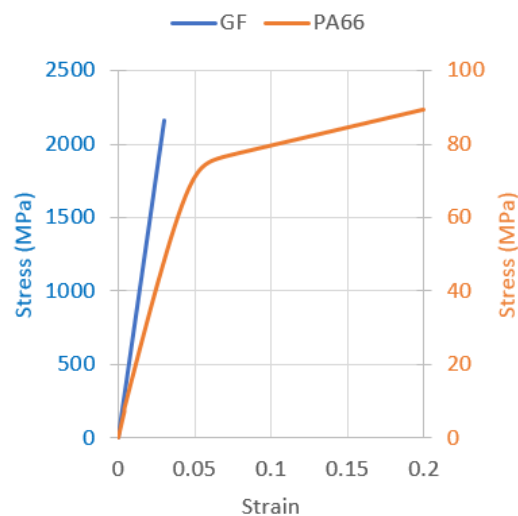


Figure 4-5 General Stress-Strain curves for GF and PA66 used for the MFH technique.

As a quick summary, the J_2 -plasticity model is defined as [66]:

$$\sigma_{eq} = \sqrt{J_2(\sigma)} = \left[\frac{1}{2} [(\sigma_{11} - \sigma_{22})^2 + (\sigma_{22} - \sigma_{33})^2 + (\sigma_{33} - \sigma_{11})^2] + 3[\sigma_{12}^2 + \sigma_{23}^2 + \sigma_{31}^2] \right]^{\frac{1}{2}}$$

Equation 4-1

Where σ_{eq} is the Von Mises equivalent stress, and $J_2(\sigma)$ the second invariant of the deviatoric stress tensor. This model considers the response to be linear elastic as long as the equivalent stress is lower than the material yield stress:

$$\sigma_{eq} \leq \sigma_y$$

When this is exceeded, the behaviour is now considering as nonlinear with plastic deformation, where the stress is then given by the sum of the yield stress and the hardening stress, or:

$$\sigma_{eq} = \sigma_y + R(p)$$

From then, different laws are applicable for either isotropic hardening, as well as, for kinematic hardening.

Additionally to the constituents' material properties, the microstructure also needed to be defined in terms of the aspect ratio of the inclusions, as well as, of the fibre orientation. For the present case, the nominal aspect ratio of 20 was used. In terms of the fibre orientation, and for the purpose of calibrating the model, a first guess was taken from the injection moulding simulation results.

With the constituents' material properties, the definition of the fibre orientation tensor and with the overall shape and volume fraction of the inclusions; then the MFH procedure could be started. First, it is good to mention that the M-T model is an approximation of the single inclusion problem, solved by Eshelby in 1957 [67], and proposes that the *strain concentration tensor* relating the volume average of strain over all inclusions related to the matrix, or B^ε in:

$$\langle \varepsilon \rangle_{w1} = B^\varepsilon : \langle \varepsilon \rangle_{w0}$$

is given by:

$$B^\varepsilon = H^\varepsilon (I, C_0, C_1)$$

Which is the definition of the Eshelby's single inclusion problem. Where $\langle \varepsilon \rangle_{w1}$ is the volume average strain field over all inclusions and $\langle \varepsilon \rangle_{w0}$ is the volume average strain

field over the matrix, H^ε is the single inclusion strain concentration tensor, I is the ellipsoidal volume of the inclusion and, C_0 , and C_1 are the uniform stiffness for the matrix and the single inclusion, respectively. In other words, the M-T method models each inclusion behaviour as it were isolated in the matrix [70].

In the case of Digimat, the homogenization is done in two stages. First, by decomposing the random fibre orientation into pseudo-grains with similar orientation. Each pseudo-grain is then homogenized using the above described M-T technique. Finally, the effective response of all the pseudo-grain is computed by assuming a one dimensional, 1D, problem, by either: 1) considering the strain field as uniform inside the domain, therefore, the macro stiffness is the volume average of the pseudo-grain stiffness. Or 2) by assuming that the stress field is uniform inside the domain, therefore, the macro compliance matrix is the volume average of the pseudo-grain compliances. This is per Voigt and Reuss models [66]. A depiction of this procedure is shown in Figure 4-6. With the definition of the MFH process, the material response could be computed, which would be correlated to the fibre orientation tensor on each element via the two stage MFH technique above explained.

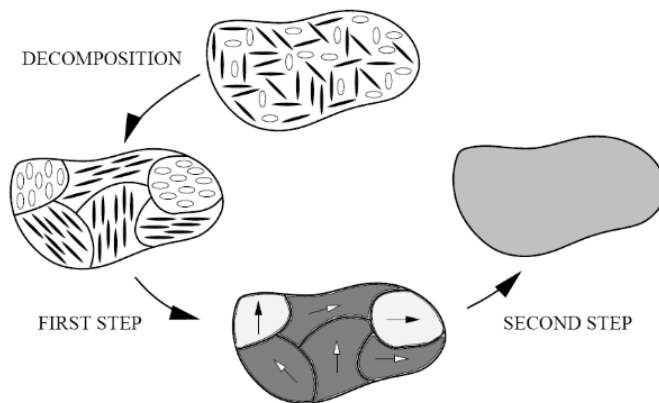


Figure 4-6 Digimat procedure for the 2-step MFH in a composite with misaligned inclusions [66].

4.3.2 Reverse engineering

In terms of the reverse engineering (RE) approach, experimental monotonic data was used to further calibre the material model. This is done by using experimental data, in the form of Stress-Strain curves from coupons oriented at 0° , 45° and 90° , to reduce the difference between this data and the material model produced during the MFH stage. To visualise this, Figure 4-7 shows a comparison of the macro behaviour between the material model computed using the MFH approach for PA66GF50, before

and after the RE, and material data from experimental testing, from a 0° reference specimen, which was used for further calibration of the model. Validation of the final material model was done using experimental data of coupons oriented differently to the ones used for calibration. The parameters to optimise during the RE are shown in Table 4-1. Additionally, during the optimization stage, other parameters like the loading conditions are also updated from the original MFH model to correlate to the experimental data.

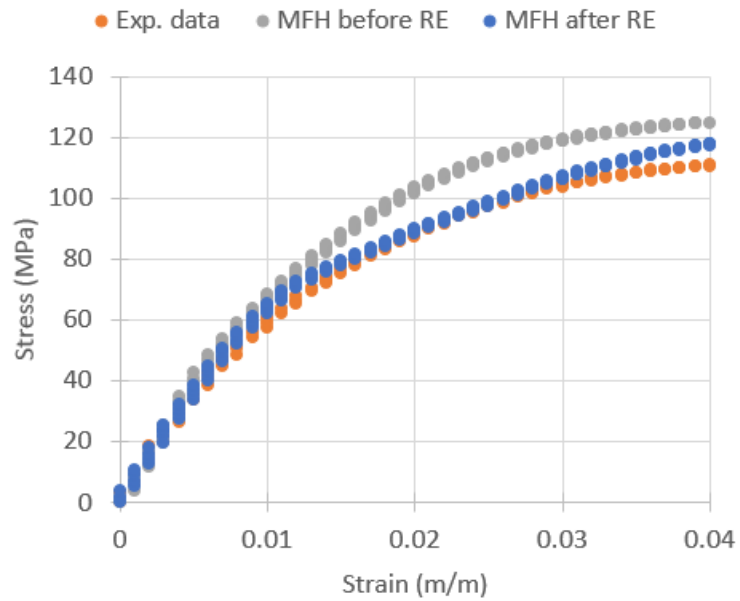


Figure 4-7 Comparison of the macro behaviour between material experimental data, and the before and after RE MFH material model for a 0° reference specimen of PA66GF50 (thickness=4mm and $V_f=30\%$).

Table 4-1 Optimisable parameters during RE.

Elastic model	Matrix Young's modulus, matrix Poisson's ratio, filler aspect ratio.
Elasto-plastic model	Matrix yield stress, matrix hardening modulus, matrix hardening exponent. Plus the ones from the Elastic parameters.

The actual method that Digimat uses for optimization is the DIRECT method available in DAKOTA [147], the specifics of which can be accessed in reference [66]; but suffice it to say that the iterative optimization used in this approach is based on minimizing the difference between the computed MFH curve and the input experimental curves. This difference between curves is represented by an error estimator, or e . If the

experimental curve is formed by a set of $n(X_r, Y_r)$ points, then the error estimator is defined as the relative error between the experimental curves and the MFH one, such that [66]:

$$e = \frac{\sum_{i=1}^n (Y_c(i)/Y_r(i) - 1)^2}{n}$$

Equation 4-2

Where $Y_c(i)$ is the interpolated value in the Y-coordinate of the computed curve at X-coordinate equal to $X_r(i)$. If $Y_c(i)=0$, the corresponding term in the sum is replaced by the absolute error. When more than one experimental curve is used to calibrate the material model, then the optimization is considered as a multi-objective problem, and weight functions are introduced (w_j). Therefore the global estimator error is defined by the sum of the individual error estimators, or:

$$e = \sum_{j=1}^m w_j e_j$$

Equation 4-3

The general process was then: First, to calibrate the elastic part of the material curve, as well as, the microstructure parameters. Once this was done, then the plasticity parameters were optimized.

4.3.3 Cyclic Stress-Strain behaviour

Due to the material's behaviour under cyclic loading, the total deformation under fatigue would be larger as the polymeric matrix experiences cyclic softening [82]. Therefore, for the present case, the Ramberg-Osgood relationship was used to draw the cyclic Stress-Strain curves, and thus, to describe the material behaviour under these conditions. This relationship has been implemented in the past on different SFRP's (reinforced nylon-6 and reinforced polybutylene terephthalate) to model the material's cyclic stress-strain behaviour [91]. Although it has been shown that this model is able to capture the cyclic softening that occurs in the polymers under fatigue conditions, it has also been shown that the non-linear part of the resultant curve tends to diverge from experimental measurements, at ambient temperature, showing higher strain hardening than the one seen in the testing data [148]; it also cannot capture time dependent effects, this means that no creep or other time-dependent processes can be reproduced by this approach [149]. The Ramberg-Osgood relationship in terms of the true strain amplitude can be defined as:

$$\epsilon_a = \frac{\Delta\epsilon}{2} = \frac{\Delta\epsilon_e}{2} + \frac{\Delta\epsilon_p}{2} = \frac{\Delta\sigma}{2E} + \left(\frac{\Delta\sigma}{2K}\right)^{\frac{1}{n'}} = \frac{\sigma_a}{E} + \left(\frac{\sigma_a}{K'}\right)^{\frac{1}{n'}}$$

Equation 4-4

Figure 4-8a shows the definition of the different terms based on the stabilised fully-reverse hysteresis loop. From Equation 4-4 the first term represents the true elastic strain range, while the second term the true plastic strain range. Coefficients K' (cyclic strength coefficient) and n' (cyclic strain hardening exponent) are obtained by plotting the true stress amplitude (σ_a) and, the true plastic strain amplitude ($\frac{\Delta\epsilon_p}{2}$) in a log-log graph [91], as is shown in Figure 4-8b.

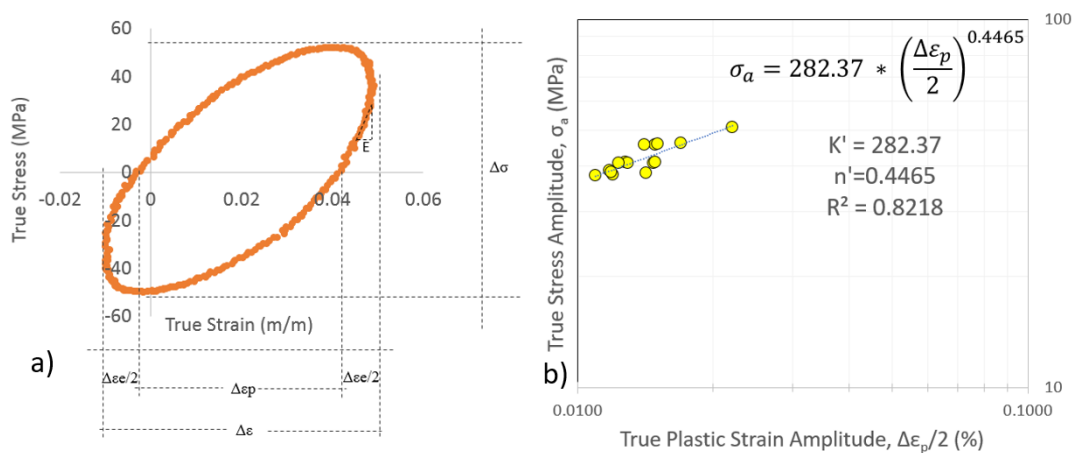


Figure 4-8 a) Definition of terms for the cyclic Stress-Strain curves. b) True stress amplitude vs True plastic strain amplitude log-log plot.

4.4 Stress Analysis

The specimens' structural models, as well as, the finite element analyses, were carried out using Abaqus [150]. This section describes in detail the individual models for the uniaxial specimens, the boundary conditions and the different type of analysis run. The procedure for mapping the fibre orientation tensor results, product of the injection moulding simulation, into the finite element mesh is also explained.

4.4.1 Structural model

A linear eight-node brick element with only one integration point [151], located in the middle of the element, was chosen for the structural mesh. The element composition is shown in Figure 4-9.

This element type allowed linking a single stress result to a single fibre orientation tensor for each element in the mesh. Due to this reduced number of integration

points, a typical hexahedral element has a 2x2x2 integration point scheme [152], and to correctly capture the stress concentrations in the specimen's gauge length, a maximum element size <0.2mm was used in the region of interest. In the same manner, to accurately map the change in fibre orientation, a total of 50 elements through the thickness were used. To avoid false element deformation, due to zero-energy modes, caused by the lack of element stiffness (hourglass phenomenon [153]) inherent of using reduced integration elements, a hourglass control was set in Abaqus [150] to mitigate this effect, i.e. introducing an artificial stiffness.

Finally, a mesh independence study was also carried out to determine that the stress results seen in the gauge length region are product of the actual material response and not due to the quality/density of the mesh. The results of this study can be seen in Figure 4-10, with a change in stress results of less than 0.4% for the mesh chosen. The final structural model used for the finite element analyses of uniaxial specimens was composed by a total of 178,000 solid brick elements and is presented in Figure 4-9.

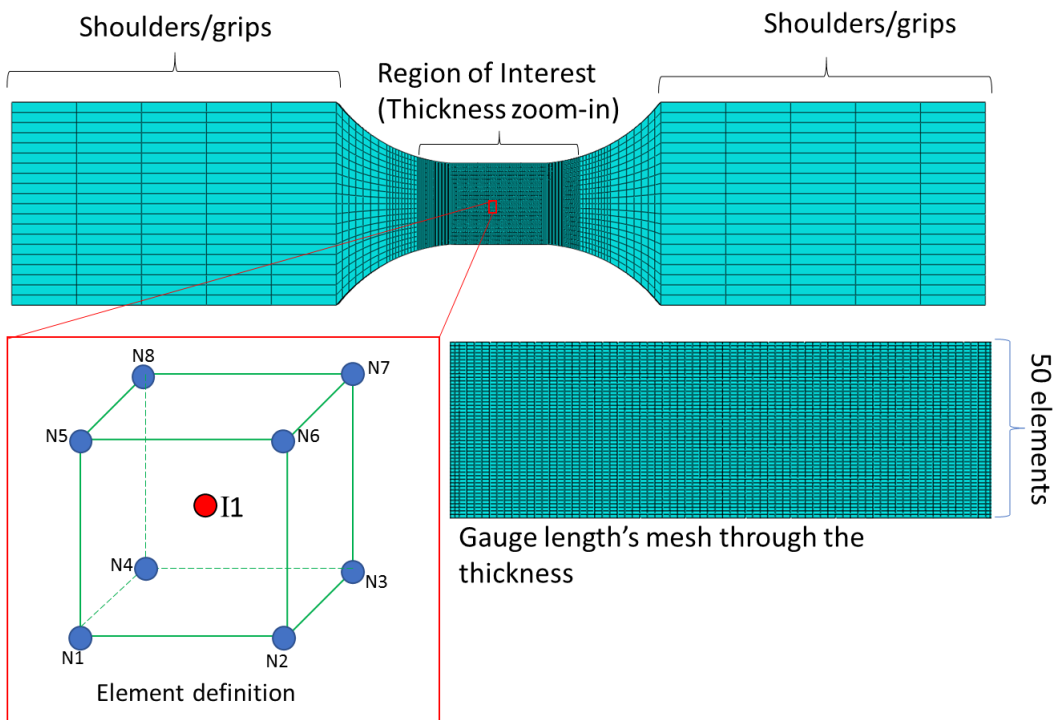


Figure 4-9 Uniaxial specimen's structural mesh, showing element's nodes (N1-N8) and integration point (I1) location.

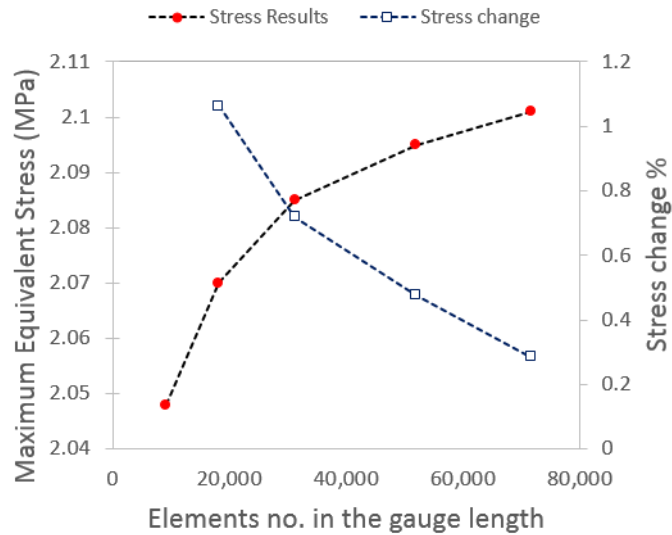


Figure 4-10 Mesh independence analysis conducted over the gauge length. Stress results from a unitary load case in tension.

4.4.2 Analysis setup

4.4.2.1 Boundary conditions

The details of the coupons' meshes were explained in the previous section, the next step was the setup of the actual analysis. The boundary conditions used for the uniaxial specimens are shown in Figure 4-11. On one end of the specimen all translations were constrained, i.e. $U_x=U_y=U_z=0$. On the other side of the specimen a kinematic coupling constraint [154], was setup to a single reference point (RP). Said kinematic coupling allowed to constrain all the nodes on that end of the specimen to the rigid body motion of a single node, RP. It was on this reference point where the uniaxial load (either Force or displacement) was applied and then uniformly transmitted to the specimen.

4.4.2.2 Analysis type

Linear, as well as, non-linear analyses were carried out on all specimens' models and orientations. Similarly, monotonic, as well as, cyclic material properties were used depending on the type of assessment being conducted. This assured the correct results in terms of material deformation, strains. All analyses were conducted under quasi-static conditions in Abaqus.

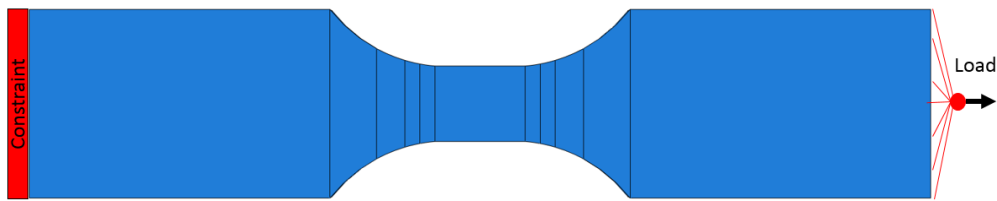


Figure 4-11 Uniaxial specimen boundary conditions.

4.4.2.3 Input of material properties

During the stress analysis a coupling process between Digimat and Abaqus was done. This allowed the calculation of local material properties on each element by following the MFH technique explained in the previous section. This was done by using the calibrated material model, via Reverse Engineering, and the material orientation tensor result for each element. The input material card contains the constituents' (GF and PA66) material properties, the orientation tensor for all the elements in the mesh, and information on regards the type of MFH method to use (M-T in this case). For an example of the type of information inside the material card please see the Appendix A.1.

4.4.3 Fibre orientation tensor mapping

In order to compute the anisotropic stresses and strains in the composite material the fibre orientation tensor results from the injection moulding simulation were *mapped* into the structural meshes. This step is important as the fibre orientation is not homogeneous and tends to change along, and throughout, the plate. Thus, depending of the location where the specimens are taken from the plate, different fibre alignment and mechanical behaviours will be observed. Figure 4-12 shows an example of this change of fibre alignment depending of the location the specimens are taken from the plate. Red values show higher local alignment, whereas, blue values show less local alignment.

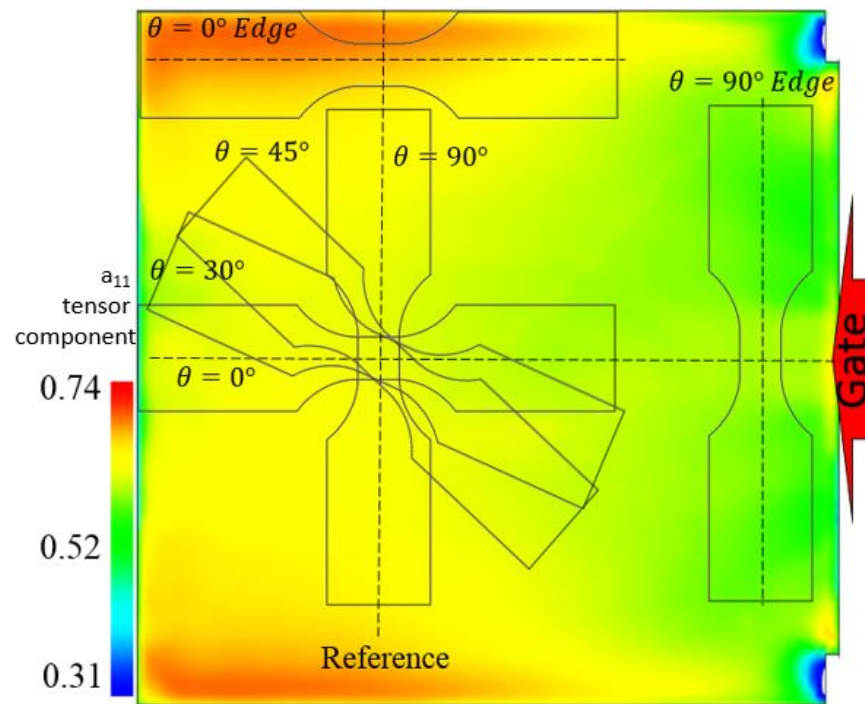


Figure 4-12 Example of fibre orientation distribution along the flow direction. Superposition of Donor (plate) and Receivers (uniaxial specimens) meshes.

In-depth results of the fibre orientation alignment are presented and explained in the Modelling results chapter of this thesis. At this moment, suffice it to say that to correctly capture the anisotropic stresses, the transfer of the orientation tensor to the structural models (meshes) was a key procedure within the modelling methodology. This is due to the stiffness at each element would change depending of the orientation tensor in that element. The result of the fibre analysis product of the injection moulding prediction is in the form of a second order fibre orientation tensor, or a 3x3 symmetric matrix, which is a nodal result [44]; i.e. is calculated at each of the plate's mesh's nodes. During the mapping procedure, this information is transferred into the integration points in the specimens' meshes. This process is done through Digimat [144] via a Node-to-Integration point technique.

The general procedure is the following: First, the specimen's mesh (Receiver) and the plate's mesh (Donor) are superposed. The Receiver is positioned on the Donor mesh at the particular location and orientation corresponding to the testing specimens, as shown in Figure 4-12. At the element level, the single integration points, corresponding to the elements in the specimen's mesh, are located on the superposed Donor's mesh. Then, via an interpolating/extrapolating algorithm [66], the orientation data from the plate's nodes are transferred into the integration points of the

specimen's mesh. This is similar to how nodal stress and strain results are calculated by extrapolating, and averaging, elemental results (at integration points) in standard finite element analyses. Figure 4-13 presents a representation of how the elements and nodes match during the procedure. Figure 4-14 shows an example of the mapped orientation data into the specimens' mesh, where for each element in the mesh, 178,000 elements in total for the case of uniaxial specimens, there is a set of matrix components corresponding to the second order orientation tensor going from a_{11} to a_{13} .

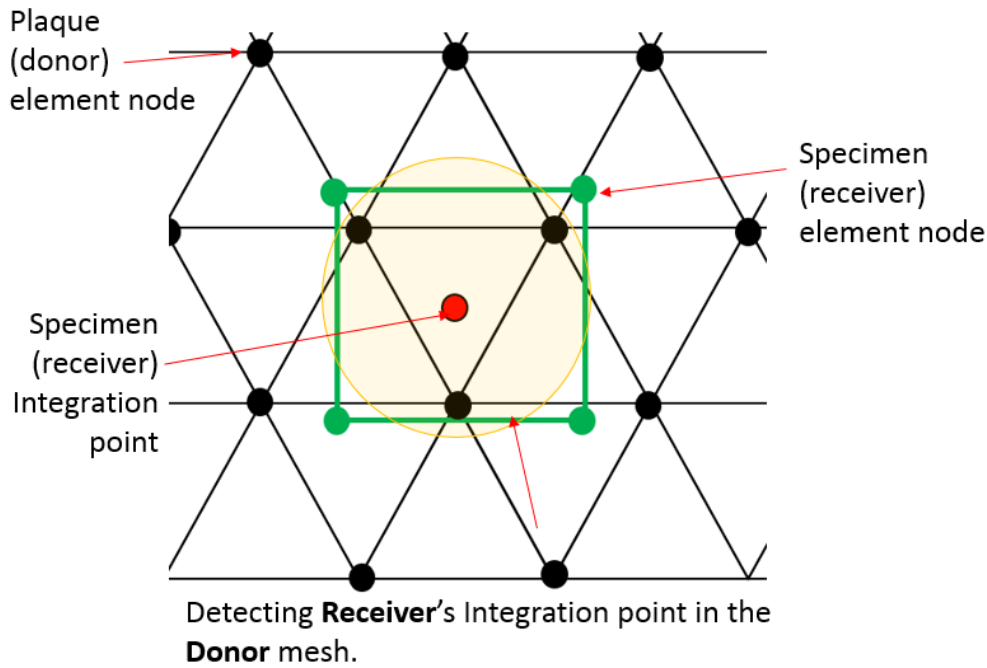


Figure 4-13 Visualization of the mapping of fibre orientation tensor results from the injection moulded plate (Donor) to the specimens structural mesh (Receiver).

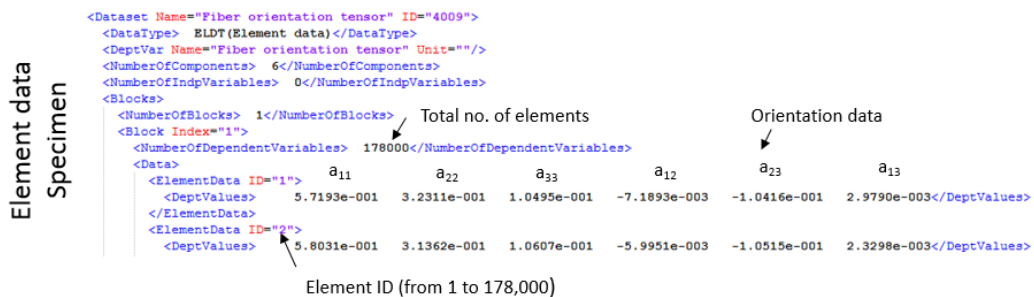


Figure 4-14 Specimen's mapped fibre orientation data.

Finally, to assess the accuracy of the transferred data, a global error analysis was conducted between the *plate's* and *specimens'* results by comparing the orientation tensors for each of the Donor and Receiver meshes. This error was calculated based

on the relatively total number of elements, in both meshes, that contained a specific value of orientation tensor component. This is shown in Figure 4-15 for the case of a 0° specimen, where the sum of all *Relative no. of elements* values is equal to 1. The data was transferred relatively well with similar amount of elements presenting a specific value of orientation tensor, and this is considering the dissimilarities between both models (plate and specimens). The error analysis results for the rest of the specimens are presented in the Appendix A.2. The back-to-back comparison of orientation tensor results through the thickness between plate and the different specimens is presented in the Modelling results section of this thesis.

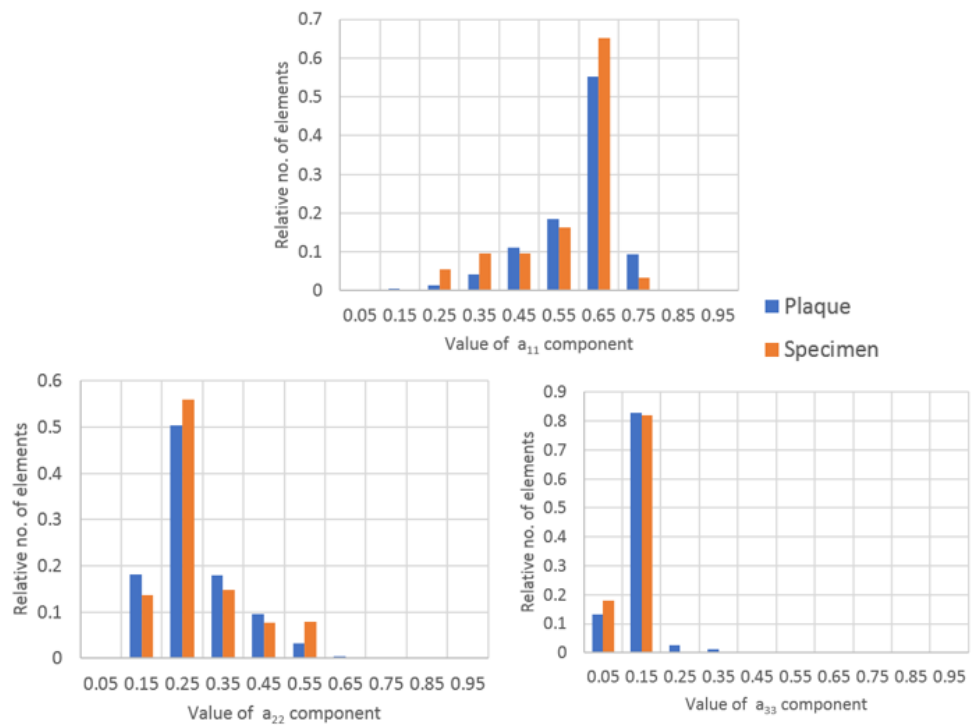


Figure 4-15 Error analysis in terms of transferred of orientation tensor data between the composite Plate and the 0° Specimen.

4.5 Fatigue modelling

4.5.1 Stress-Life (S-N) approach

4.5.1.1 Introduction

The following section explains in detail the methodology followed to apply the Stress-Life (S-N) approach in the prediction of the fatigue life of SFRP's. Firstly, and due to the relatively low stress levels experienced during fatigue testing, the material was assumed to be linear-elastic within the region of the cyclic testing. This same premise has been used in the past in industrial applications of the S-N approach on short fibre

composites [3], [71]. For the present case, HBM nCode [155] was used to automate the fatigue calculations on all elements in the model; but the application of this methodology could be carried out using any other scripting tool, e.g. Matlab, Python, etc..

The modelling approach can be summarized as follows: The stress results, the fatigue load case and the cyclic material data were input into the fatigue model. Predicted S-N curves were compared against coupon experimental data for calibration of the model. If the error is high, an iteration on the material data was done and the fatigue calculations was repeated. If the error in the calibration was low (within 5%), then the predicted life was validated against different coupon experimental data. Each of the steps of this model are explained next in this section. Figure 4-16 shows a schematic of the overall modelling procedure for this approach. Experimental coupon data from 0°, 45° and 90° specimens was used to calibrate the fatigue model. Experimental coupon data for 30° specimens was used for validation of the model.

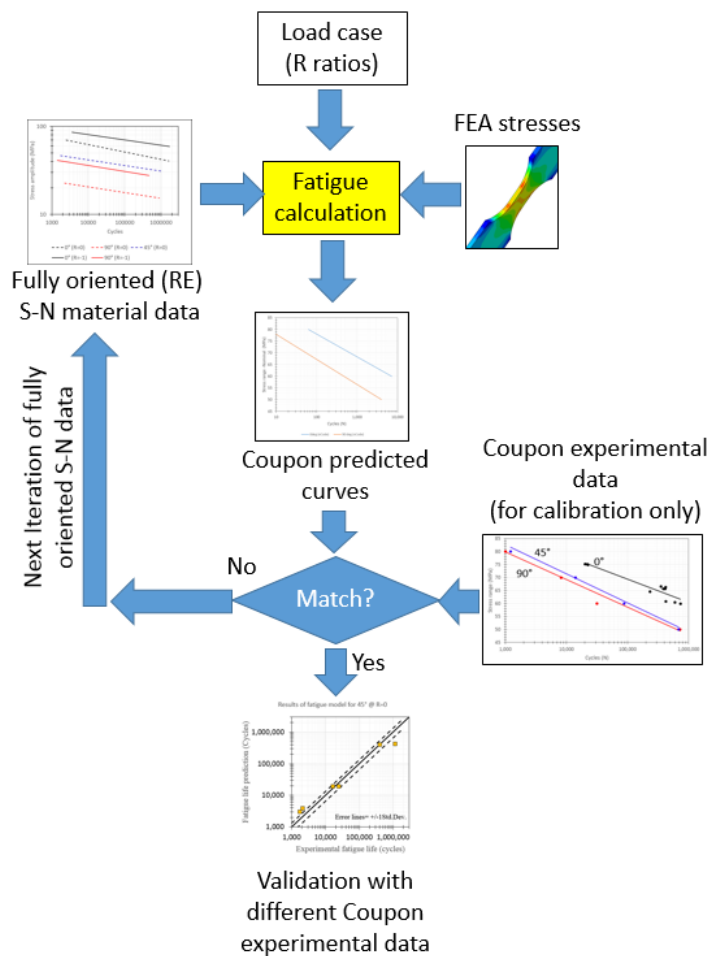


Figure 4-16 High level schematic of algorithm for S-N approach.

4.5.1.2 Stress tensor results and stress combination method

During the stress analysis step, a set of anisotropic stress results were calculated for each of the elements in the structural model. This stress state depends of the particular fibre orientation and material information, corresponding stiffness for each element. As explained previously due to the type of element used, single integration point, these stress results are in the form of a singular second order stress tensor located at the centroid of each element in the structural model. This result was then used for the subsequent fatigue calculations.

The present fatigue model is based on the S-N approach using Basquin's material curves [74]. Therefore a stress combination was needed in order to compute an equivalent stress value per element which was later used to evaluate the life against local material curves. Due to the type of loading used in this project, purely axial, the material is assumed to be exposed to proportional loading only, i.e. the components of the stresses state are proportional to each other through the cyclic loading. Therefore, it was possible to use a simpler multiaxial stress assessment using the Absolute Maximum Principal Stress, i.e. the largest value when the absolute of the three principal stresses are compared against each other [71], this was calculated for each elemental result. This assessment meant that the largest stresses would apply to the material in each cycle. One caveat of this criterion is that it does not account for the direction of the crack initiation, nor for non-proportional loadings, like a combination of asynchronous axial plus torsion loading, for such cases a multiaxial assessment using the critical plane method [156] might prove to be more adequate.

4.5.1.3 Calibration of the model and fatigue calculations

Before a fatigue life value could be computed, material curves needed to be input to characterise the cyclic behaviour of the composite. Different to metals, experimental coupon based S-N curves cannot be used directly to assess the fatigue life. This is because coupons made out of SFRP's behave, in reality, as simplified structures, due to the variation of the fibre orientation which produces an inhomogeneous stress state throughout the specimen. Nevertheless, this coupon based data can be used to calibrate a set of reverse engineered (RE) fully fibre-oriented S-N curves that represent a more homogenous fibre distribution, i.e. all fibres oriented along a single direction, from where any other particular fibre distribution can be calculated. A schematic representation of this is shown in Figure 4-17a, where RE fully-longitudinally and

transversally oriented curves were obtained by calibrating the model against experimental coupon based curves.

The description of these RE curves is, for the most part, the same as for any other Basquin curve. This is, by defining the fatigue intercept, where a comparison was done against the material ultimate tensile strength (UTS) to assess whether it has been exceeded and static failure had occurred; and by defining the fatigue exponent, where the endurance limit was assumed at 10^7 cycles. An extra parameter was used to define the specific fibre orientation of each curve, this parameter is called fibre share (λ) [46]. It can be defined as the portion of the fibre, or share, that is oriented toward the direction of critical stress (in this case the Abs. Max. Principal corresponding to each individual element on the structural model); or:

$$\lambda = l a l^T$$

Equation 4-5

Where l is the 3D orientation vector of the critical stress and l^T its transpose; while a is the fibre orientation tensor. To better explain this parameter, let us assume that the maximum principal stress in a given element in the mesh has a vector direction of [1 0 0], and the fibre orientation tensor corresponding to that element is oriented completely in that direction, therefore the fibre share of that element corresponds to:

$$\lambda = [1 \ 0 \ 0] \begin{bmatrix} 1 & 0 & 0 \\ 0 & 0 & 0 \\ 0 & 0 & 0 \end{bmatrix} \begin{bmatrix} 1 \\ 0 \\ 0 \end{bmatrix} = 1$$

This means that all the fibre, or $\lambda = 1$, is oriented toward the load direction. In the opposite case, if the fibre is completely orthogonal to the critical stress, then the fibre share would be:

$$\lambda = [1 \ 0 \ 0] \begin{bmatrix} 0 & 0 & 0 \\ 0 & 1 & 0 \\ 0 & 0 & 0 \end{bmatrix} \begin{bmatrix} 1 \\ 0 \\ 0 \end{bmatrix} = 0$$

Which indicates, no portion of the fibre is oriented toward the load direction. If the fibre orientation is set at an in-plane 45° , then its fibre share would be $\lambda=0.5$, and so on.

This parameter then was calculated for each element in the mesh, based on their individual orientation tensor, and local S-N curves were defined on each element based on that fibre share value. These local S-N curves were obtained by linearly interpolating in-between the calibrated RE curves with known fibre alignment, as it is

shown in Figure 4-17b. This procedure is done by using an interpolating factor defined as [46]:

$$I = \frac{\lambda_i - \lambda_1}{\lambda_2 - \lambda_1}$$

Equation 4-6

Where λ_i is the fibre share of the local curve to be calculated, and λ_1, λ_2 represent the fibre share of the known RE curves. In other words the curves with fully-fibre alignment. Using this interpolating factor the next step was to calculate the UTS, and the fatigue intercept (FI) of new curve by:

$$UTS_{\lambda_i} = UTS_{\lambda_1} + (UTS_{\lambda_2} - UTS_{\lambda_1}) * I$$

Equation 4-7

and,

$$FI_{\lambda_i} = FI_{\lambda_1} + (FI_{\lambda_2} - FI_{\lambda_1}) * I$$

Equation 4-8

The fatigue exponent, n , of the local curve is calculated by interpolating in-between the endurance limits for the RE curves. This is done by:

$$n_{\lambda_i} = n_{\lambda_1} * \left(\frac{n_{\lambda_1}}{n_{\lambda_2}} \right)^I$$

Equation 4-9

The depiction of the previous procedure is shown in Figure 4-17b. After the interpolations were done, standard fatigue calculations were then carried out on each element based on the stress state at that element, and on their local S-N curve described by the respective fibre share value.

The calibration of the model, and in specific of the RE curves, was done by first assuming an initial set of fully fibre-oriented S-N curves, defined by a set fibre share value (e.g. $\lambda = 0$ and 1), a fatigue intercept and a fatigue exponent. Experimental data served as a first guess. The stress analysis results from the uniaxial coupons (0° , 45° and 90°) were then used, together with the first guess of RE curves, to compute coupon S-N curves for these same specimens' orientations, which were based on the element with lowest life. These newly calculated coupon curves were then compared against their respective experimental counterpart, same coupon orientation. If the error was high, then a new guess of RE was guessed and the process was repeated

until the error between the calculated and the experimental coupon based SN curves was minimised, at which point the model is calibrated. This is shown in Figure 4-17a.

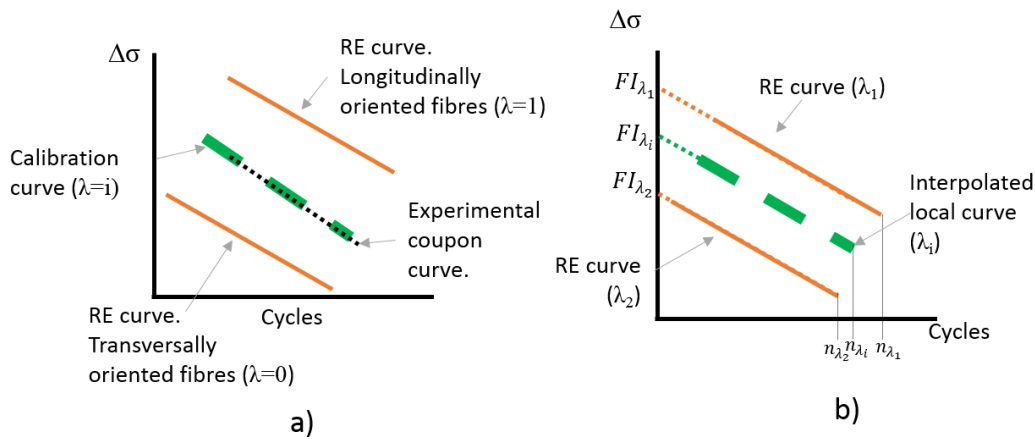


Figure 4-17 a) Schematic representation of the calibration of fully fibre-oriented Stress-Life material curves. b) Interpolation of S-N parameters

Finally, with the material S-N curves calibrated and with the multiaxial stress assessment done. The loading history, in case of non-constant amplitude loading, was then passed through a standard Rainflow counting process, e.g. ASTM E1049 [157], to separate the total number of reversals for later assessment against the local S-N curves for each element in the finite element model. In the same manner, a linear damage accumulation procedure was carried out using Miner's rule [158]. This damage assessment is based on the different stress amplitudes for each loading case, such that:

$$D = \frac{1}{N} = \sum_i \frac{n_i}{N_i}$$

Equation 4-10

Where n_i is the number of cycles experienced at one specific magnitude and ambient condition, N_i is the total life at the same conditions. Failure of the specimens was expected when $D=1$. As it was mentioned in Chapter 3.6.2, Miner's rule has several limitations such as: it does not account for the effects that the load sequence has in material degradation; it does not distinguished any particular damage mechanism; and due to the its linear nature it does not account for any non-linear damage accumulation caused by the progressive degradation of the material properties due to the propagation of damage inside the composite. Finally, to validate the model, fatigue calculations were conducted on specimens with orientations different to the

ones used for the model calibration. The results of this prediction were then compared against experimental results.

4.5.2 Mean stress correction

One of the main problems faced in fatigue analysis is the effect that the mean stress have in the material response. As there is an infinite number of stress ratios theoretically possible in real applications; it is impossible to obtain material curves for each one of those conditions. On metals, several methods have been proposed in the past to correct for these stresses. The most common methodologies are [159]:

the Goodman relationship,

$$\frac{\sigma_a}{\sigma_{eq}} + \frac{\sigma_m}{\sigma_{uts}} = 1$$

Equation 4-11

the Gerber relationship,

$$\frac{\sigma_a}{\sigma_{eq}} + \left(\frac{\sigma_m}{\sigma_{uts}}\right)^2 = 1$$

Equation 4-12

and the Soderberg relationship.

$$\frac{\sigma_a}{\sigma_{eq}} + \frac{\sigma_m}{\sigma_{yield}} = 1$$

Equation 4-13

However, these equations depend on specific material parameters, such as the UTS or Yield strength. For metals, material parameters are easily obtainable, but for composites not so much, as these parameters might change depending of the conditions of the material and orientation of the fibres. Nevertheless, these relationships have been implemented in the past in SFRP's with a wide range of results. In specific, in [160] it was shown that Goodman presented inaccuracies with regards to the slope of the corrected S-N curves for different R ratios when used in reinforced PA6. In a work by Lu et.al. [161], it was presented that for Polycarbonate and Acrylonitrile Butadiene Styrene (PC/ABS) neither Gerber, Soderberg nor Goodman relationships were able to correlate the experimental data. On the other hand, for the case of Polypropylene (PP) and Nylon and Acrylonitrile Styrene Acrylate (PA/ASA), only Gerber failed to correlate. Therefore, the aforementioned shows that the usage of these relationships depends mainly in whether or not they are able to directly fit the

available experimental data for that specific material, and therefore unable to be used as generic equations.

An additional relationship for the correction of mean stresses in short fibre reinforced polymers has been investigated; this was the Walker's relationship, which has been used in the past with reasonable results for un-reinforced and reinforced polymers under the stress-life regime [54]. In fact, the use of the Walker's relationship has been shown to better correlate with experimental data than the previous formulations, i.e. Goodman, Gerber and Soderberg, [160]–[162]. The main advantage of this approach is that it is not formulated in function of the composite material properties, like the previous models, but instead in function of the cyclic stresses that the specimen is subjected to. In this regard, the Walker equation is defined as [163]:

$$\sigma_{walker} = \sigma_{max}^{1-\gamma} \cdot \sigma_a^\gamma$$

Equation 4-14

Where; σ_{walker} is the equivalent stress after the correction, σ_{max} the maximum stress. σ_a the stress amplitude, and γ the Walker's coefficient, which is different for each material. Some of the limitations of this relationship is that the driving γ value is influenced by the type of material, the material fibre orientation and environmental conditions (temperature). In a work by Mortazavian and Fatemi [160], a wide range of γ values for reinforced PA6 and PBT (polybutylene terephthalate) were found. For example, for PA6 specimens at 90° and tested at -40°C, the best fit was achieved with a $\gamma = 0.4$, whereas for the same material and specimen orientation but tested at 125°C the data would best correlated with a $\gamma = 0.6$, and so on. This means that a caveat with using this method is that the results are inherently empirical, and thus the best γ value for a specific material is just the one that provides with the best fit of the available experimental data.

Finally, Equation 4-14 can be further simplified in terms of the Stress ratio, R, by recalling that:

$$R = \frac{\sigma_{min}}{\sigma_{max}}$$

Thus,

$$\sigma_{max} = \frac{\sigma_a}{(1 - R)}$$

Equation 4-15

Substituting Equation 4-15 into Equation 4-14, let us then defined the Walker equation as:

$$\sigma_{walker} = \sigma_a \left(\frac{2}{(1-R)} \right)^{1-\gamma}$$

Equation 4-16

Which only depends of the Stress amplitude and the Stress ratio used, and not on specific material properties of the composite.

4.5.3 Energy-based approach

One of the main limitations of using the previously described Stress-Life approach was that it assumed the fatigue behaviour of the experimental material data to be approximately equidistant between orientations, linearly distributed. This behaviour is not always the case under all stress ratios, as it has been reported in the literature [3], [75], [76], etc. and as it is shown in the Experimental results, Chapter 5, of this thesis. For this particular material, the behaviour changes depending on the stress ratio and fibre orientation. Another limitation of this method is the need of several material, S-N curves, depending of the orientation, as it is depicted in Figure 4-18a. Therefore, there is a need for a different, more holistic, approach that could overcome these restrictions. This ideal case is depicted in Figure 4-18b, where, as presented in the published literature, an energy formulation could, in theory, circumvent the S-N approach limitations by minimizing the effects of the fibre distribution.

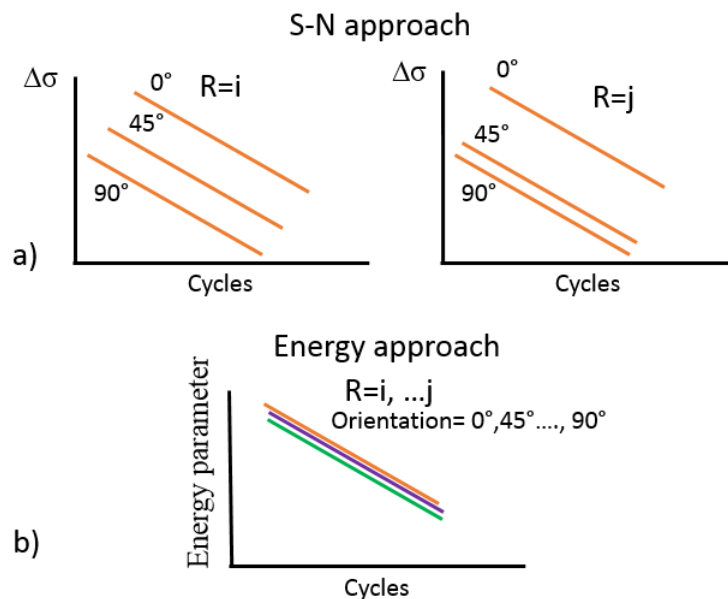


Figure 4-18 a) Simplified schematic description of the limitations of the S-N approach and, b) the advantages of using an Energy formulation.

Different energy-based approaches have been proposed in the past, as it was documented in Chapter 2, e.g. [2], [92], [94]. Upon close examination of these formulations, it could be concluded that the material was assumed to behave linear-elastically, and/or transverse isotropic (only one direction of anisotropy), with low energy dissipation; and thus implemented models mainly focused on the elastic strain energy density. In contrast to this, the results obtained during the experimental program of this project, presented in Chapter 5, showed clearly defined hysteresis loops for all the specimen orientations and stress ratios, e.g. Figure 5-19. The hysteresis areas represent the amount of energy dissipated by the material on each fatigue cycle throughout the life of the specimen. Analysis of these areas showed a clear stabilised region that covered more than 90% of the life of the specimens at all orientations, e.g. Figure 5-21. Additionally, it was observed that the cyclic stabilised dissipated energy data and the total specimen's life followed a linear relationship, power equation in a log-log plot, at each stress ratio in the form of:

$$W = AN^{-b}$$

Equation 4-17

This is shown in Figure 6-32. This meant that the stabilised dissipated energy, defined by area of the stabilised hysteresis loop, could be used as a fatigue parameter due to the specimens being subjected to this level of energy most of the time. This also seems to suggest that by using the dissipated energy as fatigue parameter, instead of stress, the effect of the fibre orientation distribution could then be reduced. Figure 4-19 shows a high level schematic of a possible application of using the dissipated energy to conduct the fatigue assessment based on Dissipated energy vs Life (W-N) curves. Although this method looks promising, based on the results presented in this thesis, it also good to have in mind some of its limitations. To start with, it is purely empirical and based on the early experimental results and observations seen in the material tested in this project where a large amount of dissipated energy has been seen and measured. As it is also based on the stabilised hysteresis loops, meaning that no low cycle fatigue is considered as in this fatigue regime no stabilisation is reached, as observed in Figure 5-21a-d for samples with <10,000 life cycles. Finally, this method still considers a certain amount of testing for the calibration of the method to obtain said curves, similar to typical S-N data, but this is significantly reduced due to the apparent insensitivity to the fibre orientation. What this means is that to obtain the fatigue material data, a single specimen orientation might be enough. In the same matter, the observed power law relationship represented in Equation 4-17 was drawn

from the experimental data, this means that A and b are purely empirical calibration factors representing a linear fit in a log-log scale, with A being the intercept and b the slope of the curve. Meaning that the W-N curve for a given material and stress ratio is the one that best fits the given experimental data into a power law equation. However, as this approach appears to be insensitive to the fibre orientation of the material, as shown in Figure 6-32, it implies that once a W-N curve has been fitted to for a specific fibre distribution and stress ratio, e.g. R=0 for 0° specimens, this curve could be representative of the material at any other system of fibre distribution for that stress ratio, this however would need to be validated, but the results shown in Chapter 6.4.2 suggest a that this statement is not entirely erroneous as data for different specimen orientations seem to come together into a singular curve.

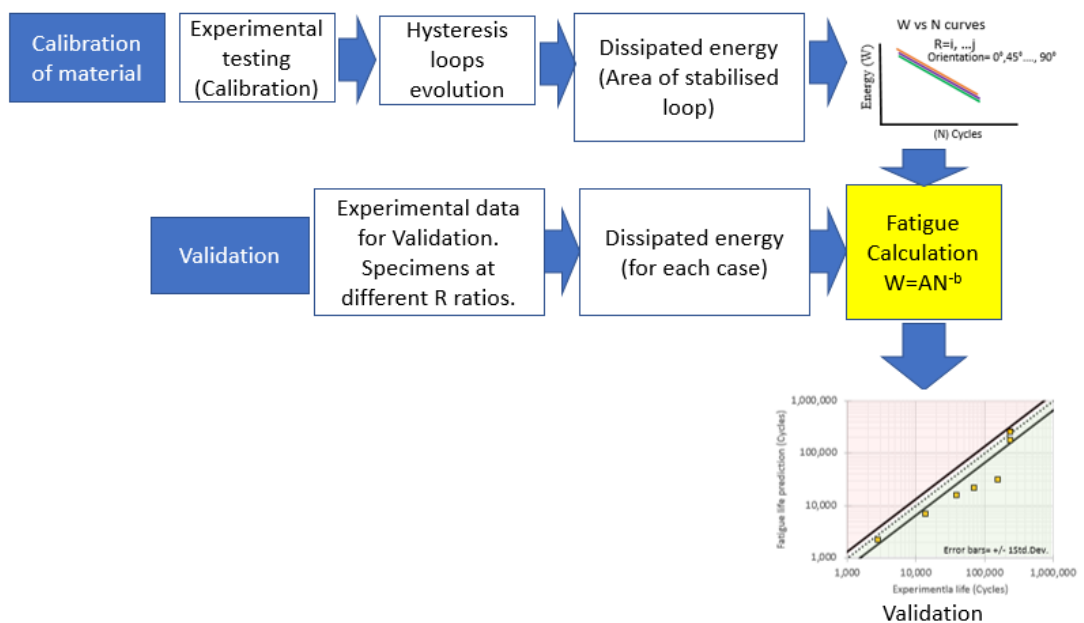


Figure 4-19 High level schematic of algorithm for a W-N approach for SFRP's.

4.6 Conclusion

This chapter presented and documented the full CAE methodology followed in this project, with detailed description of each of the modelling steps. An analysis of the variation of the simulations results, in terms of the fibre orientation tensor components and the stress results, with the mesh density/quality was presented for the Moldflow and Abaqus finite element meshes. Similarly, error levels obtained during the mapping of the orientation tensor information into the structural mesh was also documented. All this information, which allows to detect sources of inaccuracies inherent of the finite element modelling, is rarely reported in the literature. Unlike other published work [71], and due to the load levels used on this project, the

proposed material model for the prediction of the monotonic material properties considers the composite's behaviour as elasto-plastic, instead of linear elastic. Further calibration of the material model using experimental data was also conducted. The description of the Stress-Life approach was also documented in detail, including different mean stress correction relationships. Different to other proposed energy-based approaches, e.g. [2], [92], [94], this work recognises the effect of the material's plasticity. Therefore, if a fatigue parameter based in energy is to be introduced, this work understands that such parameter needs to consider the dissipated energy seen on the material measured via the stabilised hysteresis loops areas.

5. EXPERIMENTAL RESULTS

5.1 Fibre orientation distribution

5.1.1 Fibre distribution

A sample from a pristine 0° reference sample was used to measure the fibre orientation distribution throughout the plate at the centre of the reference location. The analysis was done via computed tomography (CT), with the preparation of the specimen done as described in Chapter 3 of this thesis. Figure 5-1 shows the 2D X-ray slices at the specimen's middle section. A clear distribution of fibres longitudinal and transversal to the flow direction can be observed in the *Thickness view*, describing the skin-shell-core microstructure. A clearer orientation of the fibres in the core section can be seen in the *Cross-section* view, where fibres are mostly aligned opposite to the flow direction in this layer. Finally, a more random fibre orientation belonging to the skin layers can be seen in the *Surface* view, where no particular fibre distribution can be distinguished.

Additionally, using optical microscopy, close up images of the three different layers were taken using polished samples, the results are shown in Figure 5-2 to Figure 5-4. A particular distinction can be made for fibres located at the central region, or core layer, where they are more transversally aligned to the flow direction. In contrast, in the shell layer, the fibres are mostly aligned towards to the flow direction, or out-of-plane. Finally, at the skin layer a more mixed orientation of fibres is visible. It is also good to mention that some voids were clearly observed in the matrix, these are seen as black features on the images. Accurate measurement of the different fibre orientation layers was not possible, as there was not a clear boundary between the different sections (skin-shell-core). Nevertheless, approximate measurements were taken on regions, through the thickness, where the fibres were visually more aligned toward a particular orientation. The core layer was seen to vary from ~0.76-1.3 mm; whereas, each shell layer fluctuated around ~1.0 mm. It is good to point out that these measurements varied heavily depending how much of the transition zones, sections with more visible mixed fibre alignment, was considered. Finally, an analysis was conducted to assess the approximate typical portion that each of the skin, shell and core layers represent from the total material thickness. To obtain a more generalized idea of the typical size for the layers, the results obtained herein were analysed together with the information documented in the literature in terms of fibre

orientation tensor components through the thickness obtained from [29], [33], [50]. The thickness of each layer was considered to be the point where there is a sudden drop, for the skin layer; and where the a_{11} and a_{22} curves seem to cross each other, for the core and shell layers. The considered sections are labelled in Figure 5-6. Figure 5-5 shows that approximately the skin layers represent a ~13% of the overall thickness of the material (or ~6.5% each); ~56% for the shell layers (or ~28% each); and ~31% for the central core layer. The results for the present material used in this project laid within this range.

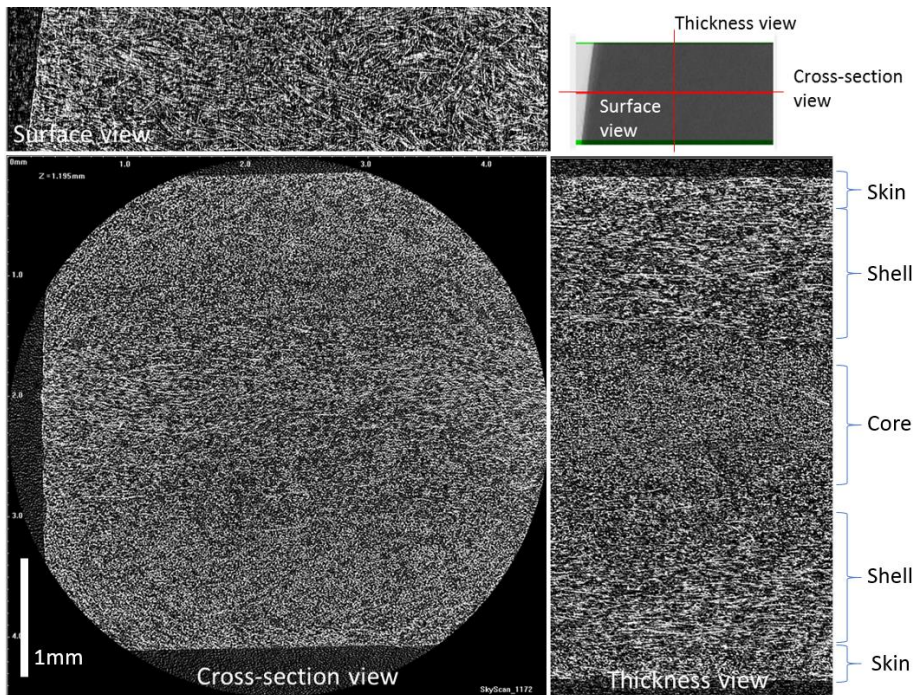


Figure 5-1 CT 2D slices at the centre of the gauge length of specimen showing the qualitative distribution of fibres through the thickness. Flow in the out-of-plane direction with respect to *Cross-section view*.

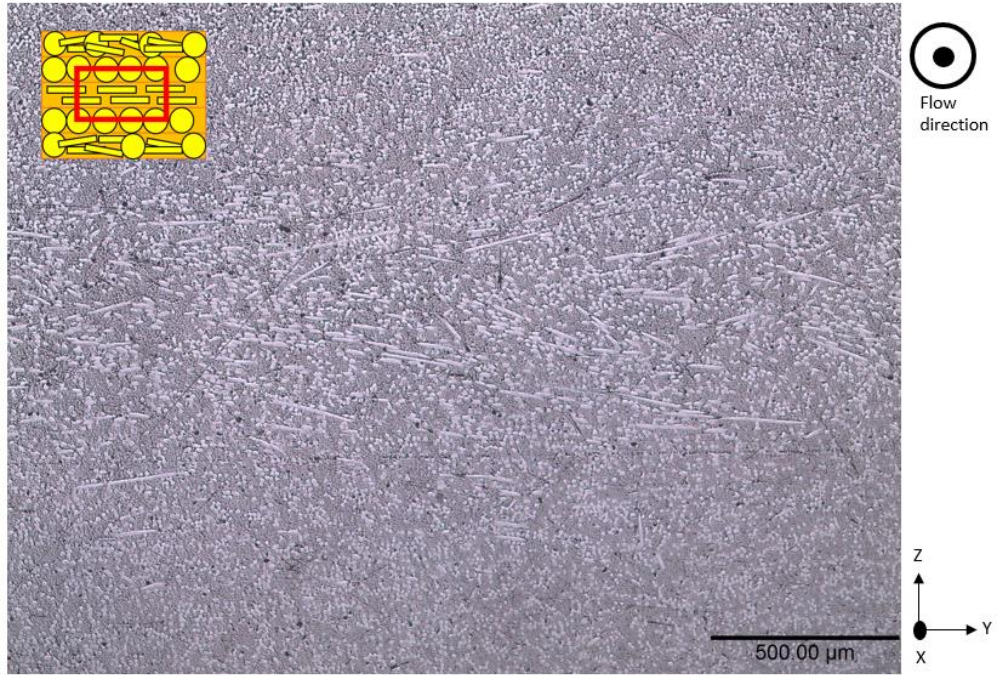


Figure 5-2 Optical microscopy picture of fibre distribution at the core layer of a 0° specimen with nominal thickness of 4mm. Flow in the out of plane direction.

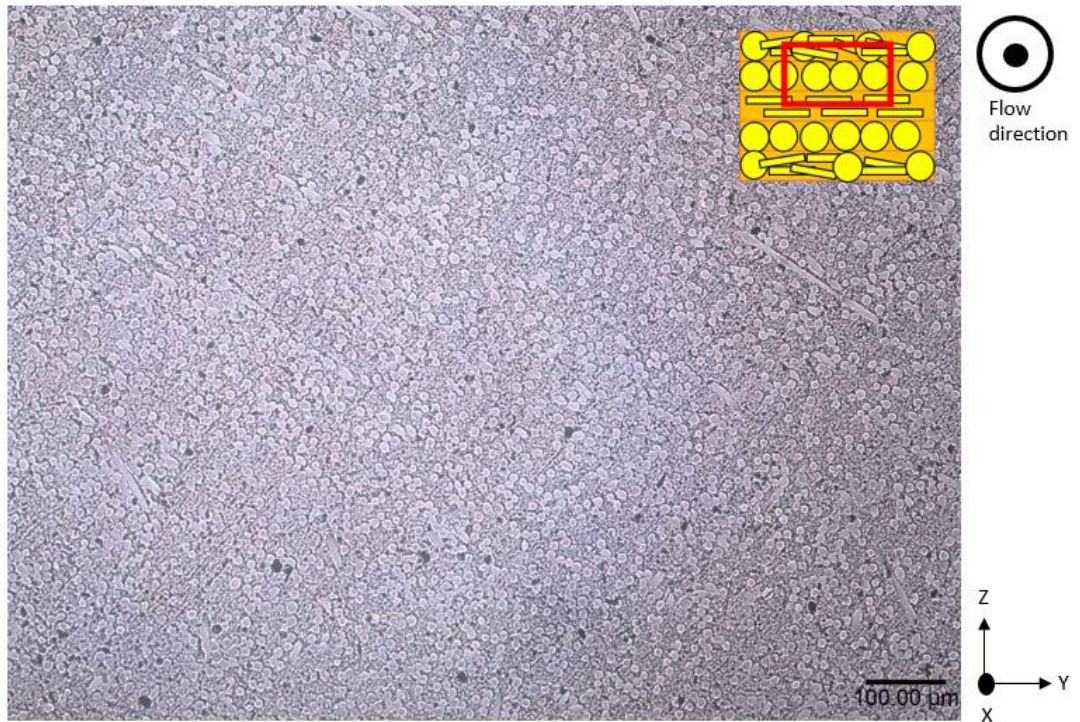


Figure 5-3 Optical microscopy picture of fibre distribution at the shell layer of a 0° specimen with nominal thickness of 4mm. Flow in the out of plane direction.

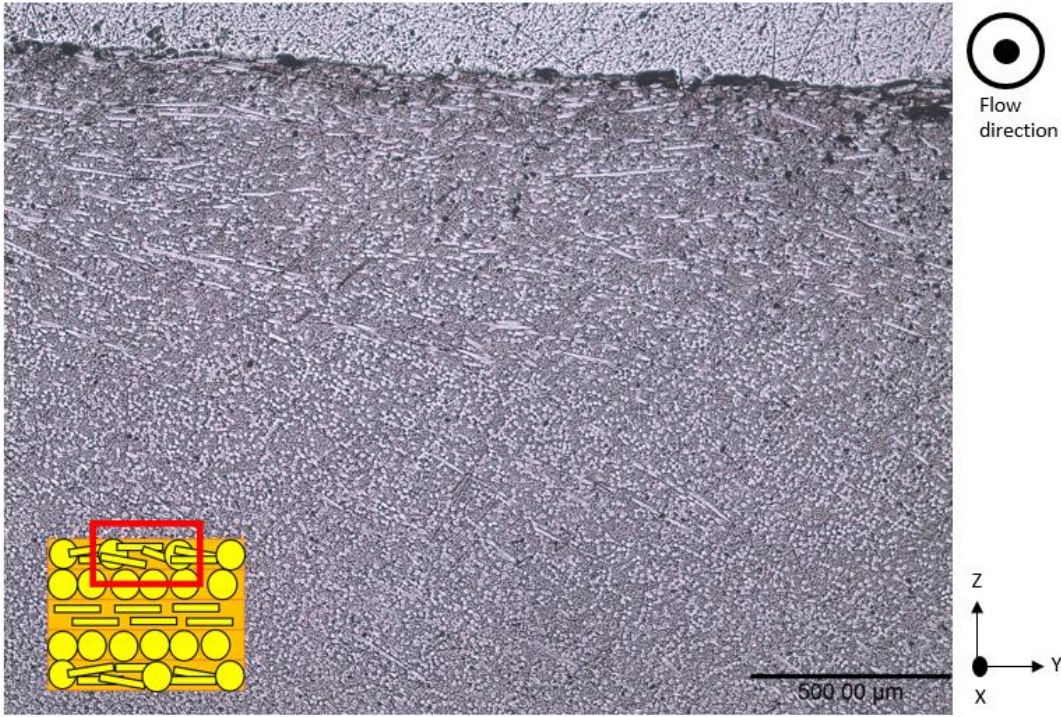


Figure 5-4 Optical microscopy picture of fibre distribution at the skin layer of a 0° specimen with nominal thickness of 4mm. Flow in the out of plane direction.

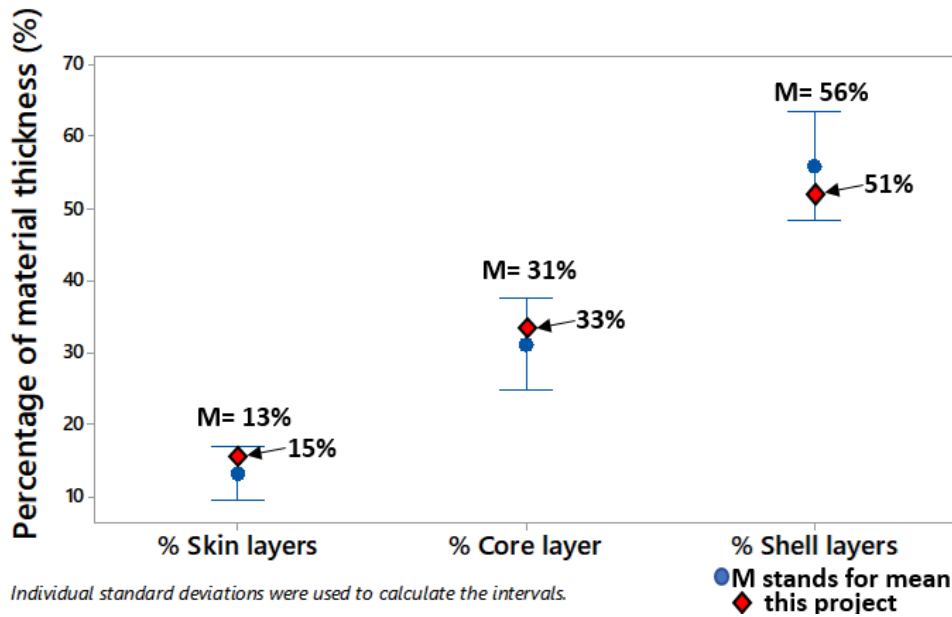


Figure 5-5 Interval plot (95%CI) of the percentage that the Skin, Shell and Core layers represent from the total material thickness. Created with information documented in [29], [33], [50].

5.1.2 Fibre orientation tensor

Computed tomography was also used to measure the fibre orientation tensor through the thickness at the centre of the reference location, as shown in Figure 3-8. As presented in the literature review, Chapter 2, the orientation of the fibres was first defined in terms of a probabilistic distribution function, which for ease of use is presented in terms of a second order fibre orientation tensor (3x3 matrix). Each of the principal diagonal components of this tensor represents the strength of alignment toward each coordinate direction. For the present project, a_{11} corresponds to the injection flow direction; a_{22} the direction orthogonal to the flow; and a_{33} the out-of-plane direction.

Two independent set of measurements were taken at the centre of the specimens. One at the composite manufacturer facilities (BASF), and another one at the industrial partner facilities (JLR); respectively, CT scanner 1 and CT scanner 2. This double measurement allowed to account for the difference in the equipment used. For reference to the reader, the CT scanner 1 was a phoenix nanotom m nanoCT scanner [164] with a maximum 180kV and 15W power and minimum voxel size of down to 300nm. CT scanner 2 was a NSI X5000 [165] with dual power trains of 225kV and 450kV, with an overall maximum system resolution of ~500nm. Five different composite samples were analysed using CT scanner 1, where the orientation data was measured every 2.33 μ m through the thickness. On the other hand, one composite sample was analysed using CT scanner 2; where the orientation data was measured every 10.1 μ m, through the thickness.

Figure 5-6 shows the results in terms of the orientation tensor components for the six different composite samples analysed using the above described CT scanners, together with the results of the FEA simulation. A clear distribution, in terms of the skin-shell-core microstructure, can be observed. Following the a_{11} tensor component, a high alignment with the flow direction at the very surface layers of the specimens can be seen, followed by a steep drop. These sections would represent the skin layers. After this region, another increase in the alignment of the fibres is seen covering a larger section of the specimen thickness. These parts would correspond to the shell regions, where fibres are mostly aligned parallel to the injection direction. Finally, at the centre of the specimen, a marked increment in the a_{22} tensor component is seen. This represents the strength of fibre alignment transversally to the flow, which mostly concentrates at the core layer of the material. It can also be observed that the out-of-plane component, a_{33} , of the fibre alignment is significantly low and consistent

through the thickness of the material, which implies that the fibres are mostly aligned in-plane.

Additionally, a comparison between the two different sets of experimental data, shown in Figure 5-6, can also be made. It can be seen that, for the most part, there is a good agreement between the CT scanner 1 and CT scanner 2 measurements, up to the start of the core region. At this point a more marked divergence can be seen, where the results of CT scanner 2 showed more randomly oriented fibres, tensor component closer to 0.5. This could be due to the maximum resolution achievable by this scanner.

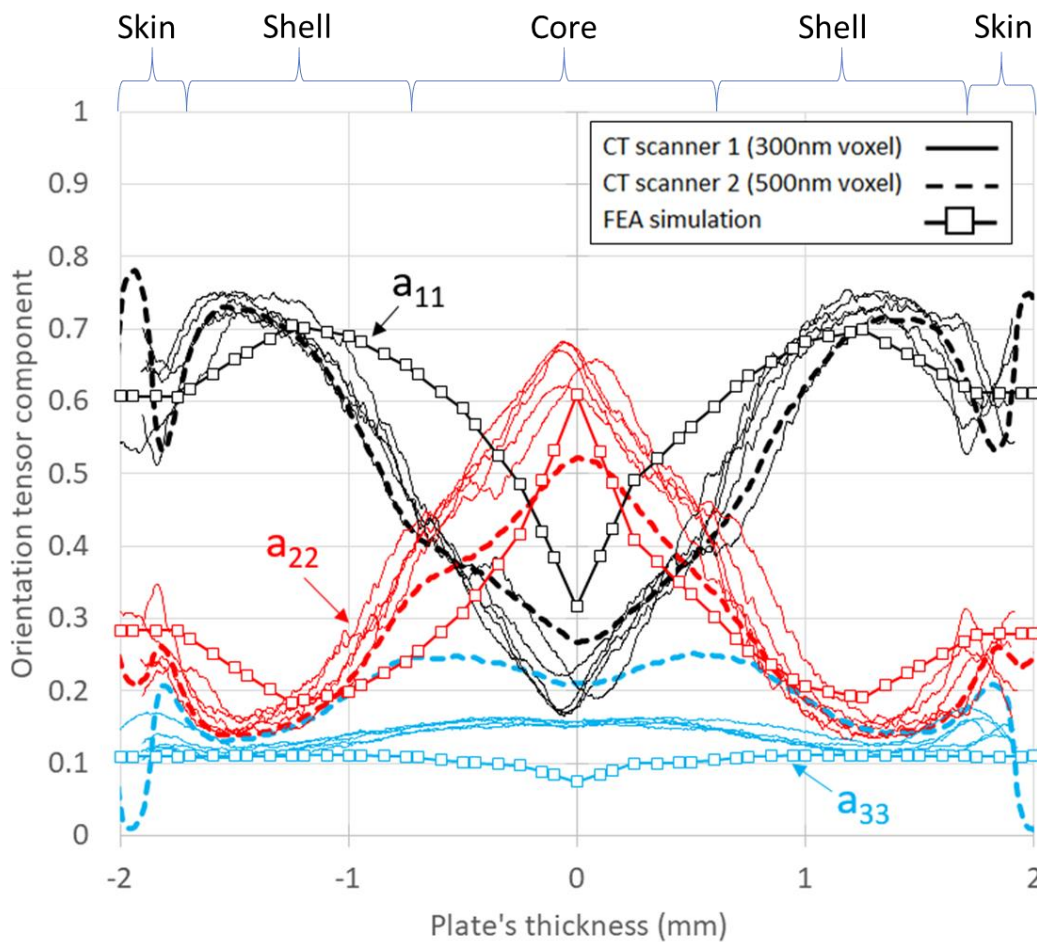


Figure 5-6 Orientation tensor components (a_{11} , a_{22} and a_{33}) measurements using two different CT scanners in a 4mm thick plate.

5.2 Monotonic testing

5.2.1 Stress-Strain behaviour

Tensile, quasi-static, testing was conducted on specimens at different orientations and locations, as shown in Figure 3-8 and Figure 3-9, to characterise the material behaviour.

The details of the testing have been described previously in Chapter 3 of this thesis. Figure 5-7 shows the obtained Stress-Strain curves. The engineering stress was calculated by using the measured applied force and the specimen's cross section. The strain was calculated by using the digital image correlation technique explained in Chapter 3.7.1; where a virtual extensometer was used inside the correlation software. The engineering strain was then calculated by dividing the change in length by the initial length. In Figure 5-7, a clear non-linear behaviour can be seen for all different specimens' orientations and locations. 0° Edge specimens presented the highest strength, with an average of 112MPa. Material ductility seemed to increase with mid-axis specimens, 30° and 45°, as these samples exhibited significant larger deformations, ϵ_{max} . In average, 90° curves laid below any other coupon orientation, presenting the lowest strength with an average of 85MPa. 45° and 90° Edge specimens showed a close behaviour in terms of strain hardening, although 45° coupons presented larger final deformations. It is good to mention that one coupon for 90° and one for 30° overlapped with the 45° and 90° Edge curves. That a similar behaviour is experienced by different coupons, suggests that the matrix was a contributor to the material response on these orientations.

Figure 5-8a-d show a comparison of the calculated values, per BS EN ISO 527-1 [113], for: the tensile (chord) Young's modulus (E), which describes the ratio of the applied stress to the change in shape due to the stretching of an elastic body, was measured from the obtained stress-strain curves, Figure 5-7, between 0.05% - 0.25% strain; the Yield strength at 0.2% strain ($\sigma_{Y0.2\%}$); the tensile Strength (σ_{UTS}), and the strain-at-break (ϵ_{max}). Figure 5-8c shows the positive fibre alignment effect produced by the mould's side walls, as 0° Edge specimens presented the highest average values for Young's modulus (E=7,885MPa). This specimen also showed the smallest strain-at-break, Figure 5-8a, with an average of 4.8%. The 90° and 90° Edge samples presented similar level of deformation with an average of 5.4% and 5.5%, respectively. However, 90° Edge specimens presented a larger Young's modulus than 90° coupons, 5,364MPa against 4,775MPa, respectively. These results seemed to imply that the plate's gate had a particular positive effect in terms of fibre alignment. Finally, Figure 5-8b depicts the general effect that the fibre orientation distribution has in the material response, where 90° specimens shows the lowest strength, followed by 90° Edge, 45°, 30°, 0° and 0° Edge.

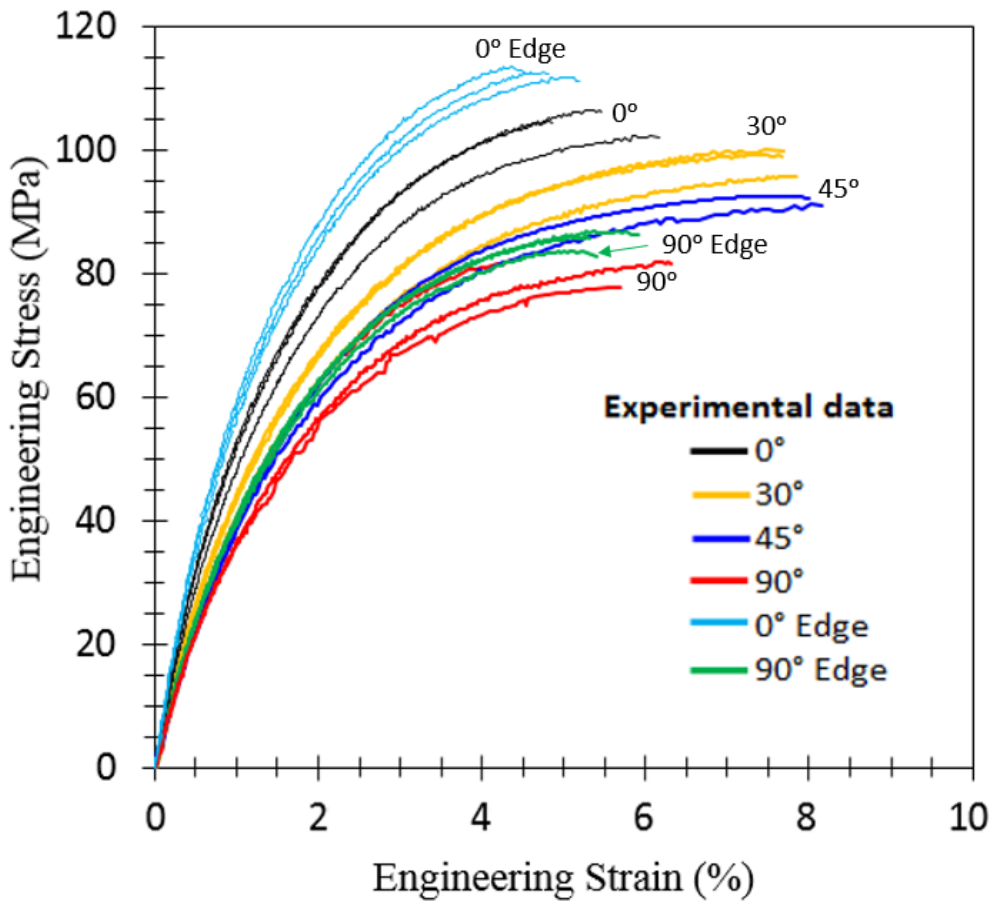


Figure 5-7 Stress-Strain curves for conditioned PA66GF50 at room temperature.

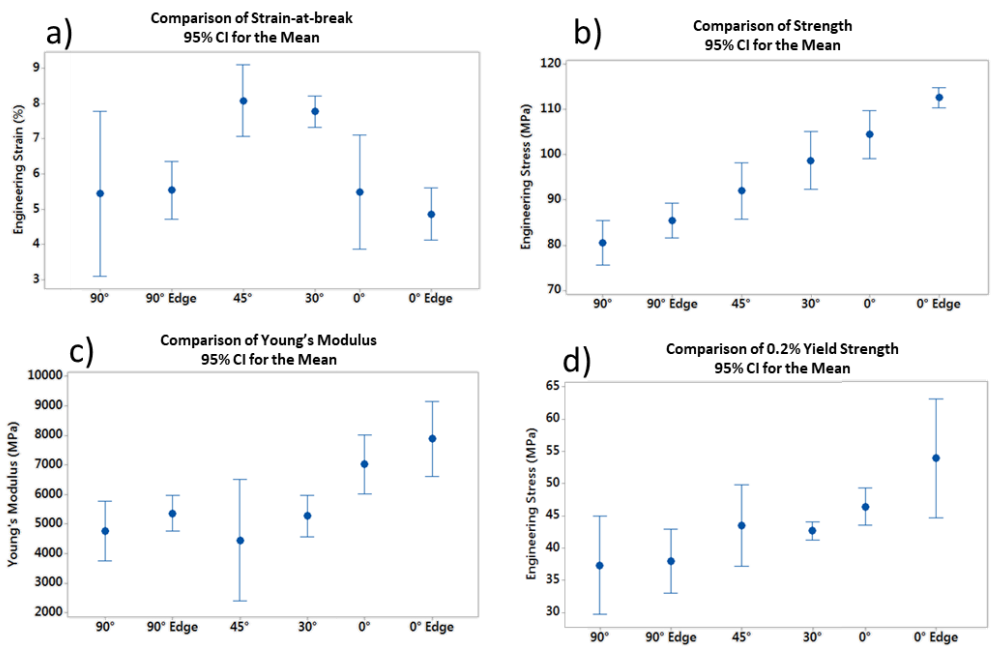


Figure 5-8 Interval plots for PA66GF50 specimens. a) Strain at break, b) Strength, c) Chord (Young's) modulus, and d) 0.2% Yield strength.

5.2.1.1 Poisson's ratio

The Poisson's ratios (μ) for the different coupon orientations were also calculated per BS EN ISO 527-1 [113]. This was done by comparing the strain decrease in the specimens' transverse direction ($\Delta\varepsilon_n$) and the strain increase in the longitudinal direction ($\Delta\varepsilon_l$) at the gauge section. Similar to the stress-strain curves, the strain was calculated by using the digital image correlation technique explained in Chapter 3.7.1, where virtual extensometers were used inside the correlation software, and positioned along and transversal to the specimens gauge section, on the width, to measure the material elongation and contraction during the test. The engineering strains were then calculated by dividing the change in length by the initial length. Individual Poisson's ratios were calculated for each specimen orientation using the following equation:

$$\nu = -\frac{\Delta\varepsilon_n}{\Delta\varepsilon_l}$$

Equation 5-1

Figure 5-9 shows the interval plot comparison of the calculated Poisson's ratios for all orientations. A clear distinction can be made between the different coupons. The material seemed to contract more on 0°, 30°, 45° and 0° Edge orientations. However, 90° and 90° Edge specimens presented similar values for ν , but almost 50% smaller than the other orientations. This implies that the transversal aligned fibres in these samples considerably diminish the lateral contraction of the composite. 0° and 0° Edge also presented almost identical values of ν , with 0.35 and 0.36, respectively. Finally, 30° and 45° had the highest values of ν , with 0.40 and 0.38 respectively, which are close to the theoretical value of pure nylon 6,6 ($\nu = 0.41$) [166]. This seems to indicate that on mid-axis specimens, i.e. coupons with more mixed-fibre orientation, the effect of the matrix is more present.

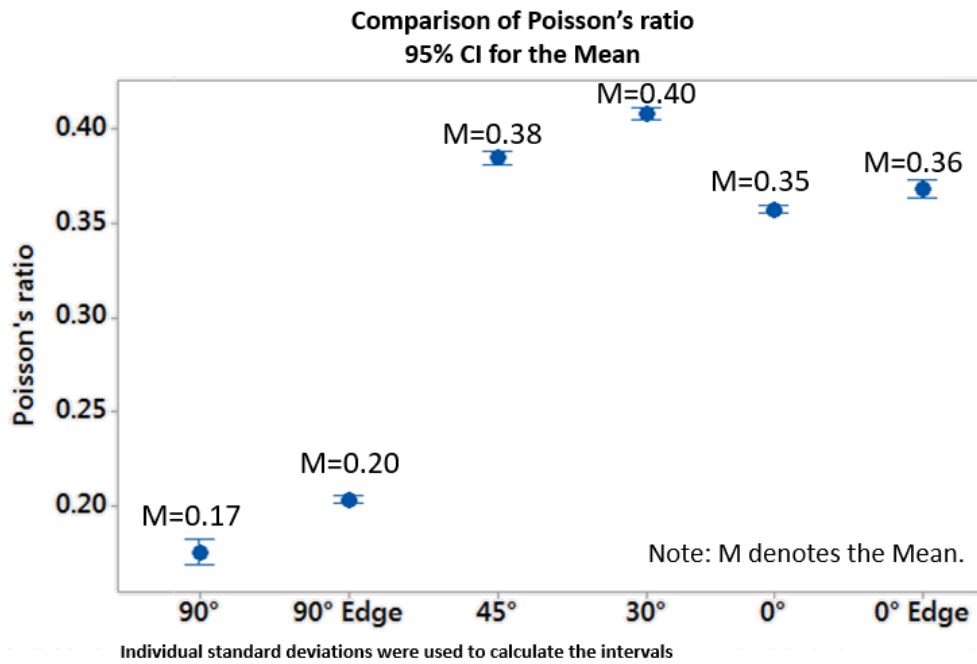


Figure 5-9 Interval plots for Poisson's ratio of PA66GF50 specimens.

5.2.2 Tension-Compression behaviour

Monotonic (quasi-static) tension-compression testing was conducted on 0° and 90° reference specimens to analyse the behaviour of the material under this condition. The same parameters used to obtain the quasi-static Stress-Strain curves were applied for this testing, i.e. 2mm/min loading rate. Figure 5-10a-b shows the stabilised loops for both specimen orientations at different stress levels. For both cases and from zero up to +/-25MPa the material behaved linearly, under both tension and compressive loads. It was at higher stresses, +/- 50MPa, that presence of the Bauschinger effect could be seen taking place in the compressive part of the curves. It is interesting to see that under the maximum applied tensile load of +50MPa, the 90° specimens deformed more than the 0° coupons; which is similar to what was seen in the Stress-Strain curves in Figure 5-7. It can also be observed that in compression, the Bauschinger effect takes place at a lower load for the 90° specimens (~46MPa). This could imply an early failure of this specimen orientation, due to the reduced Yield strength, in comparison to the 0° coupons. This could be correlated to the results of the fatigue testing at R=-1, presented in Figure 5-10, where the 90° coupons presented lower fatigue lives than those for 0° specimens.

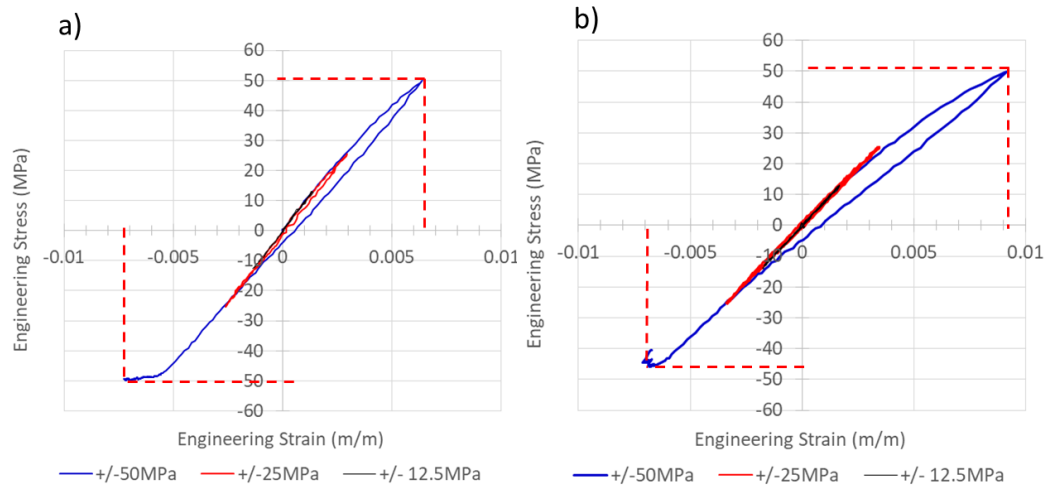


Figure 5-10 Quasi-static (2mm/min) tension-compression (R=-1) test for a) 0° and b) 90° reference specimens.

5.3 Fatigue testing

5.3.1 Constant amplitude

The first stage of the fatigue testing was the characterisation of the material fatigue performance in the form of Stress-Life (S-N) curves. Three different R ratios were used: -1.0, 0.0 and 0.3, at a frequency of 5Hz. In the same manner, four different coupon orientations were used, 0°, 30°, 45° and 90°, all cut at the same reference location per Figure 3-8. A cut-off limit of 10^6 cycles was established as endurance limit.

The results of the material characterisation under stress-controlled fatigue conditions is shown in Figure 5-11. In general, all the fatigue data seemed to follow a Power law equation, or linear relationship in a log-log plot. Therefore, it could be described using the Basquin's equation,

$$\sigma_a = AN^B$$

Equation 5-2

by defining the stress amplitude at cycle 1 (A) and the slope of the curve (B). Table 5-1 shows the values for these parameters at the different R ratios and specimens' orientations.

Under fully reverse conditions (R=-1), the fatigue life data for 45° and 90° specimens seemed to overlap, with no clear difference between orientations. This behaviour is particular of this stress ratio and these two orientations, as this was not observed in

any other case. For the case of 30° specimens, the fatigue data laid in-between 0° and 45°-90° coupons. Finally, 0° presented the highest life of all the sets of data, and at all stress ratios.

Under R=0 and R=0.3 similar observations can be made. A clear effect of the mean stress was observed for both conditions. Fatigue data at these stress ratios presented lower lives than at R=-1. For 0° and 90° specimens, data showed the highest and lowest lives, respectively, for both R ratios. 30° and 45° specimens' curves laid in-between 0° and 90° curves, with 30° coupons showing a higher fatigue performance than 45° samples.

It was then clear that the fibre orientation had a significant effect on the fatigue performance of the material. 0° specimens showed the longest lives, and 90° the shortest. R=-1 also represents a particular case where a more complex material behaviour was seen, in particular at 45° and 90° coupons. Additionally, a clear effect of the mean stress was also observed, presenting lower lives with increasing stress ratios.

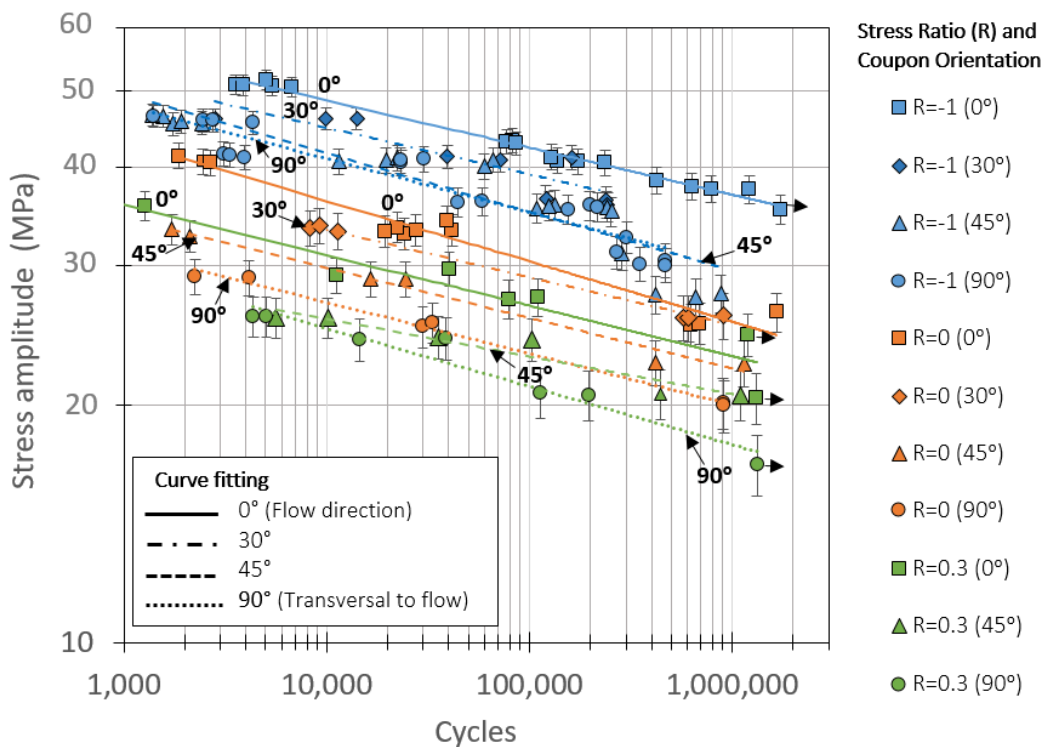


Figure 5-11 Constant Amplitude, coupon based S-N curves for conditioned PA66GF50 at ambient temperature and at different R ratios.

Table 5-1 Basquin's equation parameters in terms of Stress amplitude (σ_a), and life cycles (N).

Stress ratio	Orientation	A	B	Fitting R ²
-1	0°	84.3	-0.060	0.98
	30°	75.2	-0.055	0.81
	45°	82.5	-0.074	0.85
	90°	76.4	-0.68	0.88
0	0°	73.2	-0.076	0.96
	30°	58.0	-0.06	0.99
	45°	53.6	-0.064	0.98
	90°	49.0	-0.065	0.99
0.3	0°	55.8	-0.064	0.90
	45°	49.2	-0.074	0.94
	90°	39.7	-0.047	0.90

5.3.1.1 Stiffness evolution

It was presented in the literature review, Chapter 2, that the degradation of the material's stiffness has been widely used to analyse the damage accumulation in this type of composites. Based on this, a dynamic stiffness was calculated for the different specimens' orientations and R ratios during fatigue testing, such that:

$$K_d = \frac{\Delta F}{\delta}$$

Equation 5-3

Where K_d is the dynamic stiffness, and ΔF and δ are, respectively, the dynamic force and dynamic displacement. In order to compare the decay of the different specimens' stiffness at different stress ratios and lives, the results were normalized using the total life (N_f), and the original stiffness (K_0).

The evolution of the specimens' stiffness at different stress amplitudes is shown in Figure 5-12 to Figure 5-14. For all stress ratios, a clear difference can be made when comparing the results for samples under high stresses against the rest. On these specimens, the stiffness decay was never stabilised and a steep degradation was seen from the beginning of the test up to failure. A maximum drop of 60% of the original stiffness was seen on 45° specimens at R=-1, as presented in Figure 5-12c. On the other hand, a minimum drop of 15% of the original stiffness was seen on 0° specimens

at $R=0.3$, as shown Figure 5-14a. It is good to mention that at this particular stress ratio, $R=0.3$, the degradation of the stiffness seemed to have a gentler slope than at the other R ratios.

On specimens with intermediate lives, between 10,000 to 500,000 cycles, a sudden drop in stiffness was seen at the beginning of the test. This was then followed by a longer stabilised region for most of the specimen's life, between 60-70% of the component life. This was seen on all stress ratios. In contrast, at longer lives, $>500,000$ cycles, the initial stiffness drop was not seen, and the decay stabilised from the beginning of the test until failure. A clear example of this can be seen in Figure 5-13b. For both cases, this stabilised decaying region could suggest a consistent propagation of micro-cracks during most of the life of the specimens.

Finally, at around the 90% of the life of the sample, a sudden drop in stiffness leading to failure was also observed. This could imply the propagation of a single, or several, macro-cracks in the material.

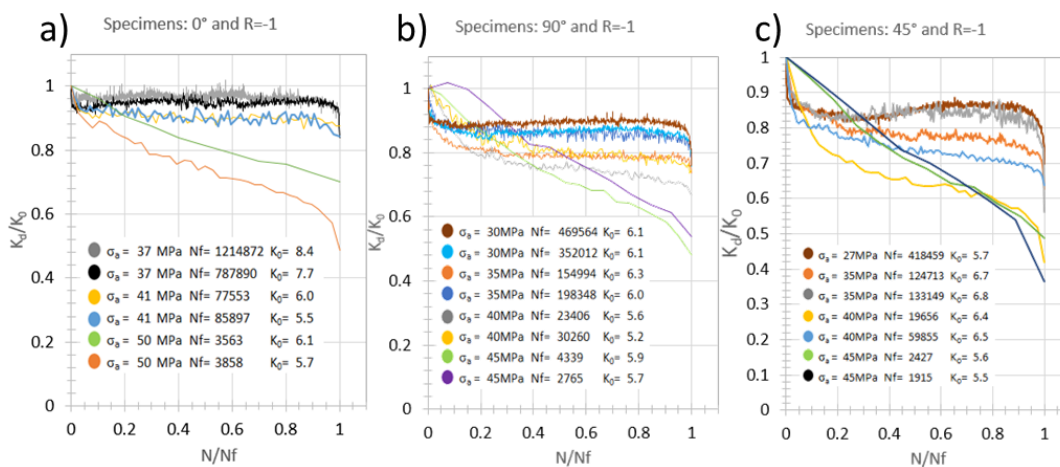


Figure 5-12 Stiffness evolution for PA66GF50 specimens at $R=-1$. Total life (Nf) is given in Cycles. Initial stiffness (K_0) is given in kN/mm.

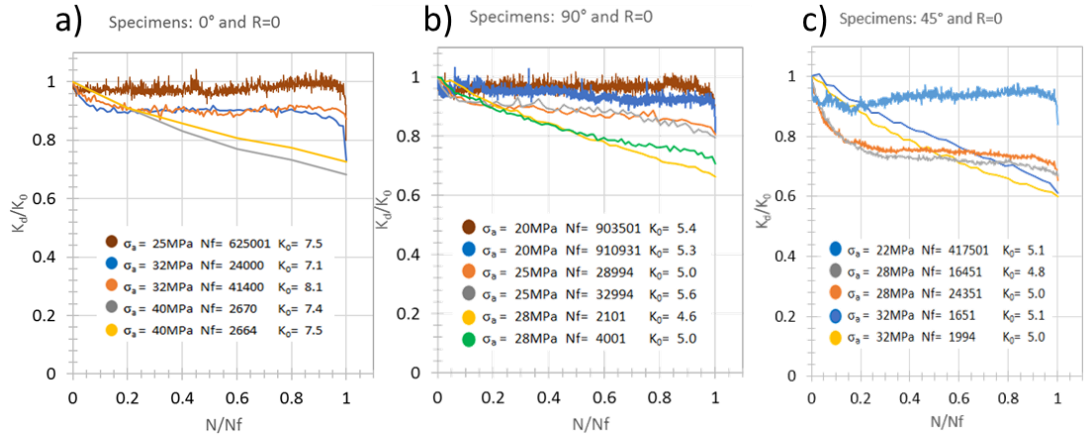


Figure 5-13 Stiffness evolution for PA66GF50 specimens at R=0. Total life (Nf) is given in Cycles. Initial stiffness (K0) is given in kN/mm.

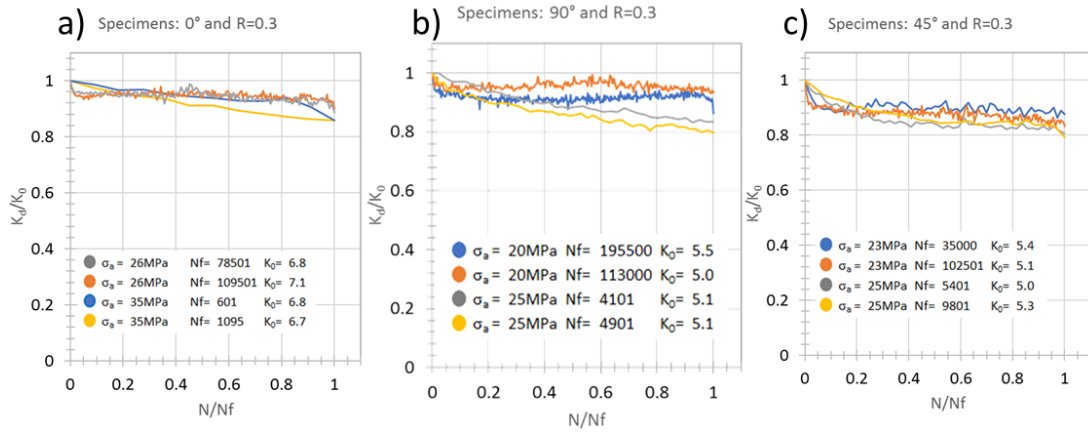


Figure 5-14 Stiffness evolution for PA66GF50 specimens at R=0.3. Total life (Nf) is given in Cycles. Initial stiffness (K0) is given in kN/mm.

5.3.1.2 Temperature evolution

Surface temperature measurements were taken at the centre of the specimens' gauge lengths via a thermocouple type T. In order to compare the data at different stress levels and lives the temperature readings were normalized with respect to the specimen's total life (N_f). Additionally, in order to account for the ambient temperature fluctuations, readings of the laboratory environment were also taken. The specimen's surface temperature at any given time (ΔT) was defined as:

$$\Delta T = T_{coupon} - T_{ambient}$$

Equation 5-4

To give the reader an idea of the ambient temperature conditions in the laboratory during all the experimentation phase, a random set of 1000 measurements were taken

from several testing conducted during different dates. Figure 5-15 shows the histogram of this data. The experimentation took approximate two years to complete, and the temperature in the laboratory averaged 21°C.

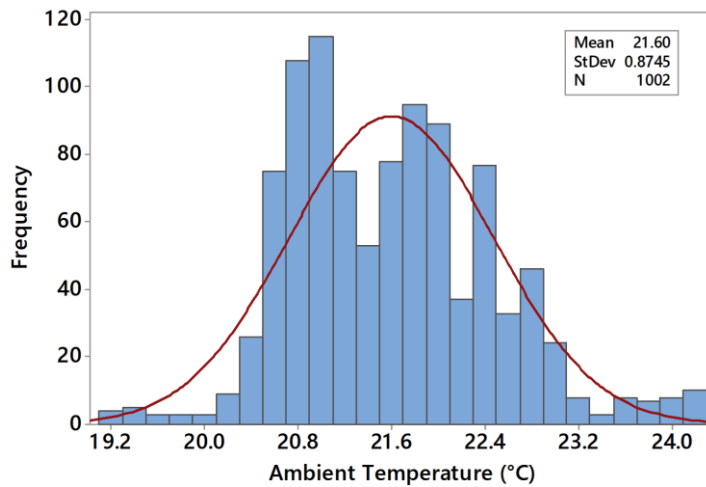


Figure 5-15 Histogram of ambient temperature.

Figure 5-16 to Figure 5-18 present the temperature readings for the specimens at different orientations and stress ratios. A clear observation can be made on specimens tested under $R=-1$ and at higher stress levels, as shown in Figure 5-16a-c. On these coupons a rapid increase of temperature was observed through the life of the specimens, with a maximum reading of approximate 17°C on 90° coupons. It is good to mention that such high levels of temperature are only seen under $R=-1$ conditions. At this same stress ratio but under intermediate and lower stresses, a stabilisation of the temperature evolution was observed and fluctuated between 2°C to 8°C.

For the case of positive R ratios, Figure 5-17 and Figure 5-18, the surface temperature fluctuated between 2°C-5°C. This was independent of the stress level and orientation. 45° specimens presented the lowest temperature increase for both R ratios, $R=0$ and 0.3. On the other hand, 0° specimens presented the highest temperature measurements but still under 5°C.

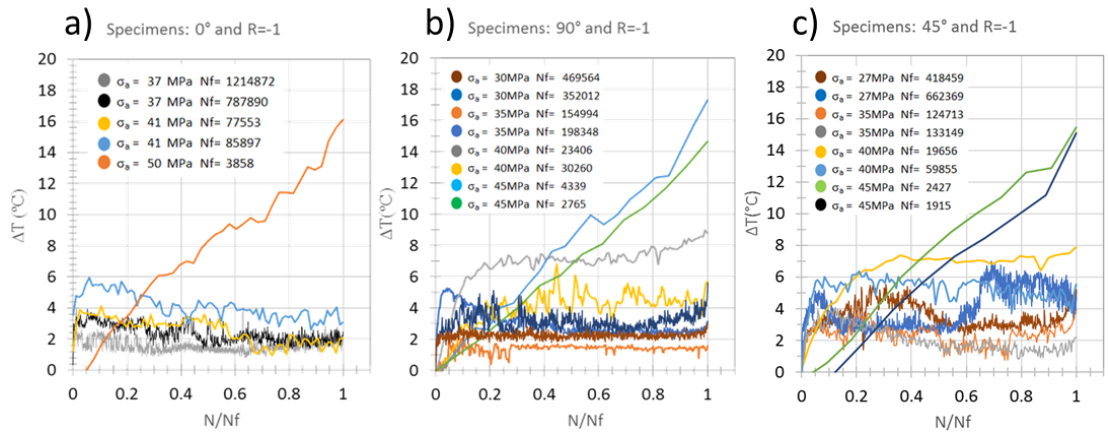


Figure 5-16 Temperature evolution for PA66GF50 specimens at R=-1. Total life (Nf) is given in Cycles.

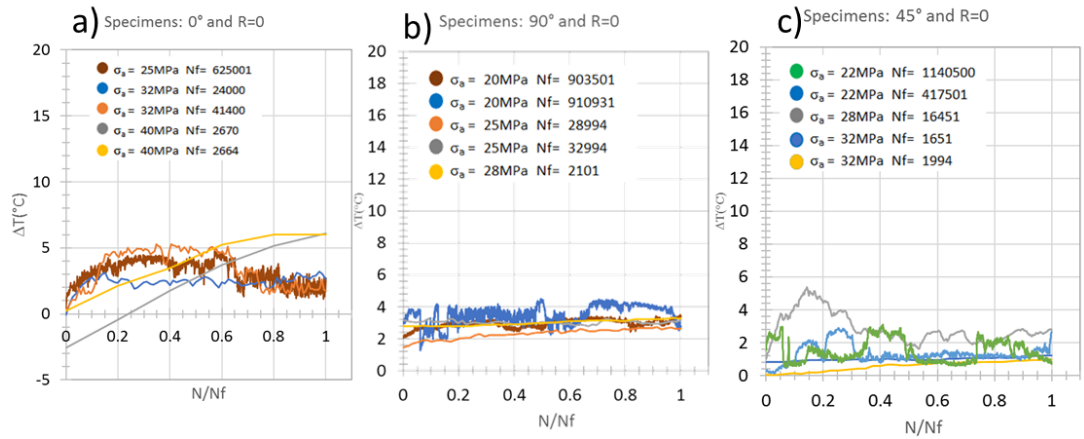


Figure 5-17 Temperature evolution for PA66GF50 specimens at R=0. Total life (Nf) is given in Cycles.

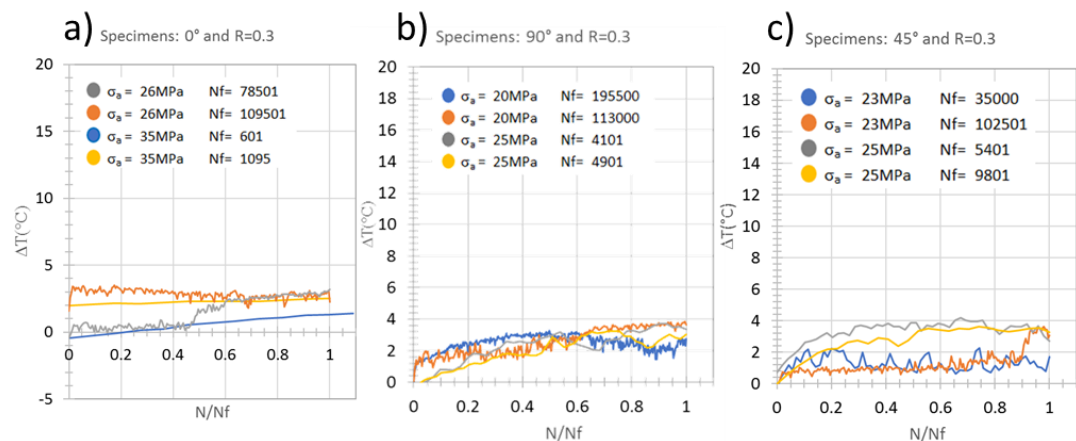


Figure 5-18 Temperature evolution for PA66GF50 specimens at R=0.3. Total life (Nf) is given in Cycles.

5.3.1.3 Hysteresis loops

Figure 5-19 and Figure 5-20 shows the hysteresis loops and the strain evolution for $R=-1$ and $R=0$ at different stress amplitudes for 0° and 30° specimens, respectively. The behaviour observed on these particular samples was also seen on 90° and 45° specimens. The results for these orientations are presented in the Appendix B.1.

First, by analysing both figures it can be seen that the composite presented a clear viscous behaviour under cyclic conditions. This is observed by the clear hysteresis loops, which represent energy loss or energy dissipation. This behaviour was seen on all orientations.

At relatively high stresses, and independent of the R ratio, the strain never stabilised and kept increasing up to failure. This was observed on 0° specimens (Figure 5-19a and c), as well as, in 30° specimens (Figure 5-20a and c). On the other hand, at relative intermediate to low stresses, the strain built-up reached a stabilised stage. This is shown in Figure 5-19b and d for 0° specimens; and in Figure 5-20b and c for 30° coupons. On the other hand, at $R=0$, a clear presence of ratcheting was observed in the material. This meant there was an accumulation of plastic strain throughout the testing, for both 0° and 30° specimens. This behaviour is shown in Figure 5-19c-d and Figure 5-20c-d. This result was very similar to metals under non-zero mean stress conditions.

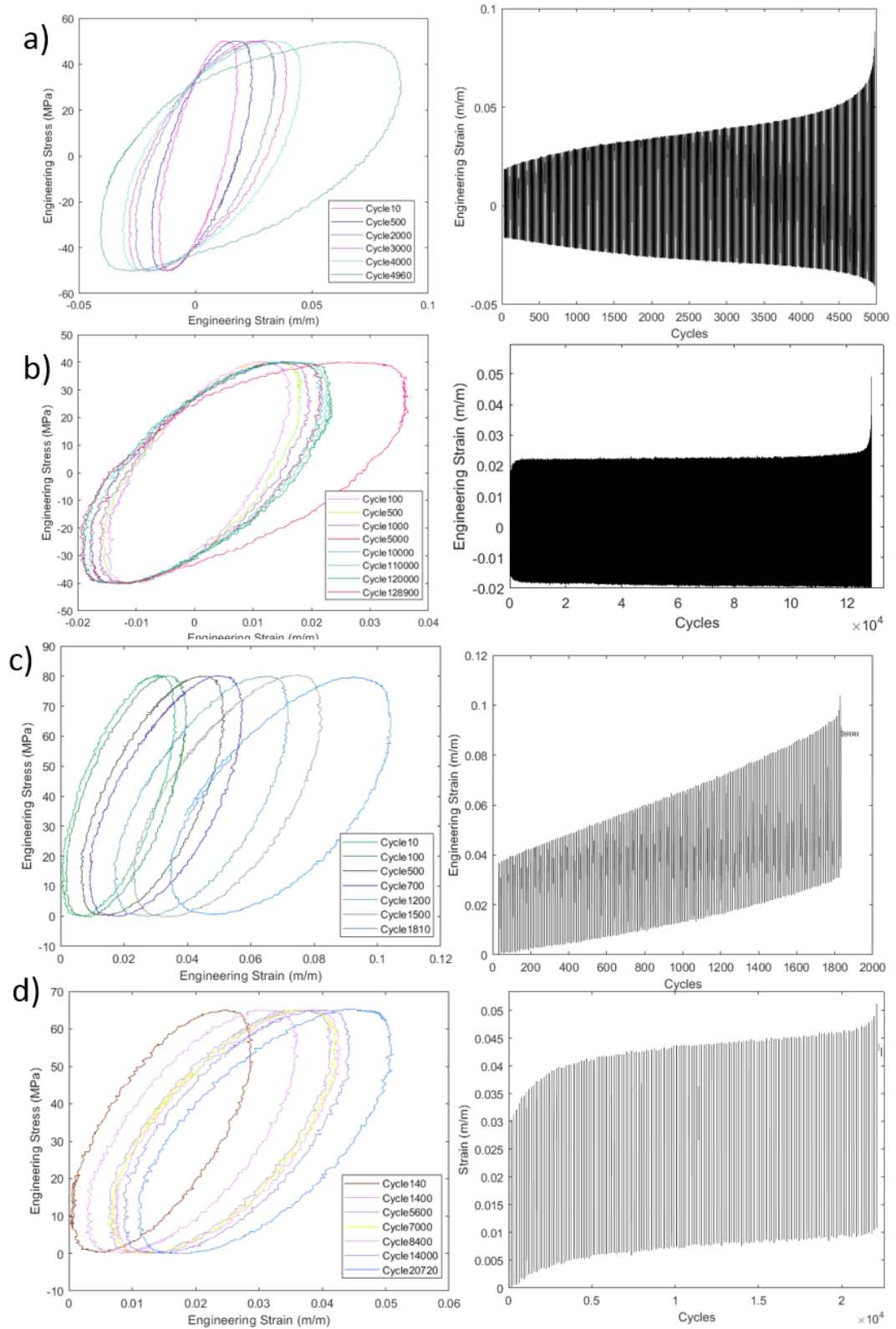


Figure 5-19 Hysteresis loops (Stress vs Strain), and evolution of strain (Strain vs Cycle) curves for 0° , $R=-1$ at a) $\sigma_a=50\text{MPa}$, b) $\sigma_a=40\text{MPa}$ and $R=0$ c) $\sigma_a=41\text{MPa}$, d) c) $\sigma_a=33\text{MPa}$.

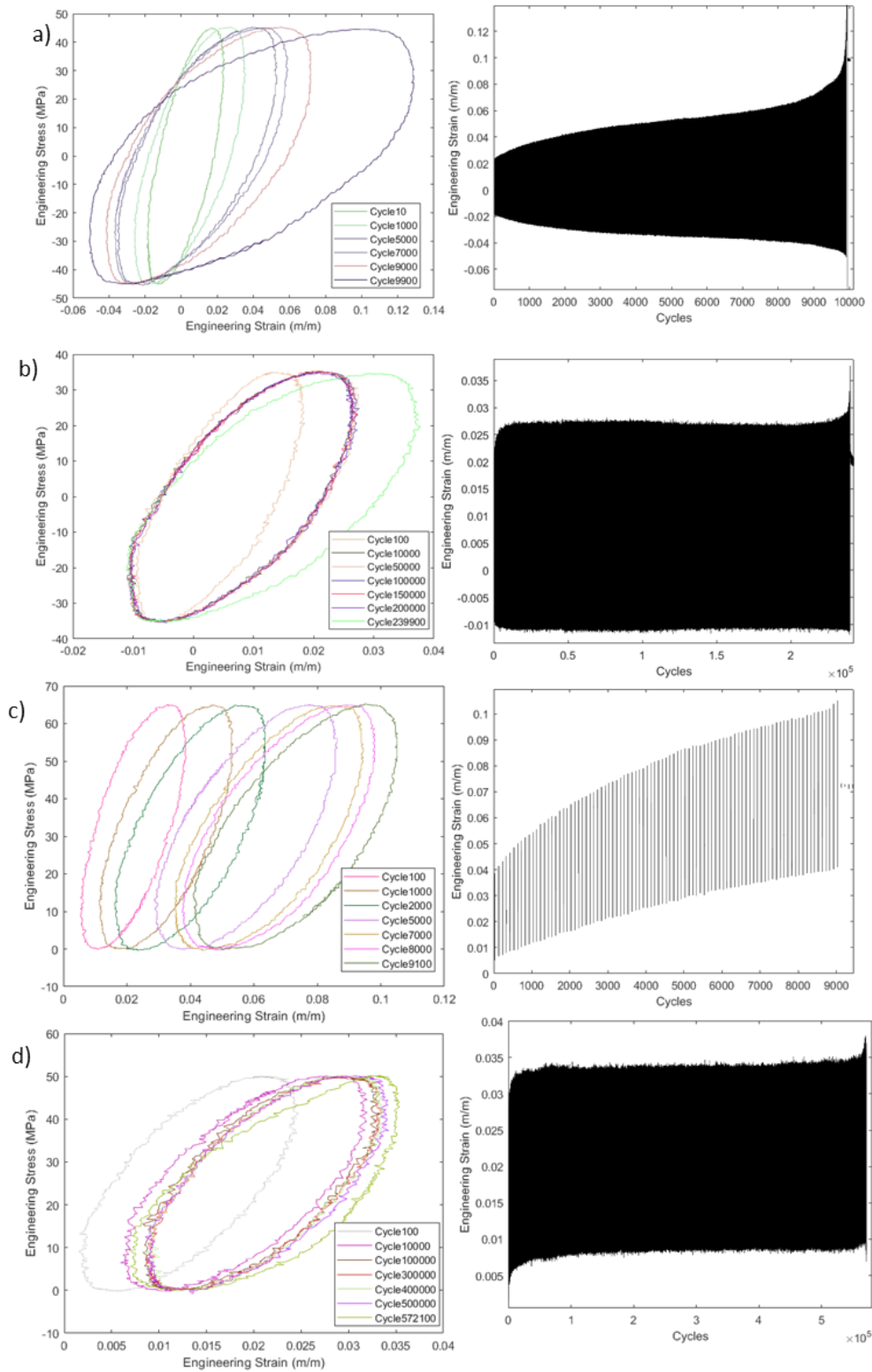


Figure 5-20 Hysteresis loops (Stress vs Strain), and evolution of strain (Strain vs Cycle) curves for 30°, R=-1 at a) $\sigma_a=46\text{MPa}$, b) $\sigma_a=36\text{MPa}$ and R=0 c) $\sigma_a=33\text{MPa}$, d) c) $\sigma_a=25\text{MPa}$.

5.3.1.4 Hysteresis area

The dissipated energy, or energy loss, is represented by the area inside of the hysteresis loops. This energy was calculated for the different orientations and at different stress levels throughout the life of the specimens. Figure 5-21 shows the evolution of the hysteresis area for 0°, 30°, 45° and 90° samples. It can be seen that at relatively high loads, or lower lives, the energy shows an exponential increase from the start of the test and until failure. No particular stabilization was seen under these conditions. In particular, 45° and 0° specimens showed the highest increase of energy with maximum values of 8.45 and 8.1 MJ/m³ respectively, as shown in Figure 5-21 a and c. This step increase was observed on specimens with lives of less than 10,000 cycles. From Figure 5-21, it can also be seen that on all orientations, and at intermediate to low stresses, a clear stabilisation of the energy is observed. This steady state is present for about 80% of the life of the specimens. Therefore, this energy could be used as a fatigue parameter to describe the cyclic performance of the material.

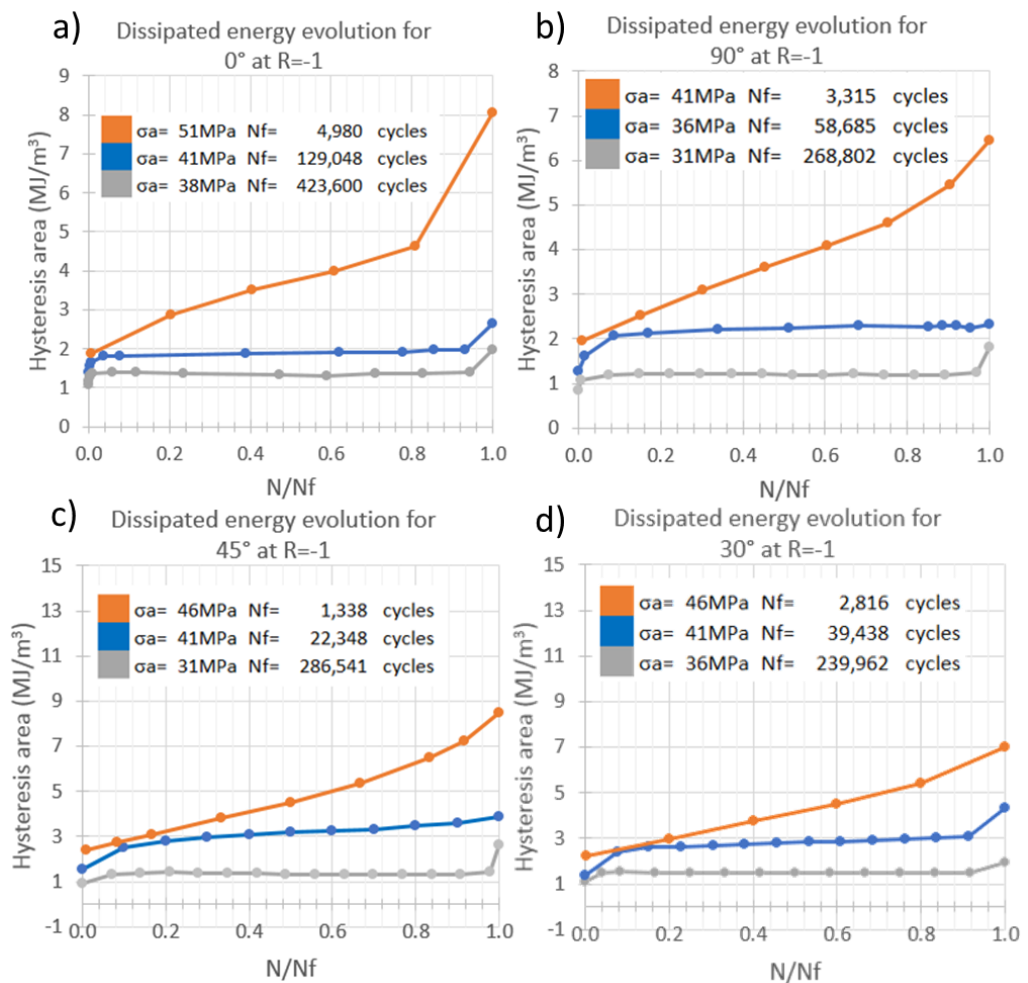


Figure 5-21 Evolution of the hysteresis area at R=-1 for a) 0°, b)90°, c)45° and d) 30° specimens.

5.3.1.5 Cyclic Stress-Strain behaviour

Cyclic Stress-Strain curves for 0°, 45° and 90° were calculated using the stabilised hysteresis loops obtained during fatigue testing. As presented in Chapter 4 of this thesis, the cyclic material behaviour was represented using the Ramberg-Osgood relationship. Figure 5-22 shows the calculated cyclic curves and the experimental stabilised hysteresis loops at different stress levels. For each of the curves, the cyclic strength coefficient (K') and the cyclic strain hardening exponent (n') were calculated using the true stress amplitudes and the true plastic strain amplitudes obtained from the hysteresis loops, as shown in Figure 4-8a and b. The calculated coefficients and exponents for each curve are presented in Table 5-2. It is good to mention that the Young's moduli (E) used were the same as the ones obtained for the monotonic curves, as shown in Figure 5-8. Figure 5-22 shows the presence of cyclic softening on the material behaviour, in comparison to the monotonic results, in particular for the 45° coupons. 45° and 90° specimens' curves showed a close behaviour. This is similar to the results seen in the S-N curves for $R=-1$, in Figure 5-11. However, it is clear that for this case the 45° curve laid below than 90° one. This could imply that there is a larger effect of the matrix on the material performance when the fibres are more mixed-oriented as is the case for 45° specimens. In regards to the results presented in Table 5-2; the influence of these parameters, K' and n' , in the fatigue life of short fibre reinforced composites was investigated by Tevatia and Srivastava [167]. It was found that high values of cyclic strain hardening exponents and low values of cyclic strength coefficients tend to increase the fatigue life of the material, at the same time, higher levels of plastic strain amplitude ($\frac{\Delta\epsilon_p}{2}$) caused shorter fatigue lives. Similar increase of the fatigue resistance with increasing values for the cyclic strain hardening exponent was also found by Slaughter and Fleck in [168], when implementing the Ramberg-Osgood relationship. Some of the limitations of this particular model were investigated by Krempl and Hong in [149], although their work was based on orthotropic visco-plastic composites, the conclusions in regards to the limitations of the usage of this model are also applicable to the present SFRP. In specific, the main caveat of this model is that the plastic deformation is considered to be time-independent. This means that no creep or other time-dependent processes can be reproduced by this approach. A combine approach of plasticity with creep theories was proposed as a way to capture these effects.

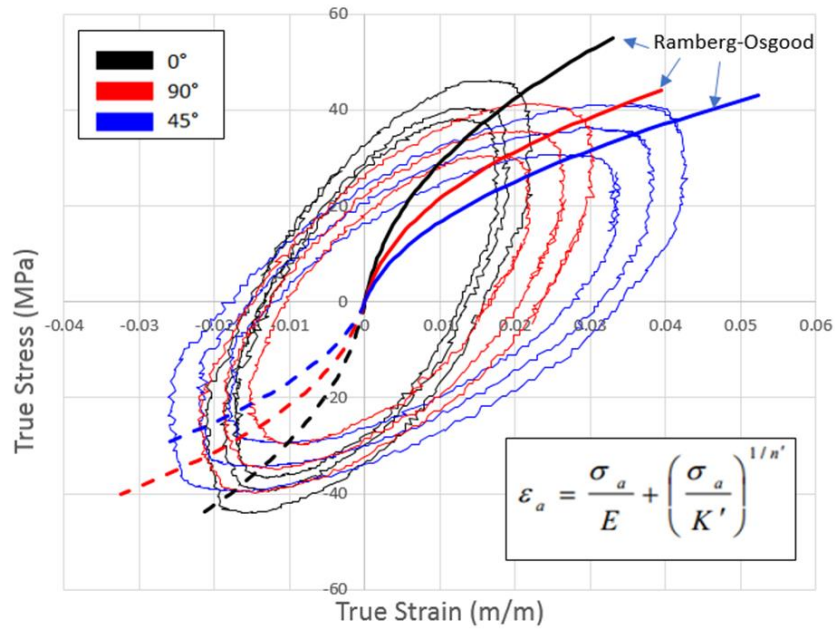


Figure 5-22 Cyclic Stress-Strain curves for PA66GF50 at different orientations, overlapping the stabilised hysteresis curves at different stress amplitudes.

Table 5-2 Calculated Ramberg-Osgood's cyclic strength coefficient (K') and cyclic strain hardening exponent (n') values for the different specimens orientations.

Orientation	K'	n'
0°	285	0.44
45°	203	0.49
90°	194	0.42

5.3.1.6 Stress-Life at 1Hz

Previously, it was shown that at R=-1 and under relative high stresses the specimens present larger levels of temperature increase, as shown in Figure 5-16. A common technique to reduce excessive heat dissipation is to reduce the frequency on high-stressed samples. However, nylon is strain rate dependent, which suggests that changing the testing frequency could change the overall performance of the material presenting completely different conditions than the ones under study in this project. Therefore, a test was conducted to assess whether the change in testing frequency affected the performance of the material. For this comparison a 90° specimen was chosen, as this orientation presented the largest temperature readings (Figure 5-16b). The frequency used was 1Hz, and the test was carried out at R=-1.

Figure 5-23 shows the comparison between different frequencies, in terms of S-N data. It can be seen that the specimen tested at the slower speed presented a significant improvement of life, approximate 6.6 times more than at 5Hz. Whereas, the temperature increase was kept within 5°C, Figure 5-24b. Additionally, a more stabilize degradation of the stiffness was also seen on this specimen, Figure 5-24a. This suggests that comparing experimental data taken at different testing frequency may not be adequate, at least for the present material, as the composite is showing a significant change in the behaviour. Therefore, and for consistency, a decision was made to keep testing a 5Hz. Nevertheless, for calculations including stabilised hysteresis loops, or stabilised stiffness, data with lives under 10,000 cycles was not considered.

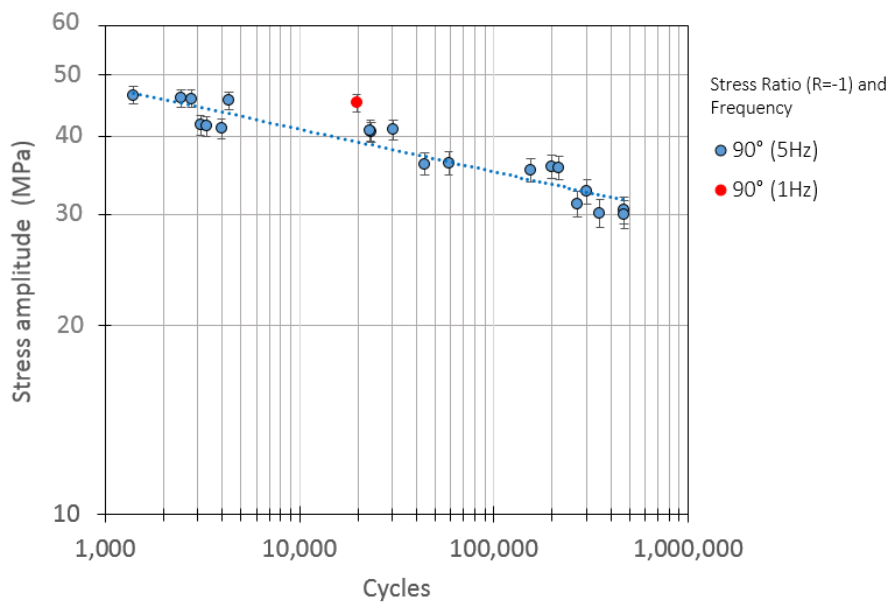


Figure 5-23 Effect of the frequency on the fatigue life of PA66GF50.

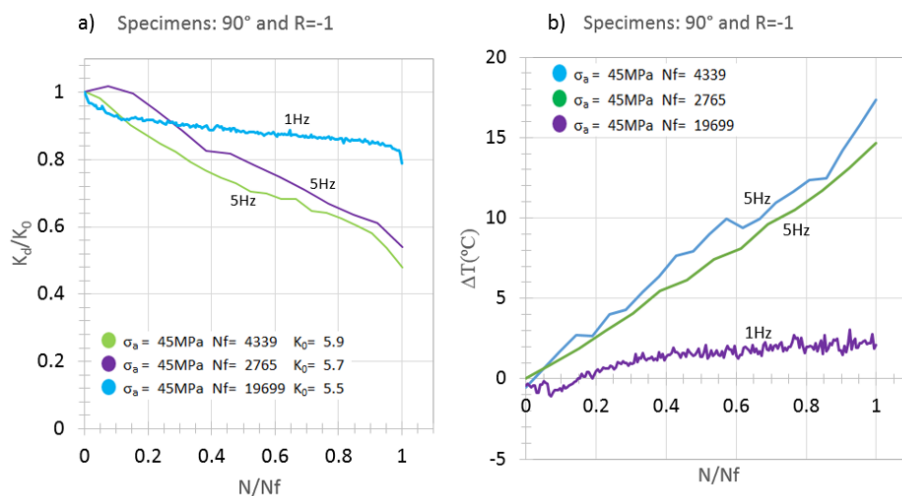


Figure 5-24 Evolution of a) Stiffness and b) Temperature with frequency.

5.3.2 Block loading

Block loading testing was conducted in order to investigate the material fatigue behaviour under different stress amplitudes and load sequences. The details of the number of cycles per block can be seen in Table 3-3 in Chapter 3 of this thesis. A table with a summary of the load conditions and the results of the block loading testing can be seen in Table 5-3. Miner's rule (Equation 4-10) was used for damage accumulation. An estimation of specimen failure was considered when $D=1$. The estimated total life, in blocks, to reach failure for each case is also presented in the same table.

Figure 5-25 shows the average number of blocks to failure for the different orientations and load sequences. The theoretical number of blocks to reach $D=1$ is marked in red. In the same manner, Figure 5-26 shows the comparison between the estimated fatigue life, for $D=1$, and the actual number of blocks reached. From both figures, it can be observed that 0° specimens showed experimental lives below the expected ones, with failure occurring in average between 60% to 79% of the total expected damage. A seemingly out-layer data point was also seen on this orientation under L-H sequence (Figure 5-26). For the case of 90° specimens, both load sequences showed good agreement with the estimated number of blocks, in average. However, two seemingly out-layer points were also seen on this orientation (Figure 5-26). Finally, 45° specimens tested under H-L sequence showed an approximate 37% higher lives, in average.

Table 5-3 Block loading testing results.

R ratio	Orientation	Load sequence (MPa)		Estimated Miner's rule damage per block	Estimated total life for D=1 (no. of Blocks)	Repeat	Experimental life (no. of Blocks)
-1	0°	H->L	45-40-37.5	0.0033	300	Repeat 1	97
						Repeat 2	147
						Repeat 3	163
						Repeat 4	274
						Repeat 5	229
		L->H	37.5-40-45	0.0033	300	Repeat 1	133
						Repeat 2	165
						Repeat 3	181
						Repeat 4	290
						Repeat 5	428
	90°	H->L	40-35-30	0.0045	222	Repeat 1	128
						Repeat 2	189
						Repeat 3	105
						Repeat 4	253
						Repeat 5	454
		L->H	30-35-40	0.0045	222	Repeat 1	241
						Repeat 2	206
						Repeat 3	196
						Repeat 4	140
						Repeat 5	352
45°	H->L	40-35-30	0.0052	192	Repeat 1	314	
					Repeat 2	177	
					Repeat 3	303	
	L->H	30-35-40	0.0052	192	Repeat 1	244	
					Repeat 2	100	
					Repeat 3	230	

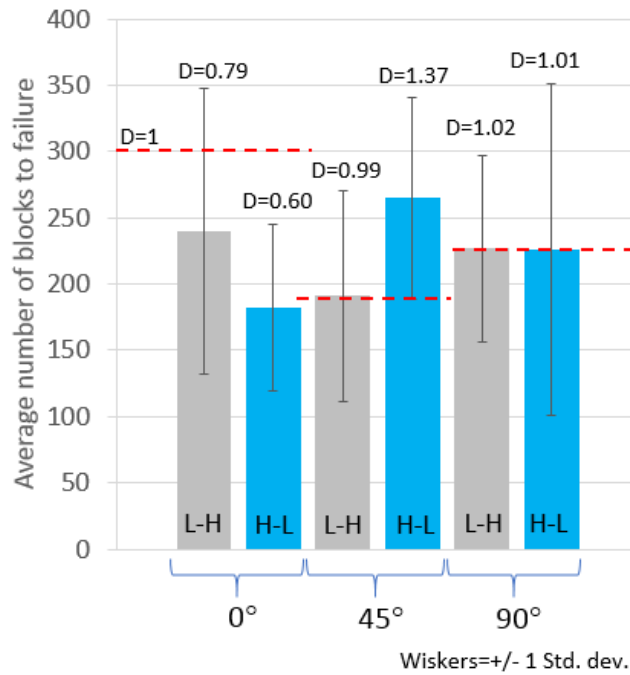


Figure 5-25 Average number of BL blocks to failure for each specimen orientation and load sequence.

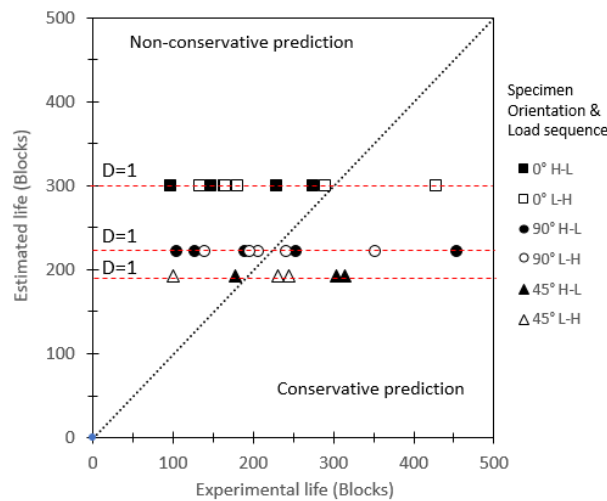


Figure 5-26 Estimated number of blocks to failure (D=1) VS Experimental number of blocks to failure for different specimens orientations and load sequences.

5.3.2.1 Block loading hysteresis loops

The hysteresis loops of the specimens subjected to block loading conditions were also recorded. Figure 5-27 show the evolution for 0°, 45° and 90° specimens under High-to-Low sequence. Whereas, Figure 5-28 shows the evolution for Low-to-High sequence. For both cases, a stabilization of the hysteresis loops and of the strain can

be seen, covering most of the life of the specimens. This is similar to the behaviour observed on constant amplitude specimens (Figure 5-19 and Figure 5-20).

A clear larger hysteresis area was also seen at higher loads, which would indicate a correlation of the amount of energy dissipation with the load level. This was seen to be independent of the stress sequence.

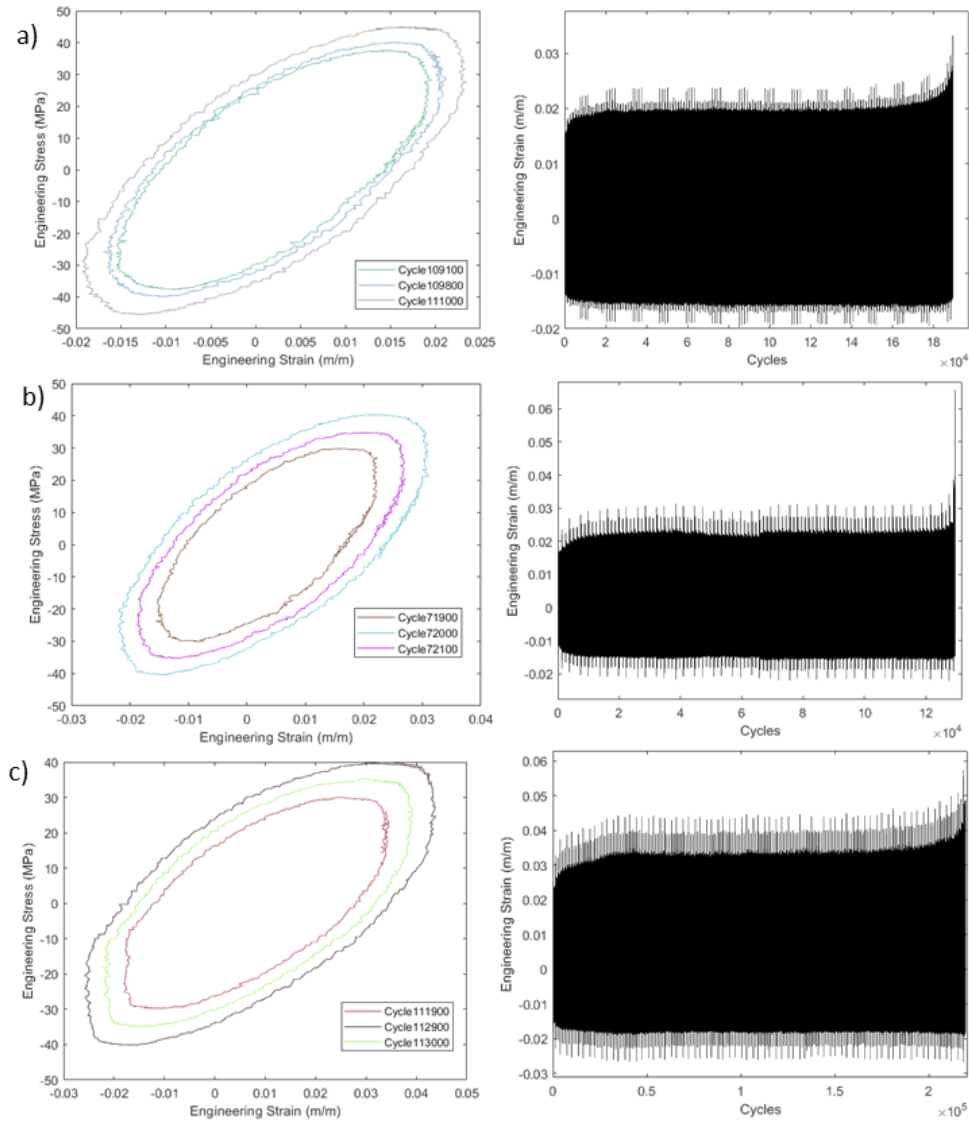


Figure 5-27 Stabilised hysteresis loops (Stress vs Strain), and evolution of strain (Strain vs Cycle) curves for a) 0°, b)90° and c)45° specimens under Block loading High-Low sequence.

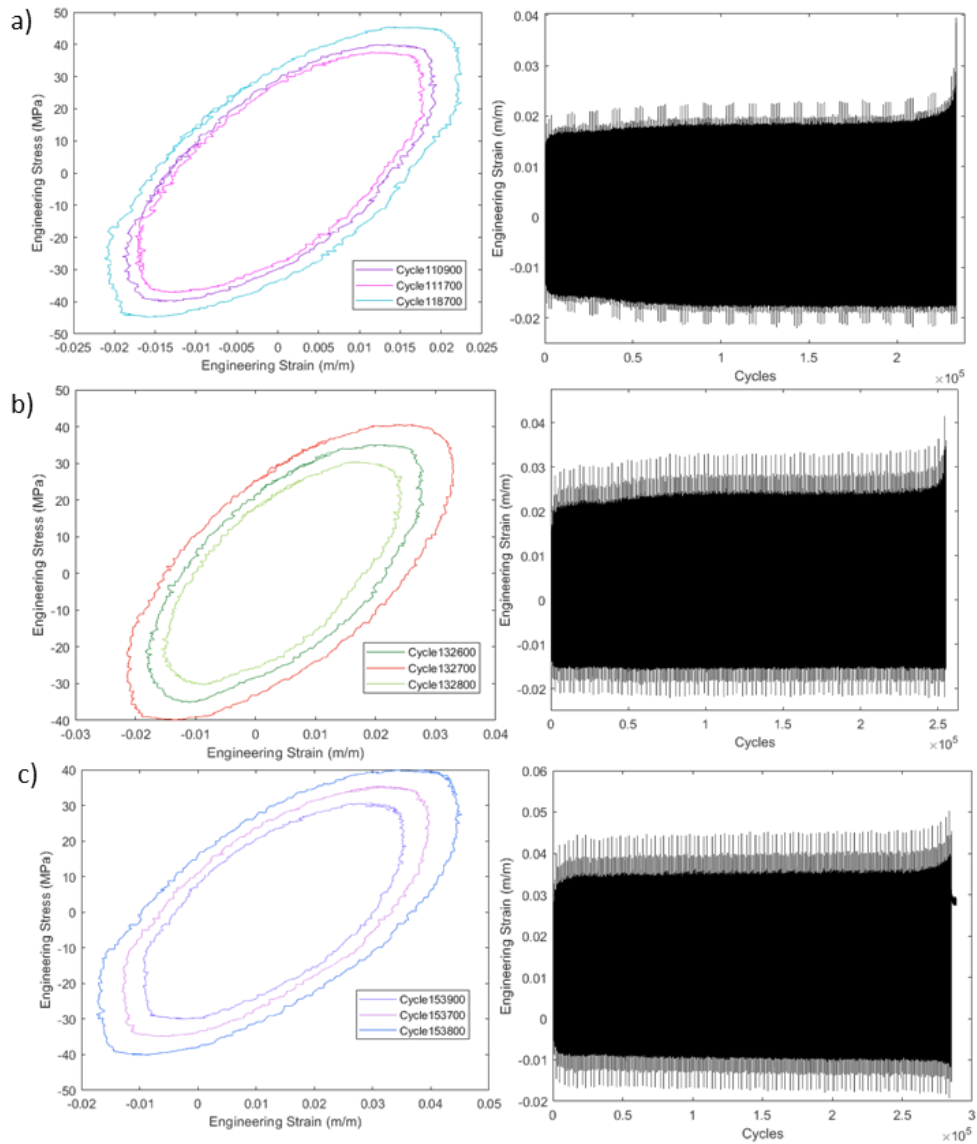


Figure 5-28 Stabilised hysteresis loops (Stress vs Strain), and evolution of strain (Strain vs Cycle) curves for a) 0°, b)90° and c)45° specimens under Block loading Low-High sequence.

5.4 Full-field strain measurements

5.4.1 Tensile strain fields (DIC)

Digital image correlation, as explained in Chapter 3.7.1, was used to analyse the evolution of the strain-field on the specimens' surfaces. It was also used to detect strain localization that could indicate the mechanisms for crack initiation. Due to the material anisotropic behaviour, two different surfaces were studied: The *main surface*, or as-moulded, which is the face in contact with the mould; and the *thickness surface*, or as-machined, which is the thickness of the specimen. Figure 5-29 shows a schematic

of both faces. A virtual extensometer was used inside the correlation software to obtain the longitudinal strain by following the deformation/elongation of the specimen. The engineering strain was then calculated by dividing the change in length by the initial length between two reference points from the extensometer. The engineering stress was calculated by dividing the applied force by the measured specimen's cross section.

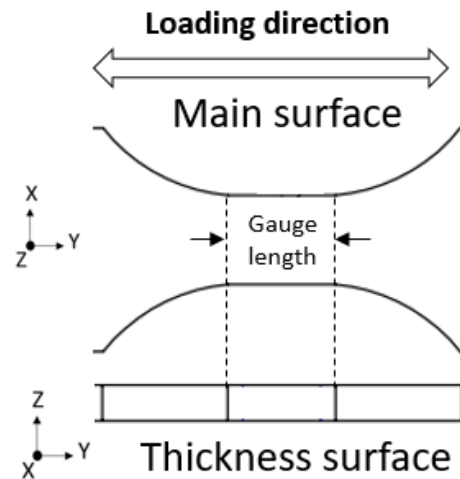


Figure 5-29 Definition of the specimen's surfaces.

Figure 5-30a-b and Figure 5-31a-b show the strain fields on the “Main surface” for, respectively, a 0° and a 90° reference specimen loaded at two different stress levels. It can be seen that at intermediate loads, and seemingly within the linear part of the curves, the strain field on the material is highly homogeneous through the specimens' gauge areas, on both orientations. At relative high stresses, and after onset of strain hardening, a change in the strain field is observed, with larger values concentrated on the gauge area, mainly located through the middle and on the side of the specimens. These results suggest that there is an effect of the fibre orientation distribution of these faces, formed by the skin layer, on the overall strain localization.

On the other hand, Figure 5-32a-c shows the strain distributions on the thickness surface for 0° , 45° and 90° samples loaded at the same stress level. On these surfaces, strain localizations can be immediately observed. For the case of the 0° specimen, Figure 5-32a, the localization is seen close to the end of the gauge length and in areas that correspond to the shell layers through the thickness, these regions are where the fibres are more aligned with the load direction. On the 90° sample, Figure 5-32b, higher strain is also seen at the end of the gauge area, but in this specimen, the localization is also observed at the centre of the specimen. This region corresponds to the core layer, and for this particular orientation, where the fibres are more aligned

with the load direction. Finally, Figure 5-32c, shows the strain field on the thickness surface for a 45° sample. Again, higher strain levels are seen at the end of the gauge area; but for this case localization of the strain is also observed at the centre of the specimen at a clear angle of 45° degrees. The comparison of the strain results for both surfaces, main and thickness, suggests that the localization of strain happens faster in the thickness than in the main surface.

These measurements, on the *main surface* and on the *thickness surface*, suggest that there is a clear change of the strain distribution as we progress inside the material. A change in the strains also implies a change in the stresses. Unfortunately, DIC is a surface level technique and is not possible to observe the internal distributions, or the change of it. Nevertheless, an assumption was made by comparing these measurements to the results of the numerical simulations. Comparable values between the DIC fields and the FEA results were found, and are presented in Chapter 7.3. Therefore, it was sensible to assume that the internal distributions in terms of stress and strains, from the FEA model, could be said to be representative of the actual distributions inside the coupons. The numerical results for the internal strain and stress fields are shown and discussed later on this thesis in Chapter 6.3.1.

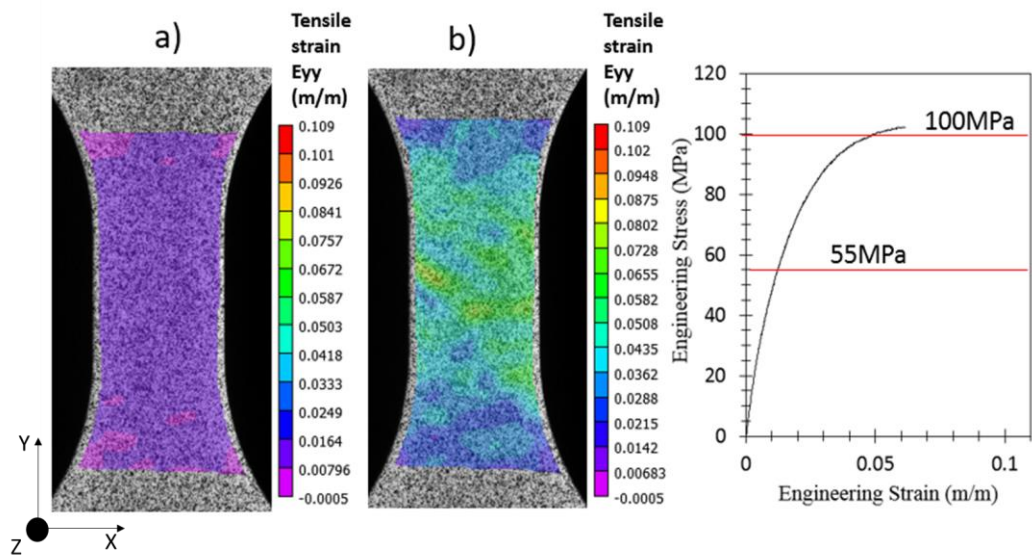


Figure 5-30 Strain distribution on the main surface for a 0° specimen loaded in tension at a) 55MPa, and b) 100MPa with $V_f=30\%$.

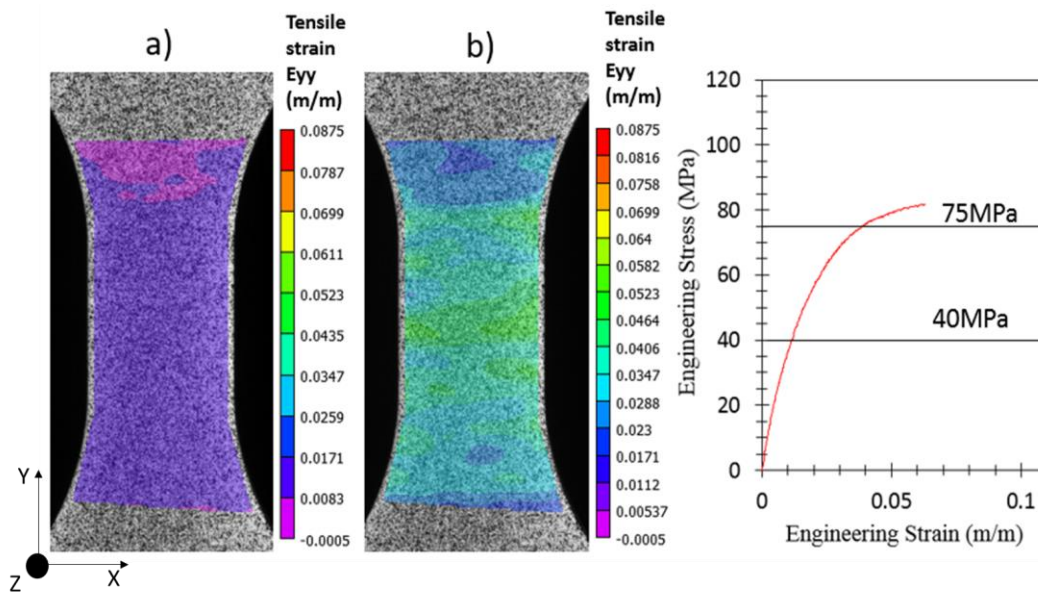


Figure 5-31 Strain distribution on the main surface for a 90° specimen loaded in tension at a) 40MPa, and b) 75MPa with $V_f=30\%$.

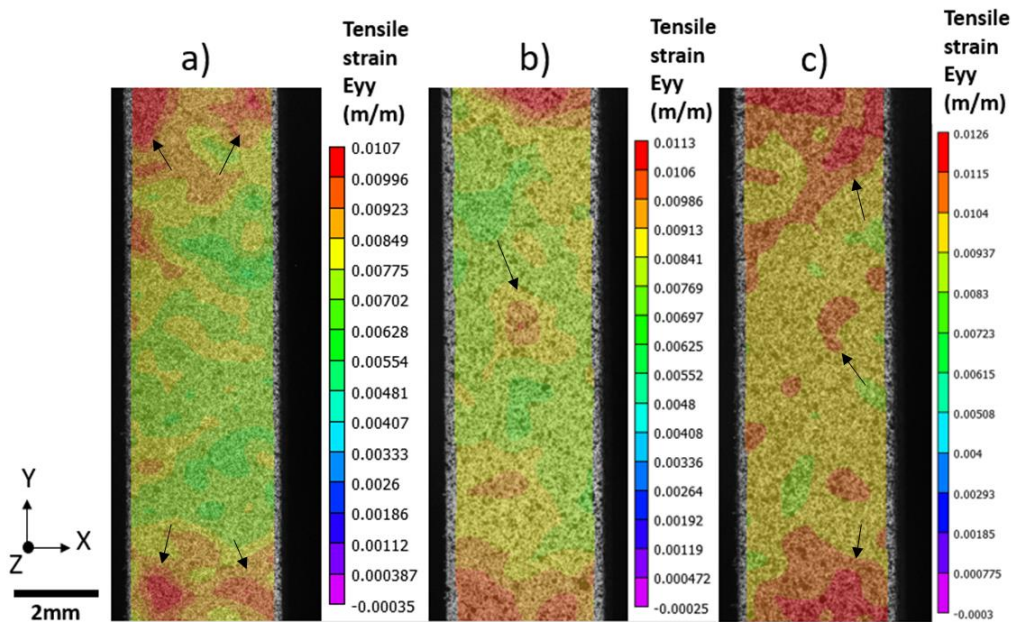


Figure 5-32 Strain distribution on the thickness surface for a a) 0°, b) 90° and c) 45° specimen loaded in tension at 40MPa.

DIC analysis was also done on the main surface of the specimens at higher stress levels, to the point of measuring the strain localization. On this face, defects/cracks were detected to start either at the middle of the sample, or near the edge of the specimens.

Figure 5-33 shows the strain distribution of a 0° specimen prior to failure. A macro crack of ~4.18 mm can be seen in the middle of the specimen, most of the strain is

localized around this flaw. The failure plane of this specimen was at an angle, forming a V shape, and it seems to have started at the macro crack location.

Figure 5-34 shows the strain distribution of a 0° specimen, and the evolution of macro crack; from the onset to failure of the sample. A clear localisation of strain can be seen at areas located close to the sides of the coupon, and in the middle of the width. Additionally, the evolution of the macro crack followed an exponential growth, taking an estimated 800ms from the onset to the final failure.

Figure 5-35 presents the strain distribution, prior to failure, of two 90° specimens. Strain localisation can be observed in areas close the specimens' side edges and in the middle of the width, especially for Specimen A. A macro crack of ~2.82mm was also observed in Specimen B, which was located close to the side of the specimen.

Figure 5-36 shows the strain distribution, prior to failure, of two 45° specimens. For this orientation, the localization of strain occurred at an angle of ~45° and covered from one side of the sample to the other. This was also observed in the case of the 30° samples, Figure 5-37. The strain distribution on these specimens also occurred at an angle, and macro cracks were seen to have started at the specimens' edges, specimens A and C.

Figure 5-38 presents the strain distribution and crack evolution corresponding to a 0° Edge specimen. Similar to Figure 5-34, the crack showed an exponential growth, taking ~2.38 seconds from onset to failure of the specimen. The final length of the crack, before complete failure, was ~2.5 mm. For this specimen, the crack also started at the specimen's edge.

Figure 5-39 shows the strain distributions prior to failure, for three different 90° Edge specimens. For this orientation the strain localization happened at the edges of the samples, and on the middle section.

From the inspection of the presented results, for the different specimen orientations, it can be said that:

- 1) The DIC distributions on all specimen orientations showed a clear path along which the crack would propagate and lead to final failure of the sample. This high strain path was seemingly dependent of the orientation of the coupon, with 0° and 90° (reference and edge coupons) showing strain localization, and macro cracks, that were for the most part normal to the load direction; as seen in Figure 5-34, Figure 5-35 and Figure 5-39. Whereas, on mid axis specimens,

30° and 45°, the path of strain localization, and crack propagation, occurred at an angle, as shown in Figure 5-36 and Figure 5-37.

- 2) For 0° and 0° Edge it took more time for the final failure to occur after the onset of a macro crack. 0° Edge being the one where the crack took the longest to propagate, 2.38s. This could be due to the more consistent alignment of fibres toward the load direction in this coupon orientation, as it can be seen in the fibre orientation tensor distribution plot in Figure 7-2, which suggest that this fibre orientation might not be ideal for crack growth.
- 3) Finally, strain localization seem to be concentrated in particular in the centre of the specimens and in the regions close to the shoulder of the samples. This being the case for all specimen orientations.

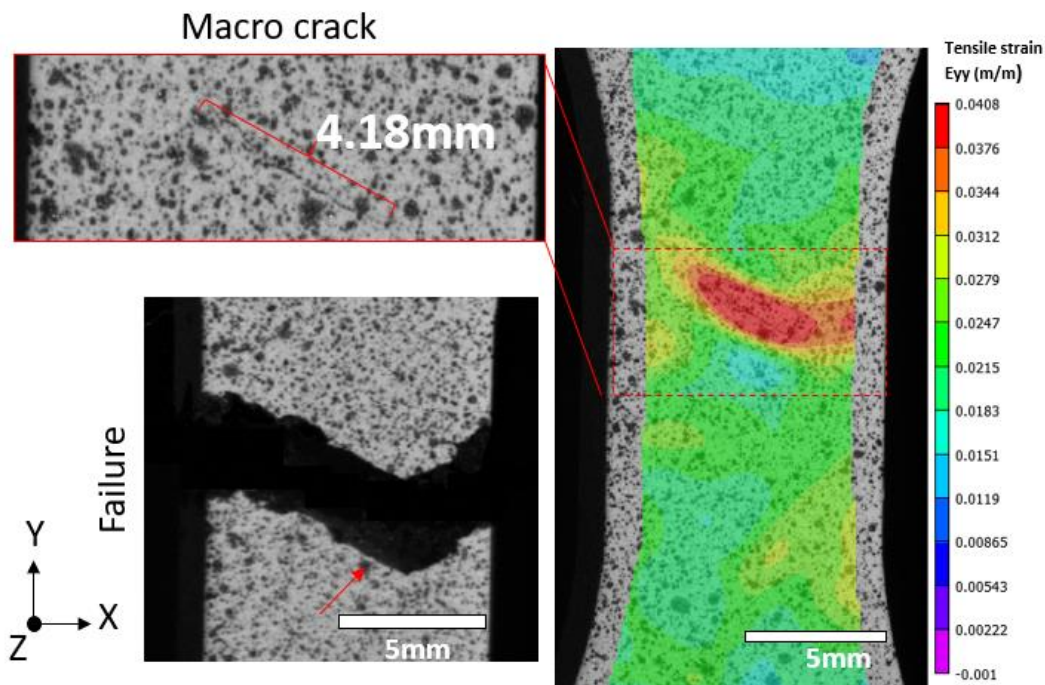


Figure 5-33 Main surface for 0° specimen tested in tension showing the strain distribution and a macro crack of 4.18mm in the centre prior to failure , and the failure plane.

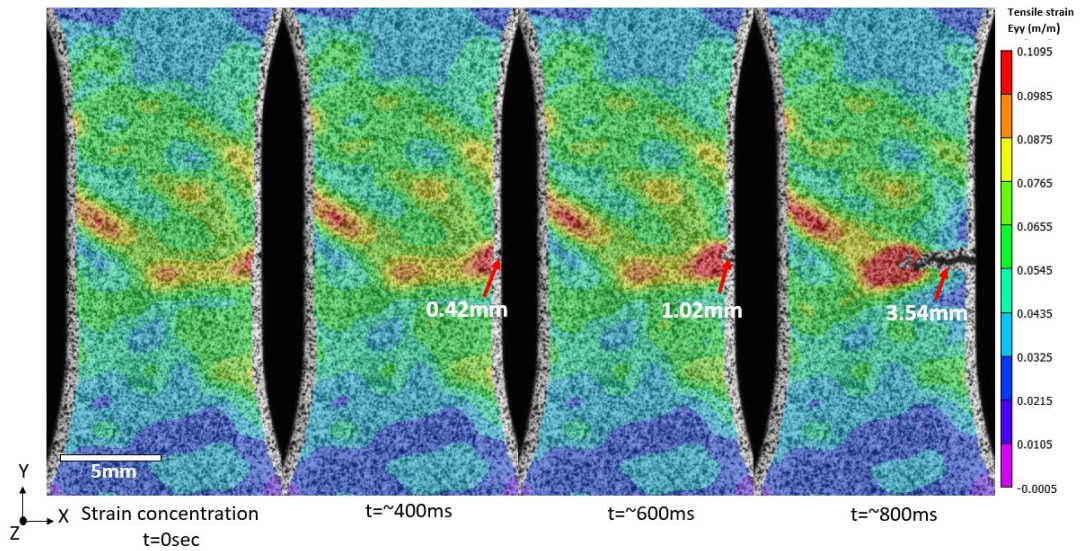


Figure 5-34 Main surface for 0° specimen tested in tension showing the strain localization, and the exponential evolution of a macro crack from onset to failure.

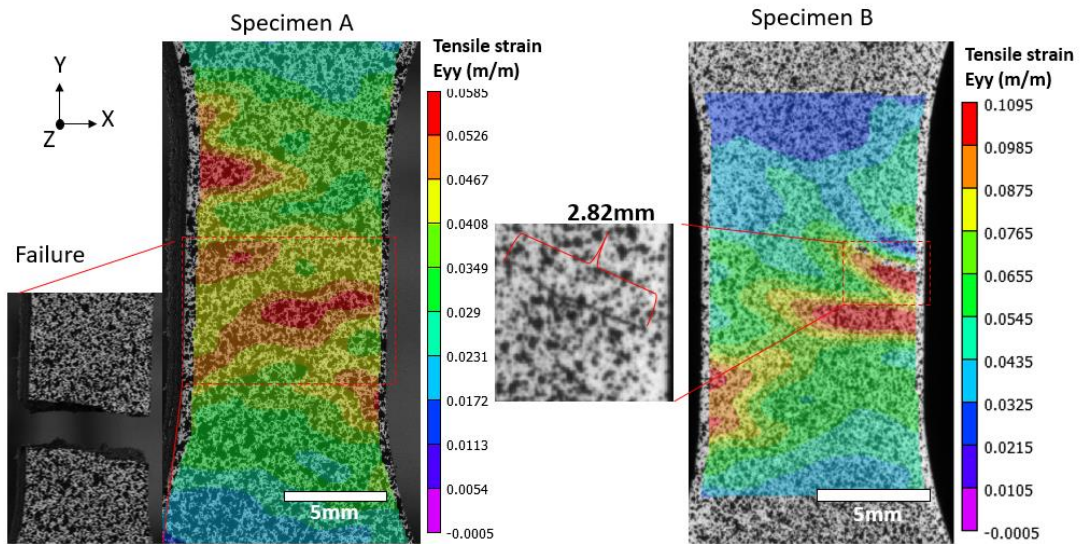


Figure 5-35 Main surface for 90° specimens tested in tension showing the strain distribution prior to failure. Specimen B showing a 2.82mm macro crack close to the edge.

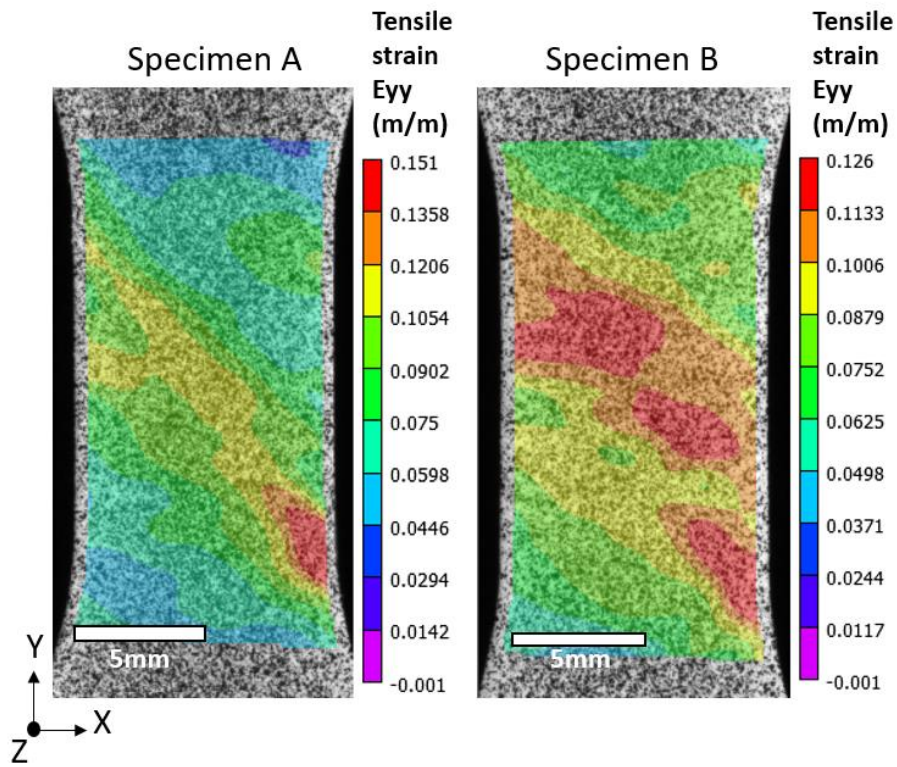


Figure 5-36 Main surface for 45° specimens tested in tension showing the strain distribution prior to failure.

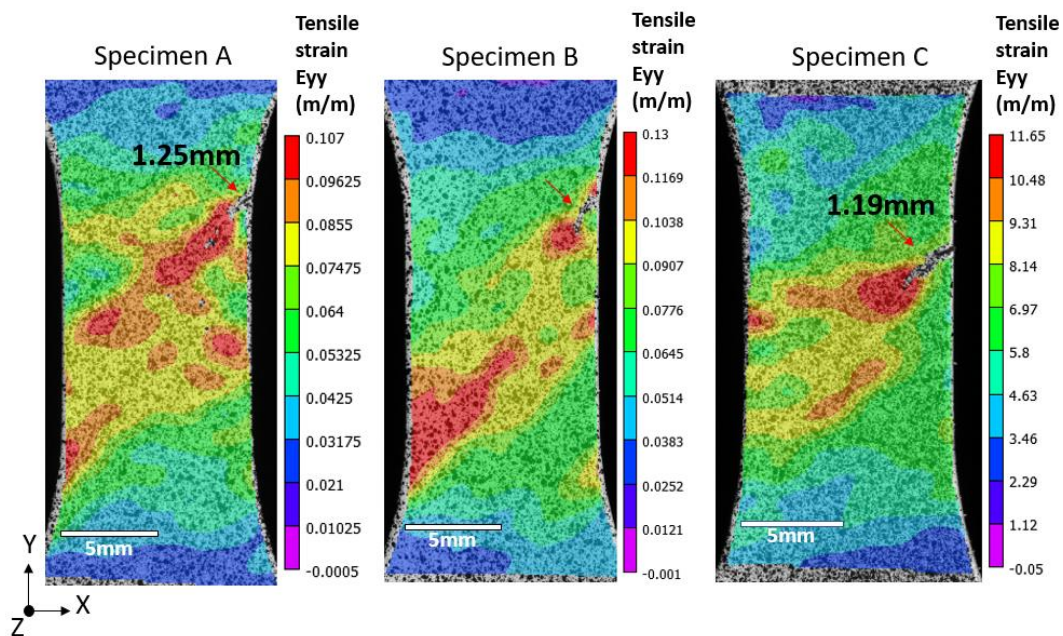


Figure 5-37 Main surface for 30° specimens tested in tension showing the strain distribution and macro cracks prior to failure.

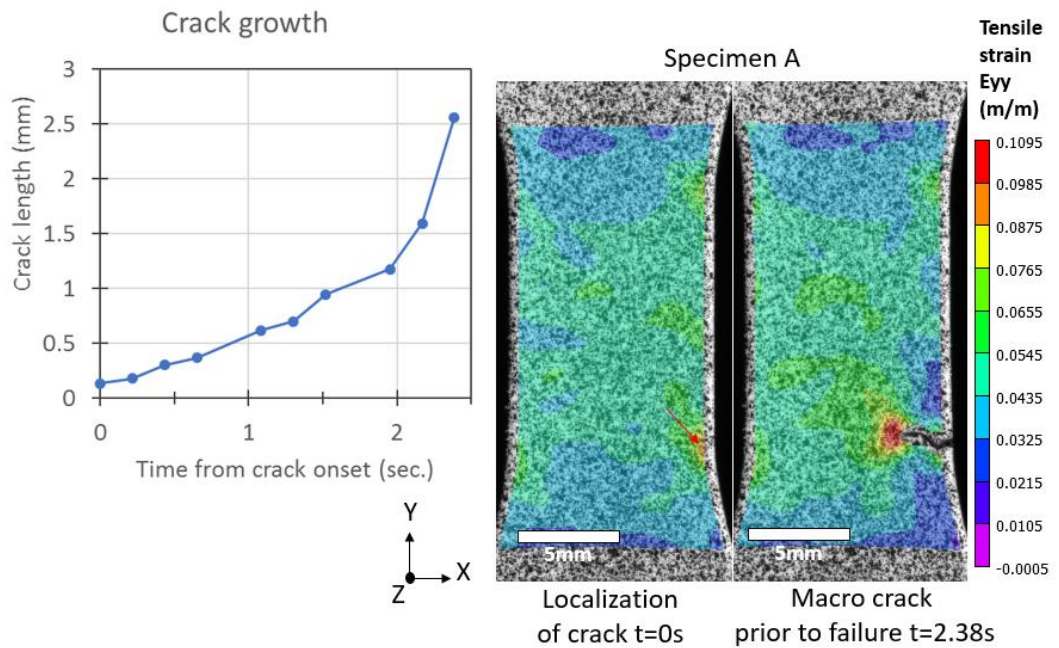


Figure 5-38 Main surface for 0° Edge specimen tested in tension showing the strain distribution and macro crack growth evolution.

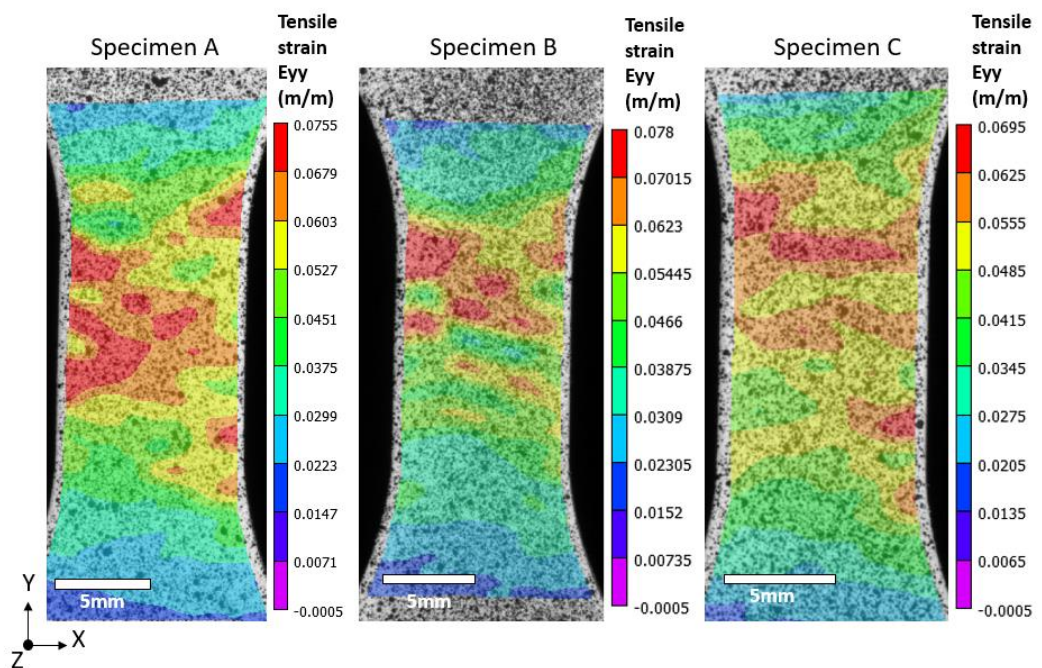


Figure 5-39 Main surface for 90° Edge specimen tested in tension showing the strain distribution prior to failure.

5.4.2 Fatigue strain fields (high speed DIC)

High speed DIC measurements were taken on specimens tested under cyclic conditions. Similar to the behaviour seen on the monotonic specimens, the strain distribution in the gauge area of the coupons seemed to be homogeneous. An

example of this is shown in Figure 5-40 for a 0° specimen tested at a stress amplitude of +/- 33MPa and at R=-1. However, for this case a clear strain accumulation occurred. This was observed by measuring two particular points, P0 and P1, located close to the final fracture plane of the coupon. Measurements were taken at different stages in the life of the specimen. An increase of 15% and 9% strain was seen for P0 and P1, respectively, between Cycle 1 and Cycle 45,000.

Similarly, HS-DIC measurements were taken on the thickness surface of a 0° specimen tested at a stress amplitude of 35MPa and at R=0. The first complete 26 cycles were measured and are presented in Figure 5-41. It took approximate 10 cycles for the strain to stabilise, and before this point, no particular localization of strain was observed. After cycle 10, the strain levels were, for the most part, constant. However, regions of high strain were seen. These point were located at the corners of the gauge area, with an approximate 40% higher strain than in the middle of the thickness. This was similar to the measurements taken on the 0° monotonic sample, Figure 5-32. In the same manner, the particular locations of high strain were seen in regions close to the shell layers, areas where the fibres are more aligned with the load direction. This measurements suggest that, for the case of the thickness surface, the localization strains is present from the early stages of the test. A different 0° specimen was also analysed, using HS-DIC, under the same testing conditions. This time the measurements were taken throughout the life of the specimen, and the results are shown in Figure 5-42a-d. Figure 5-42a shows the failure of the specimen, from where it can be observed that two cracks started near the sides of the *thickness surface* and progressed towards the centre of the specimen. These two macro cracks were observed to have started at the points of strain localization, P0 and P1, taking approximate 104 milliseconds from when they were initially observe to propagation. A visible ligament of composite is seen between the two macro-cracks prior to complete failure of the specimen. Similarly to the previous case, a clear strain localization can be seen early in the life of the sample, cycle 50, in particular at the corners of the gauge area, near the end of the shoulder, as shown in Figure 5-42b. An exponential growth, in terms of strain accumulation was seen throughout the life of the specimen, as presented in Figure 5-42c. Both locations saw an increase of approximate 2.5 times the initial strain value by the time final failure occurred. Additionally, the specimen also showed evidence of accumulation of plastic strain during the fatigue testing, i.e. ratcheting, which is typically seen in positive stress ratio testing, as presented in Figure 5-42d. It also clear from this image that there is a drop in the stiffness, observed from the decrease of the slope of the curve at 35k cycles that

indicates a progressive damage development in the specimen. Finally, Figure 5-43 presents the time lapse of the evolution of the crack initiation and propagation on the specimen' thickness surface. Figure 5-43a and b, show the left crack, P0, appearing with some intact ligament below the surface. Figure 5-43c, shows the appearance of the right crack, P1, also below the surface of the specimen. For both cracks the location of initiation corresponded to the shell layers, where fibres are more aligned with the load direction. Figure 5-43d-e show the progressive growth of both cracks.

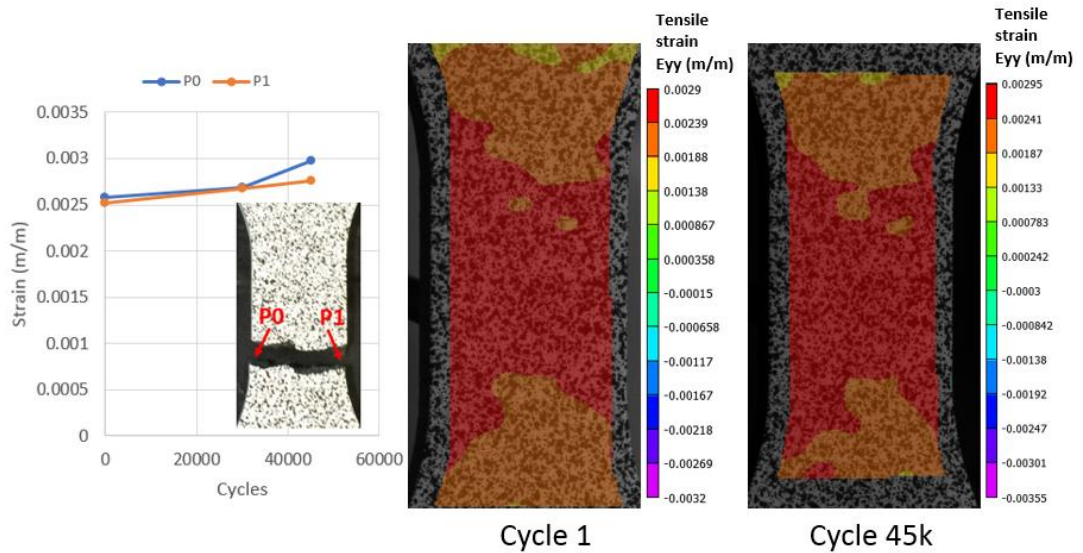


Figure 5-40 Main surface of 0° specimen tested at R=-1 and $\sigma_a=33\text{MPa}$.

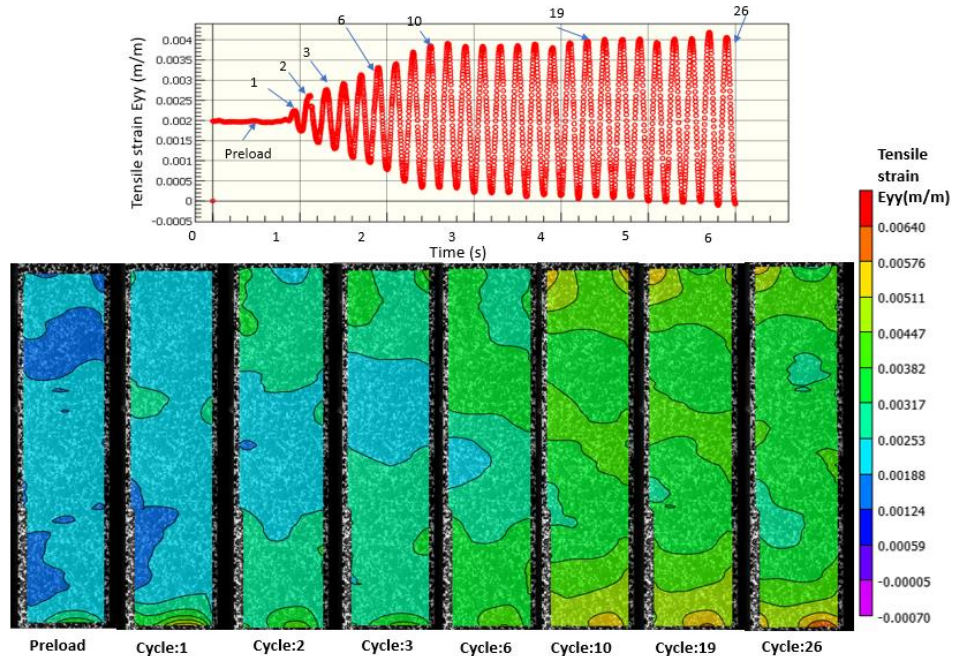


Figure 5-41 Thickness surface strain evolution at the beginning of a fatigue test for a 0° specimen at R=0 and $\sigma_a=35\text{MPa}$. Showing the gauge length area only.

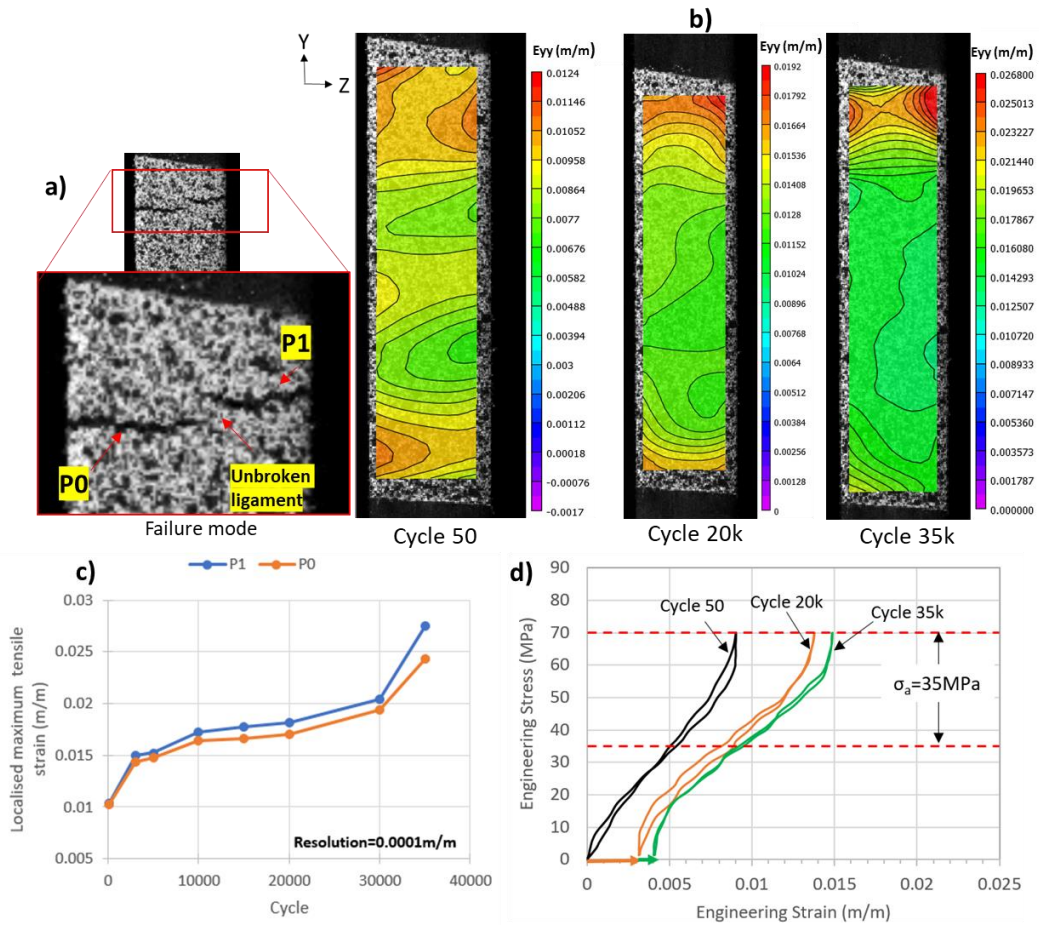


Figure 5-42 Thickness surface tensile e_{yy} strain evolution throughout the life of a 0° specimen at $R=0$ and $\sigma_a=35\text{MPa}$. a) Specimen failure. b) DIC Strain fields at different number of cycles. c) Evolution of the localised tensile strain. d) Eng. Stress vs Eng. Strain (virtual extensometer) curves at different number of cycles.

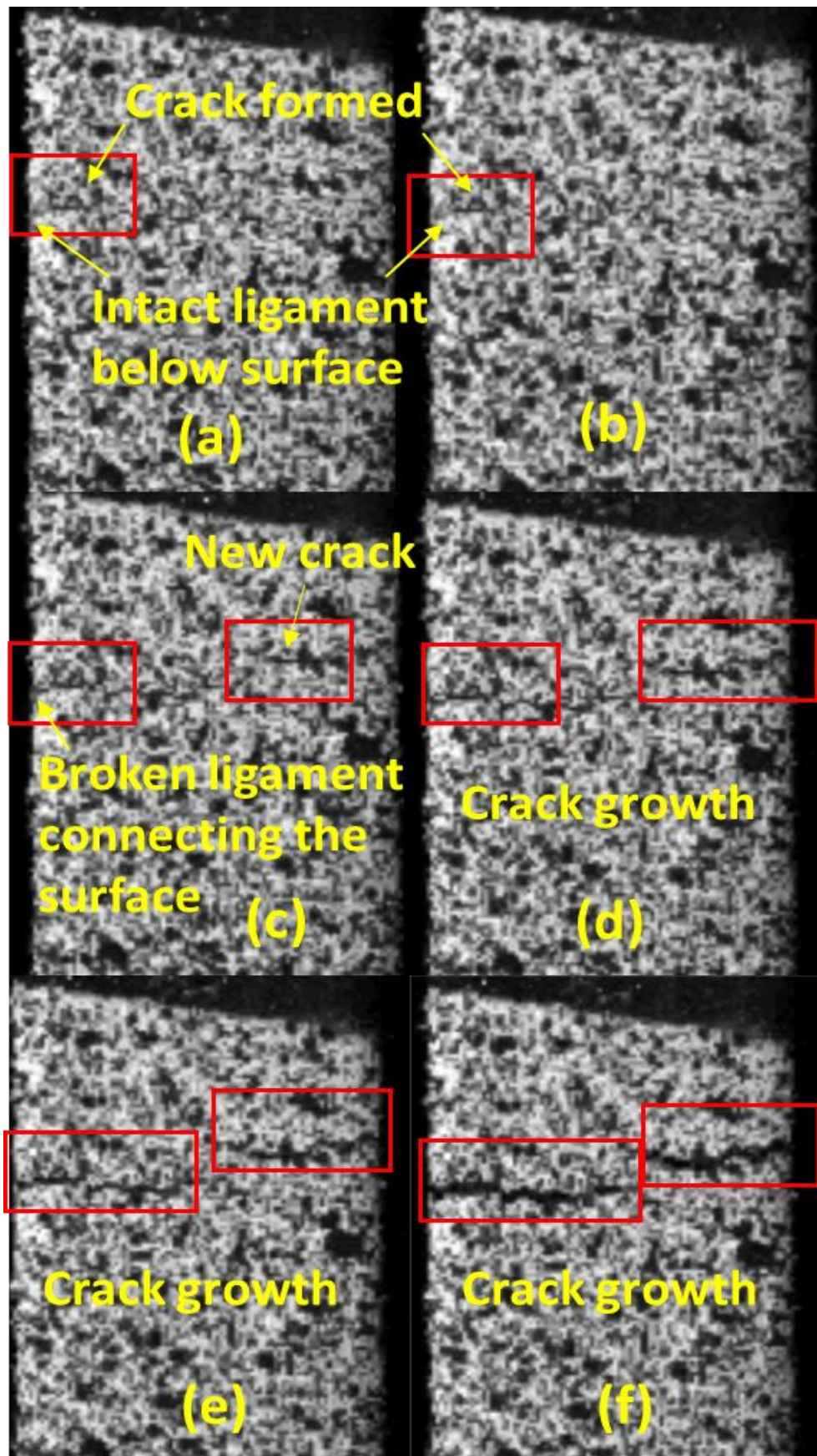


Figure 5-43 Evolution of fatigue crack through the thickness. a) to f) show a sequential time lapse capture via High speed cameras.

5.5 Material damage and failure

5.5.1 Optical inspection of failed specimens

5.5.1.1 Uniaxial tensile specimens

Tensile specimens were observed under the optical microscope to study the different failure mechanisms. Figure 5-44 shows the failure surfaces for 0°, 45° and 90° specimens. A clear distinction of the different fibre layers, shell and core in particular, can be seen for 0° and 90° specimens. On the other hand, the distribution of the fibres on the 45° coupon is more randomly orientated, with no clear distinction between the layers. For the case of 0° and 45° coupons, Figure 5-44a and c, the failure plane was at an angle, showing presence of debris. On the other hand, for the 90° specimen, a flat and clean fracture plane was seen. The presence of a second macro crack starting from the edge and growing below the failure plane was also observed on this specimen.

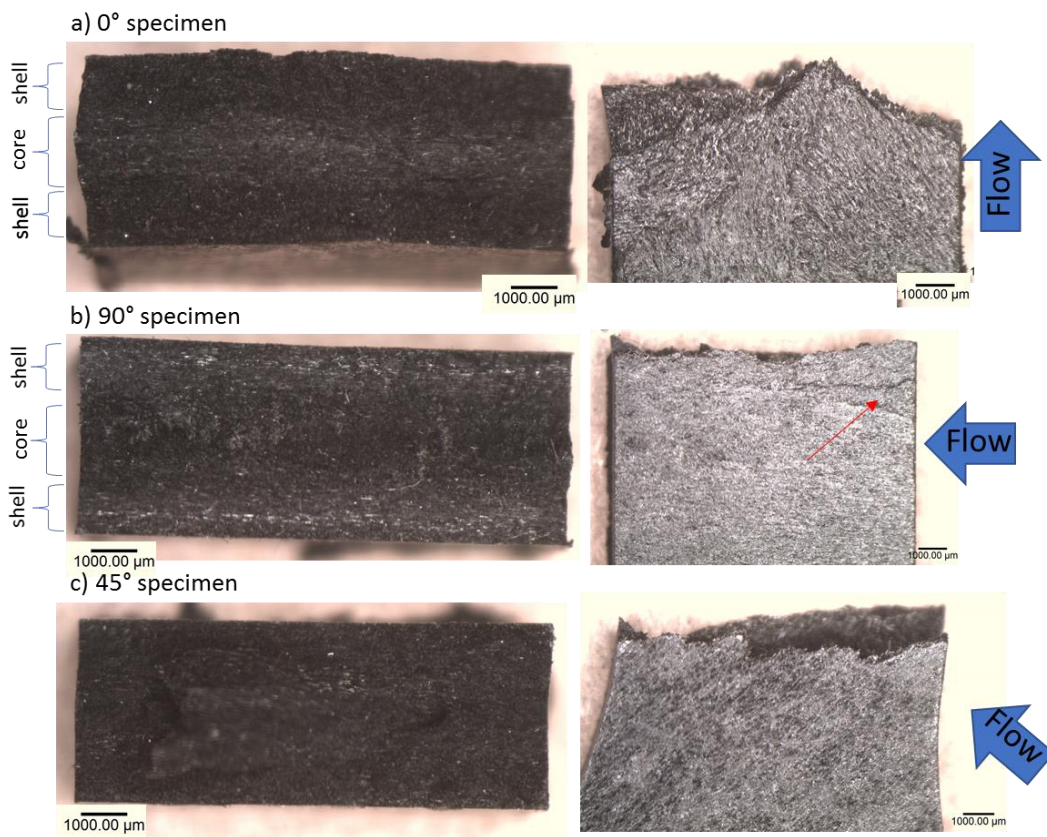


Figure 5-44 Optical view of the fracture surface for tensile tested specimens at a) 0°, b) 90° and c) 45° orientations.

The fracture plane for different specimens tested under monotonic conditions are shown in Figure 5-45. On 0°, 90°, 0° Edge and 90° Edge specimens, the failure seemed to occur, for the most part, normal to the tensile load. A 0° specimen showed a “V” failure plane. However, this corresponded to the presence of a macro crack detected prior to the failure of the sample, as shown in Figure 5-33. 90° specimens showed a cleaner failure surface. On the other hand, 0° Edge specimens showed more debris around the failure surface. Finally, for the case of 30° and 45° specimens, the failure plane occurred at an angled of approximate 45°.

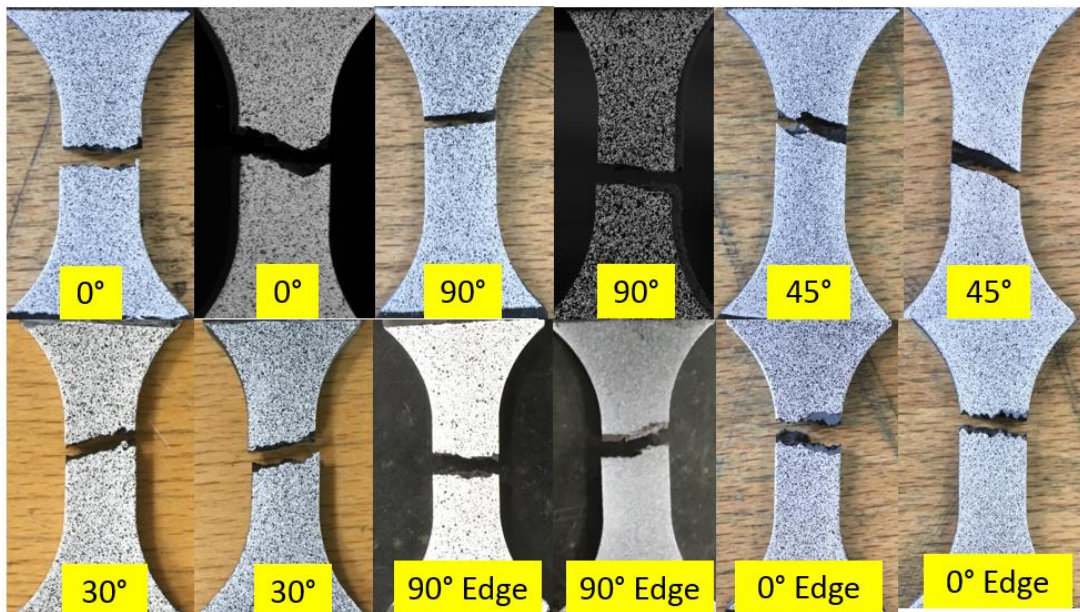


Figure 5-45 Visual inspection of failure plane for tensile specimens.

5.5.1.2 Uniaxial fatigued specimens

The following section presents the failure plane for fatigued specimens at different stress ratios. Only a couple of samples are shown for each orientation, but the rest of the specimens are accessible in the Appendix B.2.

Figure 5-46 shows the failure plane for the different orientations under $R=-1$ conditions. Similar to the case of the monotonic specimens, 0° and 90° specimens showed, for the most part, failures normal to the axial load. On the other hand, 30° and 45° specimens failed at angle corresponding to the particular orientation. Similar failures are also observed on specimens tested under $R=0$, Figure 5-47. However, for the case of 90° samples, two additional macro cracks were seen below the failure plane. This was similar to the monotonic case shown in Figure 5-44b. Angled failure planes were also seen on 30° and 45° specimens at this stress ratio. Finally, Figure 5-48 presents the fatigued specimens under $R=0.3$ conditions for 0°, 45° and 90°

orientations. The failure plane at this stress ratio is similar to the previous ones, with 0° and 90° , being normal to the load; and 45° failure occurring at an angle. That similar failures occurred under different stress level seems to imply that the mechanisms of damage are due to the distribution of the fibres, caused by the specimen orientation, rather than the type of load applied. The distinctive "horizontal" or "flat" fracture plane seen on 0° and 90° specimens could also be related to the critical length (l_c) of the fibres in the composite. From Figure 3-1d, it can be seen that the l_c for this composite is approximate $665\mu\text{m}$, whereas the average fibre length is $215\mu\text{m}$. Based on this, an assumption can be made, that by having shorter fibres cracks might be able to propagate more easily through the matrix due to a lower probability of finding a fibre in its way than in the presence of a composite with longer fibres of critical length; as suggested in Figure 2-7, longer fibres tend to increase the crack path length, so propagation will take more time and the toughness of the material would improve in consequence.



Figure 5-46 Failure plane of fatigued specimens at $R=-1$.



Figure 5-47 Failure plane of fatigued specimens at R=0.

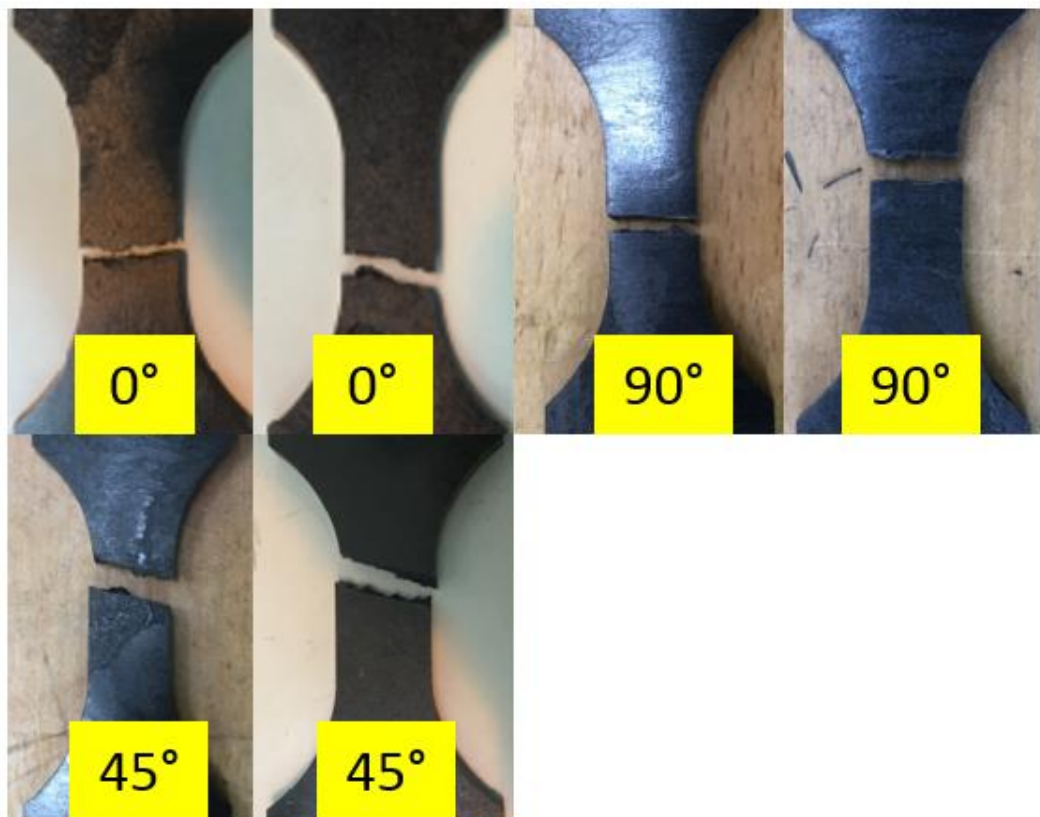


Figure 5-48 Failure plane of fatigued specimens at R=0.3.

5.5.2 Surface quality, as-moulded and as-machined

The surface quality of the specimens was analysed using scanning electron microscopy (SEM), on non-tested samples. This was conducted in order to assess the influence of the surface quality on crack initiation. A schematic of the inspected faces is shown in Figure 5-29.

5.5.2.1 As-moulded surface

Figure 5-49 shows the as-moulded, or main surface, of a pristine 90° specimen. The analysed region corresponds to the centre of the gauge length, showing the full width. A clear distinction between the fibres and the matrix can be seen in the surface. It is good to mention that this face was not machined, and is only product of the injection process and of interaction of the composite with the mould's walls.

Close ups of one side and of the centre of the specimen are shown in Figure 5-50 and Figure 5-51. Both figures show the presence of defects that are mainly located close to the reinforcement. These flaws are seen to be near the length and at the end of the fibres, and present a seemingly random distribution throughout the surface. Similar features were also seen on the surfaces of other specimens, as is shown in Figure 5-60.

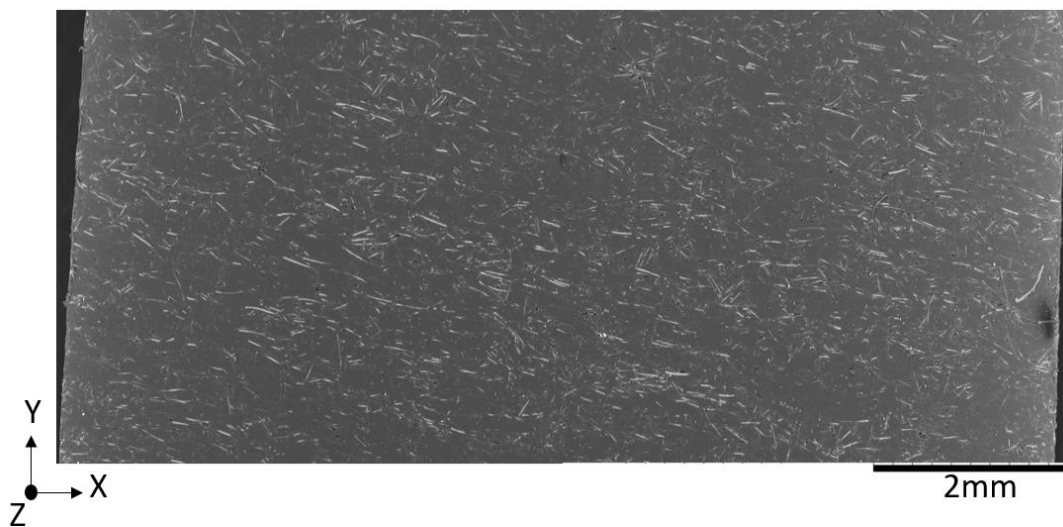


Figure 5-49 As-moulded surface, full specimen' width (10mm). Specimen not tested. $V_f=30\%$.

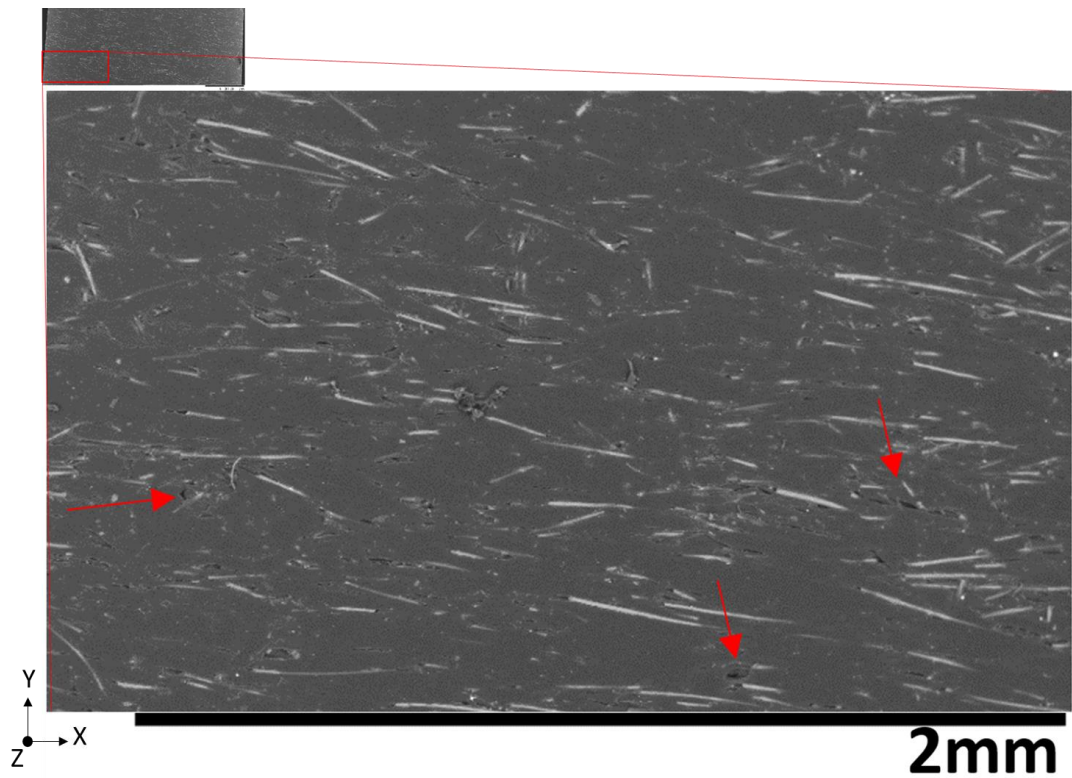


Figure 5-50 Close-up of the as-moulded, near the edge. $V_f=30\%$.

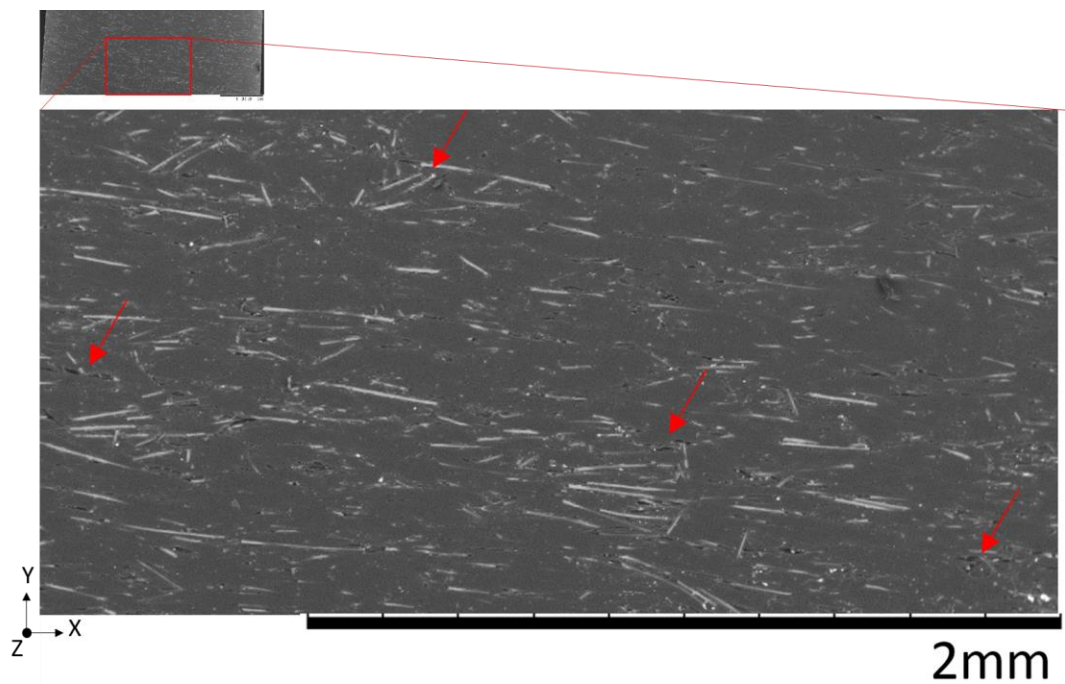


Figure 5-51 Close-up of the as-moulded, near the middle. $V_f=30\%$.

5.5.2.2 As-machined surface

Figure 5-52 shows the as-machine, or thickness surface, of a pristine 90° specimen. The analysed region corresponds to the centre of the gauge length, showing the full thickness. Similar to the previous surface, a clear distinction between the fibres and

the matrix can be observed on this face. For this particular surface, the different microstructure of the composite can be identified. On the outer regions, fibres aligned transversal to the flow represent the shell layer. In the inner section, fibres aligned along with the flow represent the core layer.

Close inspection of one side of the specimen and on the core layer are shown in Figure 5-53 and Figure 5-54. For both cases, evidence of debris in the surface can be observed, mostly nearby the reinforcement. Fibre ends and lengths seem to be regions where these flaws mostly localised.

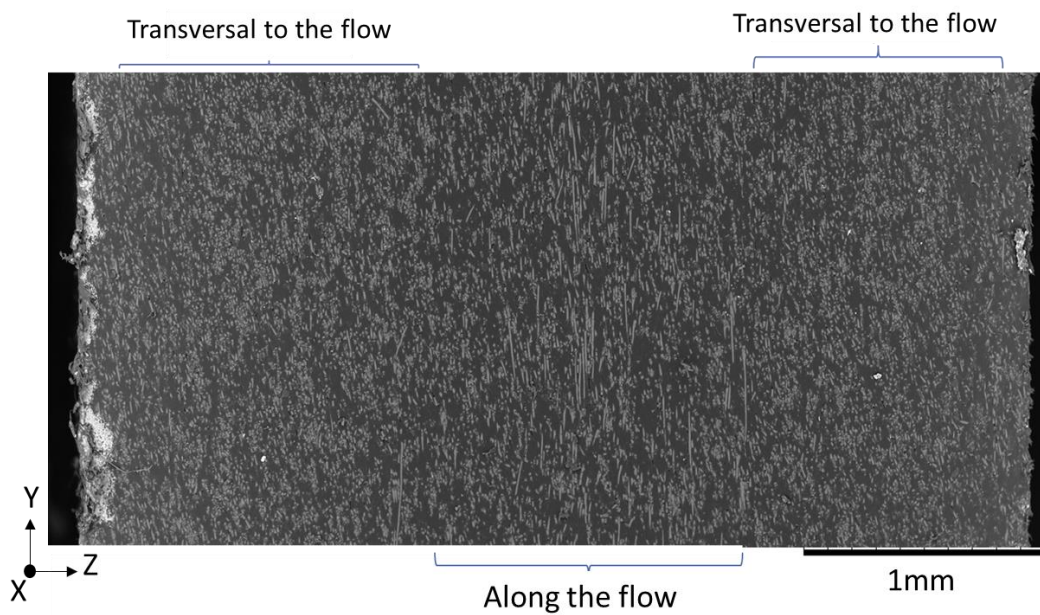


Figure 5-52 As-machined surface showing the different fibre orientation layers through the thickness. Specimen not tested. $V_f=30\%$.

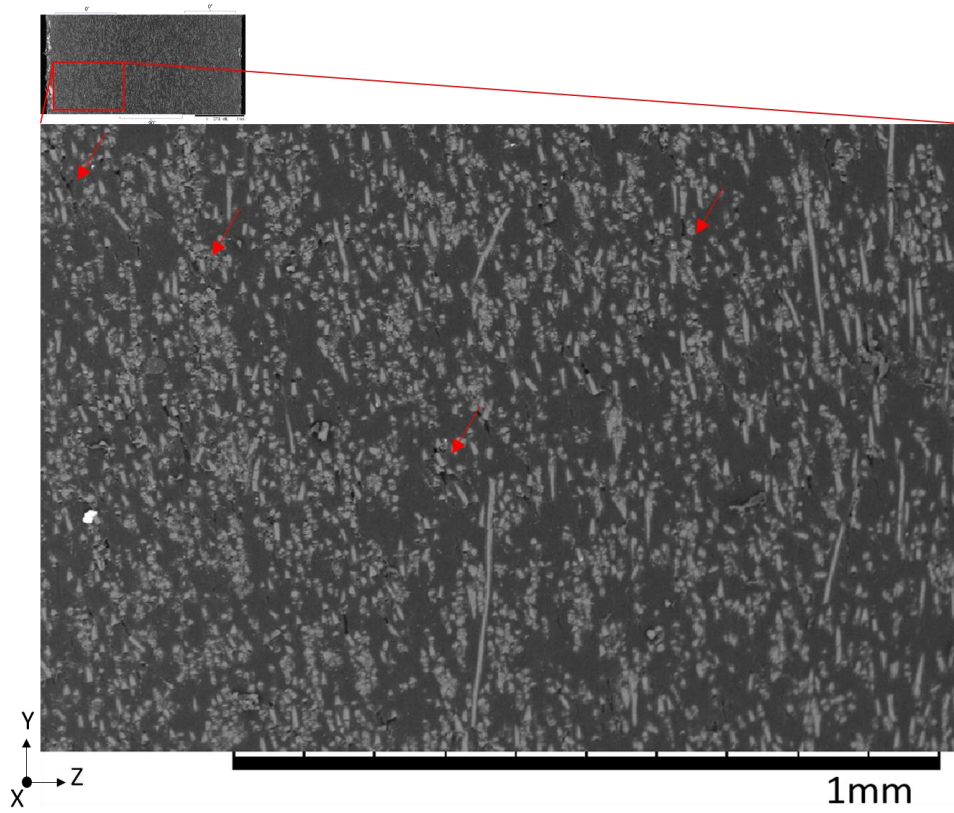


Figure 5-53 Close-up of the as-moulded, near the edge. $V_f=30\%$.

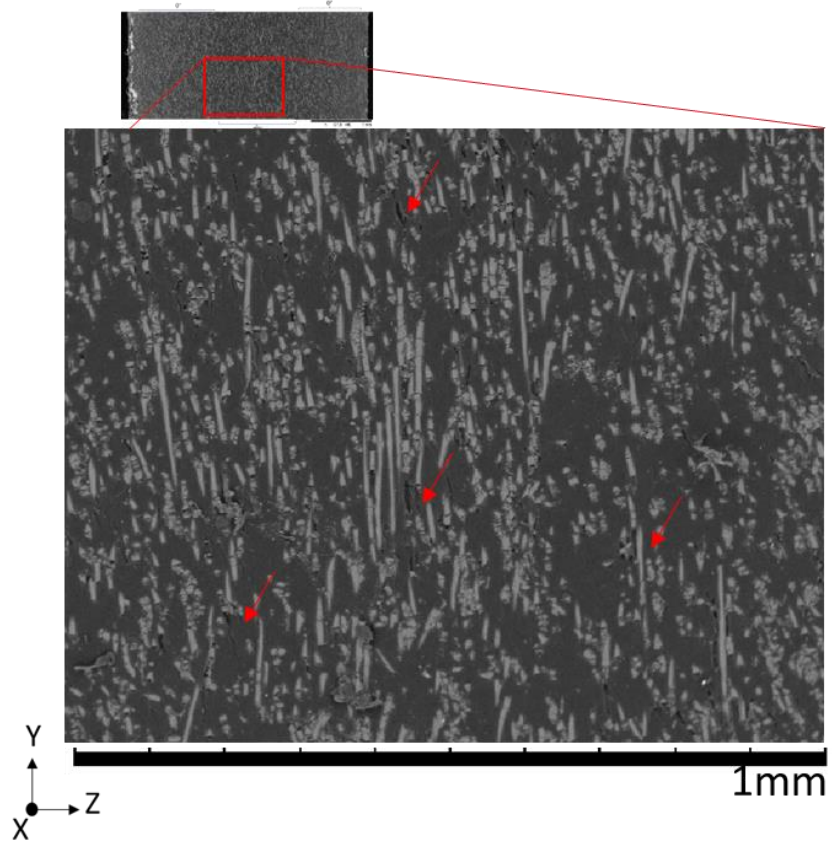


Figure 5-54 Close-up of the as-moulded, near the middle. $V_f=30\%$.

5.5.3 Tensile specimens, fracture surface

Specimens tested under monotonic conditions were analysed using SEM to gather information of the different failure mechanisms occurring inside the composite material, and at the different layers throughout the thickness.

5.5.3.1 Fracture surface of 0° reference specimens

Figure 5-55 and Figure 5-56 show the fracture surface of two 0° reference specimens tested in tensile. A distinction between the different regions in the microstructure can be seen, in specific the shell and core layers. In the outer regions, fibres appeared to be mostly aligned with the flow. On the other hand, a clear middle section with fibres aligned transversal to the flow is also present. A mostly plane fracture surface is seen on the core layer of both specimens, whereas a very messy surface is seen on the shell layers. On specimen 1, several fracture planes seem to occur denoted by "step" looking fractures on the core layer. Figure 5-55a shows a close up near the upper left corner on the shell layer of specimen 1. On this section fibres are mostly aligned with flow direction, out of plane. A very messy fracture surface can be seen, with clear evidence of large deformation of the matrix. A layer of resin seems to cover most of the fibres, and at the fibres ends the matrix is also largely deformed. This type of surface is seen on several regions on the whole fracture surface of the specimen. Figure 5-55b shows a close up of specimen 1 on the core layer. It can be seen that on this layer the fibres are mostly aligned transversally to the flow and load. Evidence of largely deformed matrix is also seen on this region, with some leftover matrix covering the fibres' sides. On this area, two fracture planes seem to occur, an upper and a lower one separated by a fracture > shape. Figure 5-55c presents a closeup of specimen 1 near the middle of the specimen on the upper shell layer. On this region the matrix also seems to have significantly deformed. A "hole" looking feature is seen on this area, implying that a section of the material was pulled out during the failure of the specimen. Figure 5-55d shows a closeup view of the transition between the shell and the core layer in the middle of specimen 1. On the shell layer, it can be observed that the matrix seems to have deformed significantly, while on the core layer a more quasi-brittle, flatter, surface can be observed. On this latter surface, the fibres seem to be cleaner, with almost no fibre covering them. A "step" looking feature is also seen, which implies two different fracture planes occurring on this section. Figure 5-56a shows a closeup image near the lower left end of specimen 2 on the shell layer. Similar to the previous sample, evidence of highly deformed matrix is seen on this section. Remnants of the matrix seem to be covering the fibres. . Figure 5-56b presents a

higher magnification closeup image on the middle of specimen 2 on the lower shell layer. The higher deformation of the matrix is seen on this picture, with matrix debris seen to be covering the most of fibres.

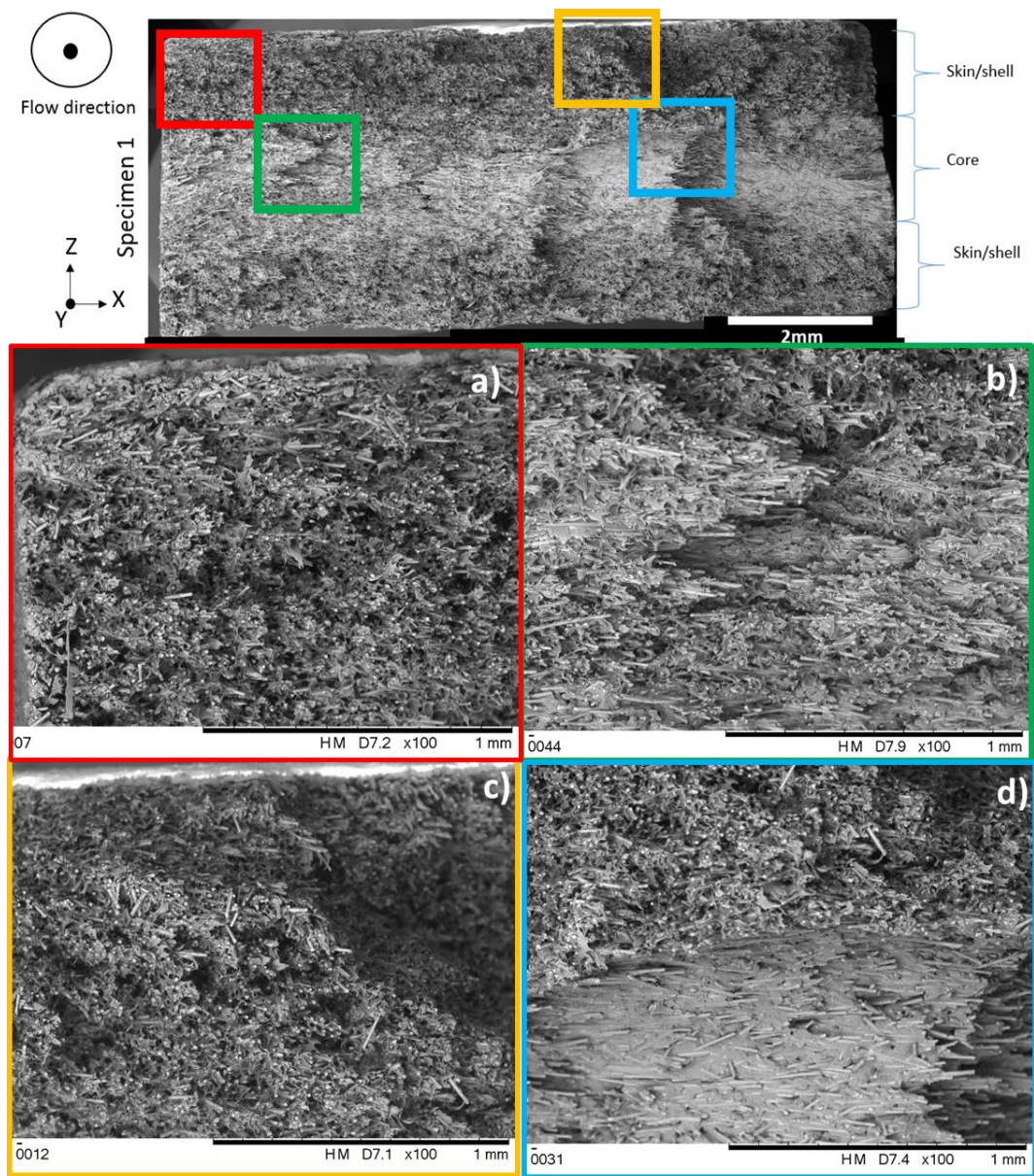


Figure 5-55 Fracture surface of 0° reference specimen 1 tested in tension and close-up images. $V_f=30\%$.

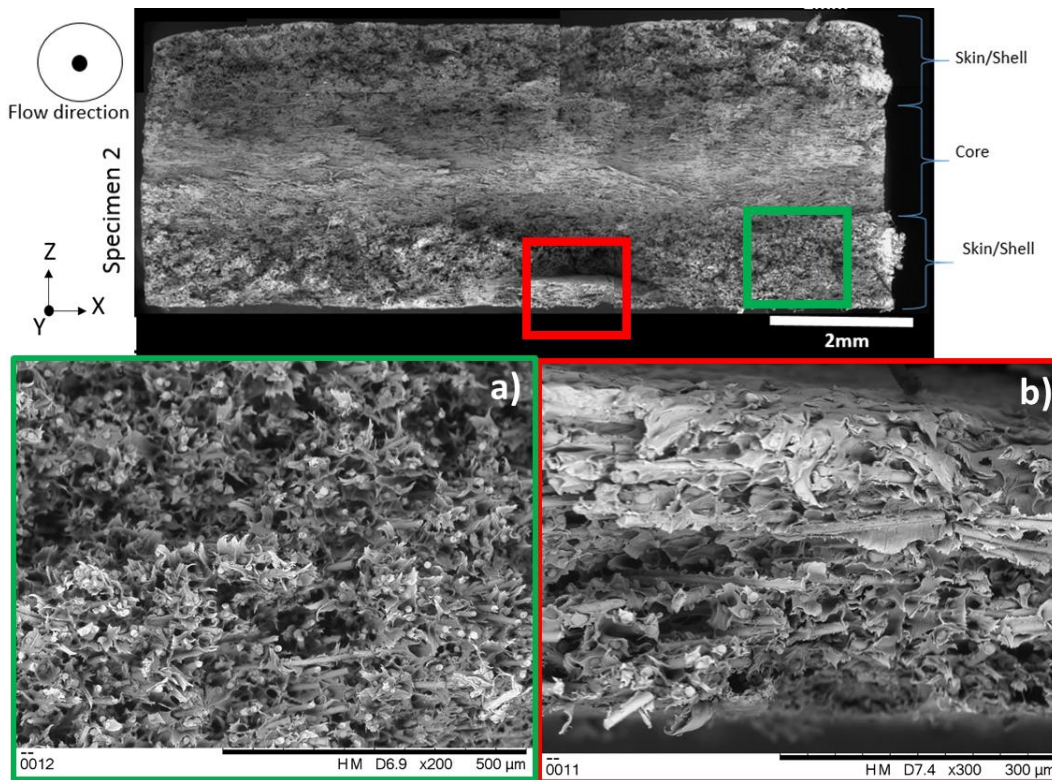


Figure 5-56 Fracture surface of 0° reference specimen 2 tested in tension and close-up images. $V_f=30\%$.

5.5.3.2 Fracture surface of a 90° reference sample

Figure 5-57 shows the fracture surface for a 90° reference specimen tested under monotonic tensile conditions. Similar to the specimens at 0°, a clear distribution of the different microstructure layers can be seen. In the outer regions, the shell layers, the fibres appear to be aligned mostly along the flow. These layers would correspond to the core layer on a 0° reference specimen due to the orientation of the sample. On the inner region, core, fibres appear to be aligned transversally to the flow, out-of-plane. This layer would correspond to the shell layers on a 0° specimen. Figure 5-57a shows a closeup on the middle of the core layer. It can be seen that the matrix on this region seems to have deformed quite significantly. With debris covering most of the fibres. Figure 5-57b shows a closeup of section near the right side of the specimen on the core layer. Two "chunks" of material can be seen on this area, this seems to indicate two different fracture surfaces. On the top of these chunks the matrix appears to be flat, with no deformation. However on the parts outside of these two regions, the matrix seems to have deformed significantly. Figure 5-57c shows a closeup image of the upper shell layer of the sample. On this area, the matrix seems to have failed on a quasi-brittle manner, with little deformation. Fibres sides appear to be clean with little

resin debris covering them. Some evidence of fibre pull-out is also clearly observed on this area.

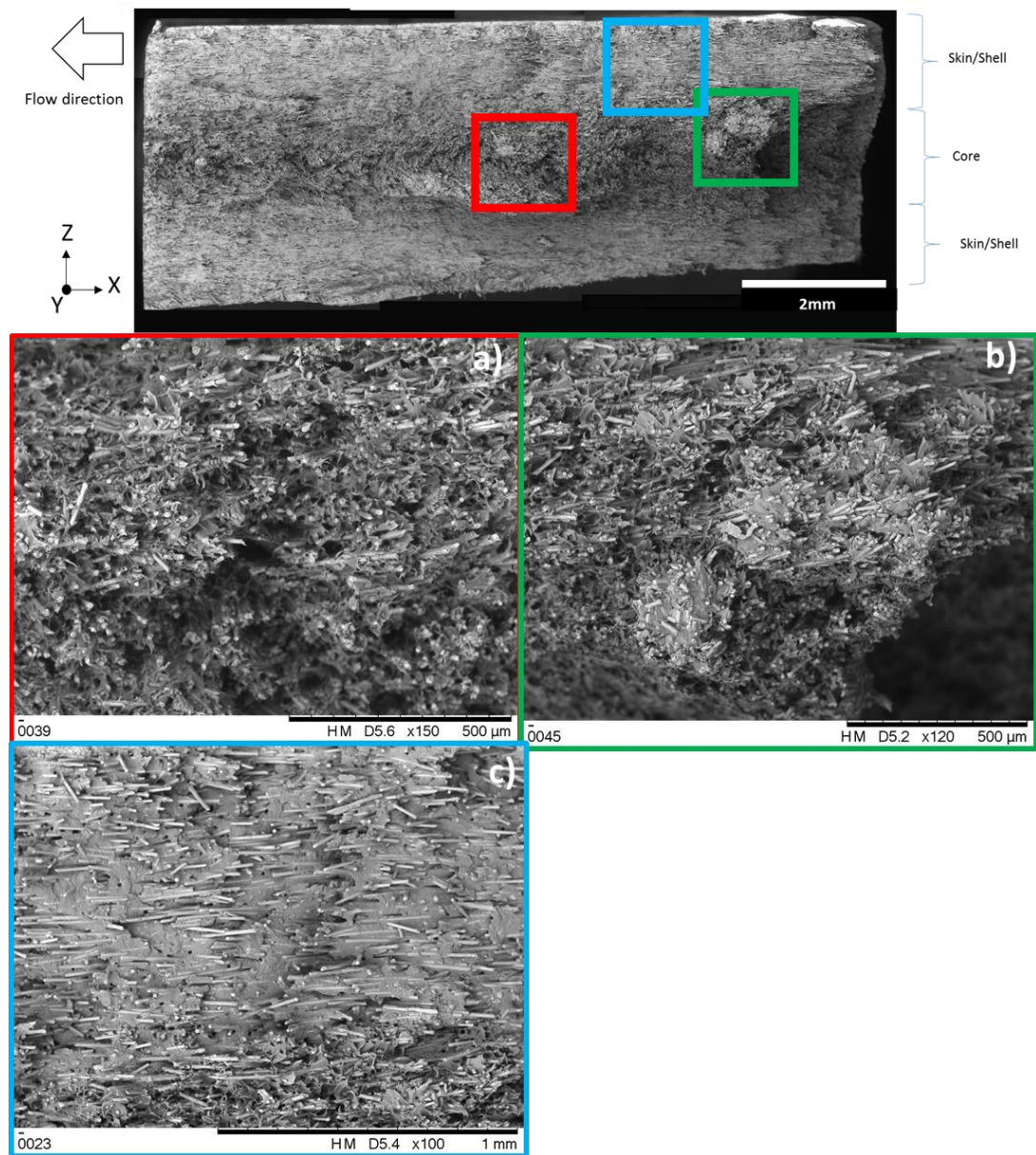


Figure 5-57 Fracture surface of 90° reference specimen tested in tension and close-up images. $V_f=30\%$.

5.5.4 Fatigue specimens, fracture surface

Similar to the previous section, specimens tested under fatigue conditions were analysed using SEM to obtain information of the different failure mechanisms occurring throughout the material under cyclic loading.

5.5.4.1 Fracture surface of 0° reference specimens

Figure 5-58 and Figure 5-59 present the fracture surface of two 0° reference specimens tested under R=-1 conditions. Similar to the monotonic specimens, the different fibre distributions throughout the thickness can be seen. However, on these surfaces a clear difference can be detected on the shell layers. On these regions, presence of "chunks" of material is clearly seen covering most of the shell layers of the specimens. On the core layer, a mostly flat surface is also observed.

Figure 5-58a presents a closeup image of the top left corner of specimen 1 on the shell layer. On this picture, presence of the chunks of material is seen. Little deformation of the matrix is also observed, with the sides of the fibres presenting a mostly clean surface. Presence of fibre breakage and fibre pull-out is also seen. Figure 5-58b presents a closeup image on the upper shell layer of specimen 1. On this area, more chunks of material can be observe, and similar to the previous section, the matrix on these parts seem to present very little deformation. Evidence of fibre failure and fibre pull-out is also visible. Figure 5-58c shows a closeup image on the middle of the core layer on specimen 1. A transition zone can be seen on this area. On the left, the matrix seem to be flat, with very little debris and fibres' sides mostly clean. On the right side, the matrix seems to have deformed more, and with matrix debris covering the sides of the fibres. Figure 5-59a presents a closeup image of the left side core layer on specimen 2. The matrix on this region seems to have failed mostly flat with very little deformation. The fibres' sides appear to be very clean, with no matrix debris. There is evidence of fibre pull-out on this area, marked by almost perfect circles left by the fibres, example of this is denoted by the arrows on the figure. Figure 5-59b shows a close up image of specimen 2 on the lower shell layer of the sample. Similar to specimen 1, "chunks" of material appear on this section, as denoted by the arrow. On the top of these "chunks" the matrix seems to have deformed very little, presenting a mostly flat surface. Below these packages, Figure 5-59c, the material seems to have deformed more, with the matrix on the fibre ends looking elongated. Finally, on a different fatigue sample the main surface was also inspected. Figure 5-60 shows the full width of the sample close to the fracture plane. A close inspection of the regions close the failure plane shows secondary cracks propagating through the matrix and bridging fibres, as is shown in Figure 5-61 and Figure 5-62.

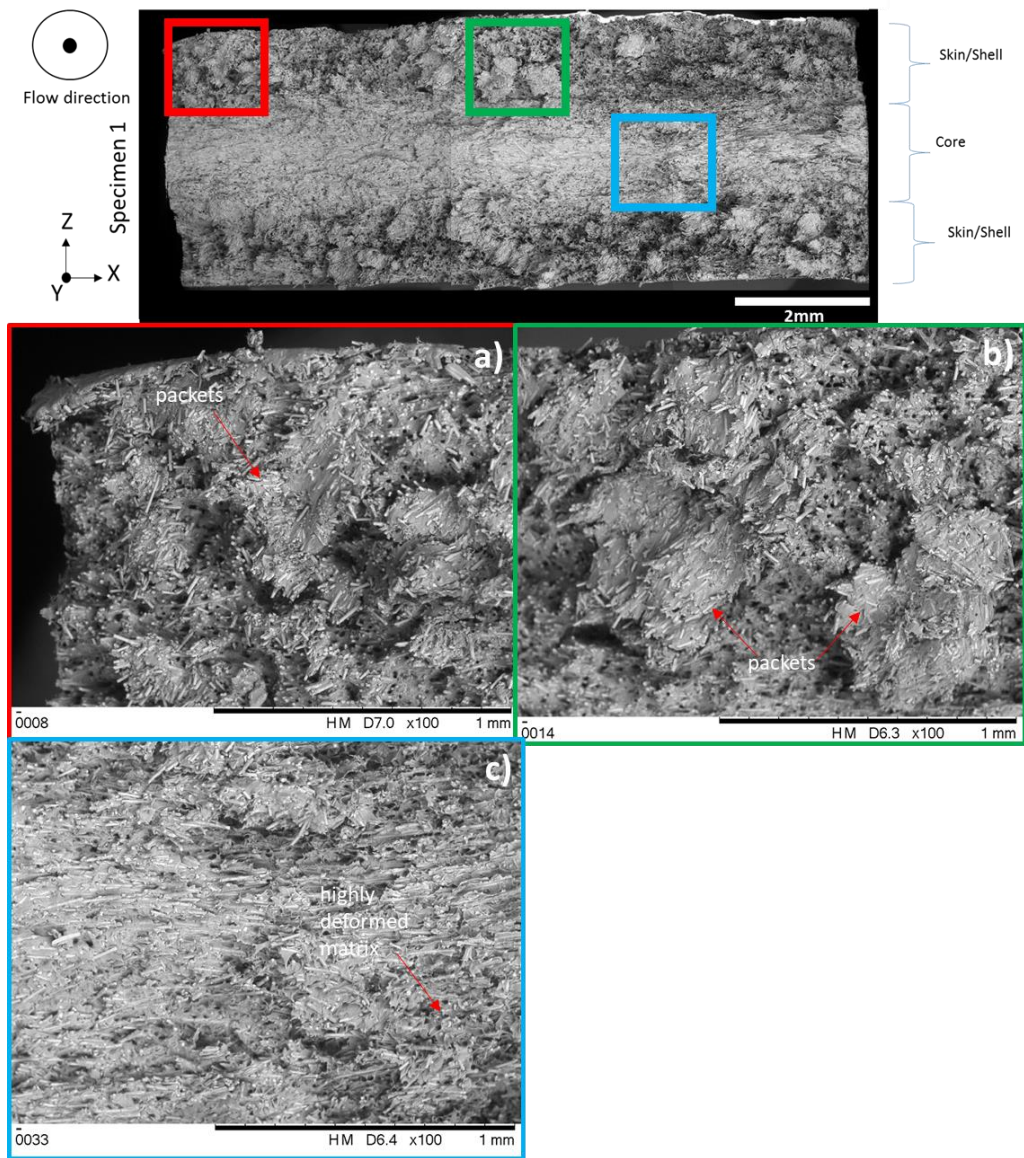


**Figure 5-58 Fracture surface of 0° reference specimen 1 tested in fatigue
R=-1 and close-up images. $V_f=30\%$.**

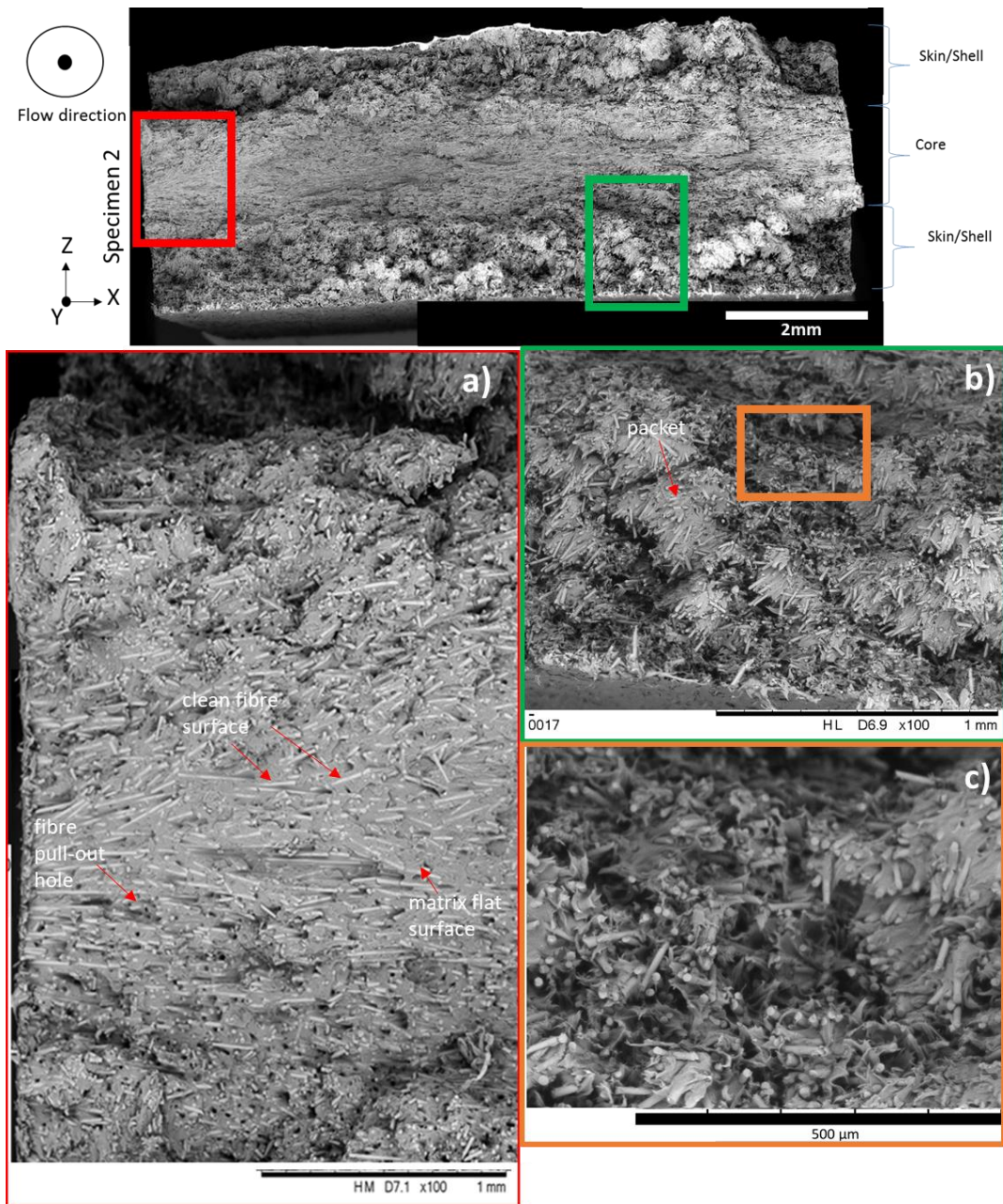


Figure 5-59 Fracture surface of 0° reference specimen 2 tested in fatigue R=-1 and close-up images. $V_f=30\%$.

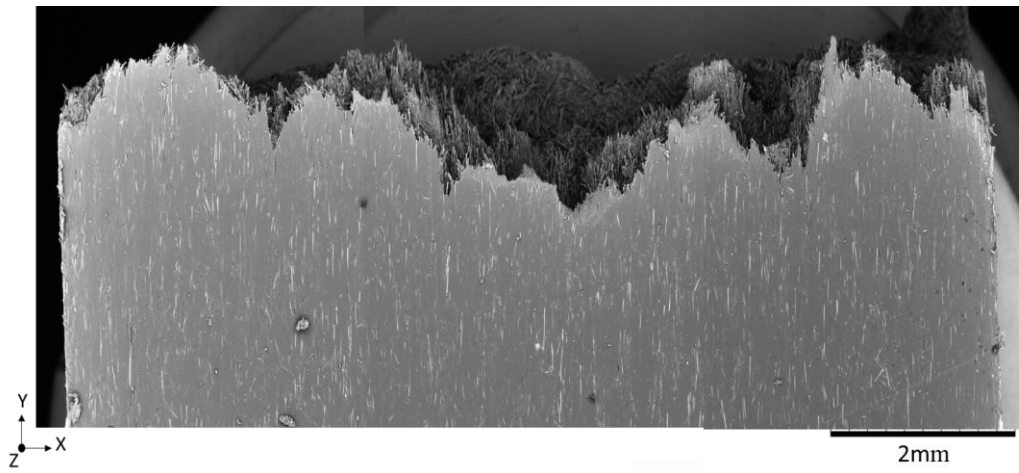


Figure 5-60 View of the main surface of a failed 0° specimen at R=-1. $V_f=30\%$.

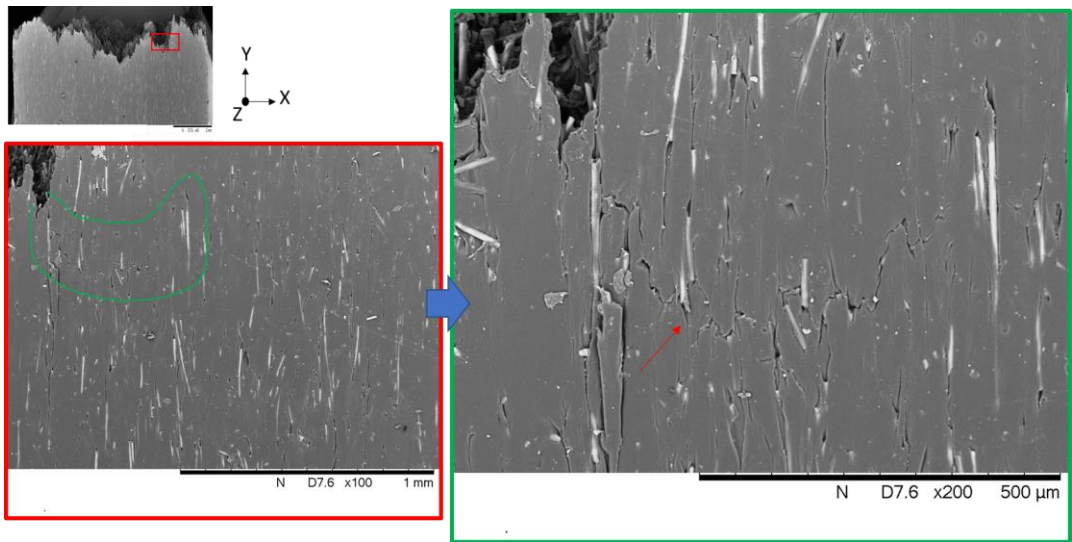


Figure 5-61 Close up near the fracture surface showing a macro crack. $V_f=30\%$.

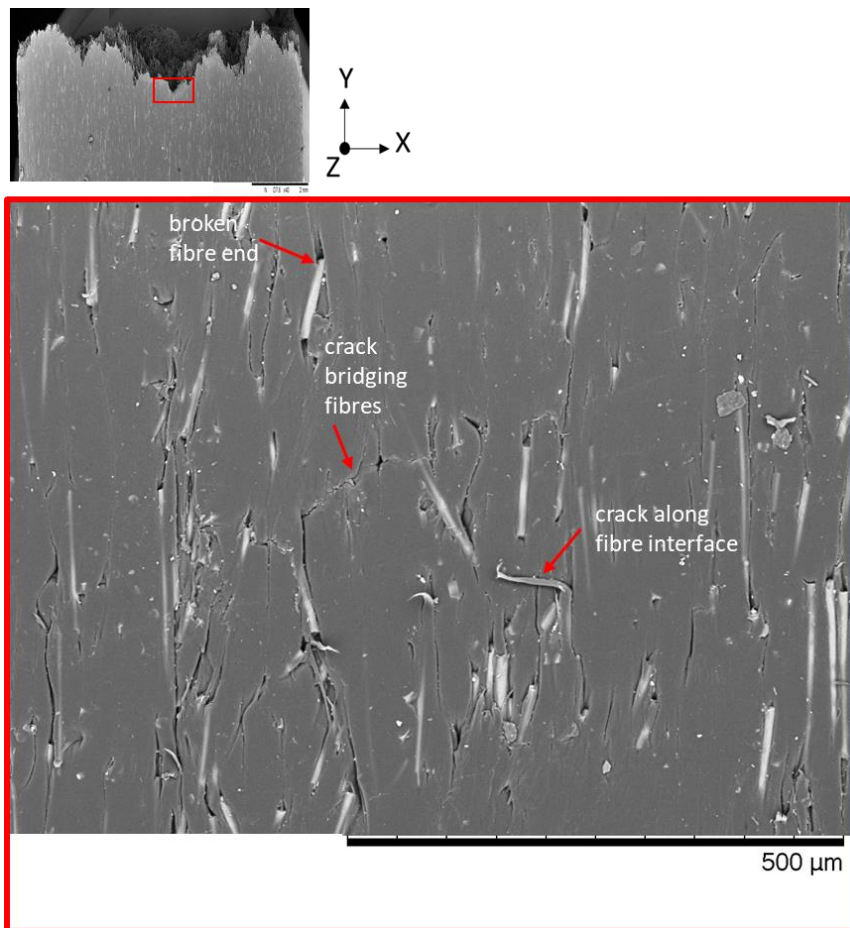


Figure 5-62 Close up near the fracture surface showing a macro crack between fibres. $V_f=30\%$.

5.5.4.2 Fracture surface of a 90° reference sample

Figure 5-63 presents the fracture surface of a 90° reference specimen tested at $R=-1$ fatigue conditions. Similar to previous samples, the division of the microstructure can be seen on this specimen, with the skin and core layers being visible. "Chunks" or "packets" of material can be seen on the core layer of this sample. The overall orientation of the fibres on this section correspond to the shell layers on a 0° reference specimen, which also presented the same packets of material on the layer where the fibres were mostly aligned with the load direction, as shown in Figure 5-58 and Figure 5-59.

Figure 5-63a presents a closeup on the upper shell layer of the sample. A "step" like feature is seen, which seems to indicate two different planes of fracture. On the upper plane, a transition zone is visible. On the left, the matrix appears to be quasi-brittle and flatter, with fibres' sides presenting a cleaner surface. On the right side, the matrix seems to have deformed significantly. Debris of matrix covering the sides of the fibres is also visible. Figure 5-63b shows a closeup image of the lower shell layer of the

sample. On this section the matrix seems to have deformed more, presenting a more messy fracture surface. On the side of the fibres, elongated matrix debris is present. Figure 5-63c presents a higher magnification image of the lower right corner of the sample. The matrix on this region shows a very flat fracture surface, with very little deformation. Some evidence of fibre pull-out is seen on this area. "Steps" like features are also seen on the surface, suggesting the presence of several fracture planes. Finally, Figure 5-63d shows the closeup image on the left side of the sample on the core layer. Similar to 0° reference specimens, presence of "chunks" or "packets" of material is seen on this region. On top of this sections, the matrix seems to be mostly flat with very little deformation. Some evidence of fibre pulling out is also present, denoted by almost perfectly round circular holes on the matrix, as shown in Figure 5-64.

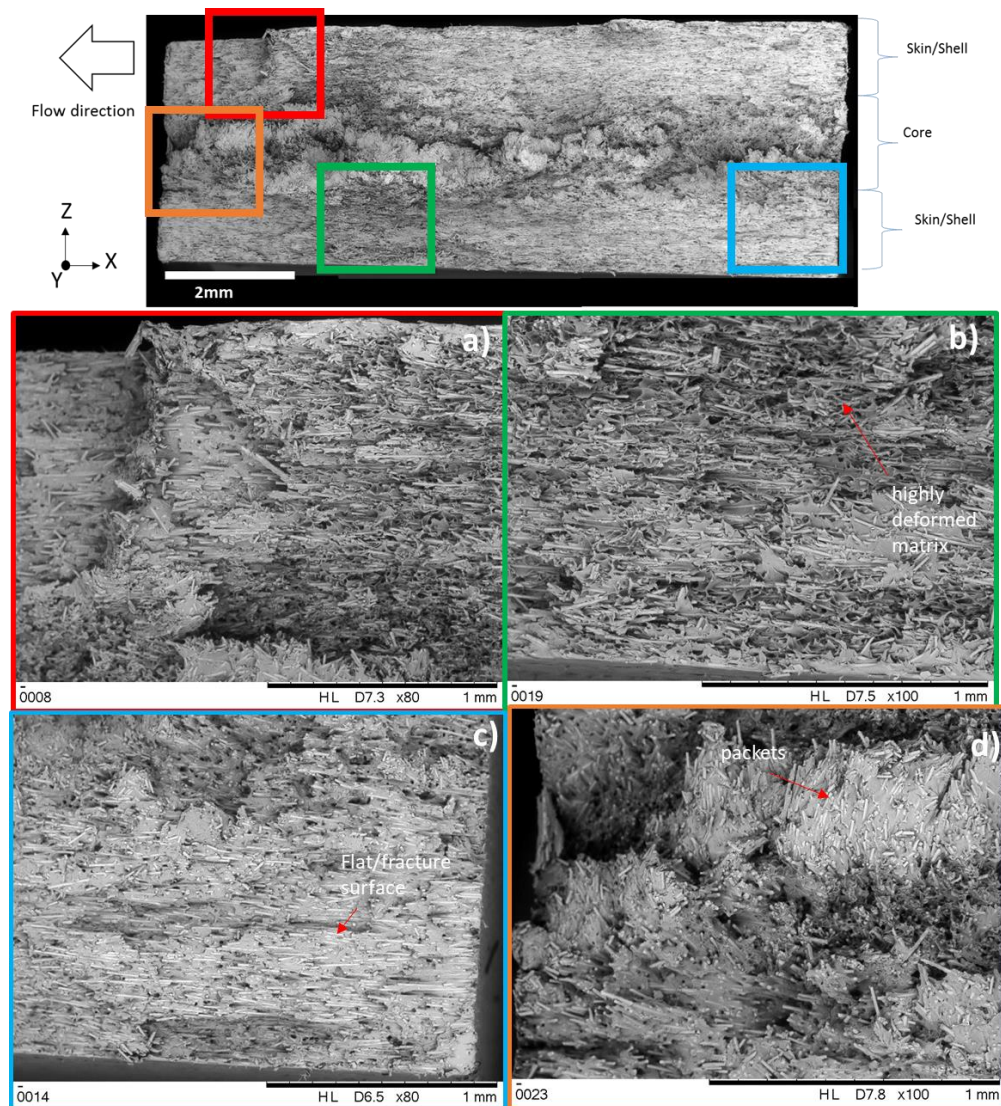


Figure 5-63 Fracture surface of 90° reference specimen tested in fatigue R=-1 and close-up images. $V_f=30\%$.

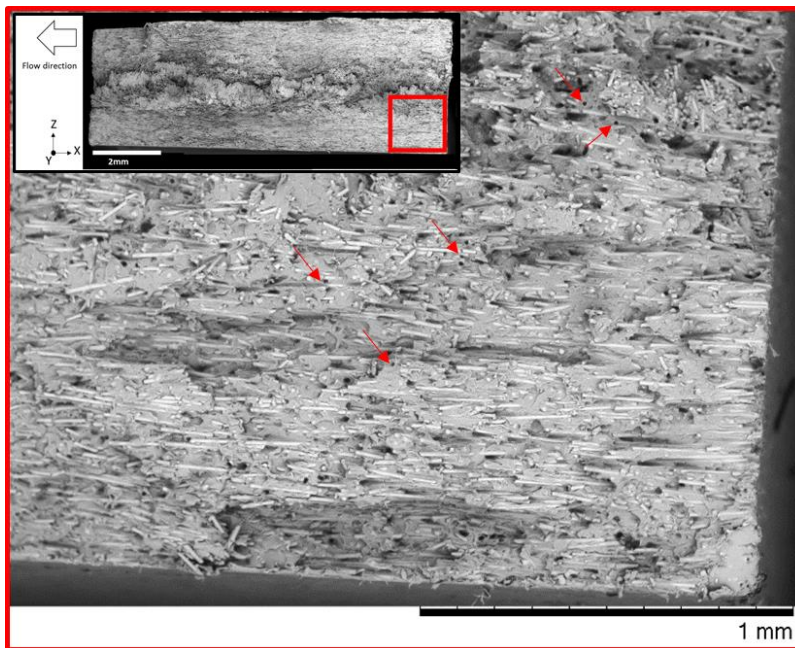


Figure 5-64 Close-up of the fracture surface of a 90° reference specimen tested in fatigue at $R=-1$ with $V_f=30\%$; showing holes in the matrix due to possible fibre pull-out.

5.5.4.3 Fracture surface of a 45° reference sample

Figure 5-65 shows the fracture surface of 45° reference sample tested in fatigue under $R=-1$ conditions. Due to the angle orientation of these samples, and to better analyse the fracture surface and fibre orientation, the specimen for SEM inspection was cut at an angled that corresponded with the fracture plane of the specimen, which was at an almost 45°. On this orientation, it can be seen that the shell layers seems to be aligned more transversally to the flow/load direction, as in the 90° reference specimens. On these layers, some "steps" like features are present, which seem to suggest the presence of several fracture planes developing on these regions. On the core layer, the fibres seems to be more aligned with the flow direction. Some "chunks" or "packets" of material can be seen on one side of the specimen.

Figure 5-65a shows a closeup image of the upper skin layer of the sample. The overall transversal orientation of the fibres can be seen. On this section the matrix seems to have deformed, producing a very messy fracture surface. Figure 5-65b presents a higher magnification image of the left side part of the sample, on the core layer. Two different matrix surfaces can be seen, on the top of the "chunks" the matrix seems to be flatter with little deformation. On the sides, the matrix seems to have deformed heavily. Figure 5-65c shows a closeup image of the core layer on the right side of the

sample. On this region, the matrix material seems to be flat for the most part, with almost no deformation. Evidence of fibre pull-out is visible on this area. Finally, Figure 5-65d presents a closeup image of the bottom shell layer of the sample. On this region the matrix seems to have deformed more, presenting a very messy fracture surface. Some debris of matrix seems to be covering the sides of the fibres. A "step" like feature is also visible, which indicates a section of material that was pulled out during the final failure of the specimen.

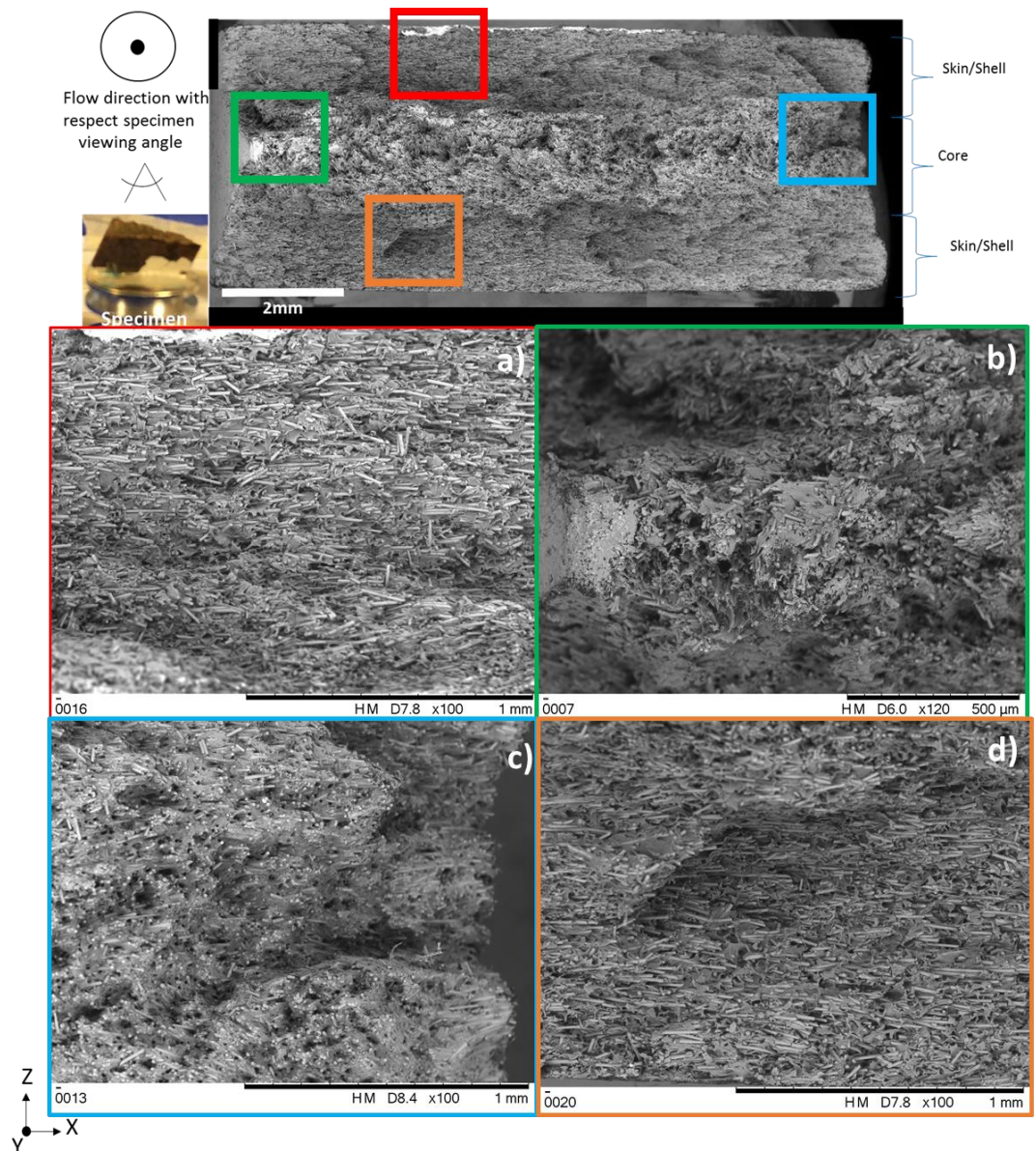


Figure 5-65 Fracture surface of 45° reference specimen tested in fatigue R=-1 and close-up images. $V_f=30\%$.

5.6 Conclusion

This chapter presented the results of the experimental program. To further corroborate the distribution of the fibres, described by the measured fibre orientation tensor, two different CT scanners were used. This double-blind validation is not commonly possible due to the CT equipment being prohibitively expensive. Histograms for the fibre diameter and length were presented, together with the calculated critical length of $l_c=665\mu\text{m}$, which was larger than the nominal and average lengths, of $200\mu\text{m}$ and $215\mu\text{m}$, respectively. From the literature [17], [20], it seems that using fibres of length below the critical length is very common in the manufacture of injection moulded short fibre reinforced composites. This could be because the difficulty of manufacturing composites increases with the aspect ratio (function of length) [78], larger fibres also have a higher probability of breaking [169]. Documented works [21], have shown a reduction of up to 62% of the original fibre length between the before and after injection moulding process, where to minimize the breaking of fibres modifications would need to be conducted to the injection screw design. Additionally, as it was seen in Figure 2-30, shorter fibres tend to have a higher strain-at-break limit, which could be desired for certain applications. Nevertheless, in short fibre reinforced composites, it is true that larger fibres produce higher tensile strengths and moduli, about 30% and 10% higher [21], respectively. Fatigue lives, and composite self-heating during cyclic loading, also seem to improve with the inclusion of larger fibres [57], [78], [79]. Frequently in the literature, e.g. [20], [56], only mechanical properties such as stress-strain behaviour, Youngs' moduli, tensile strengths and strains-to-failure are measured/calculated. However, this work also presented an analysis of the variation of the Poisson's ratio with the specimen orientation as an additional source of information regarding the effects of the fibre orientation distribution in the material behaviour. High-speed camera images provided with clear evidence of the most-likely location for crack initiation, as well as, of the strain distribution during actual cyclic conditions. This is very difficult to capture without specialised equipment and careful test control due to the speed of damage development. To the author's knowledge this is the first time that such clear evidence of damage initiation is observed in this material. Unlike other published work, e.g. [75], this thesis documents the coefficients for the obtained Basquin's relationships that describe the fatigue material data for different specimen orientations and stress ratios. The coefficient of determination, or R^2 , for each relationship that describes the quality of the data fitting is also presented to allow further assessment of the different sources

of error in the methodology. The evolution of the material's hysteresis loops areas, together with the dissipated energy was also presented. It was shown that the commonly known Ranberg-Osgood material model could be used, where clear evidence of cyclic softening was observed. Uncommonly in the literature, evidence of strain localization and measurement of the crack growth, following a clear exponential behaviour, in tensile specimens' faces was documented. Similarly uncommon, assessment of the quality of the surfaces due to the injection moulding process and specimens' machining was also presented. Finally, SEM micrographs of the fracture surface of tensile and fatigue specimens were documented to allow an analysis of the different fatigue damage mechanisms.

6. MODELLING RESULTS

6.1 Predicted fibre orientation distribution

6.1.1 Injection moulding simulation results

The simulation of the injection moulding provides with information of the composite microstructure in terms of estimates of the fibre orientation distribution and, in specific, the through-thickness fibre orientation tensor. The details of the set up and boundary conditions used were presented in Chapter 4 of this thesis. Figure 6-1 shows the evolution of the melted material filling the cavity, which takes approximate 2s. The effect of using an assembly system formed by: the mould, fan gate, runner and sprue is clearly seen, as it produced a more straight flow front during the filling process right after the composite leaves the fan gate. This consistent flow helps in minimizing the presence of weld lines (point where two or more flow fronts meet) once the material solidifies. This uniform flow also leads to a more consistent fibre orientation distribution around the middle of the composite plate, which served as the reference location for the subsequent analysis.

In terms of the fibre distribution, Figure 6-2 shows the results for the surface and a cross sectional view for the fibre orientation tensor component in the direction of the flow, or a_{11} . It is good to recall that the a_{11} , a_{22} and a_{33} tensor components represent, respectively, the strength in alignment of the fibre in the direction of the flow, transversal to the flow and out-of-plane direction. It is clear from this figure that the fibre distribution in the surface of the plate presents a higher concentration of aligned fibres near the side edges of the plate, represented by a red colour. On the other hand, closer to the gate the fibre alignment seems to be more randomly aligned, represented by a green colour. Additionally, closer inspection of the thickness view reveals a steep reduction in the alignment of the fibres with respect to the flow, from the surface of the plate to the centre. This is in line with the known Skin-Shell-Core microstructure present on this type of materials.

Figure 6-3 shows the statistical proportion of the fibres aligned towards the principal direction, or 1st eigenvalue as shown in Figure 2-18, which for the case of this model it closely corresponds to the direction of the flow. Sections a) and b) show the through-the-thickness distribution at the locations from where the specimens were taken, indicating the location of the coupons' gauge section. It is clear that the for the case of the 0° Edge specimen the fibre distribution is very consistent and highly

aligned through the specimen, as seen in Figure 6-3a. On the other hand, for the case of the reference and 90° Edge specimens, the classic skin-shell-core distribution is more clearly visible, as presented in Figure 6-3b. Again, the advantage of obtaining a straight flow front is seen in this figure, as the region surrounding the reference location produces a clear division in the distribution of the fibres through the plate.

Finally, calibration of the injection moulding simulation was done using the experimental results at the reference location. This was done by comparing the simulation results against CT measurements taken by two different scanners. The results of this analysis, as well as, the assessment of the differences, is presented in the Discussion section of this thesis in Chapter 7.

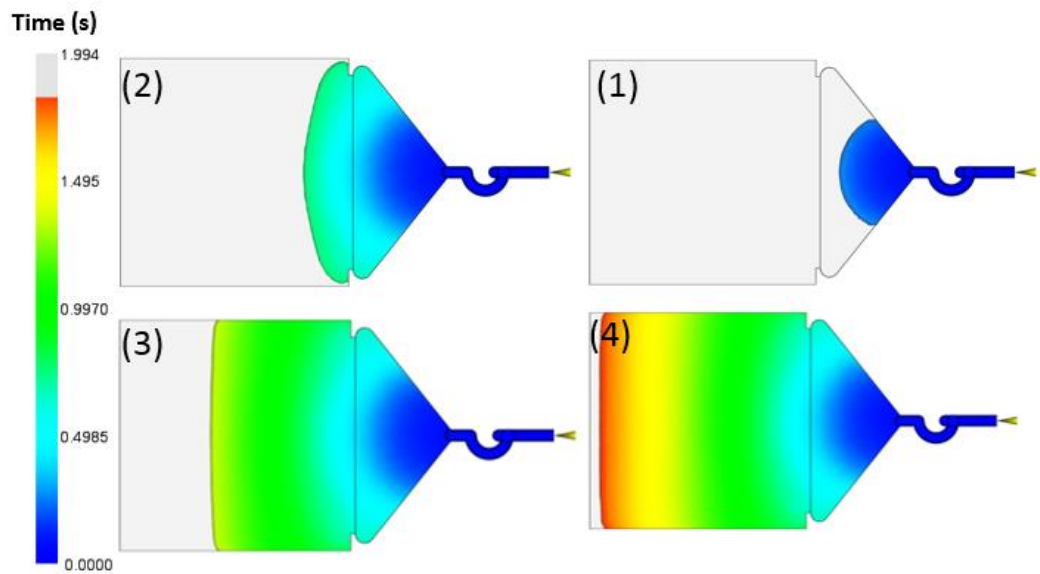


Figure 6-1 Cavity filling.

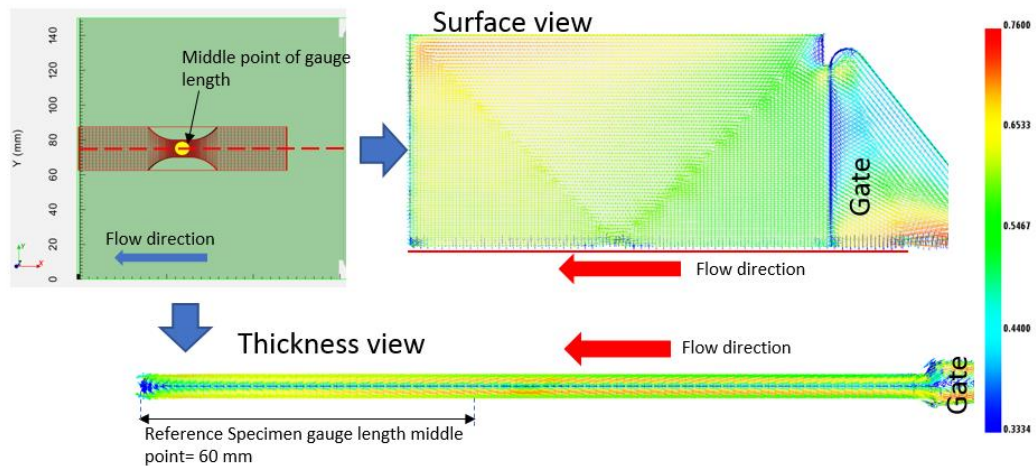


Figure 6-2 Moldflow a_{11} component results. Surface and thickness view for reference location.

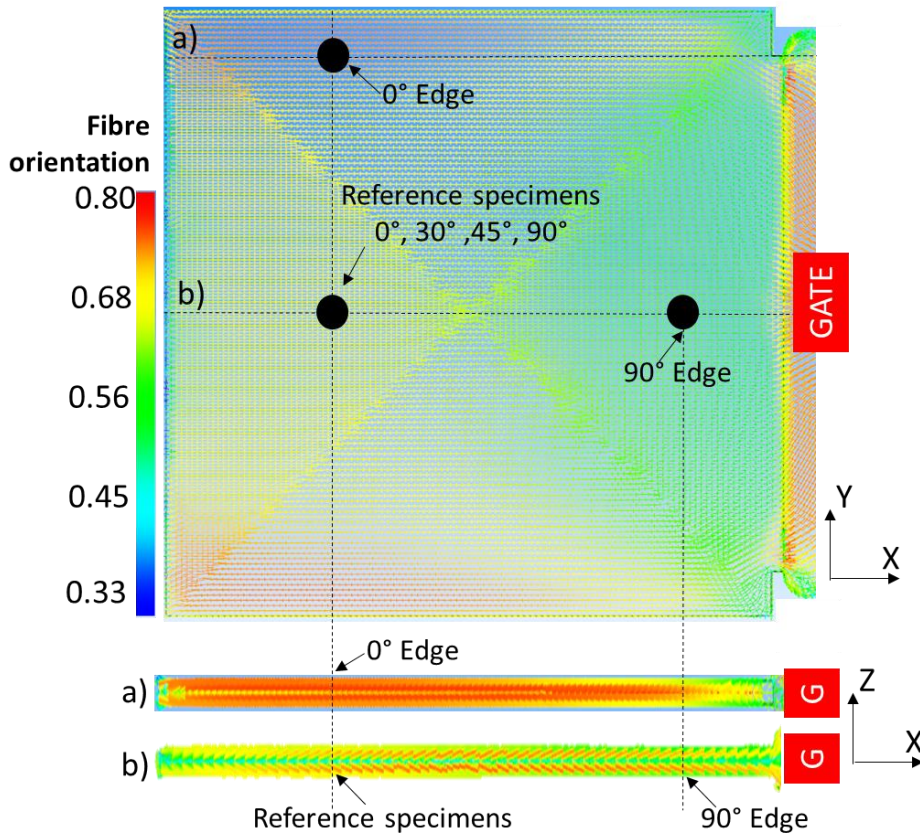


Figure 6-3 Fibre orientation distribution across the surface and through the thickness of the plate showing the location of the centres of the different specimens.

6.1.1.1 Plate's through-thickness fibre orientation tensor

As previously said, from the injection moulding simulation the through-thickness fibre orientation tensor information was extracted at different locations in the plate. This locations corresponded with the centre of the reference, 0° Edge and 90° Edge specimens, as depicted in Figure 6-3. With this information, Figure 6-4 presents a comparison of the orientation tensor components, through the thickness, at these three specified locations. It can be observed that the reference and 90° Edge locations show a very close distribution of the fibres in the shell layers. However, a clear divergence can be observed in the core and in the skin layer for the a_{11} and a_{22} components, Figure 6-4a and b. For the case of a_{11} , Figure 6-4a, the 90° Edge location showed a 22% higher tensor component than the reference location at centre of the core layer. On the other hand, for the case of a_{22} , Figure 6-4b, the 90° Edge location showed a 10% lower tensor component than the reference location at centre of the core layer. This implies that the closeness to the fan gate is having an effect on the fibre alignment in the core layer. A significant difference can also be observed when

comparing the results of the 0° Edge location against the other two. It is clear that the closeness to the mould's side walls is having a positive effect in the fibre alignment. This is seen as the component of the fibres oriented in the flow direction, Figure 6-4a, is 90% higher in core and is more consistent through the thickness than in the reference and 90° Edge locations. On the other hand, the component of the fibres transversal to the flow direction (a_{22}) was significantly reduced with a drop of 50% in the core, in comparison to the reference location. This is shown in Figure 6-4b. Finally, the comparison of the values for the out-of-plane tensor component, Figure 6-4c, shows not significant difference between the three locations, which implies that the distribution of the fibres occurs mainly in-plane, or a_{11} and a_{22} . Finally, a comparison between these FEA simulation results and the actual experimental CT measurements for the different specimen orientations can be found in Figure 7-2.

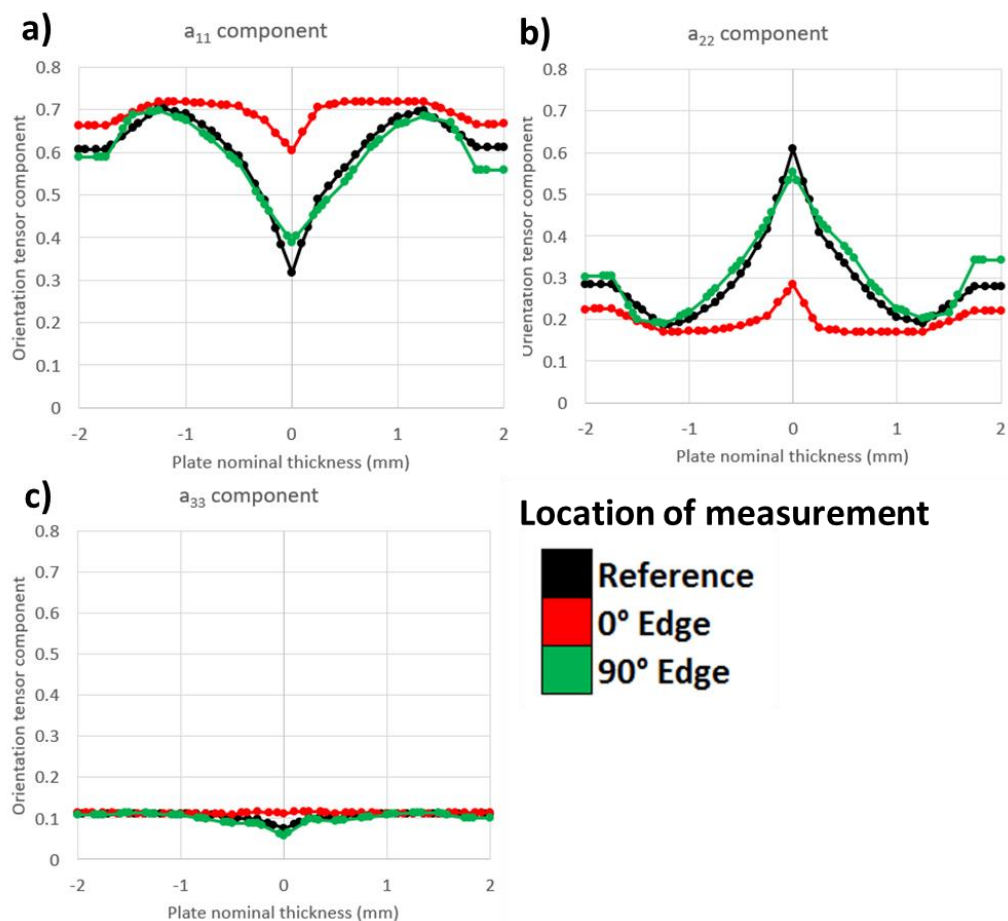


Figure 6-4 Through-thickness orientation tensor components at different points in the plate. Moldflow results only.

6.1.2 Fibre orientation tensor after mapping onto structural mesh

As described in Chapter 4, prior to the finite element analysis the results of the injection moulding simulation, in terms of the fibre orientation tensor information, were mapped onto the structural meshes of the specimens. A comparison of the results between the before and after-mapping was conducted to assess any loss of information occurring during the process of transferring the data.

Figure 6-5a to c show the comparison of the orientation tensor components for: before (Moldflow) and after (Abaqus) the mapping process; for the reference, 0° Edge and 90° Edge locations. As it can be seen, the mapping procedure correctly transferred the fibre orientation data from the plate onto the different structural meshes. The typical skin-shell-core layers can be observed on all the specimens. A close comparison showed that good agreement between Moldflow and Abaqus results was obtained, in particular, in the skin and shell layers. A maximum difference, between Moldflow and Abaqus, of ~9% was found for the case of the reference location at the core layer, Figure 6-5a. Similarly, a maximum difference of ~8% and ~10% were found for the 0° Edge and 90° Edge locations at the core layer, Figure 6-5b and c respectively.

Finally, Figure 6-6a-c show the a_{11} orientation tensor component distribution for reference, 0° Edge and 90° Edge specimens after the mapping procedure. Recall that this tensor component represent the strength of fibre alignment with the flow direction. It can be seen that in terms of the through thickness fibre distribution for the reference and 90° Edge specimens, Figure 6-6a and c, show a clearer division between the different microstructure layers. This is, higher alignment in the shell layers and lower alignment in the core layer. For the case of the reference specimen, the shell sections seem to cover a more significant area of the thickness than the core section. On the other hand, in the 90° Edge specimen, the shell and core regions seem to be of similar size, with a more distinguishable transition zones denoted by intermediate levels of alignment. Finally, the 0° Edge specimen (Figure 6-6b), presents a more uniform fibre distribution through the thickness, with relatively high levels of alignment in the shell and core layers alike. This is similar to the results shown in Figure 6-4a.

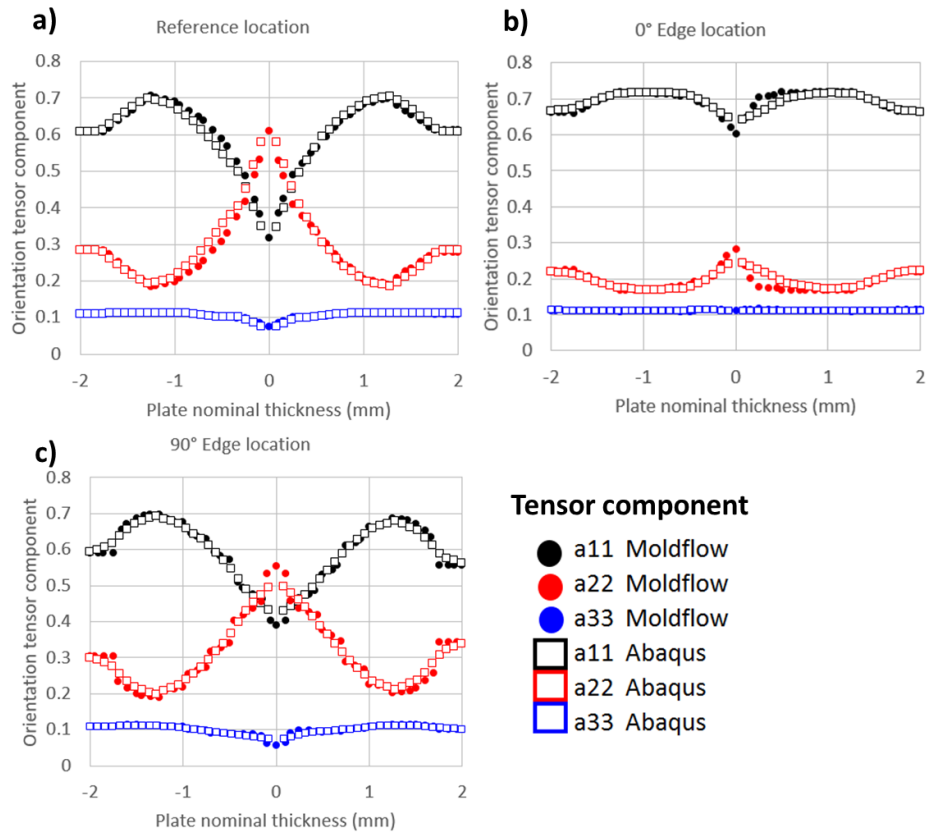


Figure 6-5 Through-thickness orientation tensor between Moldflow (before mapping) and Abaqus (after mapping) at different locations.

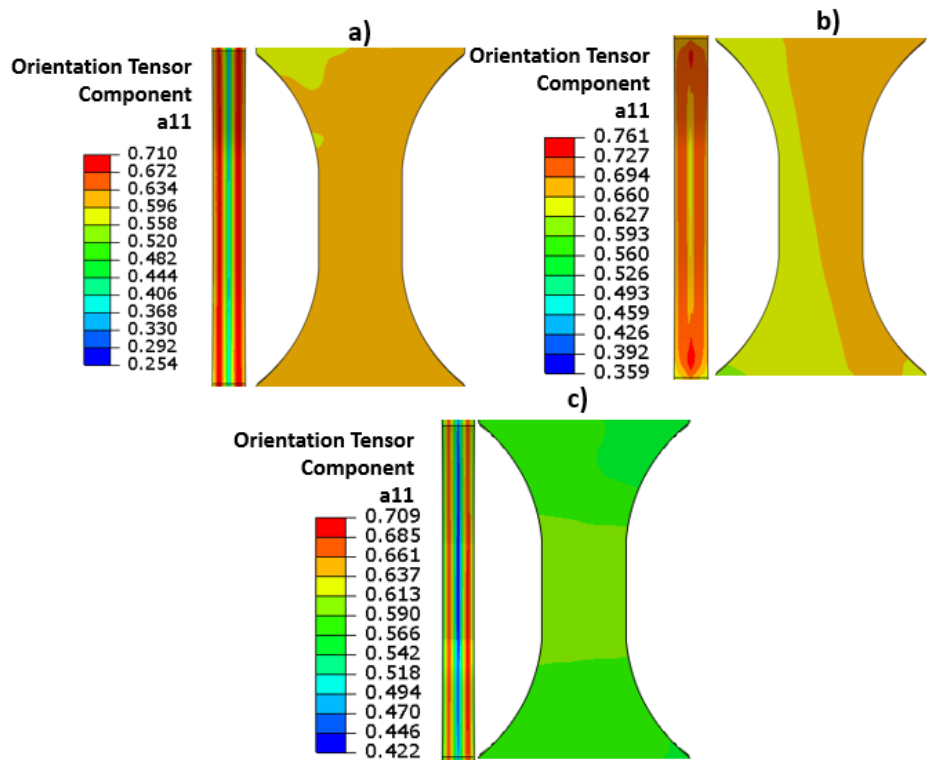


Figure 6-6 a₁₁ orientation tensor distribution for a) reference, b) 0° Edge and c) 90° Edge specimens.

6.2 Predicted material properties

6.2.1 Mean Field Homogenization and Reverse engineering results

The main result of the injection moulding simulation was the fibre orientation tensor. This information is key in the prediction of the material properties, as it is used to assess the specific directions of the fibre reinforcement during the Mean Field Homogenization (MFH) technique. This is done to calculate individual material properties on each element of the specimens' meshes. This tensor information, relating to the direction of the inclusions, together with the specific material parameters of the phases, which in simplified terms represent the matrix's and fibre's properties, are the main input for the MFH technique. A depiction of this technique was presented in Figure 2-40 and Figure 4-6.

Initially, and as described in Chapter 4, the pure MFH material model was calibrated using a simplified version of the orientation information at the reference location. This first guess was done using three different orientation tensors, corresponding to: the skin, the shell and the core layers. This is, where the fibres are, respectively, more randomly distributed, more oriented with the flow and more transversally oriented to the flow. This assumed distribution is shown in Figure 6-7 for each of the different layers. The second input corresponded to the material properties for the phases. Elastic parameters for the fibres, and elastoplastic parameters for the matrix. These values are shown in Table 6-1, where "MFH" corresponds to this initial model prior to the further calibration using experimental data. The resultant material model was then compared against averaged experimental data for 0° and 90° reference specimens, calculated from the individual test the results shown in Figure 5-7. These orientations corresponded to the material being loaded in the flow and in the transversal-to-the-flow directions. The comparison of the results is shown in Figure 6-8. The dotted-lines represent the MFH model response in the axial and transversal directions, compared against the averaged experimental data under the same conditions. It can be seen that for the case of the parallel to the flow direction, 0°, the material model shows good agreement within the linear part of the curve. It is on the onset of the non-linear part of the curve where the MFH material response starts to diverge, showing a 18% higher maximum stress than the experimental data. On the other hand, in the transversal to the flow direction, 90°, the MFH material shows a softer response than the experimental data with a reduction of 13.7% in terms of maximum stress.

The previous results showed the necessity to further calibrate the analytical model to better represent the actual response of the material. To do this, the next step was the implementation of an iterative reverse engineering (RE) approach that used experimental data to adjust the phases' material parameters, as described in Chapter 4 of this thesis. For the calibration of the model, average experimental data for 0°, 45° and 90° reference coupons were used. This averaged data was again calculated from the testing results shown in Figure 5-7. The results for the new calibrated material parameters, for the fibre and matrix, are shown in Table 6-1 in the "Reverse Engineering" row. It can be seen that for the most part the values corresponding to the fibre reinforcement stayed the same, with the matrix's parameters being the ones that changed the most. This is as the matrix is the responsible for the non-linear behaviour of the composite. As a sanity check, the new optimised values were compared against known ranges for glass fibre and nylon matrix. This allowed to assess that the levels obtained after calibration were realistic. Typical Young's modulus values for silica (Si) based glass-fibres are about 69-81GPa [15], depending on the specific composition. On the other hand, values for nylon 66 are about 1,100-3,000MPa [145], with the variation being dependant of humidity condition. Similarly, the obtained Poisson's ratios for glass fibre and matrix were very close to the documented values of $\nu = 0.2$ for glass [16]; and $\nu = 0.33-0.41$ for PA66 [16], [166], [170].

Figure 6-8 shows the comparison using the average experimental data, used for calibration, and the Reverse Engineered material model. In regards to the direction parallel to the flow, 0°, the correlation of the model with the experimental data showed a maximum difference of 5% for the maximum stress. A good agreement was also obtained for the transversal to the flow orientation, 90°, where the model and the experimental curves almost overlapped. These new material parameters, for the fibre and matrix, were the ones used to predict the composite material's properties during the MFH step conducted along the finite element stress analysis. It is good to mention that the validation of this model was carried out using experimental data from different orientations and locations than the ones used for calibration, i.e. 30° reference, 45° reference, 0°Edge and 90°Edge samples. This validation is shown in the Discussion part of this thesis.

Skin	Shell	Core
$\begin{bmatrix} 0.5 & 0 & 0 \\ 0 & 0.5 & 0 \\ 0 & 0 & 0.0 \end{bmatrix}$	$\begin{bmatrix} 0.8 & 0 & 0 \\ 0 & 0.18 & 0 \\ 0 & 0 & 0.02 \end{bmatrix}$	$\begin{bmatrix} 0.18 & 0 & 0 \\ 0 & 0.8 & 0 \\ 0 & 0 & 0.02 \end{bmatrix}$
More random orientation	More oriented with flow direction	More oriented transversal to flow direction

Figure 6-7 Assumed fibre distribution for the MFH model.

Table 6-1 Composite phases' material parameters

Material Model	Glass Fibre		Matrix			
	Young's Modulus	Poisson's ratio	Young's Modulus	Poisson's ratio	Hardening Modulus	Hardening Exponent
MFH	72 GPa	0.2	1,000 MPa	0.35	22MPa	50
Reverse Eng.		0.22	1,834 MPa	0.42	70MPa	256

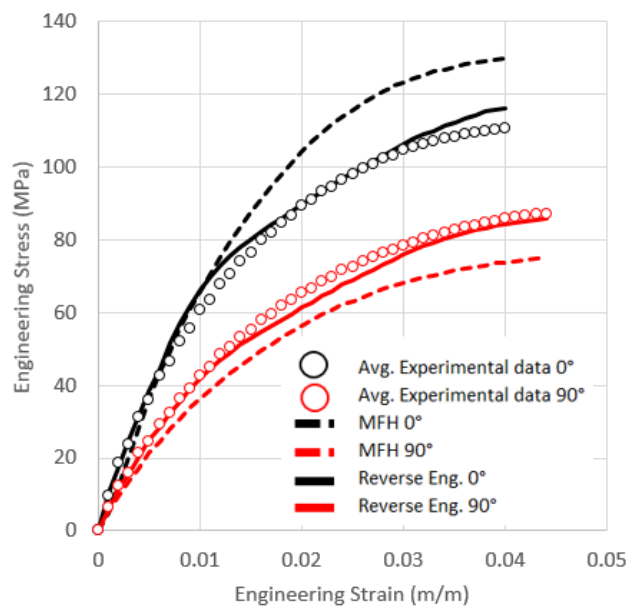


Figure 6-8 Comparison between MFH using standard values and further calibration via Reverse Engineering.

6.2.2 Finite Element Stress-Strain curves

After the material model was calibrated in the step described above, and with the fibre orientation tensor mapped into the individual structural meshes; stress analysis was then conducted on the different specimens. The boundary conditions used were described in Chapter 4 of this thesis.

With the results of the stress analysis, coupon based Stress-Strain curves were then drawn for the different specimens' orientations and are shown in Figure 6-9. In the first instance, it can be observed that the simulated material curves present a clear non-linearity, represented by strain hardening occurring on all specimens' orientations, which is characteristic of this type of composites.

The anisotropic effect caused by heterogeneous fibre orientation distribution can also be observed on these results. The 0° Edge specimen presents the highest strength and stiffness, followed by the 0°, 30°, 45°, 90° and 90°Edge samples; with the last three orientations being very close to each other.

The predicted results for 0° Edge specimen seems to be in line with the simulated orientation tensor distribution, shown in Figure 6-5b and Figure 6-6b, as it presents a higher level of fibre alignment caused by the mould's walls effect. 90° and 90° Edge coupons showed the softest material behaviour of the set of curves and with very close results, no apparent difference is seen. Close to this pair of curves also lays the 45° specimen. Additionally, 30° and 45° curves lay in between 0° and 90° specimens, with 30° showing a clearer distinction and with higher strength than the later. The validation of this predicted material curves was carried out by comparing the results against experimental data. This comparison is presented in the Discussion section of this thesis, in Chapter 7.

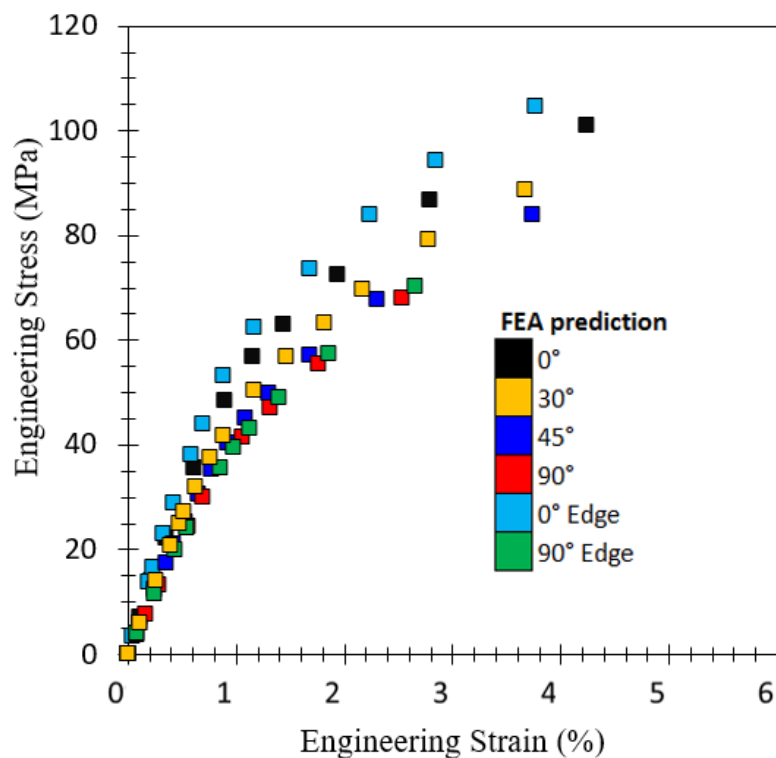


Figure 6-9 Predicted coupon Stress-Strain data.

6.3 FE Stress and Strain results

6.3.1 Dog-bone specimens

The following section, presents the finite element analysis results, in terms of stress and strain distributions for the different specimens' orientations. A clear non-homogeneous distribution of stresses and strains was observed on all specimens. In particular, the concentration of stresses seems to occur in the regions where fibres are more aligned with the load direction; with lower stress levels in areas where fibres are more aligned transversally to the load. On the other hand, in the terms of strain; the highest values seem to be located in sections right below the surface of the specimens. This is observed by inspecting the thickness view on all the coupons.

6.3.1.1 0° specimens

Figure 6-10a to f, present the stress and strain distributions for a 0° reference specimen under different load levels. With respect to the stress field, a clear distinction can be made in regards to the thickness view. The concentration of stress is occurring immediately below the surface in regions located within the shell layers, where the fibres are more aligned with the load direction, and closer to the end of the shoulders. Stresses then drop at the middle of the sample. This corresponds to the core layer, where fibres are more transversally aligned with the load. In terms of the main surface view the stresses at the centre of the gauge length present a more homogenous distribution. However, visible higher stress can be seen in the corner of the gauge area at intermediate loads, Figure 6-10b. Nevertheless, the higher stresses are always seen below the surface of the specimens, and are approximate 16% higher in the shell layers, where the fibres are mostly aligned towards to the load/flow direction, than the ones present on the main surface's gauge area, Figure 6-10c. The strain distributions on this specimen orientation show a clear concentration below the surface at higher loads, as shown in the thickness view in Figure 6-10f. Concentration of strain is also observed on the sample, in particular in the middle and at the corners of the gauge length section. This concentration of strain in the central area starts to be more noticeable under intermediate and high loads, Figure 6-10e and f.

Figure 6-11a and b shows the through thickness stress distribution near the shoulder and in the middle of the 0° reference specimen at the maximum simulated tensile load of 4kN. It can be seen that there is a clear distribution of the stresses which corresponds to different skin-shell-core layers. It is also clear that in the shoulders,

Figure 6-11a, the maximum stresses are concentrated along the thickness of the specimen from surface to surface; whereas, in the middle of the sample, Figure 6-11b, the maximum stresses are located the strain distribution under the same loads. It can be seen that in the shoulder section, Figure 6-11c, the highest strain is located through the thickness and in the surface of the sample; whereas, in the middle of the sample, Figure 6-11d, the maximum strain are located in one side of the coupon. From this, it can also be seen the effect of the fibre orientation distribution, as the strain results are not completely symmetric.

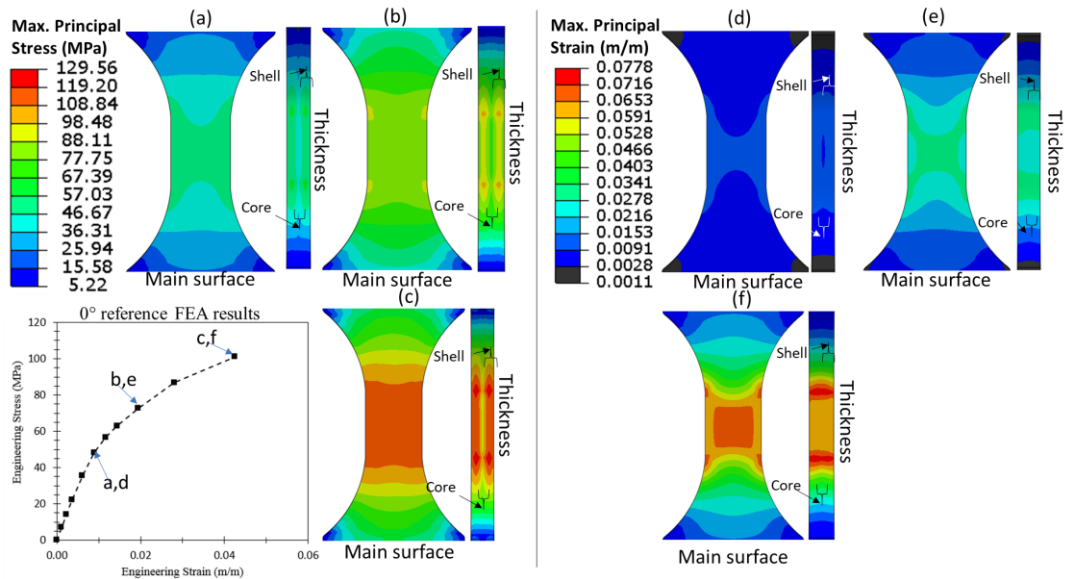


Figure 6-10 Evolution of the FE stress/strain distribution for a 0° reference specimen with $V_f=30\%$. Braces denote the approximate division between the shell and core layers in the structural model.

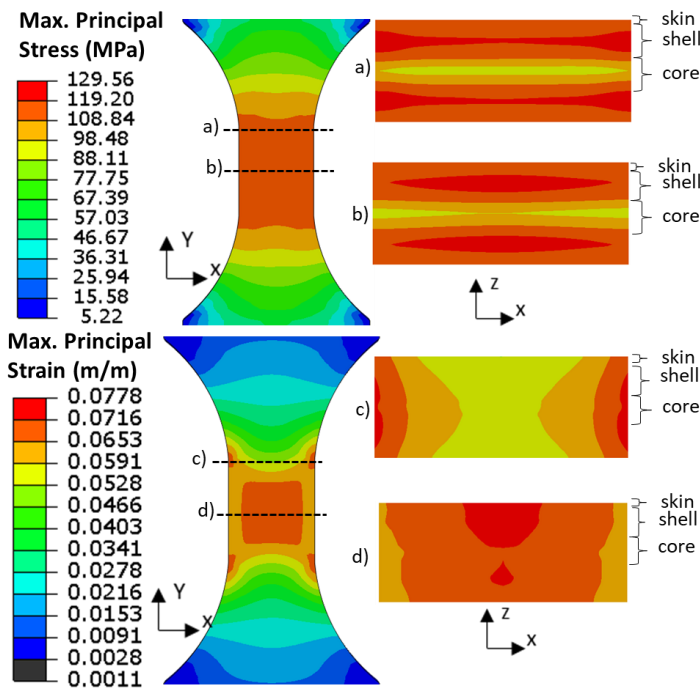


Figure 6-11 Cross sections of a 0° coupon under a 4kN tensile load showing the stress (a, b) and strain (c, d) distributions through the specimen's shoulder and middle section.

6.3.1.2 90° specimens

Figure 6-12a to f, show the stress and strain distribution for a 90° reference specimen under different load levels. On this sample the stresses are highly concentrated in the middle of the thickness, as shown in Figure 6-12a to c. This region corresponds to the core layer of the microstructure, and is where the fibres are more aligned with respect to the load direction. Higher stresses are also seen closer to the end of the shoulders of the coupon, with onset at relatively low loads, Figure 6-12a. On the main surface, the stresses show a more homogeneous distribution, concentrating more on the gauge area of the coupon. The stresses seen on this surface are approximate 22% lower than the ones seen in the core region on the samples' thickness-surface at the maximum load, Figure 6-12c. On the other hand, at lower and intermediate loads, the strain seem to distribute more homogeneously through the main and thickness surfaces of the coupon, as shown in Figure 6-12d and e. Under higher deformations, Figure 6-12f, the specimen does show a clear concentration of strain on both surfaces, particularly located at the corners and the centre of the gauge section. However, below the surface is the area with the highest strain with an approximate 3%.

Figure 6-13a and b show the through thickness stress distribution near the shoulder and in the middle of the 90° reference specimen at the maximum simulated tensile

load of 3kN. It can be seen that there is a clear distribution in the stresses which corresponds to the different skin-shell-core layers. It is also clear that in the shoulders, Figure 6-13a, the maximum stresses are concentrated all along the thickness of the specimen from surface to surface in the core layer, corresponding to the region where the fibres are mostly aligned with the load direction; this same distribution happens in the middle of the sample, Figure 6-13b, although the skin and shell layers are not clearly distinguishable. Figure 6-13c and d show the strain distribution under the same loads. Similar to the case of the 0° coupon, it can be seen that in the shoulder section, Figure 6-13c, the highest strain is located through the thickness and in the surface of the sample; whereas, in the middle section, Figure 6-13d, the maximum strains are distributed for the most part from one main surface to the other.

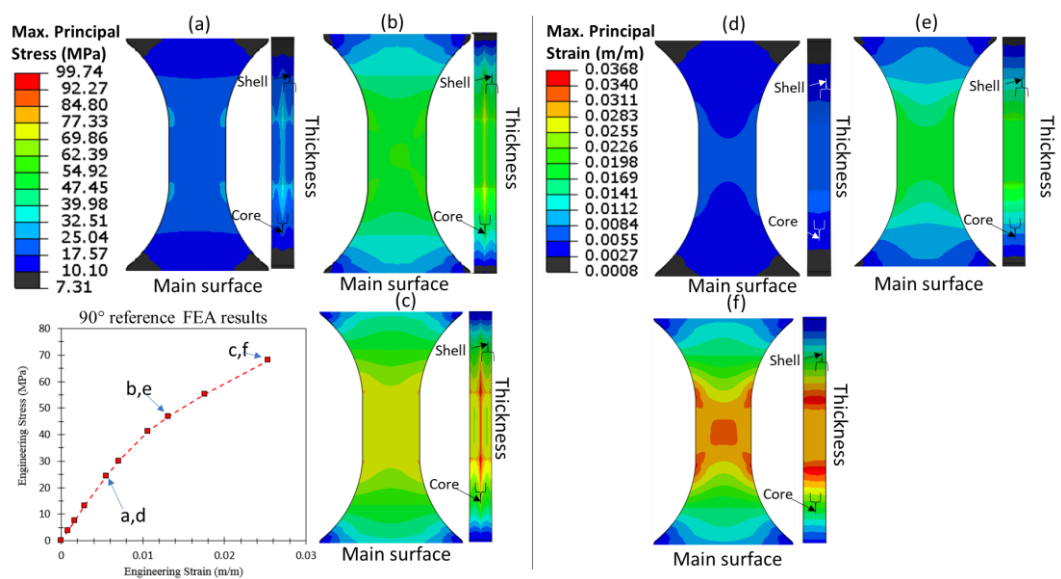


Figure 6-12 Evolution of the FE stress/strain distribution for a 90° reference specimen with $V_f=30\%$. Braces denote the approximate division between the shell and core layers in the structural model.

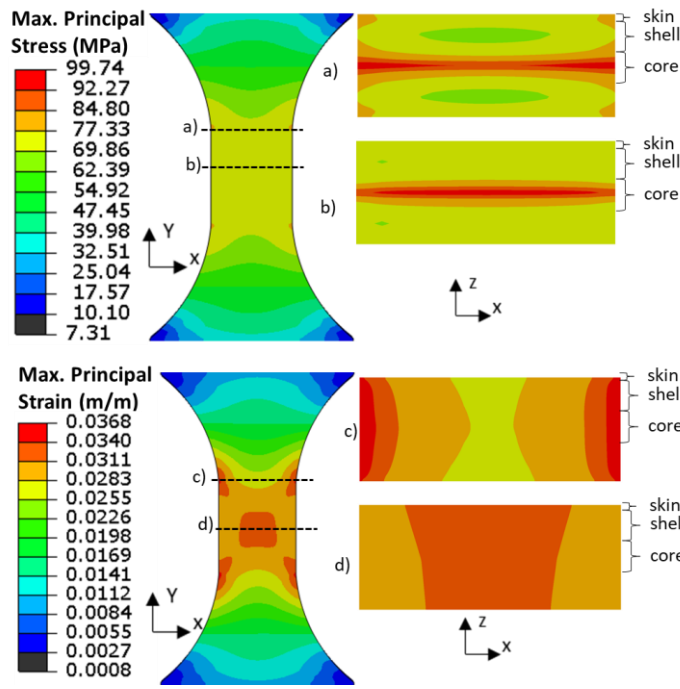


Figure 6-13 Cross sections of a 90° coupon under a 3kN tensile load showing the stress (a, b) and strain (c, d) distributions through the specimen's shoulder and middle section.

6.3.1.3 45° specimens

In contrast to the previous specimens, the 45° coupon presents a more mixed fibre orientation condition due to the angle at which the coupons are taken from the composite plate. In terms of stresses, there is a clear concentration occurring below the surface in a region located right in the middle of the thickness, as shown in Figure 6-14a. This section would correspond to the core layer on the known composite microstructure. However, opposite to the 0° and 90° specimens, this concentration of stress is not symmetrical. This difference is even clearer under higher loads, Figure 6-14c. The maximum stresses present at the middle of the coupon's thickness are approximate 20% higher than the surrounding areas. At these higher loads, another clear concentration of stress is seen on the main surface, which is located at the centre and at the corner of the gauge length section of the specimen. In terms of strain, a more homogeneous distribution is seen under low and intermediate loads, as presented in Figure 6-14d and e. With the largest values, up to 1.6%, located within the gauge length area. However, under higher loads the presence of strain concentrations is seen in the main and thickness surfaces, with the highest strain of approximate 4.5% located below the surface of the specimen, as shown in Figure 6-14f.

Figure 6-15a and b show the through thickness stress distribution near the shoulder and in the middle of the 45° reference specimen at the maximum simulated tensile load of 3.3kN. In the shoulder section, Figure 6-15a, is clear that the distribution of stresses is not symmetrical, probably due to the differences in the fibre orientation distribution and the particular orientation of this coupon. Similar is the case in the middle section, Figure 6-15b, although the asymmetry of results is not as clear. The maximum stress is located in the shoulder section and close to the surface of one of the specimen's sides. This skew of the results towards one side of the specimen is also seen on the strain field, Figure 6-13c and d. The highest strain is located in the shoulder section and towards one side, Figure 6-13c. The middle section, Figure 6-13d, shows a more evenly distributed strain, although the asymmetry is still observed.

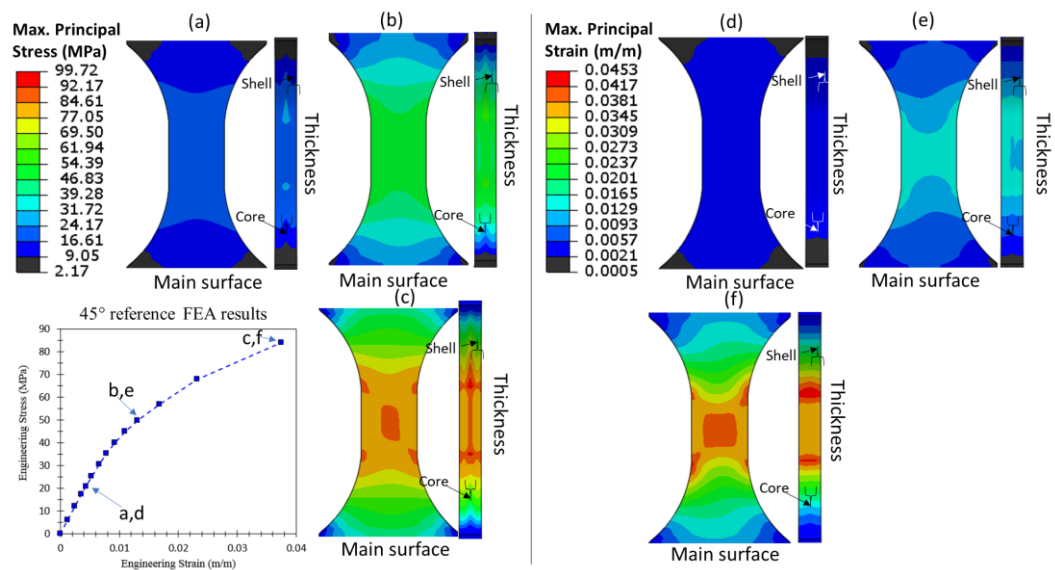


Figure 6-14 Evolution of the FE stress/strain distribution for a 45° reference specimen with $V_f=30\%$. Braces denote the approximate division between the shell and core layers in the structural model.

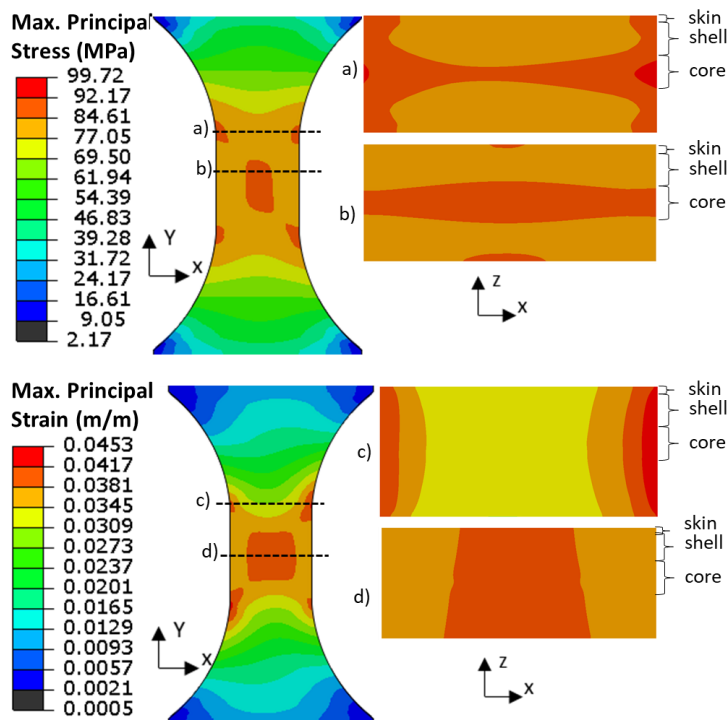


Figure 6-15 Cross sections of a 45° coupon under a 3.3kN tensile load showing the stress (a, b) and strain (c, d) distributions through the specimen's shoulder and middle section.

6.3.1.4 30° specimens

In a similar manner than the 45° specimen, the 30° reference coupon characterises by the mixed fibre orientation distribution that is product of the specific angle the specimens are cut from the composite plates. For this particular orientation the stresses on the main surface seem to be, for the most part, homogeneous in the gauge length area with particular higher levels at the corners of this section, as shown in Figure 6-16a and c. The stresses are particularly concentrated on areas closer to the specimen's shoulders, and below the surface (thickness view). Additionally, the stresses are not symmetrical. On the lower section of the specimen, the concentration is mostly located in regions that correspond to the shell layers, from the known composite's microstructure. On the other hand, in the upper section, the stresses mostly cover the full thickness of the specimen, Figure 6-16c. The strain fields also present asymmetrical results. At intermediate and higher loads, Figure 6-16e and f, a clear concentration of strain is observed on the thickness of the sample, and is mostly locate in the upper part of the coupon. On the main surface, the concentration is also asymmetrical and on opposite corners of the gauge section.

Figure 6-17a and b show the through thickness stress distribution near the shoulder and in the middle of the 30° reference specimen at the maximum simulated tensile load of 3.9kN. In the shoulder section, Figure 6-17a, one of the sides shows a larger zone with higher stresses than the other side. This is opposite to the results in the middle section, Figure 6-17b, where the stresses show a symmetry around the X axis. In terms of the strain field, the region closer to the shoulder, Figure 6-17c, shows a clear concentration below the surface and in one particular side; whereas in the middle section, Figure 6-17d, the strains are more evenly distributed from surface to surface.

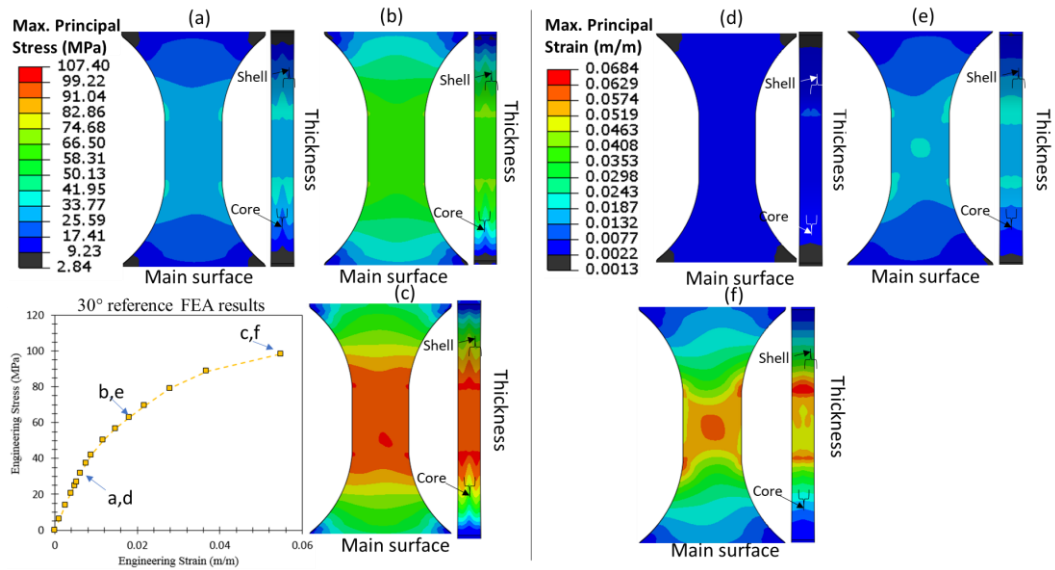


Figure 6-16 Evolution of the FE stress/strain distribution for a 30° reference specimen with $V_f=30\%$. Braces denote the approximate division between the shell and core layers in the structural model.

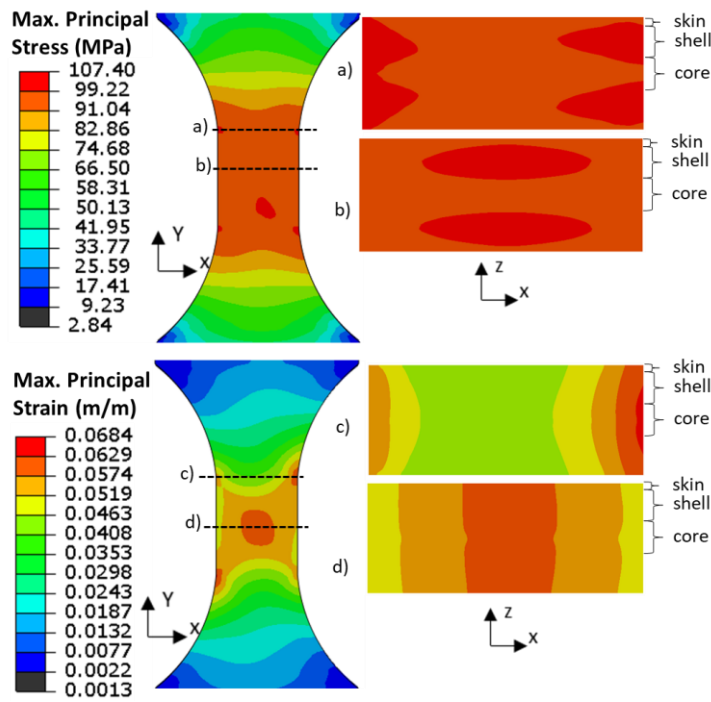


Figure 6-17 Cross sections of a 30° coupon under a 3.9kN tensile load showing the stress (a, b) and strain (c, d) distributions through the specimen's shoulder and middle section.

6.3.1.5 0° Edge specimens

Figure 6-18a to f, show the stress and strain fields for a 0° Edge specimen under different loads. The particular characteristic of this orientation is the location from where the samples are taken, as presented in Figure 6-3, and therefore the fibre orientation distribution. Looking at the main and thickness surfaces of the sample, it can be seen that the stress results are not symmetrical. On the main surface the concentration of the stresses seems to be located at the centre and at the corners of the gauge length section, Figure 6-18. On the thickness surface, higher stresses are located in the regions below the surface where fibres are expected to be more aligned with the load direction. Similarly, the strain field also shown an asymmetrical behaviour. On the main surface, the concentration of strain seems to be located at the centre and at corners of the gauge length area, Figure 6-18e and f. At higher loads the maximum strain, approximate 5%, seems to concentrate below the surface on the thickness of the coupon, as shown in Figure 6-18f.

Figure 6-19a and b show the through-the-thickness stress distribution near the shoulder and in the middle of the 0° edge specimen at the maximum simulated tensile load of 4.2kN. The stresses located near the shoulder, Figure 6-19a, show a clear

concentration towards the thickness sides; whereas in the middle section, Figure 6-19b, the stress distribution is fairly symmetrical and concentrated inside the specimen. It is good to mention that for both sections, the stresses are almost uniform, which could be due to the high alignment of the fibres in this orientation, as shown in Figure 6-3. On the other hand, the strain distribution, Figure 6-19c and d, show a variability with the location of inspection. The region around the shoulders, Figure 6-19c, presented a concentration of strain below the surface and was skewed toward one side. In the middle section of the specimen, Figure 6-19d, the highest strain was located in the region close to one of the main surface's sides, presenting an asymmetrical distribution.

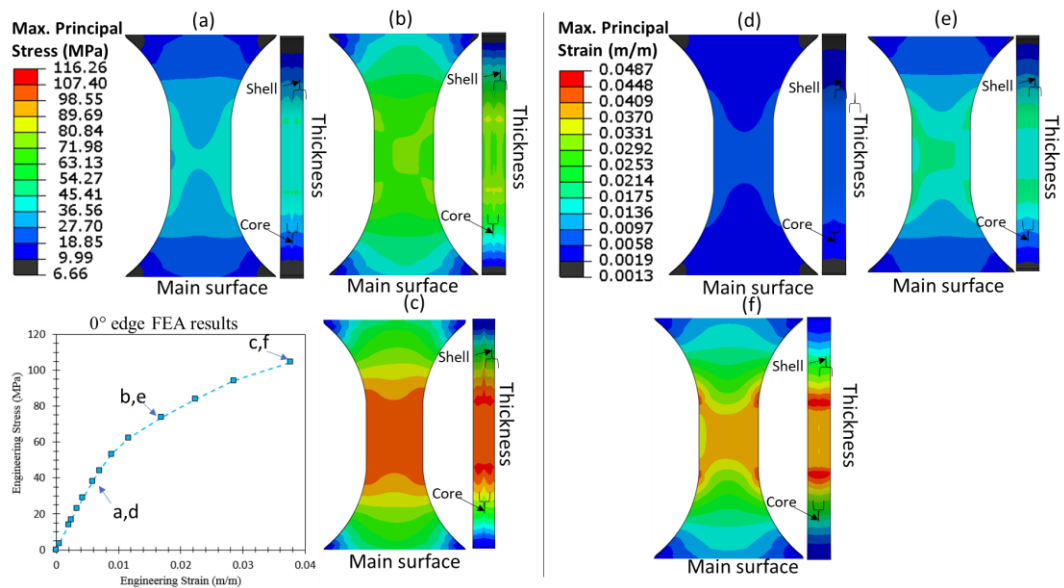


Figure 6-18 Evolution of the FE stress/strain distribution for a 0° Edge specimen with $V_f=30\%$. Braces denote the approximate division between the shell and core layers in the structural model.

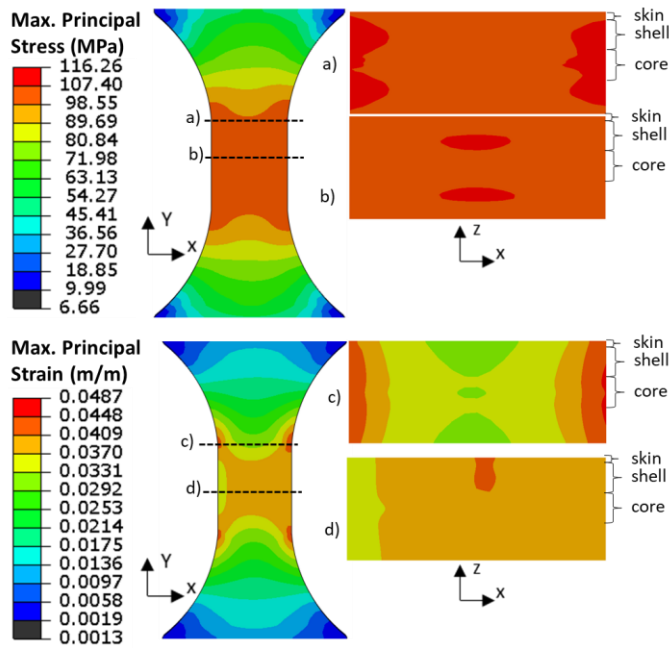


Figure 6-19 Cross sections of a 0° edge coupon under a 4.2kN tensile load showing the stress (a, b) and strain (c, d) distributions through the specimen's shoulder and middle section.

6.3.1.6 90° Edge specimens

Similarly to the previous sample, Figure 6-20a to f present the stress and strain fields for a 90° Edge specimen under different loads. The samples with this particular orientation are located closer to the fan gate, as shown in Figure 6-3. On this coupon, it can be seen that the stresses are mostly concentrated on the centre of the thickness, Figure 6-20c. This region, as in the case of the 90° reference specimen, corresponds to the core layer and is where the fibres are expected to be more aligned with respect to the load direction. In regards to the strain field, and at low and intermediate loads, the sample shows a more uniform distribution through the main surface, Figure 6-20d and e. At higher loads the strain seems to concentrate mostly below the surface, on the thickness, and closer to the end of the shoulders. A more uniform strains distribution is seen on the middle of the thickness of the sample.

Figure 6-21a and b show the through-the-thickness stress distribution near the shoulder and in the middle of the 90° edge specimen at the maximum simulated tensile load of 3kN. The stresses located near the shoulder, Figure 6-21a, show a clear concentration towards the centre in the core layer, with the highest being below the specimen's surface and on the sides. A similar layered distribution can be seen in the middle section of the coupon, Figure 6-21b, where the highest stress is located in the

centre of the core layer inside the specimen; on this section the classic skin-shell-core distribution is easily identifiable. In regards to the strain distribution, Figure 6-21c and d, the region near the shoulders, Figure 6-21c, shows a clear concentration below the surface and on the sides of the specimen, with a clear symmetry around the Z axis. On the other hand, in the middle section, Figure 6-21d, the strain are mostly skewed towards one of the specimen's main surface's sides, with also symmetry around the Z axis.

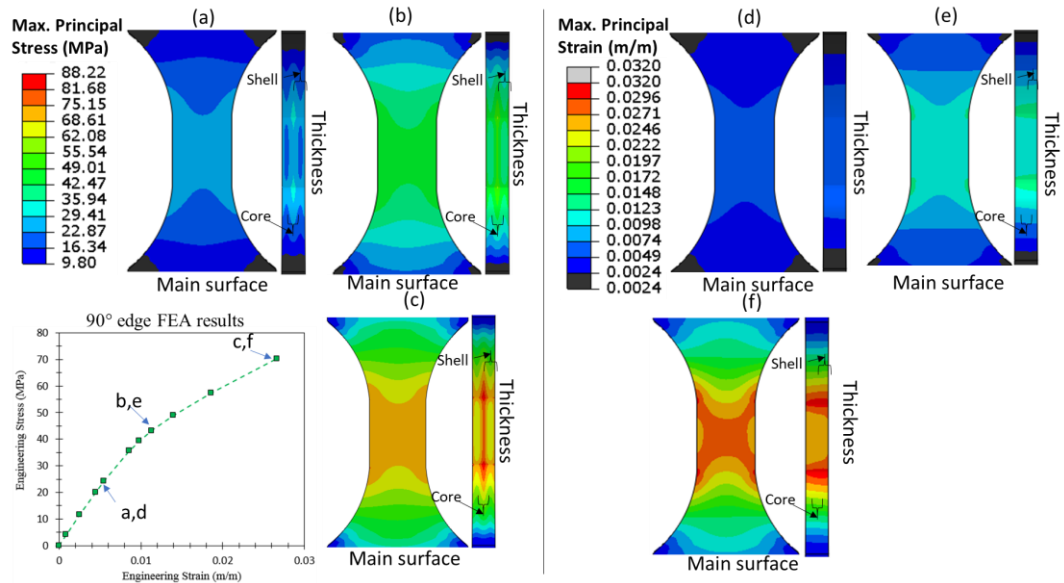


Figure 6-20 Evolution of the FE stress/strain distribution for a 90° Edge specimen with $V_f=30\%$. Braces denote the approximate division between the shell and core layers in the structural model.

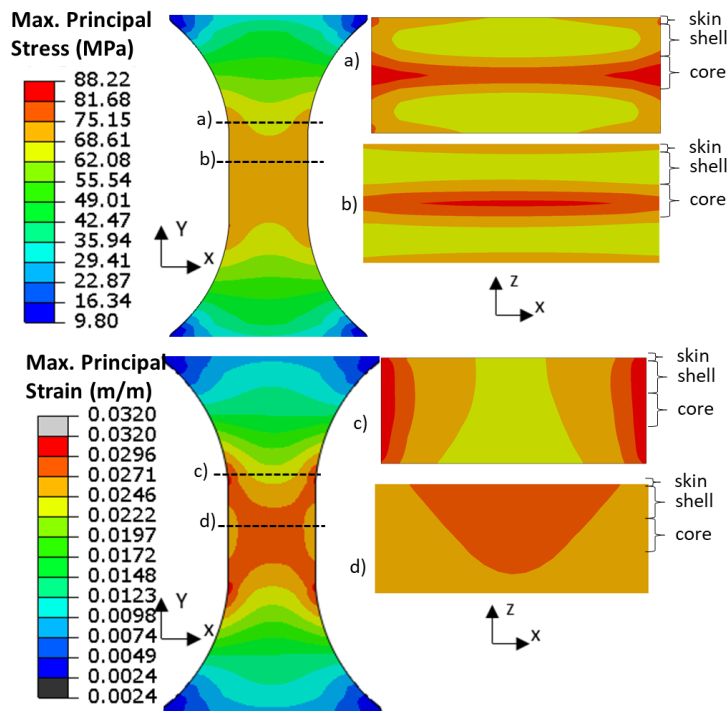


Figure 6-21 Cross sections of a 90° edge coupon under a 3kN tensile load showing the stress (a, b) and strain (c, d) distributions through the specimen's shoulder and middle section.

6.4 Fatigue modelling results

The following section details the results of the fatigue modelling. The initial results shown correspond to the Stress-Life approach, under two different stress ratios, $R=0$ and $R=-1$. The resultant Basquin's equations, power law equations, for each of the SN curves are also presented. The second methodology corresponds to the Energy based approach results, which is based on the calculation of the dissipated energy (total hysteresis loop area). The results of the methodology proposed to correct for mean stresses, i.e. Walker's equation, is also documented on this section.

6.4.1 Stress-Life fatigue modelling

6.4.1.1 Stress ratio $R=0.0$ results

The first part of the fatigue modelling corresponded to the analysis under $R=0$. This was because the results for each different orientation, in terms of SN data, are equidistant from each other, i.e. 30° and 45° experimental results lay between 0° and 90°. This can be observed in Figure 5-11.

Figure 6-22 shows the S-N modelling results at $R=0$ for different orientations. For this particular case, experimental data for 0° , 45° and 90° reference specimens (square points) was used to calibrate the model. The "Model calibration" curves are represented by the dash lines on this figure. Finally, 30° reference, 0° Edge and 90° Edge specimens were used for the model prediction. Figure 6-23 shows the FEA life distribution for the reference specimens used to calibrate the model, i.e. 0° , 45° and 90° specimens, under a stress amplitude of 30MPa. Figure 6-24 shows the distribution of lives for the samples used for validation, i.e. 30° reference, 0° Edge and 90° Edge, at the same stress level. For all cases the element with the lowest life was located under the surface of the specimen, on the thickness. It is good to mention that the location of lowest fatigue life shown in these modelling results, which is through the thickness and around the shoulders, is also the location where most of the actual failures occurred. As is presented in Figure 7-15, approximate 75% to 88% of the specimens failed around this region. Additionally, as captured by the high speed cameras, cracks were also observed to have first appeared on this region, as shown in Figure 5-43.

On Figure 6-22 the resultant fully oriented curves for 0° , 45° and 90° reference curves can be seen (solid lines). These curves assumed that the fibres on each specimens are all oriented at the same direction, as in unidirectional composites. The 0° fully oriented curve, all fibres aligned with respect to the load, presents the best performance of all specimens. The 90° fully oriented curve, all fibres aligned orthogonal to the load, the worst. It is good to mention that all the rest of the data lay in between these two curves.

In terms of modelling prediction, in Figure 6-22 it can also be observed that the predicted curve for the 30° reference specimen lays close to the experimental data, almost overlapping with each other. The 0° Edge specimen model predicted curve presents a better fatigue performance than the 0° reference specimen, and the rest of the other orientations. This is due to the more consistent alignment of the fibres towards to load direction, as it is shown in Figure 6-4. In this regard, the 90° Edge specimen model predicted curve shows a very close behaviour to the regular 90° reference specimens, although slightly better. This is also due to the fibre alignment presented in this specimen orientation, Figure 6-4.

The actual predicted curves, in terms of the Basquin's equation, for each of the specimens can be seen in Table 6-2. Comparison between the Model calibration curves and the Experimental data (linear regression curves) shows a very close agreement. Predicted curves are highlighted in green on this table.

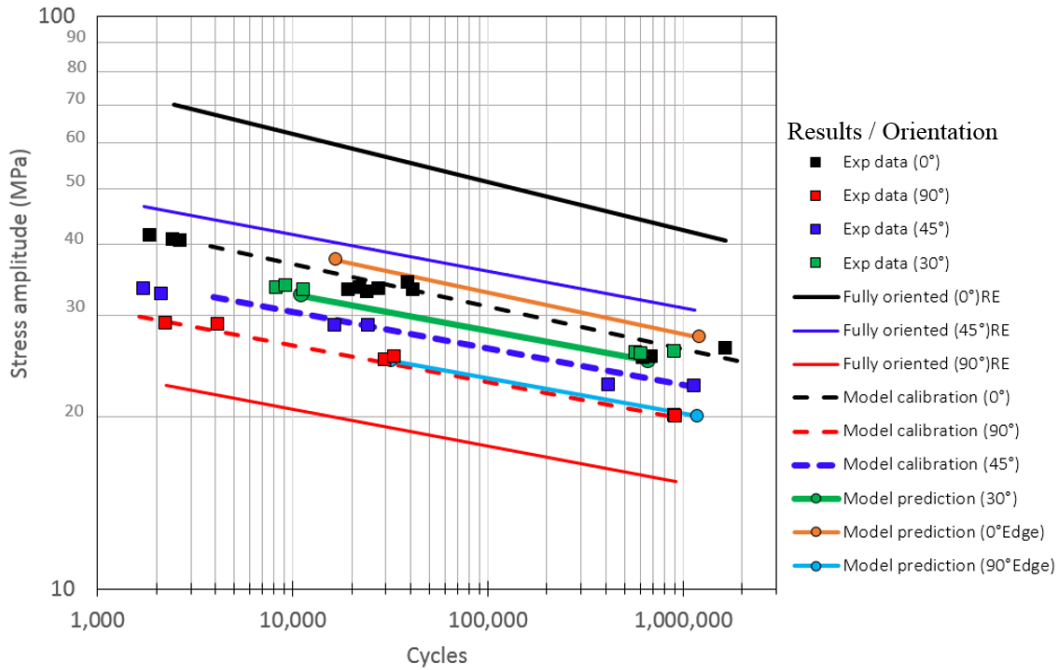


Figure 6-22 Result of the S-N fatigue modelling for R=0.0. Model uses 0°, 45° and 90° reference specimens for calibration.

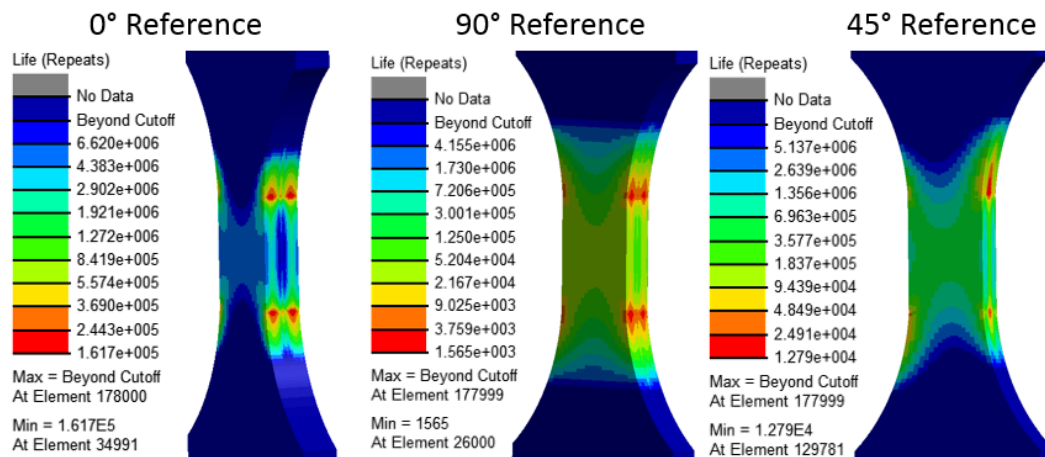


Figure 6-23 FEA-Life distribution for 0°, 45° and 90° reference specimens under R=0 and $\sigma_a=30$ MPa (Cut-off at 1×10^7 cycles).

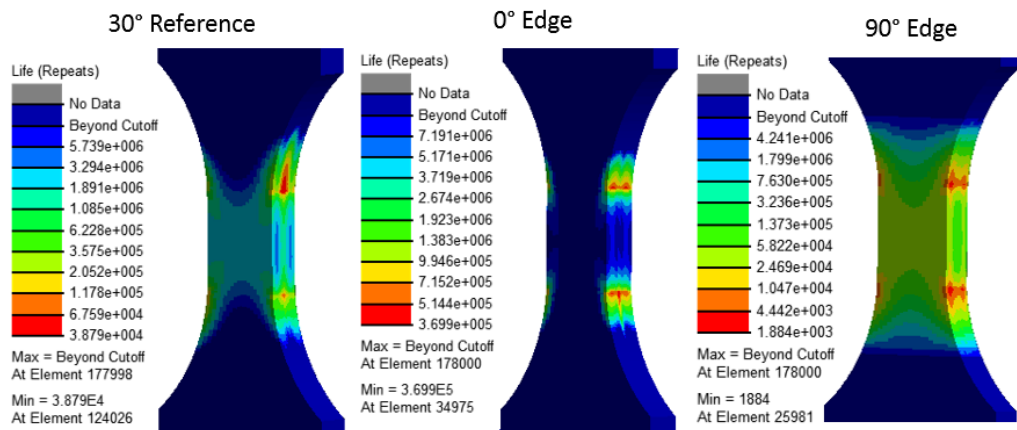


Figure 6-24 FEA-Life distribution for 30° reference, 0°Edge and 90°Edge Specimens under R=0 and $\sigma_a=30$ MPa (Cut-off at 1×10^7 cycles).

Table 6-2 Experimental and modelling Basquin's equations for R=0. Model uses 0°, 45° and 90° reference specimens for calibration.

Basquin's equations				
Specimen	Exp. Data	Modelling results		
	Linear regression	RE Fully aligned	Model calibration	Model Prediction
0°	$\sigma_a=73N^{-0.076}$	$\sigma_a=135N^{-0.084}$	$\sigma_a=73N^{-0.074}$	-
90°	$\sigma_a=49N^{-0.065}$	$\sigma_a=37.5N^{-0.065}$	$\sigma_a=48N^{-0.064}$	-
45°	$\sigma_a=54N^{-0.064}$	$\sigma_a=75N^{-0.064}$	$\sigma_a=55N^{-0.064}$	-
30°	$\sigma_a=58N^{-0.060}$	-	-	$\sigma_a=59N^{-0.064}$
0° Edge	-	-	-	$\sigma_a=75.7N^{-0.072}$
90° Edge	-	-	-	$\sigma_a=47.4N^{-0.062}$

Fatigue predictions were recalculated, but this time with the minimum amount of experimental data. This was done to test the limitations of the model. Therefore, for this case only 0° and 90° reference curves were used for calibration. In Figure 6-25 it can be observed the predicted curve for the 45° reference specimen shows good agreement with the experimental data, in particular at intermediate and longer lives. For the case of the predicted 30° reference curve, the agreement is good at lower lives, and shows a more conservative results at longer lives. The predicted curve for 0° Edge specimen still presents relative higher lives than the 0° reference specimen, although the difference is reduced in comparison to Figure 6-22. This is also the case for the predicted 90° Edge specimen curve.

Table 6-3 presents the Basquin's equations, power law, for the predicted curves for each of the different specimens orientations (highlighted in green). A comparison between fatigue predictions obtained by using these functions and by using the ones presented in Table 6-2 indicate that with only two curves for calibration of the model, the life predictions for the 30° reference, 0°Edge and 90° Edge specimens are reduced by, respectively, 50%, 70% and 77% in average. This comparison was done by calculating lives at different stress amplitudes for each curve shown in Table 6-3, and then comparing them against the results using the curves shown in Table 6-2; for each particular orientation.

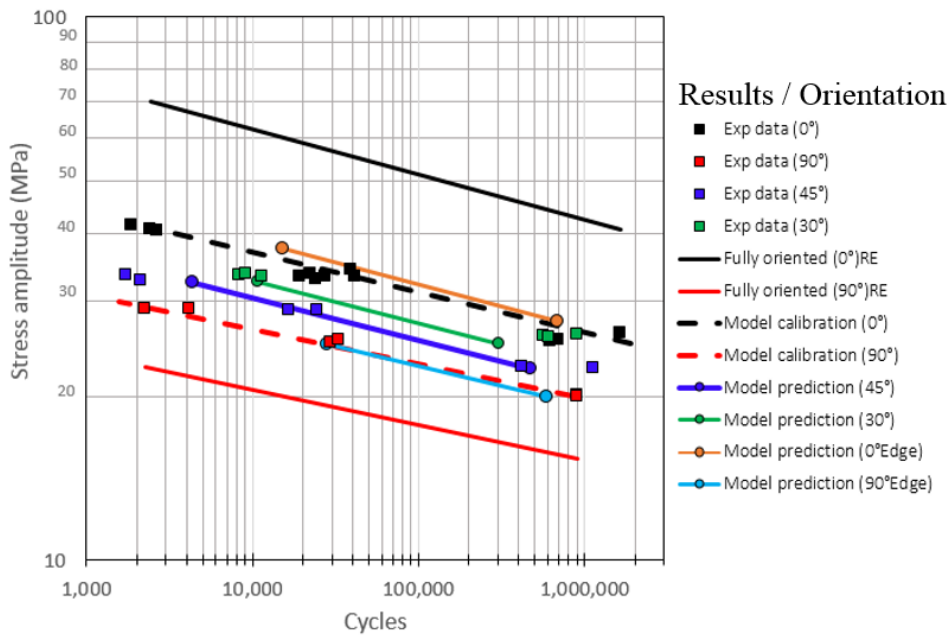


Figure 6-25 Result of the S-N fatigue modelling for R=0.0. Model uses only 0° and 90° reference specimens for calibration.

Table 6-3 Experimental and modelling Basquin's equations for R=0. Model uses only 0° and 90° reference specimens for calibration.

Basquin's equations				
Specimen	Exp. Data	Modelling results		
Orientation	Linear regression	RE Fully aligned	Model calibration	Model Prediction
0°	$\sigma_a=73N^{-0.076}$	$\sigma_a=135N^{-0.084}$	$\sigma_a=73N^{-0.074}$	-
90°	$\sigma_a=49N^{-0.065}$	$\sigma_a=37.5N^{-0.065}$	$\sigma_a=48N^{-0.064}$	-
45°	$\sigma_a=54N^{-0.064}$	-	-	$\sigma_a=62.7N^{-0.079}$
30°	$\sigma_a=58N^{-0.060}$	-	-	$\sigma_a=67.4N^{-0.079}$
0° Edge	-	-	-	$\sigma_a=81.8N^{-0.081}$
90° Edge	-	-	-	$\sigma_a=53N^{-0.073}$

6.4.1.2 Stress ratio R=-1.0 results

After the model was implemented with success under R=0 stress ratio, the same methodology was used for fully reversed conditions. The first step was to calibrate the model using 0°, 45° and 90° reference experimental data. Figure 6-26 and Table 6-4 show the results of the model under R=-1, where for this particular condition no convergence was obtained using this methodology. In Figure 6-26, it can be seen that the Model calibration curves (dash lines) do not correlate with their respective experimental data (square points). This unsuccessful calibration is due to the behaviour of the 45° and 90° reference data. From Figure 5-11 it can be seen that both orientations shown a very similar behaviour, with specimens' data points overlapping with each other; and as explain in Chapter 4 of this thesis, the SN approach uses a linear interpolation between the different specimens curves to calculate a particular fibre orientation, Figure 4-17. What this means is that if the data used for calibration is no equidistant to each other, as in the case of R=-1, the modelling cannot be successfully calibrated. The life predictions resultant under such conditions are then heavily conservative and not real.

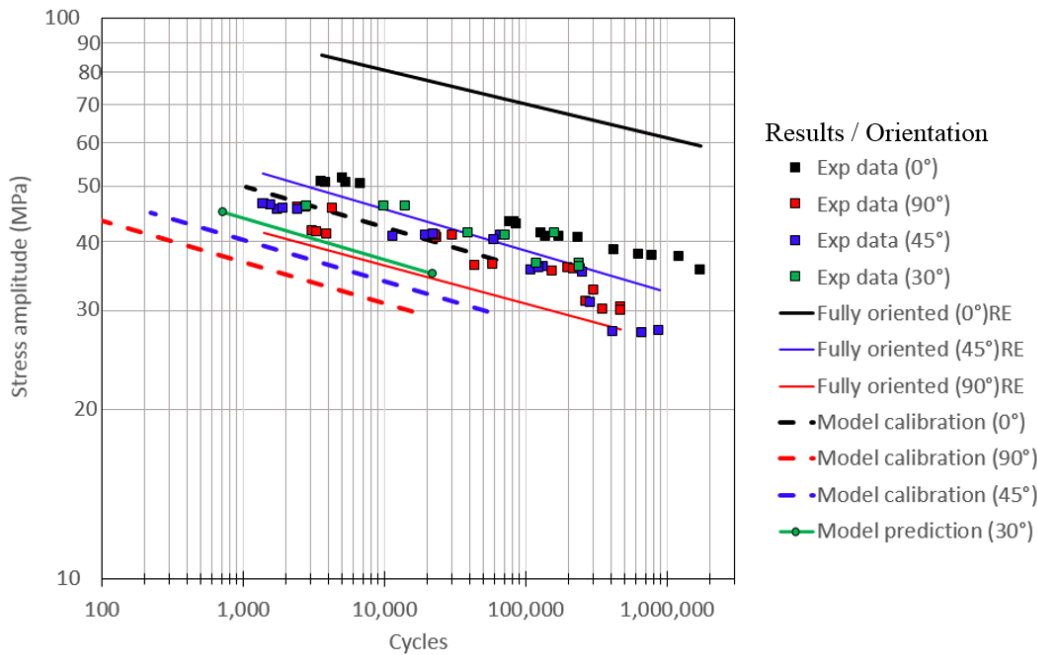


Figure 6-26 Result of the S-N fatigue modelling at the reference location for R=-1.0. Model uses 0°, 45° and 90° reference specimens for calibration.

Table 6-4 Experimental and modelling Basquin's equations for R=1. Model uses 0°, 45° and 90° specimens for calibration.

Basquin's equations				
Specimen	Exp. Data	Modelling results		
Orientation	Linear regression	RE Fully aligned	Model calibration	Model Prediction
0°	$\sigma_a = 84.3N^{-0.06}$	$\sigma_a = 140N^{-0.06}$	$\sigma_a = 83.6N^{-0.074}$	-
90°	$\sigma_a = 76.5N^{-0.068}$	$\sigma_a = 67.5N^{-0.068}$	$\sigma_a = 61.1N^{-0.074}$	-
45°	$\sigma_a = 82.5N^{-0.074}$	$\sigma_a = 90N^{-0.074}$	$\sigma_a = 67N^{-0.074}$	-
30°	$\sigma_a = 77.4N^{-0.059}$	-	-	$\sigma_a = 73N^{-0.074}$

A simplified version of the previous methodology was tested by using only two curves to calibrate the model. This is, using only 0° and 90° reference data. Figure 6-27 and Table 6-5 show the results in terms of predicted SN curves and their respective Basquin's equations. As it can be seen in Figure 6-27 a better calibration was obtained for this particular case, the model calibration curves (dash lines) correlate better with the same orientation experimental data (square points), for 0° and 90° specimens. Fatigue predictions for 30° and 45° specimens correlate better with the experimental data. However, although better results were obtained using only two curves, this

action overlooks the effect of the fibre orientation under R=-1 conditions, and might not represent the actual material behaviour.

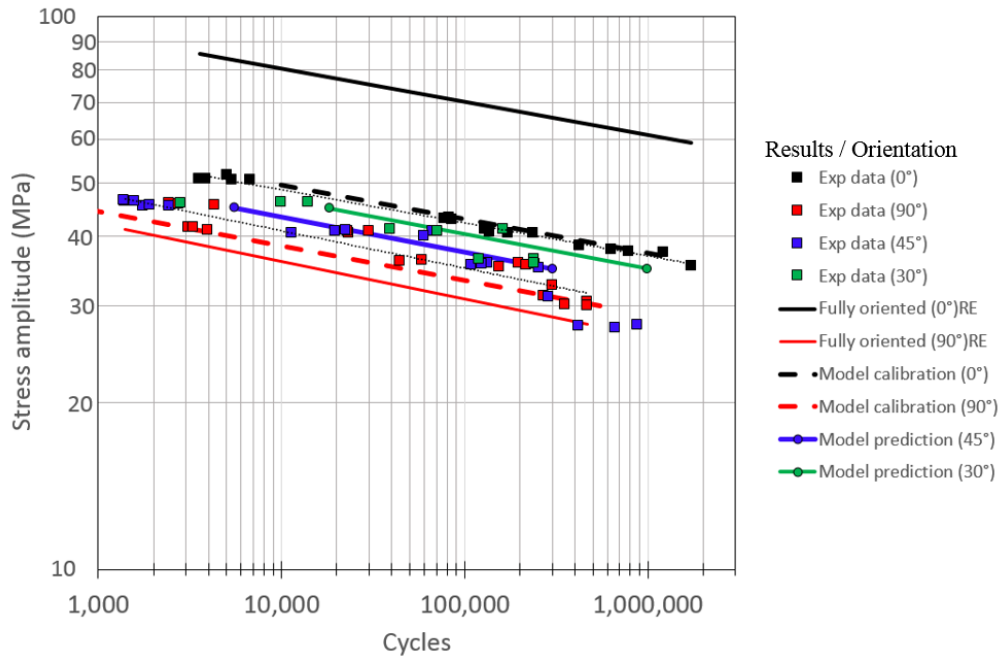


Figure 6-27 Result of the S-N fatigue modelling at the reference location for R=-1.0. Model uses only 0° and 90° reference specimens for calibration.

Table 6-5 Experimental and modelling Basquin's equations for R=1. Model uses only 0° and 90° reference specimens for calibration.

Basquin's equations				
Specimen	Exp. Data	Modelling results		
Orientation	Linear regression	RE Fully aligned	Model calibration	Model Prediction
0°	$\sigma_a = 84.3N^{-0.06}$	$\sigma_a = 140N^{-0.06}$	$\sigma_a = 87N^{-0.061}$	-
90°	$\sigma_a = 76.5N^{-0.068}$	$\sigma_a = 67.5N^{-0.068}$	$\sigma_a = 68N^{-0.062}$	-
45°	$\sigma_a = 82.5N^{-0.074}$	-	-	$\sigma_a = 77.4N^{-0.063}$
30°	$\sigma_a = 77.4N^{-0.059}$	-	-	$\sigma_a = 83.5N^{-0.063}$

6.4.1.3 Mean stress correction

The different mean stress correction relationships described in Chapter 4, i.e. Goodman, Gerber, Soderberg and Walker; were applied on the fatigue stress-life data for the different orientations and stress ratios. The results of implementing this correction methodologies in R=0 and R=0.3 data are presented below. Additionally, when a particular relationship called for the UTS or Yield strength, those values were

taken from the average of the calculated material parameters for each particular orientation, as presented in Figure 5-8.

Figure 6-28 shows the mean stress correction for the 0° reference specimens. From the four different relationships applied, it can be seen that the Goodman, Gerber and Soderberg equation, showed results far from the experimental data. However, the one that provided with the better correction was the Walker equation with a coefficient of $\gamma=0.45$, obtained by comparing R-squared values. Similarly, Figure 6-29 presents the mean stress correction for the 90° reference. As with the case for the 0° reference specimens, Goodman, Gerber and Soderberg presented with least accurate correction of stresses. The Walker correction provided again the with best fit when using a $\gamma=0.30$. Finally, Figure 6-30 presents the results of the mean stress correction for 45° reference specimens. Again and similarly to the previous cases, Goodman, Soderberg and Gerber corrections showed very poor correlation with R=-1 data. The walker equation achieved the best agreement with the fully reversed data when a $\gamma=0.45$ was used. Table 6-6 presents a compilation of the different Walker coefficients, γ , obtained for the different orientations and stress ratios. Interestingly, with the exception of 90° reference specimens, the same values for the Walker coefficient were obtained for 0° and 45° reference under R=0 and R=0.3 stress ratios. Nevertheless, it is also clear that the application of the Walker equation provided with a sensible correction of mean stresses, which was mainly due to the fact that the Walker coefficient, γ , acted as a fitting parameter that could be varied until reaching the best correlation between the data at different R ratios.

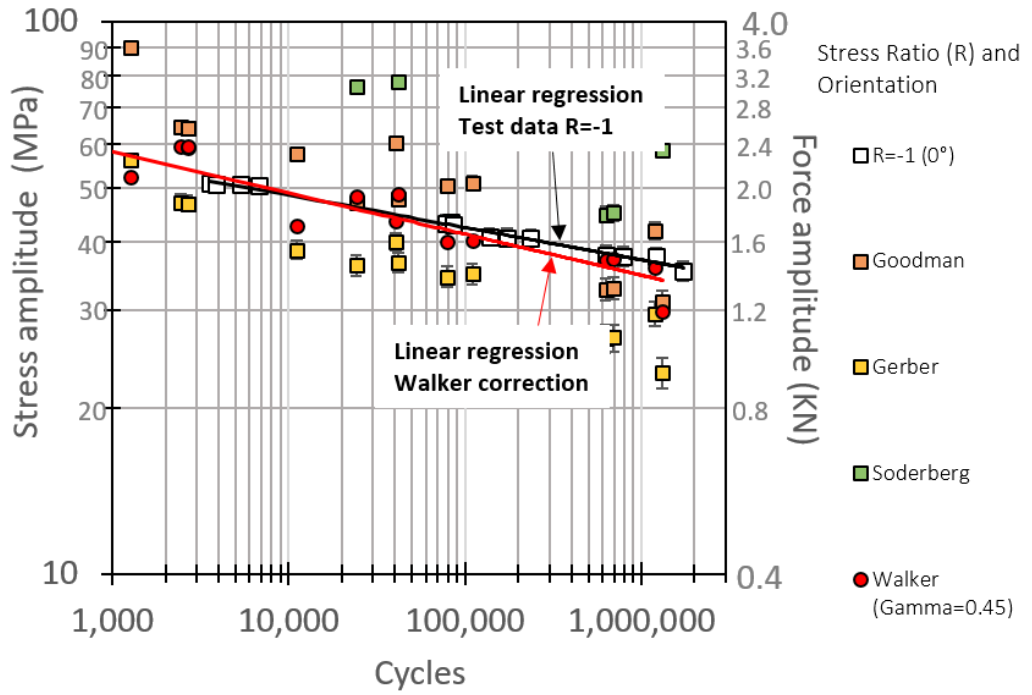


Figure 6-28 Mean stress correction for 0° reference specimens at R=0 and 0.3.

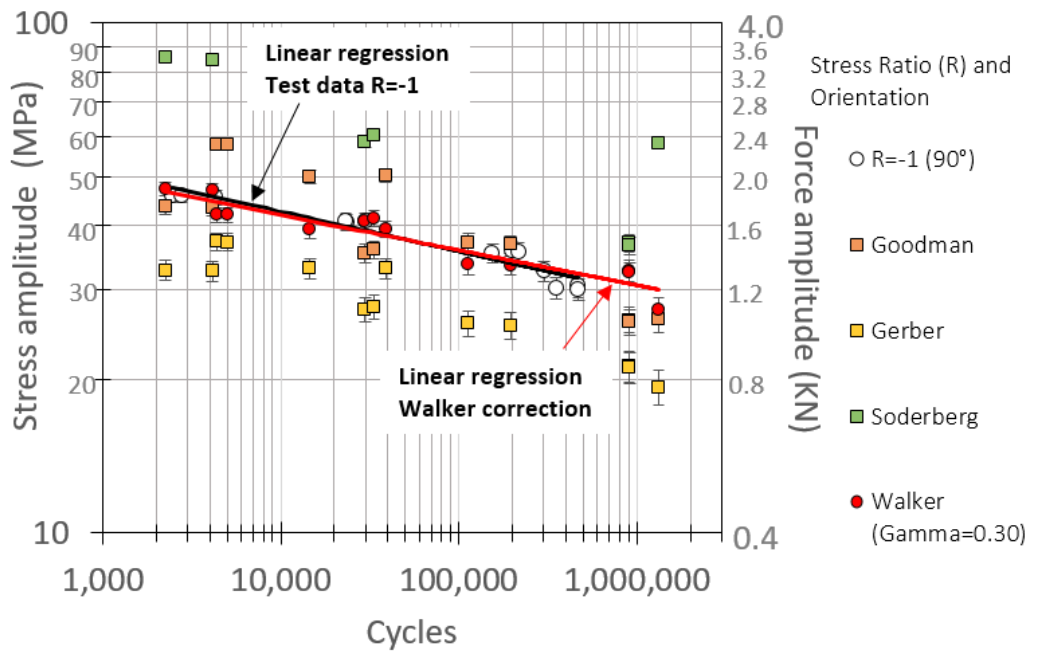


Figure 6-29 Mean stress correction for 90° reference specimens at R=0 and 0.3.

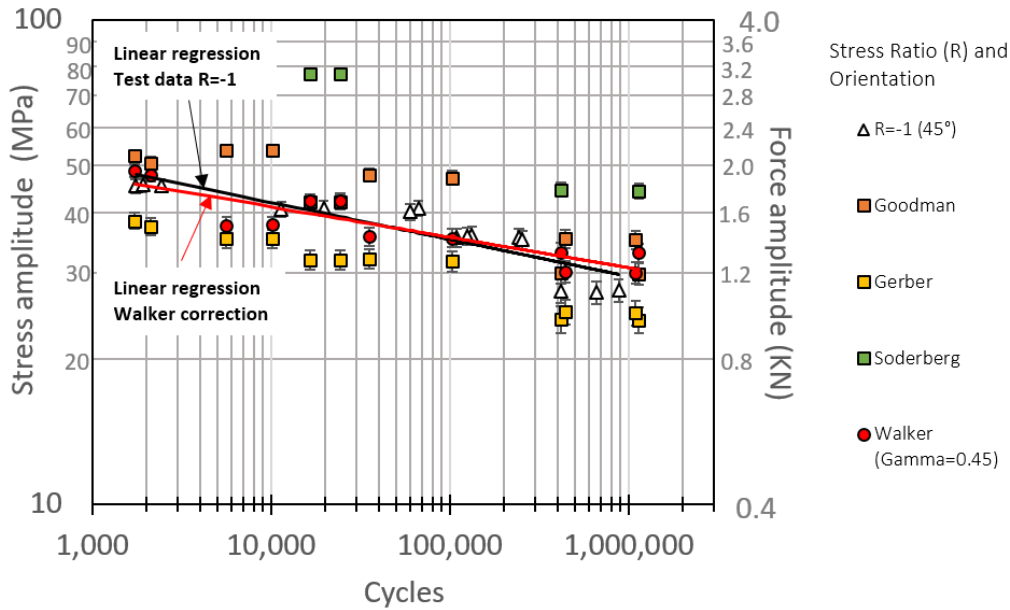


Figure 6-30 Mean stress correction for 45° reference specimens at R=0 and 0.3.

Table 6-6 Walker coefficient (γ) for different orientation and stress ratios.

Orientation	Stress ratio	Walker coefficient γ
0°	R=0	0.45
	R=0.3	
90°	R=0	0.30
	R=0.3	
45°	R=0	0.45
	R=0.3	

6.4.2 Extension of the Energy-based approach

Based on the results obtained with the Stress-Life based approach two things were clear: First, the material behaviour is highly dependent of the fibre orientation. Second, there is a clear influence of the mean stress in the material's fatigue performance. Therefore, a different approach was needed that could take into account these two factors. To this effect, an Energy approach was proposed based on the obtained experimental data. From Chapter 2, in the literature short fibre reinforced nylon is normally considered as linear elastic to simplify the fatigue calculations. However, as seen on Chapter 5, the experimental results indicate that the material experiences a

significant loss of energy, most likely due to the plastic and viscous effects of the matrix. Therefore, to try to better characterise the behaviour of the material, an energy method based on the dissipated energy, instead of the elastic strain energy density, was proposed.

From the experimental results presented in Chapter 5, the stabilised hysteresis areas that represent the energy dissipated were calculated for different specimen orientations under $R=0$ and $R=-1$ stress ratios. These hysteresis areas were then considered as the fatigue parameter, instead of stress, and were plotted against the total life of the specimens. Only specimens with stabilised hysteresis loops were used for this, which means that any specimen with less than 10,000 cycles of life were discarded. This is because on specimens with low lives, $<10,000$ cycles, the hysteresis loops never stabilised, and the total dissipated energy keep increasing until failure, as shown in Figure 5-21.

Figure 6-31 shows the Dissipated energy vs Life curves for different specimen orientations at $R=0$ and $R=-1$. It can be seen that the spread of the data caused by the orientation of the specimen seems to have diminished, with points laying close to each other. This is different to what was seen using the SN approach, Figure 6-22.

To assess the spread of the data, a linear regression, power law, was carried out on the data. The coefficient of determination, or R^2 , was used to provide with means of measurement on how well the curve fits the data points. Figure 6-32 presents the fits for each stress ratio. For both cases a large positive linear association is seen with values of 0.86 and 0.94, where following the notation presented in Equation 4-17,

for $R=-1$

$$W = 72.691N^{-0.31}$$

Equation 6-1

and for $R=0$

$$W = 19.314N^{-0.253}$$

Equation 6-2

This indicate that for each stress ratio, even though the data comes from different specimens' orientations, they seem to behave as part of the same data sample and can be described as a whole by a single function.

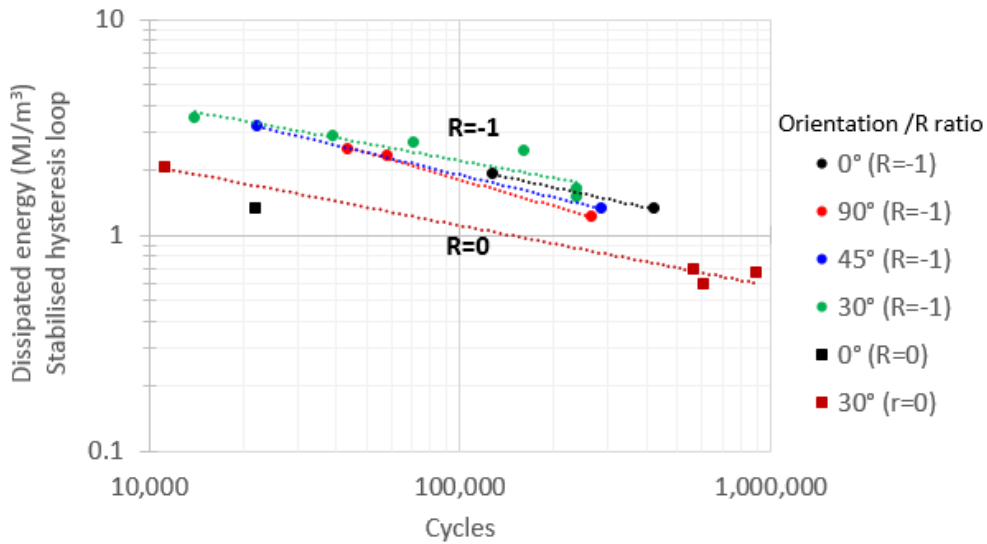


Figure 6-31 Experimental Dissipated Energy vs Life data for specimens at different orientations.

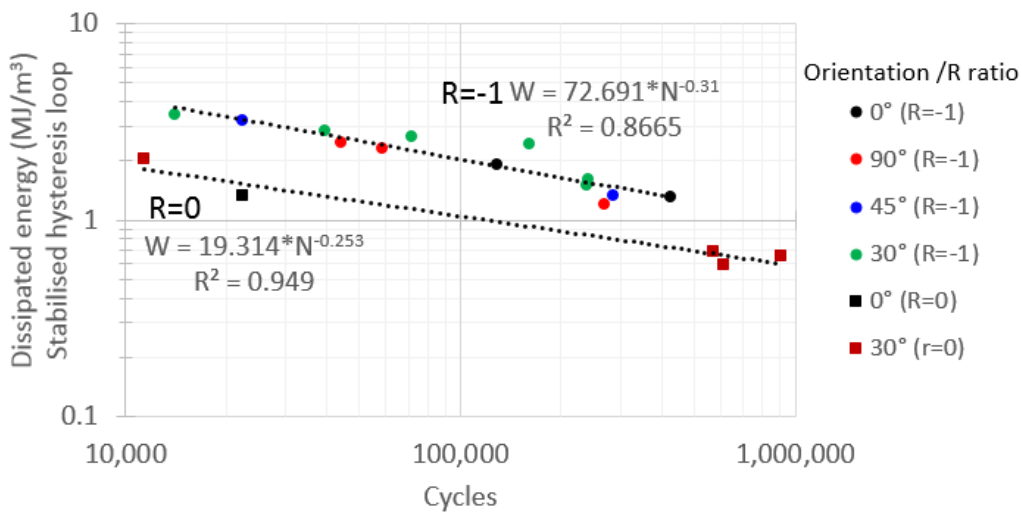


Figure 6-32 Experimental Dissipated Energy vs Life curves for specimens at different orientations at R=-1 and R=0.

6.4.2.1 Mean stress correction

Based on the previous results, Figure 6-32, a clear effect of the mean stress was seen. Therefore, and as detailed in Chapter 4, an approach using the Walker correction was postposed, but considering the dissipated energy instead of the stress amplitude. Per Equation 4-16 the Walker correction can be described in terms of stress amplitude and stress ratio as:

$$\sigma_{walker} = \sigma_a \left(\frac{2}{1-R} \right)^{1-\gamma}$$

Following the concept that the dissipated energy follows a similar trend to the S-N approach. If the Walker equivalent stress (σ_{walker}) and stress amplitude (σ_a), are then substituted by an equivalent "Walker dissipated energy" ($W_{corrected}$) and by the dissipated energy of the stabilised loop (W_a), respectively. Then, a new relation can be derived, such that:

$$W_{corrected} = W_a \left(\frac{2}{(1-R)} \right)^{1-\gamma}$$

Equation 6-3

Where the main driver of the mean stress correction would be: the stress ratio and a fitting coefficient (γ). γ can be thought as a of mean stress sensitivity material parameter [160]. A high value, like $\gamma=1$, would mean no mean stress sensitivity at all. This is, no matter the stress ratio, the material fatigue response does not change with any non-zero mean stress, and there is no correction done because the material is not affected by it. In the opposite, a lower γ value would suggest that the material has a higher mean stress sensitivity, i.e. the change of the material response under non-zero mean stresses is very large. Data for 0°, 45° and 90° reference specimens, at R=0 and R=-1, was used to find the coefficient that best fitted the experimental data using Equation 6-3. This is shown in Figure 6-33, where it can be seen that with $\gamma = 0.1$, a R² of 0.91 was achieved. Therefore the corrected dissipated energy is given by:

$$W_{corrected} = 56.238N^{-0.296}$$

Equation 6-4

From Figure 6-33 it can be seen that using this dissipated energy based mean stress correction approach seems to provide with adequate results for R=0.

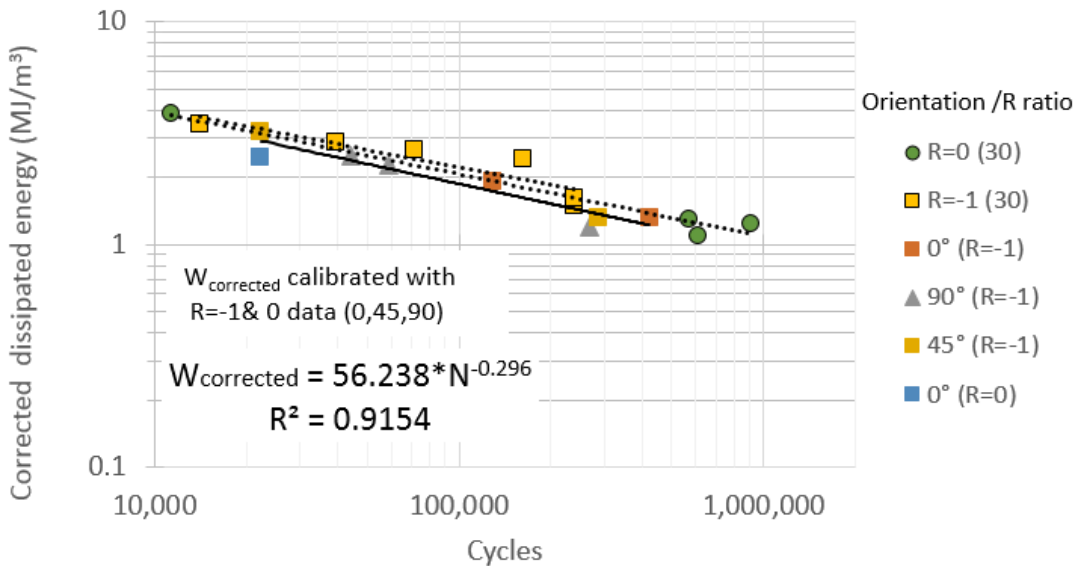


Figure 6-33 Mean stress correction. Corrected dissipated energy vs Life curve.

6.5 Conclusion

This chapter presented the results of the modelling program and CAE methodology. Unlike other published work, e.g.[71], the present thesis showed that for the current application, a non-linear elasto-plastic model better defines the mechanical response of the composite under study. The clear heterogeneity in terms of the stress and strain fields, produced by the fibre orientation distribution, was mapped successfully with the presented finite element model. Different to other similar applications of the S-N approach [71], [171], the presented methodology has mapped all the modelling stages needed for the multi-scale modelling of the fatigue behaviour of this type of composites, and it has also shown that fatigue material data obtained from thicker specimens is adequate to calibrate the model. Additionally, unlike other reported results, e.g. [171], [172], this work has shown that calibration using two specimens curves can provide with sensible results, therefore minimising the amount of experimentation needed. The effectiveness of different means stress correction techniques has also been shown. Likewise, the current limitations of the S-N approach has also been investigated. Different to other published energy-based approaches, e.g. [2], [92], [94], this work showed the effect of using a fatigue parameter based in the dissipated energy, instead of the elastic energy density, to account for the plastic behaviour inherent of this type of materials. Commonly known Walker's relationship for means stress correction seemed to provide with sensible results when applied to the energy data, although this was based only on experimental results. It is good to mention that determining the correct value for γ is purely empirical. This is, finding

the curve that best minimizes the difference between $R=0$ and $R=-1$ data (i.e. correcting for non-zero mean stresses), and this would need to be obtained for different materials through testing. Another remark is that γ could be considered as a mean stress sensitivity material parameter [160]. This is, different materials will show different sensitivities to the non-zero mean stresses. If γ is large it would mean that the material is not sensitive to mean stresses. The opposite is the case for lower γ values. Finally, this combination of the use of Walker equation in the energy realm, and the proposed Dissipated Energy-Life approach, seems to provide with a way of correcting for non-zero mean stresses in the composite, while being less sensitive to the material microstructure, i.e. fibre orientation tensor. However, this is based on these initial results, further testing and validation is needed to arrive to a more conclusive answer.

7. DISCUSSION

7.1 Introduction

In this chapter the previous experimental and numerical results are analysed and discussed together, in a holistic manner, in order to seek a better understanding of the composite material under study.

7.2 Fibre orientation distribution

The first step of the analysis related to the fibre orientation characterisation and prediction. This was key, as the fibre orientation has a huge impact in the composite's monotonic and fatigue response, as shown in Chapter 5. Due to the large amount of fibres that could potentially be at any given point in the material, the standard form of representing the general probability of the fibre orientation is by means of a second order tensor. First proposed by Advani and Tucker [48], this formulation is applicable for both experimental measurements and numerical predictions.

In regards to the experimental results, Chapter 5.1.2 presented the orientation tensor distribution through the thickness measured by two different CT scanners. The results, shown in Figure 5-5, presented the characteristic microstructure distribution inherent of injection moulded short fibre-reinforced plastics. This is, skin-shell-core structure [29]. From the measurements, two points seemed to be clear: First, the fibres mainly orient themselves in plane, along and transversally to the flow. Second, the shell and core layers cover most of the total thickness area. Similar results have been observed in the past, regarding the through thickness fibre distribution on different short fibre reinforced composites [32], [41], [43]. For this particular case, both scanners showed consistent results for most of the skin and shell layers, with values almost overlapping each other. A progressive disparity was seen to start around the middle of the shell layers with the highest mismatch found at the centre of the core region, middle of the thickness, with a difference between scanners of approximate 20%. At the point of highest mismatch the second scanner (CT scanner 2) produced more randomly aligned fibres (closer to 0.5 in the scale). This divergence of results between scanners could have been due to the fact that they have different energies. Going by the maximum resolution possible, it is reasonable to assume that the Energy CT scanner 1 > Energy CT scanner 2, and therefore the progressive attenuation of the x-ray beam with the thickness of the material will be faster for the CT scanner 2 [173]; and the

highest divergence is located at the centre due to the fact that, as the samples rotate 360°, the deepest point for the X-ray will be that middle point in the core region.

The location for the experimental measurement consisted of the centre of the testing specimens' gauge length, Figure 3-8. CT measurements were then used to calibrate the numerical model, Moldflow simulation, as it was explained in Chapter 4.2. The fibre distribution model used on this project was the Folgar-Tucker model [47], as it is one of the first and most widely used fibre interaction models. In the formulation of this model, detailed in Chapter 2.3.3, the key parameter that modifies the final orientation of the fibres is the interaction coefficient, or C_i . A value close to zero would produce almost no interaction between the fibres, and with higher values the fibres are less aligned [142]. To understand the effect that this coefficient had on the numerical predictions of the fibre orientation distribution, and as part of the calibration, a parametrical study was conducted with ranges of C_i going from 3×10^{-5} to 2×10^{-3} , with the one used being $\sim 5 \times 10^{-5}$. Higher and lower values produced results significantly outside of the experimental measurements. Figure 7-1a shows the variation of the a_{11} orientation tensor component, corresponding to the flow direction, with the changes in the interaction coefficient, Figure 7-1b shows the location of measurement. This study demonstrated that the C_i coefficient significantly changes the distribution of the fibres through the thickness of the material, with higher values affecting more the orientation on the shell layers. Vincent et. al. [32] had observed a similar behaviour on the C_i coefficient when comparing two composite materials made out of the same matrix (PAA) but with different level of reinforcement (30wt% and 50wt%). For the case of 50wt%, the best fit with numerical data was found $\sim 2 \times 10^4$, a full order of magnitude smaller, in terms of C_i value, than the one found for 30wt% fibre reinforcement. A similar increment in the value of the C_i coefficient with lower levels of reinforcement, i.e. weight fraction, was also observed by Jerabek et.al. [51].

A comparison of the model results against the CT measurements is presented in Figure 7-2, for all the three main tensor components (a_{11} , a_{22} and a_{33}). The model simulation at the reference location show sensible results with good agreement in specific for the a_{22} component, where numerical and experimental results almost overlap and presented a difference of $\sim 5\%$ between measurements and simulation on the skin and shell layers. Similarly, good agreement was obtained on the skin and shell layers for the a_{11} component. However, the measurements showed that the model is estimating a more in-plane random distribution in the core region of the specimen, denoted by the peak values closer to 0.5 at this location. On the core the predictions showed a

~46% smaller tensor component value than that in the CT measurements. This is a well-known weakness of the Folgar-Tucker model, and as reported by Launay et.al. [137], this formulation in particular tends to overestimate the a_{11} component of the orientation tensor right in the central part of the thickness of the material. Similar results to the comparison showed in Figure 7-2 were observed by Gsellmann et. al. [33], Figure 2-22, where lower agreement of a_{11} component at the core layer was achieved. Different types of flow and material thicknesses were tested with similar results in the orientation distribution of fibres at the centre of the material. Additionally, from both the experimental measurements and numerical results, the tensor component corresponding to the out-of-plane fibre orientation distribution, a_{33} , always remains low with values within 10%. This effect has also been observed on other short-fibre reinforced composites [43], [137]. This further supports the assessment that the orientation of the fibres through the material happens mostly in-plane, with tensor components a_{11} and a_{22} being determinant to define the overall orientation of the fibres. A comparison was also conducted between the predictions for the 0° and 90° Edge specimens' tensor components and the measured CT data at the reference location, also shown in Figure 7-2. A very close correlation between the reference location and the 90° Edge prediction was observed, with just a small difference at the core layer and on one of the surfaces. On the other hand, the predictions for the 0° Edge specimens showed very little change in terms of fibre orientation, an almost constant value through the thickness was seen. For both Edge specimens, the validation of these predictions was conducted by analysing the simulated and the experimental tensile response under monotonic conditions. This analysis is presented in the next section.

Finally, an analysis of the variation of the orientation tensor around the reference location was carried out. This was done to assess any significant change of the fibre distribution around the central region, covered by the specimens' gauge length area, that could influence the material's fatigue performance. The total area studied was a 12 x 12 mm² region positioned exactly around the reference point. Figure 7-3 presents the boxplot corresponding to the a_{11} component for the nine different measurements taken. The orientation of the fibres through the skin and shell layers seems to stay stable across the whole region, with the least variation occurring at the sections of highest orientation along the flow direction, shell layers. An increase in the variation of fibres is observed in the transitions zones between the shell and core layers, i.e. the transition between fibres highly aligned with the flow direction and fibres aligned

transversal to the flow. In this regions a more random distribution was expected, and it is seen on the results.

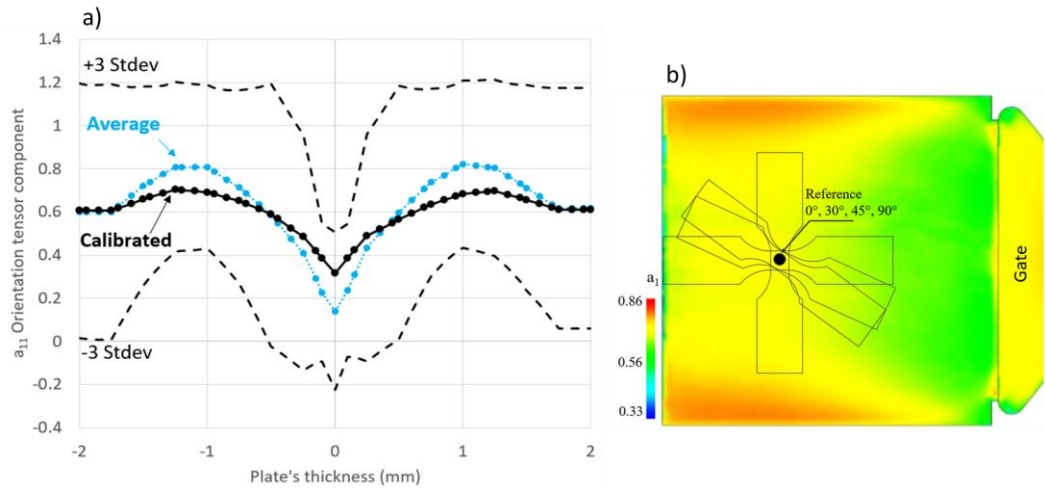


Figure 7-1 a) Variation of the predicted a_{11} orientation tensor component at reference location with the interaction coefficient (C_i). b) Location of measurement.

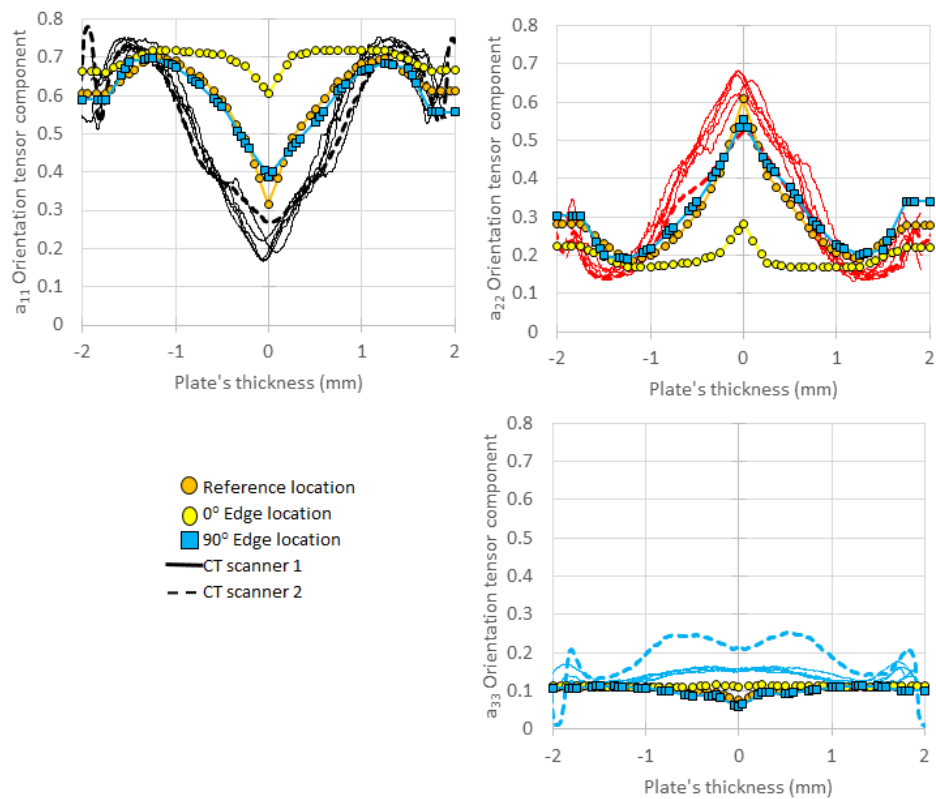


Figure 7-2 FE vs CT comparison of the orientation tensor information.

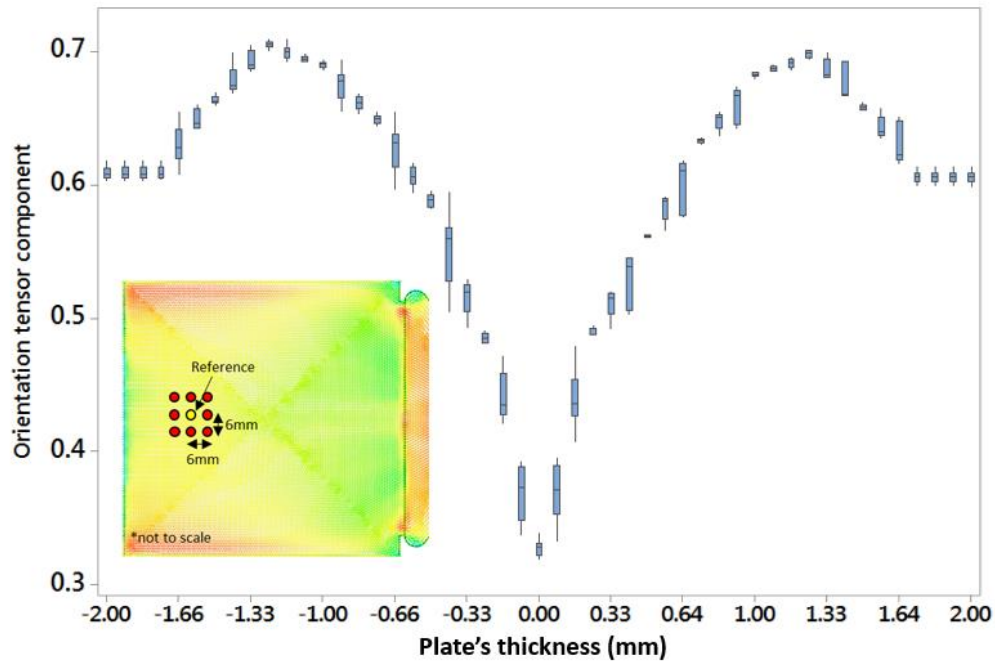


Figure 7-3 Boxplot of the variation of the predicted a_{11} orientation tensor component in a 12 x 12 mm² area around the reference location.

7.3 Monotonic tensile material behaviour

Results presented in Chapter 5.2 showed clear evidence of the anisotropic variation of the composite material properties with the fibre orientation distribution. This material variation is visible on the recorded monotonic tensile Stress-Strain curves and their respective calculated material parameters, e.g. Young's moduli, tensile strengths, maximum strain to fracture, etc.; as shown in Figure 5-7 and Figure 5-8. This observed variation of the material behaviour with the fibre orientation agrees with results reported in the literature on other short-fibre reinforced composites, e.g. [20], [52]–[54].

Analysis of the results of the predicted fibre orientation distribution at the reference and Edge locations, Figure 6-4, shows that 0° reference and, in specific, 0° Edge specimens have a higher proportion of fibres oriented with the flow direction, which on these specimens also corresponds to the load direction. Documented measurements of the length and orientation of fibres on a short fibre reinforced composite [20], presented in Figure 2-25d, showed that within the composite, longer fibres tend to orient themselves with the flow direction; while shorter fibres present a more random orientation, mostly on the 45° and 90° directions. This would mean that the 0° reference and, in specific, 0° Edge specimens, which have a larger number of flow/load oriented fibres that are also longer than the rest and thus have a better load

bearing capacity; would present higher levels of tensile strength and Young's modulus, just as the experimental results shown in Figure 5-7. This could also explain why 90° reference and 90° Edge specimens present the lowest strengths and Young's moduli, as they present a mostly inverse fibre orientation distribution to the previously explained orientations.

Additionally, the results obtained for 45° and 30° reference samples, showed that both specimens present very similar Young's modulus values to those for 90° reference and 90° Edge specimens, while having larger levels of strain to fracture than the rest of the orientations, meaning higher ductility. An analysis of the orientation tensor through the composite material, Figure 5-6, shows that the shell layers cover an approximate 60% of the total thickness area of the specimens. Therefore, as the specimens deviate from the longitudinal-to-the-flow direction, 0°, the number of longer more consistently load-oriented fibres drops and the composite behaviour might be more susceptible to the influence of the matrix, producing similar values of elastic moduli for these specimens' orientations. The higher ductility seen on the 45° and 30° reference specimens, could be explained as at these orientations the matrix has more space to deform between the fibres than in the longitudinal and transversal directions, 0° and 90° reference specimens. Additionally, examination of failed 30° and 45° reference specimens, Figure 5-45, showed an approximate 45° shear failure planes, which is characteristic of ductile failure.

Finally, of interest was also the results obtained in regards to the change in the Poisson's ratio with the overall orientation of the fibres. Chapter 5.2.1.1 showed that for specimens at 90° reference and 90° Edge their resultant values were approximately half that obtained at other orientations, with $\nu=0.17$ & 0.2 , respectively, which were very similar to the one reported by Sasayama et.al. for glass fibre ($\nu =0.2$) [16]. This implied a significantly lower lateral contraction, under tensile loading, for specimens oriented transversally to the injection moulding direction. An analysis of the distribution of the fibres through the thickness, carried out from Figure 5-6, showed that for specimens oriented transversally to the flow an approximate 60% of the internal area of the sample is filled with fibres mostly aligned with the flow direction, which could then explain the lower Poisson's ratio on these specimens as there are more fibres resisting the lateral deformation. On the other hand, for specimens oriented at 0° reference and Edge ,30° and 45° reference, the values varied between $\nu =0.35$ to 0.40 , which were again very closed to the known Poisson's for PA66 of $\nu =0.33-0.36$ [16], [170]. For the case of these specimens' orientations approximate 30%

of fibres, through the thickness, are mostly oriented with the flow direction, which could then also provide an explanation for the larger lateral contraction seen on these samples, i.e. the higher measured Poisson's ratio.

7.3.1 Predicted coupon tensile material response

As detailed in Chapter 4.3, the calibration of the material model was based on the properties of the phases, matrix and fibre, and on experimental data for 0°, 45°, 90° reference specimens. This was done to correctly characterise the material behaviour inherent of PA66GF50. Different approaches on similar SFPRs have been applied in the literature to calculate material parameters such as the Young's modulus, e.g. based on the Halpin-Tsai model [20], or have studied the material under loads low enough to consider it linear and implemented a straight forward MFH model [71], [172]. However, during the experimental program of this study a clear non-linear behaviour was observed for the composite, as shown in Figure 5-7, and thus the implementation of a different material model was needed.

The results of the numerical model presented in Chapter 6.2.2, showed that each of the different simulated FE coupons presented an elasto-plastic material behaviour, represented by the presence of different levels of strain hardening, alike the experimental curves. A comparison between the experimental and simulated curves is shown in Figure 7-4. For the specimens used as calibration, the simulation curves are very close to the experimental curves, with FEA 45° and 90° reference in particular showing a very close fit with their respective experimental curves. The good agreement of the model was more so on the 30° reference, 0° Edge and 90° Edge FE specimens that were used for validation purposes, with 30° reference in particular overlapping with the experimental results. Of special attention was the predicted response for the 0°Edge specimen, where a particular divergence is observed for stress values at approximately 50 to 60 MPa. At this stress level the FEA material curve present larger strains than the ones observed in the experiment (sky-blue lines and squares on Figure 7-4). The point where the discrepancy starts seems to be close to the calculated 0.2% Yield strength of ~55MPa, presented in Chapter 5.2.1. This implies that the material model is under-estimating the amount of strain hardening occurring for this particular specimen, where the fibres are highly and more consistently oriented with the load direction due to the effect of the mould's side edges, as shown in Figure 6-4. This also suggests that the Moldflow model might be underestimating the amount of fibres oriented with the flow direction. The difference between the FEA model and the experimental measurements, at the gauge length location, presented

in Figure 7-4, shows that the FEA model deforms ~25% more than the actual sample at maximum stresses. On the other hand, this discrepancy between the prediction and measurements is not seen for the other Edge specimen (90° Edge). A possible explanation for this is because the overall fibre orientation distribution of this particular specimen is very close to the 90° reference specimens, as shown also in Figure 6-4. These results then imply that the effect of the closeness to the mould's gate on the material behaviour is relatively low, in comparison with the material located close to the mould's side edges.

Finally, the above shows that although the M-T model is in theory restricted to low amounts of reinforcement [66], it was able to produce sensible results, in terms of monotonic material properties, for the present material which has a relatively high reinforcement level (50wt%).

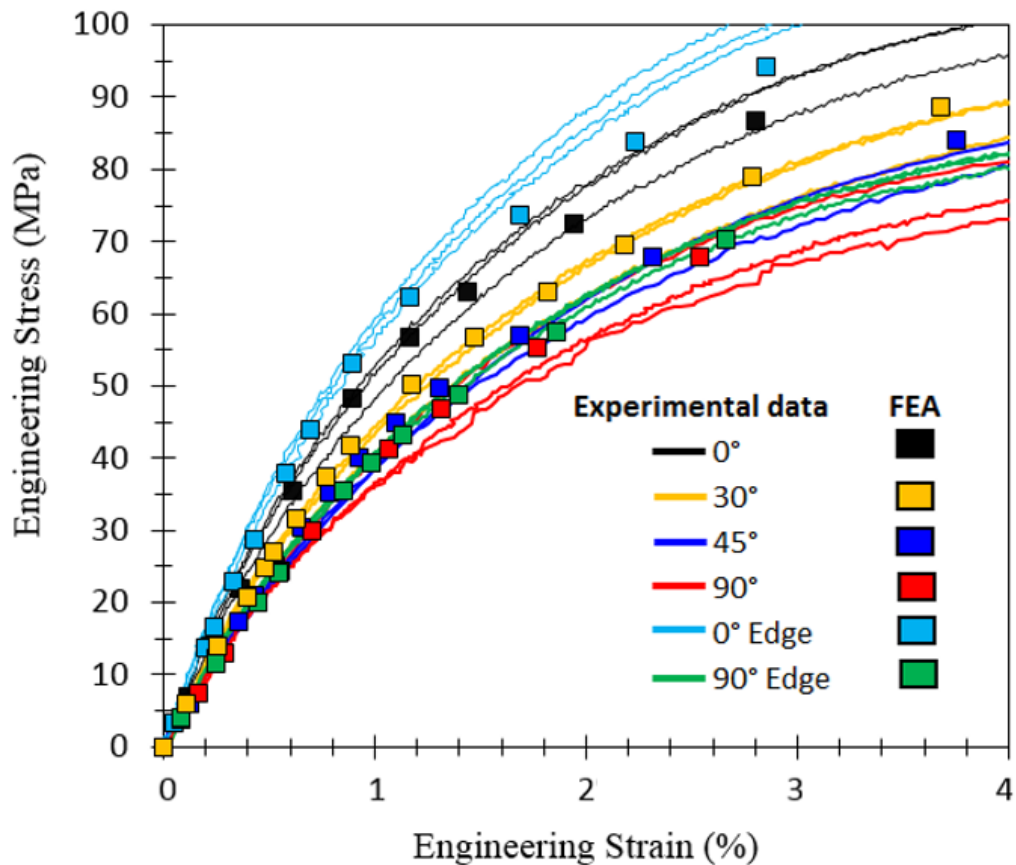


Figure 7-4 FE vs Experimental Stress-Strain curves for specimens at different orientations for PA66GF50 and $V_f=30\%$.

7.3.2 Strain field distributions

Unlike qualitative results reported in [55], digital image correlation results from this study were able to show, quantitatively, the heterogeneity of the strain field in the

material on both main and thickness surfaces, as presented in Chapter 5.4. It was seen that depending of the specimen orientation, at a certain stress level, strain localisation occurred prior to the failure of the specimen, also observed in [174]. In specific, this localisation was located in areas near the shoulder of the specimens and initiating at the free edge of the gauge area on the main surface. A comparison between DIC and FEA results with focus on the thickness surface of 0°, 90° and 45° reference specimens is shown in Figure 7-5a-c. It is clear that for all the samples the concentration of strain tends to occur closer to the shoulders and the distribution is also not symmetrical, which shows the effect of the heterogeneity caused by the fibre orientation distribution. It is interesting to see that on the DIC results the centre of the gauge length shows some patchy locations of strain, clearer in Figure 7-5b and c, which could be due to imperfections /flaws, or local fibres more or less aligned with the load direction that the presented homogenised FE model cannot captured. For the most part, these locations on the surface correlated with the locations of crack onset. In specimens with better fibre alignment with the load direction, i.e. 0° and 0° Edge, clear evidence of crack growth on the Main surface was observed to take place at those exact points, as shown in Figure 5-34 and Figure 5-38. For these particular specimens the period between crack onset and final failure was longer than for the rest of the specimens, with measured times of approximately up to 1 second for 0° reference; and more than 1 second for 0° Edge specimens. This difference on the failure of the specimens could be attributed to the overall distribution of the fibre orientations. A clear variation of the fibre alignment along the specimens' thickness was observed on the fracture surface micrographs taken from failed specimens, as presented in Chapters 5.5.3 and 5.5.4. Additionally, specimens oriented with the flow direction consist of a larger quantity of longer and better oriented fibres with the load, making the material stronger in that direction. This suggests that flaws have to pass through the fibres more often in order to propagate, possibly slowing down the crack growth. Additionally, as the stresses from the final element analysis were used as part of the fatigue analysis, a comparison between the FEA and measured strain fields was conducted as a mean to further validate the model. The idea proposed followed the assumption that if the DIC strain measurements and the finite element predictions correlated between each other, therefore the FEA calculated stresses on the specimens could be considered to be sensible enough to be representative of the actual stress state inside the specimens. As the fatigue model used on this project is based on initiation, i.e. it does not consider the actual fracture process, the comparison between the different experimental and numerical results was done right before the onset of

strain localisation is seen on the DIC measurements, which is assumed to be the point of crack initiation. Figure 7-6 presents a comparison for a 0° and a 90° reference specimens and loaded in tension at, respectively, 100MPa and 75MPa. The distribution for both cases at these stress levels presented strains mainly concentrated in the gauge section of the specimen. This is was also seen on the actual specimens used for validation, as is the case of 0° and 90° Edge specimens shown in Figure 7-7. To assess the differences between FEA predictions and DIC measurements, several values were taken at different points along the gauge section of each specimen (model and experimental), and the results compared against each other. Figure 7-8a to c, presents the boxplot comparison for the calibration and validation specimens mentioned. It is clear that the simulation results present a more uniform distribution of the strains in the gauge section of the samples. On the other hand, the strains distributions on the actual tested specimens present a larger spread of values on this section. Nevertheless, comparison of the median values for each case shows that, with the exception of the 0° Edge specimen, the difference between the models and the experiments was approximately 6%.

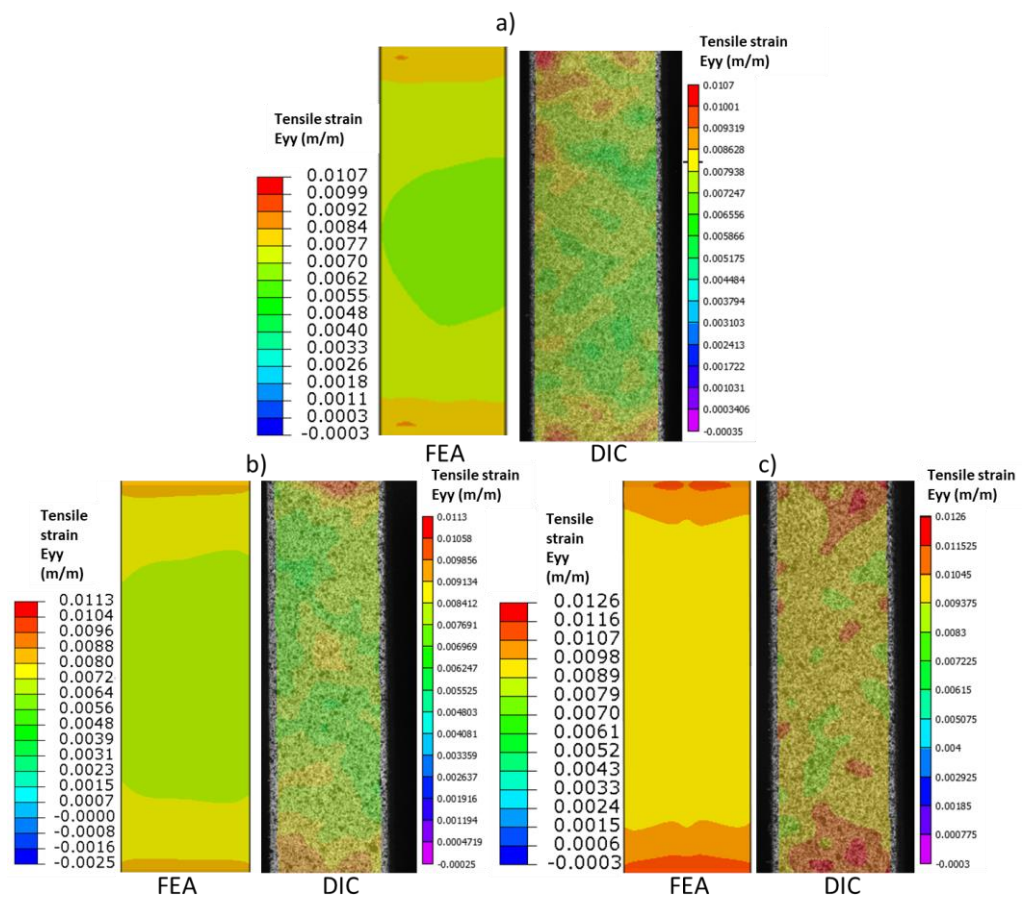


Figure 7-5 Thickness surface comparison between FEA and DIC for a) 0°, b)90°, and c) 45° reference specimens at 1.5kN tensile load.

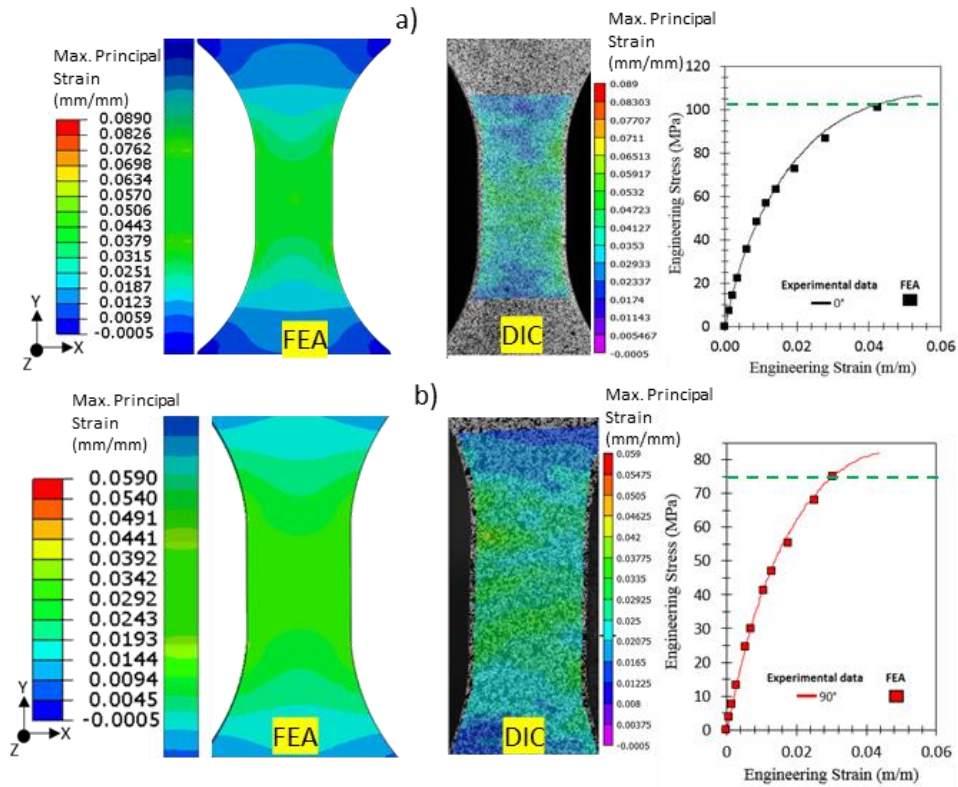


Figure 7-6 Comparison between FEA and DIC for calibration a) 0° and b) 90° reference location specimens loaded in tension ($V_f=30\%$).

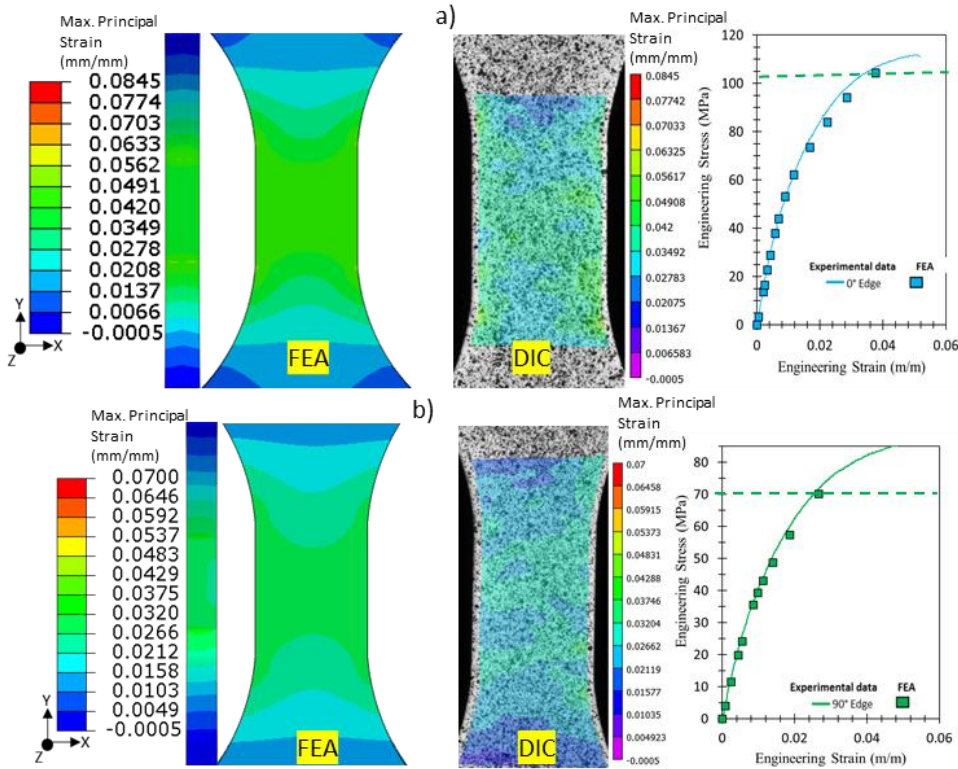


Figure 7-7 Comparison between FEA and DIC for validation a) 0° Edge and b) 90° Edge locations specimens loaded in tension ($V_f=30\%$).

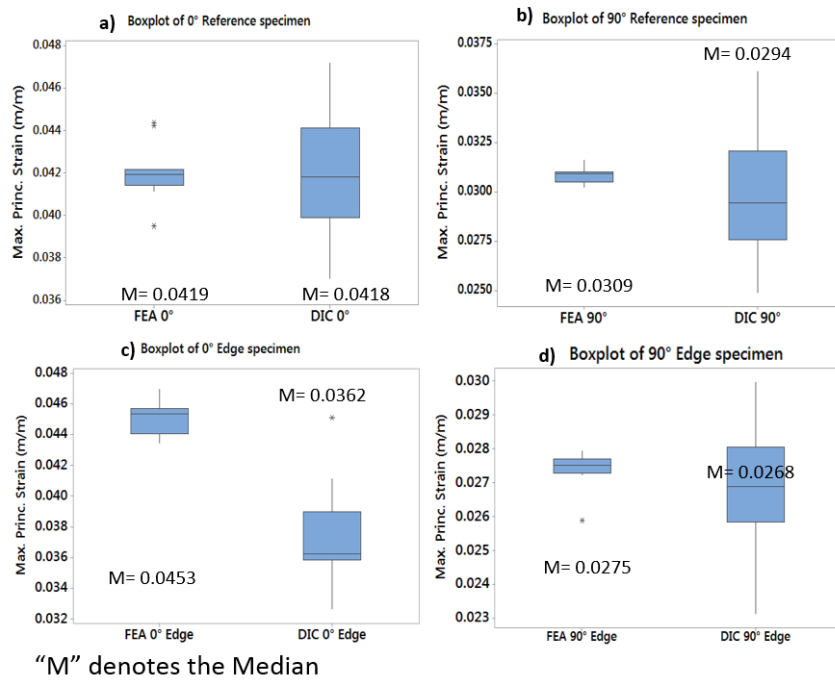


Figure 7-8 Boxplot of DIC vs FEA comparison for a) 0° reference, b) 90° reference, c) 0° Edge and d) 90° Edge specimens.

7.4 Fatigue analysis

7.4.1 Stress-Life approach

The experimental fatigue results presented in Chapter 5.3.1, in the form of stress life curves have shown the effect of the heterogeneous fibre orientation distribution on the composite material fatigue behaviour. Coupons more aligned with the mould flow direction had shown a significant higher fatigue life in comparison to any other orientation. However, a clear effect of the mean stress was observed. Results under positive stress ratios show lower lives for all the specimen orientations in comparison to fully reverse stress conditions. Additionally, under $R=-1$ stresses, 45° reference specimens presented a clear shift in their fatigue behaviour, with results closer to those for the 90° reference specimens. From these experimental results, effects of buckling were first suspected, although the 4mm thickness of the injection-moulded plates was selected on purpose to minimise risks of buckling, but this was not observed during the experimental program. An analysis of the experimental tensile stress-strain curves, Figure 5-7, shows that 45° and 90° reference specimens also presented a very close material behaviour similar to the one observed on the fully reverse fatigue conditions. Therefore, this behaviour is suspected to be from the material rather than an instability effect. Moreover, this same fatigue behaviour has

also been observed previously on other short glass-fibre reinforced polyamides [75], [77].

The combination of the complete modelling methodology, in the sense of the injection moulding prediction, material modelling and stress analysis; culminated with the application of the stress-life approach for the fatigue calculations. Unlike the very few similar applications of the stress-life approach on short fibre reinforced polymers reported in the literature [71], the methodology developed in this work included: 1) all the modelling stages needed for the multi-scale modelling of the fatigue behaviour of short glass-fibre reinforced polymers for a clear understanding of all the assumptions made in every model but also in the transfer of data between the models, and 2) validation phases for all the models through state-of-the-art experimental techniques to assess uncertainties in modelling prediction and their propagation through the various modelling steps. Also, unlike other published work [171], it has been shown that the curves used for calibration of the S-N model do not necessary have to come from thin testing specimens with almost uniform microstructure through the thickness. The present results have shown that thicker specimens, with more complex fibre distribution, as the ones used on this project can be used to adequate calibrate the model. As part of this calibration, fully oriented S-N material are calculated via reverse engineering. These RE material curves for 0° fully-aligned, shown in Chapter 6.4.1, presented higher fatigue life than the reference experimental data, as well as, the predicted Edge specimens' curves. On the other hand, the 90° fully-aligned, showed the lowest fatigue life. The particular results of the 0° Edge specimen predictions, further suggest that with the more consistent fibre alignment, due to the effect of the mould's side edges, better tensile material properties are not only produced; but also a better predicted fatigue life performance. The validation of the fatigue model under R=0 at the reference location is shown in Figure 7-9. It can be seen that it is possible to produce sensible conservative fatigue life predictions by using either two or three specimen orientations for the model calibration. Unlike results reported in the literature, for which three curves had to be used [171], [172], results from this work have shown that calibration using two specimen curves can produce very reasonable results, therefore minimising the number of test required to run such models.

However, for the case of the fully reverse stress ratio, presented in Chapter 6.4.1.2, it was shown that by using only two curves, 0° and 90° reference, the effect of the shift in the material response of 45° reference specimens, towards the 90° reference curve

seen under this type of loading condition could not be predicted. It was also demonstrated, as shown in Figure 6-26, that the calibration of the model is not possible, even when using three specimen curves, with results actually being worse than those obtained using only two calibration curves.

Finally, from the analysis of results obtained using the proposed stress-life approach two main conclusions could be drawn: 1) this methodology is limited to when the fatigue data for the different specimen orientations is almost linearly distributed between the curves of ideal 0° and 90° orientations, which has proved to be the case for positive R ratios. For this reason, this stress ratio is often used in the literature [71], [172]. 2) As shown in this thesis, it is possible to obtain sensible predictions using only two curves for validation of the model, thus reducing the amount of experimentation needed for engineering applications; 3) the approach appears to fail for alternated loading as also reported in the literature, where $R=-1$ conditions were also used [3]. This means that in order to develop a better modelling methodology a different approach is needed, and as seen in the literature review [2], [92], [94], analysis based on energy is currently being researched, albeit mostly based on the elastic energy density.

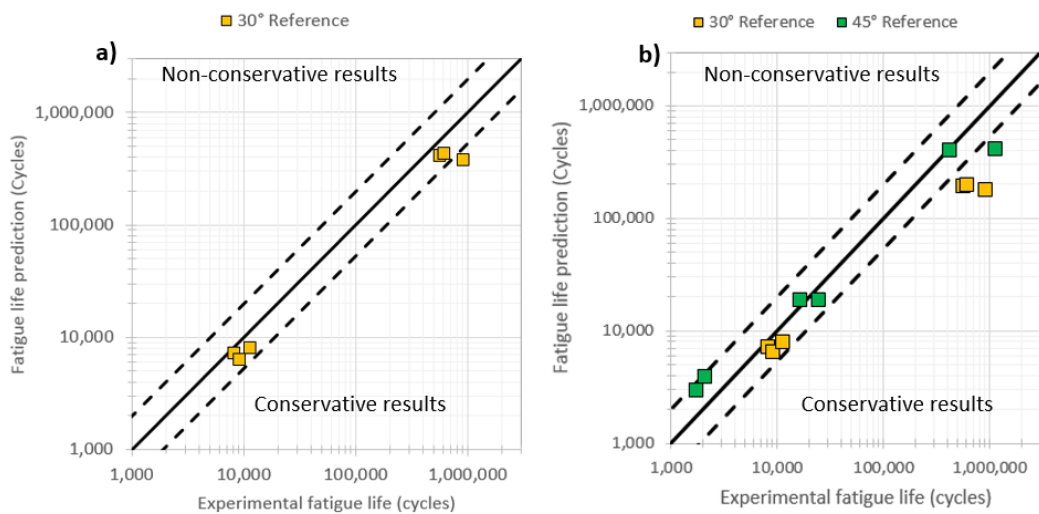


Figure 7-9 Model validation for R=0 a) using 30° reference specimens (calibrated with 0°, 45° and 90° reference); b) using 30° and 45° reference specimens (calibrated with 0° and 90° reference).

7.4.2 Energy based approach

Dissipated energy values extracted from the experimental program, in terms of the stabilised hysteresis loop areas, showed that the energy-life data for the different specimen orientations laid close to each other and could be presented by a single

power law curve, with the main differentiator being the stress ratio, as shown in Chapter 6.4.2 Figure 6-32. It also showed the possibility of applying common mean stress corrections techniques, in specific the Walker relationship as presented in Figure 6-33, and producing sensible predictions. This also implies a more comprehensive application of the energy method, as this fatigue parameter would be based on the dissipated energy via the hysteresis loops areas, instead of the elastic strain energy density calculated by assuming the material as linear elastic. This would better describe the actual behaviour of the material by incorporating the plasticity effects of the matrix.

However, a close examination of the measured stabilised dissipated energy at different stress amplitudes does show a dependency on the fibre orientation, as shown in Figure 7-10. This figure clearly shows the orientation dependency of the stabilised dissipated energy for a given stress level with the lowest energy level measured for the 0° orientation. If there is a relationship between the energy and the orientation of the fibres, then this should be visible at the local level and the finite element results should be able to show it. Figure 7-11a shows the local stress-strain curves for key elements in the cross section, through the thickness, of a 0° reference specimen with a 1.6kN applied load. Figure 7-11b-d show the stress, strain and orientation distribution on that cross-section, together with the location of said key elements. On this figure, it can be seen that the local stress/strain response for each element varies with the particular fibre orientation at that element, which implies that the energy seen on each of those elements would also be different. This same variation of the local stress-strain curves is seen for other specimens orientations as shown in Figure 7-12a and b, for 90° and 45° reference specimens respectively. Curiously, the 45° reference specimen showed the least amount of variation. The reason for this could be that the measured elements (element 1 to 7) presented the least variation in terms of the local fibre orientation, as shown in Figure 7-13c. Therefore, if the orientation is almost the same, it stands to reason that the MFH might produce similar material properties for those elements, which is seen in the local stress-strain curves in Figure 7-12b, where the individual curves for elements 1 to 7 almost overlap. Based on these local stress-strain curves, calculation of local elemental energy values for each key element was then carried out by measuring the area under the curves. The results reported in Figure 7-13 shows that the local energy values are very dependent on the main orientation of the fibres. For the 0° specimen, Figure 7-13a, the local element energy for the most aligned element (element 1) is approximately 3 times higher than the local energy for the least aligned element (element 5). For the case of the 90° specimen, Figure 7-13b,

the highest localised energy value (element 1) is approximate 1.6 times larger than the smallest energy (element 6). A similar result was also seen on the 45° specimen, Figure 7-13c.

These results indicate that a more comprehensive modelling methodology based on dissipated energy calculation under cyclic loading would therefore need to be developed to take in consideration the local elemental fibre distribution. This would, however, require extensive model development to predict the stabilised hysteresis loops using an equivalent Mori-Tanaka multi-scale model methodology under cyclic loading, in order to predict the orientation dependent stabilised cyclic curves.

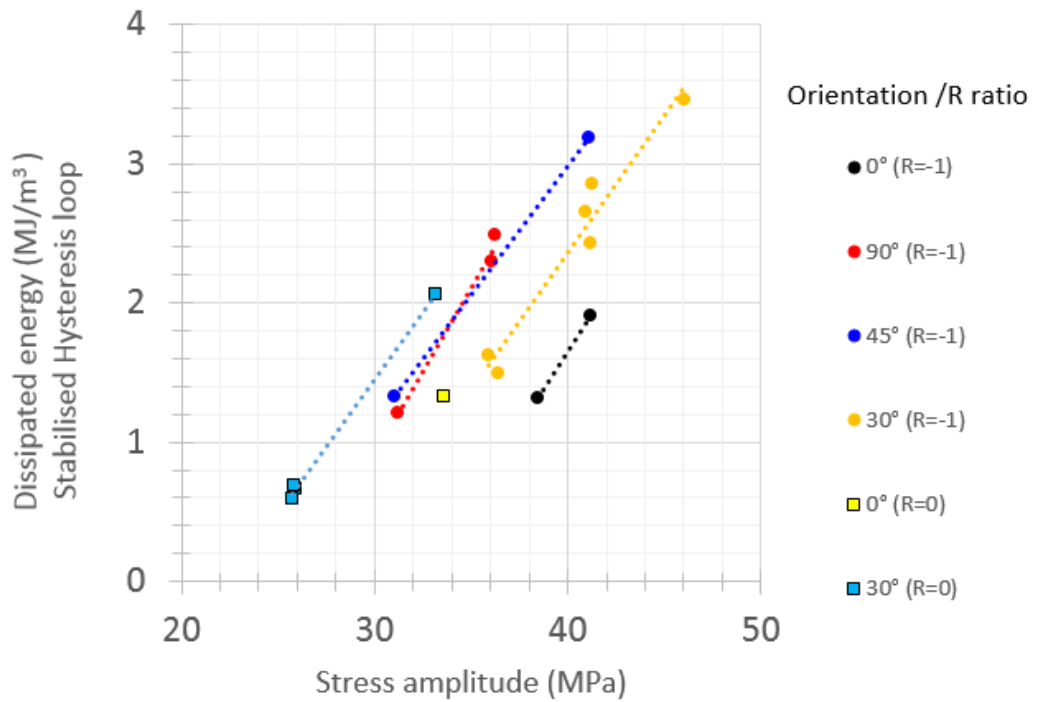


Figure 7-10 Dissipated energy vs Stress amplitude.

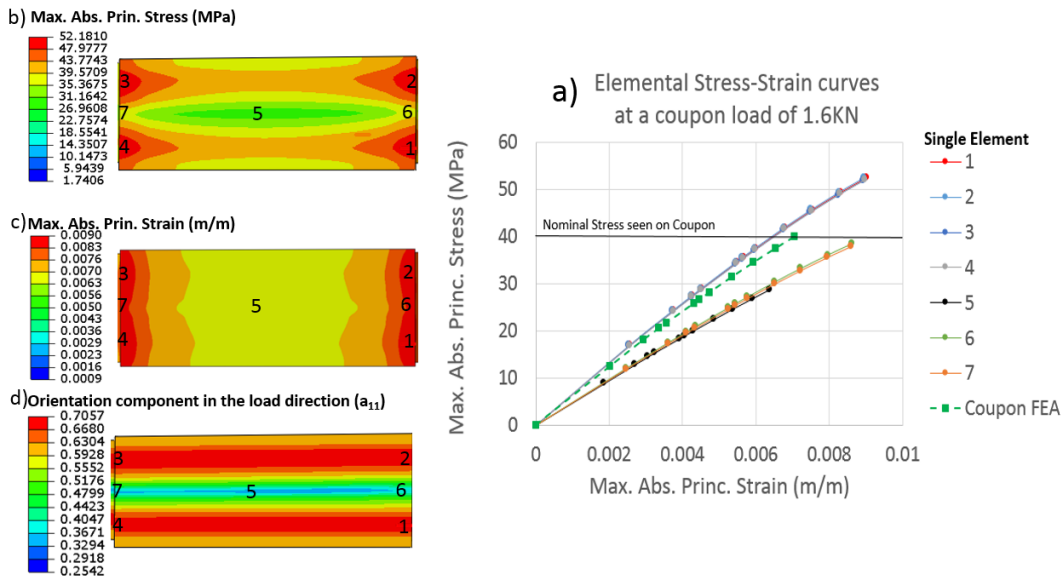


Figure 7-11 FE Elemental Stress-Strain curves of a 0° reference specimen. Location of inspection corresponded to the most common fracture plane for the specimen at that particular load level.

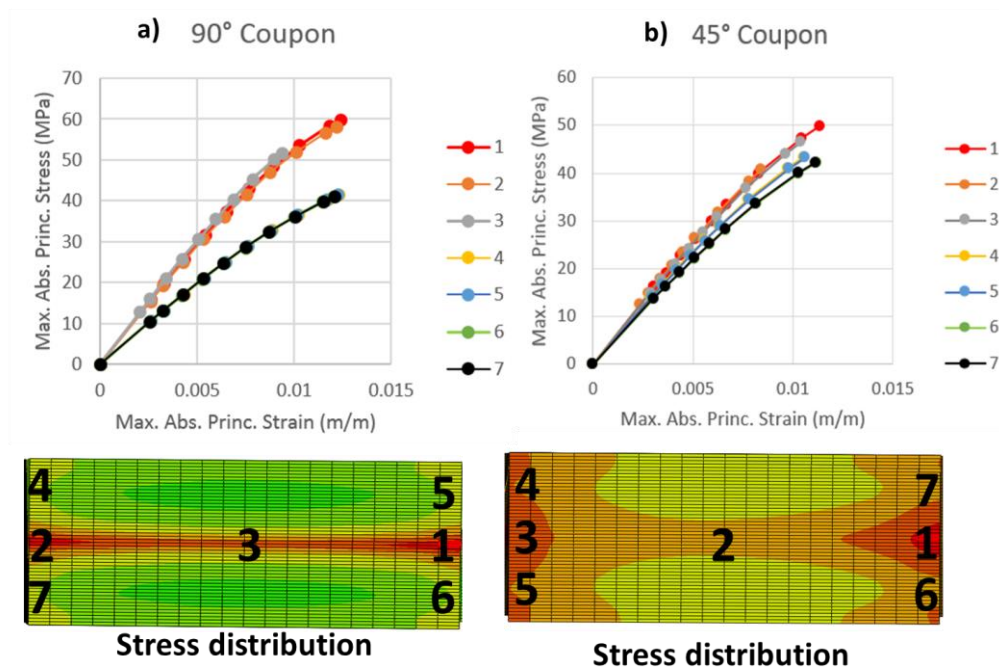


Figure 7-12 FE Elemental Stress-Strain curves at 1.6kN for a) 90° reference specimen and b) 45° reference specimen. Location of inspection corresponded to the most common fracture plane for the specimen at that particular load level.

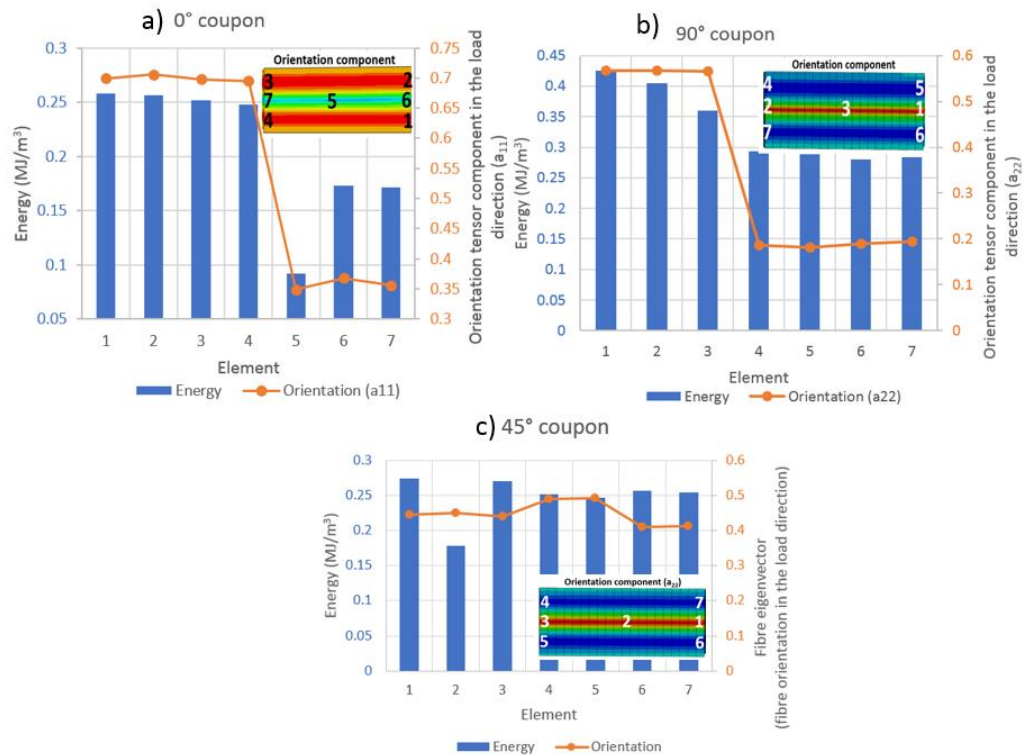


Figure 7-13 FE elemental localised energy on difference specimens seen through the thickness on the most common fracture plane. a) 0° reference, b) 90° reference and c) 45° reference.

7.4.3 Fatigue damage mechanisms

The analysis was focused on fully reverse, $R=-1$, conditions under an intermediate stress amplitude of 40MPa, or $\pm 1.6\text{kN}$. Figure 7-14a shows a comparison of the stiffness evolution of different specimen orientations under said loading conditions. In this figure, it can be seen that for 90° and 45° specimens the drop in stiffness right at the beginning of the life of the specimen is significantly steeper than the one observed for the 0° specimen. If the drop seen at the beginning of the test was due to the damage mechanisms, rather than the product of the viscoelastic response of the matrix, then there must be a visible effect of the orientation on the stiffness decay, as seen on the presented stiffness plot. A schematic of this idea is shown in Figure 7-14b, where it could be assumed that specimens with more fibres aligned orthogonally to the load, 90° and 45°, would present a bigger drop in the stiffness, as micro cracks on those specimen would be longer than the ones occurring at the fibre ends on specimens oriented parallel to the load, 0°, if debonding of the fibre/matrix interface is assumed to happen in the early stages of the test. This difference in micro-crack size at fibre ends, and due to debonding of more orthogonally-aligned fibres; has been observed in the past on fatigue tested samples in [100], as shown in Figure 2-69. For

this figure in specific, if a comparison is made at the same point in the life of the material (in this case 99.7%) the crack at the fibre end in the seemingly vertical fibre (Figure 2-69a sub-figure e) was approximate 84 μ m. On the other hand, the cracks/debonding in the seemingly horizontal fibres (Figure 2-69d sub-figures a and b) were approximate 270 and 136 μ m, respectively. This suggest that cracks in horizontal fibres grow larger than the ones in seemingly vertical fibres; which supports the above idea of why the stiffness evolution might be different depending the orientation of the specimens tested.

Chapter 5.5 presented the failure locations and planes for the different specimen orientations under tensile and fatigue conditions. In specific, the specimens' failure under cyclic loading showed two main failure locations, either: 1) near the end of the shoulder of the samples, or 2) closer to the middle of the sample. Furthermore, for 0° and 90° reference specimens, the failure occurred for the most part perpendicular to the applied load, while on the 30° and 45° failure occurred at an approximate 45° angle. An optical analysis of all the fatigued specimens is presented in Figure 7-15. It can be seen that the majority of the specimens' failure occurred in a region located near the shoulder, with 0° presenting the orientation with the highest percentage of failure in this region. Similar failure locations have been observed on the literature [77], on short fibre reinforced nylon dog-bone coupons, as shown in Figure 2-66. Correlation of these optical observations with the finite element stress results, presented in Chapter 6.3, showed that in this region, near the shoulder, the stresses and strains are highly localised; more so on the thickness surface. Similar localisation through the thickness has also been observed in the literature [55], as presented in Figure 2-42. Therefore, this near-the-shoulder location could be assumed to be the most representative case for the failure initiation of the specimens. Evidence found via high speed cameras, presented in Figure 5-43, showed the initial development of cracks right below the surface, in the shell layers, on the thickness of the sample, and close to the shoulder area. A comparison between the FEA results and the high speed camera images, presented in Figure 7-16, shows a correlation between the locations of maximum stress localisation, from the modelling results, and the regions where the cracks were observed to have initiated. This further corroborates the assessment that flaws might initiate below the surface in regions of high stress localisation, which in the case of a 0° specimen, this corresponds to the shell layers and close to the shoulders of the specimen. Figure 5-43 also suggests that the period between crack appearance and final failure is very short, which indicates that the actual process of fatigue crack initiation is most likely very slow and progressive. This means that a

fatigue model based on initiation and by looking at stresses and strains in undamaged specimens is therefore able to capture the most likely location for material failure.

SEM images of samples under the previously explained fatigue loading conditions have been shown in Chapter 5.5.4., where the failure occurred closer to the shoulder. Figure 7-17 and Figure 7-18 present a back-to-back comparison of the fracture surfaces for a tensile and a fatigue sample for 0° and 90° reference specimens. A clear distinction is visible between these surfaces. At first glance, on the fatigue specimens there is presence of "packets" of material in the regions where the fibres are more aligned with the load direction. This is not observed on the fracture surface of tensile specimens, as highlighted by the red squares and close-up view in the images, where in those regions the fracture surface is very messy and the matrix seems to be highly deformed. That these features (packets) occur only in the fatigue samples implies that there is a damage mechanism inherent of this type of loading condition. Characteristic of fatigue is the slow crack propagation with each loading cycle. This slow crack growth might cause the creation of the seen clean surfaces on the packets as the resin is not completely deformed due to the relatively low load levels experienced during fatigue, which is opposite to the significantly higher loads seen during tensile testing. A model of the creation of these planes, or plateaus, during fatigue of SFRP's was depicted in Figure 2-72; which seems to support the idea that cracks during fatigue present different propagation planes joint together by "steps" in the matrix. In previous works, analysis of fracture surfaces has been conducted by correlating the failure planes with assumed stress distributions produced by the material microstructure [99], or via correlation with different surface measurements [99], [101]. However, in order to give a better idea of the possible conditions that lead the crack initiation and failure, the conducted finite element analyses were used in conjunction with the fracture surfaces of the failed specimens, as to provide more comprehensive information about the relationship between stress and strain states in the material on the plane of failure and damage mechanisms. Figure 7-19a-d to Figure 7-21a-e, present a comparison of the whole fracture surface for failed 0°, 90° and 45° reference specimens seen under SEM, and the FE stress and strain fields on the main and thickness surfaces; and on the actual fracture plane across the thickness of the material, i.e. cross-section at the failure location. By correlating the FE results of the fracture plane with the SEM images, it is possible to observe that the highest levels of stress and strains are located below the surface. The stress is mostly localised in the regions where fibres are more aligned with the load direction. In the FE, these regions are composed by elements where their highest orientation tensor component is

aligned in the direction of the load (e.g. in a 0° specimen it is expected to present stress concentrations in locations where elements have a_{11} as the highest orientation tensor component, which for this case correlates to the shell layers, as it can be observed in Figure 7-19c). This is more clearly visible on the 0° and 90° specimens, e.g. Figure 7-19c and Figure 7-20c. From synchrotron observations documented in the literature [100], and presented in Figure 2-69a, it is possible to assume that the first fatigue micro-cracks might start at the fibre ends due to the concentration of stresses in those areas, which are located in the layers where the fibres are more aligned with the load, these regions can be inferred from the macro level FE results presented herein. These micro-cracks might not freely grow, due to the fibres being in an unfavourable orientation for propagation, as they have to go slowly through the fibres. This slow crack growth might then be producing the mostly clean surfaces on the packets of material seen on these regions, Figure 5-58b and Figure 5-59b. To this effect, Figure 5-62 shows what it looks like a crack at the interface and along the length of a seemingly horizontal fibre. Additionally, these packets could then represent several cracks' planes due to the stochastic nature of crack formation [175]. On the other hand, cracks could more easily propagate in the sections where the fibres are mostly orthogonally aligned with the load, characterised by regions of relative low stresses, and through the matrix along the fibre lengths. Some evidence of this is how clean the fibre sides are in those layers of the fracture surface, and how relatively flat and uniform the fracture surface is on that layer, as shown in Figure 5-59a and Figure 5-63c. Finally, the highly deformed matrix seen on the fracture surface and in specific below the packets in the fatigued specimen in Figure 7-18, could also provide more evidence of the final plastic failure of the sample. At this point, the higher deformation seen in the matrix could be due to the location of final failure or unstable propagation, similar to the fracture surface seen on the tensile specimens, as shown in Figure 5-56b and Figure 5-57a.

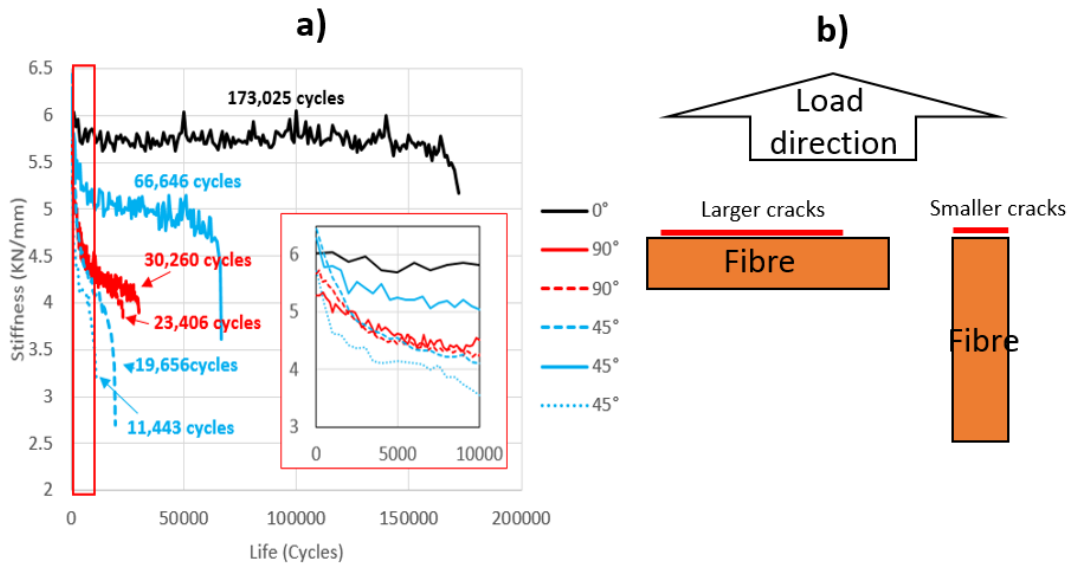


Figure 7-14 a) Comparison of stiffness evolution for different reference specimens at R=-1 and applied force amplitude of 1.6KN. b) Depiction of possible cracks lengths due to fibre orientation.

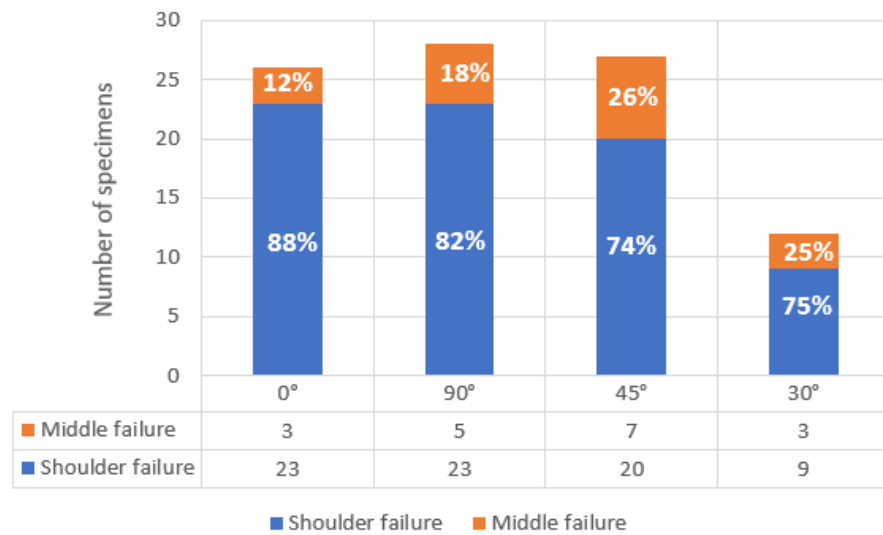


Figure 7-15 Optical analysis of specimens' fracture location.

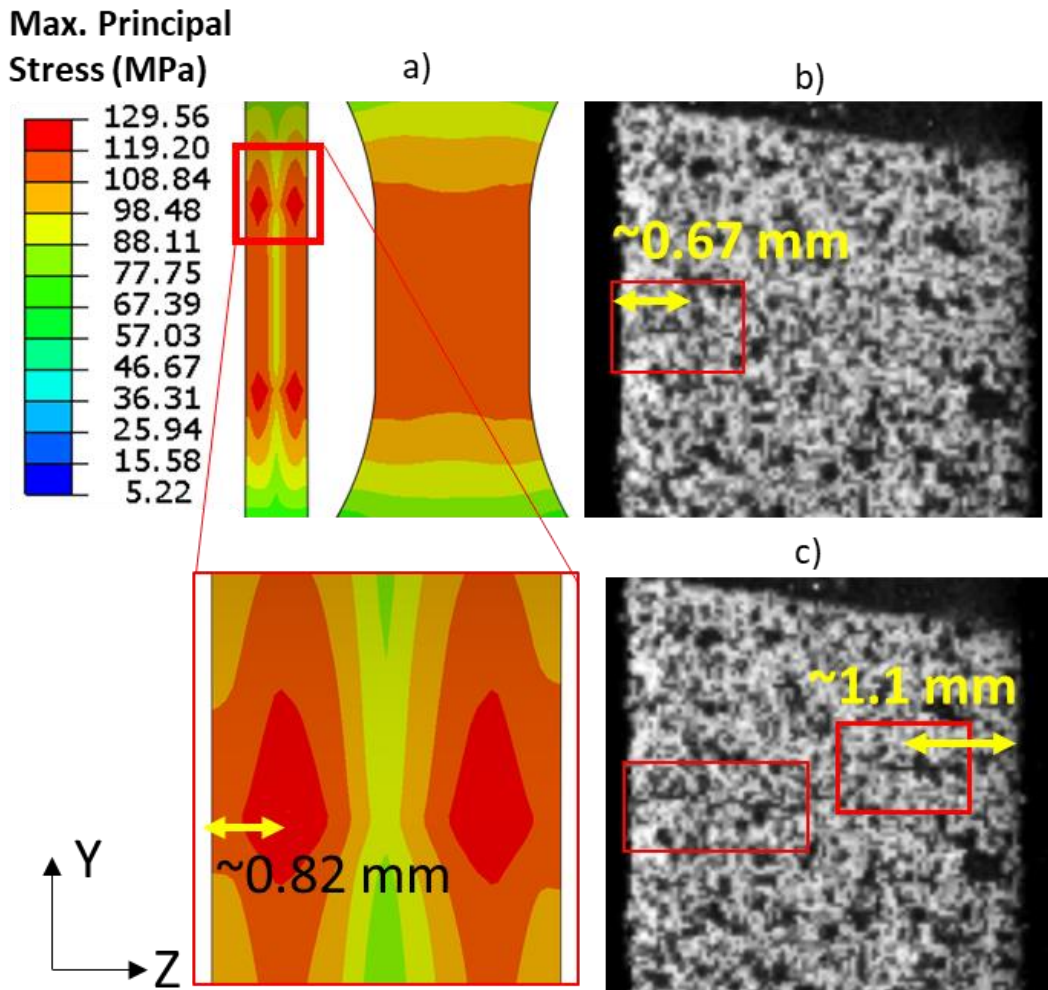


Figure 7-16 Comparison of locations of a) FEA Maximum Principal Stress and b) first crack appearance and c) second crack appearance on the thickness for a 0° reference fatigue specimen.

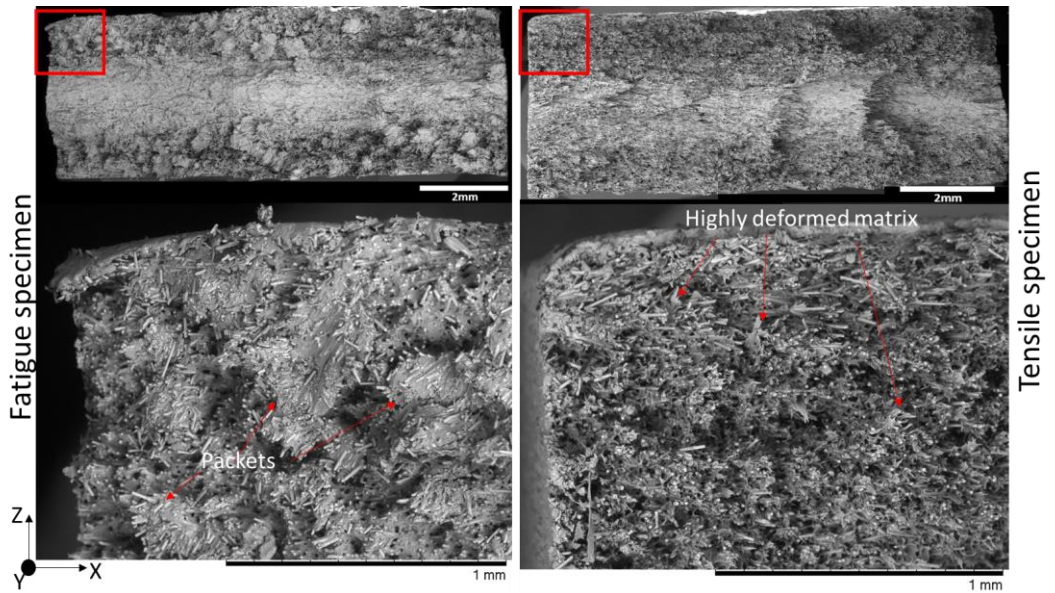


Figure 7-17 Comparison of 0° reference specimen's fracture surface with $V_f=30\%$. Tensile vs Fatigue ($N=235,800$ cycles, $R=-1$, $\sigma_a=40\text{MPa}$) samples.

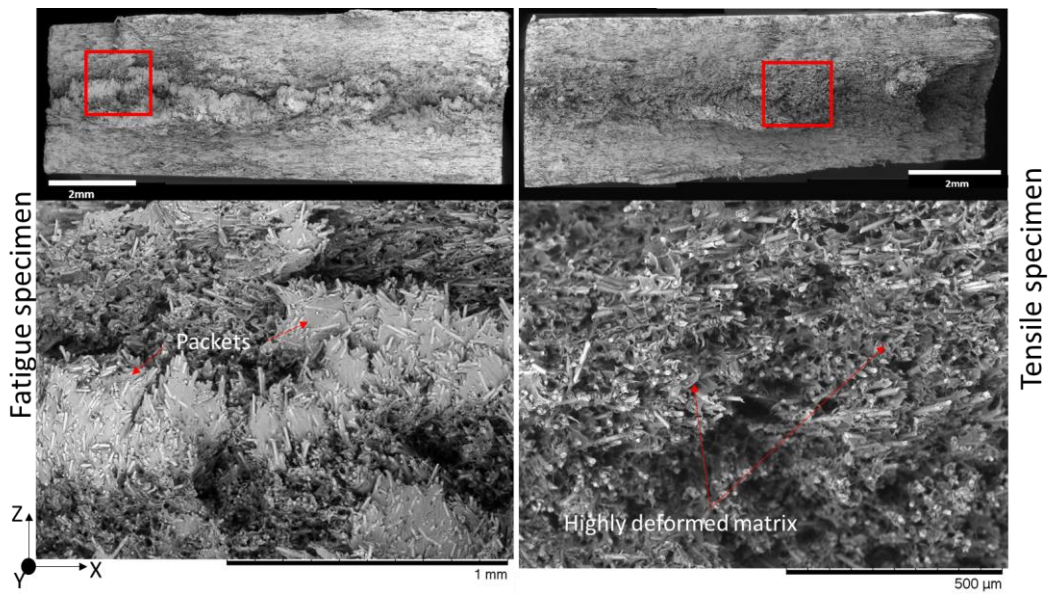


Figure 7-18 Comparison of 90° reference specimen's fracture surface with $V_f=30\%$. Tensile vs Fatigue ($N=30,260$ cycles, $R=-1$, $\sigma_a=40\text{MPa}$) samples.

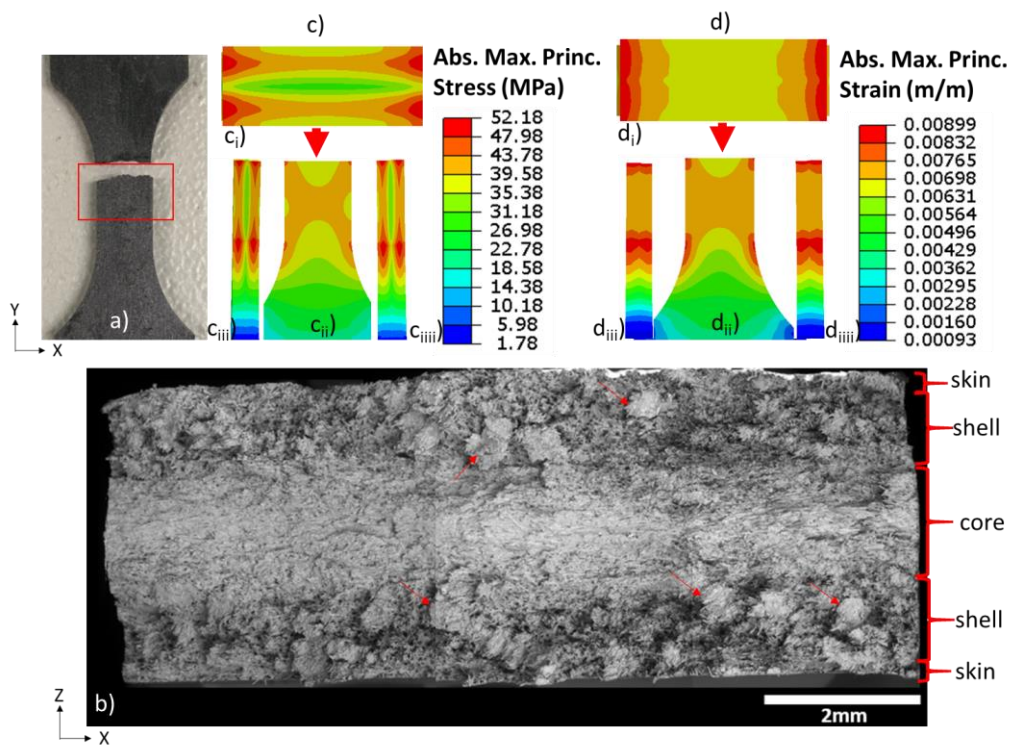


Figure 7-19 Stress and strain distributions and fracture surface of a fatigue 0° reference specimen with $V_f=30\%$ at $R=-1$ and $\sigma_a=40\text{MPa}$ ($N=235,800$ cycles).

Arrows denote example of packets seen on the fracture surface.

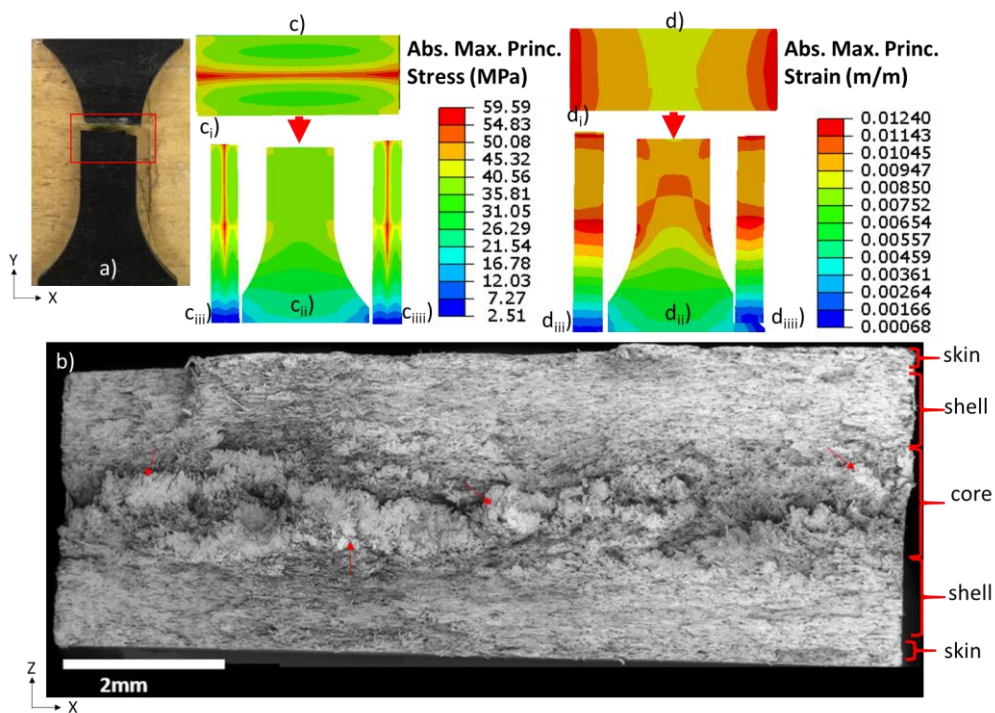


Figure 7-20 Stress and strain distributions and fracture surface of a fatigue 90° reference specimen with $V_f=30\%$ at $R=-1$ and $\sigma_a=40\text{MPa}$ ($N=30,260$ cycles).

Arrows denote example of packets seen on the fracture surface.

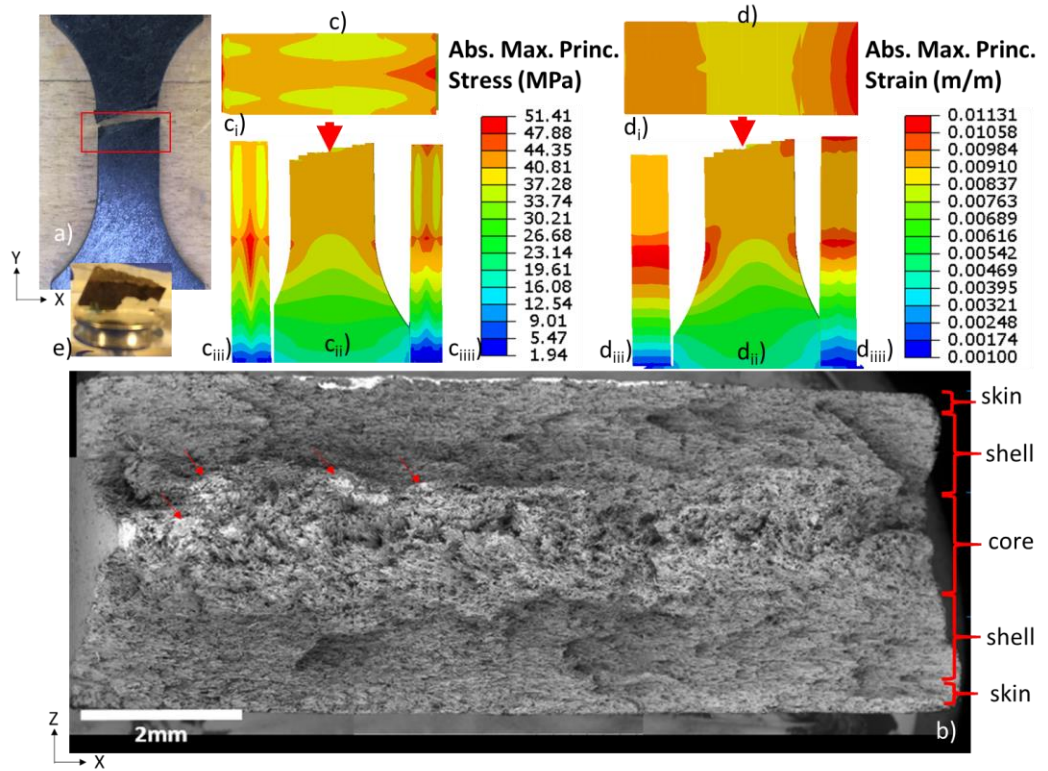


Figure 7-21 Stress and strain distributions and fracture surface of a fatigue 45° reference specimen with $V_f=30\%$ at $R=-1$ and $\sigma_a=40\text{MPa}$ ($N=66,646$ cycles). Arrows denote example of packets seen on the fracture surface.

8. CONCLUSION

The main objectives of this dissertation were to develop, and to validate, a modelling methodology for the fatigue prediction of injection moulded short glass-fibre reinforced polymers; and to generate new insight about the fatigue damage mechanisms of this type of composites. To this effect, a new multi-scale modelling approach was developed to predict the effect of the local fibre orientations and distributions on the fatigue life of these materials. This included a multi-stage computer-aided engineering methodology for the prediction of the fatigue life of dog-bone shaped specimens at different orientations and locations. Finite element models for the injection moulding, monotonic material properties, stress and strain distribution and fatigue calculations were developed. Each of the modelling steps was validated using state-of-the-art experimental techniques to assess the accuracy of the numerical predictions and the effect of the propagation of errors and inaccuracies on the final fatigue life prediction. Furthermore, new fundamental knowledge about fatigue damage development in this material has been generated in the form of the found location for multiple crack appearance below the surface of the material, in the region of high alignment of fibres along the load direction. However this result might be limited to surface measurement, and therefore, this mechanism needs to be confirmed through a more detailed CT scanning as part of future work. Analysis of high-speed camera images suggested that the time between crack appearance (multi-crack mechanism) and final material failure is very short, this therefore implied that the process of fatigue crack initiation might be very slow. This meant that by looking at stress and strain distributions in undamaged specimens it was possible to have a clear idea of the most likely location for specimen failure. Localization of stress was observed to be located below the surface in regions where the fibres are more aligned with the load direction, and in specific close to the specimen shoulders. Localization of strain was also shown to be concentrated through the thickness surface of the specimens. Analysis of the stress and strain distributions, together with SEM micrographs of the specimens' fracture surfaces and high-speed camera images, showed evidence of crack initiation occurring under the surface on locations of maximum stress/energy.

Additionally, the experimental characterisation carried out in this this project also showed that PA66GF50 exhibits a highly anisotropic material response due to the local fibre orientation distribution, product of the injection moulding process. The material's tensile and fatigue performance was observed to be significantly affected

by the fibre orientation distribution, with each tested coupon behaving as simplified structures, and producing a completely different material response depending on the location and orientation of the specimens. Under fatigue constant-amplitude conditions, the material was also seen to be affected by the mean stresses, significantly reducing the total fatigue life at higher stress ratios. Despite the overall differences observed between the experimental measurements and finite element predictions, in part due to errors propagated from the injection moulding simulation onto the stress analyses, the fatigue life predictions were shown to be close to the experimental lives under positive stress ratios. However, the results also highlighted the limitations of the modelling methodology based on the Stress-Life (S-N) approach, where under fully reverse stress ratio the calibration of the model was not possible. This could be due to the inability of the current M-T model to predict the material behaviour under cyclic conditions as it was developed, and used herein, for static loads under tensile loading. This means that it does not consider the compressive part of the cycle, as well as, the different material's cyclic mechanisms; such as the various softening and viscous effects seen in the measured hysteresis curves. To this effect, a different cyclic material model needs to be developed.

Finally, in order to overcome the limitations of the S-N method, an energy-based approach was proposed. A new fatigue parameter based on the dissipated energy calculated from the cyclic stabilised hysteresis loops was therefore introduced. It was shown that, based on the experimental results, the use of the dissipated energy seemed to reduce the effect of the fibre orientation in the cyclic response of specimens. However, a variability of the energy with the local fibre distribution was observed. Further development on this regards is however needed, in order to model the complex fibre orientation dependant local dissipated energy via simulated stabilised hysteresis loops. Nevertheless, the presented results and analysis done in this thesis regarding this approach can form the basis for future work.

8.1 Future work

- I. The humidity, moisture content, evolution in the specimen during, and after, the test was not measured on this project. In specific, the humidity level in the specimens was controlled using a hot water bath method. This technique does not provide with a consistent homogenous distribution through the material. Experimental results showed clear evidence of self-heating during the fatigue experiments, which would produce a reduction of the internal humidity and

thus affect the material response, as seen in the literature. Therefore, to produce a more controlled environment and a more consistent material condition, as well as, to assure the repeatability of the results; the humidity environment should be kept consistent at laboratory conditions (23°C and 50% R.H.). This can be achieved through the use of an environmental chamber. Similarly, to measure the change in the material moisture content, weight measurements should be taken at different points of the test, this will provided quantitative data of the effect of self-heating in the humidity content. Subsequent tests could also be carried out with specimens under as-moulded/dry conditions, to remove the effects caused by inner humidity changes.

- II. Additional testing at different stress ratios needs to be conducted to further calibrate the Walker's coefficient for the mean stress correction.
- III. As it was shown in the present Thesis, there seems to be an effect of the load sequence on the material fatigue performance under block loading conditions. In specific, preliminary results showed that the specimen orientation might have an effect on how the loading sequence affects the specimen. 0° specimens showed better fatigue lives under Low-High sequence, whereas 45° samples presented better fatigue lives under High-Low sequence. Therefore, it is sensible to assumed that this effect of the orientation would also be present under non-proportional loading, i.e. variable loading. A past work, [176], has suggested that higher frequency spectrums produce higher fatigue life, but this has only been carried out on a singular orientation, under dry conditions, and with low amount of reinforcement (30wt%). Therefore it is needed, as part of future work, to assess whether this result is still the case when accounting for different specimen orientations, while the material is conditioned and with a relatively high amount of reinforcement (50wt% or 30vf%).
- IV. The finite element implementation of the energy based model using cyclic dissipated energy is needed. For this, the numerical simulation of the stabilised hysteresis loop needs to be conducted and calibrated using experimental data. Although some testing is required, this calibration can only be conducted using a singular specimen orientation, as it has been shown in this Thesis that by using this dissipated energy approach the spread due to the specimen orientation and stress ratio seems to be minimised. Therefore, the amount of experimentation can be significantly reduced. Once this calibration is

conducted, then the model could potentially be used on specimens with different fibre distributions and under different stress ratios.

- V. It has been shown in the literature, [61], [177], that the temperature has an effect on the performance of different short fibre reinforced polymers, with higher temperatures showing a more ductile behaviour in tensile, and a lower fatigue lives during cyclic loading. Therefore, the effect of the temperature on PA66GF50 needs to be investigated. This will provide with better understanding of the material performance under conditions that could potentially be seen in the field, and thus it would increase the usability of this composite on actual structural parts.
- VI. Documented work of the effect of temperature in different short fibre reinforced polymers has shown that the creep strain and the rate of creep seem to increase as the temperature of the polymer goes above T_g [177]. As applications of the present PA66GF50 is related to the automotive industry, environments where the material is exposed to temperatures around and above T_g are highly likely to occur. Therefore, the effect of creep on the present composite needs to be studied to increase the available knowledge of the behaviour of the material under field working conditions. Finally, different specimen orientations could also be used to analyse the variation of creep with the fibre distribution.
- VII. Detailed CT scanning of specimens subjected to fatigue needs to be conducted at different number of cycles, with focus on below the surface of the specimens to further corroborate the location of multi crack appearance found in this project via the use of high speed cameras and the analysis of the FEA results.
- VIII. A different material model needs to be developed to consider the different cyclic mechanisms seen on the experimental test (hysteresis curves), that the current M-T model cannot capture, such as: cyclic softening and viscous effects.
- IX. Analysis of the applicability of the proposed S-N approach to more complex geometries needs to be investigated and validated. Is there a possibility of correlating dog-bone results with more complex, larger, geometries through the use of a calibration factor? If so, this could potentially increase the practical use of the model in real applications.

APPENDIX

A Appendix Chapter 4.

A.1 Example of material input card for stress analysis

```
#####  
MATERIAL  
name = GF  
type = elastic  
density = 2.540000000000000e-009  
elastic_model = isotropic  
Young = 7.200000000000000e+004  
Poisson = 2.200000000000000e-001  
#####  
MATERIAL  
name = PA66  
type = J2_plasticity  
density = 1.245610000000000e-009  
consistent_tangent = on  
elastic_model = isotropic  
Young = 1.795000000000000e+003  
Poisson = 3.963200000000000e-001  
yield_stress = 7.910000000000000e+000  
hardening_model = exponential_linear  
hardening_modulus = 6.577400000000000e+001  
hardening_exponent = 2.564000000000000e+002  
hardening_modulus2 = 1.036100000000000e+002  
isotropic_method = modified_spectral  
plastic_strain_multiplier = 1.136200000000000e+001  
plastic_strain_shift = 0.000000000000000e+000  
global_shear_multiplier = 1.000000000000000e+000  
plastic_shear_multiplier = 1.000000000000000e+000  
#####  
PHASE  
name = Matrix  
type = matrix  
mass_fraction = 5.000000000000000e-001  
material = PA66  
  
#####  
PHASE  
name = Filler  
type = inclusion  
mass_fraction = 5.000000000000000e-001  
behavior = deformable_solid  
material = GF  
aspect_ratio = 19.671000000000000e+000  
orientation = file  
orientation_file = C:\Users\Work\Google Drive\05-CAE\Digimat\0Degree\map\0DegOT.dof
```

```

orientation_format = Digimat
closure = orthotropic
coated = no
#####
MICROSTRUCTURE
name = Microstructure
phase = Matrix
phase = Filler
#####
RVE
type = classical
microstructure = Microstructure
#####
ANALYSIS
name = Sheffield-A3WG10CR
unit_system = METRIC/3/-3/0/0/0/0
type = mechanical
loading_name = Mechanical
final_time = 4.851400000000000e-001
max_time_inc = 2.425700000000000e-003
min_time_inc = 9.702799999999999e-005
finite_strain = off
output_name = output1
load = ABAQUS/Standard
homogenization = on
homogenization_model = Mori_Tanaka
integration_parameter = 5.000000000000000e-001
number_angle_increments = 12
stiffness = off
initial_stresses = off
orientation_usage = global
plane_strain_element = off
orientation_skin = do_not_use_moldflow_output
plane_condition_initial_guess = on
OT_trace_tol = 1.000000000000000e-001
finite_rotation = off
#####
OUTPUT
name = output1
RVE_data = Custom,Ener
Phase_data = Filler,Custom,Cglob,Ener,OT
Phase_data = Matrix,Custom,Cglob,Ener,OT
Engineering_data = None
Log_data = None
Dependent_data = Default
Fatigue_data = Default
Composite_data = Custom,A1,APS,IA

```

A.2 Mapped orientation tensor global error

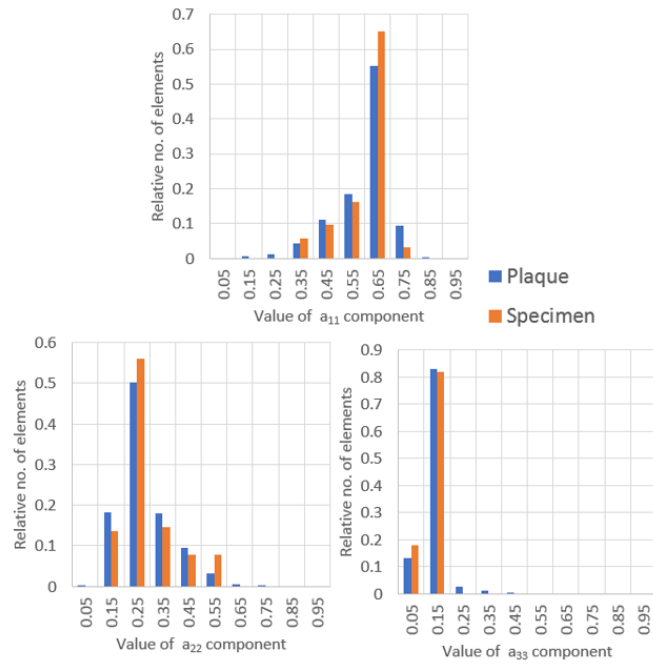


Figure A-0-1 Mapping global error for 0° Edge uniaxial specimens

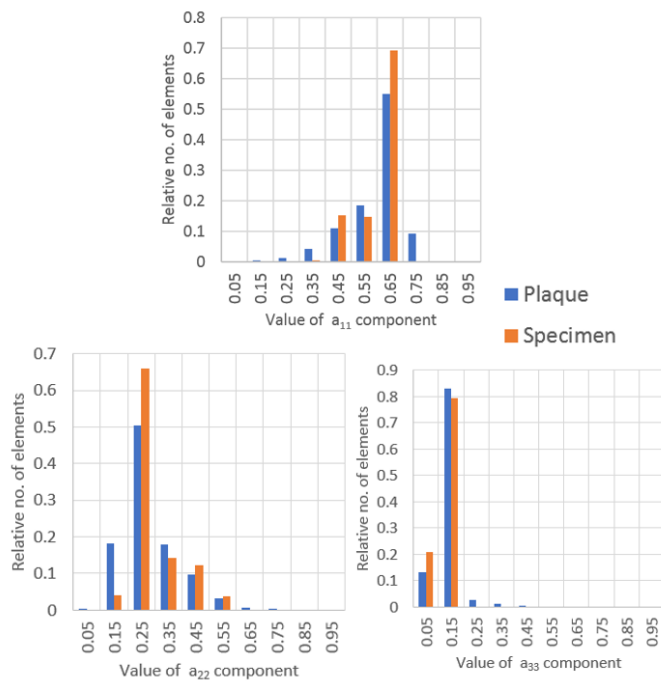


Figure A-0-2 Mapping global error for 30° uniaxial specimens

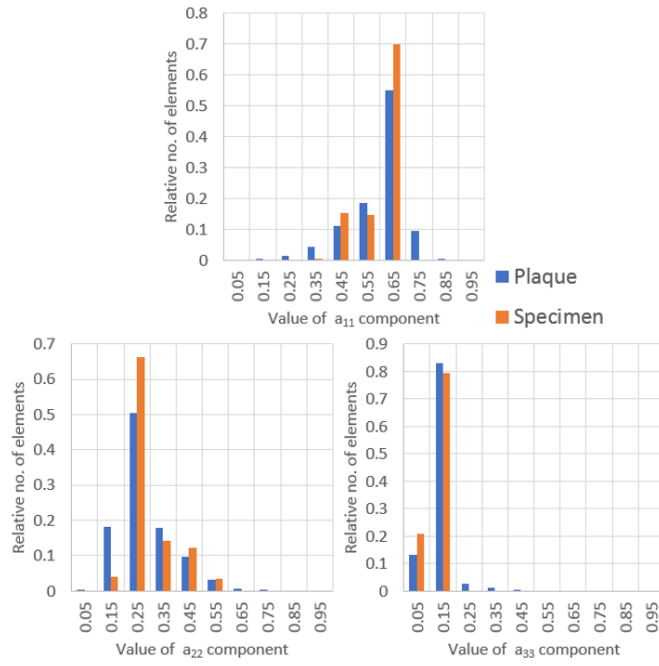


Figure A-0-3 Mapping global error for 45° uniaxial specimens

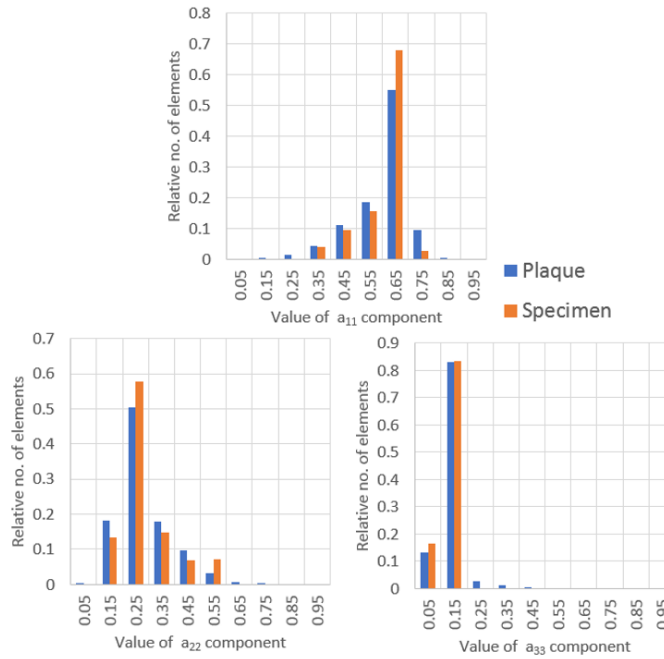


Figure A-0-4 Mapping global error for 90° uniaxial specimens

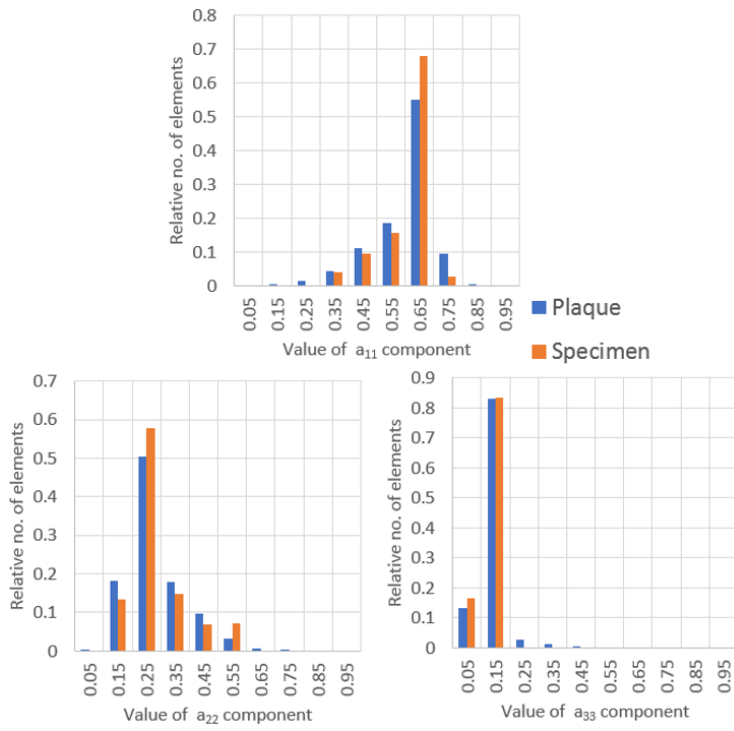


Figure A-0-5 Mapping global error for 90° Edge uniaxial specimens

B Appendix Chapter 5

B.1 Hysteresis loops

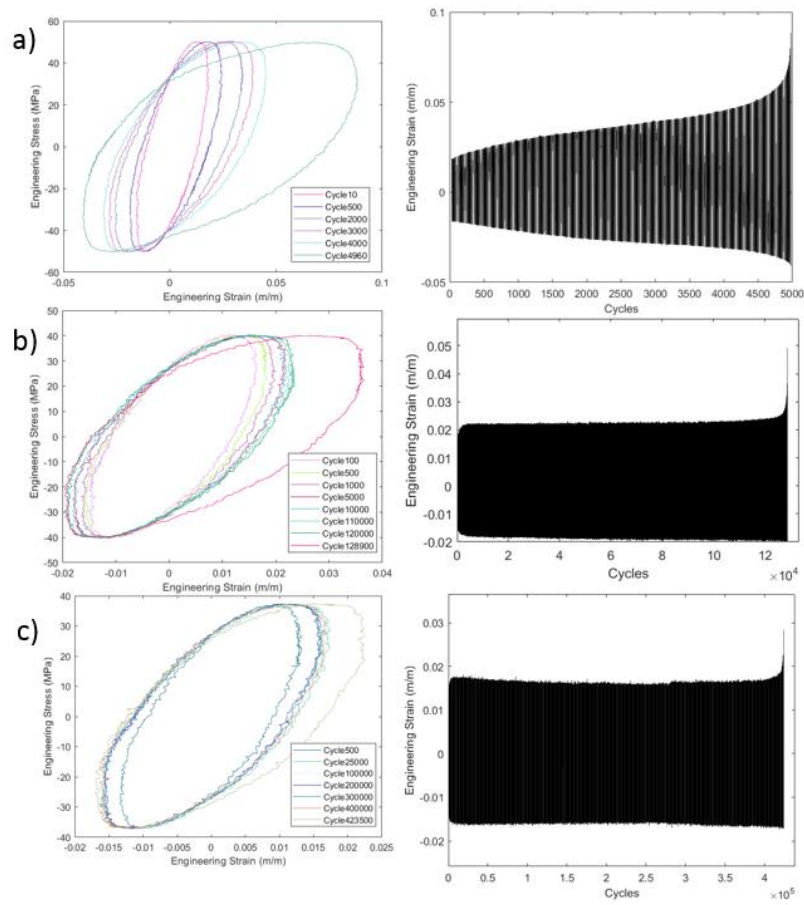


Figure A-0-6 Hysteresis loops (Stress vs Strain), and evolution of strain (Strain vs Cycle) for 0° , $R=-1$ samples at a) $\sigma_a=50\text{MPa}$, b) $\sigma_a=40\text{MPa}$ and c) $\sigma_a=38\text{MPa}$

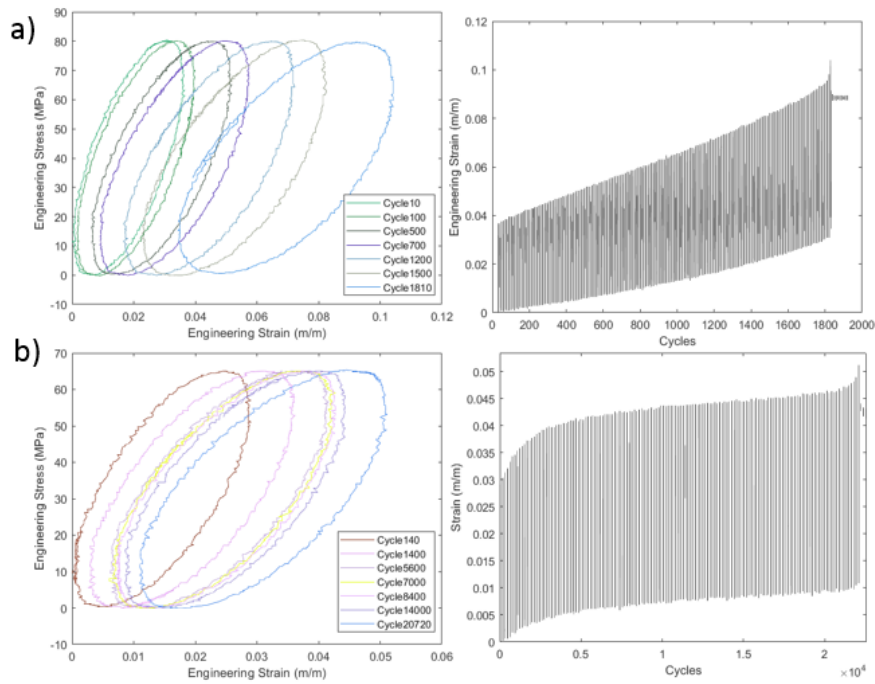


Figure A-0-7 Hysteresis loops (Stress vs Strain), and evolution of strain (Strain vs Cycle) for 0° , $R=0$ samples at a) $\sigma_a=41 \text{ MPa}$, b) $\sigma_a=33 \text{ MPa}$.

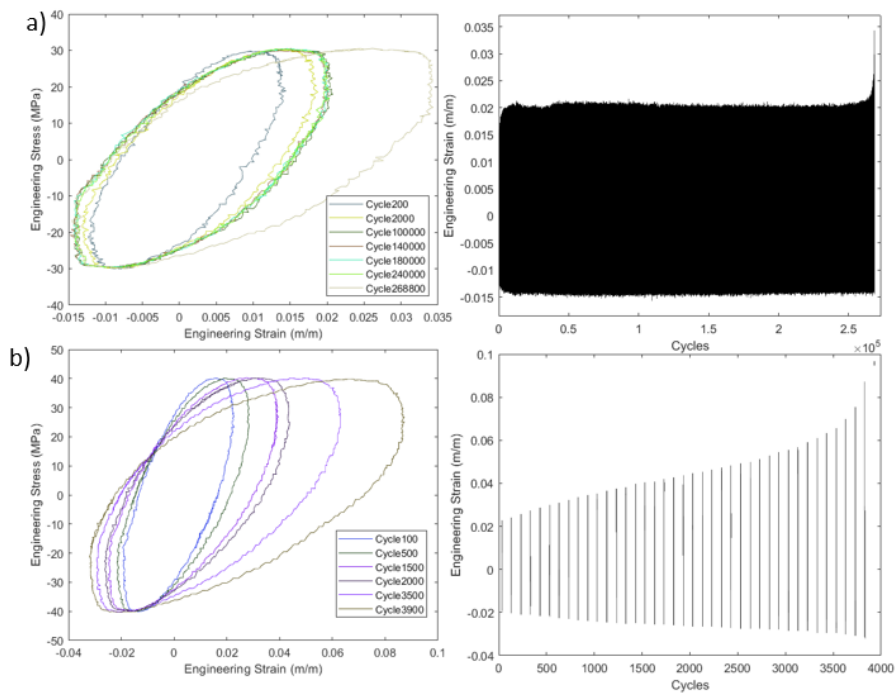


Figure A-0-8 Hysteresis loops (Stress vs Strain), and evolution of strain (Strain vs Cycle) for 90° , $R=-1$ samples at a) $\sigma_a=31 \text{ MPa}$, b) $\sigma_a=41 \text{ MPa}$.

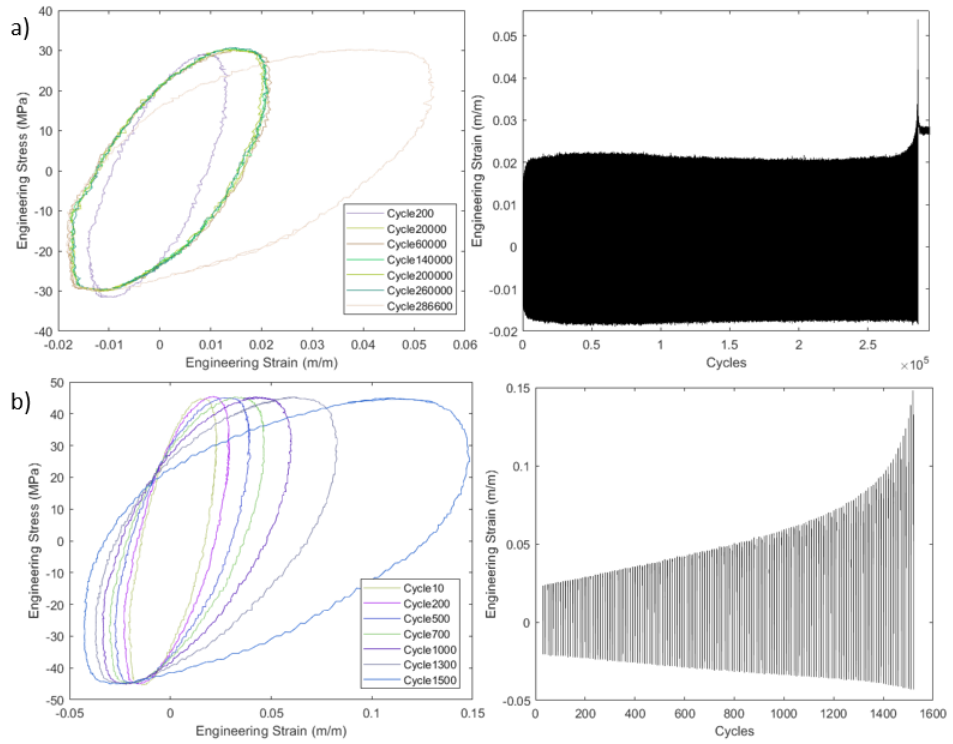


Figure A-0-9 Hysteresis loops (Stress vs Strain), and evolution of strain (Strain vs Cycle) for 45°, R=-1 samples at a) $\sigma_a=31$ MPa, b) $\sigma_a=46$ MPa

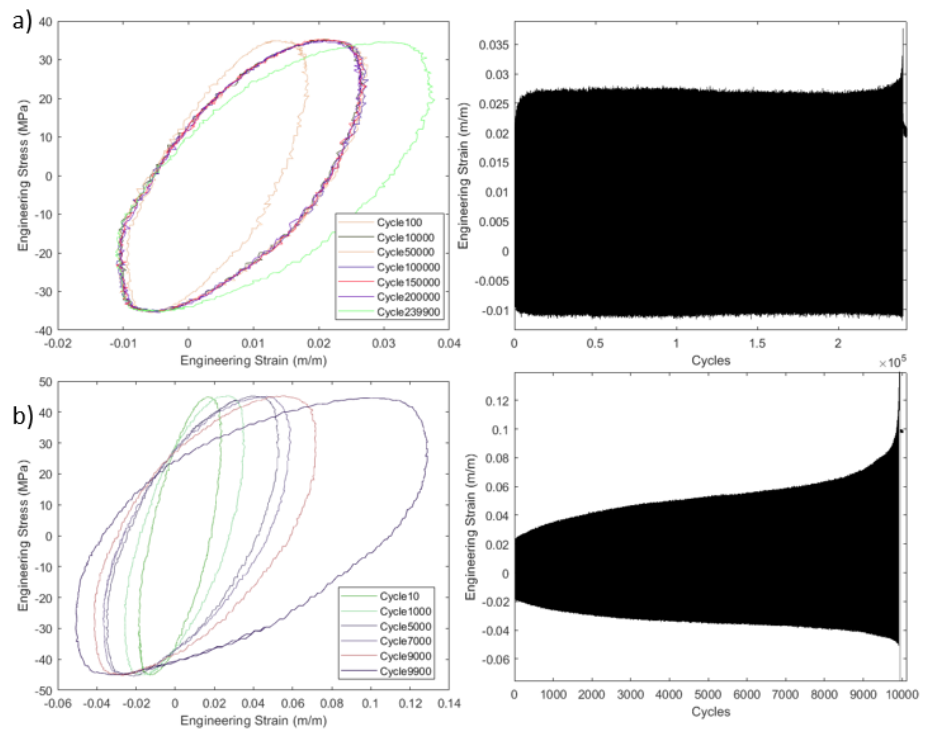


Figure A-0-10 Hysteresis loops (Stress vs Strain), and evolution of strain (Strain vs Cycle) for 30°, R=-1 samples at a) $\sigma_a=36$ MPa, b) $\sigma_a=46$ MPa

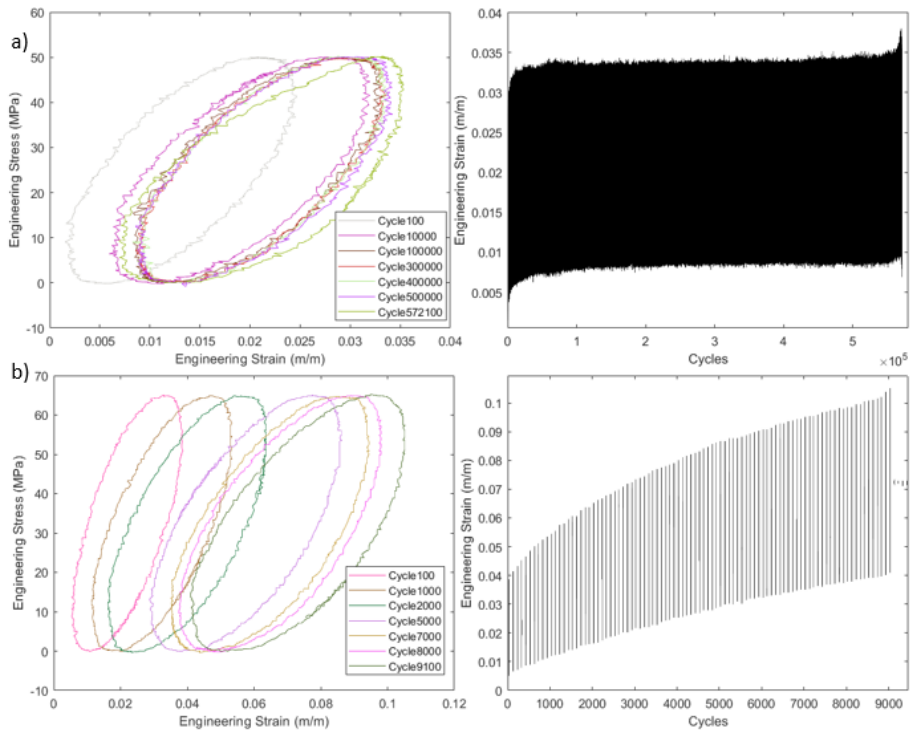


Figure A-0-11 Hysteresis loops (Stress vs Strain), and evolution of strain (Strain vs Cycle) for 30°, R=0 samples at a) $\sigma_a=25\text{MPa}$, b) $\sigma_a=33\text{MPa}$.

B.2 Fatigue failed specimens

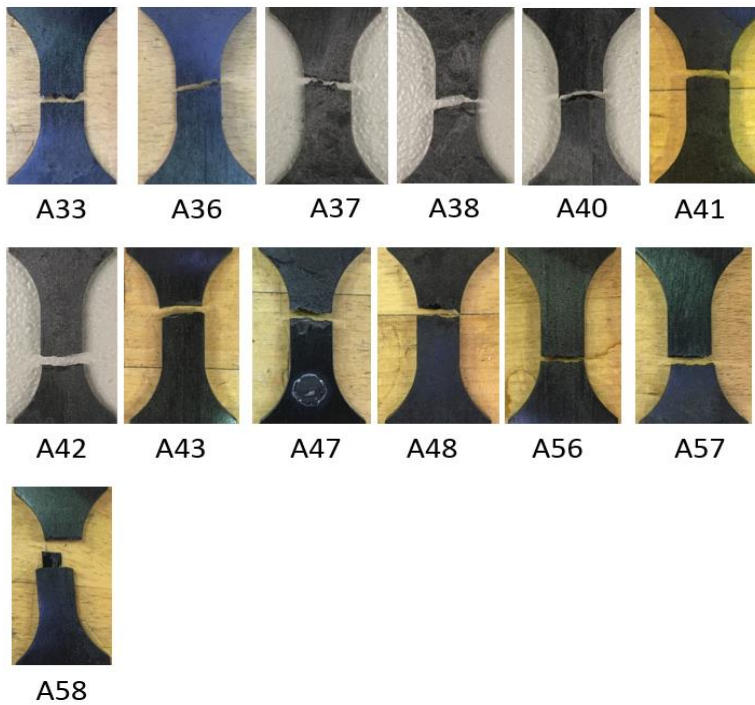


Figure A-0-12 Fracture specimens for 0° coupons at R=-1

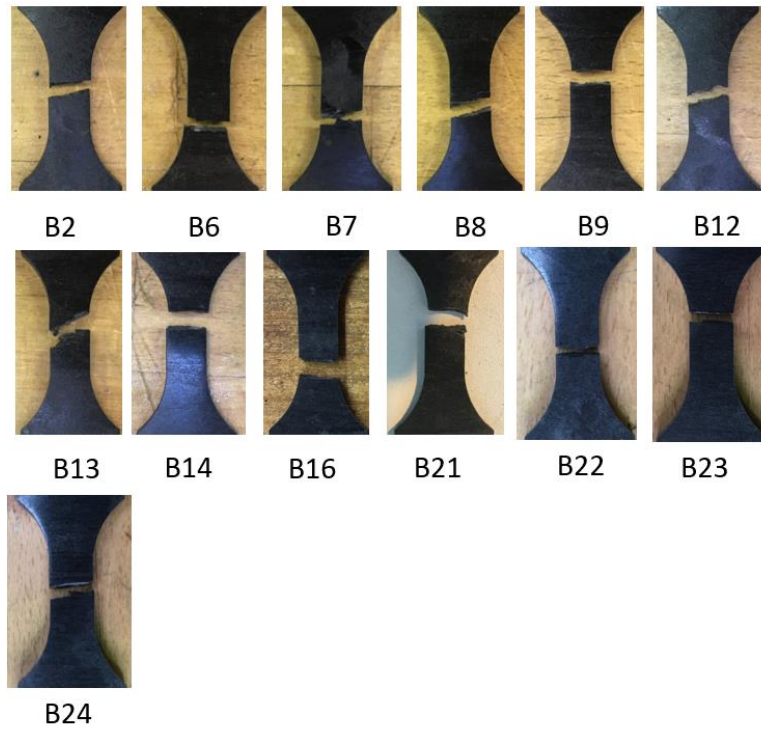


Figure A-0-13 Fracture specimens for 90° coupons at R=-1.

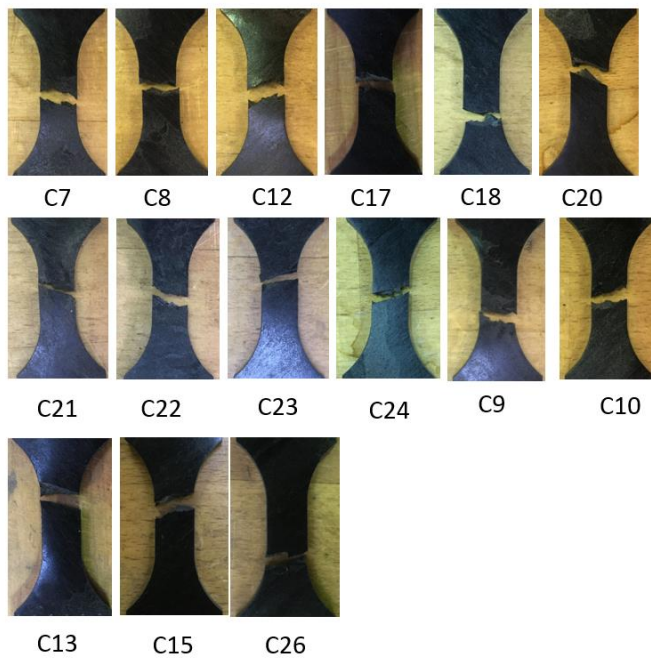


Figure A-0-14 Fracture specimens for 45° coupons at R=-1.

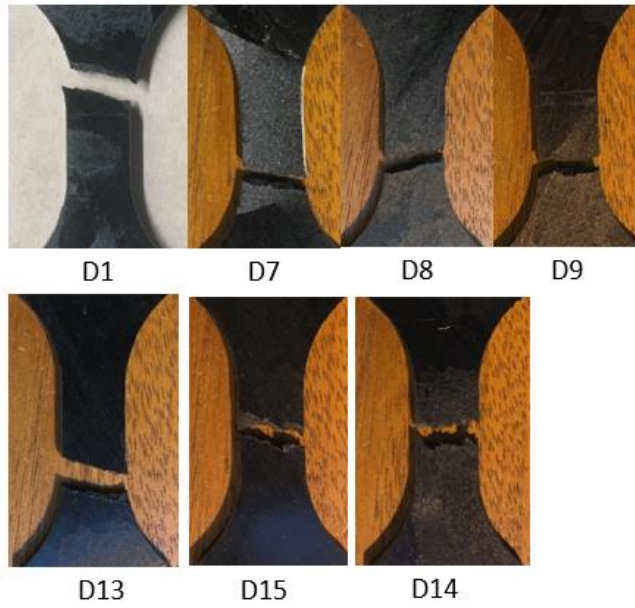


Figure A-0-15 Fracture specimens for 30° coupons at R=-1.

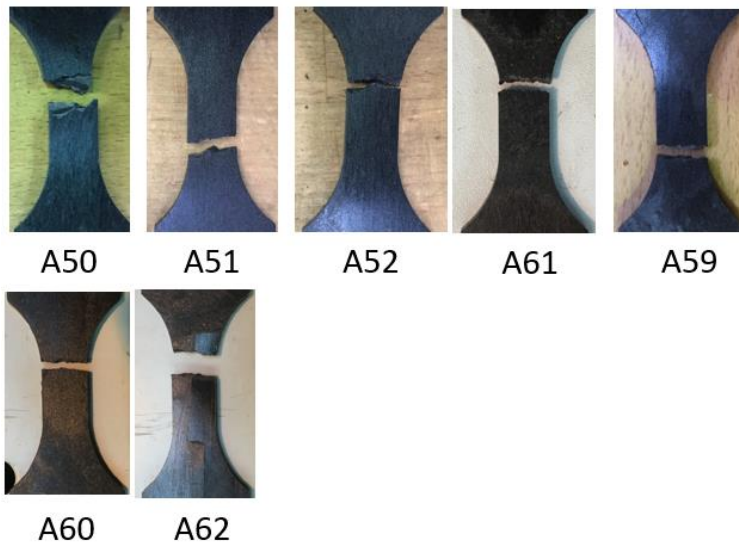


Figure A-0-16 Fracture specimens for 0° coupons at R=0.

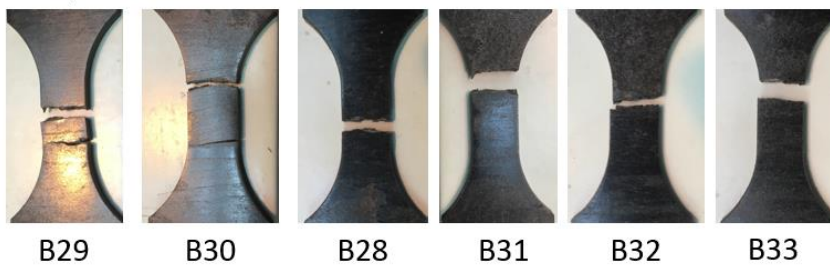


Figure A-0-17 Fracture specimens for 90° coupons at R=0.

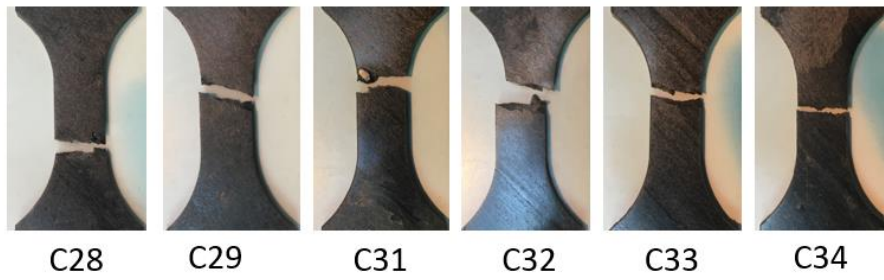


Figure A-0-18 Fracture specimens for 45° coupons at R=0.

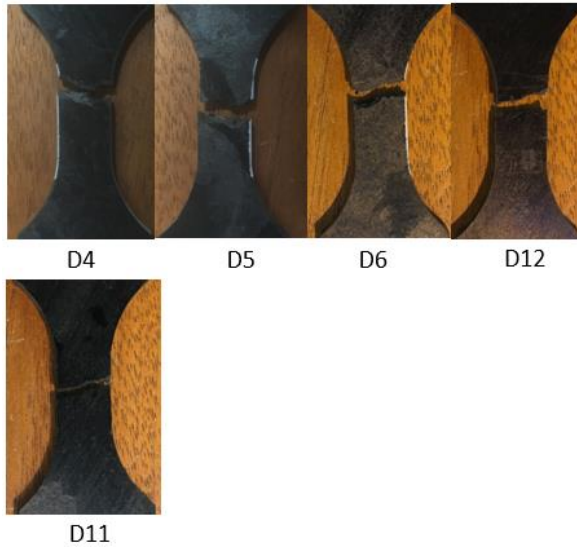


Figure A-0-19 Fracture specimens for 30° coupons at R=0.

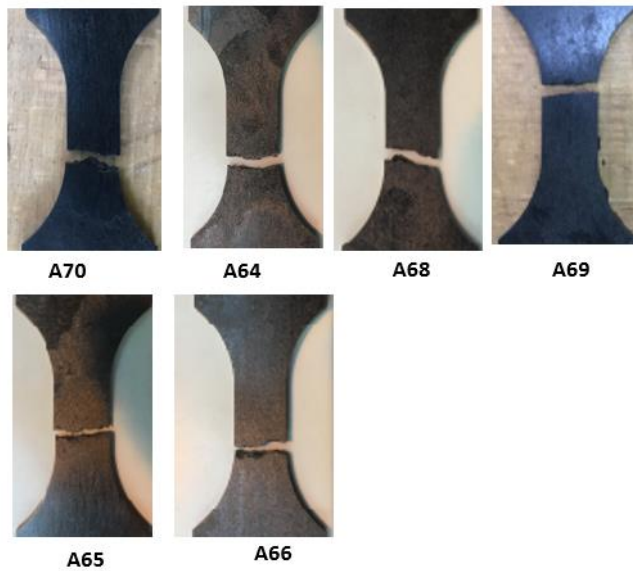


Figure A-0-20 Fracture specimens for 0° coupons at R=0.3.

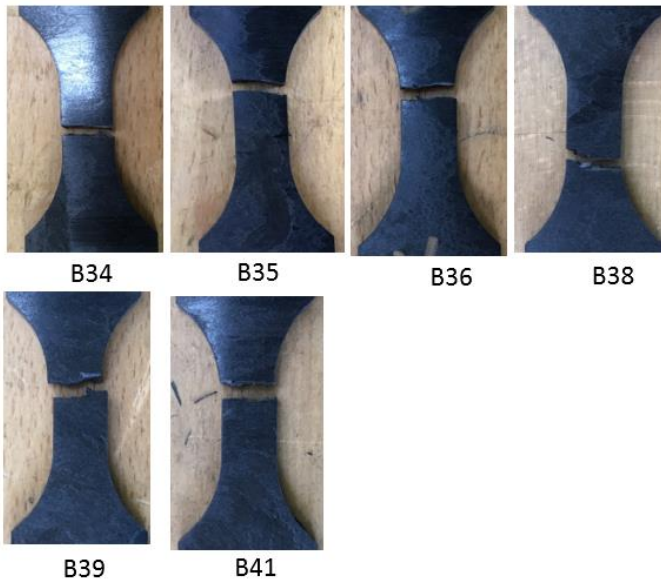


Figure A-0-21 Fracture specimens for 90° coupons at R=0.3.

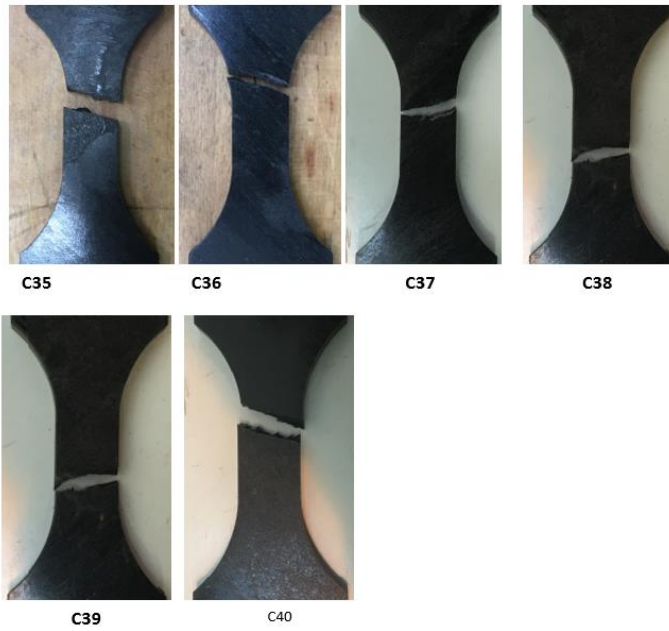


Figure A-0-22 Fracture specimens for 45° coupons at R=0.3.

REFERENCES

- [1] Y. A. Lizama Camara, C. Pinna, Z. Lu, and M. Blagdon, "Multistage modelling and experimental validation of the fatigue life of a short fibre reinforced polymer (SFRP) composite," 2018.
- [2] P. Wilson and P. Heyes, "Fatigue of short fibre reinforced polymers: from material process to fatigue life of industrial components," in *MATEC Web Conf. 12th International Fatigue Congress (FATIGUE 2018)*., 2018, vol. 165.
- [3] T. Malo, L. Adam, R. Assaker, T. Matsumoto, and R. Giacomini, "Multi-Scale Modeling of High Cycle Fatigue of Chopped and Continuous Fiber Composites," 2013.
- [4] "Regulation (EU) No 333/2014 of the European Parliament and of the Council of 11 March 2014 amending Regulation (EC) No 443/2009 to define the modalities for reaching the 2020 target to reduce CO2 emissions from new passenger cars," *Off. J. Eur. Union*, vol. 57, pp. 15–21, 2014.
- [5] J. R. Vinson and R. L. Sierakowski, *The Behavior of Structures Composed of Composite Materials*, 2nd. Kluwer Academic Publishers, 2002.
- [6] K. Chawla, *Composite Materials*, 3rd. New York: Springer, 2012.
- [7] L. Ruian Jixiang Automobile Parts Co., "Plastic Auto Engine Air Intake Manifold fit for AUDI A4 A5 Q5 VW SEAT SKODA Exeo GOLF PASSAT 2.0 TDI DIESEL 03L129711AG," *Alibaba*. https://www.alibaba.com/product-detail/Plastic-Auto-Engine-Air-Intake-Manifold_60642494958.html?spm=a2700.7724857.normalList.5.13926c85YFwfj4 (accessed Oct. 06, 2018).
- [8] D. Scorza, "Mechanical Modelling of Short-Fibre-Reinforced Materials under Static or Cyclic Loading," University of Parma, 2015.
- [9] P. Ladeveze and E. LeDantec, "Damage modelling of the elementary ply for laminated composites," *Compos. Sci. Technol.*, vol. 43, no. 3, pp. 257–267, 1992.
- [10] H. Nouri, F. Meraghni, and P. Lory, "Fatigue damage model for injection-molded short glass fibre reinforced thermoplastics," *Int. J. Fatigue*, vol. 31, no. 5, pp. 934–942, 2009.
- [11] A. P. Vassilopoulos and K. Thomas, *Fatigue of fiber reinforced composites*. London: Springer Science & Business Media, 2011.
- [12] D. D. L. Chung, *Composite Materials: Functional Materials for Modern Technologies*. Springer, 2002.
- [13] P. K. Mallick, *Fiber-reinforced composites: materials, manufacturing and design*.

CRC Press, 2007.

- [14] A. P. Vassilopoulos and K. Thomas, *Fatigue of fiber-reinforced composites*. London: Springer Science & Business Media, 2011.
- [15] F. T. Wallenberger, J. C. Watson, and L. Hong, "Glass Fibers," *ASM Handb.*, vol. 21, no. Ref 19, pp. 27–34, 2001.
- [16] T. Sasayama, T. Okabe, Y. Aoyagi, and M. Nishikawa, "Prediction of failure properties of injection-molded short glass fiber-reinforced polyamide 6,6," *Compos. Part A Appl. Sci. Manuf.*, vol. 52, pp. 45–54, 2013.
- [17] L. M. Vas, F. Ronkay, and T. Czigány, "Active fiber length distribution and its application to determine the critical fiber length," *Polym. Test.*, vol. 28, no. 7, pp. 752–759, 2009.
- [18] A. Kelly and W. R. Tyson, "Tensile properties of fibre-reinforced metals: Copper/tungsten and copper/molybdenum," *J. Mech. Phys. Solids*, vol. 13, no. 6, 1965.
- [19] F. W. J. Van Hattum and C. A. Bernardo, "Model to predict the strength of short fiber composites," *Polym. Compos.*, vol. 20, no. 4, pp. 524–533, 1999.
- [20] S. Mortazavian and A. Fatemi, "Effects of fiber orientation and anisotropy on tensile strength and elastic modulus of short fiber reinforced polymer composites," *Compos. Part B Eng.*, vol. 72, pp. 116–129, 2015.
- [21] P.K.Mallick, *Materials, Design and Manufacturing for Lightweight Vehicles*. Woodhead Publishing Series in Composites Science and Engineering, 2010.
- [22] N. Sato, T. Kurauchi, S. Sato, and O. Kamigaito, "Reinforcing Mechanism by Small Diameter Fiber in Short Fiber Composite," *J. Compos. Mater.*, vol. 22, no. 9, pp. 850–873, 1988.
- [23] J. Komornicki, L. Bax, H. Vasiliadis, I. Magallon, and K. Ong, "Polymer composites for automotive sustainability Polymer composites for automotive sustainability," *SusChem*, 2017. www.suschem.org/files/library/Publications/POLYMERS_Brochure_Web.pdf (accessed Oct. 03, 2018).
- [24] I. M. Ward and J. Sweeney, *Mechanical properties of solid polymers*, 3rd. WILEY, 2013.
- [25] S. K. De and J. R. White, *Short Fibre-Polymer Composites*. Cambridge, UK: Woodhead Publishing Limited, 1996.
- [26] M. S. Huda, L. T. Drzal, A. K. Mohanty, and M. Misra, "Chopped glass and recycled newspaper as reinforcement fibers in injection molded poly(lactic acid) (PLA) composites: A comparative study," *Compos. Sci. Technol.*, vol. 66, no. 11–12, pp. 1813–1824, 2006.

- [27] F. L. Matthews and R. D. Rawlings, *Composite materials: Engineering and science*, Reprint. Cambridge, UK: Woodhead Publishing Limited, 2008.
- [28] Carabiner development, "Composites introduction," *Carabiner development*. http://www.crabdev.co.uk/comp_manufacturing.htm (accessed Oct. 07, 2018).
- [29] F. O' Dowd, M. Lévesque, and M. D. Gilchrist, "Analysis of fibre orientation effects on injection moulded components," *Proc. Inst. Mech. Eng. Part B J. Eng. Manuf.*, vol. 220, no. 12, pp. 1909–1921, 2006.
- [30] C. Eberhardt and A. Clarke, "Fibre-orientation measurements in short-glass-fibre composites. Part I: Automated, high-angular-resolution measurement by confocal microscopy," *Compos. Sci. Technol.*, vol. 61, no. 10, pp. 1389–1400, 2001.
- [31] S. Hamanaka, K. Yamashita, C. Nonomura, T. B. N. Thi, T. Wakano, and A. Yokoyama, "Measurement of fiber orientation distribution in injection-molded composites with high filler content," *AIP Conf. Proc.*, vol. 1914, pp. 1–6, 2017.
- [32] M. Vincent, T. Giroud, A. Clarke, and C. Eberhardt, "Description and modeling of fiber orientation in injection molding of fiber reinforced thermoplastics," *Polymer (Guildf.)*, vol. 46, no. 17, pp. 6719–6725, 2005.
- [33] G. Gsellmann, M. Jerabek, and D. Salaberger, "Comparison of predicted and measured fiber orientations in injection molded parts," *Proc. 6th Conf. Ind. Comput. Tomogr.*, 2016.
- [34] G. M. Vélez-García, "Experimental evaluation and simulations of fiber orientation in injection molding of polymers containing short glass fibers," Virginia Polytechnic Institute, 2012.
- [35] E. G. Kim, J. K. Park, and S. H. Jo, "A study on fiber orientation during the injection molding of fiber-reinforced polymeric composites: (Comparison between image processing results and numerical simulation)," *J. Mater. Process. Technol.*, vol. 111, no. 1–3, pp. 225–232, 2001.
- [36] S. G. Advani and K.-T. Hsiao, Eds., *Manufacturing Techniques for Polymer Matrix Composites (PMCs)*. Cambridge: Elsevier Science, 2012.
- [37] E. Homsí, "Reinforced Plastic Material Performance," *Prospector*, 2010. <https://knowledge.ulprospector.com/1307/pe-plastic-fiber/> (accessed Oct. 07, 2018).
- [38] M. W. Darlington and P. L. McGinley, "Fibre orientation distribution in short fibre reinforced plastics," *J. Mater. Sci.*, vol. 10, pp. 906–910, 1975.
- [39] G. M. Velez-Garcia, P. Wapperom, D. G. Baird, A. O. Aning, and V. Kunc, "Unambiguous orientation in short fiber composites over small sampling area in a center-gated disk," *Compos. Part A Appl. Sci. Manuf.*, vol. 43, no. 1, pp.

104–113, 2012.

- [40] S. S. Afrookhteh, J. Jamali, M. Shakeri, and M. Baniassadi, "Stochastic reconstruction of carbon fiber paper gas diffusion layers of PEFCs: A comparative study," *Energy Equip. Syst.*, vol. 6, no. 1, pp. 51–59, 2018.
- [41] M. F. Arif, N. Saintier, F. Meraghni, J. Fitoussi, Y. Chemisky, and G. Robert, "Multiscale fatigue damage characterization in short glass fiber reinforced polyamide-66," *Compos. Part B Eng.*, vol. 61, pp. 55–65, 2014.
- [42] A. Bernasconi, F. Cosmi, and P. J. Hine, "Analysis of fibre orientation distribution in short fibre reinforced polymers: A comparison between optical and tomographic methods," *Compos. Sci. Technol.*, vol. 72, no. 16, pp. 2002–2008, 2012.
- [43] T. B. Nguyen Thi, M. Morioka, A. Yokoyama, S. Hamanaka, K. Yamashita, and C. Nonomura, "Measurement of fiber orientation distribution in injection-molded short-glass-fiber composites using X-ray computed tomography," *J. Mater. Process. Technol.*, vol. 219, pp. 1–9, 2015.
- [44] M. Insight, "Fiber orientation tensor result," *Autodesk*, 2014. <https://knowledge.autodesk.com/support/moldflow-insight/learn-explore/caas/CloudHelp/cloudhelp/2014/ENU/MoldflowInsight/files/GUID-67EA81F8-5044-461C-839E-987966065764-htm.html> (accessed Oct. 10, 2018).
- [45] Autodesk, "Theoretical basis for fiber orientation prediction," *Autodesk*, 2015. <http://help.autodesk.com/view/MFC/2015/ENU/?guid=GUID-50FF496F-0E3E-43CE-B30B-4B12CC24F7DE> (accessed Oct. 10, 2018).
- [46] HBM nCode, *DesignLife Theory Guide*. HBM United Kingdom Limited, 2013.
- [47] F. Folgar and C. L. T. III, "Orientation behaviour of fibers in concentrated suspensions," *J. Reinf. Plast. Compos.*, vol. 3, no. April 1984, pp. 98–119, 1984.
- [48] S. G. Advani and C. L. Tucker, "The Use of Tensors to Describe and Predict Fiber Orientation in Short Fiber Composites," *J. Rheol. (N. Y. N. Y.)*, vol. 31, no. 8, pp. 751–784, 1987.
- [49] J. Wang, J. F. O' Gara, and C. L. Tucker, "An objective model for slow orientation kinetics in concentrated fiber suspensions: Theory and rheological evidence," *J. Rheol. (N. Y. N. Y.)*, vol. 52, no. 5, pp. 1179–1200, 2008.
- [50] J. Wang and X. Jin, "Comparison of recent fiber orientation models in Autodesk Moldflow Insight simulations with measured fiber orientation data," *Proc. Polym. Process. Soc. 26th Annu. Meet.*, no. 2009, 2010.
- [51] M. Jerabek, A. M. Hartl, Z. Major, and R. W. Lang, "Characterization of short fiber reinforced polypropylene composites," *15th Eur. Conf. Compos. Mater.*, pp. 55–58, 2012.

- [52] V. B. Gupta, R. K. Mittal, and M. Goel, "Energy absorbing mechanisms in short-glass-fibre-reinforced polypropylene," *Compos. Sci. Technol.*, vol. 37, no. 4, pp. 353–369, 1990.
- [53] A. Bernasconi, P. Davoli, A. Basile, and A. Filippi, "Effect of fibre orientation on the fatigue behaviour of a short glass fibre reinforced polyamide-6," *Int. J. Fatigue*, vol. 29, no. 2, pp. 199–208, 2007.
- [54] S. Mortazavian and A. Fatemi, "Tensile and fatigue behaviors of polymers for automotive applications," *Materwiss. Werksttech.*, vol. 46, no. 2, pp. 204–213, 2015.
- [55] P. Heyes, "The role of stress analysis in fatigue characterisation of short fibre reinforced thermoplastics," in *NAFEMS UK Regional Conference - Engineering Simulation: The Future Begins Today*, 2016, pp. 1–4.
- [56] V. Crupi, E. Guglielmino, G. Risitano, and F. Tavilla, "Experimental analyses of SFRP material under static and fatigue loading by means of thermographic and DIC techniques," *Compos. Part B Eng.*, vol. 77, pp. 268–277, 2015.
- [57] S. A. Hitchen, S. L. Ogin, and P. A. Smith, "Effect of fibre length on fatigue of short carbon fibre/epoxy composite," *Composites*, vol. 26, no. 4, pp. 303–308, 1995.
- [58] M. Miwa and N. Horiba, "Effects of fibre length on tensile strength of carbon/glass fibre hybrid composites," *J. Mater. Sci.*, vol. 29, no. 4, pp. 973–977, 1994.
- [59] I. Carrascal, J. A. Casado, J. A. Polanco, and F. Gutiérrez-Solana, "Absorption and diffusion of humidity in fiberglass-reinforced polyamide," *Polym. Compos.*, vol. 26, no. 5, pp. 580–586, 2005.
- [60] S. Glaser and A. Wust, "Virtual development of crash-stressed parts," *Kunststoffe Int.*, vol. 96, no. 9, pp. 169–172, 2006, Accessed: Apr. 26, 2019.
- [61] Z. Wang, Y. Zhou, and P. K. Mallick, "Effects of temperature and strain rate on the tensile behavior of shod fiber reinforced polyamide-6," *Polym. Compos.*, vol. 23, no. 5, pp. 858–871, 2002.
- [62] J. C. Halpin, S. T. Louis, J. L. Kardos, J. C. Halpin, S. T. Louis, and J. L. Kardos, "The Halpin-Tsai Equations: A Review," *Polym. Eng. Sci.*, vol. 16, no. 5, pp. 344–352, 1976.
- [63] K. Jayaraman and M. T. Kortschot, "Correction to the Fukuda-Kawata Young's modulus theory and the Fukuda-Chou strength theory for short fibre-reinforced composite materials," *J. Mater. Sci.*, vol. 31, no. 8, pp. 2059–2064, 1996.
- [64] S. Y. Fu, X. Hu, and C. Y. Yue, "The flexural modulus of misaligned short-fiber-

- reinforced polymers," *Compos. Sci. Technol.*, vol. 59, no. 10, pp. 1533–1542, 1999.
- [65] S. Nemat-Nasser and M. Hori, *Micromechanics: overall properties of heterogeneous materials*. Amsterdam: Elsevier Science, 1993.
- [66] e-Xstream engineering, *Digimat user ' s manual*, 2018.0. 2017.
- [67] J. D. Eshelby, "The determination of the elastic field of an ellipsoidal inclusion, and related problems," *Proc. R. Soc. London. Ser. A. Math. Phys. Sci.*, vol. 241, no. 1226, pp. 209–229, 1957.
- [68] T. Mori and K. Tanaka, "Average stress in matrix and average elastic energy of materials with misfitting inclusions," *Acta Metall.*, vol. 21, no. 5, pp. 571–574, 1973.
- [69] M. Hori and S. Nemat-Nasser, "Double-inclusion model and overall moduli of multi-phase composites," *Mech. Mater.*, vol. 14, no. 3, pp. 189–206, 1993.
- [70] Y. Benveniste, "A new approach to the application of Mori-Tanaka' s theory in composite materials," *Mech. Mater.*, vol. 6, no. 2, pp. 147–157, 1987.
- [71] J. Lindhult and L. Miranda, "Fatigue Analysis of Anisotropic Short Fibre Reinforced Polymers-by Use of Digimat and nCode DesignLife," Chalmers University of Technology, 2015.
- [72] H. J. Bohm, "A Short Introduction to Basic Aspects of Continuum Micromechanics," *Inst. Light. Des. Struct. Biomech.*, vol. 206, p. 194, 1998.
- [73] M. A. Meyers and K. K. Chawla, *Mechanical Behavior of Materials*. Cambridge University Press, 2008.
- [74] R. P. L. Nijssen and A. P. Vassilopoulos, *Fatigue life prediction of composites and composite structures*. CRC Press, 2010.
- [75] A. Fatemi, S. Mortazavian, and A. Khosrovaneh, "Fatigue behavior and predictive modeling of short fiber thermoplastic composites," *6th Fatigue Des. Conf. Fatigue Des. 2015 Fatigue*, vol. 133, pp. 5–20, 2015.
- [76] M. De Monte, E. Moosbrugger, and M. Quaresimin, "Influence of temperature and thickness on the off-axis behaviour of short glass fibre reinforced polyamide 6.6 - Cyclic loading," *Compos. Part A Appl. Sci. Manuf.*, vol. 41, no. 10, pp. 1368–1379, 2010.
- [77] N. Fouchier, C. Nadot-Martin, E. Conrado, A. Bernasconi, and S. Castagnet, "Fatigue life assessment of a Short Fibre Reinforced Thermoplastic at high temperature using a Through Process Modelling in a viscoelastic framework," *International Journal of Fatigue*, vol. 124, pp. 236–244, 2019, doi: 10.1016/j.ijfatigue.2019.03.001.

- [78] R. E. Lavengood and L. B. Gulbransen, "The effect of aspect ratio on the fatigue life of short boron fiber reinforced composites," *Polym. Eng. Sci.*, vol. 9, no. 5, pp. 365–369, 1969.
- [79] C. Subramanian and S. Senthilvelan, "Effect of fiber length on hysteretic heating of discontinuous fiber-reinforced polypropylene," *Int. J. Polym. Mater. Polym. Biomater.*, vol. 58, no. 7, pp. 347–354, 2009.
- [80] N. E. Dowling, *Mechanical Behavior of Materials. Engineering methods for deformation, fracture and fatigue*, 4th ed. Pearson, 2013.
- [81] G. R. Ahmadzadeh and A. Varvani-Farahani, "Ratcheting assessment of GFRP composites in low-cycle fatigue domain," *Appl. Compos. Mater.*, vol. 21, no. 3, pp. 417–428, 2014.
- [82] A. Launay, M. H. Maitournam, Y. Marco, and I. Raoult, "Multiaxial fatigue models for short glass fiber reinforced polyamide--Part I: Nonlinear anisotropic constitutive behavior for cyclic response," *Int. J. Fatigue*, vol. 47, pp. 382–389, 2013.
- [83] L. Serrano Abello, Y. Marco, V. Le Saux, G. Robert, and P. Charrier, "Fast prediction of the fatigue behavior of short fiber reinforced thermoplastics from heat build-up measurements," *Procedia Eng.*, vol. 66, pp. 737–745, 2013.
- [84] S. Mortazavian, A. Fatemi, and A. Khosrovaneh, "Effect of Water Absorption on Tensile and Fatigue Behaviors of Two Short Glass Fiber Reinforced Thermoplastics," *SAE Int. J. Mater. Manuf.*, vol. 8, no. 2, 2015.
- [85] L.-W. Cai and Y. Weitsman, "Non-Fickian moisture diffusion in polymeric composites," *J. Compos. Mater.*, vol. 28, no. 2, pp. 130–154, 1994.
- [86] A. Benaarbia, A. Chrysochoos, and G. Robert, "Thermomechanical behavior of PA6.6 composites subjected to low cycle fatigue," *Compos. Part B Eng.*, vol. 76, pp. 52–64, 2015.
- [87] S. W. Tsai, "Strength Characteristics of Composite Materials," *Philco Corp*, 1965.
- [88] Dassault Systemes, "Tsai-Hill Failure Criterion," *Solidworks Help*, 2012. http://help.solidworks.com/2012/english/solidworks/cworks/tsai-hill_failure_criterion.htm (accessed Apr. 30, 2019).
- [89] Autodesk, "Tsai-Hill Criterion," *Helius Composite*, 2016. <https://knowledge.autodesk.com/support/helius-composite/learn-explore/caas/CloudHelp/cloudhelp/2017/ENU/ACMPDS/files/GUID-4A523065-8391-4FB4-AB27-6850B8CF87A8-hm.html> (accessed Apr. 30, 2019).
- [90] D. F. Sims and V. H. Brogdon, "Fatigue behavior of composites under different loading modes," *Fatigue filamentary Compos. Mater. ASTM Int.*, 1977.

- [91] S. Mortazavian and A. Fatemi, "Fatigue behavior and modeling of short fiber reinforced polymer composites including anisotropy and temperature effects," *Int. J. Fatigue*, vol. 77, pp. 12–27, 2015.
- [92] M. De Monte, M. Quaresimin, and P. Lazzarin, "Modelling of Fatigue Strength Data for a Short Fibre Reinforced Polyamide 6.6 Based on Local Strain Energy Density," 2007.
- [93] F. Meraghni, H. Nouri, N. Bourgeois, C. Czarnota, and P. Lory, "Parameters identification of fatigue damage model for short glass fiber reinforced polyamide (PA6-GF30) using digital image correlation," *Procedia Eng.*, vol. 10, pp. 2110–2116, 2011.
- [94] J. Thambi, J. Cathelin, E. Stam, S. Harsiny, and T. B. Van Erp, "A novel approach to evaluate lifetime of complex plastic applications Part I : Short fiber reinforced plastics (SFRP)," in *Spe Antec*, 2017, pp. 1234–1239.
- [95] G. Meneghetti, M. Quaresimin, and M. De Monte, "Fatigue strength assessment of a short fibre-reinforced plastic based on the energy dissipation," *Proc. 16th Int. Conf. Compos. Mater. ICCM16, Kyoto, Japan, 2007*.
- [96] H. Rolland, N. Saintier, N. Lenoir, A. King, and G. Robert, "Fatigue mechanisms description in short glass fibre reinforced thermoplastic by microtomographic observations," *Procedia Struct. Integr.*, vol. 2, pp. 301–308, 2016.
- [97] J. J. Horst, J. L. Spoormaker, and S. J. Horst JJ, "Mechanisms of fatigue in short glass fiber reinforced polyamide 6.," *Polym Eng Sci*, vol. 36, no. 22, pp. 2718–26, 1996.
- [98] M. F. ARIF, N. DESPRINGRE, Y. CHEMISKY, G. ROBERT, and F. MERAGHNI, "In situ SEM damage mechanisms investigation of short glass fiber reinforced polyamide composite," 2013.
- [99] B. Klimkeit, Y. Nadot, S. Castagnet, G. Benoit, S. Bergamo, and C. Dumas, "Damage mechanisms in multiaxial fatigue of short fibre reinforced thermoplastics," *ICCM Int. Conf. Compos. Mater.*, 2009.
- [100] H. Rolland, N. Saintier, I. Raphael, N. Lenoir, A. King, and G. Robert, "Fatigue damage mechanisms of short fiber reinforced PA66 as observed by in-situ synchrotron X-ray microtomography," *Compos. Part B Eng.*, vol. 143, no. December 2017, pp. 217–229, 2018.
- [101] E. Belmonte, M. De Monte, C. J. Hoffmann, and M. Quaresimin, "Damage mechanisms in a short glass fiber reinforced polyamide under fatigue loading," *Int. J. Fatigue*, vol. 94, pp. 145–157, 2017.
- [102] J. Karger-Kocsis, K. Friedrich, and R. S. Bailey, "Fatigue crack propagation in short and long glass fiber reinforced injection-molded polypropylene

- composites," *Adv. Compos. Mater.*, vol. 1, no. 2, pp. 103–121, 1991.
- [103] M. F. ARIF, F. MERAGHNI, N. SAINTIER, Y. CHEMISKY, J. FITOUSSI, and G. ROBERT, "Fatigue damage investigation of PA66/GF30 by X-Ray microtomography," *Sci. Arts Métiers*, 2014.
- [104] E. Belmonte, M. De Monte, T. Riedel, and M. Quaresimin, "Local microstructure and stress distributions at the crack initiation site in a short fiber reinforced polyamide under fatigue loading," *Polym. Test.*, vol. 54, pp. 250–259, 2016.
- [105] BASF, "BASF." <https://www.basf.com/gb/en.html> (accessed Apr. 29, 2020).
- [106] BASF, "Ultramid (PA) Product Range Europe," 2012. www.ultramid.de (accessed Oct. 07, 2018).
- [107] BASF, "MasterBrace Fibers." www.master-builders-solutions.basf.in (accessed Apr. 29, 2020).
- [108] J. L. Thomason, "Glass fibre sizing: A review," *Compos. Part A Appl. Sci. Manuf.*, vol. 127, no. May, 2019.
- [109] National Institutes of Health and the Laboratory for Optical and Computational Instrumentation., "ImageJ 1.52o." .
- [110] MatWeb, "Ensinger Tecamid® 6/6 Nylon (PA66)," 2020. <http://www.matweb.com/search/DataSheet.aspx?MatGUID=e95795afec4f46539c51269e453cba2b&ckck=1> (accessed Jun. 02, 2020).
- [111] BASF, "Ultramid A3WG10 CR bk564." BASF, Ludwigshafen, p. 2, 2015.
- [112] Chronos Engineering Supplies, "Digital Calipers." <https://www.chronos.ltd.uk/acatalog/Digital-Calipers.html> (accessed May 02, 2019).
- [113] BS EN ISO, *Plastics — Determination of tensile properties Part 1: General principles*. 2012, pp. 1–32.
- [114] Mettler Toledo, "Balance XPR105." https://www.mt.com/gb/en/home/products/Laboratory_Weighing_Solutions/Analytical/Excellence/xpr-analytical-balances/XPR105-30355389.html (accessed May 02, 2019).
- [115] BASF The Chemical Company, "Conditioning Ultramid® moldings." pp. 1–16, 2013.
- [116] National Instruments, "LabVIEW 2016." .
- [117] Thecni Measure, "Thermocouples." <https://www.technimeasure.co.uk/temperature/thermocouples/> (accessed May 03, 2019).
- [118] ASM International, "Introduction to Tensile Testing," *Tensile Test.*, pp. 1–13,

2004.

- [119] BS EN ISO, *Plastics — Determination of tensile properties*. 1997.
- [120] Interface force measurement solutions, "1000 Fatigue-Rated LowProfile Load Cell," 2019. <https://www.interfaceforce.com/products/load-cells/1000-fatigue-rated-lowprofile-load-cell/> (accessed May 16, 2019).
- [121] MOOG, "Test Controllers and Software." <https://www.moog.com/products/controllers-controls-software/test-controllers-software.html> (accessed May 16, 2019).
- [122] MTS, "MTS Alignment Solution." https://www.mts.com/cs/groups/public/documents/library/dev_002709.pdf (accessed May 18, 2019).
- [123] ASTM, "Standard practice for verification of testing frame and specimen alignment under tensile and compressive axial force application.," *E1012 - 14*, vol. i, pp. 1–18, 2013.
- [124] Tokyo measuring instruments lab., "General use strain gauge." https://tml.jp/e/product/strain_gauge/f_list.html (accessed May 18, 2019).
- [125] A. Scheeline, "The Nyquist sampling theorem," *Analog and Digital Conversion for Chemical Instrumentation*. https://www.asdlib.org/onlineArticles/elabware/Scheeline_ADC/ADC_NumRep_Nyquist.html (accessed May 16, 2019).
- [126] Ametek Ultra precision technologies, "DG/2.5/S MKII." <https://docs-apac.rs-online.com/webdocs/0117/0900766b801170bc.pdf> (accessed May 16, 2019).
- [127] Instron, "Dynamic Extensometer 12.5mm GL ± 5 mm Travel." <https://www.instron.us/en-us/products/testing-accessories/extensometers/axial-clip-on/dynamic/2620-601> (accessed May 18, 2019).
- [128] ASTM, "D3039-Standard Test Method for Tensile Properties of Polymer Matrix Composite Materials," *Annu. B. ASTM Stand.*, pp. 1–13, 2014.
- [129] S. Mortazavian and A. Fatemi, "Fatigue behavior and modeling of short fiber reinforced polymer composites," *Int. J. Fatigue*, vol. 77, pp. 12–27, 2015.
- [130] CorrelatedSolutions, "Vic 2D v6. Testing-Guide," [www.CorrelatedSolutions.com](http://www.correlatedsolutions.com). <http://www.correlatedsolutions.com/supportcontent/Vic-2D-v6-Testing-Guide.pdf> (accessed Mar. 25, 2019).
- [131] B. Pan, K. Qian, H. Xie, and A. Asundi, "Two-dimensional digital image correlation for in-plane displacement and strain measurement: a review," *Meas. Sci. Technol.*, vol. 20, pp. 1–17, 2009.

- [132] P. Reu, "Introduction to Digital Image Correlation: Best Practices and Applications," *Exp. Tech.*, vol. 36, no. 1, pp. 3–4, 2012.
- [133] Phantom, "Phantom VEO product family." <https://www.phantomhighspeed.com/products/cameras/veo/veo410> (accessed May 17, 2019).
- [134] Nikon, "Eclipse LV150N - Digital imaging combined with advanced optical system." <https://www.nikonmetrology.com/en-gb/product/eclipse-lv150n> (accessed May 16, 2019).
- [135] Hitachi Inspire the next, "Tabletop Microscope TM3030." https://www.hitachi-hightech.com/eu/product_detail/?pn=em-tm3030&version= (accessed May 17, 2019).
- [136] Katholieke Universiteit Leuven, "μCT equipment:Skyscan 1172." <https://www.mtm.kuleuven.be/Onderzoek/ndt/equipment/Skyscan1172> (accessed May 17, 2019).
- [137] A. Launay, M. H. H. Maitournam, Y. Marco, and I. Raoult, "Multiaxial fatigue models for short glass fibre reinforced polyamide. Part II: Fatigue life estimation," *Int. J. Fatigue*, vol. 47, no. FEBRUARY, pp. 390–406, 2013.
- [138] B. Klimkeit *et al.*, "Multiaxial fatigue life assessment for reinforced polymers," *Int. J. Fatigue*, vol. 33, no. 6, pp. 766–780, 2011.
- [139] E. Belmonte, M. De Monte, C. J. Hoffmann, and M. Quaresimin, "Damage initiation and evolution in short fiber reinforced polyamide under fatigue loading: Influence of fiber volume fraction," *Compos. Part B Eng.*, vol. 113, pp. 331–341, 2017.
- [140] Autodesk, "Moldflow Insight 2017." .
- [141] 3D Systems, "Basics of Injection Molding Design," 2019. <https://www.3dsystems.com/quickparts/learning-center/injection-molding-basics#gates> (accessed Jul. 09, 2019).
- [142] Moldflow Insight, "Moldflow' s fiber orientation models (Theory)." [https://knowledge.autodesk.com/support/moldflow-insight/learn-explore/caas/CloudHelp/cloudhelp/2018/ENU/MoldflowInsight-Analyses/files/GUID-6B3A7386-DE57-450E-BF94-B10BD629EC9B-htm.html?st=folgar tucker](https://knowledge.autodesk.com/support/moldflow-insight/learn-explore/caas/CloudHelp/cloudhelp/2018/ENU/MoldflowInsight-Analyses/files/GUID-6B3A7386-DE57-450E-BF94-B10BD629EC9B-htm.html?st=folgar%20tucker) (accessed Jul. 09, 2019).
- [143] Autodesk Moldflow Insight 2017 R2, "Fiber orientation Accuracy Validation Report," 2017. <http://help.autodesk.com.s3.amazonaws.com/sfdcarticles/kA23A000000mU1N SAU/Fiber Validation Report 2017 R2.pdf> (accessed Jul. 09, 2019).
- [144] e-Xstream engineering, "Digimat 2018.1." .

- [145] CWFG mbH, "CAMPUS - a material information system for the plastics industry," 2019. <https://www.campusplastics.com/campus/about> (accessed Jun. 10, 2019).
- [146] I. Doghri and C. Friebel, "Effective elasto-plastic properties of inclusion-reinforced composites. Study of shape, orientation and cyclic response," *Mech. Mater.*, vol. 37, no. 1, pp. 45–68, 2005.
- [147] Sandia National Laboratories, "DAKOTA, Explore and predict with confidence," 2017. <https://dakota.sandia.gov/> (accessed Jul. 30, 2019).
- [148] S. Mortazavian, "Fatigue Behavior and Modeling of Short Fiber Reinforced Polymer Composites," The University of Toledo, 2014.
- [149] E. Krempl and B. Z. Hong, "A simple laminate theory using the orthotropic viscoplasticity theory based on overstress. Part I: In-plane stress-strain relationships for metal matrix composites," *Compos. Sci. Technol.*, vol. 35, no. 1, pp. 53–74, 1989.
- [150] Dassault Systemes, "Abaqus 6.14-2." .
- [151] D. Guido, "Eight-node brick element with reduced integration (C3D8R and F3D8R)," *CalculiX CrunchiX USER' S MANUAL version 2.7*. http://web.mit.edu/calculix_v2.7/CalculiX/ccx_2.7/doc/ccx/node27.html (accessed May 23, 2019).
- [152] SAS IP Inc., "Integration point locations." https://www.sharcnet.ca/Software/Ansys/17.0/en-us/help/ans_thry/thy_et1.html (accessed May 03, 2019).
- [153] R. Vishark, "What is the 'hourglass effect' in finite element analysis? How does the reduced integration, resulting in the hourglass effect, work? How can we counter the hourglass effect?" <https://www.quora.com/What-is-the-hourglass-effect-in-finite-element-analysis-How-does-the-reduced-integration-resulting-in-the-hourglass-effect-work-How-can-we-counter-the-hourglass-effect> (accessed May 23, 2019).
- [154] Simulia, "Abaqus Analysis User' s Manual," *Abaqus 6.10*. <https://www.sharcnet.ca/Software/Abaqus610/Documentation/docs/v6.10/books/usb/default.htm?startat=pt08ch31s02aus119.html> (accessed Jun. 07, 2019).
- [155] HBM Prenscia, "nCode 2018.1." .
- [156] H. Wei and Y. Liu, "A critical plane-energy model for multiaxial fatigue life prediction," *Fatigue Fract. Eng. Mater. Struct.*, vol. 40, no. 12, pp. 1973–1983, 2017.
- [157] E1049, "Standard practices for cycle counting in fatigue analysis," *ASTM*

- Stand.*, vol. 85, no. Reapproved 2017, pp. 1–10, 2017.
- [158] P. L. N. Murthy, S. K. Mital, and J. Z. Gyekenyesi, "NASALife – Component Fatigue And Creep Life Prediction Program," *NASA/TM—2005-213886/REV2*, no. 2, p. 46, 2014.
- [159] J. Hult and F. G. Rammersdorfer, *Engineering Mechanics of Fibre Reinforced Polymers and Composite Structures*. 1994.
- [160] S. Mortazavian and A. Fatemi, "Effects of mean stress and stress concentration on fatigue behavior of short fiber reinforced polymer composites," *Fatigue Fract. Eng. Mater. Struct.*, vol. 39, no. 2, pp. 149–166, 2016.
- [161] Z. Lu, B. Feng, and C. Loh, "Fatigue behaviour and mean stress effect of thermoplastic polymers and composites," *Frat. ed Integrita Strutt.*, vol. 12, no. 46, pp. 150–157, 2018.
- [162] A. F. Stephen R. Mellott, "Fatigue Behavior and Modeling of Thermoplastics Including Temperature and Mean Stress Effects Stephen," *Polym. Eng. Sci.*, pp. 726–738, 2014.
- [163] Z. Lv, H. Z. Huang, H. K. Wang, H. Gao, and F. J. Zuo, "Determining the Walker exponent and developing a modified Smith-Watson-Topper parameter model," *J. Mech. Sci. Technol.*, vol. 30, no. 3, pp. 1129–1137, 2016.
- [164] GE Sensing & Inspection Technologies GmbH, "Phoenix Nanotom M," *Phoenix nanotom*, pp. 1–4, 2013.
- [165] NSI, "X5000 Industrial X-Ray Inspection System." <https://4nsi.com/systems/x5000> (accessed Aug. 13, 2019).
- [166] GoodFellow All the materials you need for Scientific and Industrial Research and Manufacturing, "Polyamide-Nylon 6,6 (PA 6,6) Material Information." <http://www.goodfellow.com/E/Polyamide-Nylon-6-6-Polymer.html> (accessed Aug. 06, 2019).
- [167] A. Tevatia and S. K. Srivastava, "Modified shear lag theory based fatigue crack growth life prediction model for short-fiber reinforced metal matrix composites," *Int. J. Fatigue*, vol. 70, pp. 123–129, 2015.
- [168] W. S. Slaughter and N. a. Fleck, "Fatigue of Fibre Composites," *J. Mech. Phys. Solids*, vol. 41, no. 8, pp. 1265–1284, 1993.
- [169] P. R. Lord, "Handbook of Yarn Production," *Technol. Sci. Econ.*, pp. 205–233, 2003.
- [170] A. Launay, Y. Marco, M. H. Maitournam, and I. Raoult, "Modelling the influence of temperature and relative humidity on the time-dependent mechanical behaviour of a short glass fibre reinforced polyamide," *Mech. Mater.*, vol. 56, pp. 1–10, 2013.

- [171] P. Heyes, "Multiaxial Assessment Method For Fatigue Calculations In Composite Components," 2013.
- [172] S. Vervoort, "Fatigue Analysis of Fibre-Reinforced Polymers," *Eur. Congr. Comput. Methods Appl. Sci. Eng. (ECCOMAS 2012)*, no. Eccomas, pp. 1–11, 2012.
- [173] M. H. McKetty, "The AAPM/RSNA Physics Tutorial for Residents: X-ray Attenuation," *Radiographics*, vol. 18, no. 1, pp. 151–163, 1998.
- [174] V. Crupi, E. Guglielmino, L. Scappaticci, and G. Risitano, "Fatigue assessment by energy approach during tensile and fatigue tests on PPGF35," *Procedia Struct. Integr.*, vol. 3, pp. 424–431, 2017.
- [175] Y. K. Lin and J. N. Yang, "A stochastic theory of fatigue crack propagation," *AIAA J.*, vol. 23, no. 1, pp. 117–124, 1985.
- [176] M. Eftekhari and A. Fatemi, "Variable amplitude fatigue behavior of neat and short glass fiber reinforced thermoplastics," *Int. J. Fatigue*, vol. 98, pp. 176–186, 2017.
- [177] M. Eftekhari and A. Fatemi, "Tensile, creep and fatigue behaviours of short fibre reinforced polymer composites at elevated temperatures: A literature survey," *Fatigue Fract. Eng. Mater. Struct.*, vol. 38, no. 12, pp. 1395–1418, 2015.